Abrupt change in monsoonal climate: evidence from the geochemical composition of Arabian Sea sediments

Frank Sirocko

14 September 1994

Habilitation Thesis, submitted to "Mathematisch-Naturwissenschaftliche Fakultät der Christian-Albrechts-Universität zu Kiel"

Summary / Zusammenfassung

D) Discussion **Page**

Summary

Sixty major- and trace-elements have been mapped in deep-sea sediments of the Arabian Sea at the sediment surface, the Early Holocene (8000 ^{14}C-yrBP), the Termination Ia (15,000 ^{14}C-yrBP), and the Last Glacial Maximum (about 18,000 ^{14}C-yrBP). These elements have also been determined in three high-resolution sediment cores (sampling intervals of 250 years) to reconstruct the history of sedimentation patterns on a century scale.

The lithic proportions of the elements are mainly derived from eolian sources in the western Arabian Sea, and riverine sources in the eastern part, a finding corroborated by the ^{144}Nd/^{143}Nd and ^{87}Sr/^{86}Sr composition of the clastic fraction of the sediments. Distribution patterns of zirconium (Zr) outline the tracks of the southern branch of Arabian northwesterlies, magnesium (Mg), which is found in dolomite and palygorskite, monitors the dust discharge by the northern branch of the Arabian northwesterlies. Rubidium, normalized to aluminum (Rb/Al) appears to be associated with dust discharge by the northeast monsoon winter circulation.

Concentrations of the elements cadmium (Cd) and zinc (Zn) in the sediments reveal a maximum in the region of high upwelling fertility in the western Arabian Sea, because both elements follow the cycle of nutrients in the ocean and are abundant in upwelling water. Another record of these upwelling pulses is conserved in the $\delta^{18}O$ composition of surface water plankton, because intermediate water masses in the Arabian Sea have a lighter $\delta^{18}O$ signal than the surface water; thus, the mass of water from intermediate depth that reaches the surface mixed layer causes a negative $\delta^{18}O_{(water)}$ signal in the surface water.

These key-elements have been used to reconstruct the history of the monsoonal climate during the last 24,000 years. Accordingly, the peak glacial between 20,000 and 16,000 ^{14}C-yrBP was a time of climatic stability. The summer southwest monsoon was shifted further to the south, northwesterlies prevailing over the western Arabian Sea and the northeast monsoon was at maximum strength. At 16,000 ^{14}C-yrBP, northeast monsoon derived dust proportions ceased abruptly. At the same time the most arid phase started in Arabia. This arid interval lasted until 13,000 ^{14}C-yrBP and was characterized by most intense dust discharge from Arabia and the dry Persian Gulf area, paralleled by a complete absence of southwest monsoon winds at core location 74KL. Upwelling fertility reached a minimum during that time, and open ocean conditions prevailed even in the upwelling areas off Oman. The deglaciation started at 13,000 ^{14}C-yrBP with an abrupt first increase of southwest monsoon strength and a sharp reduction in eolian flux rates, indicating increased humidity in Arabia and around the Persian Gulf. The Younger Dryas is documented as a return of high (winter) dust discharge from the northern areas, whereas the (summer) dust

discharge from Arabia did not respond to the cold spell. At 9900 ^{14}CyrBP another rapid intensification of the southwest monsoon intensity had occurred at the very end of the Younger Dryas. It is not before this age that the southwest monsoon reached its Holocene level. From 9200 to 7850 ^{14}C-yrBP, during the time of maximum solar insolation at subtropical latitudes, we observe a marked maximum of northward propagation of southwest monsoon wind tracks and precipitation, paralleled by most intense upwelling fertility in the western Arabian Sea. A second, but minor maximum in the southwest monsoon wind strength is then found between 7000 and 6000 ^{14}C-yrBP. At 4800 ^{14}C-yrBP, eolian flux from Arabia increases again, indicating a southward shift of the southwest monsoon wind tracks and its precipitation.

The cause for the abruptness of the observed climate changes cannot be explained by the orbitally controlled variations of solar radiation intensity that was shown to cause the long-term evolution of the monsoon. Instead, the rapid events appear to be synchronous with rapid climate changes in the Atlantic, and a close coupling of the monsoonal climate with north Atlantic climate became apparent. In particular, the most pronounced phase of rapid intensification of the southwest monsoon winds occurred during the Younger Dryas to Preborial transition, which was also the the most abrupt transition in the evolution of the north Atlantic/European climate. Possible causes for this relations were tested with a global atmospheric circulation model, showing that the driving force behind the rapid climate events should lie in the Atlantic, probably in the form of large-scale winter surface air pressure anomalies that have to be expected during times of ice sheet decay or shelf ice surges.

The time between subsequent phases of monsoon intensication after the Younger to Preboreal transition is 1785 years. The 1785-year period is pertinent to all records of the summer southwest monsoon driven upwelling intensity in the western Arabian Sea. In addition, a 1450-year periodicity is pertinent to the variations of dust discharge by northwesterly winds from Arabia. Dust discharge during the winter northeast monsoon season showed variability at a 950-year period. Both the 1785-year and the 1450-year period are harmonic tones of the earth´s precessional cycle (1785*13=23,205 and 1450*16=23,200) and could be interpretated as an internal response of the monsoon circulation to its major precessional forcing period of 23,200 years.

Accordingly, changes in the monsoonal climate appear to be related to two different processes: i) abrupt events as a response to abrupt climate change on the northern hemisphere, ii) an internal oscillation of the summer circulation in response to precession-controlled changes in the intensity of solar insolation at subtropical latitudes.

Zusammenfassung

Verteilungsmuster von 60 Spuren- und Hauptelementen in Tiefseesedimenten des Arabischen Meeres wurden für die Sedimentoberfläche und die Zeitscheiben des frühen Holozäns (8000 ^{14}C-yrBP), der Termination Ia (15,000 ^{14}C-yrBP), und des letzten Glazialmaximums (um 18,000 ^{14}C-yrBP) erstellt. Die gleichen Elemente wurden auch in drei Sedimentkernen mit hohen Sedimentationsraten (Zeitauflösung zwischen den Proben: 250 Jahre) analysiert, um eine detaillierte Rekonstruktion der Sedimentationsgeschichte im Arabischen Meer erstellen zu können.

Die ^{144}Nd/^{143}Nd, ^{87}Sr/^{86}Sr Werte der klastischen Sedimentfraktion spiegeln die isotopische Zusammensetzung der Gesteine im Herkunftsgebiet der Sedimente wider. Demnach stammen die lithogenen Anteile der Elementkonzentrationen im westlichen Arabischen Meer aus äolischen Quellen in Arabien, im östlichen Sektor aus fluviatilen Quellen in Indien. Die Staubfracht der verschiedenen Windsysteme ist durch eine jeweils spezifische geochemische Zusammensetzung charakterisiert; Zirkonium (Zr) zeigt den Transport in einem südlichen Arm der arabischen Nordwestwinde an; Magnesium (Mg) tritt häufig in der Staubfracht des nördlichen Arms der Nordwestwinde auf; Rubidium (Rb) ist kennzeichnend für die Staubfracht im winterlichen Nordostmonsun, der zumindest im Glazial das westliche Arabische Meer erreichte.

Die Elemente Cadmium (Cd) und Zink (Zn) zeigen Häufigkeitsmaxima in Sedimenten unterhalb von Zellen nährstoffreichen Auftriebwassers im westlichen Arabischen Meer, da beide Elemente in nährstoffreichem Wasser angereichert sind. Änderungen in der Auftriebsintensität zeigen sich aber nicht nur in den geochemischen Indikatoren, sondern auch in der δ^{18}O Zusammensetzung des Wassers (und der darin lebenden Planktonorganismen), da das Auftriebswasser aus intermediären Tiefen des Arabischen Meeres ein leichteres isotopisches Signal zeigt als das Oberflächenwasser.

Mit Hilfe dieser "Schlüsselelemente" konnte die Geschichte der Monsunzirkulation während der letzten 25.000 Jahre rekonstruiert werden. Das Hochglazial (20.000 - 16.000 ^{14}C-yrBP) erweist sich als eine Zeit klimatischer Stabilität. Die Trajektorien der sommerlichen Südwestmonsunwinde lagen weiter im Süden als heute und Nordwestwinde aus der Region des Persischen Golfes wehten über dem nördlichen Arabischen Meer. Im Winter jedoch dominierten starke Nordostmonsunwinde. Um 16.000 ^{14}C-yrBP ging die Intensität des Wintermonsuns abrupt zurück wobei zeitgleich eine Phase maximaler Aridität in Arabien begann. Diese Trockenphase dauerte bis 13.000 ^{14}C-yrBP, gekennzeichnet durch stärksten Staubflux aus Arabien und den völligen Zusammenbruch der sommerlichen Auftriebsintensität im westlichen Arabischen Meer. Auch das Ende dieser Phase um 13.000 ^{14}C-yrBP vollzog sich in einem abrupten Wechsel (Rückgang der Staubfluxraten bei gleichzeitigem Einsetzen von Auftrieb), vermutlich durch ein erstes Nordwärtsrücken der sommerlichen Südwestwindströmung verursacht.

Mit Beginn der Jüngeren Dryas kam es im westlichen Arabischen Meer zu einer abrupt einsetzenden Rückkehr von winterlichem Staubfall aus Nordostmonunwinden. Der Sommermonsun blieb allerdings unbeeinflußt von der weltweiten Klimaverschlechterung dieser Zeit. Um 9900 ^{14}CyrBP blieben die Nordostmonsunwinde unvermittelt aus, während der Sommermonsun sprunghaft auf sein heutiges Intensitätsniveau anstieg. Von 9200 to 7850 ^{14}C-yrBP erreichte die Stärke des Südwestmonsuns ein Maximum, mit kräftigem Auftriebsgeschehen und einer Verlagerung der Südwestmonsuntrajektorien weit in den Norden verbunden. In ähnlicher Weise zeigt sich ein Nebenmaximum der Südwestmonsunaktivität um 7000 and 6000 ^{14}C-yrBP.

Die Ursachen der plötzlichen Änderungen in der monsunalen Zirkulation können nicht mit langsamen Änderungen in der solaren Einstrahlungsintensität, die der Hauptanfachungsmechanismus der langfristigen Monsunvariabilität ist, erklärt werden. Es fällt dagegen auf, daß viele der abrupten Änderungsphasen mit Zeiten abrupter Änderungen im nordatlantisch/europäischen Klima einhergingen. Dies legt die Vermutung nahe, daß es eine Koppelung dieser beiden Hauptwindsysteme der Nordhalbkugel gegeben hat (gibt). Eine mögliche Telekonnektion (mit dem Monsunsystem als aktivem Parameter) wurde mit dem GISS II Modell der globalen atmosphärischen Zirkulation getestet, indem der eiszeitliche Sommermonsun durch eine großflächige Schneeanomalie über Asien unterdrückt wurde. Als Reaktion auf diese asiatische Kälteanomalie erfolgte eine drastische Abkühlung des Nordpazifik, aber eine leichte Erwärmung des Nordatlantik. Damit ist es unwahrscheinlich, daß primäre Änderungen im Monsunklima die Ursache für gleichzeitige Erwärmungsphasen der gesamten Nordhemisphäre sein können; eher können primäre Änderungen in der atlantischen Zirkulation Enfluß auf das Monsunklima nehmen.

Die verschiedenen Sprünge in der Monsunverstärkung während des Glazial-Interglazial Übergangs liegen jeweils ca. 1785 Jahre auseinander. Diese Wiederkehrperiode ist in allen Parametern der Auftriebsintensität vorhanden. Sinusoidale Schwingungen von 1450 Jahren kennzeichen dagegen die Veränderlichkeit im Staubflux aus Arabien, bzw. Schwingungen von 950 Jahren kennzeichnen die Variabilität des Wintermonsuns. Die Ursachen dieser Schwingungen sind unbekannt. Sowohl die 1785-, als auch die 1450-jährige Periode könnten Oberschwingungen des Präzessionszyklus sein. Da diese Periodizitäten auch in Meeresoberflächentemperaturänderungen des äquatorialen Atlantiks beobachtet wurden, stellen sie u.U. ein Grundmuster der Klimavariabilität in den Subtropen dar.

Die Anfachungsmechanismen der Veränderlichkeit im Monsunklima gehen damit auf zwei, voneinander unabhängige, Prozesse zurück: i) abrupte Änderungen als Reaktion auf abrupte Klimaänderungen im atlantisch/eurasischen Raum, ii) interne Oszillationen als Antwort auf präzessions-kontrollierte Änderungen in der Intensität der solaren Einstrahlung.

To Karen and Johannes

A.1. The role of the monsoons in the world's climate system

Monsoonal climate which dominates most of southern Asia and East Africa (Fig. 1) is characterized by two different seasons, (a) vigorous, rain-bearing monsoon winds from southwest during summer, (b) a rather gentle and dry winter monsoon from northeast (Hastenrath & Lamb, 1979). The southwest monsoon carries large amounts of water vapor which stems from evaporation in the subtropical areas of the southern hemisphere, and, after crossing the equator, is the major source of precipitation in East Africa, Arabia, India and China (Fig. 1). Besides its importance on agriculture and on the people living in the region, the southwest monsoon winds and their associated precipitation play a crucial role in the world´s climate system. Monsoonal clouds are the largest moisture transporting wind system in the world (Hastenrath & Lamb, 1980), and provide the greatest flux of interhemispheric latent heat as well as of the most important greenhouse gas – water vapor.

The rain that precipitates from these clouds forms the large rivers of the Asian continent, which discharge a total of 6,2 Gt of suspended sediment. Thus, about 46% of the world river discharge of suspended sediments stem from monsoonal rains over Asia (Milliman & Meade, 1983). Along with this water and sediment discharge a massive transport of dissolved ions appears to gain a major effect on the chemical mass balance of the world ocean (Froelich et al., 1992; Ittekot & Zhang, 1989; Martin & Meybeck, 1979; Raymo & Ruddiman, 1992).

The monsoon rains are not only a major climatic factor in the Asian region, but affect the composition of the atmosphere on a global scale. Swamps that develop in the tropical drainage area of the rivers provide a major source of atmospheric methan, which is formed by the microbiological oxidation of organic matter (Raynaud et al., 1988). Besides methane production, the tropical vegetation also affects the CO_2 content of the atmosphere. Keeling et al., (1987) showed that atmospheric CO_2 variations during the last 30 years have a prominent annual cycle which appears to be caused by the growing and decay of terrestrial organic biomass in the south Asian tropical forests. Sirocko & Ittekkot (1992) further discussed a likely effect of the mineral matter flux from the Asian rivers on atmospheric CO_2 variation, because an increase in the removal of organic carbon from the ocean surface water may result from particle mediated processes adding weight to marine snow aggregates (Ittekkot et al., 1992).

In the Arabian Sea, the strong monsoonal southwesterly winds have a strong impact on the hydrosphere; coastal upwelling, mixed layer depth, sea surface temperatures, nutrient content, and primary productivity are a function of monsoonal wind strength and wind tracks (Brock et al., 1992; Luther & O´Brien, 1990) (Fig. 7). Therefore, the Arabian Sea is a well suited area to study the

evolution and natural variability of this large-scale climate system, especially because sediments of the deep Arabian Sea reach high sedimentation rates up to 10 cm/1000 years, enabling us to extract high-resolution records of wind-driven oceanic upwelling, continental humidity, dust and river discharge on a century time scale.

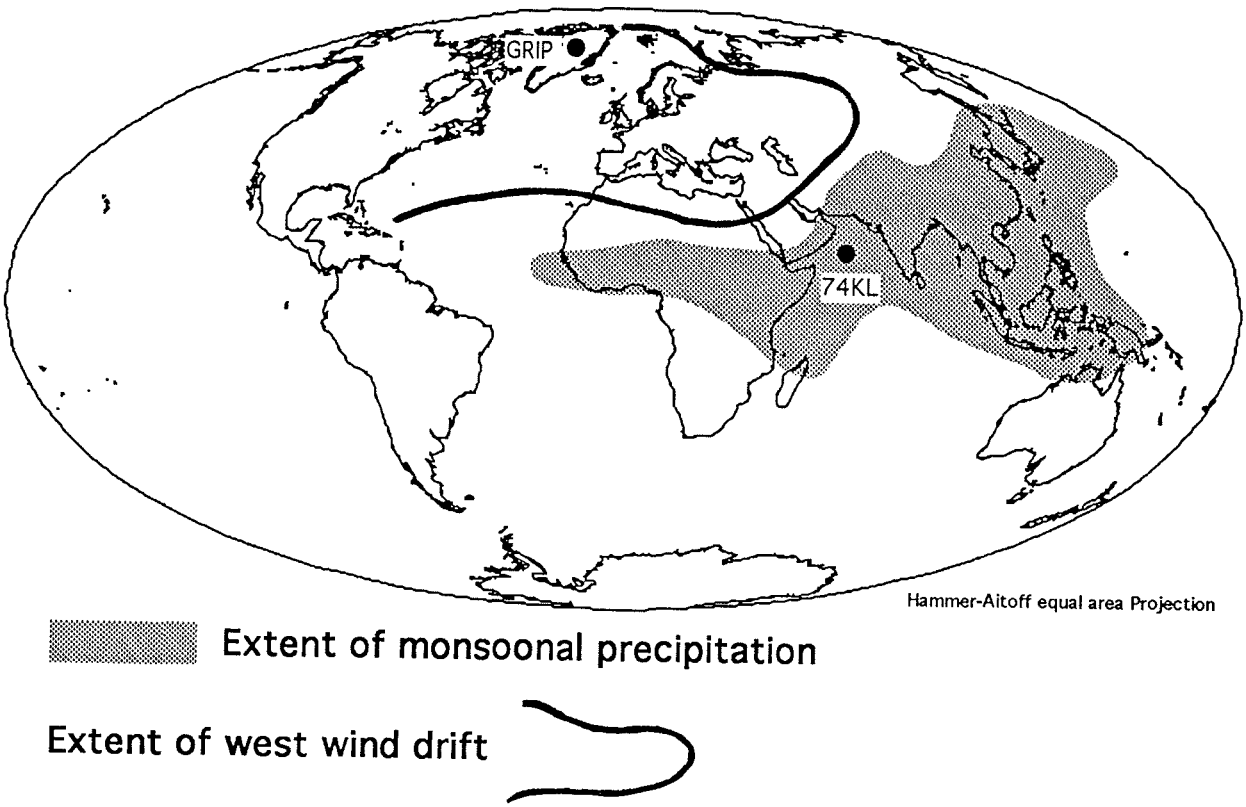

Figure 1. Areas affected by monsoonal precipitation (equal area projection, modified from IGCP-349 planning report) and by precipitation derived from the Atlantic/European westwind drift. Drilling locations of the Greenland ice-core project (GRIP) and sediment core 74KL (see B.1.) are shown for reference.

A.2. Abrupt climate changes during the last glacial to interglacial transition

During the last five years, since the pioneering work of Fairbanks (1989), increasing evidence was found in marine sediment cores and corals as well as in tree ring and peat bog records that natural climate change during the last 20,000 years occurred much faster than previously though (i.e., within hundreds of years; see for example Bard & Broecker, 1992).

Abrupt transitions were found in deep-sea records from the northern Atlantic, monitoring ice surges and meltwater discharge (e.g., Bond et al., 1992; Lehman & Keigwin, 1992; Weinelt et al., 1991). Sedimentation rate and sample spacing in marine records limit these authors to a time resolution of about hundred years. In addition, the uncertainties linked to the calendar-year-conversion of ^{14}C dates (Bard et al., 1990) increase the error margin to an extent that even the comparison between marine records from different areas of the north Atlantic may become difficult. All available records,nevertheless, agree that between 12,700 and 14,300 ^{14}C-yrBP at least one major abrupt deglaciation event has occurred in the north Atlantic region. Most probably, this event was prior to the Oldest Dryas to Bölling transition, which is recorded at 14,680 cal-yrBP in the Greenland ice-core record (Johnsen et al., 1992) (Fig. 2).

As first observed by Dansgaard et al. (1989), and confirmed during the last year by the new ice-core records in Greenland of the GRIP (Johnsen et al., 1992), and GISP projects (Taylor et al., 1993 b) natural climate change appears to happen even faster than recently reconstructed from the marine records, with events occurring within of a couple of years or decades (Alley et al., 1993). It is the unique advantage of the ice-cores that ice holds a joint information of variations in the atmospheric gas composition, dust content, and temperature. The gas composition contains a global (at least hemispheric) signal, because complete mixing of atmospheric gases occurs within 1-3 years. Changes in dust and temperature, however, are regional signals. The ice is annually laminated, and single annual laminae were counted back to about 15,000 years ago. Accordingly, the ice-cores produce a precise chronology, independent of atmospheric ^{14}C variations (Stuiver et al., 1991). Because the chronology of events in the "Summit" ice-core (Fig. 2) matches almost exactly the nearby GISP II record (Alley et al., 1993), their finding of an abrupt change at 11,640 cal-yrBP at the end of the Younger Dryas, and another event correlated with the end of the Oldest Dryas (14,680 cal-yrBP) appear to provide the best chronology of climate change in the north Atlantic region. Both events were marked by a temperature increase of 5°C, increased snow accumulation rates and a sharp drop in atmospheric dust content. The methane record, in contrast, indicates an earlier event near 16,000 cal-yrBP

(Fig. 2). Because atmospheric methane content is considered to monitor the evolution of tropical swamps, the early event should be confined to variations in tropical climate, especially, because it is not paralleled by the local Greenland temperature ($\delta^{18}O$) record (Chappellaz et al., 1993).

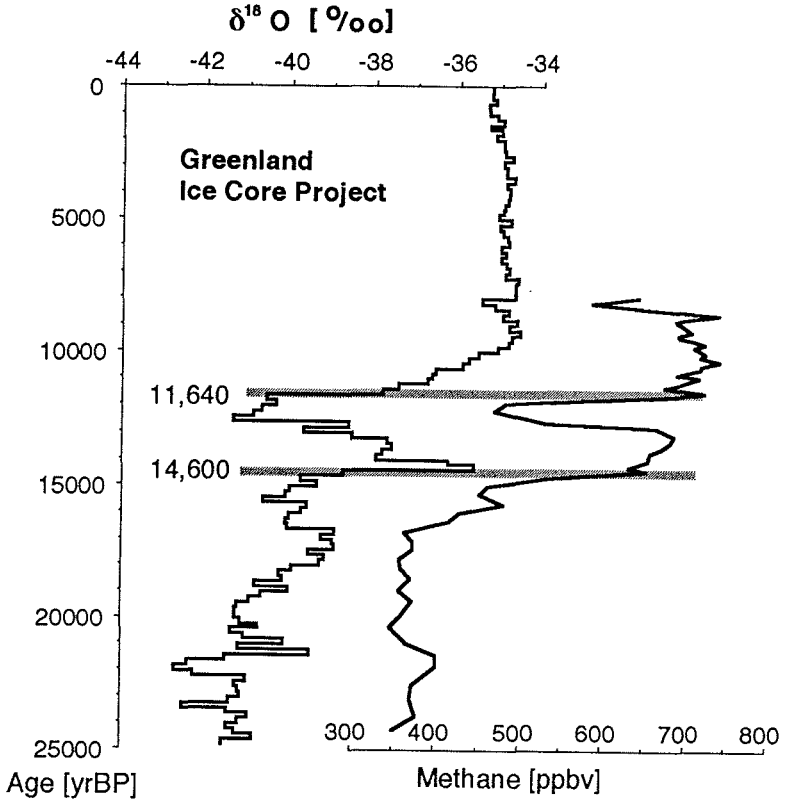

Figure 2. $\delta^{18}O$ [‰ SMOW] of snow and methane concentrations in the Greenland ice-core at " Summit" (Chappellaz et al., 1993; Johnsen et al., 1992).

A.3. Objective of this study

The objective of this study is to reconstruct and better understand the evolution of the Asian southwest monsoon climate during times of abrupt climatic change on the northern hemisphere. As shown by Sirocko et al. (1993) the monsoonal circulation of southern Asia witnessed six events of rapid change in the hydrographic and atmospheric structure during the last glacial-to-Holocene transition (compare Fig. 12). Major events were centered at 9900 ^{14}C-yrBP and 13,000 ^{14}C-yrBP; the first event occurred almost synchronous with an abrupt transition in the north Atlantic climate at 11640 cal-yrBP (Fig. 2). The nature and geographical extent of the events in the monsoon climate remained, however, unclear.

To understand the climate changes during these events in more detail, we evaluate a large number of different chemical tracers to select those few parameters that are found to be distinctive of certain transport processes (dust discharge, fluvial runoff, oceanic upwelling) and season. Geochemical tracers preserved in deep-sea sediments (analyzed by Inductively Coupled Plasma-Mass Spectrometry, ICP-MS) can provide well suited records for this pupose (e.g., Shimmield et al., 1990 b). All processes can be studied using one technique, because ICP-MS can measure 39 different elements simultanously from one small sample (Garbe-Schönberg, 1993); these are biogenically mediated components (Ba, Zn, Ni) (Elderfield, 1990), refractory elements being indicative of source area and transport pathway (Zr, Cr,) (Grousset & Chesselet, 1986), moreover, elements affected by deep ocean ventilation (Mo) (Seralatan & Hartmann, 1986) and diagenetically mobile elements (Mn) (Shaw et al., 1990) . Hence, the synchronicity and/or phase relationship in the patterns of dust-bearing, seasonally well defined winds, changes in the intensity and composition of river discharge fed by monsoonal rains, and changes in the intensity of wind-driven upwelling could provide information on the forcing mechanisms of events of abrupt climate change. Before the actual control of trace element variability by processes of climate and hydrology can be evaluated, the role of possible diagenetic and postsedimentary alterations are discussed. Accordingly, the first part of this study shows distribution patterns of element concentrations; subsequent sections will then define the most appropriate tracers for each climatic process affecting the trace element variability in the sediments. Finally, we shall look at the downcore variations of concentrations for "key-elements" during the events of abrupt change and compare the chronology of monsoonal climate with changes in the Atlantic climate. The understanding of abrupt climate change in both the Atlantic and Asian monsoon should provide a framework to evaluate the forcing and reponse mechanisms of abrupt climate change on a global scale.

A.4. The sedimentary record of monsoonal winds in the Arabian Sea

The annual monsoon cycle

After snow melt in Asia (Barnett et al., 1989), and driven by the seasonal increase in solar insolation intensity (Das, 1968), the southwest monsoon winds cross the equator in May, and subsequently shifts northward (Figs. 3, 4). During the subsequent months the northward migration of the southwest monsoon follows a stable pattern with fixed onset dates in India (Fig. 4). The maximum in wind strength over the ocean occurs in July. At the end of summer the offset of the monsoonal rains is characterized by a similar, but reversed transition. Accordingly, the duration of the moist southwest monsoon season decreases from south to north.

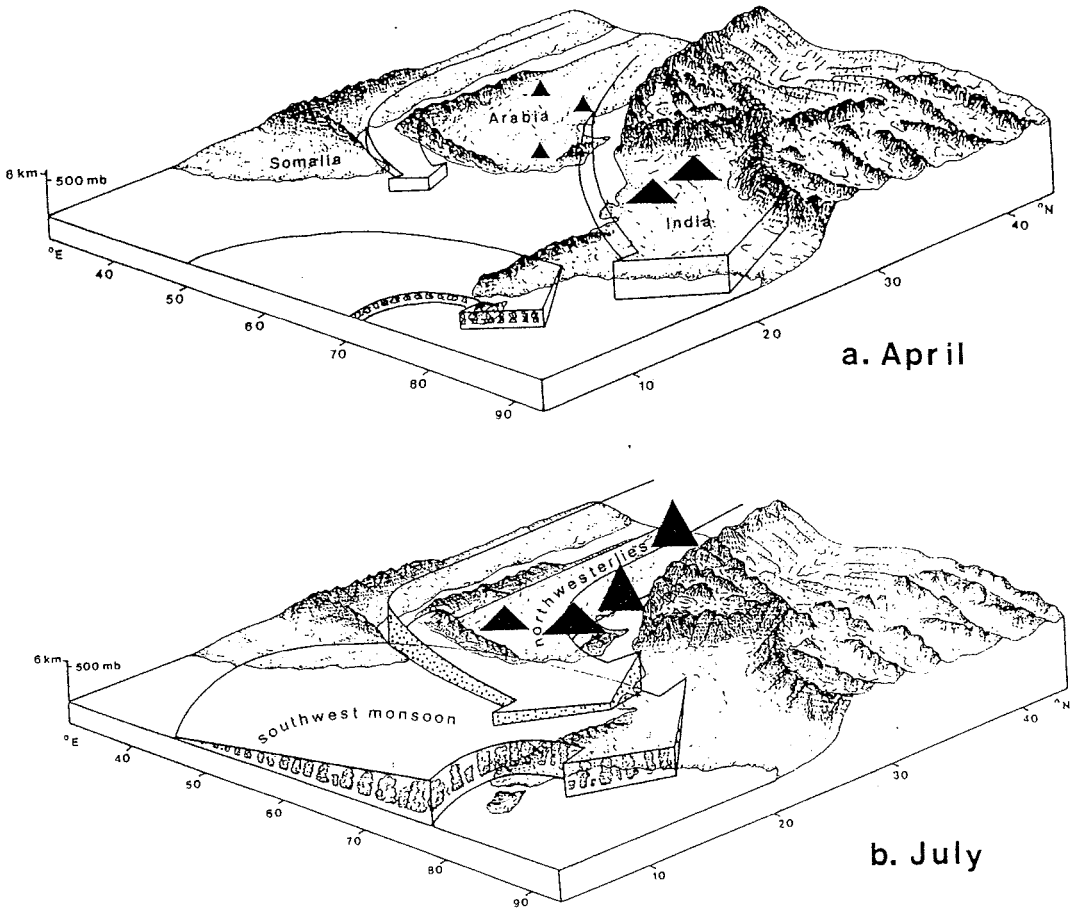

Figure 3. Internal structure of the southwest monsoon and associated northwesterlies during (a) April, (b) July. Dark triangles mark the areas of dust entrainment after (Ackerman & Cox, 1988; Chen, 1986; Middleton, 1986).

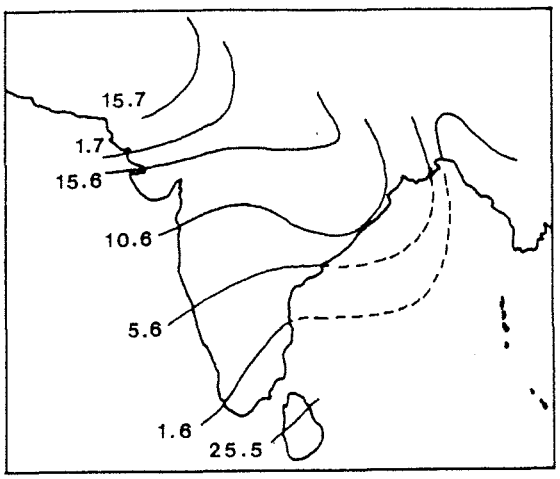

Figure 4. Average dates (day/month) of onset ofsouthwest monsoonal precipitation in India (after Das, 1968)

Dust plumes associated with monsoon winds

The maximum in southwest monsoon intensity parallels the seasonal maximum of dust discharge from Arabia (McDonald, 1938), reproduced in (Pye, 1987). Over the Arabian Sea this dust transport during summer occurs primarily with northwesterly winds in the midtroposhere (Sirocko & Sarnthein, 1989), whereas the lower troposheric southwest monsoon winds will carry the fallout from aloft to the northeast. Besides these large outbreaks during summer six other dust transporting wind systems were visible on the satellite images covering all seasons of 1979 (Fig. 5). Northeast monsoon winds that are known as moving dust in Pakistan and northern India carried a dust load too small to be observed on satellite imagery. Continuous dust transport occurred by northwesterly winds from Iran, Pakistan, through north India towards the Bay of Bengal (Fig. 5, "March to May"). An ephemeral outbreak from Pakistan towards the south is observed on 30 April. Spring dust plumes also originate from Oman with trajectories from northwest to southeast (Fig. 5, "20 April"). Large dust outbreaks start from sources in Arabia and Mesopotamia during summer. These summer dust plumes have been studied by (Ackerman & Cox, 1982, 1988; Chen, 1986). Accordingly, the northern branch of the outbreak on 25 June moves in the ground level and follows the topographic depression of the Persian Gulf trough, whereas a mid-tropospheric (700 mb) branch of the same dust storm bends to the south and traverses the Arabian Sea over the Gulf of Aden (Fig. 5, "26 June"). The satellite images of 1979 never showed dust plumes that originate directly from Somalia, thus no (or imperceptibly little) dust is raised by the southwest monsoon wind itself. Minor, but permanent plumes are visible in the Red Sea area during all seasons of the year with entrainment areas on both sides of the Red Sea. In summary, the summer southwest monsoon is strongly associated with the highest incidence of haze frequency and dust load of all seasons, nevertheless, the southwest monsoon carries no (or little) dust itself.

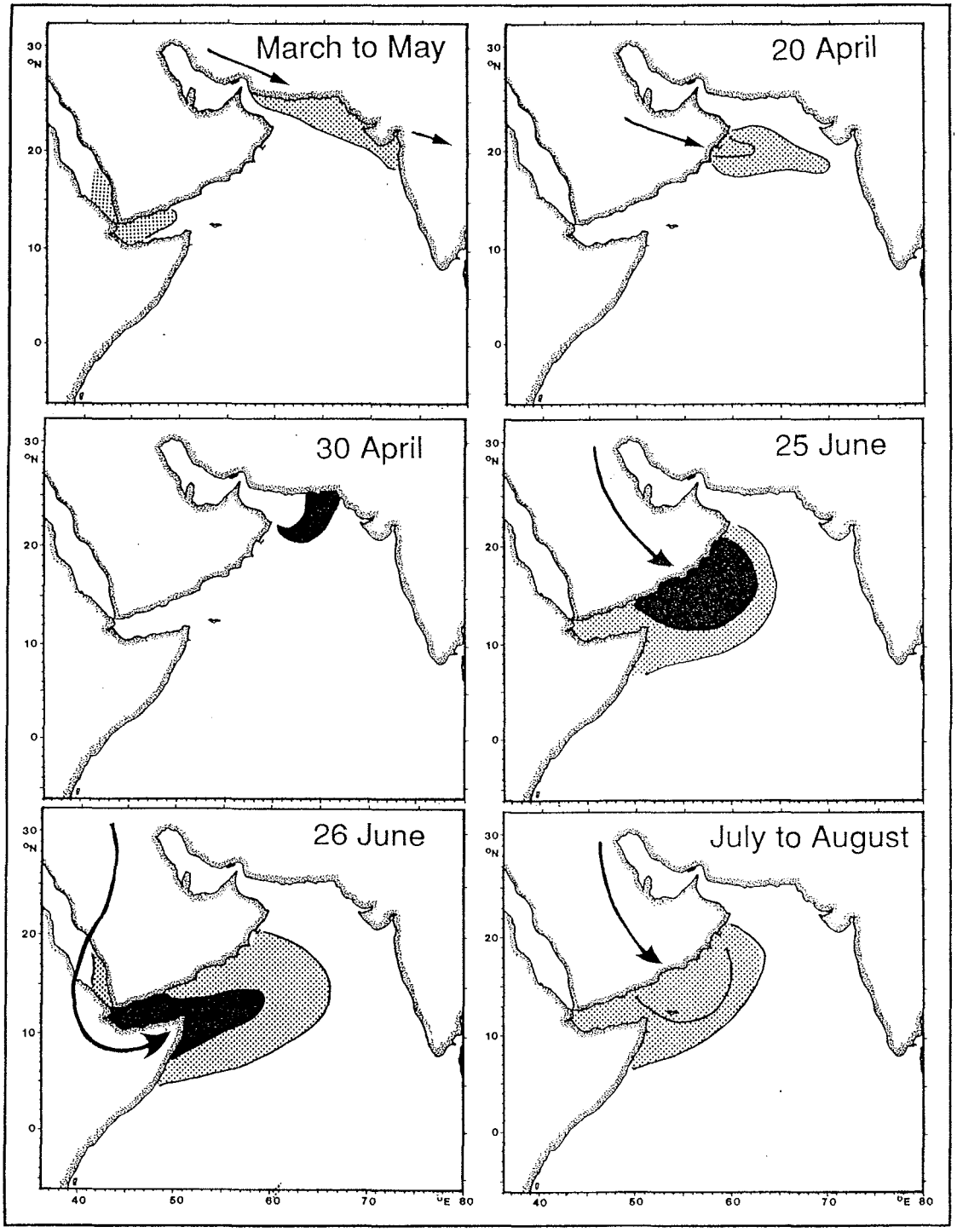

*Figure 5. Dust plumes documented on satellite images during the 1979 MONEX program (hatched areas). Dark areas show extreme mass loadings of dust, after (Chen, 1986). Arrows indicated the trajectories of dust plumes as observed on the satellite images. Total amount of dust transported in1979: 100 *10^6 tons (Sirocko & Sarnthein, 1989).*

River discharge into the Arabian Sea

The Indus, Tapti and Narbada are the largest rivers that discharge into the Arabian Sea from the Indian sub-continent, but small rivers stemming from the Western Ghats of south India can also transport large masses of water and sediment (Fig. 6). Small rivers draining the Zagros mountains of Iran and Pakistan, transport only little water masses, but dominate the sediment discharge into the Persian Gulf and into the Gulf of Oman (Sarnthein, 1972). Southwest monsoon precipitation in the Ethiopian highlands become either part of the Nile system, or find their way towards the Arabian Sea at the Kenyan and Somalian coast.

Milliman & Meade (1983) estimated the total sediment discharge from rivers into the Arabian Sea reaching a value near 1000 $*10^6$ tons (Fig. 6), that is 10 times the quantity transported by dust (see above) However, about 90% of the river discharge is generally deposited on the continental shelves (A. Wetzel, pers. comm.) or in turbidites in the deep-sea. Accordingly, the riverine contribution to the hemipelagic sediments of the Arabian Sea could be near 100 $*10^6$ tons, which is about the same quantity as being derived from dust deposition (Fig. 5). The hemipelagic sediments of the Arabian Sea could, thus, receive contributions from about 50% eolian and 50% riverine sources.

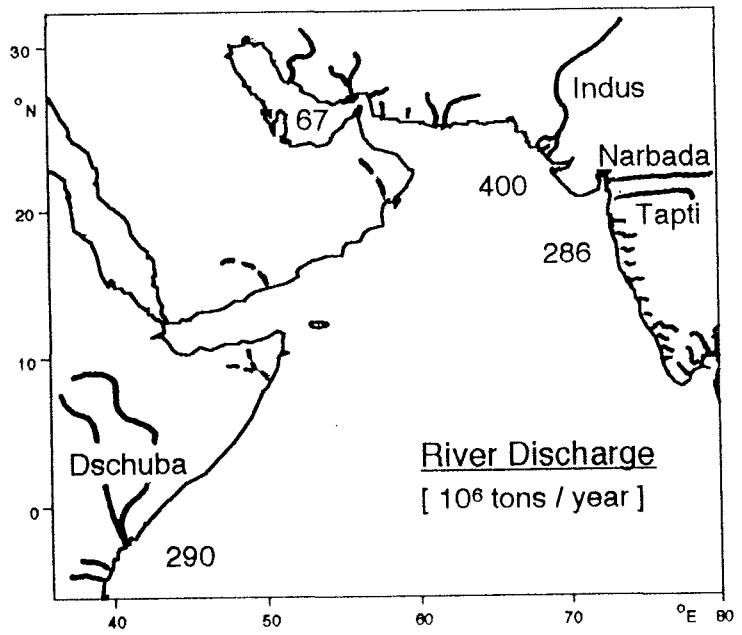

Figure 6. River discharge into the Arabian Sea, after Milliman & Meade (1983).

Hydrography and chemistry of Arabian Sea deep- and surface waters

The driving force for the surface currents is the southwest monsoon, which drives the Somali current along the coast of Africa (Schott & Fieux, 1985) and induces coastal upwelling off Somalia and Oman (Fig. 7). These upwelling waters are rich in nutrients and dissolved ion content of the trace elements Cd, Zn, Ni and Cu (Saager et al., 1992), but show low surface water temperatures (Wyrtki, 1972) The core of the southwest monsoon, called the Findlater jet (Findlater, 1969; Findlater, 1974), crosses the central Arabian Sea, leading to Ekman open ocean upwelling north of the axis, and mixed layer deepening to its south (Bauer, 1991; Luther & O´ Brien, 1990).

The vertical profile of water masses (Fig. 7 b) shows the "Arabian Sea Surface Water" on top, a highly saline water mass that forms by intense evaporation over the central Arabian Sea (Duplessy, 1982; Hastenrath & Lamb, 1979). Below, we find the highly saline "Persian Gulf Outflow Water "in the northwestern sector of the Arabian Sea. In the central Arabian Sea "South Indian Central Water" occurs at the same depth. This water mass is formed at the subtropical convergence of the southern Indian Ocean, from where it spreads towards north (Bertram, 1989). Coastal and open ocean upwelling cells mix over a depth of about 300 m (Prell & Streeter, 1982), thus, they are feeding on a mixture from three sources (ASW, PGW, SICW, Fig. 7). Below, "Antarctic Intermediate Water" mixes with "Red Sea outflow Water", which spreads on isopycnal surfaces from the Gulf of Aden as far as the coast of Australia (Lynch-Stieglitz et al., subm.). The deep Arabian Sea is filled by "North Atlantic Deep Water", and some "Antarctic Bottom Water" at depths below 4000 m, south of the Carlsberg Ridge.

The distribution of dissolved gases in the water column of the Arabian Sea is characterized by a pronounced oxygen minimum layer at subsurface depth (Slater & Kroopnick, 1984). Both the seasonal reversal of currents in the Arabian Sea (Currie et al., 1973) and a long residence time of the water in the Arabian Sea (Broecker et al., 1988), combined with high flux rates of organic matter (Haake et al., 1993; Nair et al., 1989) lead to an intense remineralisation of organic matter at 300-1200m waterdepth, where oxygen is largely consumed and the water gets anoxic. These reducing conditions are reflected in increased levels of Mn, Fe and the REE at this depth (German & Elderfield, 1990), but do not affect the profiles of nutrient, Cd and Zn content (Fig. 7d, e).

Figure 7. Hydrography of the Arabian Sea.
(a) Oceanographical names,
(b) Processes that control the surface water mass composition during summer (Luther & O´Brien, 1990),
(c) Schematic profile across the Arabian Sea from East-Africa (A) to southern India (B); ASW: Arabian Sea Surface Water; PGW: Persian Gulf Outflow Water; SICW: South Indian Central Water; AAIW: Antarctic Intermediate Water; RSW: Red Sea Outflow Water; NADW: North Atlantic Deep Water; AABW: Antarctic Bottom Water; after Bertram (1989; Wyrtki (1971). Core location of sediment core 74KL.
d, e) PO_4, H_4SiO_4, Cd and Zn content in deep and surface water, from Saager et al., (1992).

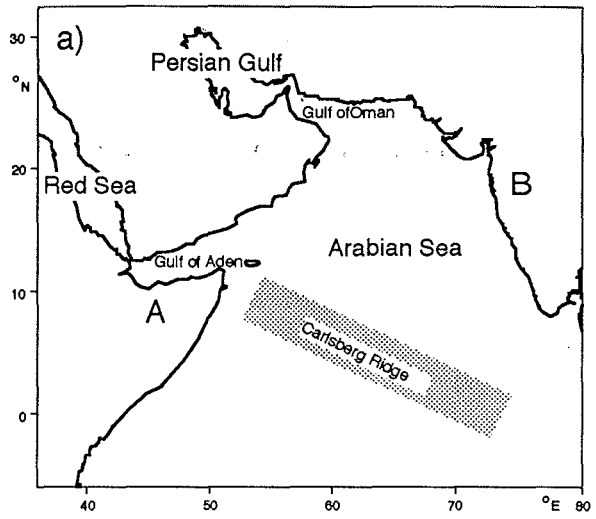

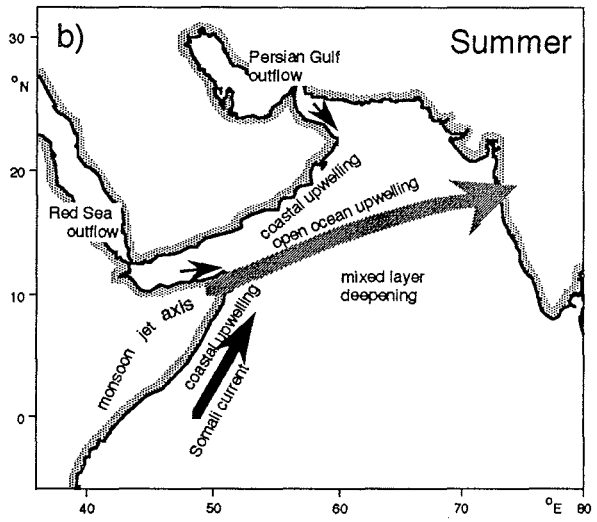

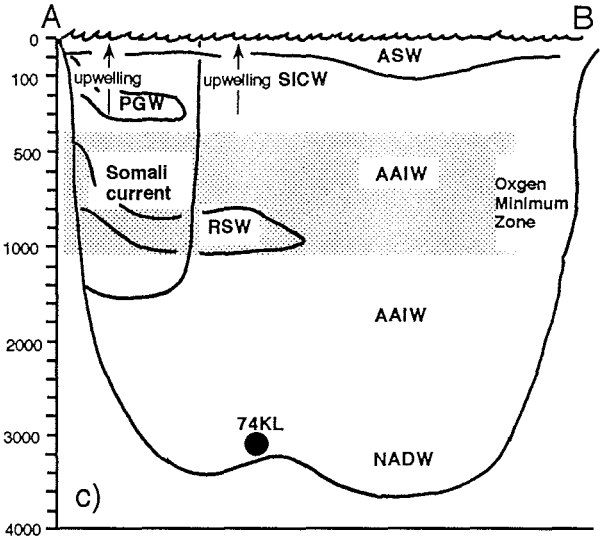

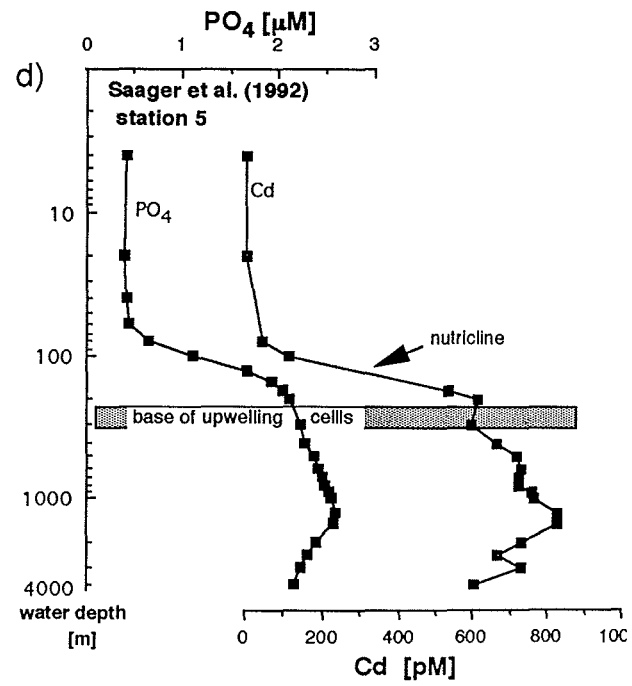

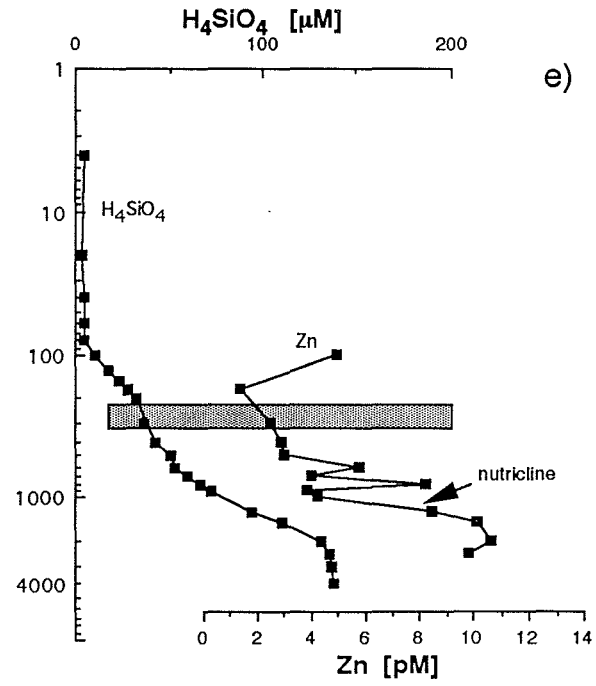

A.5 Previous work

High resolution time series and reconstructions of the monsoonal climate

The reconstruction of the monsoonal climate has attracted marine geologists since the first deep-sea studies in the Arabian Sea in the late sixties (e.g., Olausson & Olsson, 1968; Stewart et al., 1965; Von Stackelberg, 1972). The cores studied during the subsequent years were sampled on time-intervals of thousands of years, and revealed the late Pleistocene and Holocene history of the monsoons on a millenia-scale (e.g., Duplessy, 1982; Prell, 1984; Prell & van Campo, 1986; Van Campo, 1986). The only core up to now studied on a century-scale was core 162 in the pioneering paper of (Olausson & Olsson, 1968), who already described an evolution of the summer monsoon, characterized by three abrupt transitions after the Younger Dryas, and an early Holocene maximum of southwest monsoon intensity. The age model of the core was based on only three ^{14}C dates, which were not corrected for the age of sea water and had an error of "several hundred" years (*op.cit.*). Taking this error margin into acount, the transitions in the sediment composition of core 162 could be identical to the events E4, E5, E6, as described in this paper (Fig. 12). The sampling resolution in core 162 was 10 cm (i.e., a time resolution of 100 years); thus, this early paper had already shown that the events of monsoon intensification should have occurred on time-scales of decades.

Inorganic Geochemisty of Arabian Sea sediments

The first studies of the geochemistry of the Arabian Sea were done at the continental margins of Somalia (Marchig, 1974; Müller, 1967) and India (Marchig, 1972). According to these authors Cr, Fe, and Ti were concentrated in the lithogenic, quartz-rich, and coarse grained sediments of the shelf and upper slope, whereas Mn, Ni, Cu, and Zn were most frequent in the clay-mineral-rich, fine-grained sediments of the lower slope and deep ocean.

The geochemistry of the open Arabian Sea was then studied by Shankar et al. (1987), who first mapped the geochemical provinces of the whole ocean and defined by means of factor analysis the following processes that contribute to the chemical composition:

a) detrital influx from Somalia
b) accretion of Mn-nodules in the Somali basin
c) eolian transport from Arabia
d) preservation of organic-rich sediments under anaerobic conditions at the Oman margin
e) detritus from the river Indus
f) detritus from the rivers Tapti and Narbada
g) in situ weathering of basalts on the Carlsberg Ridge
h) hydrothermal activity on the Carlsberg Ridge.

The data set of Shankar et al. (1987) included all samples from (Kolla & Biscaye, 1973; Kolla & Biscaye, 1977; Kolla et al., 1976b; Kolla et al., 1981a; Kolla et al., 1981b),

who had studied the mineralogy of the Arabian Sea surface samples in every detail, and first discovered the eolian source of sediments in the western Arabian Sea. The samples that were used by Shankar et al. (1987) included sites that were affected by turbidites, channel deposits of the Indus fan, relict sediments on the shelf and weathering of basalts on the flanks of the Carlsberg Ridge. Accordingly, the distribution patterns of the geochemical properties at the sediment surface, as shown by Shankar (*op.cit.*) do not always agree fully with the distribution patterns as presented in this study (Figs. 17-56), because samples that were visually affected by any kind of disturbance were carefully avoided in this paper.

Scholten (1987) studied the mineralogy and geochemistry of the sediments on, and south of the Carlsberg Ridge. On the ridge, he found a composition of the sediments typical for a lithogenic source, but could not clearly identify provenance and transport of the particles. The most important finding was that hydrothermal activity on the Carlsberg Ridge had ceased for the last 100,000 years.

The geochemical composition of the sediments at the Oman continental margin revealed abundant lithogenic elements (Zr, Al, Ti, Cr), concentrated on the shelf as a relict after winnowing of the fine grained fraction (Pedersen et al., 1992; Shimmield et al., 1990b).

The chemistry of sediments on the Indian shelf was documented by Paropkari (1990), who attributed the high content of Al, Ti, Fe, Mg, Na, K, Mn, Cu, Ni, and Zn to the fine-grained texture of the sediments; only Ni, Cu and Zn were found to be affected by scavenging and formation of authigenic Fe- and Mn-hydroxides (op.cit.).

The geochemical information that is still missing to apply geochemical tracers for reconstruction past climate stages of the area, are ocean-wide distribution patterns of element concentrations in the non-turbiditic surface sediments and for time-slices of the past to define the transport pathways of elements and sediments during the present and the past. Hence, we present maps for various geochemical parameters at the sediment surface, the Early Holocene (8-10 ka), the Termination Ia (16-18 ka), and the Last Glacial Maximum (21-23 ka) (chapter C.1.).

B) Material and Methods

A total of 37 sediment cores, including 3 high-sedimentation rate cores were chosen to monitor the precise chronology of abrupt changes in monsoonal climate and sediment input to the Arabian Sea. Locations of the sediment cores, and of all geographical names used in the text, are shown in Fig. 8.

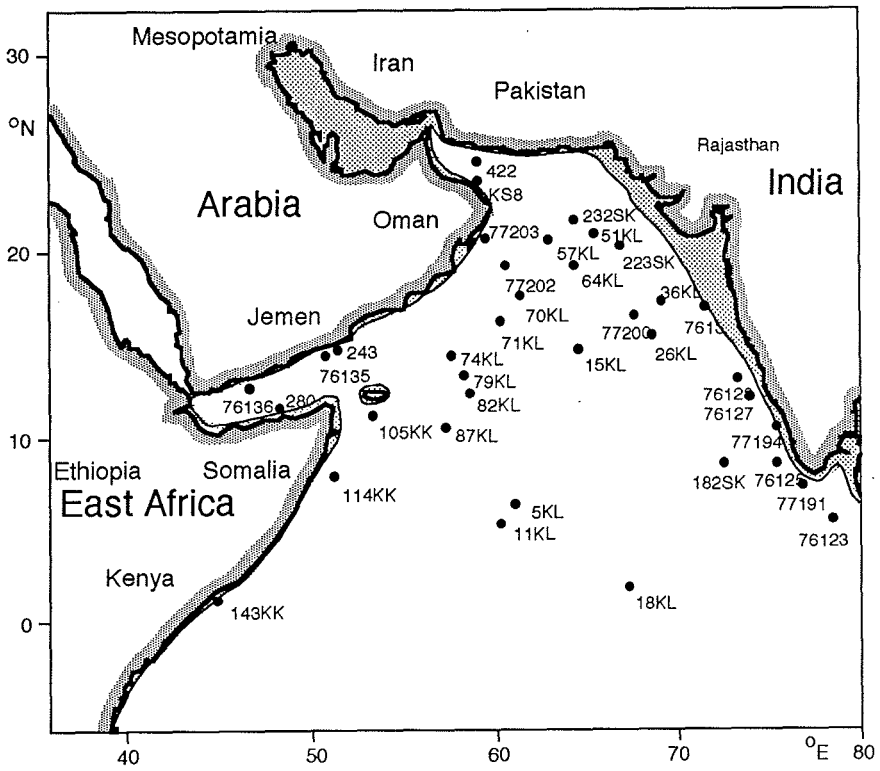

Figure 8. The Arabian Sea. Locations of sediment cores and geographical names. The high-resolution cores 74KL, KS8 and 422 are marked by an asterix.

B.1. Core locations and age control of high resolution sediment cores

Core 74KL

Core 74KL (cruise SONNE 42) was obtained from the East Sheba Ridge, 1000 m above the turbidite plain of the Indus delta, and 300 km south of the Arabian continental margin, below the upwelling region of the central western Arabian Sea (Fig. 9 a). The sediment colour of the whole core are variations of "olive grey" following the notation of the "Munsell" colour charts (Fig. 9 b). The core is 320 cm long, with the section lower than 125 cm being covered with black spots of submillimeter size. Two foraminiferal sand layers are visible at 235 and 247.5 cm. The core was sampled at 2.5 cm intervals, which corresponds to an average time resolution of 300 years (Tab. 1).

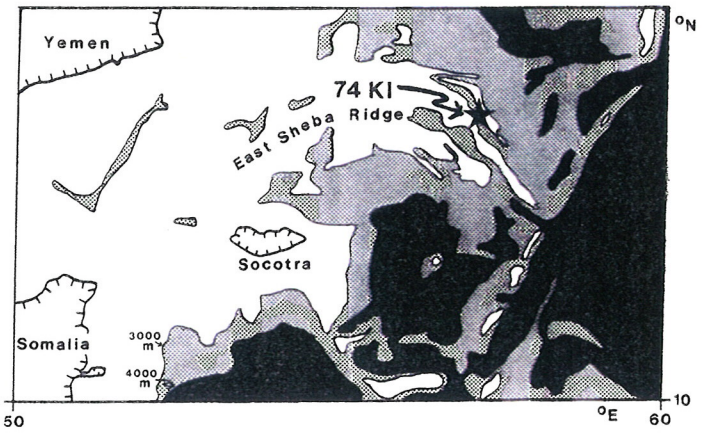

Figure 9. Core 74KL
(a) Bathymetry at core location after (GEBCO, 1975)
white: waterdepth <3000 m.
stippled : " 3000-4000 m;
black: " >4000 m;

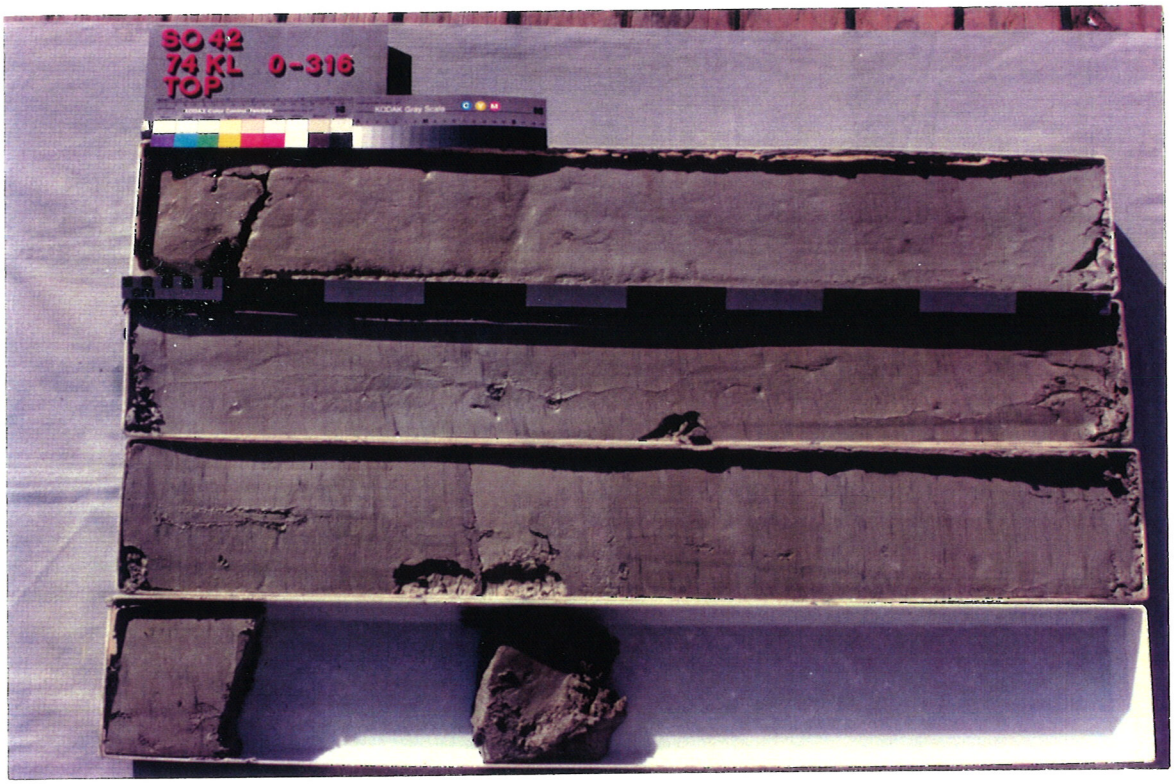

Figure 9. Core 74KL, (b) photograph.

^{14}C dates by accelerator mass spectrometry (AMS-^{14}C) were made on the same planktonic species as used for the $\delta^{18}O$ profile (i.e., *G.ruber*). This species was chosen because it is abundant in all sections of core 74KL (Fig. 10). Prior to the selection of depth levels that are suited for AMS-^{14}C analysis on this single species, the abundance of *G.ruber* was determined; it is low in the glacial section and at the sediment surface of core 74KL, but high in the early Holocene section

(Fig. 10). Maxima of *G.ruber* occur at 95-100, 127.5, 235 and 247.5 cm depth, with only the two lower maxima being located in the foraminiferal sand layers.

Based on the *G.ruber* abundance profile, sampling positions for ^{14}C analysis were chosen at depth of all maxima to obtain ages from samples that have a minimum proportion of specimens being reworked by bioturbation. The ^{14}C ages of these samples are reported in Tab. 1, and the ^{14}C-age/depth profile reveals an almost linear increase of age with depth (Fig. 11). Only at 235 and 247.5 cm depth ages of about 40,000 ^{14}C-yrBP disrupt the linear pattern. Both dates are from the two foraminiferal sand layers. These old ages in a largely linear age/depth profile reveal that these foraminifera are not from an authochtonuous source, but the result of lateral input of redeposited ancient sediments. These redeposited sediments should be eroded at a location nearby, because core 74KL is located in a small trough on the East Sheba Ridge (1000 m above the Indus plain); thus, a possible cause for the two foraminiferal layers could be a mega-event in the Indus fan, or local erosion on the flanks of the trough.

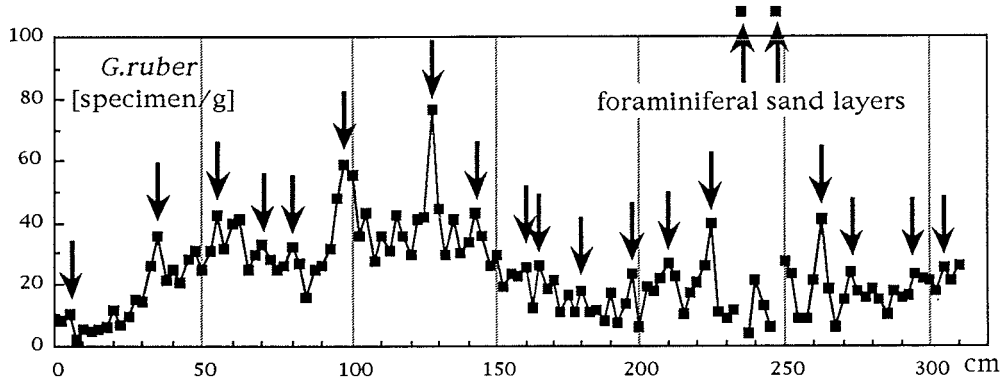

Figure 10. Abundance of Globigerinoides ruber (specimens per gram sediment) in sediment core 74KL. Arrows mark sample depth for AMS ^{14}C dates (Tab. 1). The values at 235 and 247.5 cm depth were set at >100; the real values largely exceed that number.

Frequent occurrence of *G.ruber(pink)* in the two foraminiferal layers indicates a source as old as the last interglacial, when this species became extinct in the northern Indian Ocean (Zobel, 1973). Single specimens of *G.ruber(pink)* can be traced as far as the depth of 195 cm. Accordingly, the AMS date at this depth is still affected by ancient specimens, stemming from the foraminiferal sand layers and subsequent bioturbation. This finding explains the knickpoint at 180 cm depth in the age / depth relation and the unreasonable low sedimentation rate found between 180 and 195 cm depth (Tab. 1 and Fig. 11).

Table 1a. ^{14}C age control of sediment core 74KL. All ^{14}C-ages were corrected by 400 years for the average age of surface ocean water. ^{14}C-ages were converted into calendar years by means of tree ring data and U/Th ages, using switch points at 10,400 ^{14}C-yrBP= 12,400 cal-yrBP.; and 13,100 ^{14}C-yrBP = 15,100 cal-yrBP, 13,200 ^{14}C-yrBP= 16,700 cal-yrBP (Bard et al., 1990; Winn et al., 1991). Average sedimentation rates, average dry density, and average carbonate content were calculated for the depth interval between the sample depth were they are reported and the depth of the following sample. Dry density values are from Sirocko (1989), $CaCO_3$ values from Appendix 2.

sample depth [cm]	Age AMS-^{14}C ^{14}C-yrBP	1 σ error yr	Age adjusted cal-yrBP	Sedimentation Rates average	max. cm/1000 yrs	min.	Dry density g/cm^3	$CaCO_3$ %
7.50	1230	60	1170	13.0	14.0	12.1	0.61	63.1
35.00	3350	100	3632	9.1	10.0	8.4	0.65	67.1
55.00	5540	90	6320	6.5	7.0	6.0	0.67	68.8
70.00	7850	90	8625	11.8	15.6	9.4	0.68	68.1
80.00	8700	120	9550	9.3	10.7	8.3	0.75	69.1
97.50	10580	120	11880	14.6	18.4	12.1	0.85	68.5
115.00	11780	130	13780	9.8	12.5	8.0	0.79	66.8
127.50	13060	150	16060	13.2	18.3	10.3	0.90	59.5
142.50	14200	170	17700	10.4	13.1	8.7	0.85	61.0
160.00	15880	170	19380	13.2	125.0	6.9	0.83	60.8
165.00	16260	170	19760	17.2	28.8	12.3	0.82	61.1
180.00	17130	180	20630	(5.1)	(5.8)	(4.5)	0.83	60.4
197.50	20580	260	24080 (*1)					
210.00	21860	290	*1	(*1: occurrence of *G.ruber(pink)*				
225.00	22820	320	*1					
235.00	39800	1900	*1					
247.50	45600	3700	*1, *2	(*2 foraminiferal sand layer)				
262.50	24840	430	*1, *2					
272.50	25830	410	*1					
295.00	29540	610						
305.00	30230	650						

Table. 1b. Average sedimentation- and accumulation rates for the smallest sediment sections in which stable average sedimentation rates could be calculated.

	Sedimentation Rates average	max. cm/1000 yrs	min.	Average Accumulation Rates bulk	$CaCO_3$ g/m^{2}yr	Lithogenic
7.5-35 cm:	13.0	14.0	12.1	79.1	49.9	29.2
55.0-97.5 cm:	8.4	8.8	8.1	59.0	40.6	18.5
127.5-180 cm:	12.9	14.0	11.9	109.6	66.4	43.2

Accordingly, the date at 180 cm is the oldest reliable ^{14}C date. Due to these disturbances in sedimentation patterns and their effects on the ^{14}C dates, the complete section 200-310 cm was discarded for further evaluations on the chronology and geochemistry of core 74KL.

The ^{14}C years as reported in Tab. 1 were converted to a calendar year time scale by using a tree ring calibration for ages below 10,000 years, and a U/Th adjusted time-scale for ages older than 10,000 years (see reference for the calibration scheme in Tab. 1). The determination of adjusted ages near the ^{14}C-plateaus at 9900 and 12.700 ^{14}C-yrBP is problematic, but fortunately, none of our ^{14}C ages coincides with the age of the ^{14}C-plateaus (Fig. 11 b.).

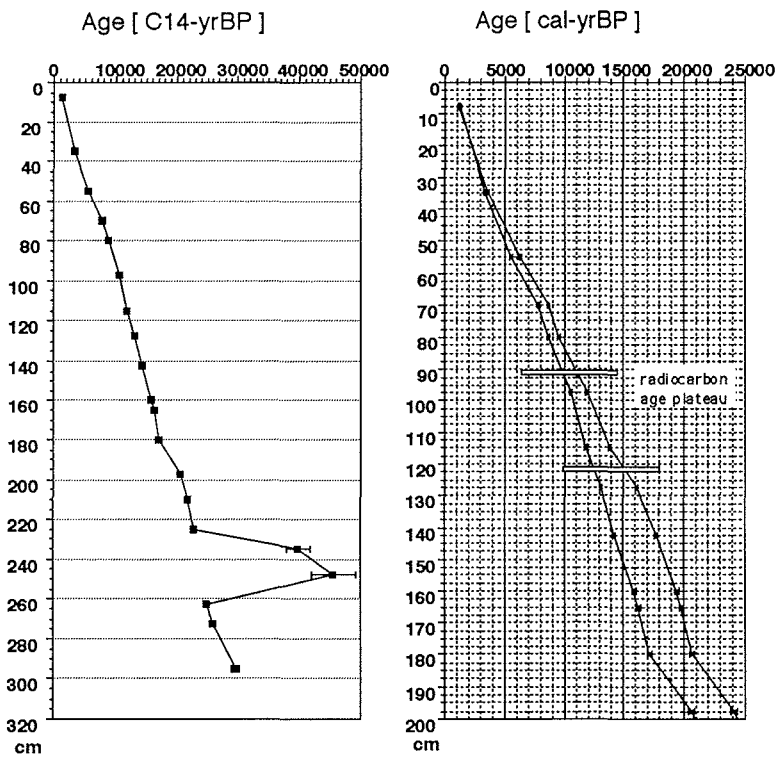

Figure 11. Age-depth relation of AMS-^{14}C dates in core 74KL: (a) the whole profile, (b) the upper 2m of undisturbed sedimentation. The calibration of the AMS dates after Sirocko et al. (1993) (Tab. 1). Error bars are given, but mostly not visible due to the size of markers. Plateaus of constant radiocarbon age after Broecker (1992), Lotter (1991).

Sedimentation rates were then calculated on the basis of the adjusted ^{14}C-stratigraphy, and Tab. 1a reports on average, minimum and maximum sedimentation rates that can be calculated within the 1sigma error bars of the ^{14}C

dates. When the distance between samples is little, the errors produce a large effect (a theoretical possible sedimentation rate of 125 cm/1000 yrs between 160 and 165 cm, Tab. 1b). Accordingly, high resolution sedimentation rates cannot be interpolated over too small sediment thickness. Instead, sedimentation rates were integrated over large depth intervals, and special care was taken by choosing only those dates, which are centered at outstanding maxima in the abundance of *G.ruber* (Fig. 10). Now stable average, maximum, and minimum sedimentation rates can be obtained for the late Holocene (13.0 cm/1000 yrs), the early Holocene (8.4 cm/1000 yrs), and glacial (12.9 cm/1000 yrs).

The $\delta^{18}O$ values of *G.ruber* in the glacial section of core 74KL range between 0.0 and -0.2‰, but three decreases up to -0.5‰ are found at 177.5, 167.5, and 135 cm depth (Fig. 12). After the last increase, the $\delta^{18}O$ value does not reach again

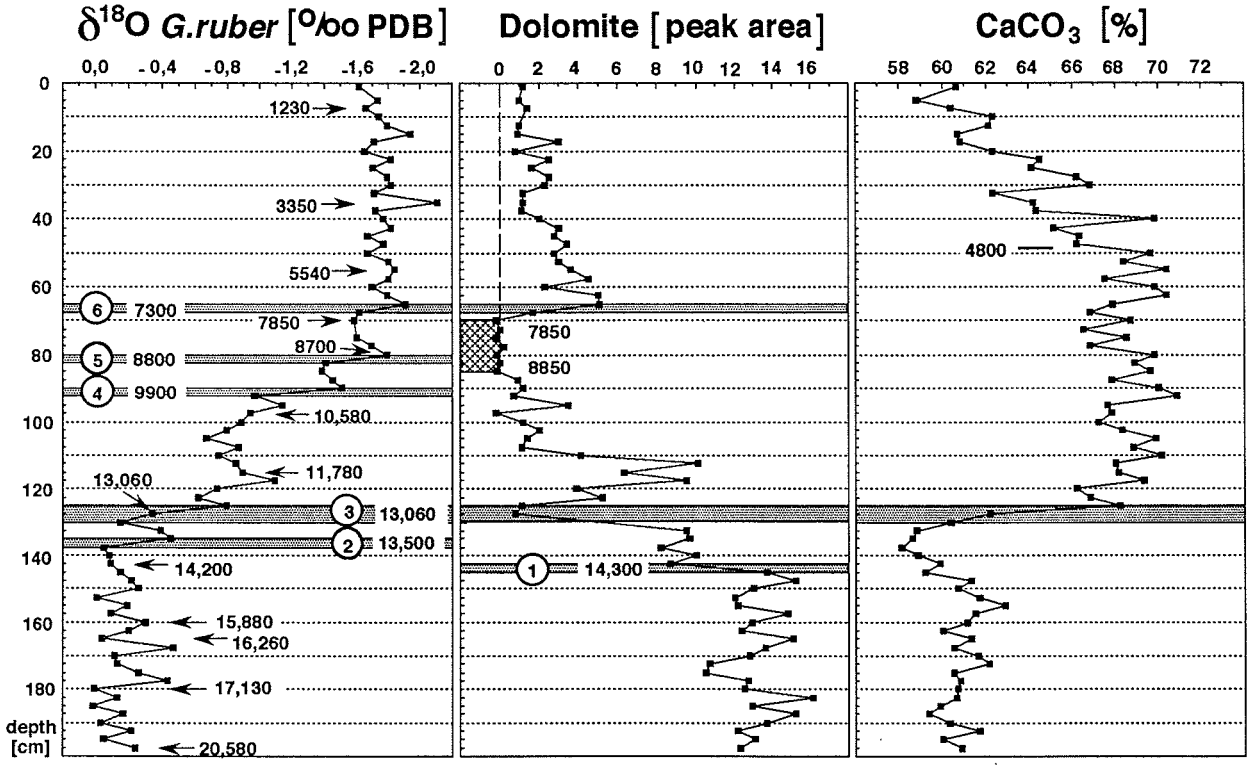

Figure 12. from Sirocko et al. (1993): AMS C-14 dates for sediment core 74KL (Tab.1), $\delta^{18}O$ values of Globigerinoides ruber, and dolomite abundance in the lithogenic fraction > 2µm, $CaCO_3$ content. The depth of events 1-5 are marked by stippled bars. The hatched dolomite minimum between 85 - 70 cm depth indicates the early Holocene maximum of southwest monsoon wind intensity.

the glacial level, thus the decrease at 135 cm depth is regarded as the first deglacial $\delta^{18}O$ event (E2, Fig. 12). The next decrease in the $\delta^{18}O$ profile of core 74KL

occurred with an amplitude of 0.5‰ between 127.5 and 125 cm, followed by rather constant values during the Bölling, Alleröd, and Younger Dryas interval. The next event of 0.5‰ is found between 92.5 and 90 cm depth (E3, Fig. 12). Immediately after E3 a gradual increase occurred between 90 and 82.5 cm, followed by another $\delta^{18}O$ event during E5 with an amplitude of 0.4‰ and another subsequent smooth increase. During E6, with a last decrease of 0.3‰, the Holocene level is reached where $\delta^{18}O$ remained largely constant at -1.7‰. A spike-like minimum of 0.4‰ at 35 cm marks the only disruption of an otherwise stable Holocene level.

According to the evolution of the $\delta^{18}O$ profile of *G.ruber* in core 74KL as described above, the complete glacial to interglacial transition of 1.7‰ has witnessed at least 5 events with a complete shift of 2.1‰ only during the events of abrupt $\delta^{18}O$ change. If the global $\delta^{18}O$ variation between the glacial and the Holocene can account for a 1.2‰ shift (Labeyrie et al., 1987), the local $\delta^{18}O$ signal in the Arabian Sea should be characterized by extremes of very negative $\delta^{18}O$ spikes that have only a short duration and return to values a little above its former level rather soon (chapter D.3.).

Table 2. ^{14}C-ages and calendar-year-ages of the $\delta^{18}O$ events and of the begin and end of the early Holocene humid interval in core 74KL The events are numbered according to Fig. 12, the calibration of the ages was done according to the calibration scheme as outlined in Tab. 1a).

Event	Event-depth cm	Event age cal-yrBP	^{14}C Event Age ^{14}C-yrBP	Refs. for adjustment
Event 6:	66,25	8050	7300	(Pearson, 1986)
Humid interval	70,00	8600	7850	(Stuiver et al., 1991)
Event 5:	81,25	9700	8800	(Stuiver et al., 1991)
Humid interval	82,50	9900	8850	(Stuiver et al., 1991)
Event 4	91,25	11450	9900	(Stuiver et al., 1991)
Event 3:	127,50	16060	13060	(Bard et al., 1990)
Event 2:	136,25	17000	13500	(Bard et al., 1990)

Core KS8

KS8 (French cruise ORGON IV) is located on the continental margin of Oman in the southern Gulf of Oman, outside the Oman upwelling area (Fig. 13). The core has been already extensively studied (Moyes et al., 1978), although not with a sampling resolution of 5 cm resulting in a time resolution of about 350 years, given a mean sedimentation rate of 13.5 cm/1000 yrs (Fig. 14). The lithology reveals scattered sand and silt layers, the origin of which were interpreted as redeposited shelf sediments (*op.cit.*).

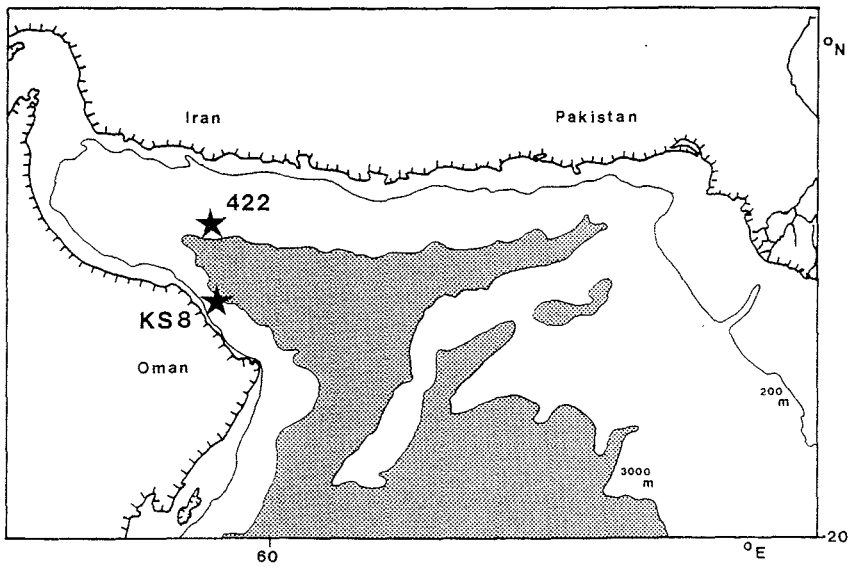

Figure 13. Core KS8
(a) Bathymetry at core location after (GEBCO, 1975)
white: waterdepth <3000 m.
stippled: " >3000 m;

Based on the results from 74KL, an event $\delta^{18}O$ stratigraphy was developed for KS8. The major events in 74KL occurred at 13,600 ^{14}C-yrBP; 13,060 ^{14}C-yrBP and 9900 ^{14}C-yrBP (Fig. 12). All three events seem to have occurred also in the $\delta^{18}O$ record of KS8 (Fig. 14). A first decrease of 0.8‰ from glacial $\delta^{18}O$ values at +0.5‰ is found at 230 cm depth. Analogous to the succession of events as shown in 74KL, this first $\delta^{18}O$ increase in KS8 should be E2. The next event with an amplitude of 0.8‰, the largest of all, occurred at 200 cm depth, and should be E3, especially because it is also paralleled by a strong decrease of lithic carbonate content, which is exactly the same pattern as observed for E3 in 74KL (Fig. 12). The strong $\delta^{18}O$ decrease at 140 cm in KS8 (at the end of the Younger Dryas) should then be E4. Event E5 and E6 are not visible in KS8, which could be caused by the low sampling resolution in KS8 in combination with the large variability of $\delta^{18}O$ values in the glacial section, which clearly exceed the variability as found in core 74KL. The full transition from the Younger Dryas to the Holocene level has an amplitude of 1.6‰ in KS8, and most probably E4, and the minor events E5 and E6 appear as one large transition which account for a $\delta^{18}O$ change of 1.6‰ between

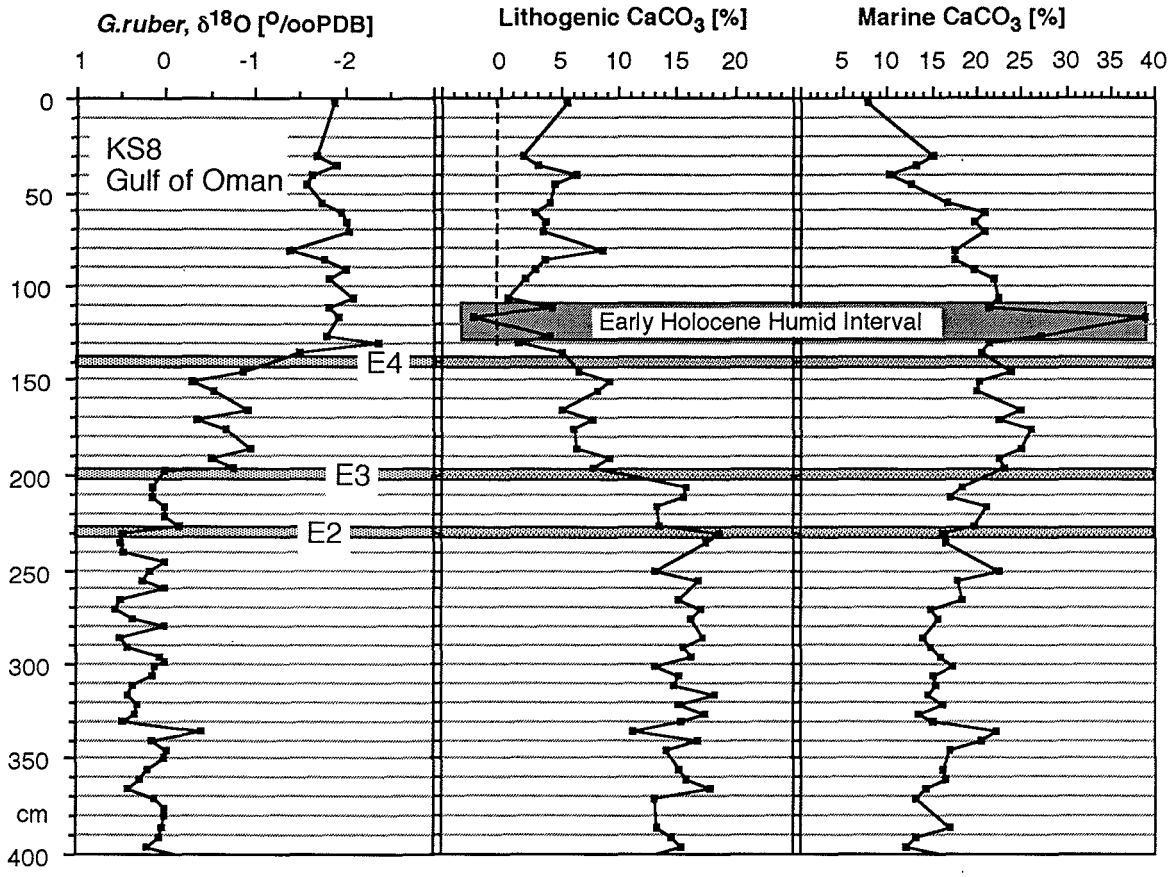

Figure 14. Core KS8, $\delta^{18}O$ G.ruber (315-400 µm), lithogenic and marine carbonate content .

150 and 130 cm in KS8. The early Holocene minimum of carbonate content in 74KL is then visible between 130 and 110 cm in KS8 (compare also sediment core 422, below), again reflecting the overregional scale of changes observed in the sediments of the Arabian Sea.

Core 422

Core 422 (METEOR cruise 5) has been retrieved from the northern (Iranian) margin of the Gulf of Oman (Fig. 13). The core was sampled at 2 cm intervals which led to a time resolution of 120 years during the Holocene where sedimentation rates reached 16.3 cm/1000 yrs (Fig. 15). The glacial section of 422 shows heaviest $\delta^{18}O$ values of about +0.5, but in addition, extremely large variations up to values of -0.5 (i.e., with an amplitude of 1 ‰).

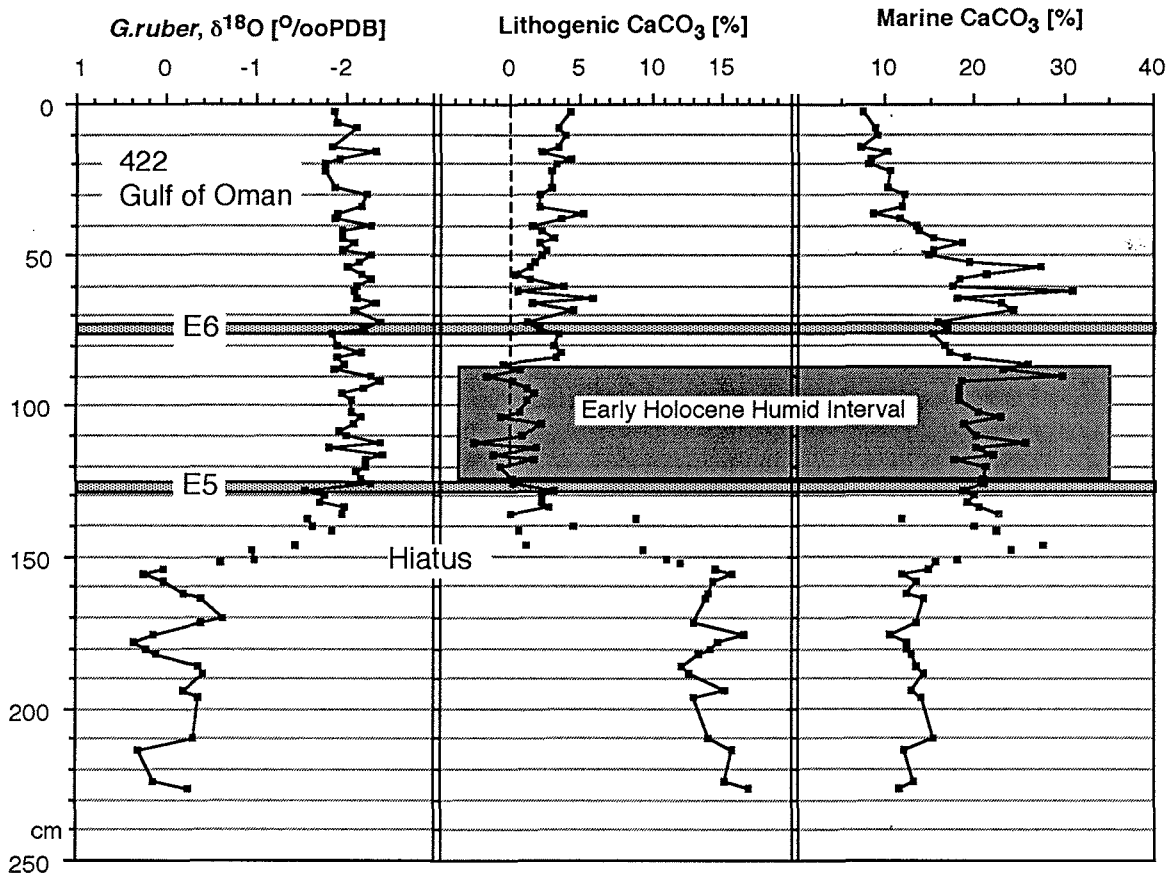

Figure 15. Core 422, $\delta^{18}O$ G.ruber (315-400 µm), lithogenic and marine carbonate content.

Thus, the values and the patterns of $\delta^{18}O$ variation in the glacial section of 422 are similar to KS8. Unfortunately, the $\delta^{18}O$ record of sediment core 422 lacks any Younger Dryas oscillation, but shows a foraminiferal sand layer at 149 cm depth, which may indicate a hiatus in the middle termination I. Based on continuous sedimentation rates, a sediment section of up to 40 cm may be lost.

A sharp decrease of 0.6‰ in the $\delta^{18}O$ signal of core 422 occurs at 127 cm, when $\delta^{18}O$ values almost reached their Holocene level. The event could represent E5, based on its occurrence immediately before the early Holocene minimum of lithogenic carbonate concentrations (compare Fig. 12). Another decrease of $\delta^{18}O$ values at 75 cm depth could then represent E6. If the decreases of $\delta^{18}O$ values at 127 and 75 cm indeed represent these events, E5 and E6 must have occurred in a time-span shorter than 120 years.

B.2. Definition of the time-slice samples: Sediment surface, Early Holocene, Termination Ia and the Last Glacial Maximum

37 sediment cores from the northern Indian Ocean were sampled at the sediment surface and at depth levels of climatic extremes (Fig. 16), which are i) the Last Glacial Maximum at 21,000-23,000 cal-yrBP (21-23 ka), ii) an interval of extreme aridity in Arabia during the Termination Ia at 16,000-18,000 cal-yrBP (16-18 ka), and iii) an Early Holocene humid interval at 8000-10,000 cal-yrBP (8-10 ka).

Samples from these time-slices can be positioned on the basis of the $\delta^{18}O$ curves, that were already available from Sirocko (1989). All $\delta^{18}O$ profiles, except for 5KL and 11KL, are done on the planktonic species *G.ruber*, which dwells in the upper 50 m of the ocean (Duplessy & Bé, 1981). The curves are presented in Fig. 16, which also shows the approximate position of the end and the beginning of the termination (events E2, E5), and the depths that were sampled for geochemical analysis. Core positions, water depth and depth of samples are reported in Tab. 3.

Table 3. Sediment core locations, water depth, and sample depth

Leg	Core	Sediment surface	8-10 ka	16-18ka	21-23 ka	Long. °N	Lat. °E	water depth m
SO42	15KL	0-5	16-20	35-39	50-54	14 52.82	64 44.79	3920
	26KL	0-5	15-19	78-82	103-107	15 30.86	68 45.61	3776
	36KL	0-5	8-12	26-30	43-47	17 04.49	69 02.68	2055
	51KL	0-5	28-32	78-82	130-134	20 57.92	65 33.54	2644
	57KL	0-5	28-32	78-82	118-122	20 54.47	63 07.32	3422
	64KL		8-12	58-62	96-100	19 04.62	64 41.01	3281
	70KL	0-10	18-22	58-62	82-86	17 30.69	61 41.82	3810
	71KL	0-20	38-40	70-74		16 14.17	60 15.35	4029
	74KL	9-15	62-66	138-142	200-204	14 19.26	57 20.82	3212
	79KL	0-2	38-42	79-83		13 38.84	58 19.56	4351
	82KL	0-2	8-10	58-62	100-105	12 41.09	58 40.62	4416
	87KL	0-5	58-62	94-98	118-122	10 30.05	57 44.22	3773
SO28	05KL			30-33	48-52	06 39.75	61 08.03	3335
	11KL	0-5	11-14	41-44	65-69	05 23.36	60 15.09	3859
	18KL	0-10	17-21	33-37	43-47	01 53.99	67 20.47	3035
IOE	105KK	3-7	57-62	111-119	138-143	11 16.00	53 32.50	3535
	114KK	3-8	44-48	104-108	137-141	08 00.50	51 12.80	3843
	143KK	12-19	156-162	215-220	253-258	01 15.00	44 47.00	1522
	182SK	4-8	27-32	38-44		08 46.20	73 42.00	2234
	223SK	8-15	19-24	67-72	98-103	20 04.00	66 53.00	2686
	232SK	5-10	22-27	77-82	110-115	21 47.00	64 36.00	3098
OSIRIS	76123	5,5	18,5	58,5	78,5	06 23.50	78 39.50	2631
	76125	6,5	50,5	88,5	132,5	08 35.00	75 20.00	1878
	76127	4,5	18,0	37,5	57,5	12 05.40	73 54.00	1610
	76128	6,5	77,0	188,5	255,0	13 08.00	73 19.00	1712
	76132		18,5	189,5		16 59.40	71 30.80	1430
	76135	4,5	108,5	207,5	247,5	14 26.60	50 31.80	1895
	76136	5,5	38,5	76,5	134,5	12 52.30	46 48.90	1649
	77191	21,5	401,5	659,5		07 30.10	76 43.00	1254
	77194	11,5	149,0	315,5	389,0	10 28.00	75 14.00	1222
	77200	4,5	18,5	45,0	69,5	16 32.50	67 53.50	2910
	77202	8,0	53,5	133,5	198,0	19 13.30	60 40.90	2427
	77203	0-20	75,0	225,0	368,5	20 41.90	59 34.10	2442
METEOR5	422	0-10	126-130	156-160	184-188	24 23.40	59 02.50	2732
ORGON4	KS8	2-4	105-112	235-247	285-292	23 28.00	59 11.50	2900
VALDIVIA1	243K	0-3	58-62	168-172		14 42.60	51 33.50	1041
	280K	0-3	58-62	118-122		11 44.80	48 15.50	2106

Most samples for geochemical analyses were taken from giant box cores (30 x 30 x 500 cm) and have a volume of 4 x 4 x 4 cm. The large sample volume serves to minimize the effects of local microenvironments, such as caused by pyrite formation, burrows, Mn-nodules, etc.. For cores with smaller diameters (i.e., the cores from the Osiris, IOE), the sample size had to be reduced to as little as 1ccm.

The large volume of most samples enables us to study various other properties of the sediments. Besides the results from inorganic geochemistry, presented in this work, the faunal composition and organic geochemistry are studied in several cooperative projects with Drs. R. Anderson, J. Scholten (U/Th flux), L. Burckle (diatoms), V. Ittekkot (^{15}N), B. Molfino (coccoliths), G. Eglinton (U^{K}_{37}), H. Schulz, W. Prell (planktonic foraminifera, SST). All these projects will obtain results from aliquots of the same samples, that will finally allow to integrate informations on biogenic and abiogenic factors affecting the chemical composition of the Arabian Sea sediment.

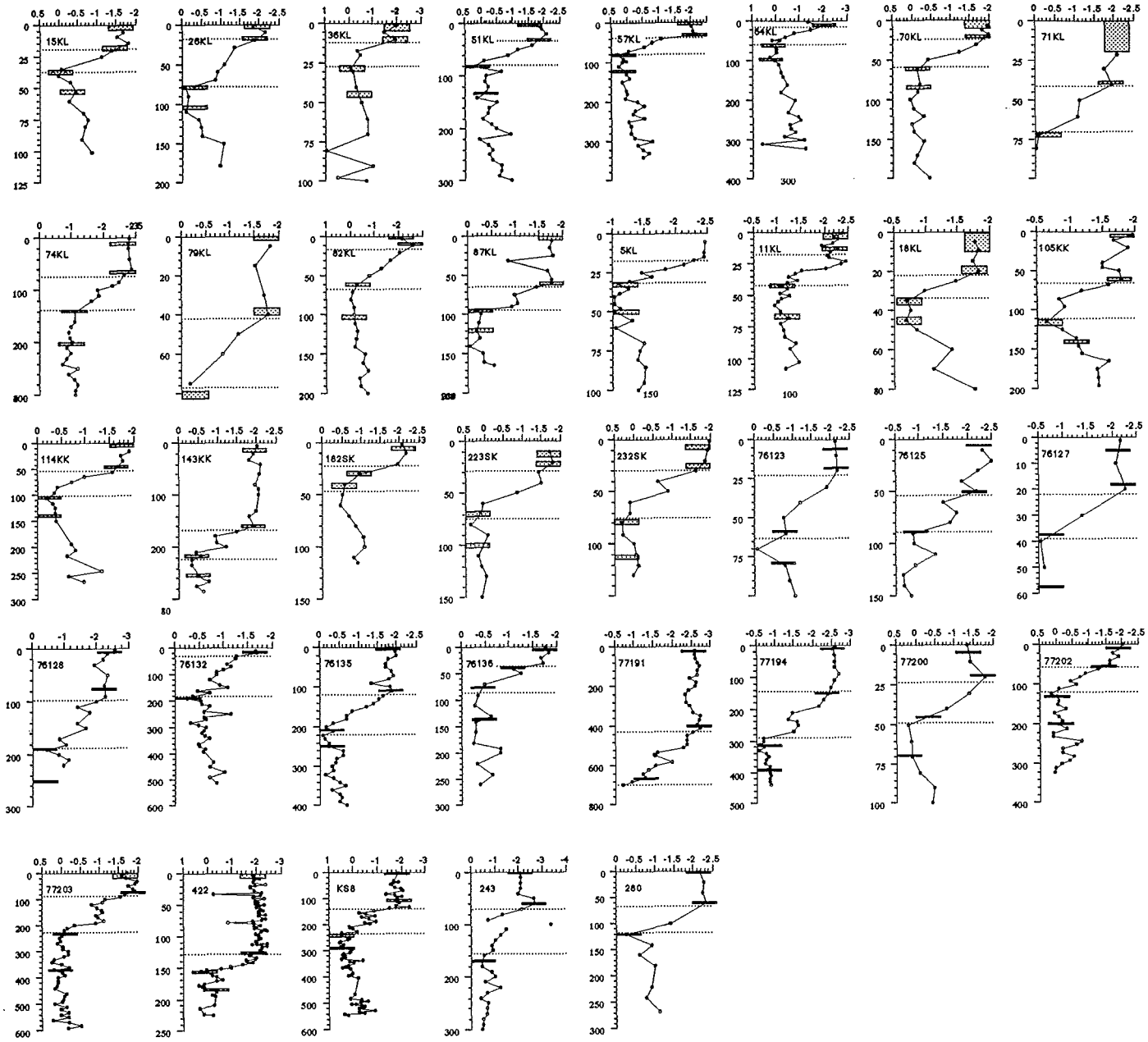

Figure 16. $\delta^{18}O$ curves of Globigerinoides ruber [‰ PDB] . Numerical values are from Sirocko (1989), except for sediment cores 243 and 280, for which values are listed in Appendix 6, Dotted lines show the stratigraphic markers (i.e., the begin of $\delta^{18}O$ increase during event E2 at 17,000 cal-yrBP and the end during event E5 at 9700 cal-yrBP) when $\delta^{18}O$ values first reached the Holocene level. Depths of sampling are shown as stippled squares. $\delta^{18}O$ values for sediment cores 5KL and 11KL were originally determined on Globigerina sacculifer, but have been corrected by subtraction of 1‰, to match the G.ruber data matrix.

B.3. Analytical methods

A total of 53 chemical elements, 4 sedimentological parameters, the $\delta^{18}O$, $\delta^{13}C$ composition of foraminifera, and the Sr- and Nd-isotope composition of the lithic fraction have been measured. $CaCO_3$, biogenic opal, organic carbon, S concentrations and the chemical analyses by ICP, ICP-MS and XRF have been determined from aliquots of the same samples (listed in Tab. 4). These samples of about 5 g were freeze-dried and powdered in an agate mortar.

Determination of $CaCO_3$ (carbonate) content

50 mg were used for $CaCO_3$ analysis on a "Ströhlein Coulomat" at the "Geologisch-Paläontologische Institut, Universität Kiel". Another aliqout of 100 mg was measured for $CaCO_3$ content at the "Zentrum für Meeres- und Klimaforschung, Universität Hamburg" using a "Westhöff Carmhograph 6".

The $CaCO_3$ data from the "Coulomat" are slightly lower than the "Carmhograph" data for core 74KL (Fig. 17), because the "Carmhograph" method uses hot 2N phosphoric acid to dissolve all carbonates, whereas the "Coulomat" method uses phosphoric acid at room temperature. Accordingly, dolomites are dissolved using the "Carmhograph", whereas the "Coulomat" only dissolves $CaCO_3$. "Camograph" data are hence used to calculate all element concentrations on a carbonate-and-opal-free-basis, because the samples from the northern Arabian Sea contain high dolomite amounts (Sirocko et al., 1991) that would dilute the concentration values of elements significantly if values were calculated on a $CaCO_3$-and-opal-free-basis only.

Determination of biogenic opal content

The biogenic opal concentrations were determined after a single extraction of silica into 2M Na_2CO_3 solution at 85°C for 5 hours at the Lamont-Doherty-Earth Observatory, using the method of Mortlock & Froelich (1989).

Determination of trace elements by ICP-MS (Inductively Coupled Plasma-Mass Spectrometry)

250 mg of the bulk sample were weighed into "Savillex" teflon beakers. The sample was moistened with 1 ml H_2O, 2 ml HNO_3 (conc.) were added to the sample, heated for 2 hours at 100°C and taken to dryness to dissolve carbonate and attack organics. 4 ml HF (conc., p.a. grade) and 1 ml HNO_3 (conc., p.a. grade) were added and heated for 24 hours in closed vials at 160°C. The solution was taken to dryness; 1 ml HNO_3 and 10 drops $HClO_4$ (conc., p.a. grade) were added to the residue, heated for 24 hours at 160°C and taken to complete dryness at 220°C. The residue was dissolved in 2 ml HNO_3 and this solution was increased to a volume of 50 ml with

deionized water.

The analyses were run on a VG PlasmaQuad PQ 1 in the ICP-MS laboratory at the "Geologisch-Paläontologische Institut, Universität Kiel", according to the procedure as outlined by Garbe-Schönberg (1993). Concentration values of all trace elements in rock standards of the USGS (United States Geological Survey) were determined routinely every day for the "BR" or "BHVO-1" standard. Certified concentration values for trace elements, their long-term average concentration reproduced with the ICP-MS at Kiel, respective data from the day when the samples of core 74KL were measured, standard deviation (n=2; i.e., the 74KL sample batch and the long-term avarage for the ICP-MS at Kiel) and relative error are listed in Tab. 4. Accordingly, except for Tl, the relative error of the analytical precision is less than 5%, below 1,2 % for the elements used for the reconstruction of the monsoon history (Zn, Zr, Rb, see chapter C.4., D.3.).

Table 4. Trace element concentrations in the "BHVO-1" standard , certified values after Govindaruju (1989), long-term average values for the ICP-MS at Kiel (Garbe-Schönberg, 1993), and values during the run of samples for this study.

Element	Isotope	BHVO-1 certified value Govindarayu, 1989	BHVO-1 long term average, Kiel Garbe-Schönberg, 1993	BHVO-1 together with sample batch 74KL	Standard deviation (s)	Relative error
		ppm	ppm	ppm	ppm	%
Lithium	Li 7	4,6	4,3	4,6	0,21	2,4
Scandium	Sc 45	31,8	31,3	30,1	0,85	1,4
Chromium	Cr 52	289	278	311	23,3	4,0
Cobalt	Co 59	45	43,9	45,8	1,34	1,5
Nickel	Ni 60	121	120	120	0,00	0,0
Copper	Cu 63	136	143	148	3,54	1,2
Zinc	Zn 66	105	122	121	0,71	0,3
Gallium	Ga 71	21	21	21	0,00	0,0
Rubidium	Rb 85	11	9,15	9,46	0,22	1,2
Strontium	Sr 86	403	364	359	3,54	0,5
Yttrium	Y 89	27,6	25,3	26,6	0,92	1,8
Zirconium	Zr 90	179	168	169	0,71	0,2
Niobium	Nb 93	19	19,7	17,5	1,56	4,2
Molybdenum	Mo 95	1,02	1,20	1,14	0,04	1,8
Caesium	Cs 133	0,13	0,13	0,1	0,02	9,2
Barium	Ba 137	139	121	121	0,00	0,0
Lanthanum	La 139	15,8	14	14,5	0,35	1,2
Cerium	Ce 140	39	34,1	36,2	1,48	2,1
Praeseodymium	Pr 141	5,7	4,81	5,22	0,29	2,9
Neodymium	Nd 146	25,2	22,4	24,4	1,41	3,0
Samarium	Sm 147	6,2	5,72	6,23	0,36	3,0
Europium	Eu 151	2,06	1,88	2,06	0,13	3,2
Gadolinium	Gd 157	6,4	5,79	6,01	0,16	1,3
Terbium	Tb 159	0,96	0,85	0,91	0,04	2,4
Dysprosium	Dy 163	5,2	5,2	5,2	0,00	0,0
Holmium	Ho 165	0,99	0,88	0,96	0,06	3,1
Erbium	Er 166	2,4	2,32	2,53	0,15	3,1
Thulium	Tm 169	0,33	0,3	0,32	0,01	2,3
Ytterbium	Yb 172	2,02	1,84	1,99	0,11	2,8
Lutetium	Lu 175	0,29	0,25	0,28	0,02	4,0
Hafnium	Hf 178	4,38	4,36	4,71	0,25	2,7
Thallium	Tl 205	0,58	0,06	0,04	0,01	14,1
Lead	Pb 206+207+208	2,6	2,08	2,4	0,23	5,1
Uranium	U 238	0,42	0,43	0,43	0,00	0,0

Minor discrepancies between the concentration values for core 74KL and the respective values of core 74KL in the four time-slice maps may occur, because downcore values represent 1 cm thick samples, and time-slice values represent 4 cm thick samples, averaging over a longer sediment section. Accordingly, the time-slice samples are more likely to include proportions from microenvironments like scattered pyrite crystals, micro Mn nodules, single fish bones etc..

The total relative error, encountered for the concentration values of an element, is the relative error of the analytical precision (Tab. 4), plus a maximum error of 4% from the calculation of concentration values on a carbonate-and-opal-free-basis (1% from the $CaCO_3$ analyis, 1% for neglecting organic carbon content, and 2% for the presence of pore water salt).

Determination of Cd by ETAAS (electrothermal atomic absorption spectrometry)

Cd was measured on a Perkin Elmer, Zeeman 5000, ETAAS from the same solution as the ICP-MS samples. These measurements were done at the "Geologisch-Paläontologische Institut, Universität Kiel".

Determination of Al, Fe and Mg by ICP (electrothermal atomic absorption spectrometry)

These three elements were measured on a Perkin Elmer ICP/6000 from the same solution than the ICP-MS samples. These measurements were also done at the "Geologisch-Paläontologische Institut, Univ. Kiel".

Determination of the major elements by X-ray fluorescence

5 g of dry sediment was heated to 700°C and the volatile fraction was determined. 1g of the residue was mixed with 5 g $Li_2B_4O_2$ (Spectromelt A10) and melted to tablets. SiO_2, TiO_2, MnO, CaO, and P_2O_5 were determined on a Phillips PW 1400 at the "Mineralogische Institut, Universität Kiel" (Devey et al., 1994). Element concentrations in the bulk sample were then calculated by use of the volatile fraction and the atomic weight of the oxides. The sum of all oxides was always between 98 and 101% of the sample.

Determination of Na and K by AA/AE (Atomic Absorption/Emission) spectrophotometry

Na and K were measured on a "Instrumentation Laboratory" spectrophotometer (IL 157/IL 257) from the same solution as the ICP-MS samples. These measurements were also done at the "Geologisch-Paläontologische Institut, Universität Kiel".

Determination of marine and lithogenic $CaCO_3$ content

The marine and lithogenic proportions of the two $CaCO_3$ fractions were quantified using the method by Sirocko & Sarnthein (1989) (i.e., by the difference in the isotopic composition of $CaCO_3$). Fossil (lithic) $CaCO_3$, derived from Mesozoic and Cenozoic strata around the Persian Gulf, exhibit an average $\delta^{18}O$ composition of -6‰, a value measured in a dust sample from Arabia (Sirocko, 1989). On the other hand, marine plankton tests from the surface water have an oxygen isotope composition near to the isotopic composition of *G.ruber* (about -2‰), which is the species measured for age control of all cores (Fig. 16). The $\delta^{18}O$ isotopic composition of the bulk sediment sample (between the two endmember values (lithic = -6‰, marine= *G.ruber* value) served to calculate the relative proportions of both the lithic and the marine fraction from the bulk $CaCO_3$ content.

Determination of carbon and nitrogen content

Total C and total N of the bulk sediment was measured on an Carlo Erba CN-analyser on a 100 mg aliqout from the bulk sample. The data were measured at the "Zentrum für Meeres- und Klimaforschung, Universität Hamburg".

Determination of organic carbon content

C_{org} was determined by subtraction of carbonate-C from total-C.

Determination of sulfur content

S was measured on a LECO CS 125 analyzer at "GEOMAR" Kiel. The analysis was repeated three times on aliqouts of 50 mg of the bulk sample, and average values have been calculated.

Determination of the $^{87}Sr/^{86}Sr$ and $^{143}Nd/^{144}Nd$ isotope composition of the siliciclastic fraction

The $^{87}Sr/^{86}Sr$ and $^{143}Nd/^{144}Nd$ isotope composition of the siliciclastic fraction was determined on the residue after dissolution of carbonates with ultraclean acetic acid, and destruction of organic compounds with H_2O_2. The residue was centrifuged and the fluid discarded. 50 mg of the residue was then dissolved in HNO_3, HF, and $HClO_4$ in closed teflon vials at 160°C. The Sr fraction and the Nd fraction were separated by cation exchange on resin filled quartz columns. The $^{87}Sr/^{86}Sr$ and $^{143}Nd/^{144}Nd$ isotopic composition was measured on a Finnigan 261 MAT mass spectrometer at the "Max-Planck Institut für Chemie, Mainz". The values were corrected for mass fractionation by normalizing to $^{86}Sr/^{88}Sr=0.11940$. $^{143}Nd/^{144}Nd$ values were normalized to $^{146}Nd/^{144}Nd=0.7219$ and expressed as $\varepsilon Nd(0)$ $=[^{143}Nd/^{144}Nd(measured)/0.512638]-1]*1000$, using the present day value for the

bulk earth composition from Jacobsen & Wasserburg (1980). The acceptable precision of the $^{143}Nd/^{144}Nd$ is 0.000030 which is equal to an $\varepsilon Nd(0)$ of 0.6.

Determination of clay content [percent of the < 2µm grain size fraction in the siliciclastic fraction]
After leaching of the $CaCO_3$ fraction with acetic acid and leaching the organic fraction with H_2O_2, the grain size distribution of the residue was determined on a Sedigraph 5000 D. Data are from Sirocko (1989).

Determination of $\delta^{18}O$, $\delta^{13}C$ of *Globigerinoides ruber, Cibicides wuellerstorfi*, and the total $CaCO_3$ fraction
Isotopic measurements of the $\delta^{18}O$, $\delta^{13}C$ composition of planktonic foraminifera (*G.ruber*), benthic foraminifera (*C.wuellerstorfi*) and of the total carbonate fraction, were made with a Finnigan MAT 251 mass spectrometer at the C-14 Laboratory of the "Institut für Kernphysik, Universität Kiel". The MAT is coupled on-line to a Carbo-Kiel automated CO_2 preparation from carbonate samples. The system measures with an accuracy of ±0.07‰ for oxygen and ±0.04‰ for carbon isotopes. Calibration was done to the NBS 20, 19 and 18 standard. All values are reported on the Pee Dee belemnite (PDB) scale.

C. Results

C.1. Distribution patterns and high-resolution time series of element concentrations

Figs. 17-56 present distribution patterns and downcore variations of sedimentological parameters (Figs. 17-19) and various chemical elements (Figs. 20-56). The chemical elements are listed according to their atomic weight. Typical concentration values of elements in igneous rocks and sediments are given in Tab. 5, from Turekian & Wedepohl (1961), for comparison of the concentrations in the Arabian Sea sediments with rock data.

Carbonate content ($CaCO_3$)

The modern distribution pattern of carbonate reveals the lowest values in the northwestern Arabian Sea, especially in the Gulf of Oman, and maximum values on the Carlsberg Ridge (Fig. 17 a). The CaCO3 values used for Fig. 17 a-d were measured on a "Coulomat", see chapter B.3., thus, represent $CaCO_3$-carbonate only, equivalent to the "average of 2., 3." profile of core 74KL (Fig. 17 e).

The correlation between low $CaCO_3$ content and increasing waterdepth (Kolla et al., 1976a; Peterson & Prell, 1985; Von Stackelberg, 1972) as a result of dissolution of $CaCO_3$ in CO_2-rich bottom waters, cannot be observed in our data (Fig. 17 b), because all core locations lie well above the carbonate critical depth at 5000 m, most of them even above the lysocline at 3900 m waterdepth. The shallowest cores originate from the continental margin just below the oxygen minimum layer, which is usually found between 200 and 1200 m all over the Arabian Sea (Wyrtki, 1971). Thus, dissolution of carbonates appears to be a process less important, at least for sediment cores from above the lysocline. Instead, as in the long Pleistocene records of Murray & Prell (1991) or Clemens & Prell (1990), dilution by siliciclastic components seems to control the relative $CaCO_3$ concentration (Fig. 17 c). Accordingly, the distribution patterns of $CaCO_3$ during the Early Holocene, the Termination Ia, and the LGM (Fig. 17 b-d) also outline siliciclastic accumulation rates, which, thus, reached a maximum during the Termination Ia, and a minimum during the Early Holocene.

The 74KL $CaCO_3$ profile (Fig. 17 e), see chapter B.3. for the differences between the three curves, exhibits minimum values during the Termination Ia and a sharp transition between 132.5 cm and 125 cm towards higher values during E3.

Figure 17. (a) $CaCO_3$ content at the sediment surface, (b) $CaCO_3$ content during the Early Holocene (8000-10,000 cal-yrBP), (c) $CaCO_3$ content during the Termination Ia (16,000-18,000 cal-yrBP), (d) $CaCO_3$ content during the Last Glacial Maximum (21,000-23,000 cal-yrBP), (e) sediment core 74KL, arrows indicate the depth of AMS-^{14}C dates, converted to calendar years according to Tab. 1, hatched areas show events as defined in Fig. 12; (h) modern $CaCO_3$ content versus waterdepth, (i) modern $CaCO_3$ content versus lithic accumulation rate.

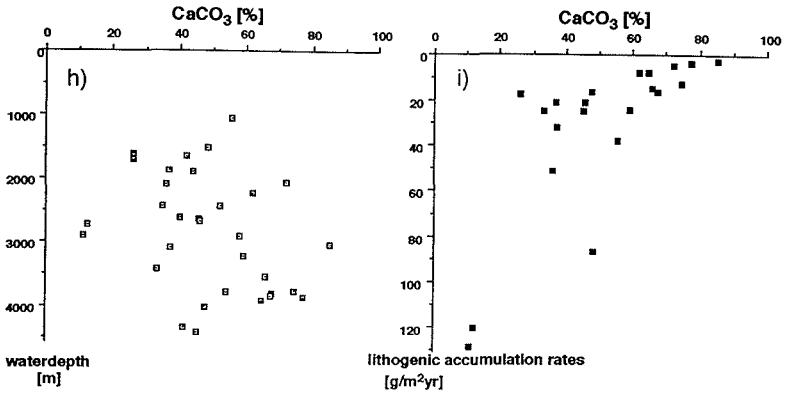

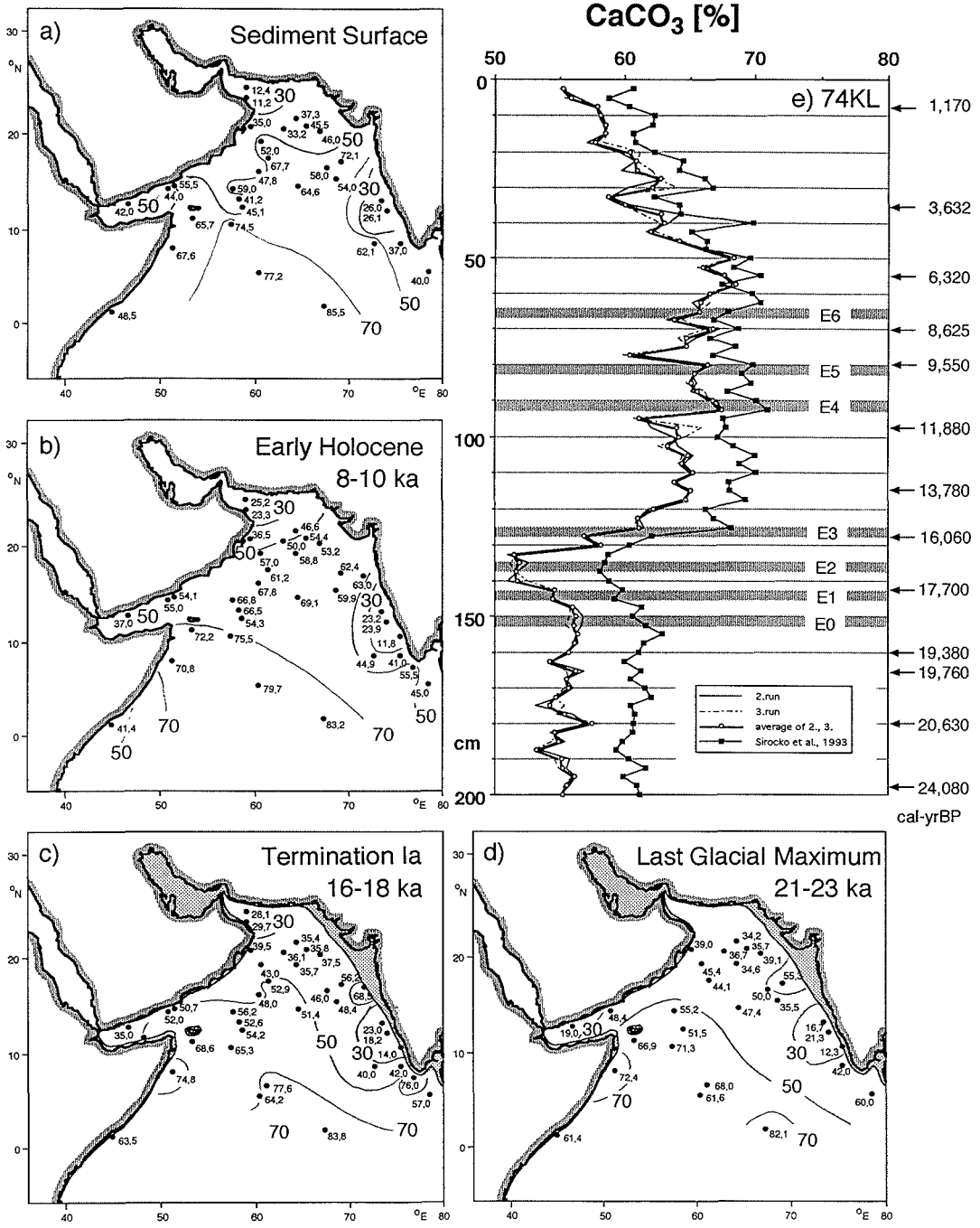

Biogenic Opal

The faunal composition of biogenic opal in the Arabian Sea was evaluated on smear slides of the silt fraction. Accordingly, opaline particles are in general highly affected by dissolution; especially the samples of the Termination Ia and of the Last Glacial maximum time-slice are extremely bad preserved. Well preserved specimens of several species can be observed only in the western Arabian Sea during the Holocene. In these samples, including core 74KL, the main components are: 80% Diatoms, 5-10% Radiolaria, 1-5% Silicoflagellates, 1% Sponge Spiculae. Thus, variations in biogenic opal content mainly reflects variations in diatom abundance.

Maximum opal concentrations, measured by leaching of the opal, occur in the western Arabian Sea during the Holocene (Fig. 18 a, b), indicating high flux values of upwelling derived biogenic particles. The concentration of opal does not outline directly the major coastal upwelling areas off Oman and Somalia, only accumulation rates of biogenic opal show this feature (Sirocko et al., 1991), because lithic flux rates are so high near the continents that they dilute the opal concentration values significantly. Accordingly, the opal concentration maximum is found about 500 km far away from the continents (i.e., where biogenic accumulation rates start to increase over lithic accumulation rates, *op.cit.).*

Biogenic opal concentrations were low all over the Arabian Sea during glacial times (Fig. 18 c, d), corroborating the finding of low upwelling intensity as reconstructed from the faunal composition of the sediments (Prell et al., 1980). The downcore profile of biogenic opal in sediment core 74KL shows the major transition between low glacial values and high Holocene values at 96.25 cm depth (i.e., 5 cm below event E4, Fig. 18 e). A further increase of opal content is observed below E5. Whether these offsets between the $\delta^{18}O$ events and the opal increase are real or being caused by a different degree of bioturbation is not known. The maximum of biogenic opal concentration during the Early Holocene is then found at the same depth as the dolomite minimum (85- 70 cm depth, Fig. 12), which is interpreted as the time of maximum northward propagation of the southwest monsoon (chapter D.3.). The synchronous maximum in opal concentrations shows that the Early Holocene was also the time of maximum upwelling strength in the western Arabian Sea.

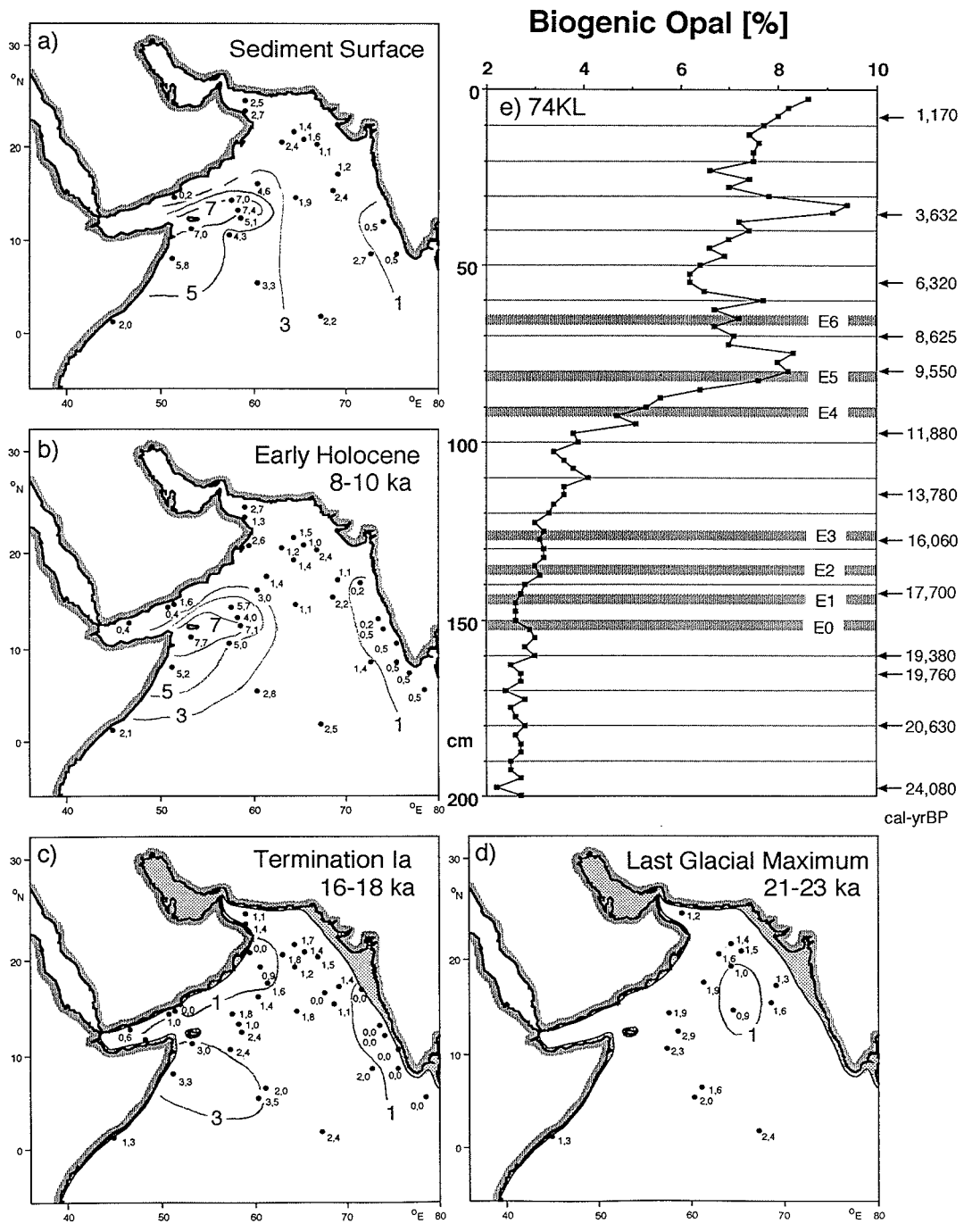

Figure 18. Biogenic opal content, (a) at the sediment surface, (b) during the Early Holocene (8000-10,000 cal-yrBP), (c) during the Termination Ia (16,000-18,000 cal-yrBP), (d) during the Last Glacial Maximum (21,000-23,000 cal-yrBP), (e) sediment core 74KL, arrows indicate the depth of AMS-^{14}C dates, converted to calendar years according to Tab. 1, hatched areas show events as defined in Fig. 12.

Grain size < 2 μm (clay fraction)

The distribution patterns of the clay size fraction for modern and glacial times exhibit continuous maxima far distant from the continents, and in addition, a local maximum in the Gulf of Oman during Holocene times (Fig. 19 a-d,). The glacial/interglacial transition in the <2μm record of sediment core 74KL starts at a depth of 130 cm, and shows a fairly continuous increase towards the Holocene, which is reached at a depth of 85 cm (Fig. 19 e).

Sirocko (1989) and Sirocko & Lange (1991) analyzed the clay mineral composition of the cores used in this study. Accordingly, the distribution pattern of palygorskite is most indicative of the transport in the mid-tropospheric northwesterly winds from Arabia (compare Fig. 5 and also Kolla et al. (1976 b). The northern branch of these northwesterlies that carry dust plumes from Iran and Pakistan is characterized by high chlorite and illite contents. Plumes derived from the Red Sea area are rich in smectite, and show significant amounts of amphiboles as far as to the Gulf of Aden. Quartz is found in the clay fraction of all samples at values of around 5%, and reveals its maximum in the northwestern sector of the Arabian Sea near the Gulf of Oman. Accordingly, the clay mineral assemblage in the western Arabian Sea is almost exclusively derived from Arabia, transported by means of wind, and consists of illite, smectite, kaolinite, chlorite, palygorskite, in decreasing order of abundance.

The clay mineral composition in the eastern Arabian Sea reflects its source from the Indian subcontinent, from where it is transported into the ocean mainly by rivers (Fig. 6). Most abundant are smectites (derived from the Deccan basalts) and illite (typical for the Indus), wheras palygorskite is completely missing in sediments derived from the Indian continent. A third source of clay minerals affects the sediments of the Gulf of Oman where an assemblage rich in illite, chlorite, kaolinte and quartz is discharged by local rivers draining the Makran ranges, and being most active during the Holocene.

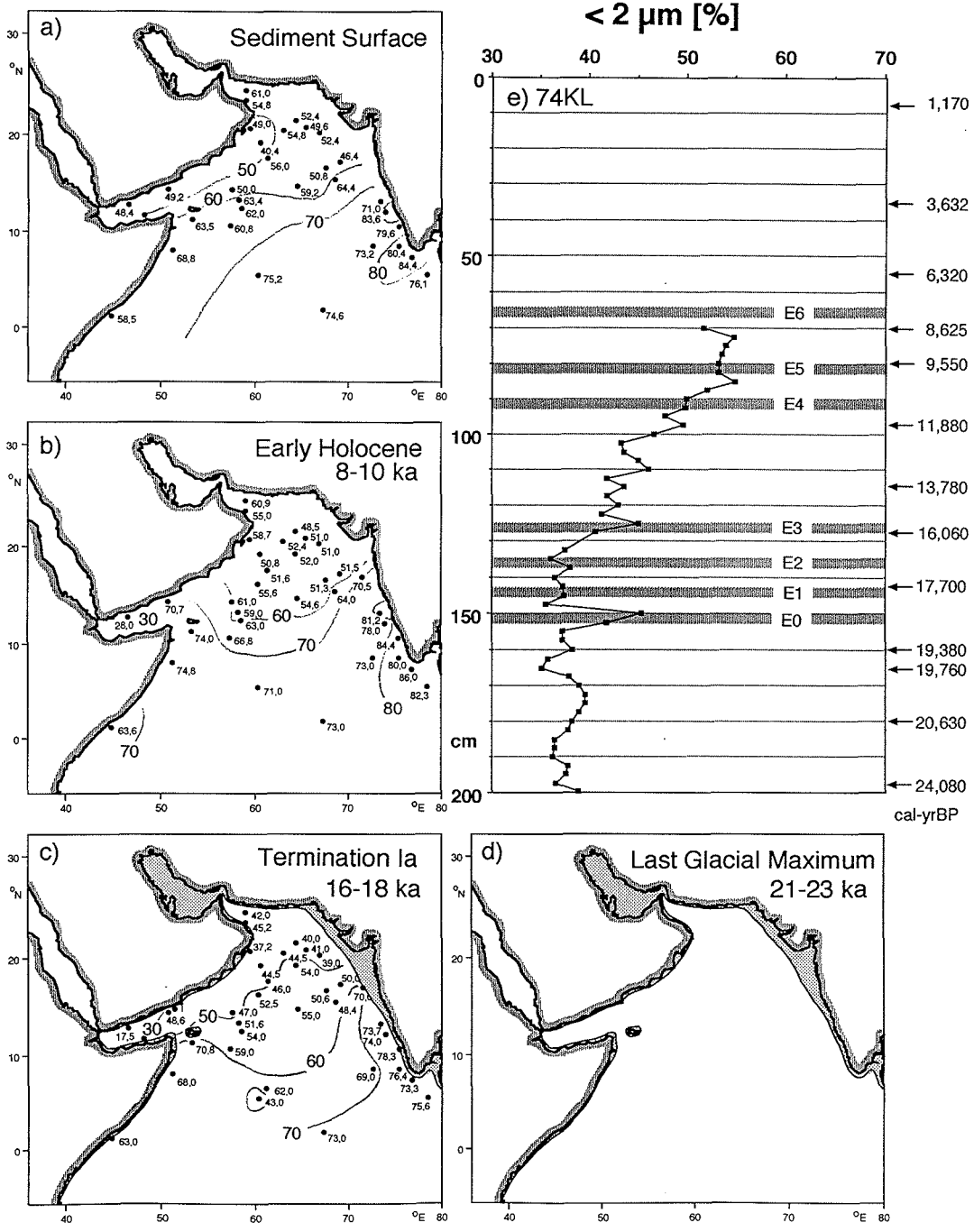

Figure 19. Grain size <2μm [%of the siliciclastif fraction], (a) at the sediment surface, (b) during the Early Holocene (8000-10,000 cal-yrBP), (c) during the Termination Ia (16,000-18,000 cal-yrBP), (d) during the Last Glacial Maximum (21,000-23,000 cal-yrBP), (e) sediment core 74KL, arrows indicate the depth of AMS-^{14}C dates, converted to calendar years according to Tab. 1, hatched areas show events as defined in Fig. 12.

Lithium (Li)

Table 5. Li content in various rock types, from Turekian & Wedepohl (1961)

	Igneous Rocks				Sedimentary Rocks			Deep-Sea Sediments	
Ultrabasic	Basalts	Ca-Granite	Granite	Syenites	Shales	Sandstone	Carbonates	Carbonate	Clay
ppm: 0.X	17	24	40	28	66	15	5	5	57

Sediments of the Arabian Sea show a persistent minimum of Li concentrations at the Oman coast (Fig. 20 a-d), where sediments have been found to be relatively coarse grained, especially during glacial times. The maximum of Li content, however, occurs in the fine grained sediments of the equatorial Arabian Sea and near to the coast of Somalia during glacial times. Li content in core 74KL decreases gradually between the glacial and the Holocene level and minimum contents are reached at a depth of 50 cm (i.e., during the middle Holocene, Fig. 20 e).

The leachable fraction of Li in core 74KL is negligible (Tab. 13), showing that only minor proportions of Li are adsorbed to particle surfaces. Li is, instead, highly enriched in the clay fraction (Tab. 13). The areal distribution of Li resembles the pattern of clay content (Fig. 19), thus corroborating this link. The downcore profile of Li, however, is opposite to the profile of clay content in core 74KL, indicating that the element is in particular incorporated into a specific clay mineral. This clay mineral could be illite, because biotite minerals can enrich Li to an extreme content and the illite content of core 74KL is lower during the Holocene than during the glacial (Sirocko, 1989; H. Lange, unpubl. data).

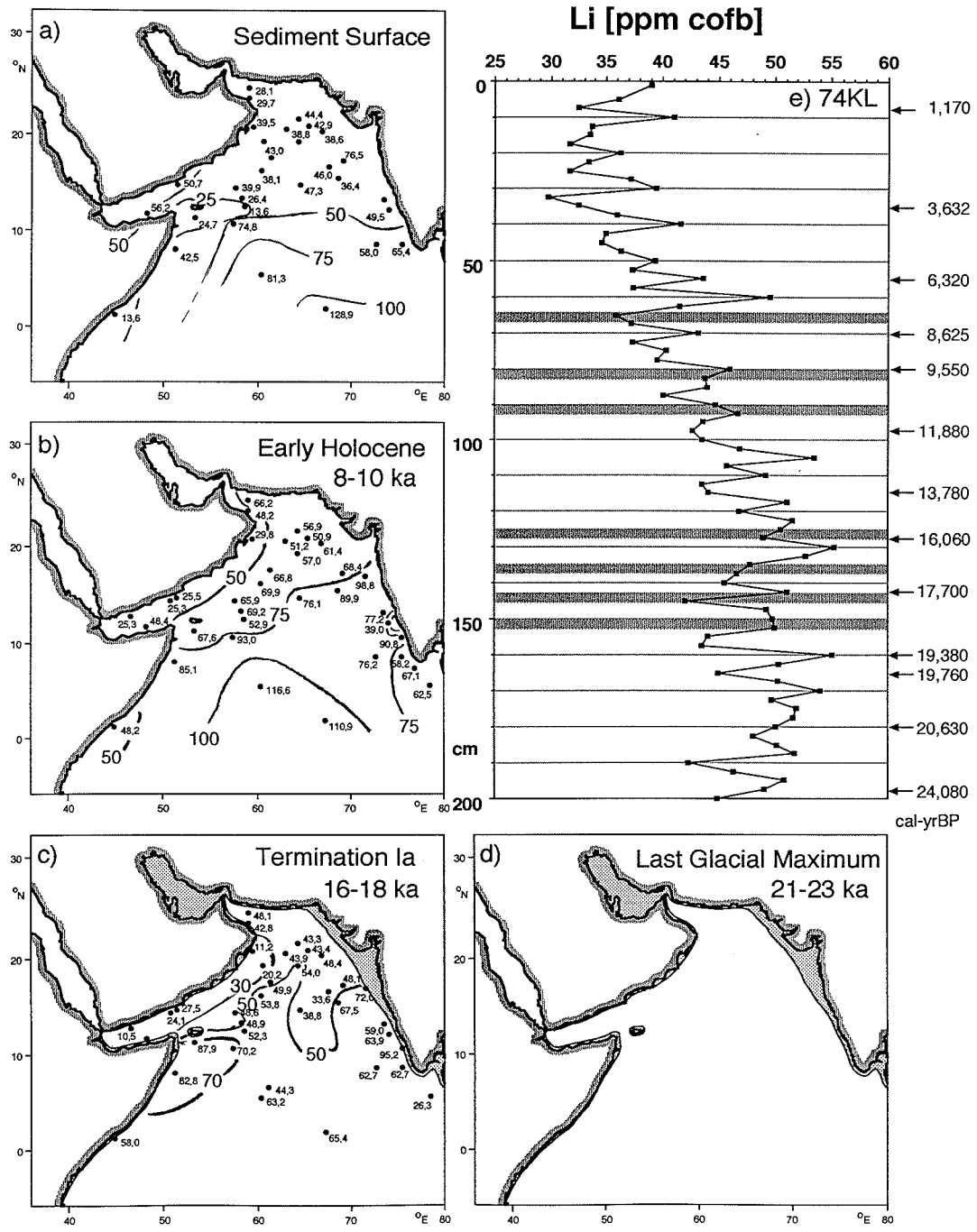

Figure 20. Lithium content, (a) at the sediment surface, (b) during the Early Holocene (8000-10,000 cal-yrBP), (c) during the Termination Ia (16,000-18,000 cal-yrBP), (d) during the Last Glacial Maximum (21,000-23,000 cal-yrBP), (e) sediment core 74KL, arrows indicate the depth of AMS-^{14}C dates, converted to calendar years according to Tab. 1, hatched areas show events as defined in Fig. 12.

Organic Carbon (C_{org})

The mechanisms that determine C_{org} concentration in the sediments of the Arabian Sea are being discussed with great controversy (Paropkari et al., 1992, versus Pedersen et al., 1992), especially for sediments being deposited at depth of the oxygen minimum zone. Physical mechanisms relating the C_{org} accumulation rates to surface water productivity have been found by Sarnthein et al. (1988), a relation to bottom water O_2 content has been described by Slater & Kroopnick (1984), and a first order correlation to sedimentation rate has been observed by Sirocko & Ittekkot (1992) and Emeis (1994). Near the continents, a terrestrial organic carbon fraction could in part explain these discepencies. At the location of core 74KL, however, the organic carbon fraction is known to be derived primarily from marine sources (Haake et al., 1992; Reemtsma & Ittekkot, 1992).

The distribution patterns of C_{org} concentrations at the sediment surface in the deep Arabian Sea reveal lowest values in the remote open ocean areas where both sedimentation rate and biogenic productivity are low, whereas high values are found in the western Arabian Sea (i.e., below the areas of high surface water productivity, Fig. 21 a, b). Accordingly, the distribution patterns of C_{org} content in the deep-sea sediments appear to reflect surface water productivity. Note that all cores studied in this work are located at depths below the oxygen minimum zone where mechanisms affecting the C_{org} preservation are probably more complex (Pedersen et al., 1992; Paropkari et al., 1992).

Following this line of evidence, the ocean-wide low C_{org} content during the time-slice of Termination Ia could be interpreted as representing low surface water productivity (Fig. 21 c, d). The high-resolution profile of C_{org} content in core 74KL shows this minimum to occur exactly between E0 and E3. C_{org} content during the LGM, however, was relatively higher than during Termination Ia. Either surface water productivity was higher during the LGM, or the preservation of C_{org} was increased during that time when deep-water ventilation was sluggish in the western Arabian Sea (see S and Mo (Figs. 28, 47), chapter D.1.).

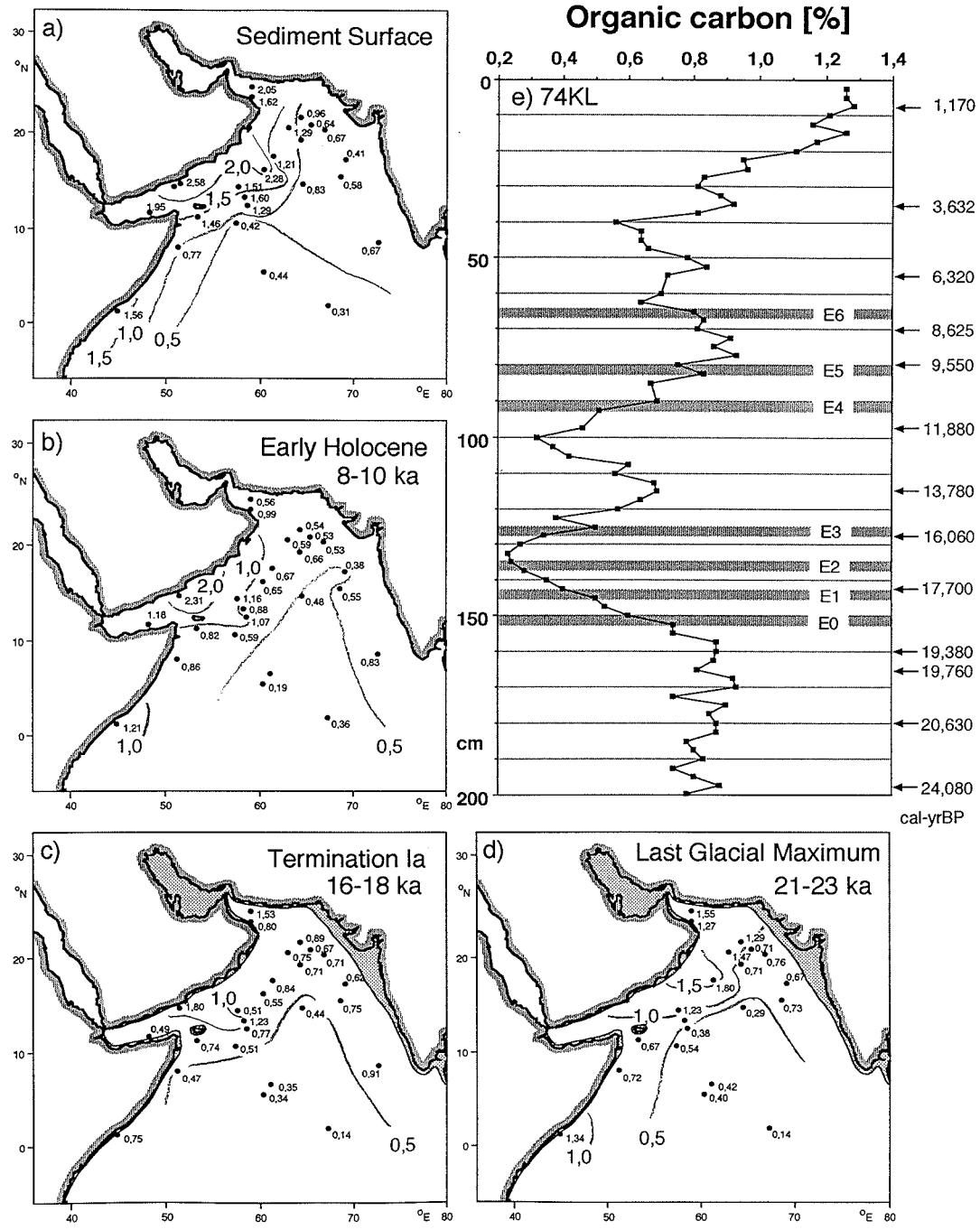

Figure 21. Organic carbon content, (a) at the sediment surface, (b) during the Early Holocene (8000-10,000 cal-yrBP), (c) during the Termination Ia (16,000-18,000 cal-yrBP), (d) during the Last Glacial Maximum (21,000-23,000 cal-yrBP), (e) sediment core 74KL, arrows indicate the depth of AMS-^{14}C dates, converted to calendar years according to Tab. 1, hatched areas show events as defined in Fig. 12.

Nitrogen (N)

Nitrogen concentrations in marine sediments are related directly to C_{org} contents, because marine organisms incorporate both elements in a fixed molar ratio of C/N = 7/1, which represents the ratio of abundance in the dissolved phase in ocean water. Accordingly, distribution patterns and downcore variations of both elements should be very similar. Subtle differences in the behaviour of both elements are best recorded as the C/N ratio, and only C/N values are shown and discussed in this N-chapter.

In the Arabian Sea, most C/N values are close to the expected Redfield value of 7, but minimum values <5 characterize the open ocean, wheras values >10 are found in the northwestern Arabian Sea off Arabia and in the Gulf of Oman (Fig. 22 a-d). The major feature in the C/N record of core 74KL is a pronounced minimum at 130-140 cm depth (Fig. 22 e). Based on the modern pattern, where low C/N values reflect open ocean conditions, we may conclude that open ocean sedimentation patterns prevailed during that depth interval, and that the Termination Ia section between 130-140 cm depth represents the time of lowest upwelling productivity in the Arabian Sea, an interpretation which is corroborated by low C_{org}, Zn, Cd and Ba content during that interval (Figs. 21, 39, 48, 50), and a clear maximum in the abundance of tropical foraminifera at the same depth (Schulz, 1994). An explanation for the low N content during the glacial and also in the sediments of the modern open ocean may be that both C and N are remineralized to an extent that nondegradable, nonbiogenic proportions of N (those bound on clay mineral surfaces) become quantitatively important and lower the C/N ratio.

Another explanation of the low C/N ratios <5 in sediments at the Oman shelf and upper continental slope was given by Hermelin & Shimmield (1990), who proposed low C/N ratios as being indicative of winnowing, with a preferential removal of organic carbon. It appears unlikely, that core 74KL at 3212 m waterdepth experienced winnowing during Termination Ia times, but we cannot exclude this possibility, because the two foraminiferal layers in the deeper section of the core show that bottom water movements may occur sometimes also in the region of core 74KL (Fig. 11).

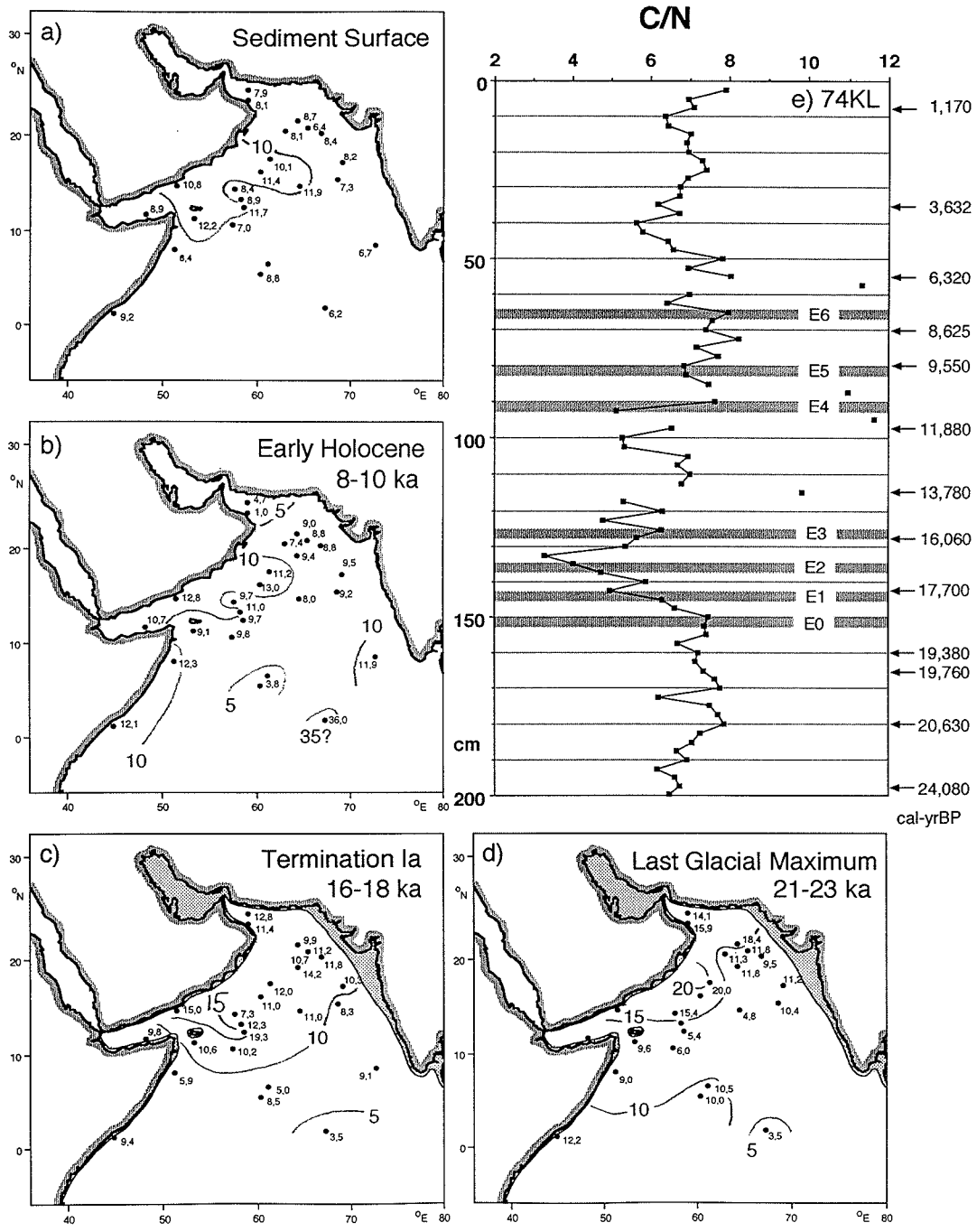

Figure 22. Nitrogen content, (a) at the sediment surface, (b) during the Early Holocene (8000-10,000 cal-yrBP), (c) during the Termination Ia (16,000-18,000 cal-yrBP), (d) during the Last Glacial Maximum (21,000-23,000 cal-yrBP), (e) sediment core 74KL, arrows indicate the depth of AMS-^{14}C dates, converted to calendar years according to Tab. 1, hatched areas show events as defined in Fig. 12.

Sodium (Na)

Table 5 continued. Na content in various rock types, from Turekian & Wedepohl (1961)

	Igneous Rocks				Sedimentary Rocks			Deep-Sea Sediments	
Ultrabasic	Basalts	Ca-Granite	Granite	Syenites	Shales	Sandstone	Carbonates	Carbonate	Clay
ppm: 4.2	1.8	2.8	2.6	4.0	1.0	0.3	0.04	2.0	4.0

Na content in igneous rocks is largely controlled by the abundance of Na-rich feldspars, clinopyroxenes or clinoamphiboles (Tab. 5). Clastic sediments usually show low Na contents, because Na is completely dissolved during weathering of the source rock and dissolved ions are concentrated in the river runoff to the ocean and its salt content. Deep-sea shales reveal higher Na levels because salt-derived Na is enclosed in the pore water of the sediments.

This interstitial Na is still present also in our samples, because samples were not desalted before measuring their chemical composition. The bulk Na concentrations, (expressed on a carbonate-and-opal-free-basis =cofb) appear to be highly affected by this pore water Na, because the distribution pattern of Na shows continuous maxima on the Carlsberg Ridge (Fig. 23 a-d), where $CaCO_3$ content is also highest (Fig. 17). These changes in carbonate content must effect the Na concentration values (cofb), because carbonate tests add to the pore volume, causing a higher pore water volume per unit of lithic sediments. Thus, any change in carbonate or opal content has to be monitored by the Na (cofb) content and distribution patterns and downcore variations of Na are not interpretable in our data set.

The Na-problem, as outlined above, is a good example to show how critical the choice of the right calculation algorithm (here cofb) is. For elements that are enriched in pore water the cofb-approach is not well suited. Fortunately, Na^+ is the only kation that is highly abundant in interstitial waters. Other elements are also prominent, except that their concentrations are magnitudes lower than the respective concentrations in the particulate fraction (Shaw et al., 1990). Thus, the problems arising for Na hold true for all elements, but except for Na they are of negligible importance.

The occurrence of hygroscopic NaCl (up to about 3%) in the samples introduces an error into the data evaluation, because all concentration values are presented on a carbonate-and-opal-free-basis. This error is as large as the error origination from the precision of the CaCO3 and biogenic opal analyis (±1%) and neglecting Corg content (up to 1,5%). In total, a maximum error of up to 5% has to be added to the relative error of the analytical precision (Tab. 4).

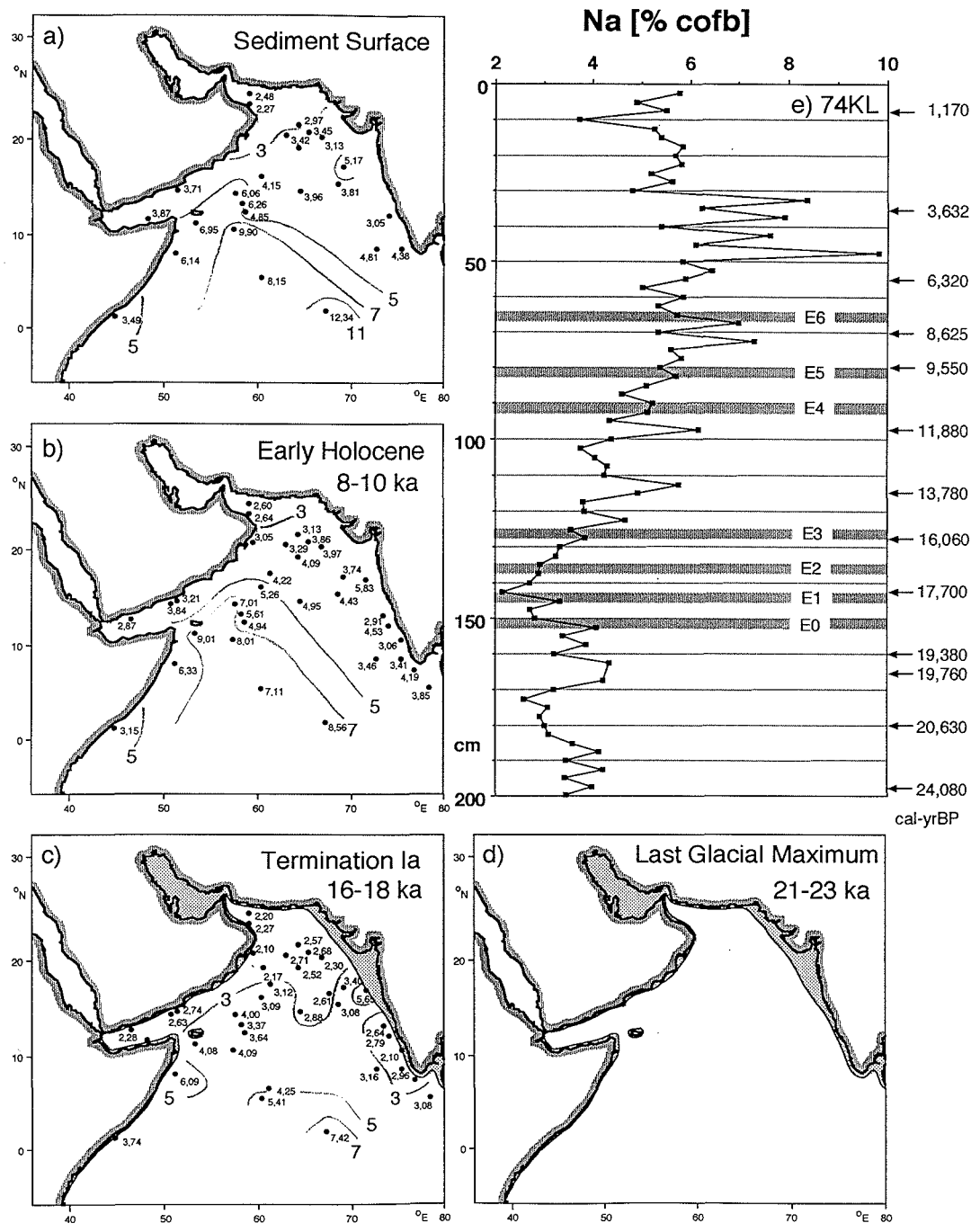

Figure 23. Sodium content, (a) at the sediment surface, (b) during the Early Holocene (8000-10,000 cal-yrBP), (c) during the Termination Ia (16,000-18,000 cal-yrBP), (d) during the Last Glacial Maximum (21,000-23,000 cal-yrBP), (e) sediment core 74KL, arrows indicate the depth of AMS-^{14}C dates, converted to calendar years according to Tab. 1, hatched areas show events as defined in Fig. 12.

Magnesium (Mg)

Table 5 continued. Na content in various rock types, from Turekian & Wedepohl (1961)

	Igneous Rocks				Sedimentary Rocks			Deep-Sea Sediments	
Ultrabasic	Basalts	Ca-Granite	Granite	Syenites	Shales	Sandstone	Carbonates	Carbonate	Clay
ppm: 20.4	4.6	0.94	0.16	0.58	1.5	0.7	4.7	0.40	2.10

The variations of Mg in rocks can largely be attributed to three processes that enrich Mg^{2+} ions in rock forming minerals. i) A substitution of Mg^{2+} for Fe^{2+} in crystal structures of Fe-rich minerals, preferentially in ultramafic olivines, pyroxenes, biotite and chlorite. ii) A substitution for Ca^{2+} in carbonates. The magnitude of the Mg incorporation into the carbonates depends on the Mg concentration of the solution, where the carbonates precipitate, culminating in the formation of dolomite in coastal sebkhas (e.g. around the Persian Gulf). iii) The Mg^{2+} ions have a large cation exchange capacity, and large amounts of Mg can be adsorbed onto clay particles.

The distribution pattern of Mg in the sediments of the Arabian Sea shows a persistent maximum in the western Arabian Sea off the coast of Yemen (Fig. 24 a-e). The source of the Mg-maximum are most likely dust plumes being transported from the Arabian desert towards the Arabian Sea during summer (compare Fig. 5) and which are rich in Mg-bearing minerals (i.e., palygorskite and dolomite, compare Sirocko et al., 1991).

Mg content (Fig. 24 c, e) in core 74KL reached highest values at 160-130 cm depth (i.e., during Termination Ia, when also $CaCO_3$ concentrations showed a minimum, interpreted as reflecting maximum dust discharge and maximum aridiy in Arabia during the deglacial, Fig. 17). The maximum of Mg during the $CaCO_3$ minimum reflects that these high dust loads were derived from Arabia.

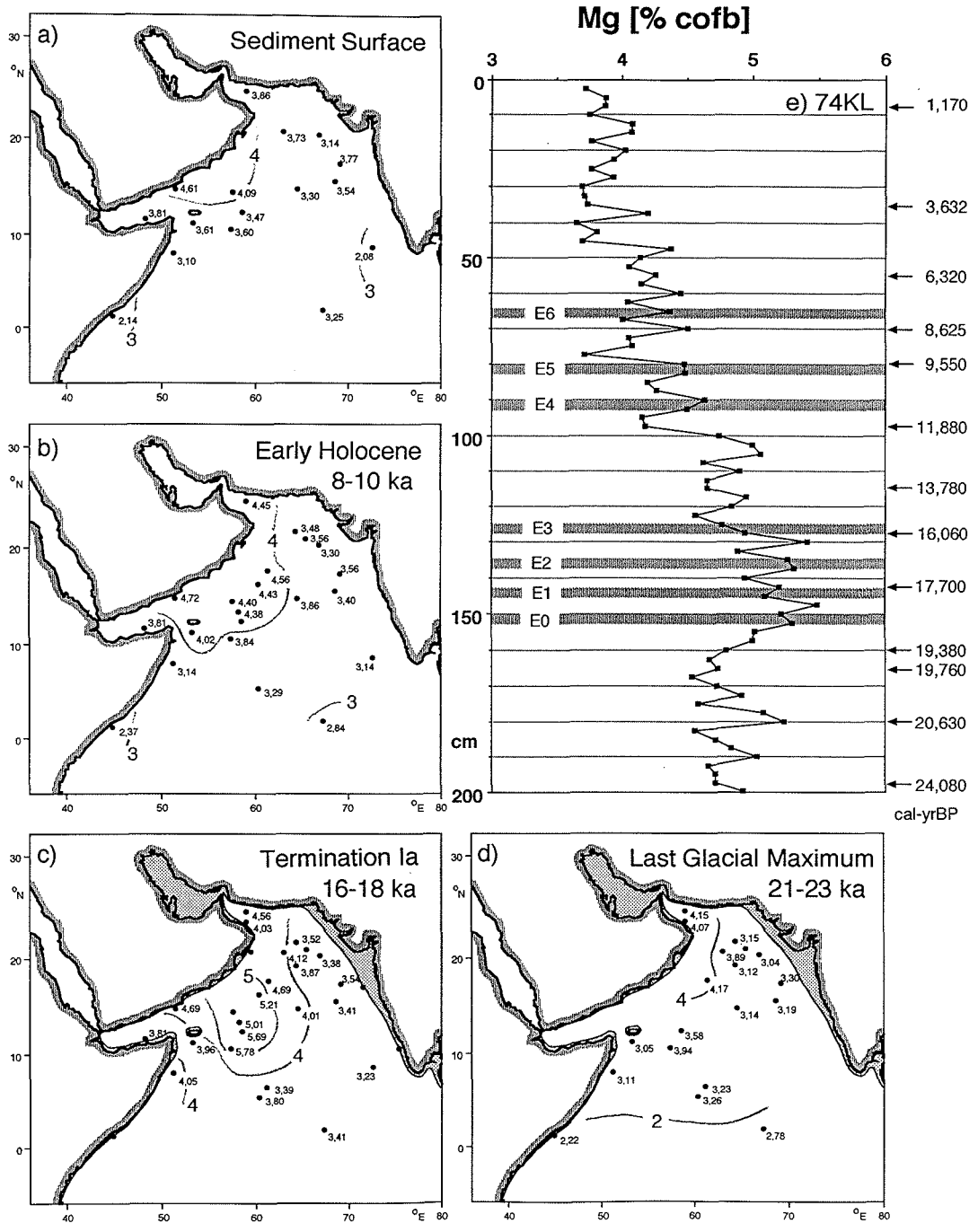

Figure 24. Magnesium content, (a) at the sediment surface, (b) during the Early Holocene (8000-10,000 cal-yrBP), (c) during the Termination Ia (16,000-18,000 cal-yrBP), (d) during the Last Glacial Maximum (21,000-23,000 cal-yrBP), (e) sediment core 74KL, arrows indicate the depth of AMS-^{14}C dates, converted to calendar years according to Tab. 1, hatched areas show events as defined in Fig. 12.

Aluminum (Al)

Table 5 continued, Al content in various rock types, from Turekian & Wedepohl (1961)

	Igneous Rocks				Sedimentary Rocks			Deep-Sea Sediments	
Ultrabasic	Basalts	Ca-Granite	Granite	Syenites	Shales	Sandstone	Carbonates	Carbonate	Clay
% 2.0	7.8	8.2	7.2	8.8	8.0	2.5	0.4	2.0	8.4

The tongue of low Al values (<6%) in the western Arabian Sea with a prevailing minimum off Yemen (<5%) could be a result of provenance, if the ultrabasic gabbros (low in AL content, Tab. 5) around the Red Sea would provide a significant source of dust (Fig. 25 a-d). A proof for such an inference would be a plume of high values of elements typically enriched in ultrabasites (Cr, Co, Ni, Figs. 33, 36, 37) in the area of the Al minimum; however, there is no such evidence. Another explanantion of the plume of low Al values in the western Arabian Sea could be a dilution with lithic components that are low in Al, like dolomite or palygorskite. Indeed the plume of palygorskite (Sirocko & Lange, 1991), as well as the maximum in the Mg distribution pattern (Fig. 24), match the area of low Al values. 10% of palygorskite in the clay fraction (Sirocko & Lange, 1991), see also (Faugères & Gonthier, 1981; Kolla et al., 1976b) plus (unquantified) contributions from the silt fraction could quantitatively account for the low Al values (cofb) off Arabia. This dilution affects all other elements that are not enriched in dolomite or palygorskite; accordingly, distribution patterns of all refratory elements, except Mg, reveal minimum concentrations off Arabia.

At core position 74KL, the glacial to interglacial change has to be seen in that regional context. The core is located at the very northern edge of the low Al plume and the southward shift of dust plumes during glacial times brings the core position under the influence of relatively Al-rich dust plumes from the Persian Gulf area. The maximum in Al concentrations in core 74KL is found between 150-130 cm depth (i.e., during the Termination Ia) when dust discharge from the west (Mg, Fig. 24) and also from north reached a maximum (Fig. 25 e).

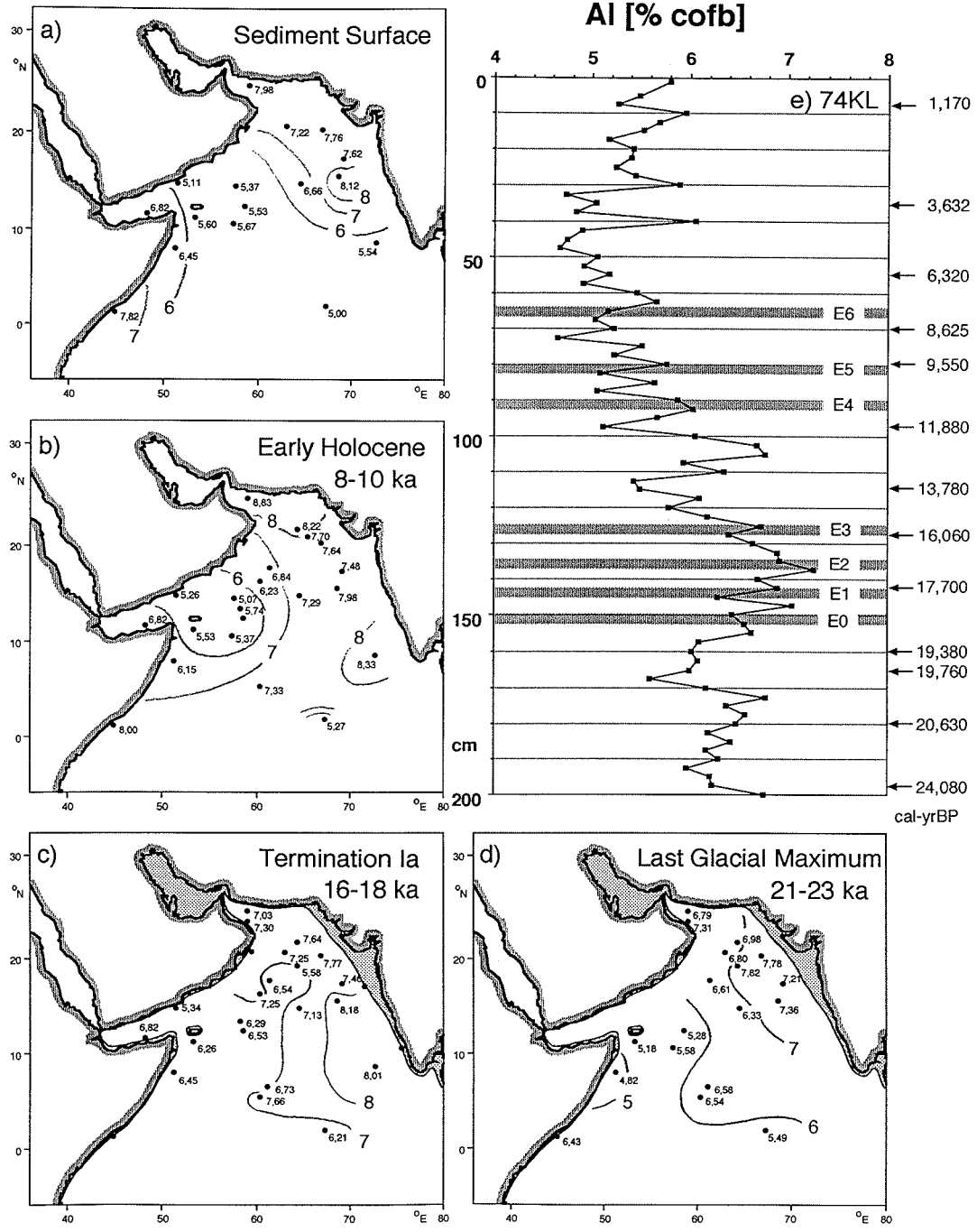

Figure 25. Aluminum content, (a) at the sediment surface, (b) during the Early Holocene (8000-10,000 cal-yrBP), (c) during the Termination Ia (16,000-18,000 cal-yrBP), (d) during the Last Glacial Maximum (21,000-23,000 cal-yrBP), (e) sediment core 74KL, arrows indicate the depth of AMS-^{14}C dates, converted to calendar years according to Tab. 1, hatched areas show events as defined in Fig. 12.

Silicon (Si)

Table 5 continued. Si content in various rock types, from Turekian & Wedepohl (1961)

	Igneous Rocks				Sedimentary Rocks			Deep-Sea Sediments	
Ultrabasic	Basalts	Ca-Granite	Granite	Syenites	Shales	Sandstone	Carbonates	Carbonate	Clay
ppm: 20.5	23.0	31.4	34.7	29.1	7.3	36.8	2.4	3.2	25.0

Si concentrations are corrected for biogenic opal derived Si by subtracting SiO_2 (opal) from the total SiO_2 content; the SiO_2 (opal) values were already corrected for water content of the diatomacous silica (Mortlock & Froelich, 1989).

The $Si_{(lithic)}$ content of the Arabian Sea sediments reveals a pertinent maximum off the coast of Pakistan and a gradient towards the south (Fig. 26 a-d). This pattern resembles the distribution pattern of quartz (Sirocko & Lange, 1991), although these authors had analyzed the clay-sized quartz content. Besides its direct relation to quartz content, the patterns of $Si_{(lithic)}$ concentrations reveal resemblance to the distribution patterns of the <2µm clay fraction. In particular, the very low $Si_{(lithic)}$ content below 15% on the remote Carlsberg Ridge can only be explained by very low Si content of the clay minerals that contribute up to 75% of the clastic fraction in this area (Fig. 19). The pertinent maximum of $Si_{(lithic)}$ off Pakistan does not follow grain size variations, and can be thought to reflect a provenance of clastic particles in the Indus alluvial plain of northern India and Pakistan.

Sediment core 74KL shows high values during the glacial, followed by a decrease near events E3 and E4 towards low Holocene values (Fig. 26 e). Unfortunately, $Si_{(lithic)}$ content in 74KL was measured only at 5 cm intervals, and the interpretation of the downcore variations remains rather vague at this sample resolution. The variations of Si content in 74KL in the western Arabian Sea are most similar to the pattern of Al variations (Fig. 25), thus, like Al, reflecting dust discharge from the Persian Gulf area.

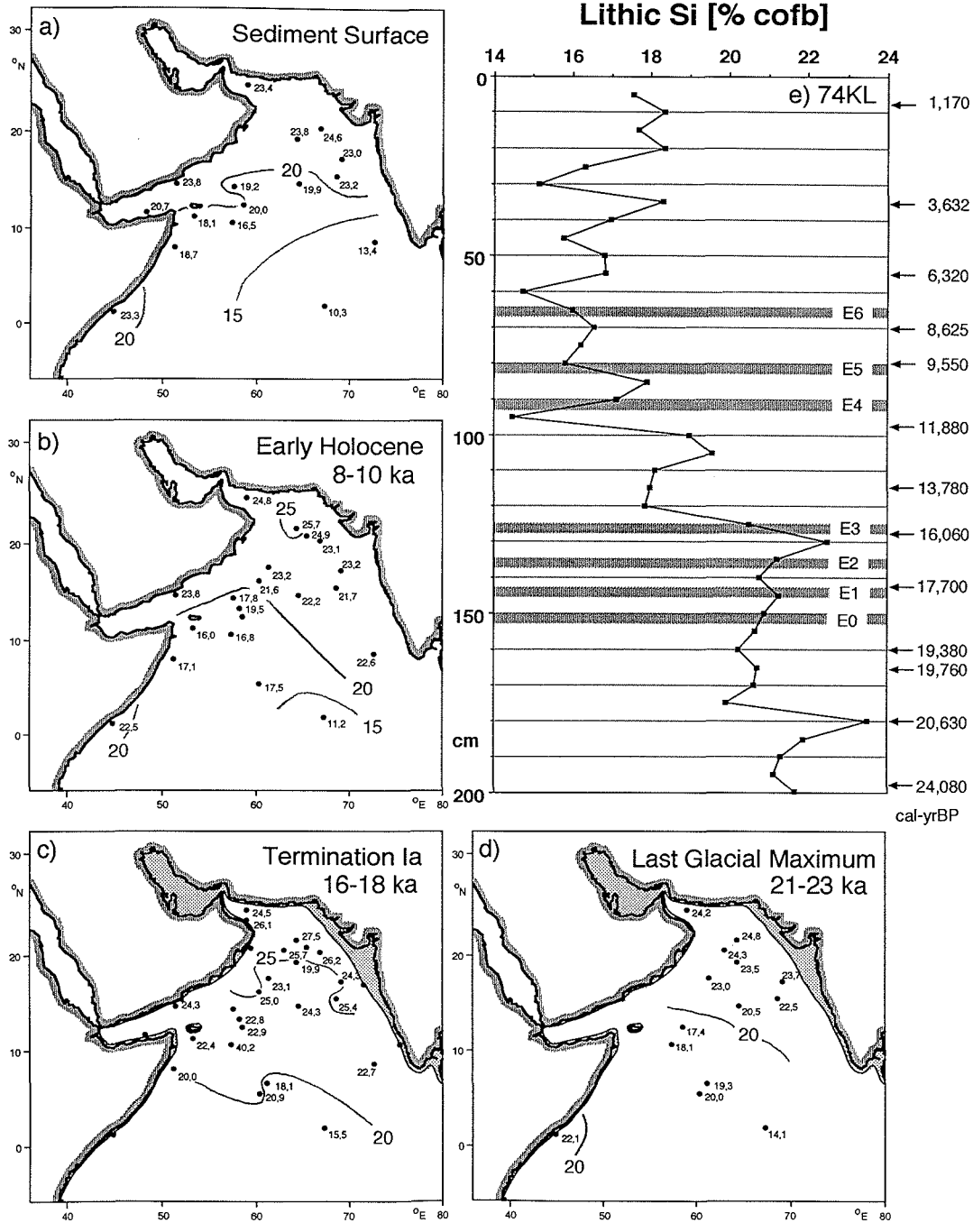

Figure 26. Silicon content, (a) at the sediment surface, (b) during the Early Holocene (8000-10,000 cal-yrBP), (c) during the Termination Ia (16,000-18,000 cal-yrBP), (d) during the Last Glacial Maximum (21,000-23,000 cal-yrBP), (e) sediment core 74KL, arrows indicate the depth of AMS-^{14}C dates, converted to calendar years according to Tab. 1, hatched areas show events as defined in Fig. 12.

Phosphorus (P)

Table 5 continued. P content in various rock types, from Turekian & Wedepohl (1961)

Igneous Rocks					Sedimentary Rocks			Deep-Sea Sediments	
Ultrabasic	Basalts	Ca-Granite	Granite	Syenites	Shales	Sandstone	Carbonates	Carbonate	Clay
%: 0.02	0.11	0.09	0.06	0.08	0.07	0.02	0.04	0.04	0.15

Concentration values of P in igneous and sedimentary rocks are usually below 0.1%, but values >0.15% may occur in deep-sea clays. P contents of sediments can reach maximum values (7.6-9.4%) when apatite, a Ca-phosphate, is abundant, a mineral which is formed from all kinds of organic debris, but preferentially from fish bones. Another P-rich authigenic mineral is xenotime (a HREE phosphate; 5.0-7.5% P content), whereas the heavy mineral monazite (a LREE phosphate; 4.3-7.0% P content) is of terrestrial origin. Other lithic minerals, like quartz, feldspar, biotite, always show values of <0.03% P.

P contents in the Arabian Sea sediments reach values between 0.07 and 0.15% (Fig. 27 a-d), thus within the range of normal deep-sea clays. The maxima on the Carlsberg Ridge can be caused by minor apatite contents in the carbonate fraction, that result in computed maximum values when bulk P content is expressed on a carbonate-free basis.

Core 74KL shows five spikes of high P content (Fig. 27 e). These spikes are unique to the P profile, thus, could be caused by the occurrence of scattered fishbones in the sediments. The abundance of fish remains have not been analysed, and thus, this explanation is mere speculation. A general increase in P content can be observed at depth above 95 cm (i.e., in the Holocene section of 74KL). Higher surface water productivity during the Holocene, thus higher P-flux, would be in accordance with the increase in concentration values of other biologically mediated elements like Ni, Zn, Ba and biogenic opal content during that time (Figs. 37, 39, 50, 18).

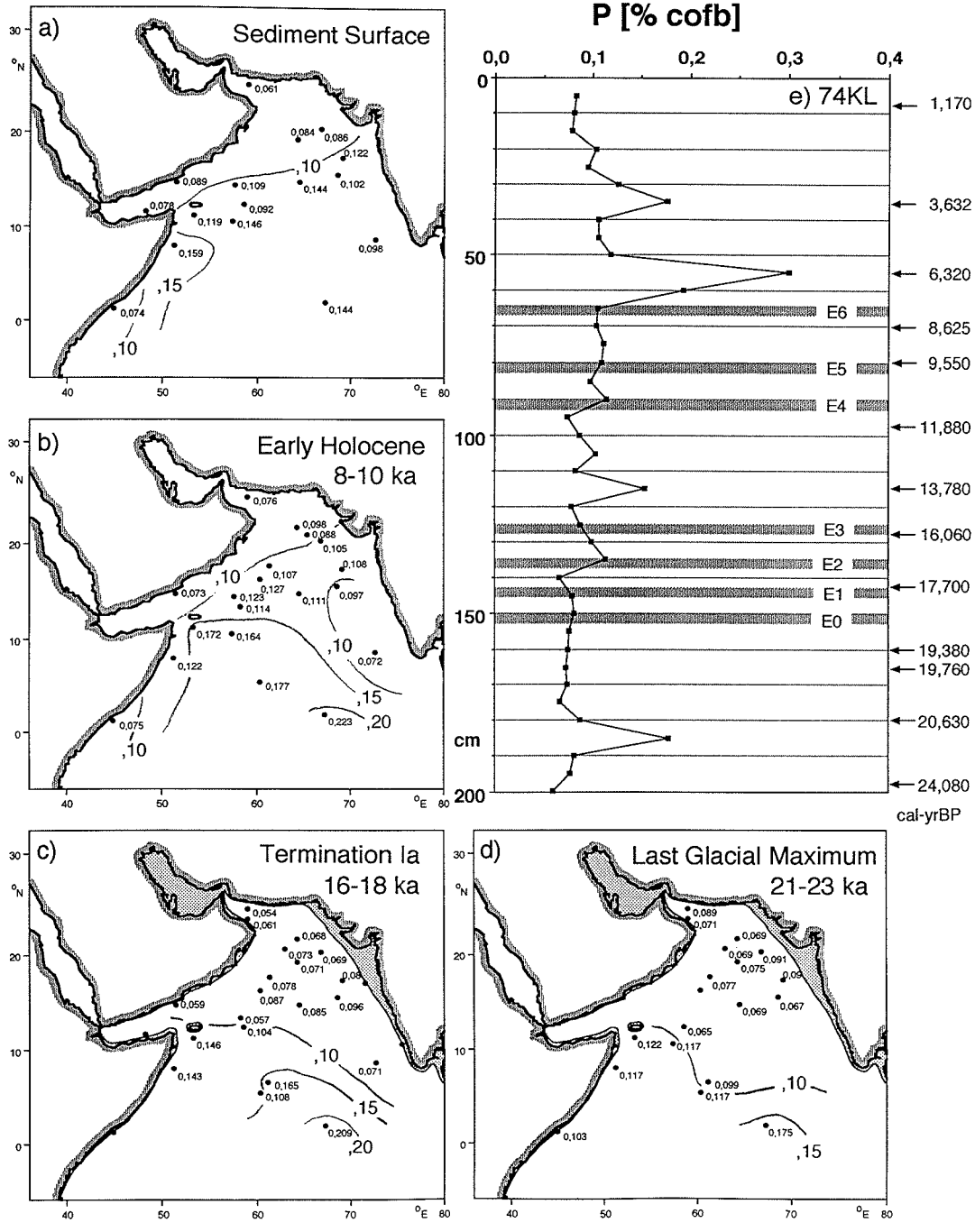

Figure 27. Phosphorus content, (a) at the sediment surface, (b) during the Early Holocene (8000-10,000 cal-yrBP), (c) during the Termination Ia (16,000-18,000 cal-yrBP), (d) during the Last Glacial Maximum (21,000-23,000 cal-yrBP), (e) sediment core 74KL, arrows indicate the depth of AMS-^{14}C dates, converted to calendar years according to Tab. 1, hatched areas show events as defined in Fig. 12.

Sulfur (S)

Table 5 continued, Na content in various rock types, from Turekian & Wedepohl (1961)

	Igneous Rocks				Sedimentary Rocks			Deep-Sea Sediments	
Ultrabasic	Basalts	Ca-Granite	Granite	Syenites	Shales	Sandstone	Carbonates	Carbonate	Clay
%: 0.03	0.03	0.03	0.03	0.03	0.24	0.02	0.12	0.13	0.13

Distribution patterns of S show a permanent maximum off Arabia (Fig. 28 a-d), depicting large similarities with the patterns of dolomite, representing dust plumes stemming from northern Arabia (Sirocko et al., 1991). The mineral composition of dust collections in the Persian Gulf region reveals indeed high amounts of dolomite, paralleled by high content of gypsum and anhydrite (14% of total lithic, Kukal & Saadallah, 1973). Dolomite, gypsum and anhydrite are frequent in the Mesozoic strata around the gulf (Chapman, 1978).

According to the similarities between S and dolomite abundance it seems plausible that S found in the deep-sea sediments of the western Arabian Sea was originally derived from an eolian, Arabian source. In the sediments, however, gypsum must dissolve and its S content adds to the formation of pyrite, if organic carbon and dissolved Fe-ions are available. High pyrite contents are observed in the glacial sections of sediments from the Gulf of Oman where S content reached maximum values during glacial times (Fig. 28 d) when dust discharge from the Persian Gulf/Mesopotamian region was at a maximum (Sirocko et al., 1991).

The most prominent change in the downcore variations of S is an abrupt decrease of bulk concentrations between 162.5 and 160 cm depth from high values during the Last Glacial Maximum to low values during the Termination Ia (Fig. 28 e). This decrease is also found in other easily reducible elements like Cr and Mo (Fig. 33, 47), which indicates that 162.5 cm is a level of major change in the reducing strength of sediments (chapter D.1.).

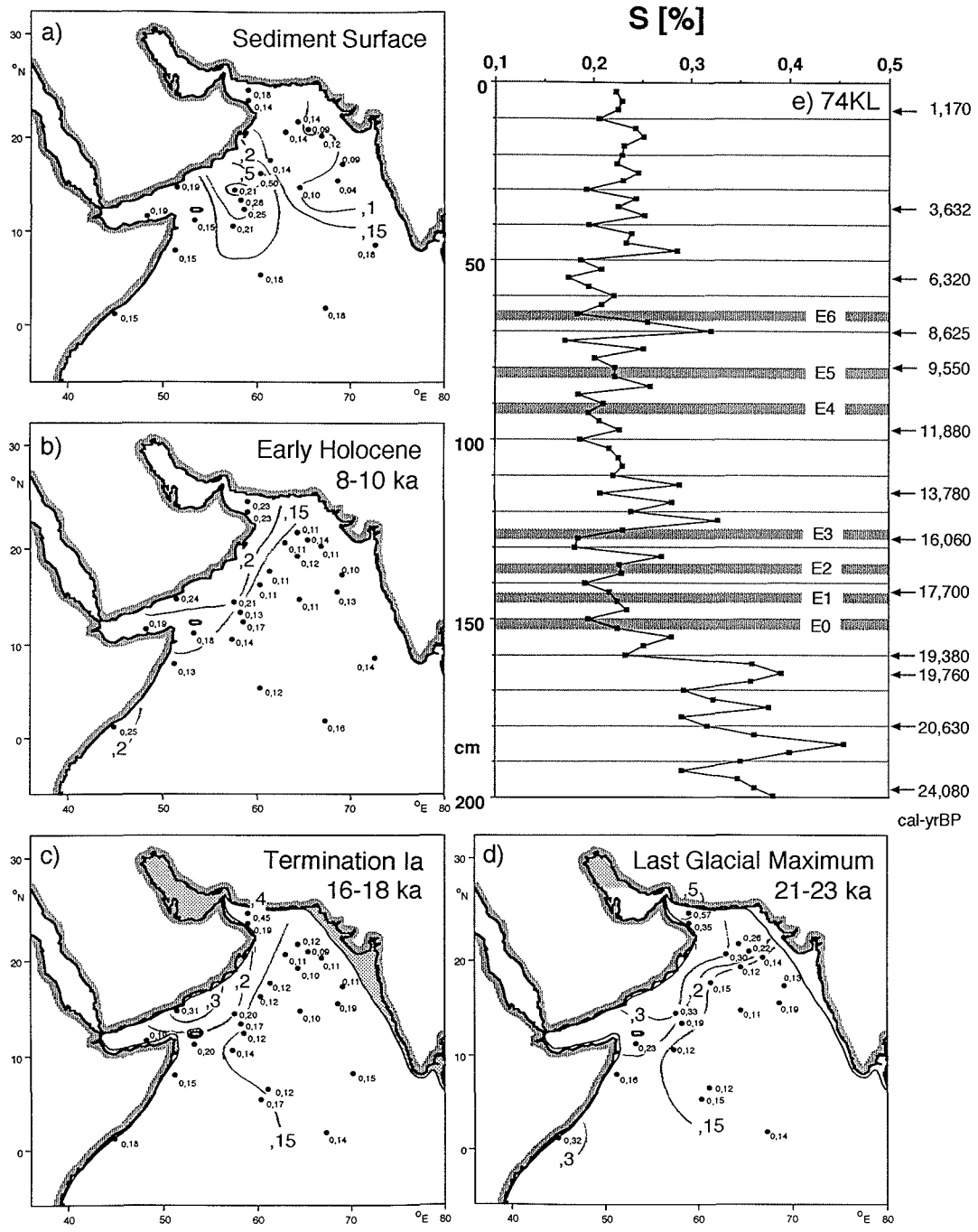

Figure 28. Sulfur content, (a) at the sediment surface, (b) during the Early Holocene (8000-10,000 cal-yrBP), (c) during the Termination Ia (16,000-18,000 cal-yrBP), (d) during the Last Glacial Maximum (21,000-23,000 cal-yrBP), (e) sediment core 74KL, arrows indicate the depth of AMS-^{14}C dates, converted to calendar years according to Tab. 1, hatched areas show events as defined in Fig. 12.

Potassium (K)

Table 5 continued. K content in various rock types, from Turekian & Wedepohl (1961)

	Igneous Rocks				Sedimentary Rocks			Deep-Sea Sediments	
Ultrabasic	Basalts	Ca-Granite	Granite	Syenites	Shales	Sandstone	Carbonates	Carbonate	Clay
ppm: 0.004	0.08	2.5	4.2	4.8	2.7	1.1	0.27	0.29	2.5

In the Arabian Sea sediments we observe three source areas of K, best depicted in the distribution patterns of surface sediments, which reveal plumes stemming from Oman/Pakistan, middle India, and Somalia (Fig. 29 a). The Indian source dominates the patterns at the sediment surface and at 8-10 ka (Fig. 29 a, b), but the Somalian source was not active at 8-10 ka. K contents are in general higher all over the Arabian Sea during the Termination Ia, but are lower in the Gulf of Oman. Maximum values are observed in the central Arabian Sea during Termination Ia, possibly caused by an overlap of the Arabian and the Indian plume.

In core 74KL we observe a pronounced maximum between 150 and 125 cm depth (Fig. 29 e), a maximum which can be also seen in the Mg and Al record (Fig. 24, 25). Apparently, dust discharge from northern and central Arabia was at a maximum during the Termination Ia. If the K content in these dust plumes is concentrated in the clay- or feldspar fraction of the eolian particles remains unresolved, because not only illite (rich in K) is abundant in the glacial sediments (Sirocko & Lange, 1991); alterated feldspar crystals are also frequently observed on smear slides of the glacial sediments. Unfortunately, the mineral composition of the silt fraction in the Arabian Sea sediments has not been studied yet.

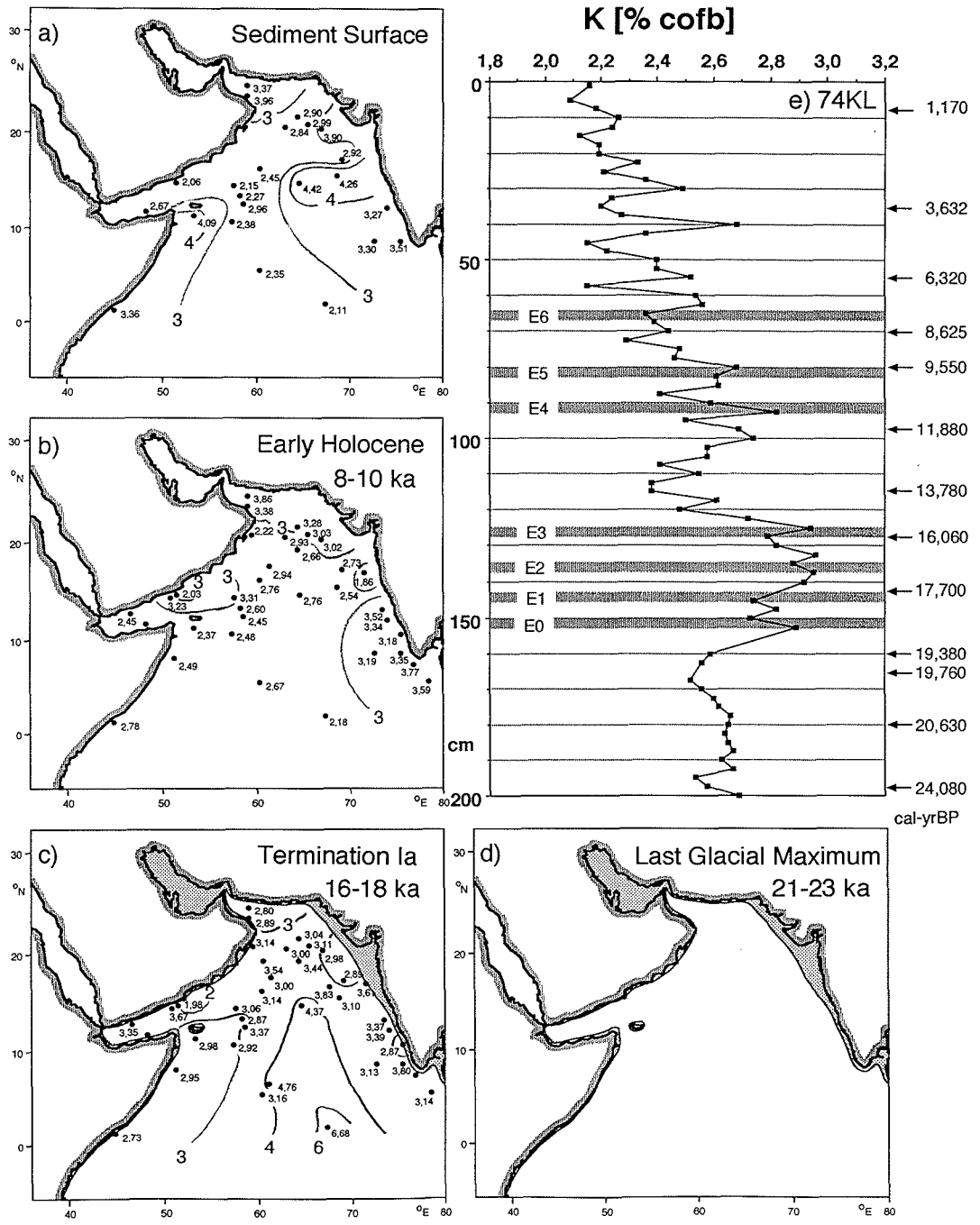

Figure 29. Potassium content, (a) at the sediment surface, (b) during the Early Holocene (8000-10,000 cal-yrBP), (c) during the Termination Ia (16,000-18,000 cal-yrBP), (d) during the Last Glacial Maximum (21,000-23,000 cal-yrBP), (e) sediment core 74KL, arrows indicate the depth of AMS-^{14}C dates, converted to calendar years according to Tab. 1, hatched areas show events as defined in Fig. 12.

Table 5 continued. Ca content in various rock types, from Turekian & Wedepohl (1961)

Igneous Rocks					Sedimentary Rocks			Deep-Sea Sediments	
Ultrabasic	Basalts	Ca-Granite	Granite	Syenites	Shales	Sandstone	Carbonates	Carbonate	Clay
%: 2.5	7.6	2.5	0.5	1.8	2.2	3.9	30.2	31.2	2.9

Ca content is primarily concentrated in carbonates (Tab. 5), sedimentation patterns of which have been evaluated above (Fig. 17). Besides the various carbonates, non-carbonate Ca is found in feldspars and rocks rich in this minerals. Another Ca-rich mineral, which frequently occurs in marine sediments is apatit, a Ca-phosphate, which is formed from fish bones and other biogenic detritus. The calculation of non-$CaCO_3$-Ca content was done by subtracting the $CaCO_3$-Ca concentration from total CaO-Ca concentrations. Accordingly, dolomite-Ca is still incorporated in the Ca content as discussed below.

The distribution patterns of Ca in the Arabian Sea sediments show a continuous maximum in the equatorial region (Fig. 30 a-d). This pattern cannot be caused by dolomite-Ca, which has its maximum at the Oman coast. A possible eolian origin of feldspar-Ca on the Carlsberg Ridge is also unlikely, because eolian grain sizes are small in this remote area, and feldspar minerals are likely to dissolve in the deep ocean where sedimentation rates are low (2 cm/1000 years on the Carlsberg Ridge, Sirocko et al., 1991).

Accordingly, the only remaining source for high non-$CaCO_3$-Ca could be apatite, built by the decay of fishbones. A small amount of apatite, which must be present in all samples, must increase in relative abundance with rising $CaCO_3$ content, when concentration values are expressed on a carbonate-and-opal-free-basis (cofb). This mathematical algorithm could be responsible for the high relative Ca content in the central Arabian Sea (Fig. 30). The increase of non-$CaCO_3$-Ca in core 74kL at 95 cm depth, however, should show an actual increase in apatite formation (Fig. 30 e), because no $CaCO_3$ increase is observed at that depth level. This explanation is consistent with the evidence of an increase in upwelling productivity during event E4 (see chapter D.4.).

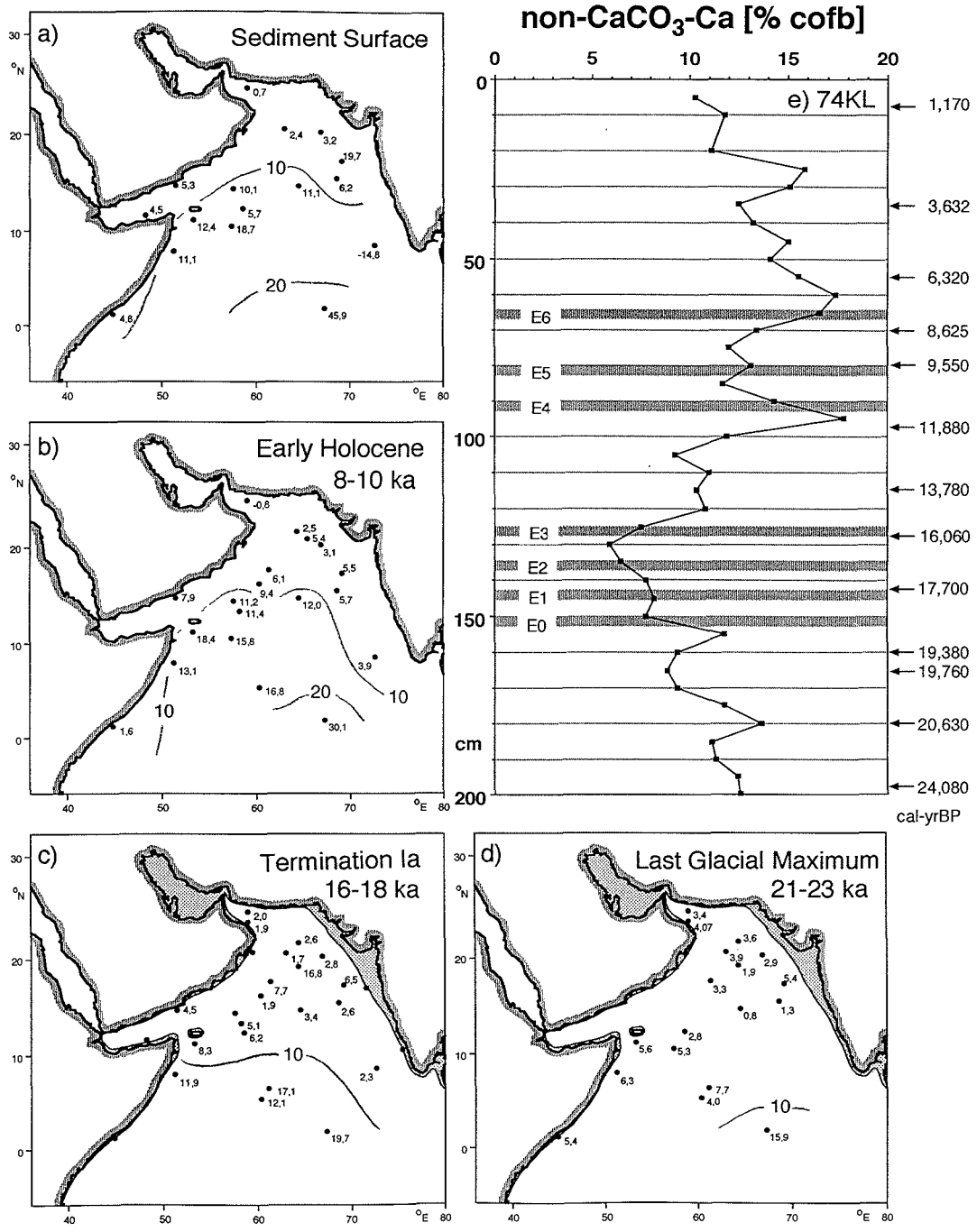

Figure 30. Non-$CaCO_3$ calcium content, (a) at the sediment surface, (b) during the Early Holocene (8000-10,000 cal-yrBP), (c) during the Termination Ia (16,000-18,000 cal-yrBP), (d) during the Last Glacial Maximum (21,000-23,000 cal-yrBP), (e) sediment core 74KL, arrows indicate the depth of AMS-^{14}C dates, converted to calendar years according to Tab. 1, hatched areas show events as defined in Fig. 12.

Scandium (Sc)

Table 5 continued. Sc content in various rock types, from Turekian & Wedepohl (1961)

	Igneous Rocks				Sedimentary Rocks			Deep-Sea Sediments	
Ultrabasic	Basalts	Ca-Granite	Granite	Syenites	Shales	Sandstone	Carbonates	Carbonate	Clay
ppm: 15	30	14	7	3	13	1	1	2	19

The distribution patterns of Sc during all three time-slices reveal maximum values off and south of the basalt plateau of the Deccan (Fig. 31 a-d), similar to what is observed in the distribution patterns of Ti, Fe and As (Fig. 32, 35, 41). The carrier phase of these elements is unknown; it could be the suspension load of the rivers Tapti and Narbada, which drain the Deccan, or could be the discharge of dissolved ions in these rivers.

High values of Sc content are also observed off Yemen, where dust plumes from gabbroic sources in south Arabia deliver their sediments to the ocean. The Holocene maximum of Sc concentrations at the southern coast of the Gulf of Aden could come from the same source, or indicate contributions from Ethiopian basalts, transported to the Gulf of Aden by southwest monsoon winds or small local rivers from the north Somalian mountains.

The profile of Sc content in core 74KL shows extremely high values of Sc at 142.5-137.5 cm depth (i.e., during the middle of Termination Ia, Fig. 31 e). The high Sc content at this depth might be real, because it was duplicated in repeated runs of ICP-MS analysis of that section; on the other hand, it cannot be excluded that the extremely high values present a contamination, because the sample from 74KL in the Termination Ia time-slice does not show the extreme enrichment of Sc at that time. Slightly higher values (significantly higher values, if the extremes at 140 cm depth are neglected) of Sc content are then found in the Holocene section of core 74KL above 87.5 cm depth, indicating a Holocene maximum in the abundance of mineral detritus derived from a mafic source, probably the Ethiopian or Red Sea area, where Sc-rich basalts are prominent .

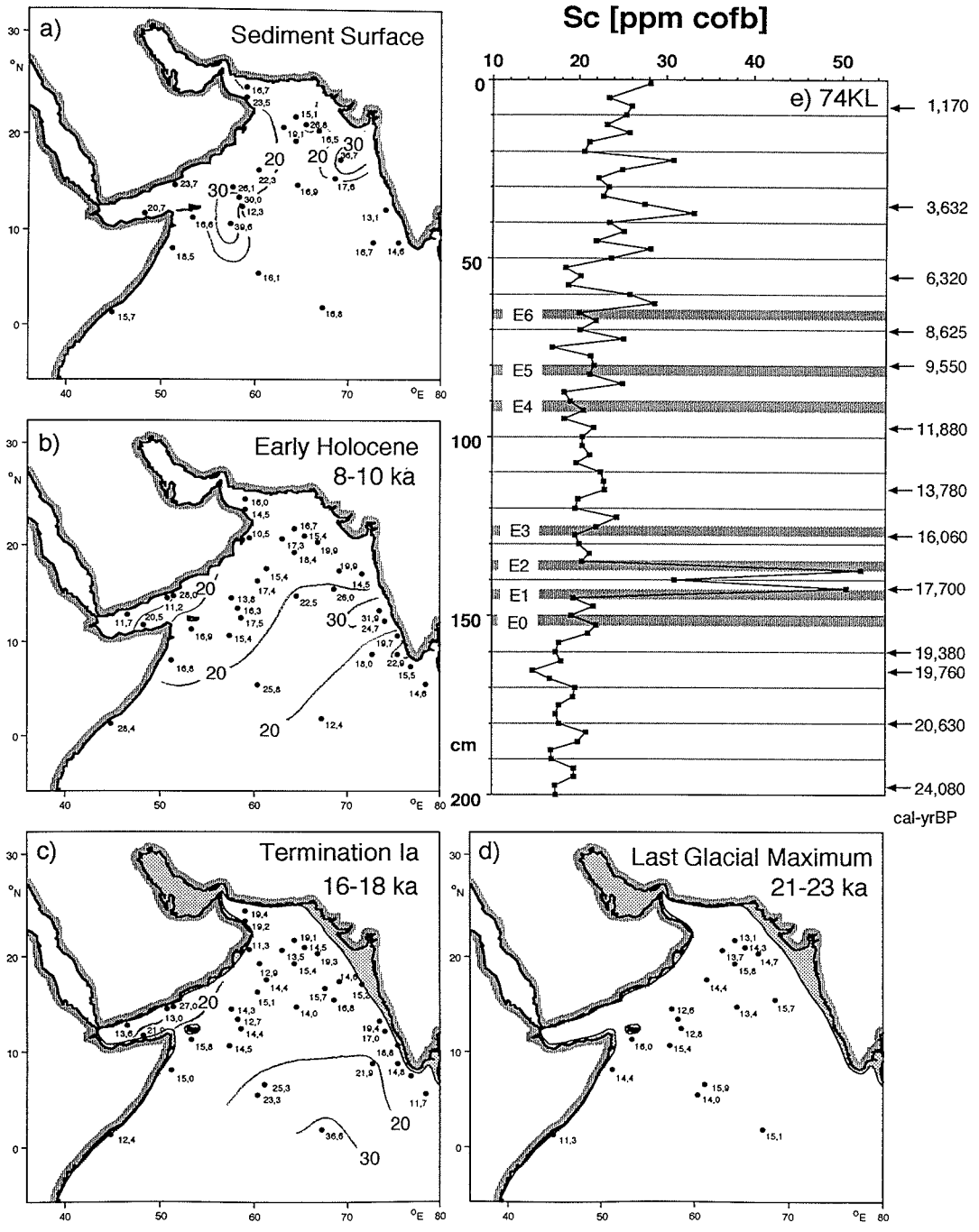

Figure 31. Scandium content, (a) at the sediment surface, (b) during the Early Holocene (8000-10,000 cal-yrBP), (c) during the Termination Ia (16,000-18,000 cal-yrBP), (d) during the Last Glacial Maximum (21,000-23,000 cal-yrBP), (e) sediment core 74KL, arrows indicate the depth of AMS-^{14}C dates, converted to calendar years according to Tab. 1, hatched areas show events as defined in Fig. 12.

Titanium (Ti)

Table 5 continued, Ti content in various rock types, from Turekian & Wedepohl (1961)

Igneous Rocks					Sedimentary Rocks			Deep-Sea Sediments	
Ultrabasic	Basalts	Ca-Granite	Granite	Syenites	Shales	Sandstone	Carbonates	Carbonate	Clay
ppm:0.03	1.38	0.34	0.12	0.35	0.46	0.15	0.04	0.08	0.46

Ti content in surface sediments of the Arabian Sea sediments show a maximum of Ti off the East African coast during the Holocene (Fig. 32 a), and another persistent maximum off middle India (Fig. 32 a-d); in both cases adjacent to basaltic source rocks (Deccan, Red Sea, Ethiopia), which are rich in Ti (Tab. 5). High Ti contents occur in shallower waters near the coast, an observation, which might be explained by two processes: i) winnowing at the sediment surface by current activity that concentrates Ti-rich heavy minerals (Shimmield et al., 1990b), ii) fast settling of heavy mineral particles out of dust plumes, which results in an enrichment of heavy minerals near the entrainment area of dusts. Both processes might operate in the coastal and marginal waters of the Arabian Sea near to basaltic source rocks.

Sediment core 74KL shows highest Ti content during the LGM, and a downcore profile similar to that of Al (Fig. 32 e). Accordingly the variations of Ti concentrations in the sediments over the open ocean resemble the dust flux from the Persian Gulf region, dominate the sedimentation patterns in the western and central Arabian Sea during glacial times (see chapter C.3.).

The pattern of Ti excess (Ti/Al, not shown) display a Holocene maximum off east Africa and an increase from low values during the glacial to high values subsequent to event E4 and E5, similar to the the pattern of Hf/Zr (Fig. 53 f). This probably reflects the increased contributions from the basalt provinces of East Africa and the Red Sea that deliver higher dust loads after the onset of the strong southwest monsoon during E4 (see chapter D.4.).

The Ti/Al values at the sediment surface have a correlation of 0.65 to the susceptibility of the same samples (deMenocal and Sirocko, unpubl. data). Accordingly, the relative abundance of Ti-bearing heavyminerals, derived from the East African/Red Sea basalts, control the susceptibility values of sediments in the Arabian Sea, corroborating the results (Bloemendal & deMenocal, 1989; Bloemendal et al., 1993). Susceptibility values at the coast of Arabia, where quartz-rich dust accumulation is highest, are, however, low.

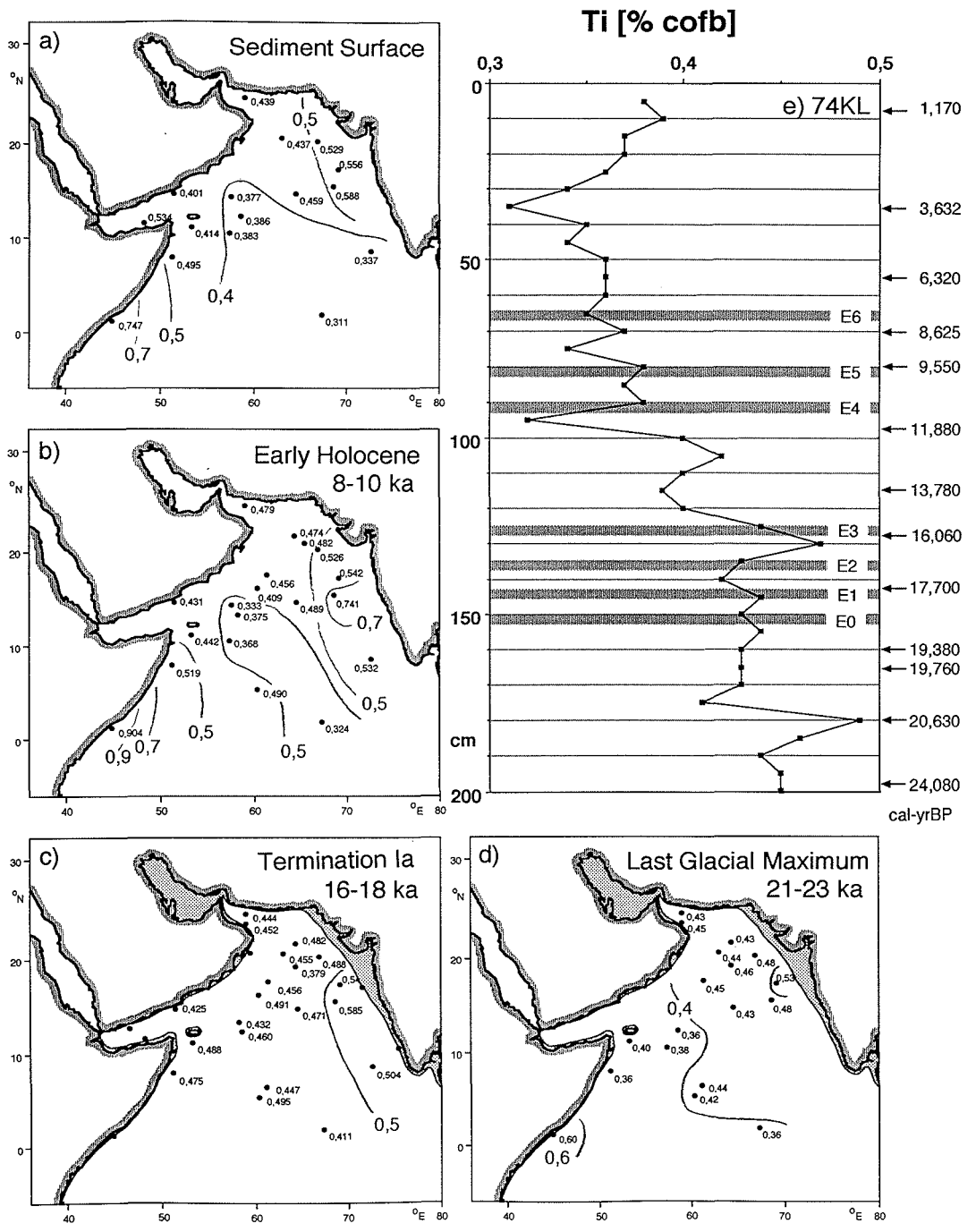

Figure 32. Titanium content, (a) at the sediment surface, (b) during the Early Holocene (8000-10,000 cal-yrBP), (c) during the Termination Ia (16,000-18,000 cal-yrBP), (d) during the Last Glacial Maximum (21,000-23,000 cal-yrBP), (e) sediment core 74KL, arrows indicate the depth of AMS-^{14}C dates, converted to calendar years according to Tab. 1, hatched areas show events as defined in Fig. 12.

Chromium (Cr)

Table 5 continued, Na content in various rock types, from Turekian & Wedepohl (1961)

Igneous Rocks					Sedimentary Rocks			Deep-Sea Sediments	
Ultrabasic	Basalts	Ca-Granite	Granite	Syenites	Shales	Sandstone	Carbonates	Carbonate	Clay
ppm: 1600	170	22	4.1	2.0	90.0	35.0	11.0	11.0	90

The Cr content of Arabian Sea sediments reveals a tongue-shaped distribution pattern with maximum values at the coast of Oman; these values of more than 150 ppm are higher than usually found in deep-sea sediments (Fig. 33 a). We can imagine three processes that lead to this Cr enrichment: i) High proportions of detrital chromite in dust particles derived from the ophiolites of Oman, Pakistan, and Iran, which contain Cr contents up to 5900 ppm (Mosley & Abbots, 1979). ii) High Cr contents in clay-minerals (illite) that are derived from soils in the ophiolite areas. iii) Enrichment of Cr in strongly reducing sediments.

The lack of Cr enrichment in the clay fraction and its minimal leachable proportion (Tab. 13.) indicate that most of the Cr in the northernmost Arabian Sea is, and was, of a clastic source. In this case, the source rocks of high Cr content are most likely the ophiolite-rich strata of Iran, Pakistan, and Oman, and the transport agent could be the prevailing northwesterly winds from the Persian Gulf region (compare Fig. 5).

The downcore variations of Cr in 74KL (Fig. 33e) look very similar to Al, which, like Cr, is preferentially derived from the Persian Gulf region. The occurrence of a Younger Dryas event at 110-97.5 cm depth in the Cr profile indicates that the northwesterlies from the Persian Gulf regions responded to that cold phase, whereas the northwesterlies form central Arabia (reconstructed from the Mg record, Fig. 24) did not show that response (see chapter D.4.).

Enrichment of Cr in stronlgy reducing sediments could be an alternate/ additional explanation of the high Cr content in the sediments of the Gulf of Oman during the LGM (Fig. 33 d), because the modern bottom water O_2 contents in the Gulf of Oman is less than 2 ml/l (Wyrtki, 1971) and glacial values can be expected to have been even lower (chapter D.1.). The highest Cr values in the LGM section of core 74KL, could be caused by this mechanism, because the decrease of Cr content at 160 cm (Fig. 33 e) parallels a decrease (probably caused by a intensification of deepwater ventilation, see chapter D.1.) of S, Mo and C_{org} content (Figs. 28, 47, 21) at the same level.

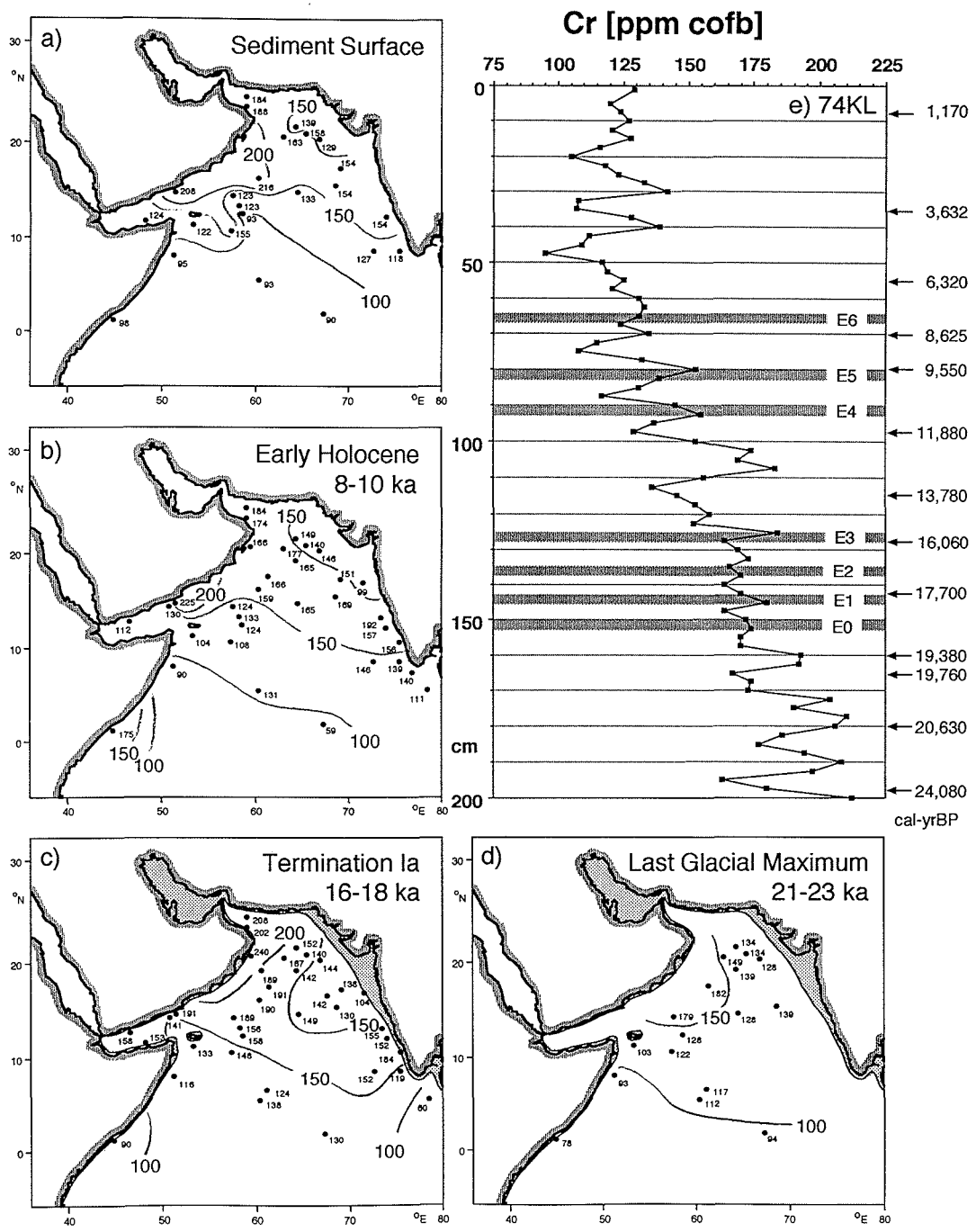

Figure 33. Chromium content, (a) at the sediment surface, (b) during the Early Holocene (8000-10,000 cal-yrBP), (c) during the Termination Ia (16,000-18,000 cal-yrBP), (d) during the Last Glacial Maximum (21,000-23,000 cal-yrBP), (e) sediment core 74KL, arrows indicate the depth of AMS-^{14}C dates, converted to calendar years according to Tab. 1, hatched areas show events as defined in Fig. 12.

Manganese (Mn)

Table 5 continued, Mn content in various rock types, from Turekian & Wedepohl (1961)

Igneous Rocks					Sedimentary Rocks			Deep-Sea Sediments	
Ultrabasic	Basalts	Ca-Granite	Granite	Syenites	Shales	Sandstone	Carbonates	Carbonate	Clay
ppm: 0.16	0.15	0.05	0.04	0.09	0.09	X0.	0.11	0.10	0.67

The spatial distribution pattern of Mn shows high values >0.5% at the sediment surface in the central Arabian Sea, indicating enrichment in the surface layer under open ocean conditions (Fig. 34 a). During the Early Holocene and especially during the Termination Ia, the Mn enrichment is confined to the central ocean (Fig. 34 b-d) where sedimentation rates are low (Sirocko, et al., 1991). The low C_{org} content of the cores from equatorial latitudes must result in a redox layer of up to 30 cm depth (following the C_{org}-Mn relation as developed by Finney & Mitchell (1988)). A yellowish, well oxydized surface layer was indeed observed for cores from the central Arabian Sea (Hashimi et al., 1984). With a sedimentation rate of 2.5 cm/1000 yrs, this 30 cm level is of an age of aproximately 12,000 yrBP;thus, the Mn enrichment in the time-slice samples of Termination Ia on the Carlsberg Ridge could simply reflect the depth of the major redox boundary in that low sedimentation rate area.

The depth of the oxydizing surface layer in core 74KL would be predicted (Finney & Mitchell, 1988) to be less than 3 cm at a C_{org} concentration of 2% at the sediment surface in core 74KL (Fig. 21 e); indeed, only very little Mn enrichment is observed in the uppermost cm of core 74KL (Fig. 34 e). A Mn maximum, however, is found at depth of the Early Holocene between 90-55 cm depth, which could present an synsedimentary maximum of Mn-sedimentation (Fig. 34 e), because there is no marked increase in the amount of the leachable proportion at that depth level, but a maximum of Mn enrichment in the clay fraction (Tab. 13).

The transition from low Mn content during the glacial to high Mn content during the Holocene occurred during events E3 and E4. These increases, as well as the pronounced minimum during Termination Ia in core 74KL, exactly parallels changes in C_{org} content (Fig. 21). Thus, concentrations of Mn and organic carbon must be closely coupled in core 74KL, except for the surface values, where both elements show a different behaviour. Probably, the more Mn is kept in the sediment the more reducing (carbon-rich) the sediments are.

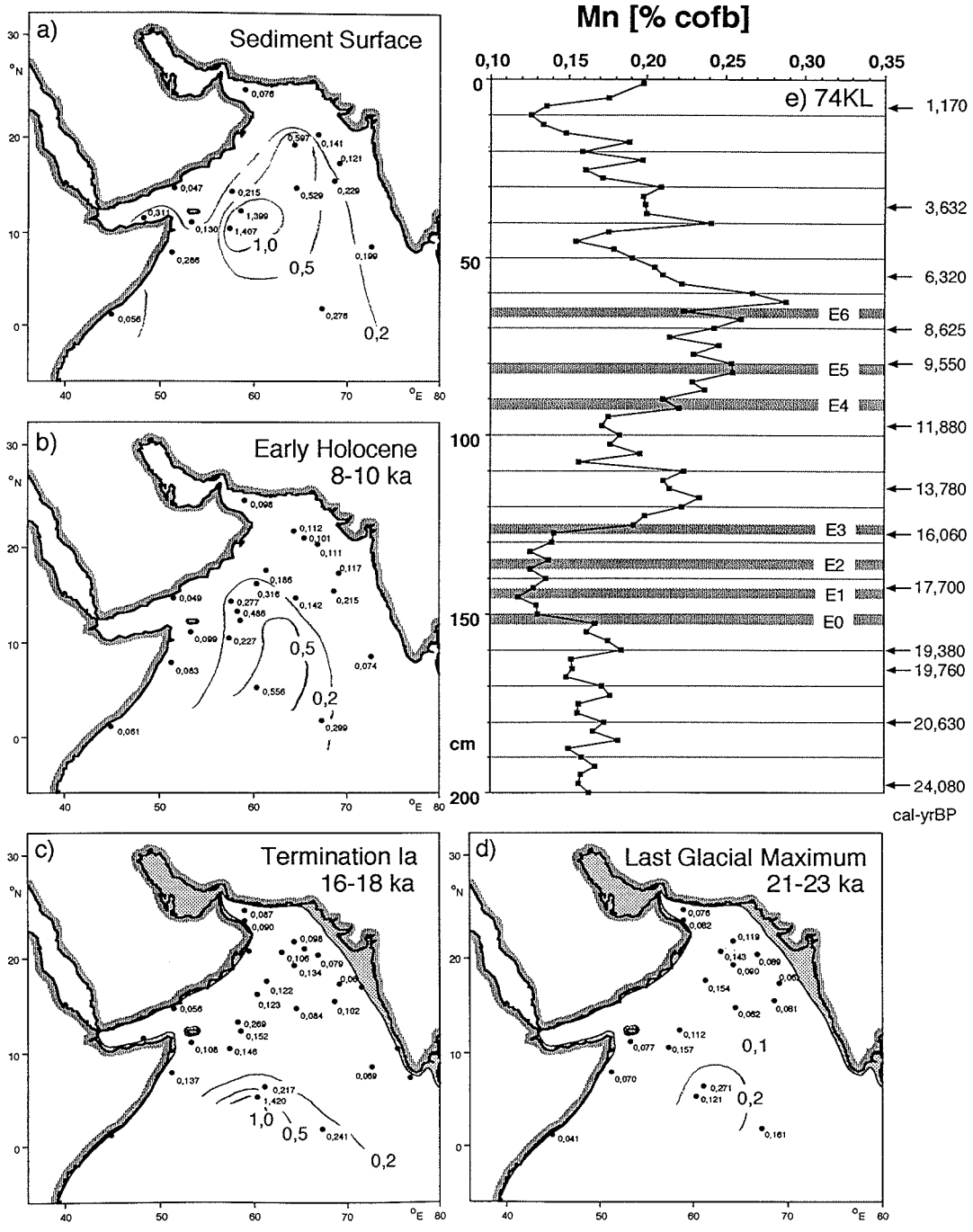

Figure 34. Manganese content, (a) at the sediment surface, (b) during the Early Holocene (8000-10,000 cal-yrBP), (c) during the Termination Ia (16,000-18,000 cal-yrBP), (d) during the Last Glacial Maximum (21,000-23,000 cal-yrBP), (e) sediment core 74KL, arrows indicate the depth of AMS-^{14}C dates, converted to calendar years according to Tab. 1, hatched areas show events as defined in Fig. 12.

Iron (Fe)

Table 5 continued. Fe content in various rock types, from Turekian & Wedepohl (1961)

	Igneous Rocks				Sedimentary Rocks			Deep-Sea Sediments	
Ultrabasic	Basalts	Ca-Granite	Granite	Syenites	Shales	Sandstone	Carbonates	Carbonate	Clay
ppm: 9.4	8.7	3.0	1.4	3.6	4.7	1.0	0.38	0.90	6.5

Fe content in Arabian Sea sediments ranges from 2.5% to 6%, thus being in the range of values typical for rock forming minerals (Tab. 5, Fig.35 a-d). A continuous maximum of Fe is found in the eastern Arabian Sea off India, where large amount of Fe are leached from the Fe-rich basalts of the Deccan traps (C. Devey, pers. comm.). Low values of Fe content are found in the western Arabian Sea with a persistent minimum off Yemen, where dust discharge from Arabia is at its maximum (see Mg, Fig. 24). Thus, the source of Fe in the western Arabian is probably eolian, whereas it is fluvial in the eastern part. The central Arabian Sea should then see a mixture between the two sources (see Nd, Sr isotopes, chapter C.3.).

Sediment core 74KL lies in the western sector of predominantly eolian source of Fe, but if Fe is transported within a dissolved or kolloidal phase in the eastern sector, 74KL still might be effected by Fe stemming from Indian rivers (Fig. 35 e). If the variations of Fe in 74KL thus present variations in the proportions from eolian (Arabian) or riverine (Indian) sources cannot be finally evaluated at this stage. The similarity of the distribution patterns and downcore variations of Fe and Al (Fig. 35, 25), though, suggest that the eolian dust derived Fe proportions from the Persian Gulf area are the dominating source of Fe in the western Arabian Sea.

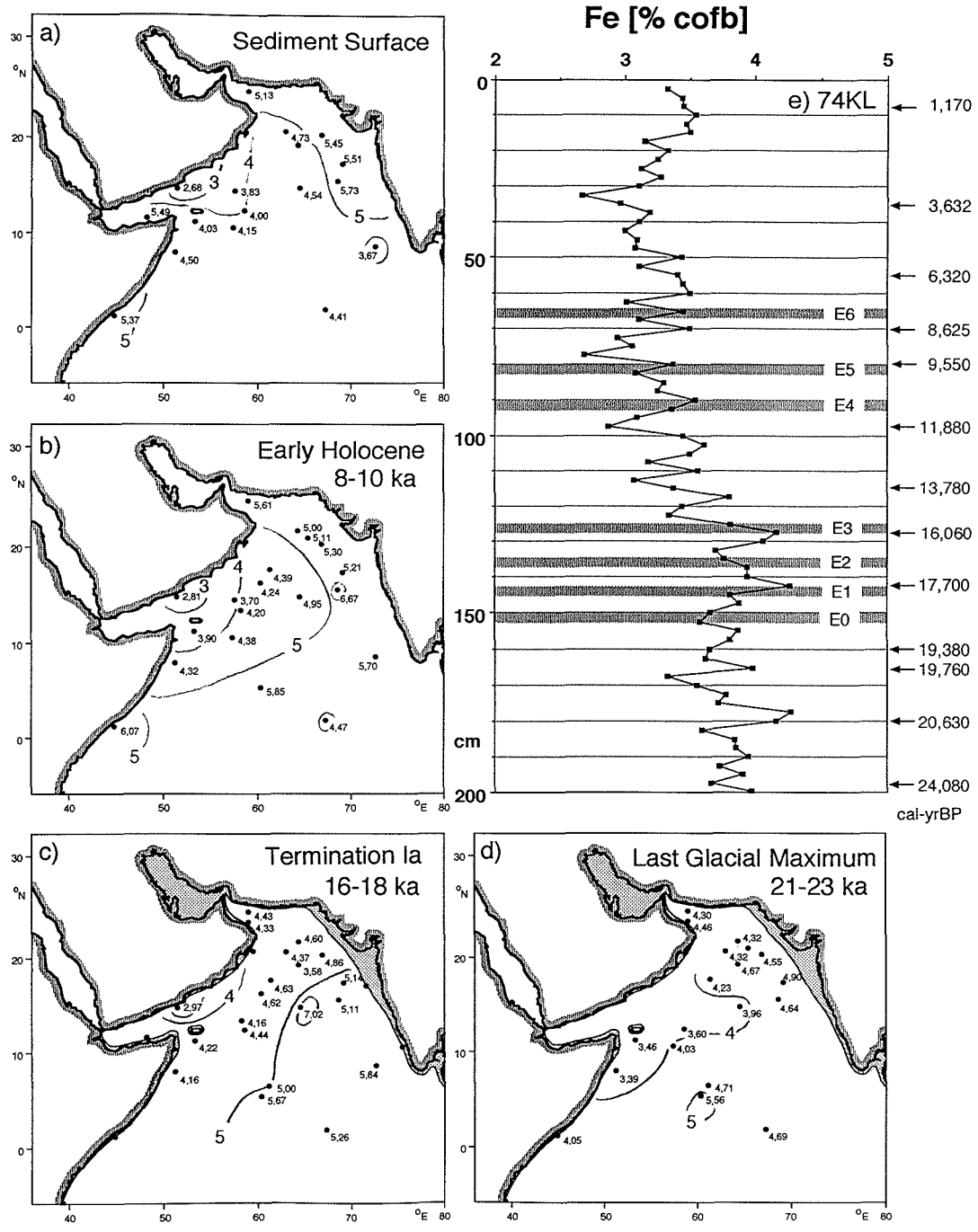

Figure 35. Iron content, (a) at the sediment surface, (b) during the Early Holocene (8000-10,000 cal-yrBP), (c) during the Termination Ia (16,000-18,000 cal-yrBP), (d) during the Last Glacial Maximum (21,000-23,000 cal-yrBP), (e) sediment core 74KL, arrows indicate the depth of AMS-^{14}C dates, converted to calendar years according to Tab. 1, hatched areas show events as defined in Fig. 12.

Cobalt (Co)

Table 5 continued. Co content in various rock types, from Turekian & Wedepohl (1961)

	Igneous Rocks				Sedimentary Rocks			Deep-Sea Sediments	
Ultrabasic	Basalts	Ca-Granite	Granite	Syenites	Shales	Sandstone	Carbonates	Carbonate	Clay
ppm: 150	48.0	7.0	1.0	1.0	19	0.3	0.1	7.0	74

The areal distribution of Co shows enrichment in the open ocean (Fig. 36 a-d), very much like Mn (Fig. 34). In contrast, downcore variations of Co are nearly identical to the Ni profile, which was interpreted as being controlled by scavenging and fixation of Ni from the surface waters. The biogenic source of Co in the Holocene section of 74KL is corroborated by extremely low concentrations of Co in surface waters of the Arabian Sea (Topping, 1969) showing Co uptake by biogenic organisms in the euphotic layer or removal of solid Mn- and Co-phases in the oxygen minimum zone (German & Elderfield, 1990). After deposition, the labile Co^{3+} can be transformed to Co^{2+} in the reducing section of the sediments, and like Mn becomes mobile. Accordingly, it can be expected that Co shares parts of its behaviour with Ni and other parts with Mn.

It cannot be by pure coincidence that the highest values of Co concentrations occurred during the interval of highest biogenic opal content and upwelling strength at 82.5 to 75 cm depth (Fig. 36 e). Organic matter is known to contain up to 100 ppm Co and high flux rates of organic carbon seem to transfer high amounts of Co to the deep-sea, where C_{org} is than remineralized, but substantial proportions of Co and Ni can be kept in the sediments. On the other hand, an Early Holocene ultrabasic source area, like the Iran/Oman ophiolites, could also deliver Co-rich clastics. In this case, high amounts of both Cr and Ni should parallel the Co maximum during the early Holocene. This is, however, not observed for these elements (Figs. 33, 37). Accordingly, it seems to be the organically mediated uptake of Co and Ni that is responsible for the Early Holocene maximum of these two elements in core 74KL.

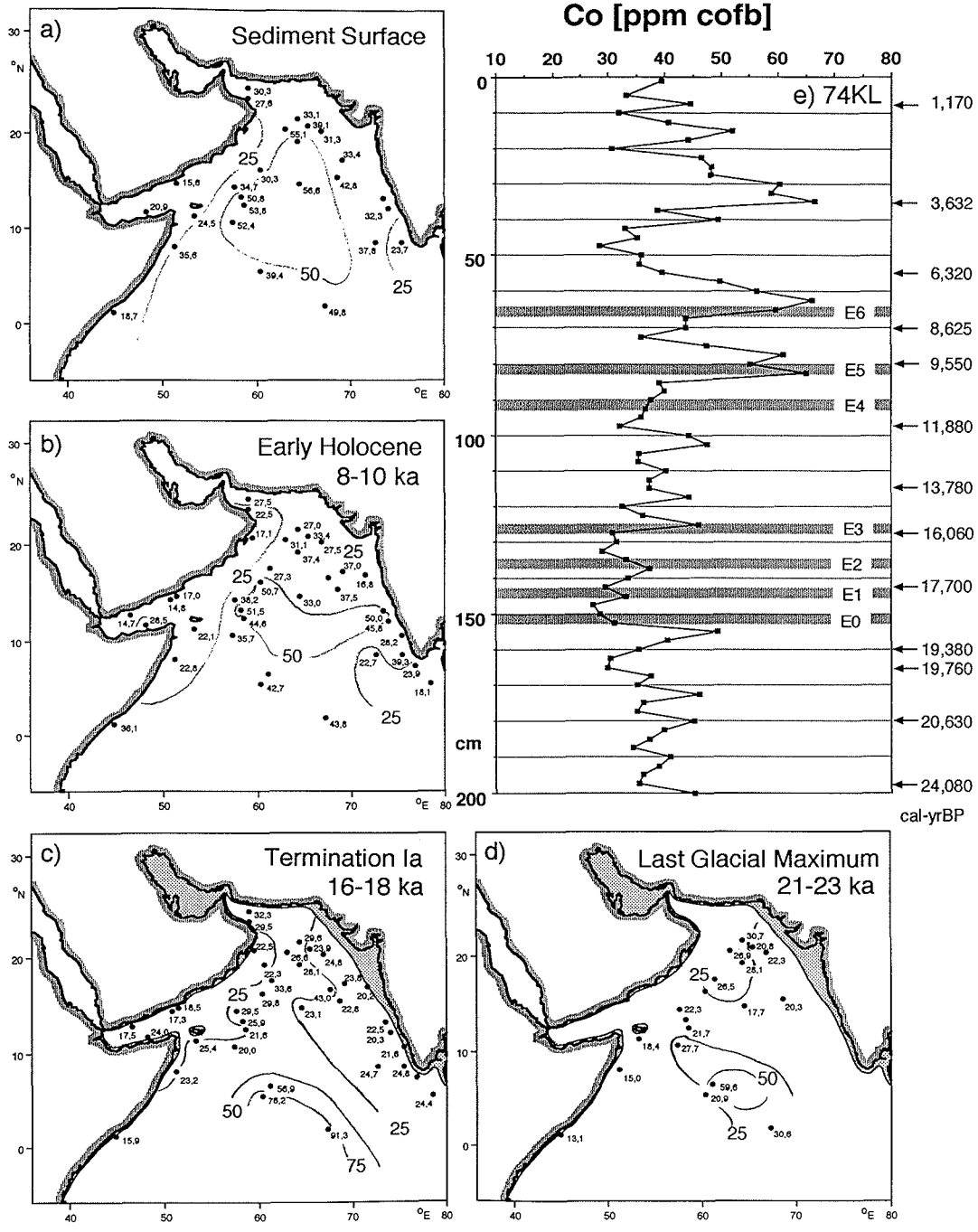

Figure 36. Cobalt content, (a) at the sediment surface, (b) during the Early Holocene (8000-10,000 cal-yrBP), (c) during the Termination Ia (16,000-18,000 cal-yrBP), (d) during the Last Glacial Maximum (21,000-23,000 cal-yrBP), (e) sediment core 74KL, arrows indicate the depth of AMS-^{14}C dates, converted to calendar years according to Tab. 1, hatched areas show events as defined in Fig. 12.

Nickel (Ni)

Table 5 continued. Ni content in various rock types, from Turekian & Wedepohl (1961)

Igneous Rocks					Sedimentary Rocks			Deep-Sea Sediments	
Ultrabasic	Basalts	Ca-Granite	Granite	Syenites	Shales	Sandstone	Carbonates	Carbonate	Clay
ppm:2000	130	15	4.5	4.0	68	2.0	20.0	30.0	225

Like Cr and Co, Ni concentrations are highest in ultramafic rocks (Tab. 5). In ocean water dissolved Ni content reveals higher values at depth than at the surface and the depth profile is similar to dissolved Zn content, which is highly correlated to the nutrient H_4SiO_4 content (Broecker & Peng, 1982). This connection of Ni to the nutrient cycle is also reflected by high Ni contents found in marine organic matter (Collier & Edmond, 1984). A third factor affecting Ni concentrations in sediments is its affinity to metallic binding, especially in sulfides together with Fe (pyrite).

The distribution of Ni in the Arabian Sea shows a plume of values > 150 ppm stretching from Oman towards the southeast (Fig. 37 a-d). The ophiolite rocks around the Persian Gulf and the prevailing northwesterly winds in this area seem to deliver large proportions of both Cr and Ni (Figs. 33, 37), but on the other hand, Ni is enriched relative to Cr in the western offshore areas of the Arabian Sea where marine accumulation rates start to exceed the lithic accumulation rates (compare distribution patterns of biogenic opal, Fig. 18). Ni is, however, not enriched in the immediate coastal upwelling areas of Somalia or Arabia where accumulation rates of lithic dust particles largely exceed the marine contributions.

In core 74KL, the Ni enrichment reveals a rapid change during E3 and E4, as well as a steep maxima during the Early Holocene and at 62 and 40 cm depth (i.e., immediately below similar maxima in biogenic opal content, Fig. 18 e). A similar sharp increase in Ni content during E4 is found in sediment core KS8 from the Gulf of Oman (Appendix 5). Accordingly, like Co, Ni has a potential to serve as a productivity indicator, however, masked by variations of lithic Ni proportion.

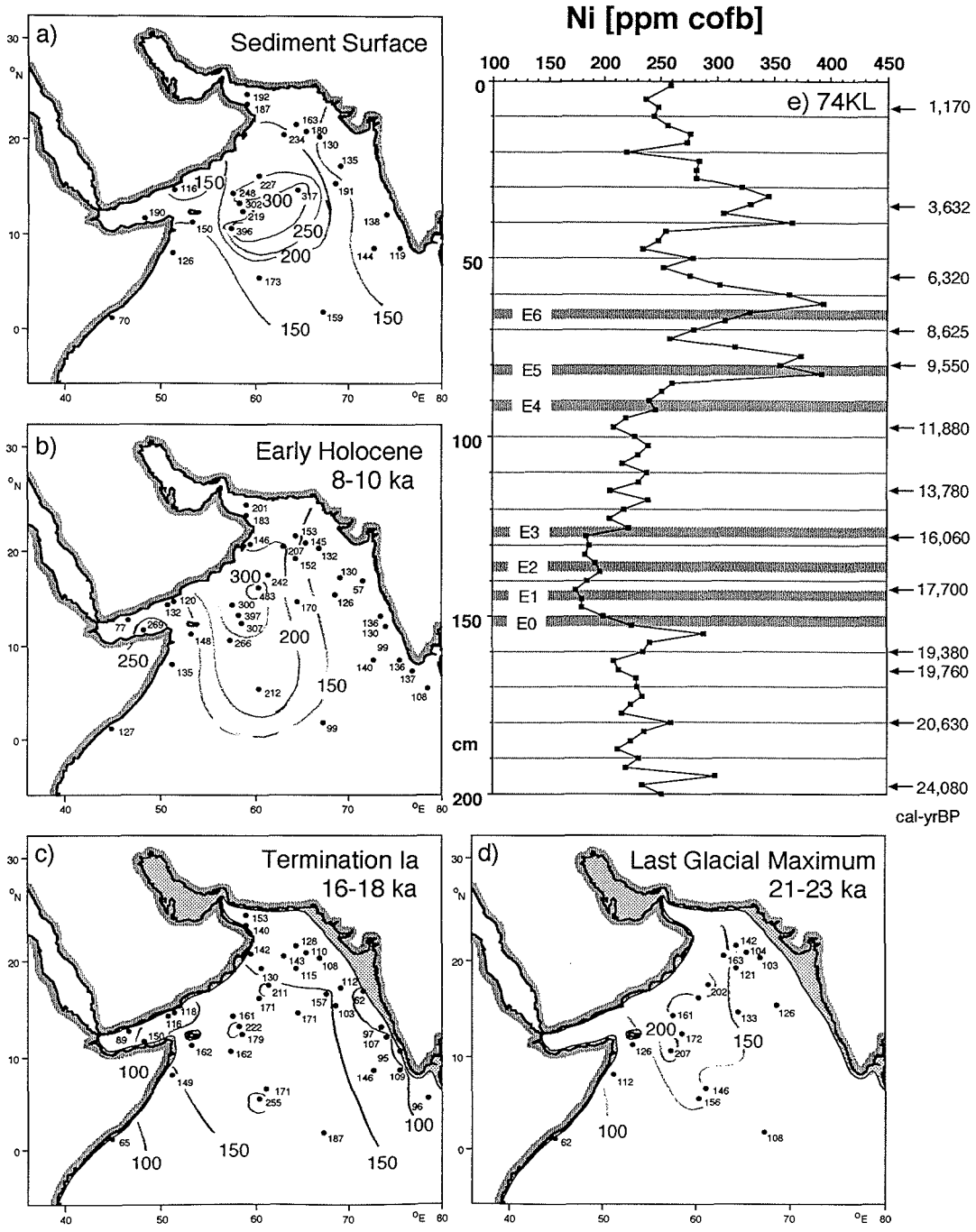

Figure 37. Nickel content, (a) at the sediment surface, (b) during the Early Holocene (8000-10,000 cal-yrBP), (c) during the Termination Ia (16,000-18,000 cal-yrBP), (d) during the Last Glacial Maximum (21,000-23,000 cal-yrBP), (e) sediment core 74KL, arrows indicate the depth of AMS-^{14}C dates, converted to calendar years according to Tab. 1, hatched areas show events as defined in Fig. 12.

Copper (Cu)

Table 5 continued. Cu content in various rock types, from Turekian & Wedepohl (1961)

	Igneous Rocks				Sedimentary Rocks			Deep-Sea Sediments	
Ultrabasic	Basalts	Ca-Granite	Granite	Syenites	Shales	Sandstone	Carbonates	Carbonate	Clay
ppm: 10.0	87.0	30.0	10.0	5.0	45.0	X.	4.0	30.0	250

Copper concentrations in rocks reveal average values between 5 and 100 ppm, with highest values in basalts and lowest values in feldspar rich rocks (Tab. 5). Bruland, (1980) and Broecker & Peng (1982) have shown, that Cu concentrations in ocean waters increase with waterdepth, a pattern that follows the nutrient content of the water and which is reflected in the chemical composition of plankton (Collier & Edmond, 1984). The same relation was found by Saager et al. (1992) in the Arabian Sea.

The distribution patterns of Cu show a persistent maximum over the Carlsberg Ridge in the equatorial Indian Ocean, far away from the continents, and far away from the region of increased upwelling productivity in the western Arabian Sea (Fig. 38 e). The lithic sediment fraction in this remote region is extremely fine grained (see <2μm grain size variations, Fig. 19) and Cu is found to be extremely enriched in the clay fraction (Tab. 13). Thus, the Cu enrichment in the equatorial Indian Ocean appears to be caused by the fine grained texture of sediments in this region alone.

The downcore variations of Cu in core 74KL, however, reveal a tight relation to the element Zn (Figs. 38 e, 39, 50), which, like Cu, is highly enriched in nutrient-rich waters of the Arabian Sea (Saager et al., 1992) . Especially, the sharp increase of Cu content at 95-92.5 cm depth (immediately below event E4) cannot be caused by grain-size variations, because the pattern of clay content does not show an abrupt change at that depth (Fig. 19). Instead, event E4 is the major event of upwelling intensification in the western Arabian Sea (chapter D.1.), an event that is obviously depicted in the Cu content of the sediment. Accordingly, only the broad scale distribution patterns of Cu concentrations follow primary variation in grain-size composition of the sediments, whereas surface water fertility dominate the Cu flux under the upwelling cells in the western Arabian Sea.

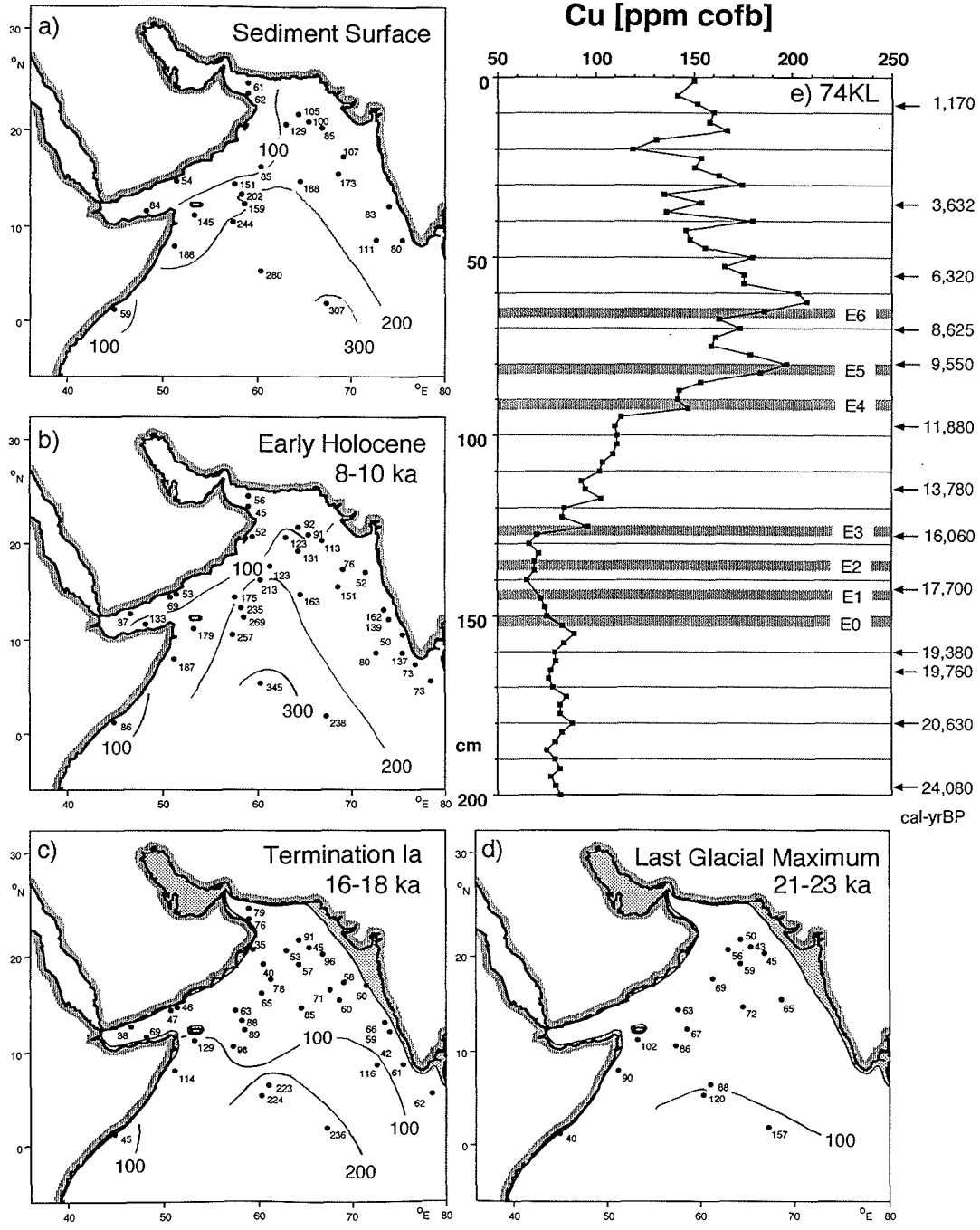

Figure 38. Copper content, (a) at the sediment surface, (b) during the Early Holocene (8000-10,000 cal-yrBP), (c) during the Termination Ia (16,000-18,000 cal-yrBP), (d) during the Last Glacial Maximum (21,000-23,000 cal-yrBP), (e) sediment core 74KL, arrows indicate the depth of AMS-^{14}C dates, converted to calendar years according to Tab. 1, hatched areas show events as defined in Fig. 12.

Zinc (Zn)

Table 5 continued, Zn content in various rock types, from Turekian & Wedepohl (1961)

	Igneous Rocks				Sedimentary Rocks			Deep-Sea Sediments	
Ultrabasic	Basalts	Ca-Granite	Granite	Syenites	Shales	Sandstone	Carbonates	Carbonate	Clay
ppm: 50	105	60	39	130	95	16	20	35	165

The distribution of Zn in the sediments of the Arabian Sea shows two maxima; one in the area of upwelling fertility off Arabia and another one off southern India (Fig. 39). The Zn content in both areas largely exceed what could be expected from Zn content in ignous rocks (Tab. 5).

An explanation of the maximum in the western Arabian Sea could come from the observation that Zn concentrations in ocean water closely follow the concentration of the nutrient H_4SiO_4 (Bruland, 1980); thus, Zn together with H_4SiO_4 is enriched in the upwelling waters of the western Arabian Sea (Saager et al., 1992). Mediated by the uptake or adsorption of Zn to organic matter or fine grained particles, Zn from the surface waters can reach the sediments easily (Martin & Knauer, 1973; Collier & Edmond, 1984) determined Zn concentrations up to 400 ppm in dry plankton). Accordingly, the Zn maximum in the sediments of the western Arabian could be explained by high biogenic flux rates and high Zn content in the surface waters of the region.

The maximum of Zn in the eastern Arabian Sea, however, must have another reason, because nutrient content of surface waters is low in that region (Wyrtky, 1971). The center of the Zn maximum off southern India is core 76127 (1610 m waterdepth) where values reach a maximum of 15,000 ppm at the sediment surface. The origin of this Zn could stem from a deepwater source, or from the small rivers of southern India, draining the western Ghats, which have some extemely Zn-rich soils in their drainage area (Katyal & Sharma, 1991). In any case, the extreme Zn values are paralled by extreme Pb and Mo concentrations (Figs. 47, 55), which indicates an anoxic environment at the continental slope of souther India.

Core 74KL lies in the area of upwelling derived Zn in the western Arabian Sea, thus should monitor the history of nutrient fluxes in the upwelling cells (Fig. 39 e). Accordingly, after a Termination Ia productivity minimum, upwelling intensified during E3 and E4, reaching maximum values during E5 and E6.

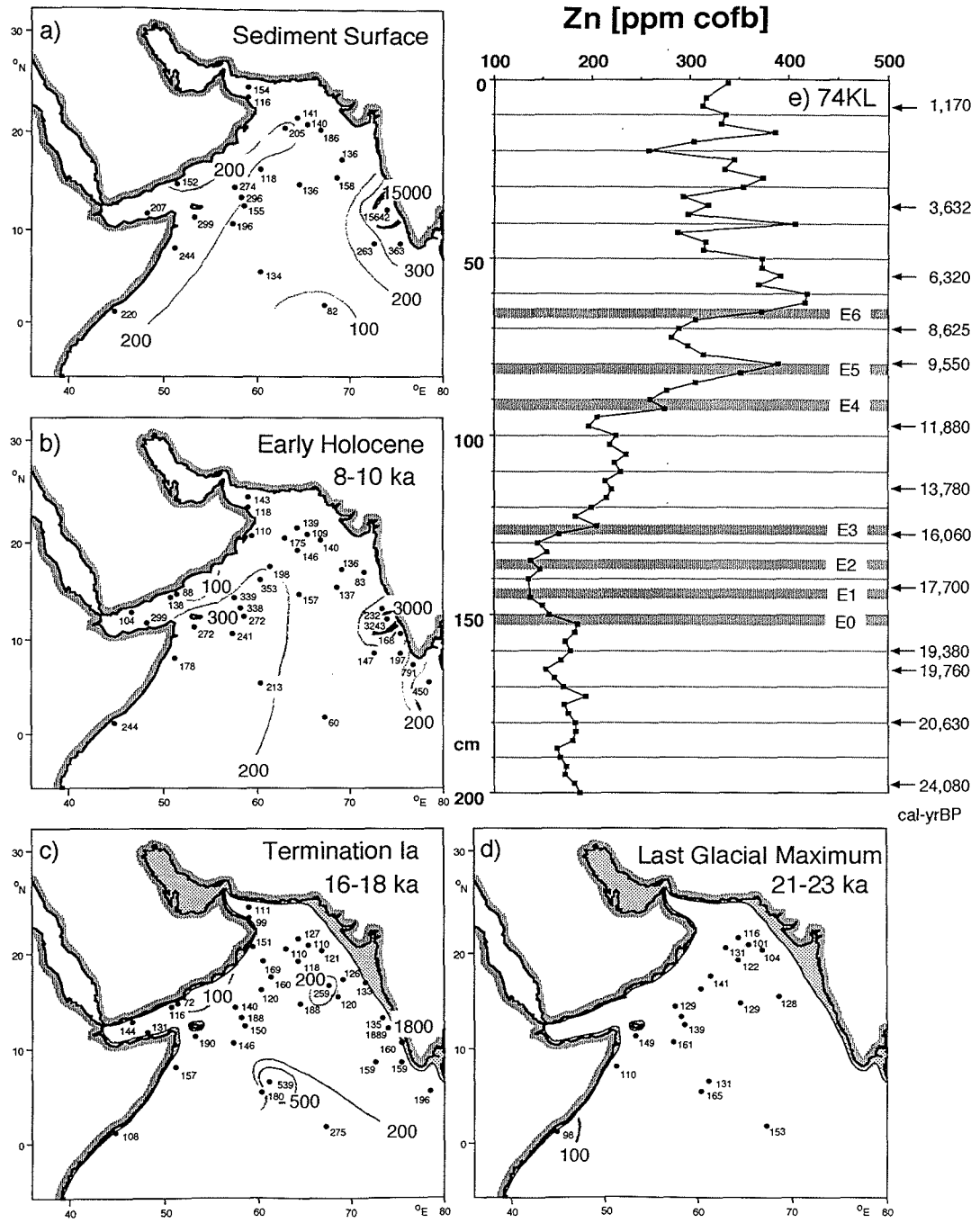

Figure 39. Zinc content, (a) at the sediment surface, (b) during the Early Holocene (8000-10,000 cal-yrBP), (c) during the Termination Ia (16,000-18,000 cal-yrBP), (d) during the Last Glacial Maximum (21,000-23,000 cal-yrBP), (e) sediment core 74KL, arrows indicate the depth of AMS-^{14}C dates, converted to calendar years according to Tab. 1, hatched areas show events as defined in Fig. 12.

Gallium (Ga)

Table 5 continued. Ga content in various rock types, from Turekian & Wedepohl (1961)

	Igneous Rocks				Sedimentary Rocks			Deep-Sea Sediments	
Ultrabasic	Basalts	Ca-Granite	Granite	Syenites	Shales	Sandstone	Carbonates	Carbonate	Clay
ppm: 1.5	17	17	17	30	19	12	4	13	20

The relative proportions of Ga in the various rock types closely follow the variability of Zr. In contrast to Zr, Ga is also concentrated in clay minerals and can be largely enriched in clay particles during soil formation.

The distribution of Ga reveal no distinct pattern, only indications of lower values in the western Arabian Sea and a plume out of East Africa that resembles the Zr distribution pattern during the Early Holocene (Fig. 40 a-d). Like Zr, enrichment of Ga in the clay fraction of Arabian Sea sediments is low, and no leachable proportions of Ga are observed (Tab. 13). It is only during the Last Glacial Maximum that distinct differences between Zr and Ga are observed when a Ga-rich plume enters the Arabian Sea from the Thar desert area of northern India. The shape of the plume looks most similar to the distribution of Rb (Fig. 42), which is discussed as showing dust transported in northeast monsoon winds during the peak glacial.

The downcore variations of Ga in sediment core 74KL (Fig. 40 e) closely follow the Zr profile (Fig. 45). Like with Zr, there is a tendency for a higher amplitude in the rhythmic variations of maxima and minima in the Holocene section when compared to the glacial section. The nature of these oscillations is discussed in chapter D.6.

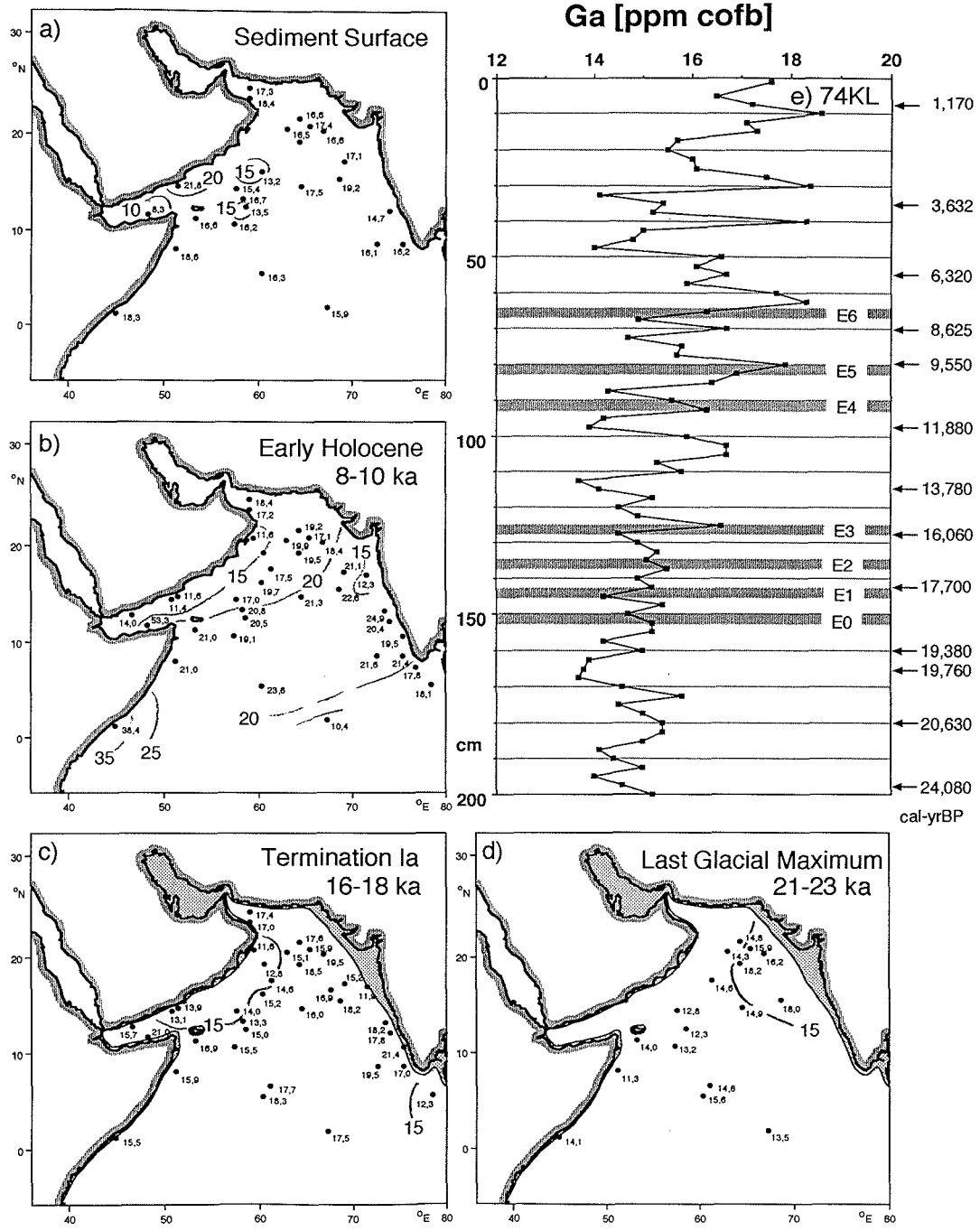

Figure 40. Gallium content, (a) at the sediment surface, (b) during the Early Holocene (8000-10,000 cal-yrBP), (c) during the Termination Ia (16,000-18,000 cal-yrBP), (d) during the Last Glacial Maximum (21,000-23,000 cal-yrBP), (e) sediment core 74KL, arrows indicate the depth of AMS-^{14}C dates, converted to calendar years according to Tab. 1, hatched areas show events as defined in Fig. 12.

Arsenic (As)

Table 5 continued. As content in various rock types, from Turekian & Wedepohl (1961)

Igneous Rocks					Sedimentary Rocks			Deep-Sea Sediments	
Ultrabasic	Basalts	Ca-Granite	Granite	Syenites	Shales	Sandstone	Carbonates	Carbonate	Clay
ppm: 1.0	2.0	1.9	1.5	1.4	13.0	1.0	1.0	1.0	13.0

As concentrations in igneous rocks are usually less than 2 ppm, but may reach a maximum of 8 ppm, which is still lower than our maximum values of >15 ppm in the western Arabian Sea off the Deccan (Fig. 41 a-e). This maximum coincides with maxima in K, Sc, Ti, Fe and Sr content (Figs. 29, 31, 32, 35, 29, 43); elements, which are known to be leached from basalts by means of chemical erosion under humid climate conditions, which is intense in the Deccan region (Devey, pers.comm.). Thus, a likely explanation of the As plume reaching as far as the central Arabian Sea could be a transport in a dissolved phase, and adsorption to clays after entering the ocean.

As, which was measured using Atomic Absorption Spectroscopy, was not determined in 74KL and not in the samples of the Last Glacial Maximum time-slice.

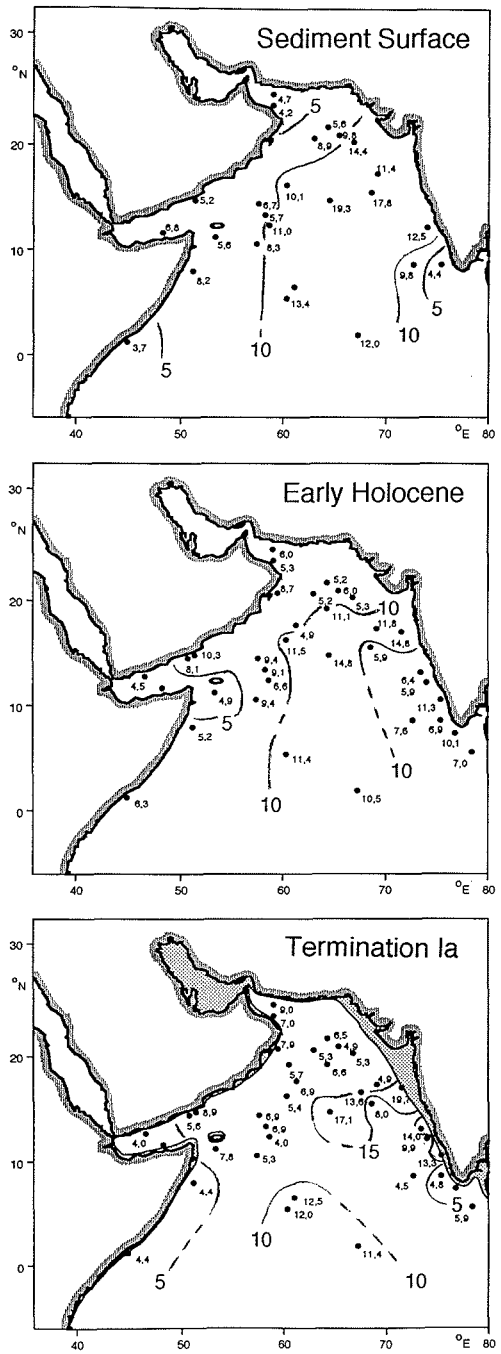

Figure 41. Arsenic content, (a) at the sediment surface, (b) during the Early Holocene (8000-10,000 cal-yrBP), (c) during the Termination Ia (16,000-18,000 cal-yrBP).

Rubidium (Rb)

Table 5 continued, Rb content in various rock types, from Turekian & Wedepohl (1961)

	Igneous Rocks				Sedimentary Rocks			Deep-Sea Sediments	
Ultrabasic	Basalts	Ca-Granite	Granite	Syenites	Shales	Sandstone	Carbonates	Carbonate	Clay
ppm: 0.2	30	110	170	110	140	60	3	10	110

Distribution patterns of Rb reveal a consistent maximum off northern India and Pakistan, whereas Rb concentrations in the western Arabian Sea are low (Fig. 42 a-d). This is corroborated by the Rb content of modern aerosols off Arabia (63 ppm Rb, F.S. unpubl. data) and loess deposits in Pakistan (>120 ppm Rb, F.S. unpubl. data).

The Rb-rich dust plumes from northern India shifted towards middle India during glacial times, indicating an increased southward extent of the glacial northeast monsoon. We can, however, not exclude that parts of the Rb bearing minerals during the glacial in the northernmost Arabian Sea were derived from the river Indus, which should have discharged its sediment load directly into the deep Arabian Sea during times of lowered sea level. Sediment core 74KL, however, being on a ridge above the Indus turbidite plain is very remote from the river Indus, and it appears very unlikely that the glacial section of 74KL could be affected by riverine contributions from the Indus (see Nd, Sr isotope chapter C.3).

The Rb content of 74KL (Fig. 42 e) shows the same downcore profile as Cs (Fig. 49). Maximum values are found between 150 to 125 cm depth, followed by a gradual evolution towards low values during the Holocene, punctuated by a return to high "glacial" values during the Younger Dryas interval.

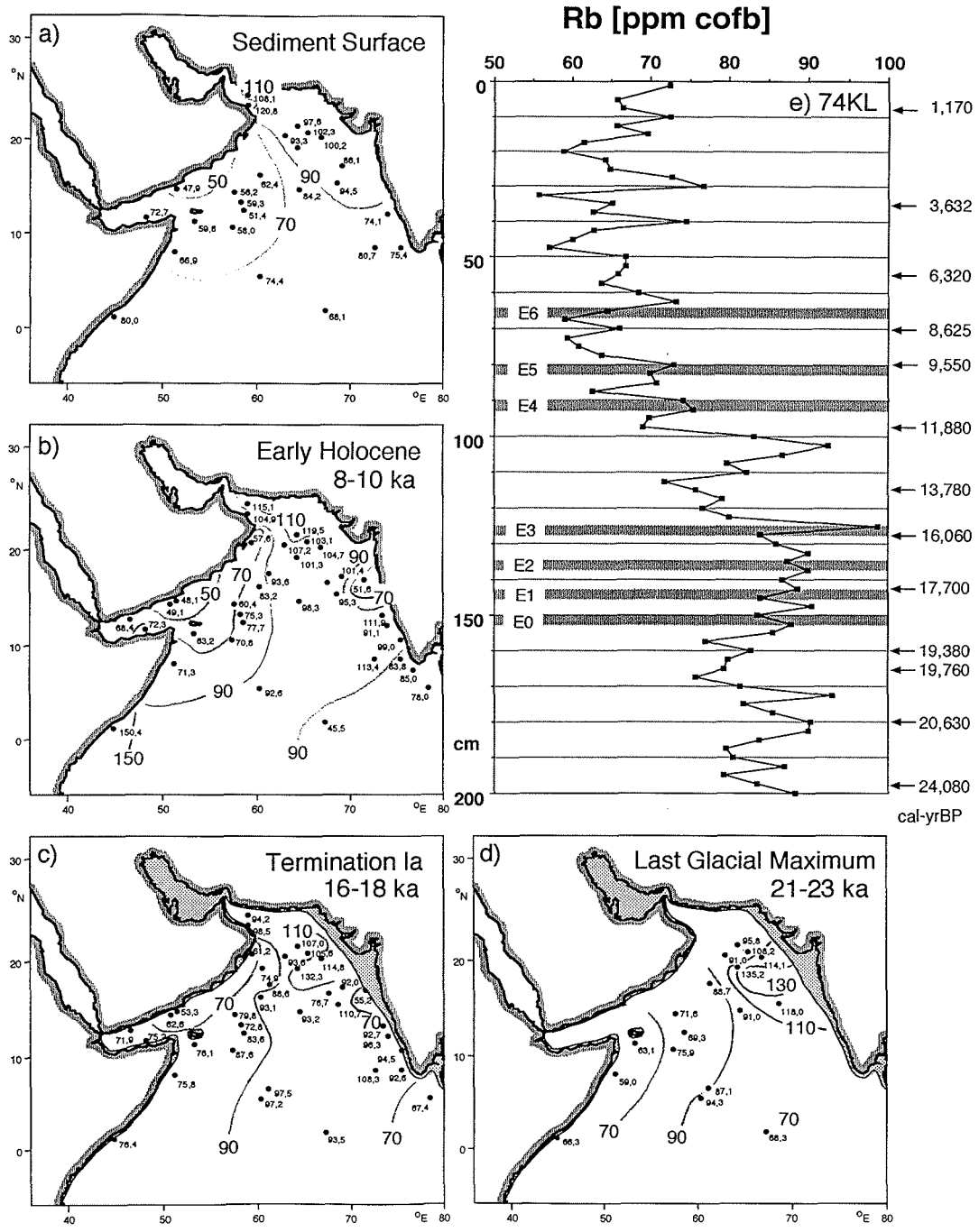

Figure 42. Rubidium content, (a) at the sediment surface, (b) during the Early Holocene (8000-10,000 cal-yrBP), (c) during the Termination Ia (16,000-18,000 cal-yrBP), (d) during the Last Glacial Maximum (21,000-23,000 cal-yrBP), (e) sediment core 74KL, arrows indicate the depth of AMS-^{14}C dates, converted to calendar years according to Tab. 1, hatched areas show events as defined in Fig. 12.

Strontium (Sr)

Table 5 continued. Sr content in various rock types, from Turekian & Wedepohl (1961)

Igneous Rocks					Sedimentary Rocks			Deep-Sea Sediments	
Ultrabasic	Basalts	Ca-Granite	Granite	Syenites	Shales	Sandstone	Carbonates	Carbonate	Clay
ppm: 1	465	440	100	200	300	20	610	2000	180

The dominating feature in the distribution patterns of Sr/Ca in Arabian Sea sediments is a pronounced maximum of Sr off middle and southern India during the Early Holocene and the Termination Ia (Fig. 43 a-d). In core 76132 (the core with extremely high values at the Indian margin) the source of Sr are irregular clusters of aragonite of 1 mm diameter with no obvious biogenic structure. The area of extreme Sr enrichment is not confined to a specific waterdepth, but is confined to the shelf and continental slope off the Deccan, see Marchig (1972), which basalts are Sr-rich (Lightfoot et al., 1990). Intense chemical weathering of the region may result in a surface water runoff rich in dissolved Sr content, which precipitates as aragonite after entering the ocean

During glacial times the plume of high Sr content was shifted towards the south, indicating more intense chemical weathering also in southern India (Van Campo, 1986), or a more effective longshore southward transport in the surface currents at times when the low-salinity Bay of Bengal water was absent on the south Indian shelf (Duplessy, 1982).

Core 74KL shows a decrease of Sr/Ca during the Termination Ia, followed by a sharp transition to the Holocene level during event E3, corresponding to 127. 5 cm (Fig. 43 e). The cause of the Sr/Ca minimum could be a deeper position of the lysocline during the Termination Ia, leading to poor preservation of Sr-rich aragonite. The modern depth of the lysocline is at about 2900 m (Kallel et al., 1988; Kolla et al., 1976a), the waterdepth of 74KL is 3212m; thus, a lysocline deepening by only 300 m between the Holocene and the glacial, could explain the Sr/Ca minimum during the Termination Ia.

It cannot be excluded that the changes in Sr/Ca could be related to changes in the proportions of lithic Sr, because total Sr, and not carbonate Sr, content is used to calculate the Sr/Ca ratio. This source of error gets important, if dust from Arabia and the Persian Gulf area, which was at a maximum at the depth of the Sr/Ca minimum, should show low Sr content. Thus, an evaluation of the variability of the Sr/Ca ratio has to remain preliminary until the lithogenic Sr content is not quantified.

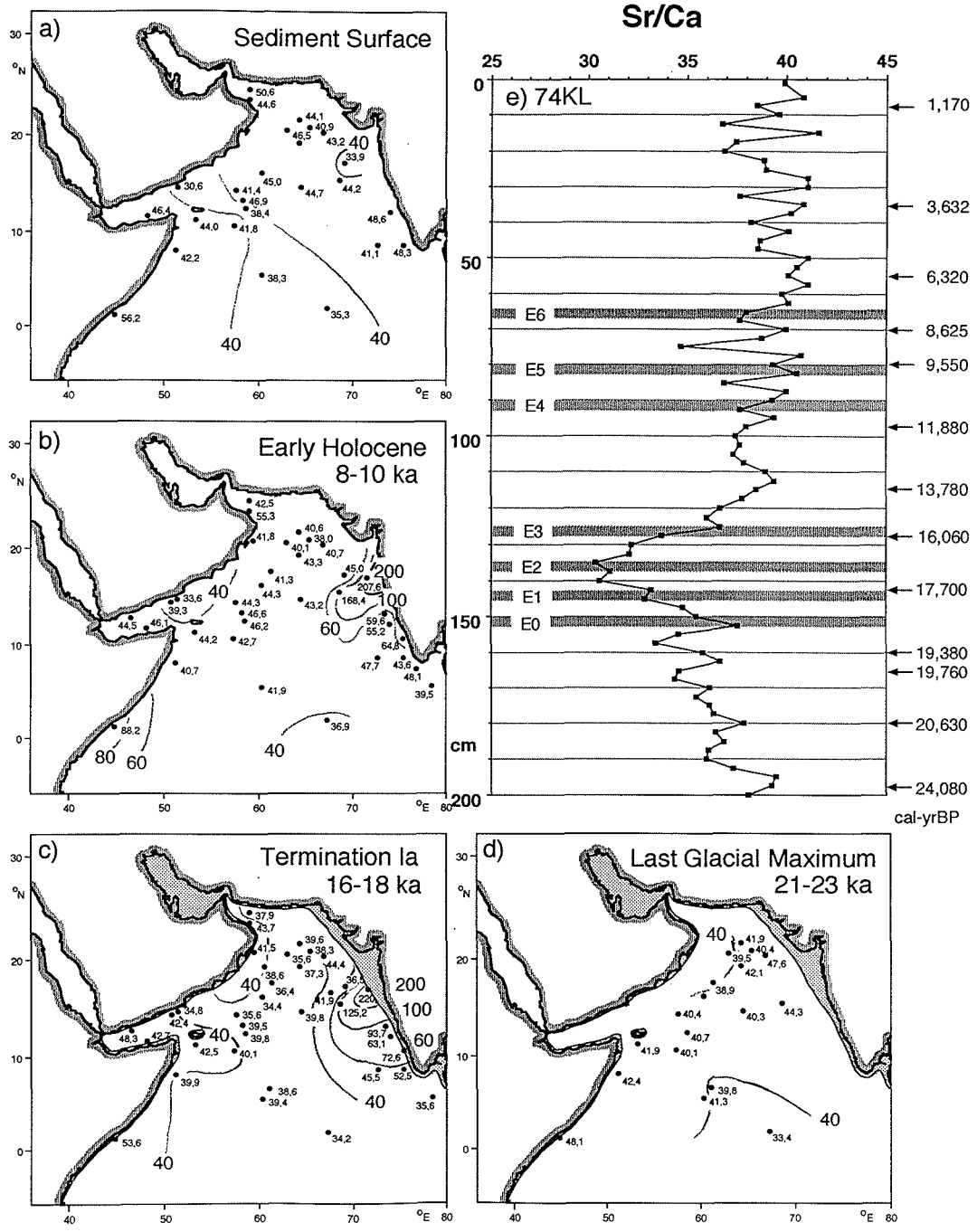

Figure 43. Strontium to Calcium ratio, (a) at the sediment surface, (b) during the Early Holocene (8000-10,000 cal-yrBP), (c) during the Termination Ia (16,000-18,000 cal-yrBP), (d) during the Last Glacial Maximum (21,000-23,000 cal-yrBP), (e) sediment core 74KL, arrows indicate the depth of AMS-^{14}C dates, converted to calendar years according to Tab. 1, hatched areas show events as defined in Fig. 12.

Yttrium (Y)

Table 5 continued, Y content in various rock types, from Turekian & Wedepohl (1961)

Yttrium:	Igneous Rocks				Sedimentary Rocks			Deep-Sea Sediments	
Ultrabasic	Basalts	Ca-Granite	Granite	Syenites	Shales	Sandstone	Carbonates	Carbonate	Clay
ppm: 0.X	21	35	40	20	26	40	30	42	90

The chemistry of Y is so similar to the chemistry of the REE that this element is discussed together with the REE (see below). The similarity between these elements is due to the lanthanide contraction, which starts with La, when electrons are added to the N-orbit of the atom instead of to the outer O-orbit. Additional electrons in an orbit near to the core of the atom cause a contraction, whereas only additional electrons in the outer orbit cause an expansion of the atom size. Such a contraction occurs for all REE. Accordingly, the atomic radius of Lu (Z=71; 0,85 Å) is smaller than for La (Z=57; 1,06 Å). Y (0,89 Å) has the same ionic radius as Ho (0,89 Å) and because both elements occur strictly in the 3+ valence state, their chemistry is almost identical.

In consequence, the distribution patterns and downcore variation of Y and the HREE are most similar (Fig. 44, 52).

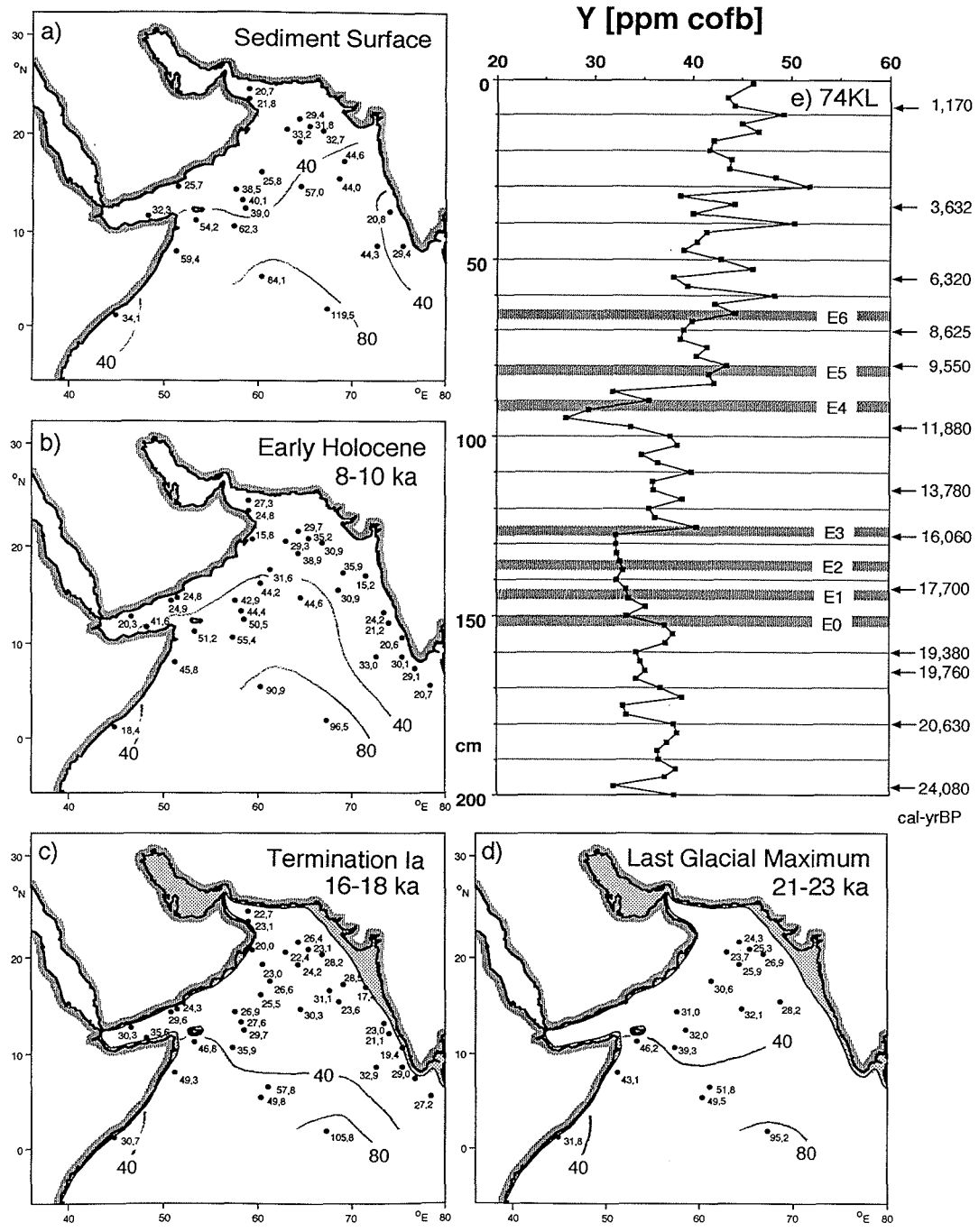

Figure 44. Yttrium content, (a) at the sediment surface, (b) during the Early Holocene (8000-10,000 cal-yrBP), (c) during the Termination Ia (16,000-18,000 cal-yrBP), (d) during the Last Glacial Maximum (21,000-23,000 cal-yrBP), (e) sediment core 74KL, arrows indicate the depth of AMS-^{14}C dates, converted to calendar years according to Tab. 1, hatched areas show events as defined in Fig. 12.

Table 5 continued. Zr content in various rock types, from Turekian & Wedepohl (1961)

Igneous Rocks					Sedimentary Rocks			Deep-Sea Sediments	
Ultrabasic	Basalts	Ca-Granite	Granite	Syenites	Shales	Sandstone	Carbonates	Carbonate	Clay
ppm:45	140	140	175	500	160	220	19	20	150

Zr^{4+} is found in most silicates, where it can replace Ti, REE, Fe, Ca, and is enriched in heavy minerals like ilmenite or rutil (Zr content: 1000 ppm). The element Zr has a clear maximum in the mineral zircon ($ZrSiO_4$), that can contain 500.000 ppm (50%) Zr. Accordingly, the Zr content of ignous rocks depends highly on the occurrence of zircon minerals in the rocks, the patterns of which are rather irregular, but with a minimum in ultrabasaltic rocks (Tab. 5).

Zircons are extremely resistant to weathering, and thus, sediments can reach extreme Zr enrichment, especially in regions of intense chemical weathering, where all other minerals are dissolved. Together with other heavy minerls, zircons can be found in all kinds of placer deposits. In wind-blown aerosols, they are, however, rather infrequent, because they are not easily entrained into the air due to their high specific weight, and if entrained, they are among the very first fallouts from that dust plume, and have no capacity for long range transport. Only vigorous, and in addition, very high (midtropospheric) dust plumes should be able to transport heavy minerals.

The distribution pattern of Zr concentrations in the Arabian Sea sediments reveals a continuous plume of values > 100 ppm stretching from the Horn of Africa towards east and northeast (Fig. 45 a-d). The high Zr content could be due to detrital zircon or inclusions of Zr in silikates and heavy minerals. Adsorbed Zr to clay minerals, mainly smectites, can be no major source, because the leachable Zr proportions are zero, and we do not oberve any Zr enrichment in the clay fraction (Tab. 13). The spikes in the Zr profile of 74KL (for example at 40 cm depth) could be caused by only a few additional Zr grains, because 1 grain of zircon can contain as much Zr as up to 3500 other grains.

The extent and shape of the Zr maximum in the Arabian Sea probably resembles summer windtracks in the mid-troposphere over the Gulf of Aden (Fig. 5, 26 June), where northwesterlies from Arabia and the 850 mb southwest monsoon wind tracks merge (Chen, 1986; Ramage & Raman, 1972). The gradient of Zr concentrations

continued on page 60

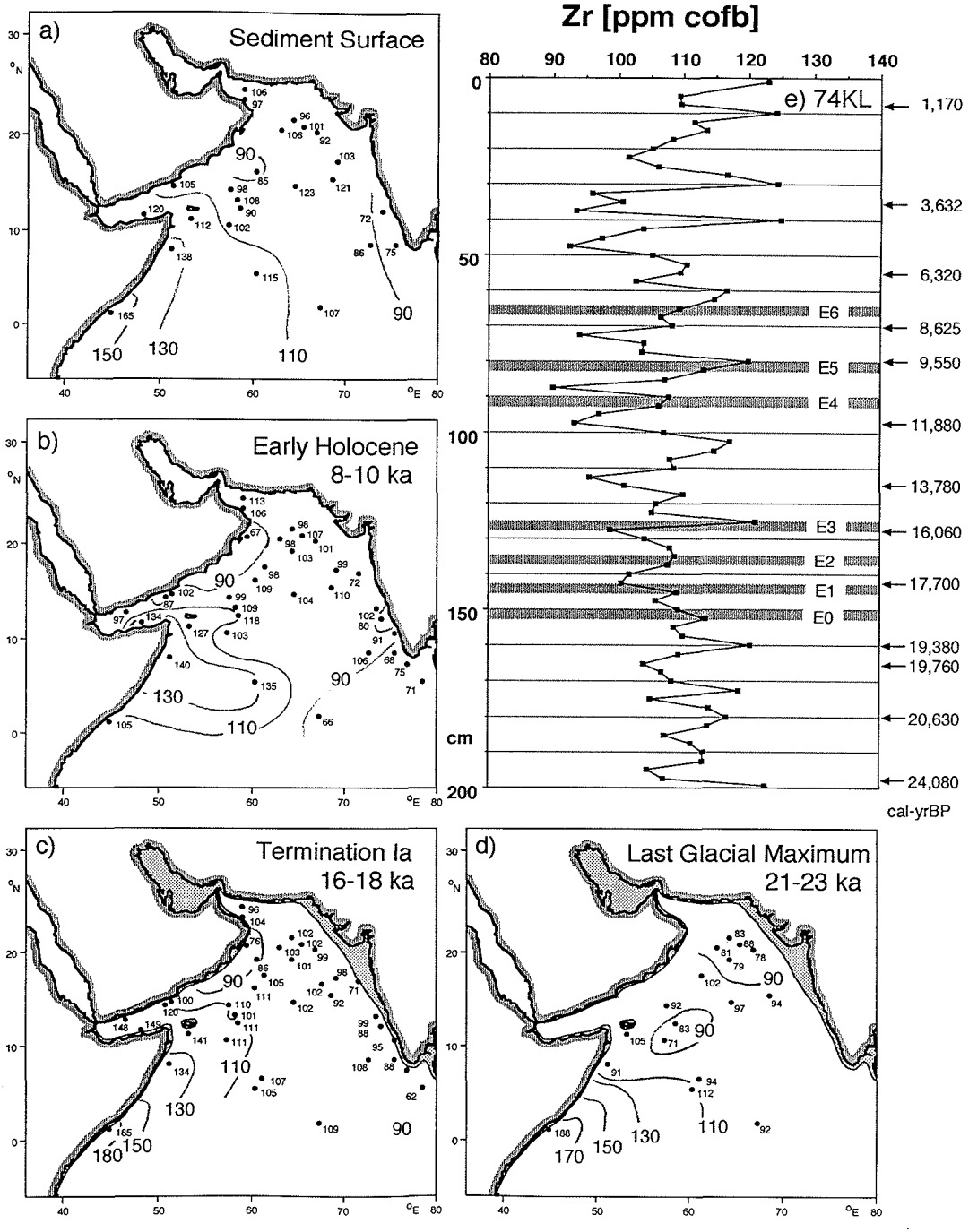

Figure 45. Zirconium content, (a) at the sediment surface, (b) during the Early Holocene (8000-10,000 cal-yrBP), (c) during the Termination Ia (16,000-18,000 cal-yrBP), (d) during the Last Glacial Maximum (21,000-23,000 cal-yrBP), (e) sediment core 74KL, arrows indicate the depth of AMS-^{14}C dates, converted to calendar years according to Tab. 1, hatched areas show events as defined in Fig. 12.

Niobium (Nb)

Table 5 continued, Nb content in various rock types, from Turekian & Wedepohl (1961)

Igneous Rocks					Sedimentary Rocks			Deep-Sea Sediments	
Ultrabasic	Basalts	Ca-Granite	Granite	Syenites	Shales	Sandstone	Carbonates	Carbonate	Clay
ppm: 16	19	20	21	35	11	0.0X	0.3	4.6	14

Nb concentrations are highest in igneous rocks, especially if they are rich in feldspar (Tab. 5). Distribution pattern of Nb in the Arabian Sea show a persistent minimum in the northwestern sector and a maximum off East Africa and on the Carlsberg Ridge (Fig. 46 a-d), which resembles the distribution pattern of Zr to some extent (Fig. 45).

Sediment core 74KL in the western Arabian Sea is dominated by the dust discharge from northern Arabia and the Persian Gulf area; accordingly, downcore variation of Nb look similar to the profile of Al (Fig. 25), which is the most representative element for a source of eolian particles from the Persian Gulf region.

Zr, continued from page 59

towards the east, which is most obvious during the Early Holocene, cannot be explained by transport in the low level southwest monsoon winds, which blow from east Africa towards the Gulf of Aden and Arabia, having trajectories almost 90 degrees different to what is observed in the Zr distribution patterns. This transport is also observed during the Termination Ia, but not during the Last Glacial Maximum when a dust plume of low Zr content stretches from Oman/Pakistan towards the whole western Arabian Sea, and high Zr contents are confined to the equatorial region.

The variations of Zr in sediment core 74KL do not reveal any trend, except an oscillation, which is enhanced in its amplitude after event E3 (see chapter D.6.).

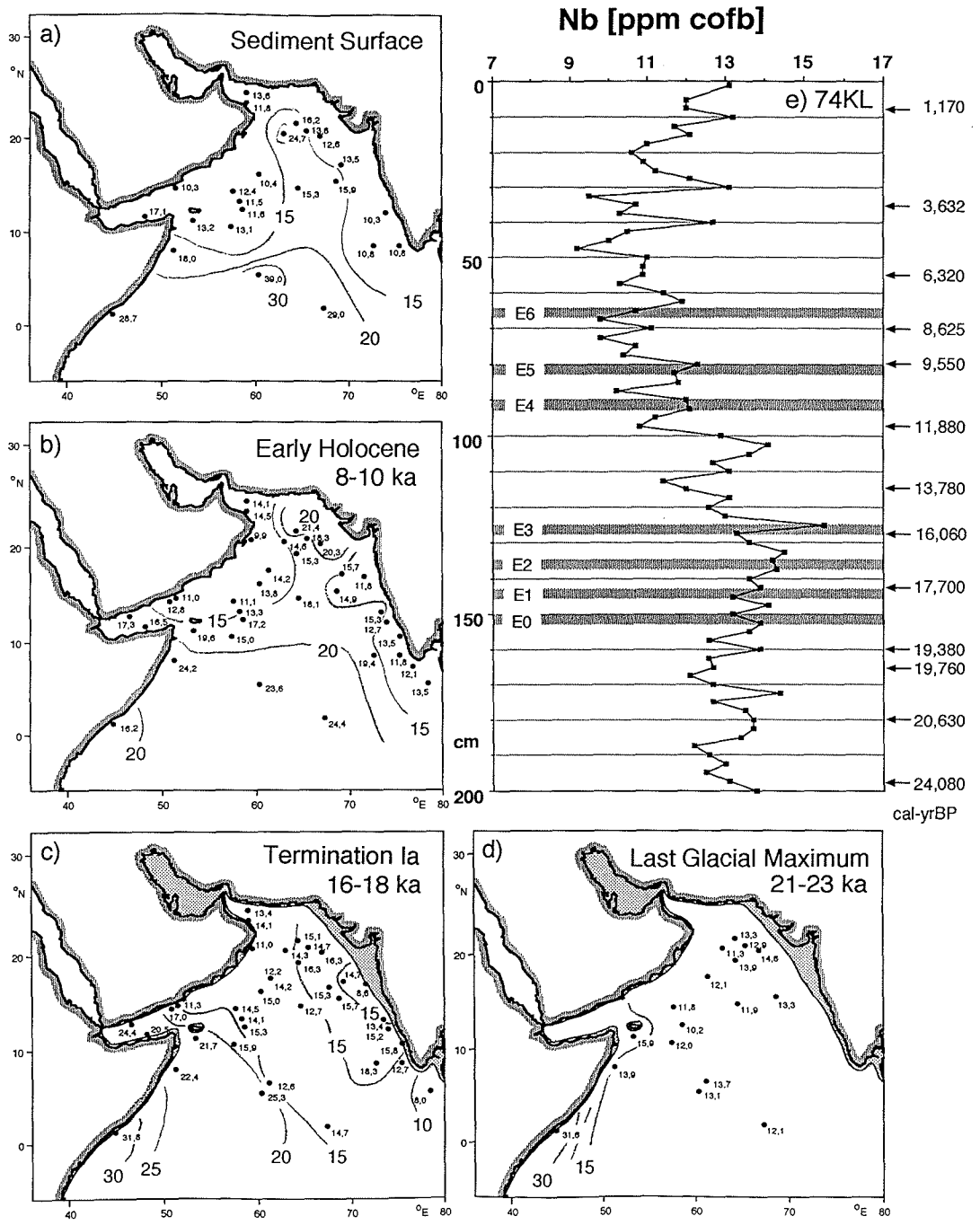

Figure 46. Niobium content, (a) at the sediment surface, (b) during the Early Holocene (8000-10,000 cal-yrBP), (c) during the Termination Ia (16,000-18,000 cal-yrBP), (d) during the Last Glacial Maximum (21,000-23,000 cal-yrBP), (e) sediment core 74KL, arrows indicate the depth of AMS-^{14}C dates, converted to calendar years according to Tab. 1, hatched areas show events as defined in Fig. 12.

Molybdenum (Mo)

Table 5 continued. Mo content in various rock types, from Turekian & Wedepohl (1961)

Igneous Rocks					Sedimentary Rocks			Deep-Sea Sediments	
Ultrabasic	Basalts	Ca-Granite	Granite	Syenites	Shales	Sandstone	Carbonates	Carbonate	Clay
ppm: 0.3	1.5	1.0	1.3	0.6	2.6	0.2	0.4	3.0	27.0

Distribution patterns of Mo in the Arabian Sea sediments reveal maximum values at the Indian continental margin (Fig. 47 a-b), where C_{org} concentrations are extremely high (Marchig, 1972; Marchig, 1974). In addition, high values of Mo occur on the Carlsberg Ridge in the glacial sediment section (Fig. 47 c-d). If this maximum on the Carlsberg Ridge is a function of deep-water chemistry, or a south Indian source of Mo, or only a diagenetic enrichment of Mo together with Mn in these slowely accumulating sediment cores cannot be evaluated.

The downcore variations of Mo in core 74KL reveal distinct similarities to the C_{org} profile (except for the upper 50 cm), and also to Mn (Figs. 47 e, 21 e, 34 e). Because Mn variability appears to be mainly a function of C_{org} flux, we have to conclude that the Mo abundance in74KL is also controlled by C_{org} content. The enrichment of Mo during the LGM in core 74KL (at depth below 155 cm) exceeds by far what could be expected from a linear response to the coherent C_{org} increase alone. In accordance, Mo together with S and Corg forms a single factor in the factor analysis of the 74KL element concentrations (F4, Fig. 61), indicating that deepwater O_2 content at core location 74KL was significantly lower during the LGM than during the Termination Ia and the Holocene (see chapter D.2.).

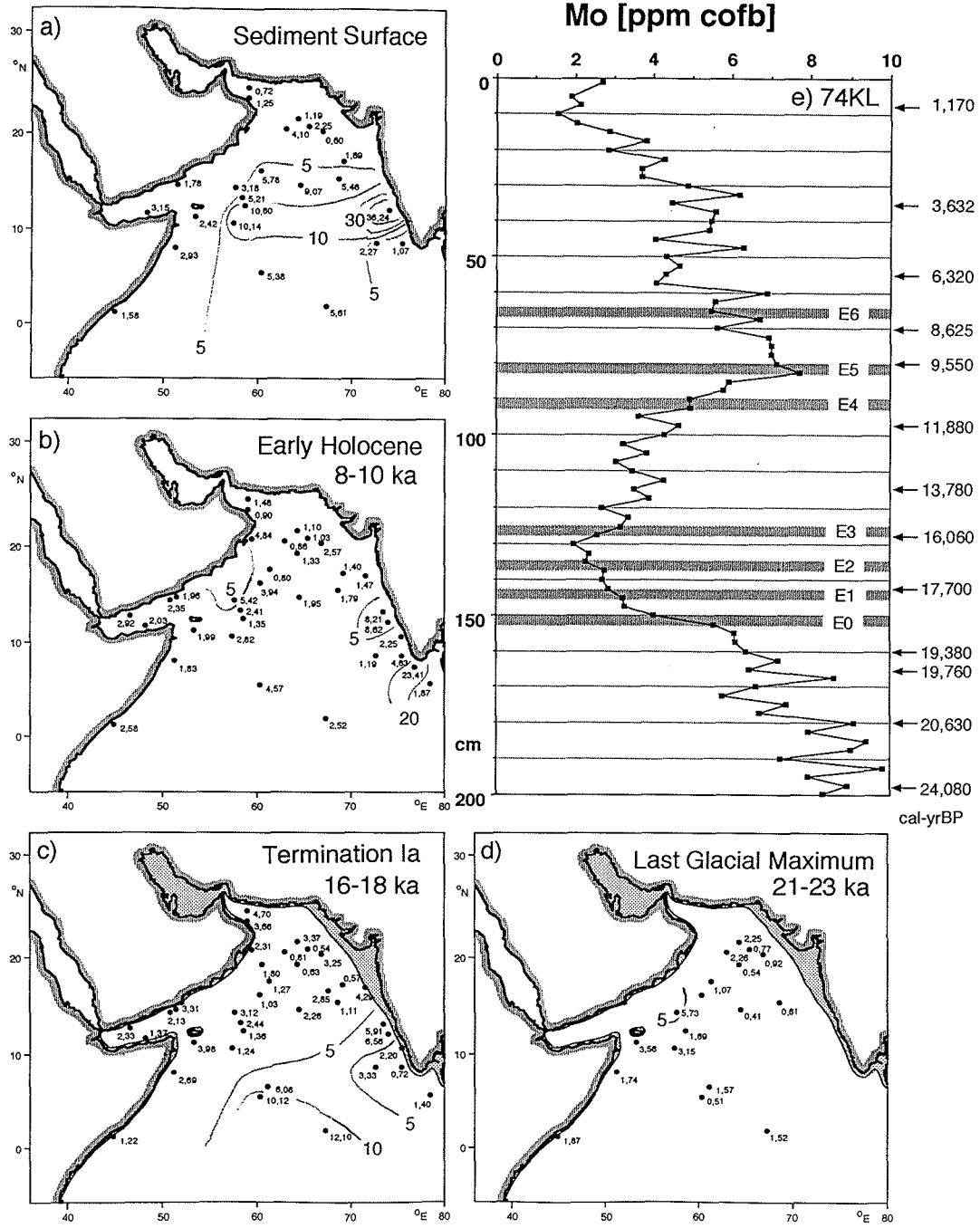

Figure 47. Molybdenum content, (a) at the sediment surface, (b) during the Early Holocene (8000-10,000 cal-yrBP), (c) during the Termination Ia (16,000-18,000 cal-yrBP), (d) during the Last Glacial Maximum (21,000-23,000 cal-yrBP), (e) sediment core 74KL, arrows indicate the depth of AMS-^{14}C dates, converted to calendar years according to Tab. 1, hatched areas show events as defined in Fig. 12.

Cadmium (Cd)

Table 5 continued, Cd content in various rock types, from Turekian & Wedepohl (1961)

	Igneous Rocks				Sedimentary Rocks			Deep-Sea Sediments	
Ultrabasic	Basalts	Ca-Granite	Granite	Syenites	Shales	Sandstone	Carbonates	Carbonate	Clay
ppm: 0.X	0.22	0.13	0.13	0.13	0.3	0.0X	0.04	0.0X	0.42

Cd content in the western Arabian Sea and Holocene section of core 74KL is near 2% thus, largely exceeding typical values in igneous rocks (Tab. 5) High values of Cd content in marine sediments can occur because biogenic tissue of marine organisms has Cd contents between 2 and 15 ppm. Calacarous tests of foraminifera and coccoliths also have high Cd contents, because they incorporate dissolved Cd from nutrient-rich water (Boyle, 1992). Cd concentrations in general closely follow PO_4 content of the water (Broecker & Peng, 1982; Bruland, 1980), and because it is incorporated into planktonic species, it has a high potential to monitor variations of surface water nutrient content and biogenic flux rates.

Cd concentrations in the Arabian Sea sediments show a clear maximum in the western Arabian Sea where PO_4-rich deepwater upwells to the surface (Fig. 48 a-b). Its distribution pattern is almost identical to Zn (Fig. 39), which reflects the H_4SiO_4 nutrient species, and to biogenic opal (Fig. 18). The maximum is strong during the Holocene, but weak and displaced to the coast of Somalia during the time of Termination Ia (Fig. 48 c, d).

Cd content in sediments at the location of sediment core 74KL show low values during the glacial, with a minimum between 150 and 125 cm (Fig. 48 e), corroborating the finding of minimum upwelling intensity during that Termination Ia interval, as being also shown in the record of C_{org}, Zn, and Ba (Figs. 21, 39, 50. The transition towards higher Cd values during the Holocene occurs at 85 cm depth. The other nutrient elements Zn, C_{org}, and Ba already reached the Holocene level at 95 cm depth. Cd content, in contrast shows spikes (remeasured twice) at 92.5 cm, 82.5-80 cm, and a sharp increase at 65 cm depth, ie. exactly during events E4, E5 and E6.

The reason for the different behaviour of Cd and Zn, C_{org}, Ba remains unexplained, but obviously Cd, which should monitor PO_4 content of surface waters, parallels more closely the $\delta^{18}O$ changes in the surface water than the other "nutrient elements". This could be due to the chemical inert nature of Cd in sediments, which could results in a better preservation of synsedimentary maxima.

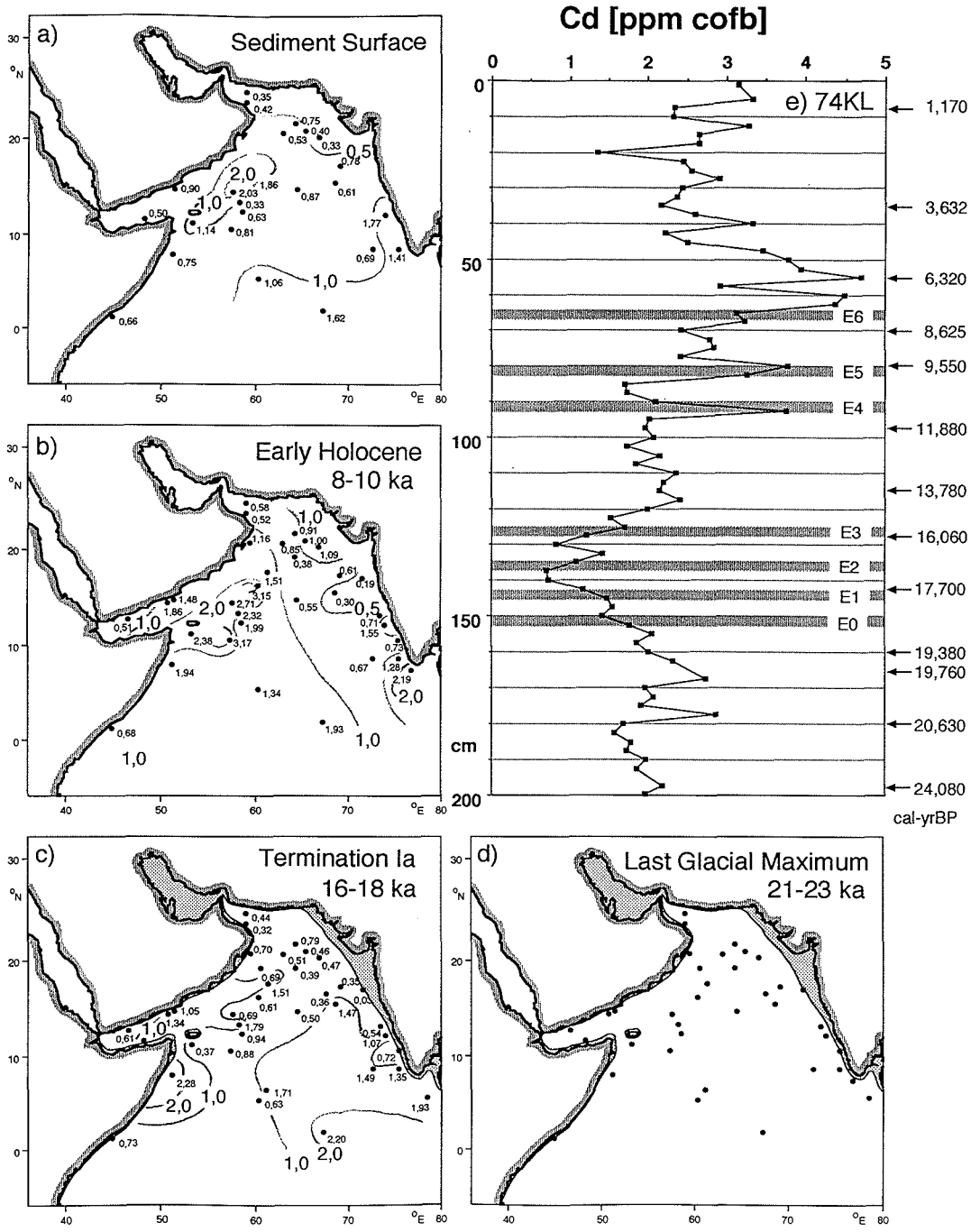

Figure 48. Cadmium content, (a) at the sediment surface, (b) during the Early Holocene (8000-10,000 cal-yrBP), (c) during the Termination Ia (16,000-18,000 cal-yrBP), (d) during the Last Glacial Maximum (21,000-23,000 cal-yrBP), (e) sediment core 74KL, arrows indicate the depth of AMS-^{14}C dates, converted to calendar years according to Tab. 1, hatched areas show events as defined in Fig. 12.

Cesium (Cs)

Table 5 continued, Cs content in various rock types, from Turekian & Wedepohl (1961)

	Igneous Rocks				Sedimentary Rocks			Deep-Sea Sediments	
Ultrabasic	Basalts	Ca-Granite	Granite	Syenites	Shales	Sandstone	Carbonates	Carbonate	Clay
ppm: 0.X	1.1	2.0	4.0	0.6	5.0	0.X	0.X	0.4	6.0

Cs easily replaces Rb and K in all K-feldspars and mica, and accordingly, igneous rocks with high feldspar or mica content reveal high Cs contents (Tab. 5). According to the mutual substitution of K, Rb and Cs we do not wonder that distribution patterns and downcore variations look nearly identical for these elements. Maximum values occur off Pakistan, in combination with a gradient towards the south, prominent during all time-slices (Figs. 29, 42, 49). The maximum off Pakistan indicates a source in the alluvial plains of northern India. Whether the transport mechanism to the Arabian Sea is eolian, riverine, or both, is hard to say; if it is eolian, the dust should be transported during spring or during the northeast monsoon winter season (Fig. 5). We cannot exclude the Indus as a possible source, because it has a high load of illite (Guptha & Hashimi, 1985), but the broad north to south gradient in the distribution pattern, suggests a transport system that reaches the elevated Oman Ridge in the western Arabian Sea, which is 700 km away from the Indus delta. Because leachable proportions of Cs are negligible in 74KL (Tab. 13), we favour the eolian source as the major contributor; dissolved proportions of the chemical rather inert Cs would have to result in a considerable leachabe proportion of Cs.

See K and Rb for a further interpretation of the distribution patterns and downcore variations of Cs.

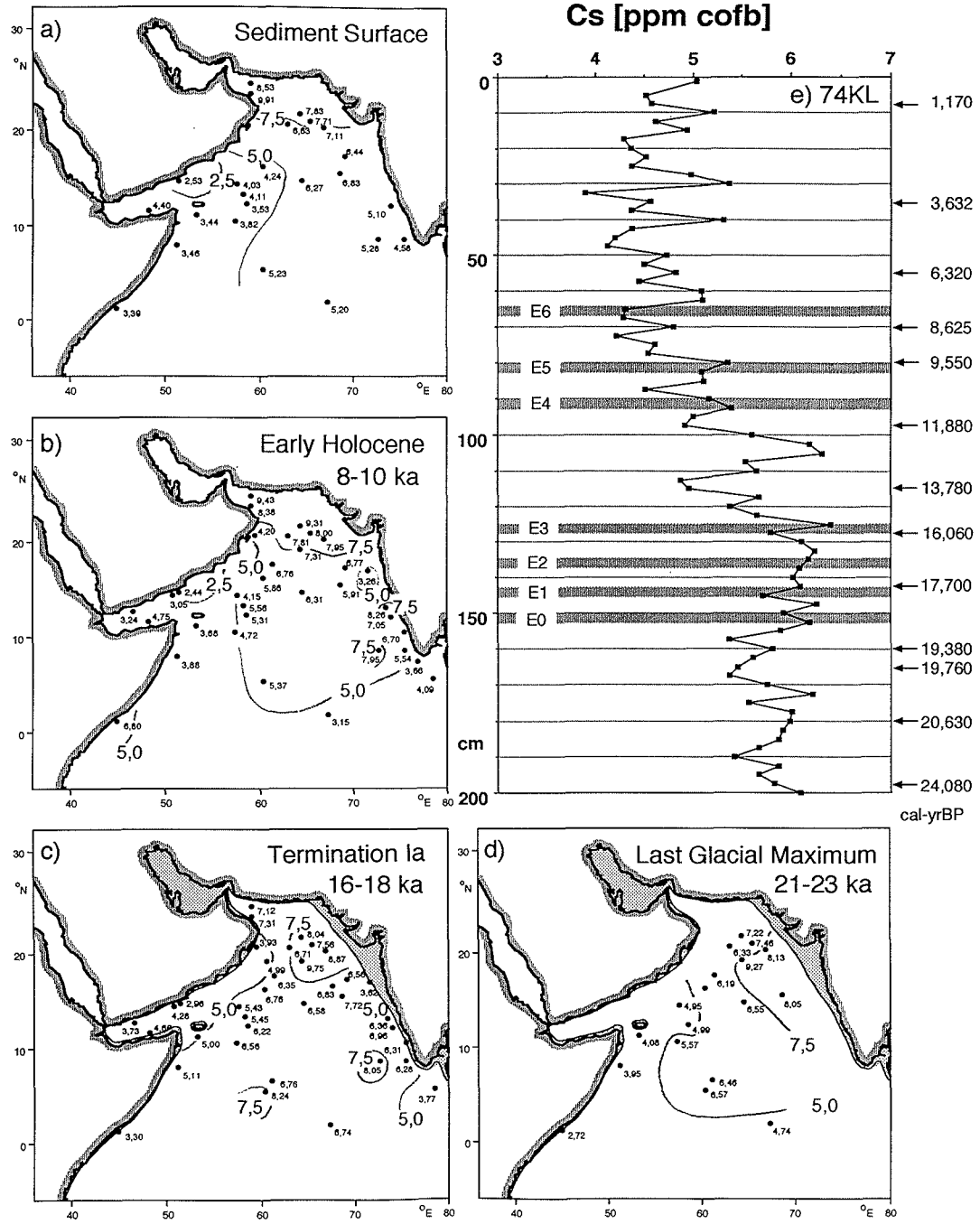

Figure 49. Cesium content, (a) at the sediment surface, (b) during the Early Holocene (8000-10,000 cal-yrBP), (c) during the Termination Ia (16,000-18,000 cal-yrBP), (d) during the Last Glacial Maximum (21,000-23,000 cal-yrBP), (e) sediment core 74KL, arrows indicate the depth of AMS-^{14}C dates, converted to calendar years according to Tab. 1, hatched areas show events as defined in Fig. 12.

Barium (Ba)

Table 5 continued. Ba content in various rock types, from Turekian & Wedepohl (1961)

Igneous Rocks					Sedimentary Rocks			Deep-Sea Sediments	
Ultrabasic	Basalts	Ca-Granite	Granite	Syenites	Shales	Sandstone	Carbonates	Carbonate	Clay
ppm: 0.4	330	420	840	1600	580		10	190	2300

Highest Ba content is found in sediments, rich in biogenic opal content (Tab. 5), because diatom frustules can contain up to 30,000 ppm Ba (Collier & Edmond, 1984). This Ba is removed from the water column by adsorption, or by formation of $BaSO_4$ crystals in reducing micro-environments of sinking organic particles (Bishop et al., 1977). The crystals are stable in the sediments and dissolve only under extremely reducing conditions (V. Marchig, pers. comm.).

The distribution pattern of Ba content (and also of Ba/Al) shows a persistent maximum over the Carlsberg Ridge in the equatorial Indian Ocean (Fig. 50 a-d). The maximum could be caused by the low content of lithic material in combination with intense dissolution of biogenic opal in that area (visible on smear slides). Thus, Ba content from the $BaSO_4$ crystals is relatively enriched over small lithic proportions, especially when concentrations are expressed on a carbonate-and-opal-free-basis (Fig. 50). The distribution pattern of accumulation rates of Ba (not shown) reveals the maximum in the region of high upwelling fertility in the western Arabian Sea.

Ba content in core 74KL is characterized by a steep increase between 100 cm and 80 cm. Using a concentration value of 20,000 ppm Ba in opaline tests (Collier & Edmond, 1984), a 500 ppm Ba content in the lithic fraction (Tab. 13), and 100 ppm content in the $CaCO_3$ fraction (*op.cit.*), the increase in opal content from 2 to 8% (observed in core 74KL between the Glacial and the Holocene section) should cause an increase in Ba content by 2000 ppm, which is indeed about the difference being found in core 74KL between the glacial and Holocene sections. Thus, variations of Ba in core 74KL mainly reflect biogenic opal content. The Ba minimum at 150-130cm depth in core 74KL, however, is not matched by respective changes in opal content (Fig. 18). The low Ba values are, however, paralleled by lowest C_{org} and Zn content (Fig. 21, 39), most probably reflecting a low upwelling fertility in the western Arabian Sea during that time (chapter D.4.).

This interpretation could be tested by applying the Ba-paleoproductivity equation of Dymond et al. (1992), but high-resolution accumulation rates cannot be calculated for core 74KL (Tab. 1b), and the fossil content of dissolved Ba in the deep Arabian Sea is not known. Both values are, however, a prerequisite for using the paleoproductivity equation.

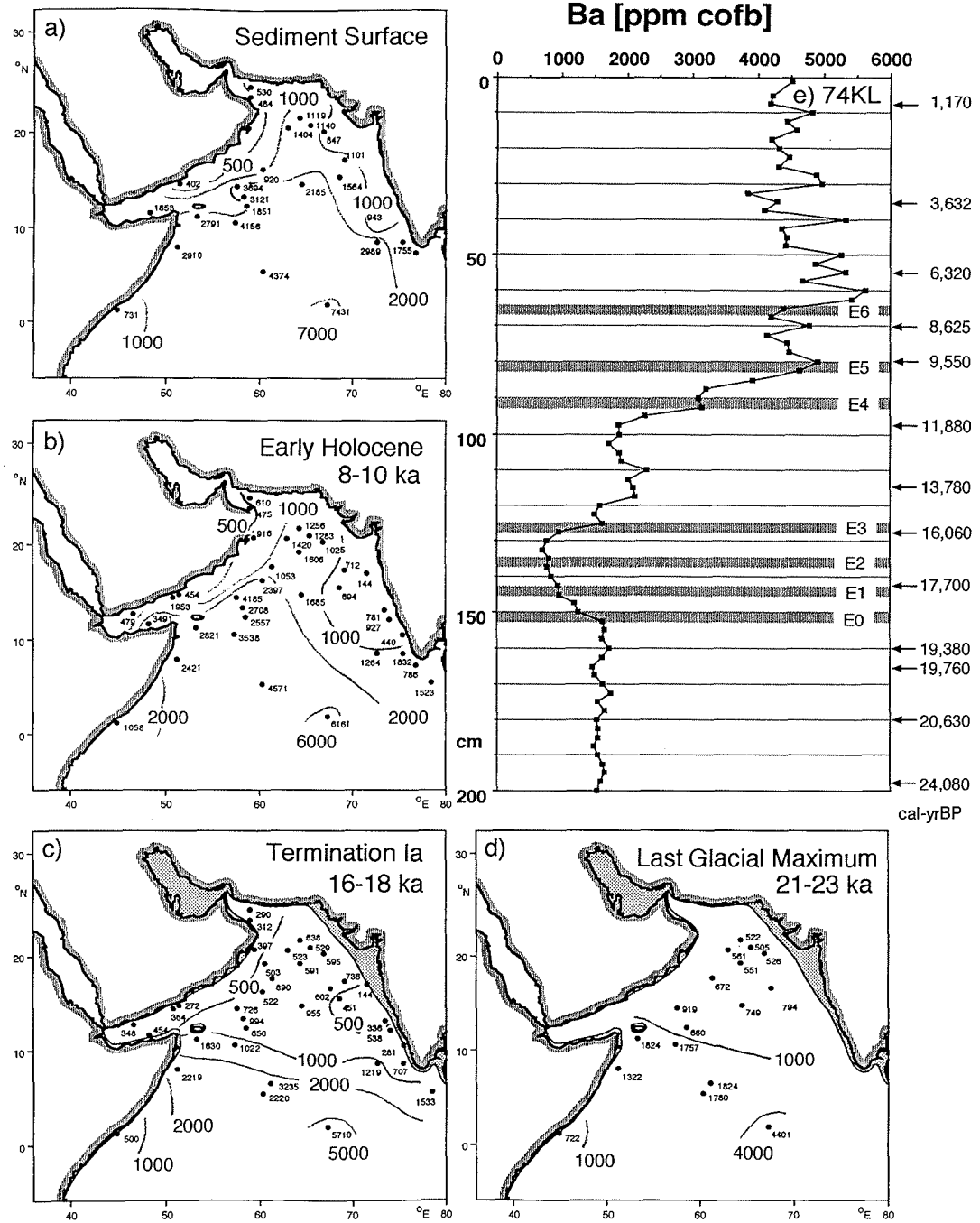

Figure 50. Barium content, (a) at the sediment surface, (b) during the Early Holocene (8000-10,000 cal-yrBP), (c) during the Termination Ia (16,000-18,000 cal-yrBP), (d) during the Last Glacial Maximum (21,000-23,000 cal-yrBP), (e) sediment core 74KL, arrows indicate the depth of AMS-^{14}C dates, converted to calendar years according to Tab. 1, hatched areas show events as defined in Fig. 12.

Lanthan (La) and the Rare Earth Elements (REE)
(Cerium-Ce, Praseodymium, Pr, Neodymium-Nd, Samarium-Sm, Europium-Eu, Gadolinium-Gd, Terbium-Tb, Dysprosium-Dy, Holmium-Ho, Erbium-Er, Thulium-Tm, Ytterbium-Yb, Lutetium-Lu)

Table 5 continued, Nd and Yb content in various rock types, from Turekian & Wedepohl (1961)

	Igneous Rocks				Sedimentary Rocks			Deep-Sea Sediments	
Ultrabasic	Basalts	Ca-Granite	Granite	Syenites	Shales	Sandstone	Carbonates	Carbonate	Clay
Neodymium:									
ppm: 0.X	20	33	37	65	24	37	4.7	14	140
Ytterbium									
ppm: 0.X	2.1	3.5	4.0	7.0	2.6	4.0	0.5	1.5	15

Only oncentration values of Nd and Yb are given in Tab. 5, because all rare earth elements (REE) reveal very similar relative proportions of concentrations in rocks. Some differences exist between the light rare earth elements (LREE) Ce, Pr, Nd, Sm and the heavy rare earth elements (HREE) Eu, Gd, Tb, Dy, Ho, Er, Tm, Yb, Lu. We will only discuss Nd and Yb being representative for the rest of the two subgroups. Numerical values of concentration values for all REE are given in Appendix 1-6. Concentrations of REE are generally higher in felsic than in mafic igneous rocks (Tab. 5). Extreme enrichment can occur in zircon minerals ($ZrSiO_4$), monazit ($Ce[PO_4]$, mainly light REE) and also in biogenic minerals, for example in xenotime ($Y[PO_4]$, mainly heavy REE).

Highest values of REE content are observed in sediments, because they can be adsorbed to clay minerals or organic matter. Similar to Zn, the REE reveal a close relation to H_2SiO_4 in ocean waters, a relation that was also found in the Arabian Sea deepwater (Bertram, 1989; German & Elderfield, 1990). Even if the REE are not believed to be an internal part of the nutrient cycle of anions, the REE kations follow the same pattern of depletion in surface waters and enrichment due to remobilisation at depth.

The distribution patterns of REE concentrations in the Arabian Sea show a very consistent picture: minumum values off Arabia and a gradient towards the open ocean, where they reveal a broad and prevailing maximum on the Carlsberg Ridge. The most likely explanation of this pattern could be the occurrence of small proportions of REE in the non-lithic fraction. This non-lithogenic proportion affects the concentration values of an element, when bulk values are expressed on a carbonate-free basis, in a way that $CaCO_3$ content must be positively correlated with element content. Accordingly, the REE maximum on the Carlsberg Ridge could simply reflect the occurrence on non-lithogenic REE in sediments. On the other hand, relatively high zircon contents on the Carlsberg Ridge might add that figure (Fig. 45).

The downcore variations of the LREE concentrations in core 74KL (Fig. 51 e)

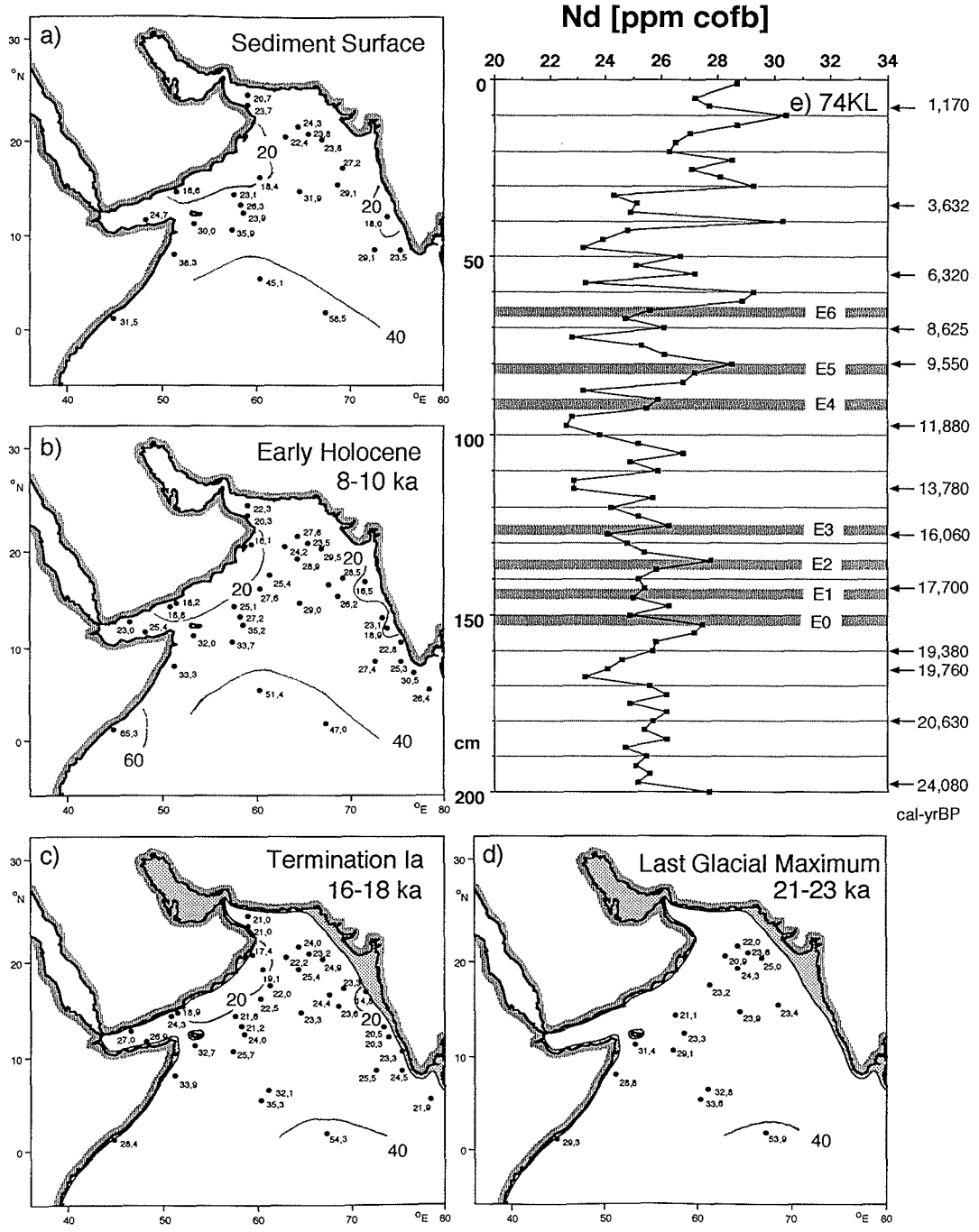

Figure 51.Neodymium (LREE) content, (a) at the sediment surface, (b) during the Early Holocene (8000-10,000 cal-yrBP), (c) during the Termination Ia (16,000-18,000 cal-yrBP), (d) during the Last Glacial Maximum (21,000-23,000 cal-yrBP), (e) sediment core 74KL, arrows indicate the depth of AMS-^{14}C dates, converted to calendar years according to Tab. 1, hatched areas show events as defined in Fig. 12.

closely resembles the Zr profile (Fig. 45 e) indicating that most the LREE have a lithic origin. The non-lithogenic REE proportions can be approximated by the REE/Zr ratio, which should account for the lithogenic REE proportions concentrated in zircons. When normalized to Zr, LREE show almost constant values or a weak enrichment in the upper meter of core 74KL (not shown). The HREE, however, Fig. 52 f, show a strong enrichment in the Holocene section of core 74KL, starting with event E4, which was shown to be the major event of monsoon intensification (see D.4.). The increase in the Yb/Zr ratio during event E4 parallels an increase in the leachable proportion of the HREE (Tab. 13), indicating that HREE were more effectively scavenged from the water column due to higher surface water productivity during the Holocene.

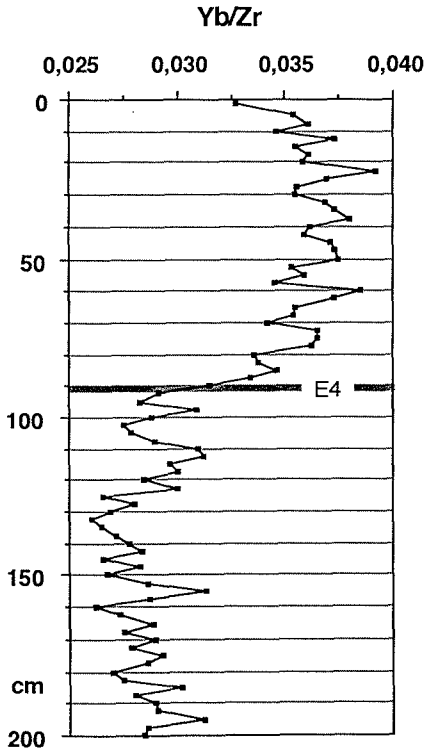

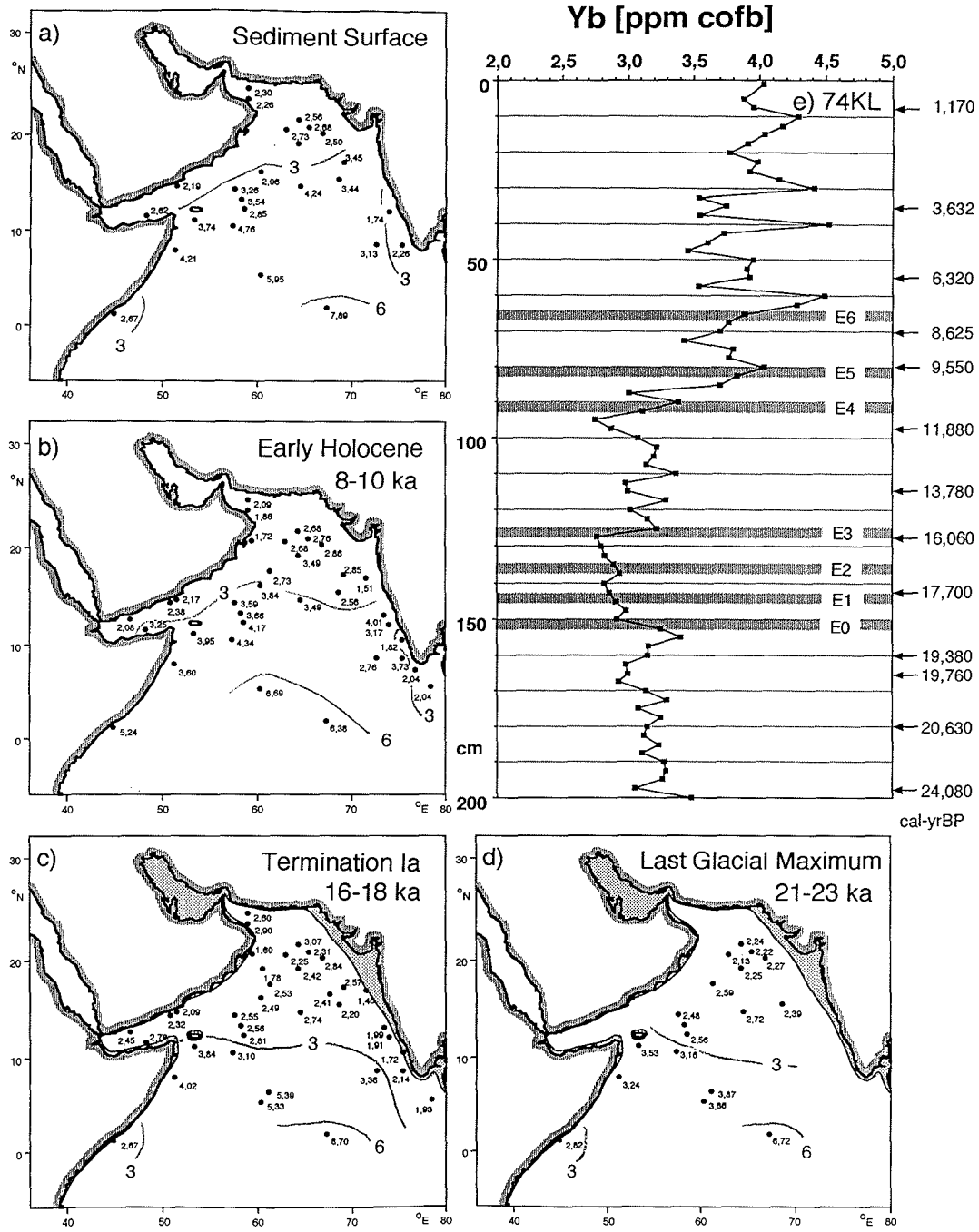

Figure 52. Ytterbium (HREE) content, (a) at the sediment surface, (b) during the Early Holocene (8000-10,000 cal-yrBP), (c) during the Termination Ia (16,000-18,000 cal-yrBP), (d) during the Last Glacial Maximum (21,000-23,000 cal-yrBP), (e) sediment core 74KL, arrows indicate the depth of AMS-^{14}C dates, converted to calendar years according to Tab. 1, hatched areas show events as defined in Fig. 12, (f) Ytterbium to zirconium ratio in sediment core 74KL.

Hafnium (Hf)

Table 5 continued. Hf content in various rock types, from Turekian & Wedepohl (1961)

	Igneous Rocks				Sedimentary Rocks			Deep-Sea Sediments	
Ultrabasic	Basalts	Ca-Granite	Granite	Syenites	Shales	Sandstone	Carbonates	Carbonate	Clay
ppm: 0.6	2.0	2.3	3.9	11.0	2.8	3.9	0.3	0.4	4.1
Zr/Hf::75	70	76	45	45	61	56	63	50	37

The chemistry of Hf closely resembles Zr, because both elements occur in the same valence status and the radius of their atoms and ions are nearly identical due to the lanthanide contraction (see Y). Like Zr, Hf does not have any biogenically mediated components in sediments, the leachable proportions are zero, and there is no enrichment in a specific size fraction (Tab.13). Accordingly, distribution patterns and downcore variations of Zr and Hf are very similar in the sediments of the Arabian Sea, revealing a minimum in the western Arabian Sea where dust plumes from Arabia dominate sedimentation patterns, and a maximum off East Africa, where detritus from the Ethiopian basalts could be frequent (Fig. 53 a-d).

An important difference between Hf and Zr is that zircons ($ZrSiO_4$) have up to 50% Zr, but significantly less Hf (Hinton & Upton, 1991). Accordingly, the Zr/Hf ratio, which is highest in mafic rocks (Tab. 5), should reflect the relative change in the abundance of zircon minerals. Distribution patterns of Zr/Hf have a pronounced maximum off East Africa (not shown) and the downcore variations of the ratio in 74KL show a abrupt increase at 81.25 cm, representing event E5 (Fig. 53 e). This increase in the abundance of Zr could be caused by more vigorous winds that can transport heavy minerals over long distances, it can be concluded that event E5 represents the event of intensification of the southwest monsoon wind strength at the location of core 74KL. This is in contrast to monsoon driven upwelling fertility, which had increased 1750 years earlier during event E4. See chapter D.4. for a further discussion.

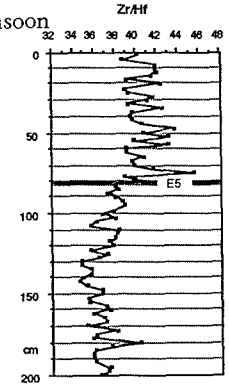

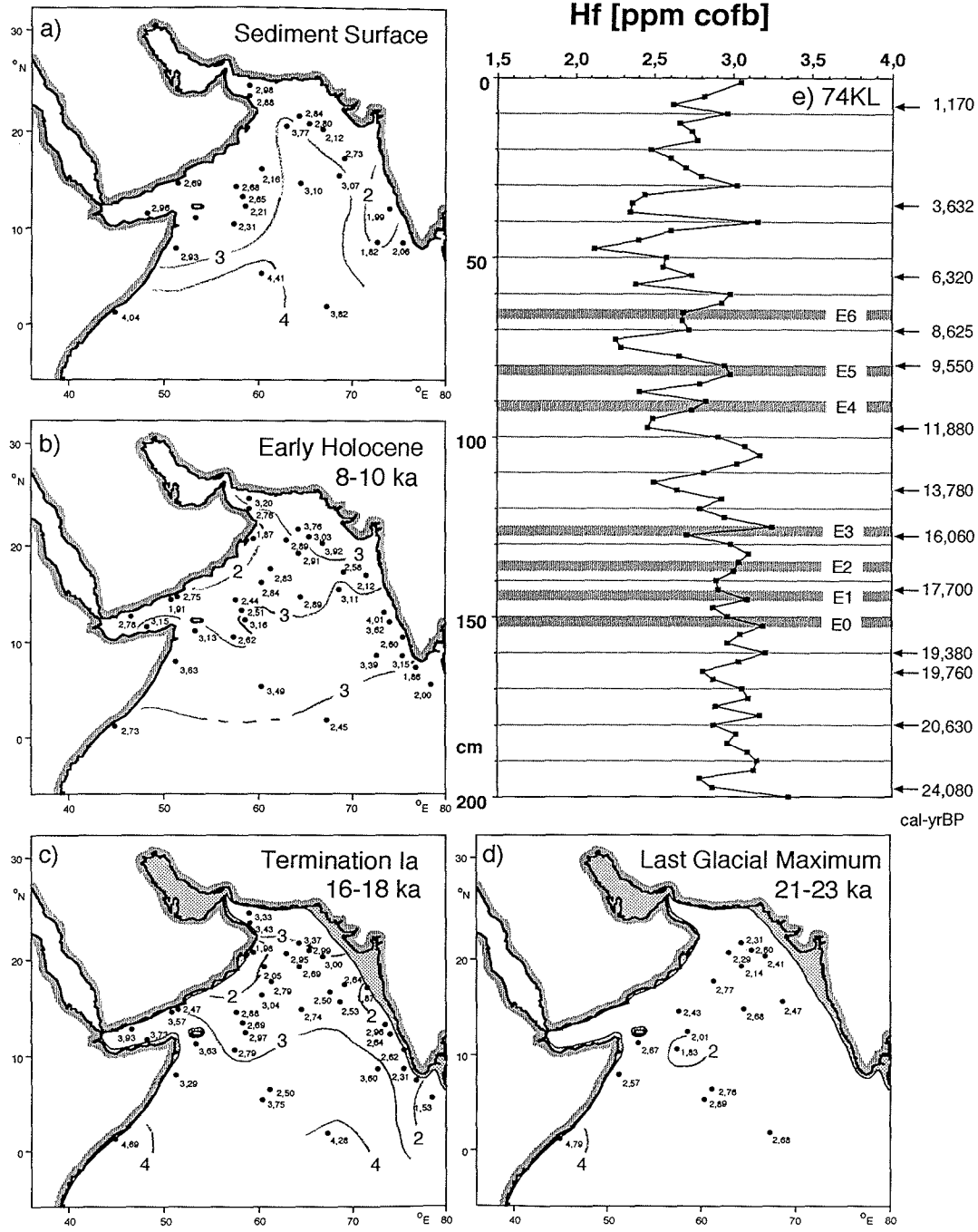

Figure 53. Hafnium content, (a) at the sediment surface, (b) during the Early Holocene (8000-10,000 cal-yrBP), (c) during the Termination Ia (16,000-18,000 cal-yrBP), (d) during the Last Glacial Maximum (21,000-23,000 cal-yrBP), (e) sediment core 74KL, arrows indicate the depth of AMS-^{14}C dates, converted to calendar years according to Tab. 1, hatched areas show events as defined in Fig. 12. (f) ratio between Zr and Hf.

Thallium (Tl)

Table 5 continued. Tl content in various rock types, from Turekian & Wedepohl (1961)

Igneous Rocks					Sedimentary Rocks			Deep-Sea Sediments	
Ultrabasic	Basalts	Ca-Granite	Granite	Syenites	Shales	Sandstone	Carbonates	Carbonate	Clay
ppm: 0.06	0.21	0.72	2.3	1.4	1.4	0.82	0.0X	0.16	0.8

Tl, an element enriched in felsic rocks (Tab. 5), reveals patchy irregular patterns in the sediments of the Arabian Sea (Fig. 54 a-d). Downcore variations in core 74KL do not follow a behaviour comparable to other elements (Fig. 54 e). The element has a substantial leachable fraction in core 74KL, but only little enrichment in the clay fraction (Tab. 13). At this stage, no interpretation of the Tl data seems to be possible.

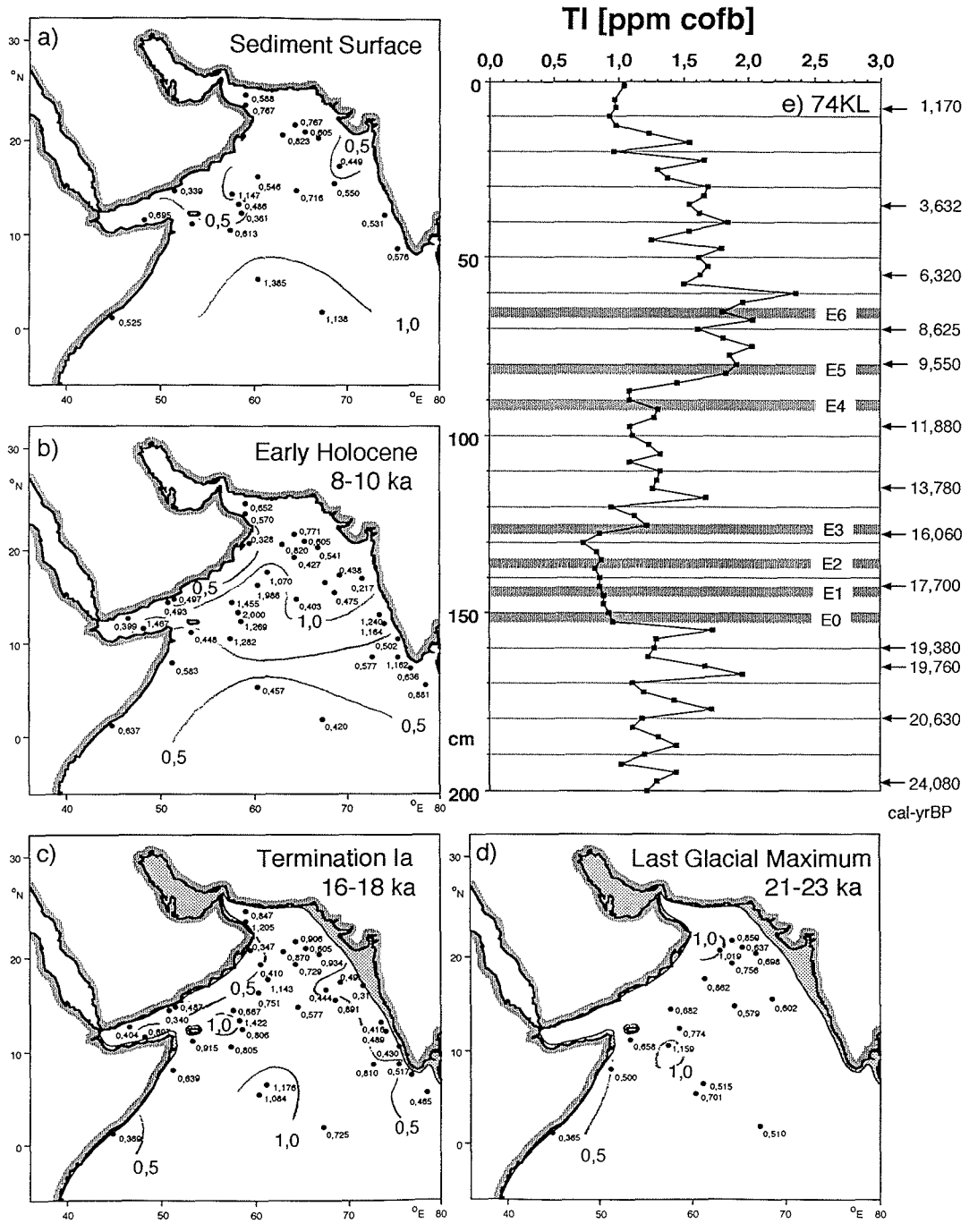

Figure 54. Thallium content, (a) at the sediment surface, (b) during the Early Holocene (8000-10,000 cal-yrBP), (c) during the Termination Ia (16,000-18,000 cal-yrBP), (d) during the Last Glacial Maximum (21,000-23,000 cal-yrBP), (e) sediment core 74KL, arrows indicate the depth of AMS-^{14}C dates, converted to calendar years according to Tab. 1, hatched areas show events as defined in Fig. 12.

Lead (Pb)

Table 5 continued. Pb content in various rock types, from Turekian & Wedepohl (1961)

	Igneous Rocks				Sedimentary Rocks			Deep-Sea Sediments	
Ultrabasic	Basalts	Ca-Granite	Granite	Syenites	Shales	Sandstone	Carbonates	Carbonate	Clay
ppm: 1.0	6.0	15.0	19.0	12.0	20.0	7.0	9.0	9.0	80.0

In the Arabian Sea sediments, we observe avarage concentrations of Pb, as being typical for igneous rocks, and a substantial leachable proportion (38%), but little enrichment in the clay fraction (Tab. 13). On the continental margin of India we find patchy maxima with extremes up to 136 ppm in the same samples that show Zn enrichment (Fig. 39).

The distribution patterns of Pb concentrations reveal consistently low values directly at the Arabian coast, but high values in the western Arabian Sea near core 74KL during the late and Early Holocene (Fig. 55 a, b). This Pb enrichment is confined to those areas where biogenic accumulation rates exceed lithic accumulation rates, probably due to scavenging of Pb from the water column.

The downcore variations of Pb in 74KL remain on the same level throughout the LGM, the Termination, Allerod/Bölling and the Younger Dryas. This is different to C_{org}, Zn or Ba content (Figs. 21, 39, 50), which show a minimum during Termination Ia (150 - 127.5 cm), being explained as an interval of lowest upwelling productivity (chapter D.4.). The only other geochemical parameter to show the same evolution as Pb content is the Yb/Zr ratio (Fig. 52 f).

A sharp increase of Pb content did not occur before event E4 at 92.5 cm depth in core 74KL (Fig. 55 e). This increase is not connected with a change in the leachable proportion or a change in a specific grain-size fraction. Its cause must be seen in the context of increases in upwelling fertility during event E4, which was found to be the event of main southwest monsoon intensification (chapter D.4.). A pronounced maximum of Pb occurs in core 74KL then during the Early Holocene (Fig. 55 e), at the same time when Co and Ni reveal a steep maxima (Figs. 36, 37) and dolomite content is zero (Fig. 12).

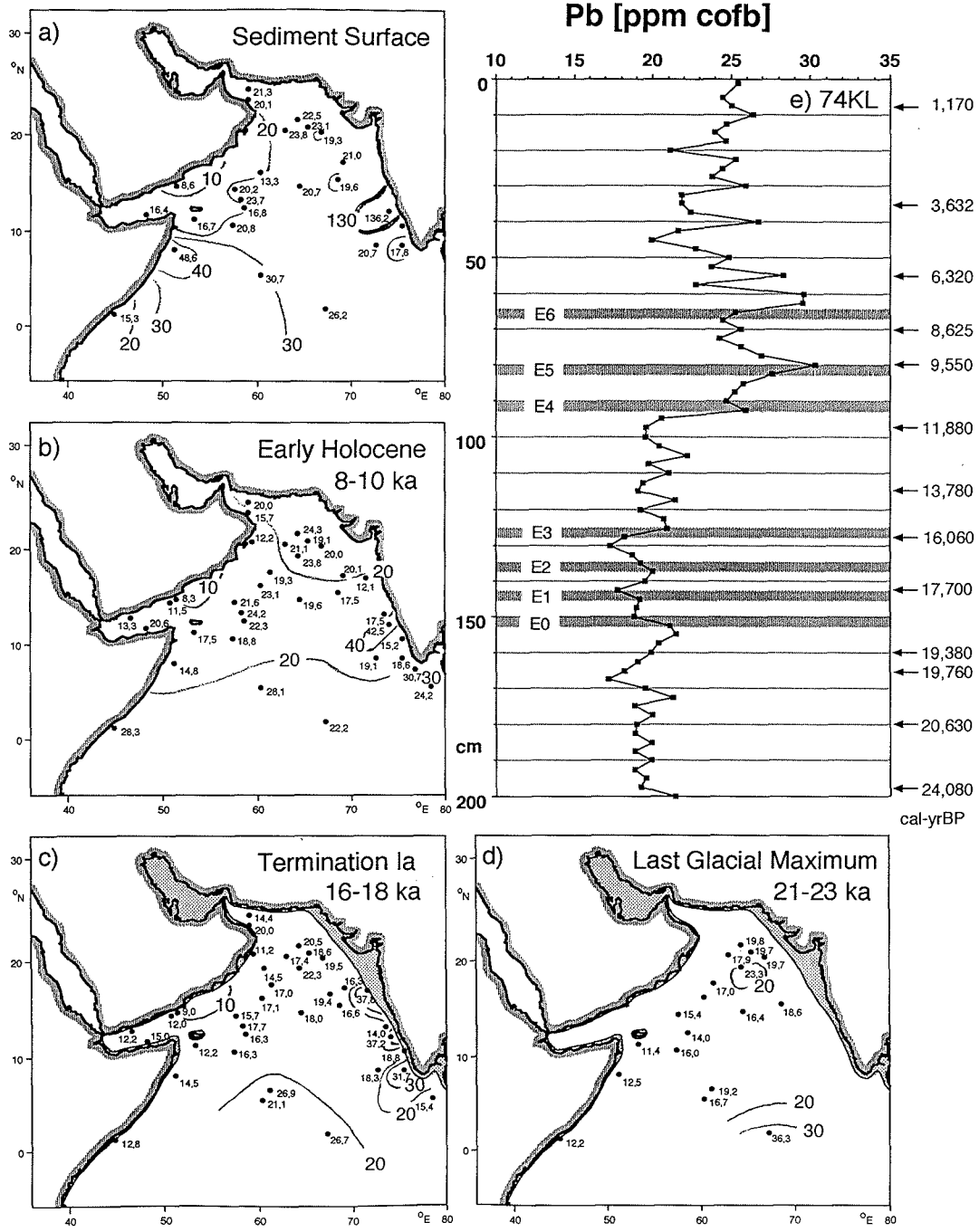

Figure 55. Lead content, (a) at the sediment surface, (b) during the Early Holocene (8000-10,000 cal-yrBP), (c) during the Termination Ia (16,000-18,000 cal-yrBP), (d) during the Last Glacial Maximum (21,000-23,000 cal-yrBP), (e) sediment core 74KL, arrows indicate the depth of AMS-^{14}C dates, converted to calendar years according to Tab. 1, hatched areas show events as defined in Fig. 12.

Uranium

Table 5 continued. U content in various rock types, from Turekian & Wedepohl (1961)

Igneous Rocks					Sedimentary Rocks			Deep-Sea Sediments	
Ultrabasic	Basalts	Ca-Granite	Granite	Syenites	Shales	Sandstone	Carbonates	Carbonate	Clay
ppm:0.001	1.0	3.0	3.0	3.0	3.7	0.45	2.2	0.X	1.3

U concentrations in the Arabian Sea sediments reveal persistant values > 3 ppm (the maximum value of U in rocks, Tab. 5), indicating large contributions from oceanic sources; indeed 80% of total U in core 74KL are found in the leachable fraction (Tab. 13). Maxima of U concentrations are observed in the western Arabian Sea, a pattern most similar to biogenic opal, Zn and Cd concentrations (Figs. 18, 39, 48). Accordingly, U concentrations in sediments of the western Arabian Sea appear to be related to the patterns of upwelling productivity even if U has no direct chemical link to the nutrient content of surface waters. Instead, organic carbon flux and organic carbon content appear to control the depth to the redox layer in the sediments (Finney & Mitchell, 1988), which then could control diffusion of U from the deepwater into the sediment (Klinkhammer & Palmer, 1991).

The downcore variations of U in 74KL reach their lowest level during the Termination Ia, intermediate values during the LGM and highest values during the Holocene above 85 cm (Fig. 56 e). Spike-like maxima of U content are found during events E4 and E5, which is similar to the profile of Zn and Cd (Figs. 39, 48).

The U-enrichment off India is, however, unlikely to be related to surface water productivity, which is rather low in this area (Wyrtki, 1971), but must be seen in the context of extreme organic carbon content on the Indian continental slope. Modern sediments reveal maximum U concentrations up to 12 ppm and C_{org} contents up to 6% (Marchig, 1974), an observation which was interpreted as a response to high preservation of organic carbon under conditions of anoxia at extremely high sedimentation rates.

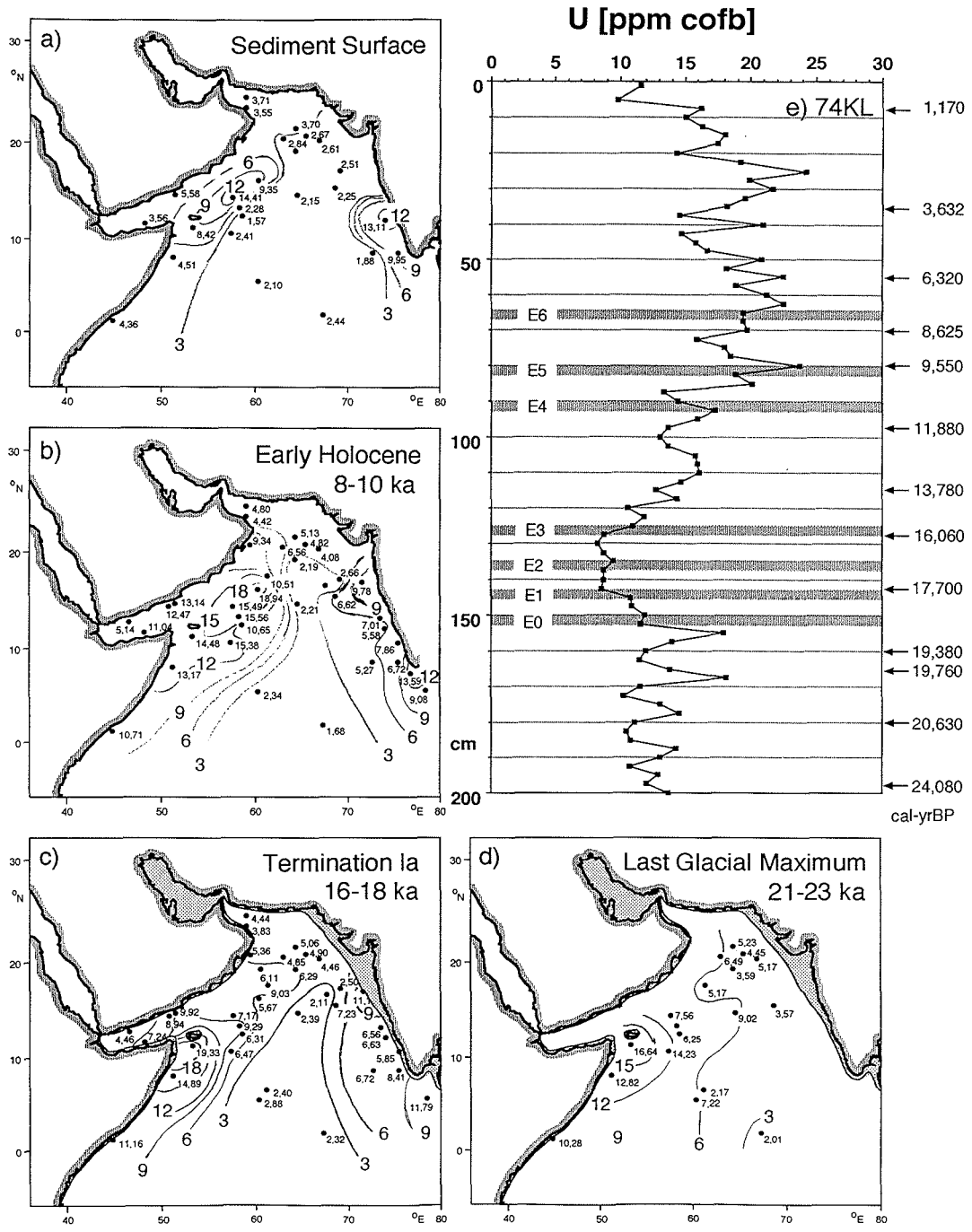

Figure 56. Uranium content, (a) at the sediment surface, (b) during the Early Holocene (8000-10,000 cal-yrBP), (c) during the Termination Ia (16,000-18,000 cal-yrBP), (d) during the Last Glacial Maximum (21,000-23,000 cal-yrBP), (e) sediment core 74KL, arrows indicate the depth of AMS-^{14}C dates, converted to calendar years according to Tab. 1, hatched areas show events as defined in Fig.

C.2. Factor analysis of element concentrations

For a joint interpretation of the distribution patterns of various elements (chapter C.1.) the complete data matrix was evaluated by factor analysis. This is a powerful statistical tool to identify groups (="factors") of elements with a similar depositional behaviour and to define the particular elements ("end members") that represent most of the variance in a group. The program SYSTAT served for calculating the principle component variability of all elements measured on a high resolution scale (2.5 cm intervals) in core 74KL. The program used a rotated correlation matrix, with a tolerance of 0.001 and 25 iterations. Because the correlation matrix was rotated, negative scores may in some cases (e.g., Figs. 57, F2) represent high concentration values. Accordingly, only the gradients in the distribution patterns of scores are evaluated.

Tabs. 6-10 and Figs. 57-61 show the factor loadings and scores for the geochemistry of all time-slices discussed in this study and downcore 74KL. In all cases, more than 90% of the variance can be explained by only seven factors. F1 always incorporates the REE, Y and Ba. The distribution patterns of the scores for F1 reveal a northwest to southeast gradient from the Arabian coast to the Carlsberg Ridge during all time-slices. In 74KL, the F1-values are higher during the Holocene than during the glacial, and the amplitude of variability is enlarged above 127.5 cm, representing event E3.

F2 primarily includes elements which show a maximum in the Persian Gulf area (Al) and/or northern India (Rb, Cs) (Figs. 57-61). The north to south gradient in the distribution pattern of factor scores for F3 indicates a provenance from dust plumes derived from Iran, Pakistan or northern India (similar to the dispersal of winter or spring dust plumes, Fig. 5) or from riverine contribution of the river Indus (Fig. 6). In 74KL, F2 also includes Mg, which is derived from wind-borne dust from Arabia, thus having another source area than Al, Rb, Cs, which are derived from areas further north (Figs. 25, 42, 49). The downcore variations of the F2 factor scores in core 74KL reveal a gradual transition from the glacial to the Holocene level, starting with an increase of amplitude after event E3 at 127.5 cm depth.

F3 is found in all time-slices with high loadings on Zr, Hf and Nb. Distribution patterns of the factor scores show a persistent, but in its position highly variable maximum off East Africa (Figs. 57-60). The most northerly position of this maximum is reached during the early Holocene. Zr, the major element of this factor, is enriched in the mineral zircon, which was observed in surface samples of core 114 SK. The distribution pattern of Zr, which has already been discussed in the context of eolian

	F1	F2	F3	F4	F5	F6	F7
CORG	-0,66	0,29	-0,14	-0,49	0,05	-0,23	0,34
N	-0,62	0,08	-0,12	-0,55	0,14	-0,35	0,29
S	-0,02	0,63	-0,22	0,05	0,09	-0,68	0,14
AL	-0,39	-0,75	0,41	-0,15	-0,22	0,14	-0,13
FE	-0,01	-0,73	0,53	-0,04	-0,19	-0,07	-0,19
MN	0,07	0,29	-0,06	0,82	-0,25	-0,34	-0,09
MG	-0,26	0,07	-0,91	-0,08	0,15	-0,02	-0,08
LI	0,90	-0,25	-0,29	-0,06	0,02	-0,03	-0,19
NA	0,90	0,25	-0,12	0,15	0,10	-0,16	-0,22
K	-0,27	-0,52	0,40	0,35	-0,22	0,47	0,21
SC	0,09	0,05	-0,32	0,04	0,08	0,00	-0,92
CR	-0,44	-0,22	-0,61	-0,26	-0,13	0,24	-0,20
CO	0,39	-0,23	-0,11	0,82	0,01	0,02	0,18
NI	0,08	-0,08	-0,22	0,80	0,19	-0,18	-0,19
CU	0,83	0,02	-0,07	0,52	0,12	0,03	0,01
ZN	-0,55	0,15	0,30	0,04	0,62	-0,31	-0,28
GA	-0,04	0,03	-0,14	-0,25	-0,04	0,76	0,00
AS	0,29	-0,30	-0,02	0,60	-0,10	0,57	0,15
RB	-0,13	-0,94	0,19	-0,14	-0,12	0,09	0,09
SRCA	-0,32	-0,40	0,71	0,00	0,11	-0,28	0,13
Y	0,98	0,05	0,02	0,14	0,02	0,06	0,06
ZR	-0,08	-0,06	0,87	-0,33	-0,06	0,22	0,02
NB	0,50	-0,19	0,62	-0,30	0,04	-0,11	0,26
MO	0,27	0,25	0,01	0,90	-0,17	-0,01	0,08
CD	0,50	0,34	-0,16	-0,04	0,75	0,12	-0,02
CS	0,01	-0,96	-0,16	0,05	-0,06	0,08	0,13
BA	0,90	0,14	-0,07	0,20	0,30	-0,18	0,02
LA	0,96	-0,05	0,25	0,03	-0,04	0,01	-0,01
CE	0,66	-0,24	0,69	-0,13	-0,08	-0,02	0,01
PR	0,95	-0,03	0,29	0,06	-0,06	0,03	0,03
ND	0,97	0,01	0,22	0,04	-0,04	0,03	0,03
SM	0,98	0,05	0,17	0,07	-0,03	-0,02	0,03
EU	0,99	0,07	0,12	0,07	0,00	-0,02	0,04
GD	0,99	0,04	0,09	0,08	-0,03	0,02	0,06
TB	0,99	0,07	0,06	0,05	0,01	0,00	-0,03
DY	0,99	0,04	0,05	0,13	-0,01	0,01	0,01
HO	0,99	0,04	0,02	0,09	0,02	0,02	0,01
ER	0,99	0,03	0,01	0,14	0,03	0,00	-0,02
TM	0,99	0,02	-0,01	0,14	0,06	0,03	0,03
YB	0,98	0,00	-0,02	0,15	0,06	0,05	0,02
LU	0,98	0,02	-0,01	0,14	0,08	0,01	0,02
HF	0,31	-0,33	0,56	-0,45	0,12	0,08	0,35
TL	0,54	-0,19	0,01	0,01	0,76	-0,22	0,17
PB	0,59	-0,65	-0,02	0,30	0,24	-0,19	0,01
U	-0,22	0,26	-0,12	-0,23	0,88	-0,04	-0,09
total variance explained:	45,30	11,60	11,20	11,30	6,50	5,30	3,80

Table 6. Factor loadings, and total variance explained by each factor, for the geochemical composition at the sediment surface.

Figure 57. Factor scores for the geochemical composition at the sediment surface. The three elements that explain most of the variance are shown in the header (from Tab. 6).

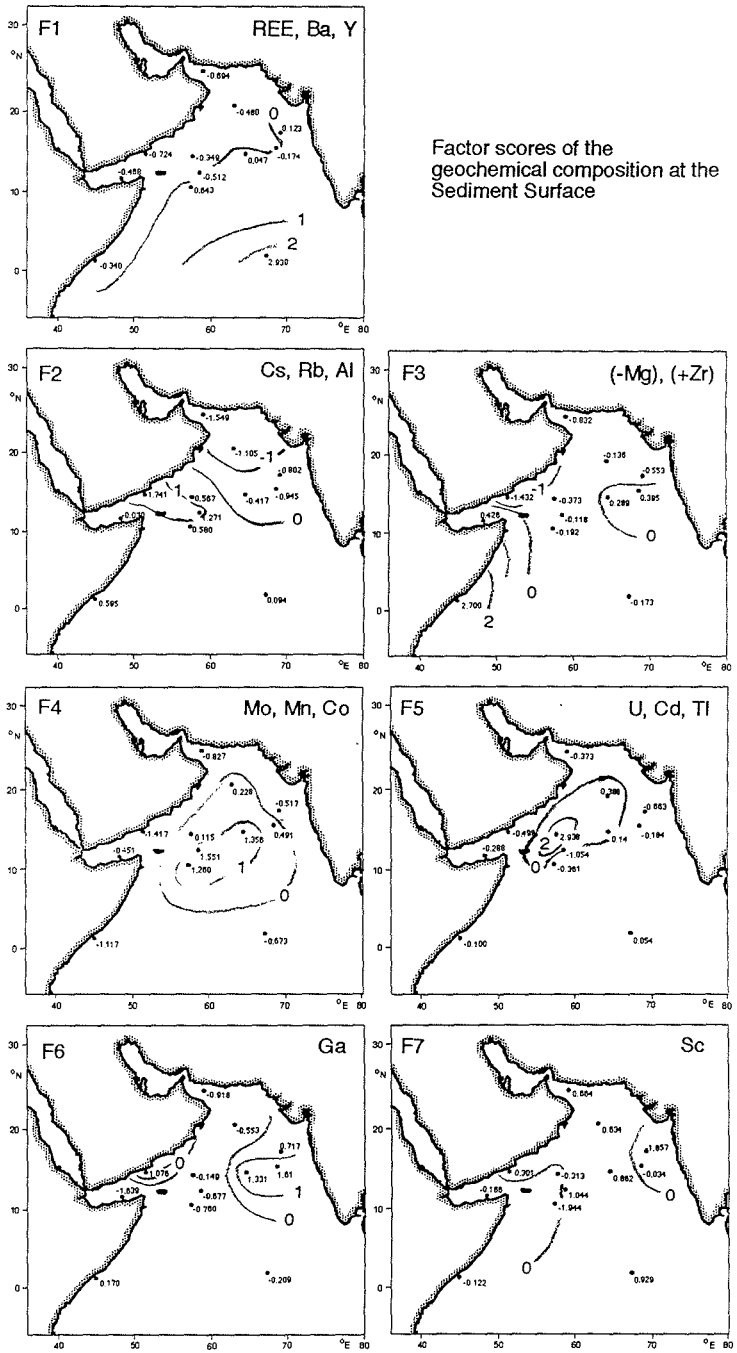

CORG	-0,20	0,33	0,02	0,03	-0,88	-0,02
N	-0,30	0,11	0,20	0,07	-0,87	0,06
S	0,16	0,08	0,00	0,02	-0,81	-0,07
AL	-0,07	-0,89	0,17	-0,33	0,11	-0,02
FE	0,26	-0,67	0,25	-0,19	0,31	0,02
MN	0,29	0,19	0,20	0,58	0,37	0,49
MG	-0,69	0,22	-0,04	0,44	-0,22	0,26
LI	0,43	0,21	0,03	-0,02	0,76	0,18
NA	0,39	0,73	0,04	0,22	0,37	-0,05
K	-0,26	-0,78	0,02	0,15	0,07	-0,10
SC	0,21	-0,14	0,28	-0,26	-0,49	0,40
CR	-0,40	-0,45	-0,06	-0,08	-0,59	0,33
CO	0,36	-0,04	-0,33	0,61	0,40	0,34
NI	-0,15	0,04	0,00	0,94	0,08	0,18
CU	0,48	0,46	0,17	0,39	0,50	0,27
ZN	0,09	0,10	0,23	0,92	-0,11	-0,07
GA	0,24	-0,24	0,56	0,25	-0,26	-0,10
AS	0,14	0,18	-0,30	0,11	0,07	0,80
RB	0,15	-0,93	0,04	-0,11	-0,06	-0,16
SRCA	0,04	-0,12	0,02	-0,03	0,05	-0,09
Y	0,53	0,48	0,04	0,00	0,53	0,33
ZR	-0,04	0,05	0,91	0,16	-0,08	-0,04
NB	0,48	0,03	0,33	-0,50	0,52	-0,17
MO	0,41	0,25	0,06	0,53	-0,03	0,38
CD	0,09	0,58	-0,24	0,57	0,10	-0,14
CS	-0,20	-0,93	-0,02	-0,07	0,20	-0,13
BA	0,53	0,53	0,04	0,28	0,34	0,15
LA	0,99	-0,09	0,00	-0,06	0,00	-0,04
CE	0,76	-0,46	0,08	0,04	-0,30	-0,16
PR	0,97	-0,17	0,01	-0,06	-0,08	-0,06
ND	0,98	-0,10	-0,01	-0,05	-0,03	-0,05
SM	0,99	-0,04	-0,02	-0,04	0,02	-0,01
EU	0,99	0,05	-0,02	-0,01	0,04	0,03
GD	0,98	0,12	-0,02	-0,03	0,14	0,04
TB	0,98	0,12	0,00	-0,02	0,13	0,07
DY	0,97	0,17	0,01	0,02	0,17	0,08
HO	0,93	0,22	0,02	0,03	0,23	0,14
ER	0,92	0,24	0,04	0,06	0,23	0,17
TM	0,93	0,19	0,00	0,05	0,25	0,16
YB	0,91	0,25	0,00	0,12	0,21	0,19
LU	0,90	0,24	0,06	0,15	0,23	0,19
HF	-0,09	-0,33	0,68	-0,37	0,20	-0,20
TL	-0,17	0,07	-0,05	0,94	-0,01	-0,02
PB	0,65	-0,52	0,00	0,43	0,26	0,09
U	-0,13	0,44	0,04	0,70	-0,36	-0,31
total variance explained:	35,20	15,50	5,20	13,10	12,60	4,90

Table 7. Factor loadings, and total variance explained by each factor, for the geochemical composition during the Early Holocene (8-10 ka).

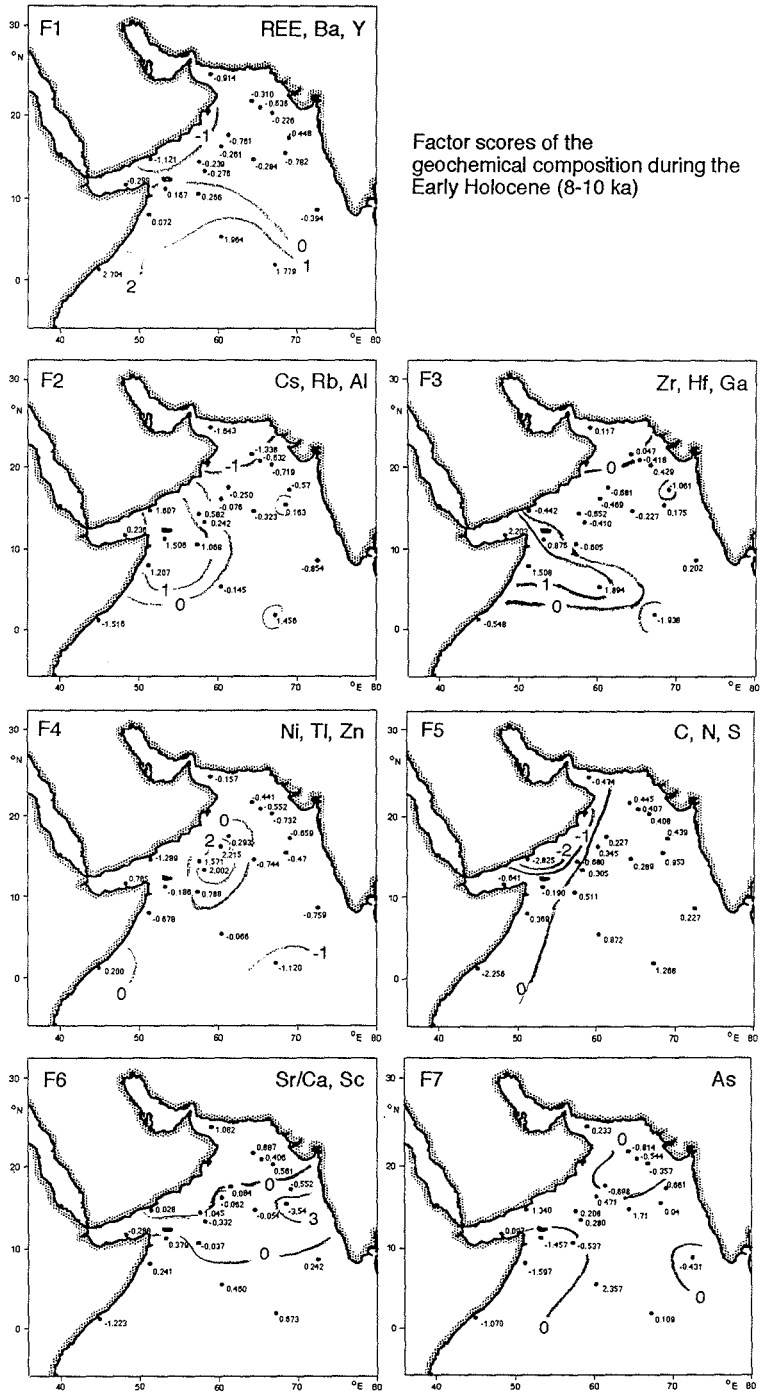

Factor scores of the geochemical composition during the Early Holocene (8-10 ka)

Figure 58. Factor scores for the geochemical composition during the Early Holocene (8-10 ka). The three elements that explain most of the variance are shown in the header (from Tab. 7).

CORG	-0,47	-0,22	-0,21	0,00	-0,75	-0,05	-0,26
N	-0,26	-0,08	-0,11	0,00	-0,81	0,34	-0,22
S	-0,02	-0,17	-0,01	-0,03	-0,90	-0,11	0,03
AL	-0,20	0,61	0,14	0,06	0,01	0,11	0,55
FE	0,19	0,23	-0,03	-0,02	0,34	0,08	0,80
MN	0,34	0,07	0,29	0,59	0,00	-0,25	0,43
MG	-0,38	-0,65	0,00	0,23	0,01	-0,37	-0,17
LI	0,33	0,08	0,73	0,09	0,10	0,37	-0,13
NA	0,83	-0,26	0,34	0,04	0,21	0,14	0,05
K	0,80	0,08	-0,33	-0,08	0,38	0,09	0,08
SC	0,82	0,07	-0,15	-0,21	-0,33	-0,11	0,07
CR	-0,41	-0,15	-0,31	0,11	-0,45	-0,54	-0,10
CO	0,89	0,13	-0,11	0,30	0,05	-0,15	0,15
NI	0,35	-0,37	0,08	0,75	0,14	-0,19	0,24
CU	0,88	0,06	0,05	0,33	0,09	0,08	0,18
ZN	0,58	-0,08	-0,29	0,25	0,28	0,37	0,08
GA	0,24	0,69	0,34	-0,22	-0,02	-0,03	0,22
AS	0,42	-0,12	-0,43	0,11	-0,03	0,07	0,57
RB	-0,02	0,92	-0,16	0,04	0,26	0,03	-0,06
SRCA	-0,20	0,34	0,11	-0,07	-0,17	0,66	0,23
Y	0,97	-0,10	0,09	-0,06	0,15	0,08	0,01
ZR	0,16	-0,36	0,74	-0,20	0,21	-0,06	-0,05
NB	0,18	0,12	0,91	0,18	0,10	-0,04	0,16
MO	0,90	0,08	-0,01	0,22	-0,24	-0,13	0,19
CD	0,49	-0,28	0,01	0,11	0,01	0,58	-0,18
CS	0,01	0,90	-0,13	0,21	0,22	-0,07	-0,01
BA	0,96	-0,08	-0,02	0,05	0,18	0,17	-0,01
LA	0,95	0,04	0,15	-0,08	0,21	0,10	-0,02
CE	0,79	0,27	0,18	-0,06	0,43	0,12	0,04
PR	0,97	0,04	0,08	-0,03	0,21	0,10	0,02
ND	0,94	0,02	0,23	-0,06	0,19	0,06	0,00
SM	0,98	0,12	0,03	0,08	0,09	0,02	0,05
EU	0,97	0,10	0,09	0,10	0,00	-0,06	0,10
GD	0,97	0,04	0,13	0,02	0,08	-0,04	0,04
TB	0,99	0,04	0,08	0,03	0,10	0,00	0,05
DY	0,98	-0,03	0,12	0,04	0,11	0,03	0,04
HO	0,98	-0,02	0,09	0,05	0,12	0,06	0,05
ER	0,98	-0,01	0,09	0,05	0,12	0,02	0,05
TM	0,92	0,13	0,14	0,24	0,03	-0,05	0,17
YB	0,99	0,03	0,04	0,07	0,11	0,02	0,05
LU	0,97	0,09	0,05	0,16	0,06	0,00	0,09
HF	0,61	0,16	0,53	-0,04	-0,11	-0,39	0,08
TL	0,03	0,16	-0,08	0,85	-0,06	0,15	-0,14
PB	0,58	0,50	-0,37	0,26	0,42	0,02	-0,03
U	-0,16	-0,44	0,64	-0,02	-0,16	0,31	-0,37
total variance explained:	48,30	9,60	8,70	5,50	8,10	4,87	4,90

Table 8. Factor loadings, and total variance explained by each factor, for the geochemical composition during the Termination Ia (16-18 ka).

Figure 59. Factor scores for the geochemical composition during the Late Glacial (16-18 ka). The three elements that explain most of the variance are shown in the header (from Tab. 8).

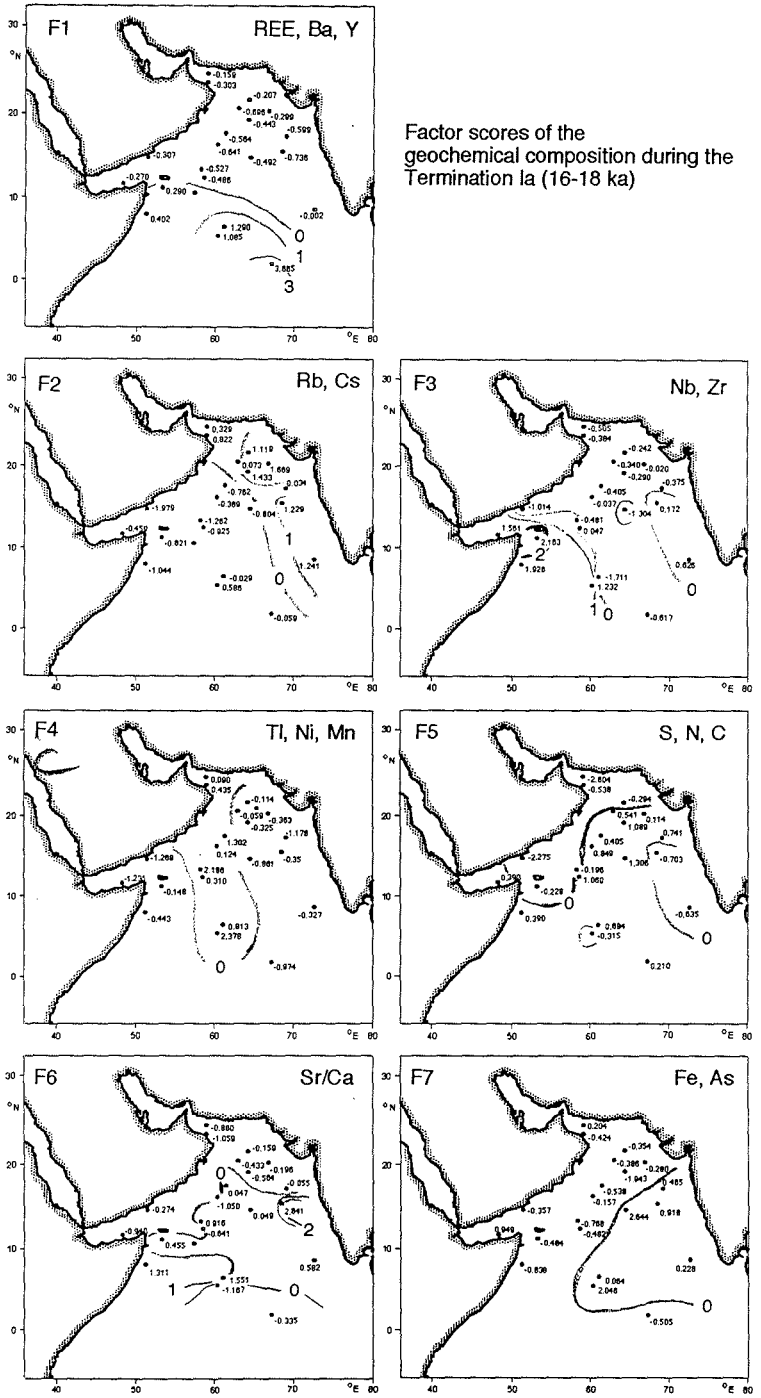

Factor scores of the geochemical composition during the Termination Ia (16-18 ka)

	F1	F2	F3	F4	F5	F6	F7
CORG	-0,58	0,07	0,17	0,12	-0,70	0,05	0,00
N	-0,55	0,32	0,13	0,13	-0,61	-0,16	0,22
S	-0,30	0,18	0,06	-0,28	-0,78	-0,12	0,00
AL	-0,49	-0,84	0,02	-0,06	-0,10	0,10	0,17
FE	0,23	-0,82	0,06	0,21	-0,01	0,18	-0,17
MN	0,34	-0,09	-0,22	0,28	0,01	0,86	-0,06
MG	-0,33	0,08	-0,62	0,45	-0,40	0,18	-0,27
SC	0,21	-0,07	-0,70	-0,03	0,34	0,23	0,14
CR	-0,50	-0,30	-0,50	0,16	-0,50	0,10	-0,24
CO	0,22	-0,20	-0,20	0,02	0,08	0,92	0,05
NI	-0,16	0,09	-0,51	0,73	-0,11	0,29	-0,26
CU	0,89	0,11	-0,15	0,19	0,28	-0,03	-0,20
ZN	0,52	0,03	-0,19	0,71	0,33	0,04	-0,13
GA	-0,29	-0,84	-0,03	0,00	0,24	-0,07	0,15
RB	-0,41	-0,85	-0,24	0,00	0,17	-0,01	0,14
SRCA	-0,52	-0,06	0,55	-0,11	0,45	-0,15	0,33
Y	0,98	0,09	0,00	-0,03	0,11	0,08	-0,07
ZR	0,04	0,13	0,95	-0,09	-0,05	-0,10	-0,13
NB	-0,08	0,15	0,92	-0,20	0,00	-0,07	0,24
MO	0,03	0,76	-0,11	0,13	-0,32	0,14	0,42
CS	-0,35	-0,77	-0,49	0,03	0,15	0,08	0,07
BA	0,98	0,12	-0,06	0,06	0,11	0,07	0,02
LA	0,96	0,04	0,18	-0,07	0,14	0,08	0,08
CE	0,52	-0,37	0,61	-0,13	0,23	0,14	0,31
PR	0,97	0,02	0,16	-0,06	0,13	0,07	0,07
ND	0,98	0,04	0,13	-0,02	0,13	0,04	0,05
SM	0,99	0,03	0,07	-0,02	0,08	0,04	0,03
EU	0,99	0,07	0,09	-0,01	0,03	0,03	0,00
GD	0,99	0,09	0,01	0,01	0,10	0,06	-0,01
TB	0,99	0,04	0,01	-0,02	0,08	0,10	-0,02
DY	0,98	0,10	-0,02	-0,06	0,07	0,07	0,04
HO	0,99	0,07	0,00	0,01	0,09	0,08	-0,03
ER	0,98	0,09	0,01	0,01	0,11	0,08	-0,06
TM	0,98	0,09	-0,02	-0,02	0,08	0,14	-0,04
YB	0,99	0,08	0,04	-0,01	0,09	0,07	-0,07
LU	0,98	0,04	-0,01	-0,02	0,07	0,17	-0,04
HF	0,08	0,09	0,96	-0,18	-0,07	-0,03	-0,13
TL	-0,24	0,00	-0,40	0,81	-0,02	0,07	0,31
PB	0,70	-0,55	-0,23	-0,04	-0,12	0,07	0,20
U	-0,13	0,81	0,13	0,24	0,32	-0,34	0,13
total variance explained:	46,50	13,80	13,80	6,00	7,40	5,40	2,70

Table 9. Factor loadings, and total variance explained by each factor, for the geochemical composition during the Last Glacial Maximum (21-23 ka).

Figure 60. Factor scores for the geochemical composition during the Last Glacial Maximum (21-23 ka). The three elements that explain most of the variance are shown in the header (from Tab. 9).

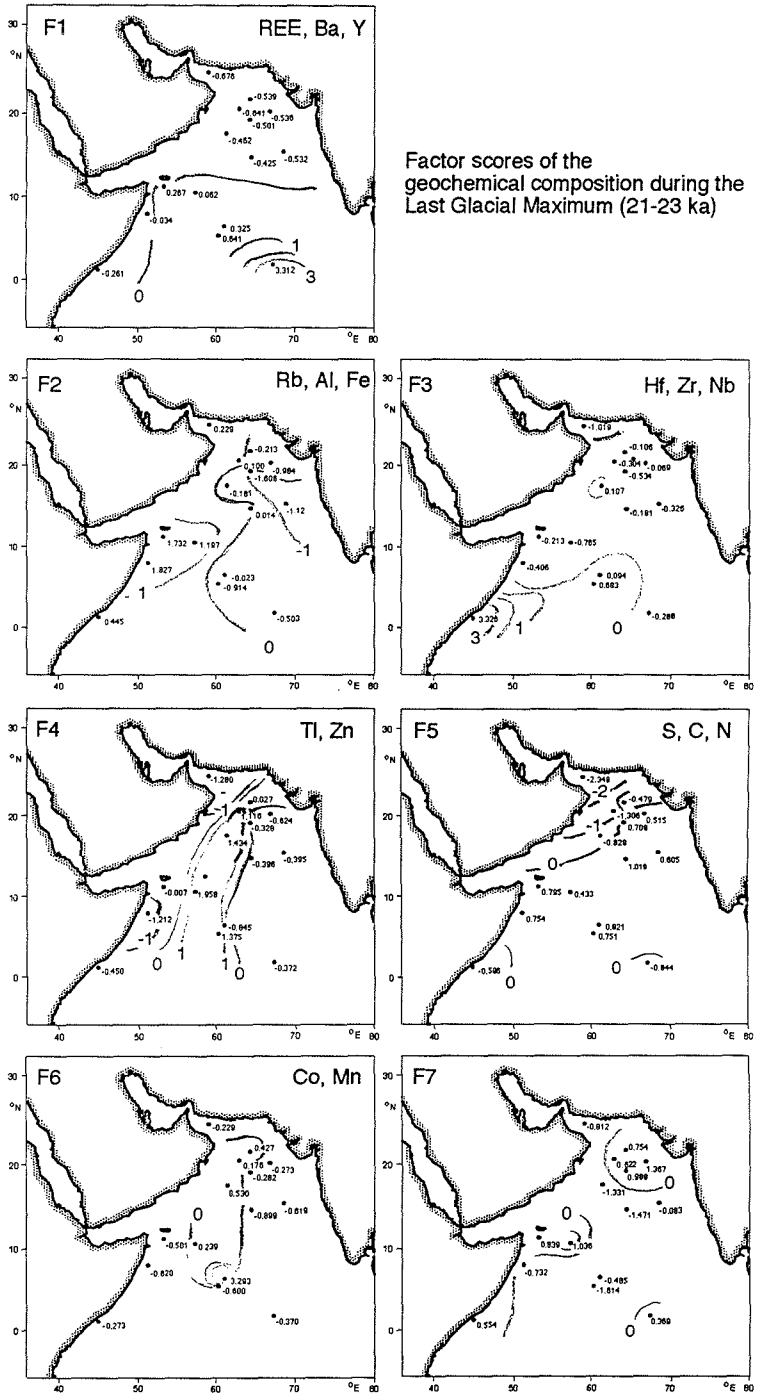

	Factor 1	Factor 2	Factor 3	Factor 4	Factor 5	Factor 6	Factor 7
CORG	0,48	0,46	-0,19	0,59	-0,19	0,06	0,18
N	0,54	0,42	-0,28	0,56	-0,13	0,08	0,13
S	-0,18	-0,29	0,01	0,85	-0,07	-0,05	-0,07
AL	-0,04	-0,93	-0,26	-0,03	0,07	0,00	-0,15
FE	-0,02	-0,88	-0,22	0,12	0,03	-0,04	-0,17
MG	-0,31	-0,90	-0,03	-0,06	0,02	0,00	-0,16
NA	0,14	0,80	0,37	-0,04	0,08	-0,04	0,01
K	-0,25	-0,84	0,15	-0,20	0,10	-0,11	-0,22
LI	-0,30	-0,85	0,10	0,04	-0,06	-0,26	0,08
SC	0,16	0,06	-0,13	-0,18	0,94	0,01	-0,03
CR	-0,22	-0,87	-0,08	0,29	-0,15	0,04	0,04
MN	0,19	0,26	0,79	-0,16	-0,04	0,08	0,22
CO	0,45	0,16	0,54	-0,01	0,01	0,66	0,05
NI	0,51	0,37	0,65	0,06	0,01	0,32	0,06
ZN	0,63	0,60	0,35	-0,19	0,07	-0,02	0,18
GA	0,88	0,00	0,14	-0,30	0,06	0,01	0,20
RB	-0,13	-0,95	-0,18	-0,01	0,02	0,06	0,05
SR/CA	0,35	0,53	0,29	0,07	-0,10	0,04	0,63
Y	0,82	0,37	0,09	0,05	0,02	0,15	0,10
ZR	0,72	-0,54	0,02	0,08	-0,25	0,03	0,16
NB	0,08	-0,93	-0,30	-0,05	0,01	0,03	0,03
MO	-0,15	-0,12	0,57	0,72	-0,11	0,03	0,04
CD	0,46	0,43	0,56	0,02	-0,15	-0,30	0,16
CS	-0,11	-0,97	-0,13	-0,02	0,00	-0,03	0,00
BA	0,61	0,70	0,32	-0,10	0,01	-0,05	0,13
LA	0,98	-0,13	0,01	0,01	-0,01	0,03	0,03
CE	0,65	-0,72	-0,10	-0,01	-0,01	-0,02	-0,01
PR	0,94	-0,29	-0,02	-0,02	0,05	0,02	-0,04
ND	0,94	-0,21	0,01	-0,02	0,05	-0,05	-0,08
SM	0,96	-0,14	0,07	0,00	0,09	0,06	0,00
EU	0,58	-0,57	-0,23	0,08	0,01	0,27	-0,34
GD	0,92	0,09	0,07	-0,03	0,05	0,25	-0,12
TB	0,97	0,12	0,10	0,04	0,03	0,04	-0,02
DY	0,95	0,20	0,19	0,03	0,02	-0,02	0,04
HO	0,92	0,30	0,22	0,05	-0,01	0,03	0,07
ER	0,88	0,37	0,26	0,02	-0,02	-0,02	0,07
TM	0,87	0,37	0,24	0,03	-0,03	0,03	0,15
YB	0,85	0,44	0,23	0,02	0,00	0,03	0,05
LU	0,83	0,47	0,24	0,01	-0,01	0,04	0,10
HF	0,27	-0,88	-0,06	0,09	-0,13	0,00	0,03
TA	0,02	-0,92	-0,30	0,00	0,07	-0,05	-0,11
TL	0,21	0,34	0,81	0,23	-0,06	0,00	-0,11
PB	0,68	0,39	0,46	-0,19	0,02	-0,08	0,08
U	0,47	0,50	0,58	-0,05	-0,13	0,05	-0,08
total variance explained:	36,5	32,9	10,8	5,3	2,6	2,0	2,3

Table 10. Factor loadings, and total variance explained by each factor, for the geochemical composition in sediment core 74KL.

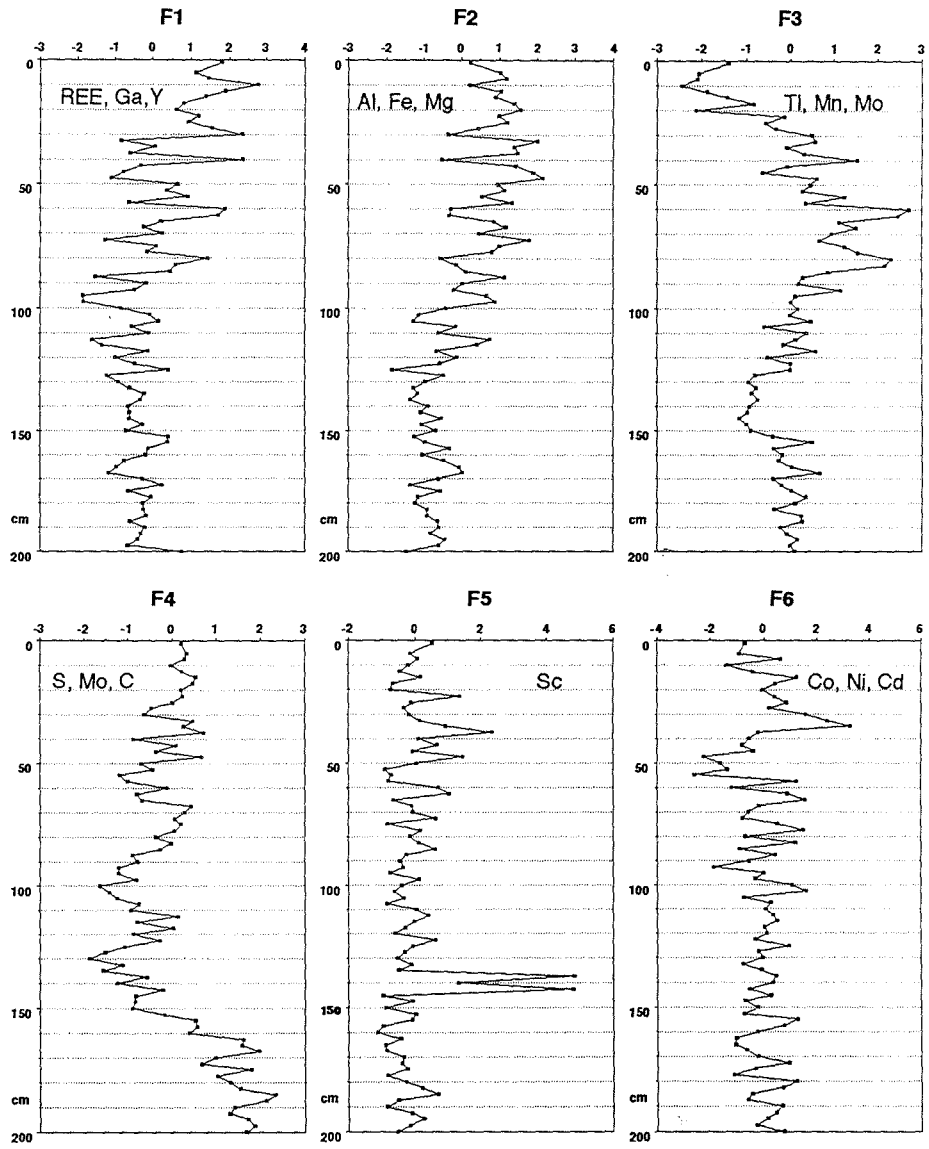

Figure 61. Factor scores for the geochemical composition in sediment core 74KL. The three elements that explain most of the variance are shown in the header (from Tab. 10).

transport in the southern branch of northwesterlies from Arabia (see chapter C.1.), is obviously a record associated with winds from the Red Sea area. The Zr-Hf-Nb factor does not appear in the core 74KL profile (Fig. 61), where these elements covary with F1 and F2 (Tab. 10).

F4 (F3 in 74KL) is rich in the elements Tl, Co and Mn, which are mobile in the reducing section of the sediment profiles. This "diagenesis-factor" shows high values in the central Arabian Sea (Figs. 57-60) and in the early Holocene section of core 74KL, where these elements are most frequent at 80 and 60 cm depth (Fig. 61). Near to the sediment surface (at 20 cm depth) the mobile elements are depleted, probably because the sediments of core 74KL are in a reducing state up to the very top, and mobile kations can be injected back into the bottom water.

F5 (F4 in 74KL) is consistently high in C_{org}, N, S, and Mo (Figs. 57-61), all of which are elements typically enriched in an oxygen depleted environment at high fluxes of organic carbon. The distribution patterns of factor scores always show negative (the data matrix was allowed to be rotated by the program) values in the northwestern Arabian Sea, with an extremely (negative) maximum in the Gulf of Oman during the Last Glacial Maximum (Fig. 60). Accordingly, the deepwater in the northern Arabian Sea should have been oxygen depleted and received the greatest input of C_{org} during that time interval. In core 74KL, F4 shows a decrease in power at 160-130 cm. It is most likely that this stage represents the first onset of better ventilated deepwater at the end of the glacial. The finding is corroborated by the beginning of an increase in the $\delta^{13}C$ values of *C. wuellerstorfi* at exactly 160 cm depth (Fig. 66).

The remaining factors for all four time-slices and 74KL represent small groups or single elements that appear only in one or the other time-slice, and present local/temporal anomalies. A problem in application of factor analysis to a matrix of samples from stratigraphically defined time-slices (Figs. 57-60) arise from elements that respond to diagenitic (i.e., depth-dependent) mobilisation. Accordingly, changes in the distribution pattern of F4 and F5 are hardly interpretable. Factor analysis of the concentrations of chemical elements in the deep-sea sediments of the Arabian Sea is, however, able to identify some groups of elements that have a common provenance (F2, F3), but the factors are not fully capable of clearly distinguishing particular source areas and transport processes of sediment input. The major disadvantage of the factor analysis approach for the evaluation of the monsoonal climate is that none of the factors can be attributed exclusively to those proportions of the trace element flux that is derived from the biogenic acivity in the surface upwelling waters. Elements that are sensitive to nutrient content and biogenic flux (e.g. Ba, Cd, Zn) do not appear as a single factor. This link between the southwest monsoon intensity and the upwelling of subsurface water is a crucial point in an

understanding of the monsoonal climate. Accordingly, the further evaluation of the geochemical variations is not done by this statistical technique, but on the basis of an evaluation of the physical and chemical processes that affect an element, and by a comparison of its distribution pattern in the surface sediments with the modern patterns of wind dispersal or river discharge.

C.3. The provenance of clastic sediments in the northern Indian Ocean: Reconstructions from the $^{143}Nd/^{144}Nd$, $^{87}Sr/^{86}Sr$ composition of the lithic fraction

As shown in chapter A.4. about 50% wind-borne and 50% river-borne particles contribute to the hemipelagic, non-turbiditic, clastic sediments of the deep Arabian Sea. In this chapter the relative sediment proportions derived from these eolian and riverine sources are quantified to estimate past variations in the mass and composition of the clastic fractions of the sediments.

The $^{87}Sr/^{86}Sr$ and $^{143}Nd/^{144}Nd$ isotopic composition of clastic particles is a well suited tool to reconstruct the provenance of sediments in the ocean (Biscaye et al., 1974; Grousset & Biscaye, 1989; Grousset et al., 1988). Goldstein et al., (1984) had shown that the $^{143}Nd/^{144}Nd$ isotopic composition of river suspensions and eolian dust still reflect the isotopic composition of source rocks on the continents. The transport processes of these particles are not directly documented in the isotopic composition of particles, but can be inferred from the areal gradients in the isotopic composition of sediments in any depositional environment. In case of the Arabian Sea we had shown that dust plumes from Arabia dominate the mass accumulation of particles in the western Arabian Sea (Sirocko & Sarnthein, 1989) (Fig. 5). The evaluation of the seasonal course of dust discharge, visible on satellite images, has shown that there is almost no dust discharge from India during modern times, whereas several large rivers discharge tremendous loads of suspended sediments from the Indian continent (Fig. 6). At the Arabian margin, in contrast, the modern sediment near the coast may stem from discharge by local wadis during ephemeral rain episodes, but dust transport clearly dominates over the deep-sea, occurring during summer by prevailing northwesterly winds. Accordingly, an unambiguous identification of the source areas of sediments in Arabia, India, or Africa by means of their $^{87}Sr/^{86}Sr$ and $^{143}Nd/^{144}Nd$ isotope composition may provide evidence for the modern kind of transport mechanism.

Distribution patterns of $^{87}Sr/^{86}Sr$ and $^{143}Nd/^{144}Nd$ in the clastic fraction of surface samples

The sediments in the modern western Arabian Sea show $^{87}Sr/^{86}Sr$ values of 0.709-0.710; in the eastern sector, values reach >0.715 (Fig. 62, Tab. 11). Both regions are separated by a steep gradient that runs NW to SE from the Gulf of Oman straight towards the southern tip of India, reflecting a sharp boundary between the western and the northern sedimentary province of the Arabian Sea. (Kolla et al., 1981b) first described similar sediment provinces based on the mineralogical and sedimentological composition of surface sediments.

The εNd(0) values are about -6 in the clastic sediments of the western Arabian Sea (Fig. 62, Tab. 11). Exactly the same value was determined for dissolved Nd in the surface water of the western Arabian Sea by Bertram (1989). The εNd(0) values of the clastic sediments in the eastern sector of the Arabian Sea, however, reach a minimum of -17 on the continental slope of southern India (Fig. 62, Tab. 11). Values for the isotopic composition of the water are not available in the eastern sector (*op. cit.*). Unfortunately, the coverage of our εNd(0) data is not as dense as it is for Sr, but nevertheless, the data indicate that the gradient between the western and the eastern Arabian Sea runs N to S, which is 45° different from the gradient in the $^{87}Sr/^{86}Sr$ distribution pattern. An εNd(0) value of -8.74 (core 114 SK) near the Somalian coast disrupts the uniformity of εNd(0 values in the western Arabian Sea.

Grain-size dependent fractionations

Grain-size dependent fractionations largely affect the $^{87}Sr/^{86}Sr$ composition, because the radiogenic ^{87}Sr can be enriched largely in clay minerals and mica. Indeed, isotope data of the clay fraction on the Indian margin reveal maxima up to 0.7250 $^{87}Sr/^{86}Sr$ in the <2μm fraction (Tab. 11), and samples rich in clay content generally show more positive $^{87}Sr/^{86}Sr$ values. The clay content of the lithic fractions shows large regional contrasts in the Arabian Sea with maxima occurring in the Gulf of Oman and on the continental slope of India (Fig. 19). The statistical correlation between the $^{87}Sr/^{86}Sr$ values of the total lithic fraction and the clay content of the lithic fraction is, however, not significant in the Arabian Sea sediments (sediment surface: r^2=0.06, early Holocene: r2=0.02, Termination Ia: 0.28). Accordingly, $^{87}Sr/^{86}Sr$ values of the total lithic fraction of the Arabian Sea reflect primarily the provenance of the clastic fraction.

The $^{143}Nd/^{144}Nd$ isotopic composition is not affected by grain-size variations (Goldstein et al., 1984) , because Sm/Nd is not enriched greatly in the clay fraction. This holds true also for the sediments of the Arabian Sea (Tab. 13, Fig. 65). Moreover, the correlation coefficient of the $^{143}Nd/^{144}Nd$ isotopic composition versus clay content is even lower as for $^{87}Sr/^{86}Sr$ in our data matrix. Thus, grain-size dependent fractionations of isotopes may play only a minor role in the isotopic composition of Arabian Sea sediments.

Table 11. $^{87}Sr/^{86}Sr$ and $^{143}Nd/^{144}Nd$ isotopic data from the siliciclastic fraction of Arabian Sea deep-sea sediments at the sediment surface, during the Early Holocene (8-10 ka), and the Termination Ia (16-18 ka). Values for Persian Gulf samples are sediment surface values. $^{143}Nd/^{144}Nd$ values have been normalized to $^{146}Nd/^{144}Nd=0.7219$ and $\varepsilon Nd(0) = [^{143}Nd/^{144}Nd(measured)/0.512638]-1]*1000$, using the present day value for the bulk earth composition from Jacobsen & Wasserburg (1980).

	$^{87}Sr/^{86}Sr$							$^{143}Nd/^{144}Nd$							εNd(0)			
		2 sigma	duplicate	2 sigma	triplicate	2 sigma	average rounded		2 sigma	duplicate	2 sigma	triplicate	2 sigma					average
Sediment Surface																		
15KL	0,710860	0,000011					0,710860 0,7109											
26KL	0,711918	0,000010					0,711918 0,7119	0,512173	0,000022	0,512215	0,000031				-9,07	-8,25		-8,66
51KL	0,712971	0,000010					0,712971 0,7130	0,512200	0,000026	0,512199	0,000038				-8,54	-8,56		-8,55
57KL	0,711518	0,000010					0,711518 0,7115	0,512212	0,000016						-8,31			-8,31
71KL	0,710444	0,000009					0,710444 0,7104	0,512272	0,000019	0,512288	0,000012				-7,14	-6,83		-6,98
74KL	0,709376	0,000024					0,709376 0,7094											
82KL	0,710391	0,000007					0,710391 0,7104	0,512241	0,000021						-7,74			-7,74
11KL	0,710019	0,000008					0,710019 0,7100	0,512235	0,000034						-7,86			-7,86
18KL	0,709483	0,000008					0,709483 0,7095	0,512193	0,000024						-8,68			-8,68
105KK	0,709784	0,000008					0,709784 0,7098	0,512303	0,000041						-6,53			-6,53
114KK	0,709884	0,000011					0,709884 0,7099	0,512190	0,000017						-8,74			-8,74
143KK	0,710147	0,000008					0,710147 0,7101	0,512270	0,000050	0,512311	0,000024				-7,18	-6,38		-6,78
182SK	0,711040	0,000008					0,711040 0,7110	0,512040	0,000030						-11,67			-11,67
223SK	0,714239	0,000018					0,714239 0,7142											
232SK	0,713511	0,000016					0,713511 0,7135											
77194	0,714650	0,000010					0,714650 0,7147	0,511746	0,000017						-17,40			-17,40
422	0,713602	0,000010					0,713602 0,7136	0,512331	0,000019						-5,99			-5,99
KS8	0,716591	0,000062					0,716591 0,7166											
280	0,709293	0,000008	0,709373	0,000014			0,709333 0,7093											
Persian Gulf																		
1060	0,709809	0,000010					0,709809 0,7098											
1063	0,713464	0,000011					0,713464 0,7135											
1177	0,710796	0,000014					0,710796 0,7108											
1199	0,712568	0,000008					0,712568 0,7126											
1203	0,709431	0,000009					0,709431 0,7094	0,512294	0,000027	0,512278	0,512278				-6,71	-7,02		-6,87
Early Holocene																		
15KL	0,712867	0,000009					0,712867 0,7129											
36KL	0,715030	0,000011					0,715030 0,7150	0,512245	0,000019						-7,67			-7,67
51KL	0,709420	0,000010					0,709420 0,7094											
57KL	0,709696	0,000009	0,709694	0,000007			0,709695 0,7097											
64KL	0,709314	0,000005	0,709332	0,000014	0,709323	0,000011	0,709323 0,7093											
70KL	0,709236	0,00009	0,709235	0,000012			0,709236 0,7092											
71KL	0,712503	0,000106	0,710146	0,000008	0,710133	0,000009	0,710927 0,7109											
74KL	0,709737	0,000018	0,709739	0,000012			0,709738 0,7097											
79KL	0,709855	0,000001	0,709878	0,000008	0,709914	0,000024	0,709882 0,7099											
82KL	0,710033	0,000015	0,710095	0,000007	0,71008	0,000008	0,710069 0,7101	0,512248							-7,61			-7,61
87KL	0,709393	0,000010					0,709393 0,7094											
11KL	0,709969	0,000008					0,709969 0,7100	0,512148		0,512253	0,000036				-9,56	-7,51		-8,53
18KL	0,709385	0,000009					0,709385 0,7094	0,512161							-9,30			-9,30
105KK	0,709295	0,000016					0,709295 0,7093											
114KK	0,709340	0,000015					0,709340 0,7093	0,512236		0,512338					-7,84	-5,85		-6,85
143KK	0,708926	0,000013					0,708926 0,7089	0,512377		0,512322					-5,09	-6,16		-5,63
182SK	0,712854	0,000009					0,712854 0,7129	0,512160							-9,32			-9,32
223SK	0,713164	0,000018					0,713164 0,7132	0,512138		0,512170					-9,75	-9,13		-9,44
232SK	0,713515	0,000017					0,713515 0,7135	0,512167							-9,19			-9,19
76123	0,714823	0,000043	0,714700	0,000031			0,714762 0,7148											
77202	0,711692	0,000024					0,711692 0,7117											
422	0,709713	0,000010					0,709713 0,7097											
KS8	0,713995	0,000050					0,713995 0,7140											
Late Glacial																		
15KL	0,712097	0,000013					0,712097 0,7121											
26KL	0,712532	0,000011					0,712532 0,7125	0,512130	0,000018	0,512110	0,000009	0,512120	0,000011		-9,91	-10,30	-10,10	-10,10
36KL	0,712588	0,000017	0,712588	0,000011			0,712588 0,7126	0,512179	0,000014			0,512156	0,000011		-8,95		-9,40	-9,18
51KL	0,714490	0,000012					0,714490 0,7145											
57KL	0,712868	0,000010					0,712868 0,7129											
64KL	0,717156	0,000008					0,717156 0,7172											
70KL	0,711819	0,000013					0,711819 0,7118											
71KL	0,712247	0,000011					0,712247 0,7122											
74KL	0,710549	0,000080					0,710549 0,7105	0,512329	0,000011	0,512336	0,000020	0,512317	0,000018		-6,03	-5,89	-6,26	-6,06
79KL	0,710574	0,000027					0,710574 0,7106											
82KL	0,711187	0,000008					0,711187 0,7112	0,512284	0,000024	0,512264	0,000015				-6,91	-7,30		-7,10
87KL	0,710619	0,000010	0,710151	0,000009	0,710198	0,000011	0,710323 0,7103	0,512249	0,000031	0,512249	0,000018				-7,59	-7,59		-7,59
5KL	0,710215	0,000010	0,710444	0,000059			0,710330 0,7103	0,512252	0,000016	0,512217	0,000024				-7,53	-8,21		-7,87
11KL	0,712165	0,000012					0,712165 0,7122	0,512222	0,000017	0,512213	0,000015	0,512227	0,000010		-8,11	-8,29	-8,02	-8,14
18KL	0,709936	0,000014					0,709936 0,7099	0,512258	0,000015	0,512236	0,000018	0,512229	0,000011		-7,41	-7,84	-7,98	-7,74
105KK	0,709802	0,000008					0,709802 0,7098	0,512335	0,000013	0,512322	0,000013	0,512320	0,000012		-5,91	-6,16	-6,20	-6,09
114KK	0,710006	0,000012	0,710201	0,000015			0,710104 0,7101	0,512334	0,000014	0,512312	0,000015	0,512301	0,000024		-5,93	-6,36	-6,57	-6,29
143KK	0,709568	0,000008					0,709568 0,7096	0,512369	0,000009	0,512352	0,000009	0,512353	0,000022		-5,25	-5,25	-5,58	-5,36
182SK	0,713328	0,000010					0,713328 0,7133	0,512125	0,000012	0,512141	0,000009	0,512123	0,000009		-10,01	-9,69	-10,05	-9,92
223SK	0,715476	0,000008					0,715476 0,7155	0,512150	0,000011	0,512141	0,000010	0,512155	0,000009		-9,52	-9,69	-9,42	-9,55
232SK	0,715426	0,000007					0,715426 0,7154											
422	0,710817	0,000010					0,710817 0,7108	0,512308	0,000016						-6,44			-6,44
KS8								0,512261	0,000008						-7,35			-7,35
243	0,709598	0,000008	0,709594	0,000008			0,709596 0,7096	0,512322	0,000021	0,512296	0,000015				-6,16	-6,67		-6,42
280								0,512417	0,000019	0,512443	0,000028	0,512414	0,000013		-4,31	-3,80	-4,37	-4,16

<2 µm fraction

core-sample	depth [cm]
74KL-10	0,712495
77194-11.5	0,723131
57KL-1	0,712971
422-0	0,720874
422-220	0,717753

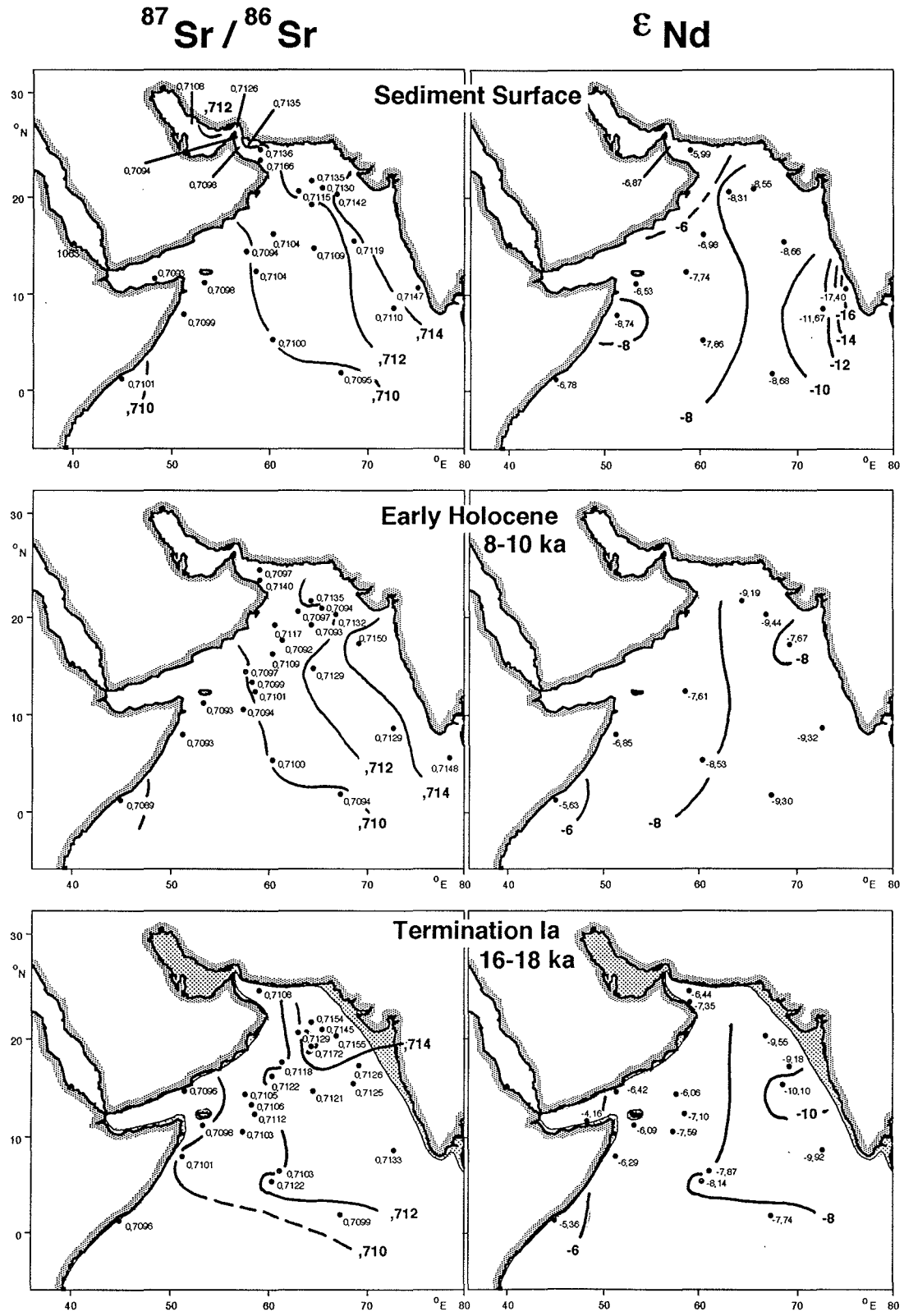

Figure 62. Distribution patterns of $^{87}Sr/^{86}Sr$ and εNd(0) in the lithic fraction of Arabian Sea sediments at the sediment surface, during the Early Holocene (8-10 ka), and during the Termination Ia (16-18 ka).

Distribution patterns of $^{87}Sr/^{86}Sr$ and $^{143}Nd/^{144}Nd$ values on the ambient continents

$^{87}Sr/^{86}Sr$ and $^{143}Nd/^{144}Nd$ values of lithic strata on the continents surrounding the Arabian Sea have been compiled from the literature to evaluate if the isotopic composition of the deep-sea sediment is consistent with the respective values in the source regions of dust and river loads (Fig. 63).

Low $^{87}Sr/^{86}Sr$ values of 0.704 are observed in the young (Late Cenozoic) lava flows of the Ethiopian rift system and the Red Sea rift (Betton & Civetta, 1984). $\varepsilon Nd(0)$ values at +5 corroborate the young age of this newly formed crust. The Pan-African (Late Proterozoic) built crust on both sides of the Red Sea shows similar $^{87}Sr/^{86}Sr$ values with an average ratio of 0.705. Extremely positive deviations of >0.800 were observed in some rocks of high biotite content, which can enrich the radiogenic ^{87}Sr to an extreme degree (Altherr et al., 1990; Barrat et al., 1990; Duyverman et al., 1982; Harris & Marzouki, 1986; Kröner et al., 1992; Reischmann, submitted).

$\varepsilon Nd(0)$ of the Pan-African rocks show a large scatter of values between -6 and +10, reflecting the inhomogeneous composition of the Pan-African terrane, which incorporated melts from the underlying old continent and the mantle below (Harris et al., 1984). The old crust below the Pan-African rocks shows modern $\varepsilon Nd(0)$ values of -13 in northwestern Kenya, as being observed in the rocks of the Congo craton (Harris et al., 1984). Metasediments of the Pre-Pan-African rocks in Kenya and Sudan reveal a $\varepsilon Nd(0)$ of -6, and $^{87}Sr/^{86}Sr$ values between 0.707 and 0.715 (Harris et al., 1984).

In the northwestern Arabian basement, $^{87}Sr/^{86}Sr$ amounts to 0.705, and $\varepsilon Nd(0)$ values are found at +4. Also the Zagros mountains of Iran reveal $^{87}Sr/^{86}Sr$ values near to 0.704, moreover a second group of data near to 0.713, which is found in plutonic intrusions of Mesozoic age (Baumann et al., 1984; Jung et al., 1984). Unfortunately, these authors do not report data on the $\varepsilon Nd(0)$ composition of these Zagros mountains. Sediment core 422 in the northern Gulf of Oman, which receives most of its modern clastic sediments from small rivers draining the Zagros, reveal $\varepsilon Nd(0)$ values of -6, which compare well with values from the Pre-Pan-African basement in Kenya and Sudan. It appears quite possible that these Pre-Pan-African rocks form the the majority of deep basement rocks of the Arabian peninsula.

We have found no reports on the Nd- or Sr-isotope composition of the Paleozoic to Cenozoic sedimentary strata of central and northern Arabia and on the isotopic composition of the Quaternary dune sands that cover the sedimentary strata. These strata represent the detritus of erosion on the old (Pre-Pan-African) continent, and on the Pan-African land mass. Accordingly, one may assume that the $^{87}Sr/^{86}Sr$ and $^{143}Nd/^{144}Nd$ composition of the Arabian Paleozoic, Mesozoic and Cenozoic sedimentary strata presents a mixture from all sources surrounding the

Arabian land mass.

Avergage εNd(0) values for northern India and the Himalaya are reflected in the sediment load of the river Indus, the suspension load of which shows an εNd(0) of -12 (Goldstein et al., 1984). This value reflects a crustal age for the Indian and Asian landmass, which is much older than in northern Arabia and the Zagros ranges.

The modern provenance of clastic sediments in the Arabian Sea

The large desert storms that transport dust from Arabia into the Arabian Sea have a large entrainment area from the lowlands of Mesopotamia all along the Persian Gulf and the central Arabian desert down to the Arabian Sea (Ackerman & Cox, 1988; Chen, 1986). The entrainment area in the central Arabian desert and the lowland of Mesopotamia for the dust storm on June 22-26, 1979 (Fig. 5) is enveloped in Fig. 63. The Sr and Nd isotopic composition of the dust, and the sands moving in the area has not been measured, but as shown above, one may expect a value resulting from a mixture from all Arabian source rocks and the debris of the Zagros ranges that is deposited in the large tectonic foreland trough that includes the Mesopotamian lowlands and the Persian Gulf. The expected mixture for the central Arabian desert should fall between 0.705 and 0.710 for the $^{87}Sr/^{86}Sr$ composition, and close to -6 for εNd(0) value (Fig. 64). These values match the respective values of the lithic sediments of the western Arabian Sea (Fig. 62), and accordingly, the Arabian desert is a likely source for the eolian fraction in the sediments of the western Arabian Sea. A direct (southwest monsoon-borne) source of the eolian particles in East Africa or the Red Sea area, however, is unlikely, because the Ethiopian basalts show an $^{87}Sr/^{86}Sr$ composition of 0.704, but a εNd(0) of +5, which is far away from the observed values in the deep-sea sediments (Figs. 63, 64). This observation agrees with the evaluation of the satellite images of 1979 (Fig. 5), where dust over the Gulf of Aden was observed only in combination with dust plumes over the Arabian peninsula or dust plumes over the Sudan. Dust plumes leaving the Somalian coast on trajectories of the southwest monsoon have never been observed during the evaluation of satellite images covering the time span of 1979 and 1980. The Mesozoic sedimentary strata, exposed at the surface in the coastal area of Somalia, are identical to the strata as being found in Arabia, because both regions were part of one continent before the opening of the Red Sea. Accordingly, the isotopic composition of the Somalian soils should be most similar to values in Arabia, and proportions transported as dust derived from the Somalian coastal plains could not be distinguished from sources in central Arabia.

The average $^{87}Sr/^{86}Sr$ value of 0.712, and the average εNd(0) value of -8 reported for the sediments in the northern sector of the Arabian Sea (Figs. 63, 64)

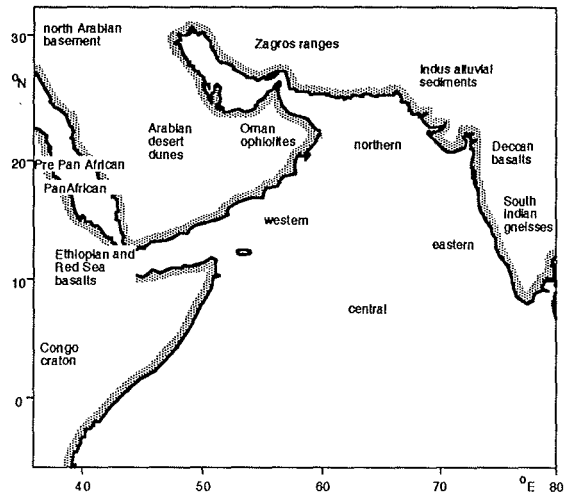

Major Geological Units on land, and modern sedimentary provinces of the Arabian Sea

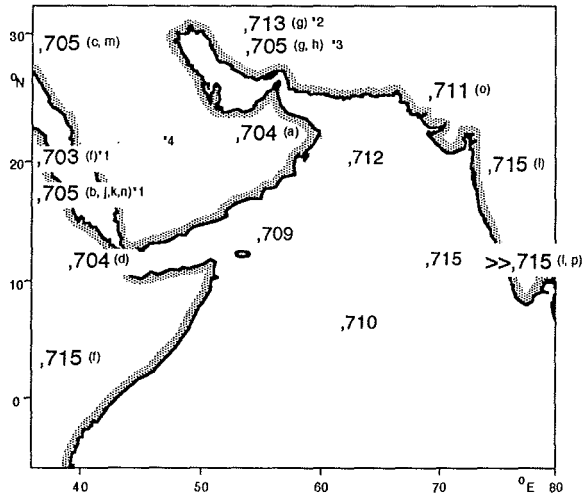

Average $^{87}Sr / ^{86}Sr$ of geological units on land and in the modern sedimentary povinces of the Arabian Sea

*1: authors working on Pan African rocks always report on scattered values much higher then 0.710

*2: values for plutonic rocks

*3: values for volcanic rocks

*4: Entrainment area of Arabian dust storms stretches from the Mesopotamien lowland to the Arabian coast (Chen, 1986)

*5: no Nd isotopic data are reported for Iran. The value shown is the modern value of sediment core 422 (Tab. 11), which averages riverine detritus from the Zagros ranges

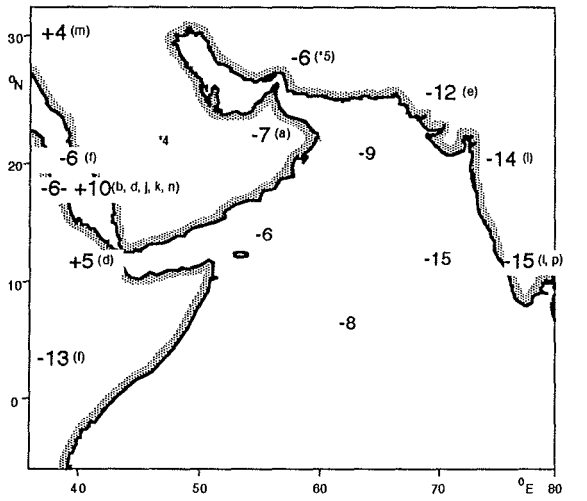

Approximate $^{143}Nd / ^{144}Nd$ of geological units on land and in the sedimentary povinces of the Arabian Sea

references:
a) McCulloch et al., 1980
b) Duyverman et al., 1982
c) Jarrar et al., 1983
d) Betton & Civetta, 1984
e) Goldstein et al., 1984
f) Harris et al., 1984
g) Jung et al., 1984
h) Baumann et al., 1984
i) Millisenda et al., 1988
j) Altherr et al., 1990
k) Barrat et al., 1990
l) Lighfoot et al., 1990
m) Stein & Hoffmann, 1992
n) Reischmann in prep.
o) Goldstein & Jacobsen, 1987)
p) Millisenda et al., 1994

Figure 63. (a) Geological provinces and (b) average values of $^{87}Sr/^{86}Sr$ and (c) $\varepsilon Nd(0)$ for the lithic strata on the continents adjacent to the Arabian Sea.

are close to the values as expected from the Zagros (εNd(0) of -6), but still too negative for a Zagros source alone. The Zagros derived proportions could be eolian (compare dust outbreak on 30 April 1979 (Fig. 5)), but could also have a riverine source from small rivers entering the Gulf of Oman. The εNd(0) value of -12 for the river Indus is too negative to account for a source from the river alone. Accordingly, the sediments of the northernmost Arabian Sea must be a mixture of sources in the Indus, and other sources in Arabia and the Zagros.

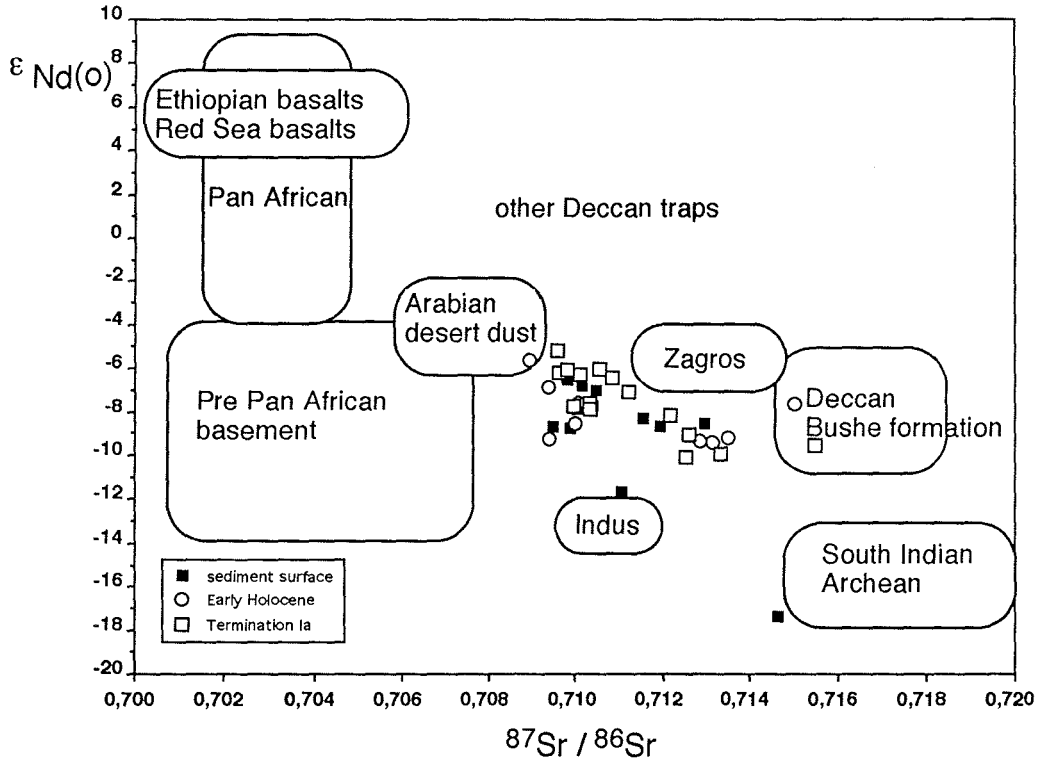

Figure 64. (a) $^{87}Sr/^{86}Sr$ of the bulk lithic versus εNd(0) of the bulk lithic fraction. Shown is also the isotopic composition on land, according to Fig. 63, and references therein.

The Sr and Nd isotope values in the eastern Arabian Sea largely agree with both the isotopic signature of the Bushe formation of the Deccan basalts (-15 and 0.714) (Lightfoot et al., 1990), and with the isotopic signature of the Archean of southern India (-15, 0.720) (Millisenda et al., 1994; Millisenda et al., 1988) (Fig. 63). The value reported for the Deccan isotopic composition has been measured at the Bushe formation, which is the lowest and largest of all Deccan trap (i.e., the unit that should be primarily eroded by the modern rivers draining middle India). Other trap series, however, have completely different isotopic composition that range

between 0.703 and 0.709 for $^{87}Sr/^{86}Sr$, and -8 to +3 for $\varepsilon Nd(0)$ (Lighfoot et al., 1990). Unfortunately, we cannot quantify the proportions that are derived from each trap, and thus, along the Indian coast we cannot calculate the relative proportions being derived from the Deccan basalt flows and the Archean gneisses of southern India.

As shown above by the comparison of land data with data from the sediments of the ocean, the isotopic signature of sediments in the western and eastern Arabian Sea reflect the gross composition of rocks on land. Specific entrainment areas of dust, or drainage areas of the rivers, however, cannot be distinguished with confidence at this stage, because some source regions (e.g. Pan-African rocks, Deccan basalts) already represent a mixture of several geological subunits, and dust loads and river suspensions can present a second-order mixture over several source regions. Accordingly, we can only define the end members of the isotopic composition of the sediments by the average composition of the sediments in the ocean near to the coast (Tab. 12).

Table 12. End members of $\varepsilon Nd(0)$ and $^{87}Sr/^{86}Sr$ isotopic composition contributing to the terrigenuous fraction of modern sediments of the Arabian Sea. The data for the Indus suspension load are from (a) Goldstein et al., 1984, (b) Goldstein & Jacobsen (1987), the other values represent the average composition as shown in Fig. 63.

	$\varepsilon Nd(0)$	$^{87}Sr/^{86}Sr$
Arabian desert dust	-6	0.709
Persian Gulf sediments (Zagros)	-6	0.712
Indus	-12[a]	0.711[b]
Middle India	-14	0.715
Southern India	-15	0.715

If we apply a simplified (two component) mixing model to the modern sediments in the northern Arabian Sea, the 50% isoline ($^{87}Sr/^{86}Sr$: 0.712) of equal Sr contributions from eolian sources in Arabia and riverine provenance in India runs from the southern Gulf of Oman straight towards the southern tip of India (Fig. 64). This simple mixing model neglects that the $^{87}Sr/^{86}Sr$ composition of the Indus suspensions is intermediate between the Arabian and Indian values, and thus, reliable calculations of the relative proportions from each sediment source can not be done on the basis of $^{87}Sr/^{86}Sr$ values and $\varepsilon Nd(0)$ values alone.

The application of the simple mixing model to the samples from the Carlsberg Ridge with an average $^{87}Sr/^{86}Sr$ of 0.7105 and $\varepsilon Nd(0)$ of -8 shows that most of the lithic compounds would be derived from an Arabian dust source (i.e., 70% at core location 11KL, and 50% at core location 18KL, if the concentrations of Nd and Sr were the same in the Arabian and Indian source areas and the remaining fraction would be derived from southern/middle India exclusively). If the Indus contribution reaches the top of the Carlsberg Ridge, a considerable

amount of the sediments could be derived from that source.

In summary, even for the modern sediments of the Arabian Sea, the precise amounts of the major fractions (Arabian dust, Indus suspensions, other river suspensions from India) in the central Arabian Sea cannot be calculated, because there are too many different possible source regions and transport pathways of clastic particles in the Arabian Sea. The clearest evidence for the provenance of particles in the western Arabian Sea during modern times are the trajectories of dust plumes visible on satellite images (Fig. 5). Unfortunately, no $^{87}Sr/^{86}Sr$ and $\varepsilon Nd(0)$ values are available for the isotopic composition of particles in these dust plumes. An average value from the compilation of land data in and around Arabia is near to 0.709 $^{87}Sr/^{86}Sr$ and -6 $\varepsilon Nd(0)$, which are the values observed in the deep-sea sediments off the Arabian coast. One could, however, calculate several alternate mixing models for the isotopic composition of the sediments in the western Arabian Sea if considerable masses from the Indus and the Ethiopian plateau are envoked.

Variations of provenance for the clastic sediment fraction during the past

During the Early Holocene, the 0.712 isoline of $^{87}Sr/^{86}Sr$ was shifted towards the coast of Arabia (Fig. 62), which could be interpreted as showing either increased fluvial runoff from India or reduced proportions from the eolian Arabian source. Lithic accumulation rates in core 74KL show a minimum during this early Holocene interval (Tab. 1b), because the southwest monsoon was shifted to its northernmost position, and dust contributions from northern Arabia were almost absent at the latitude of 74KL (compare distribution pattern and evolution of dolomite, Sirocko et al., 1991, 1993). This observed decrease in the flux rates of Arabian dust appears to be the more likely explanation for the westward shift of the 0.712% isoline during the Early Holocene than increased fluvial runoff from India.

During Termination Ia a distinct maximum of $^{87}Sr/^{86}Sr$ (0.715) is found off northern India, a maximum, which is not paralleled by a shift in the $\varepsilon Nd(0)$ composition, which had to be expected if sediments from the river Indus would be the source for the maximum. The modern $\varepsilon Nd(0)$ of the Indus is at -13 (Goldstein et al., 1984). The particles that cause the $^{87}Sr/^{86}Sr$ maximum could either be derived from the north Indian Thar desert, which lies in the tracks of springtime dustplumes from Iran and Pakistan, or the particles could be derived from Pakistan or Iran directly during spring or during winter northeast monsoon season.

At the time of Termination Ia, the 0.712 isoline of equal eolian/riverine proportions over the open ocean was shifted further westward, further than during the Late or Early Holocene (Fig. 62). Theoretically this could be caused by increased flux of clastic particles being derived from the Thar desert (see above),

but there is also an alternate explanation of this observation. (Sirocko et al., 1991) had already shown that dolomite, derived from the Persian Gulf area, was highly abundant in the western Arabian Sea during Last Glacial times. These particles from the dry Persian Gulf carry an isotopic signature of 0.712 for $^{87}Sr/^{86}Sr$, and probably -6 for $\varepsilon Nd(0)$, and the trajectories of their dispersal in the northwesterly winds run parallel to the 0.712 isoline over the ocean. Accordingly, these eolian components from the Persian Gulf area are a third factor in our simple mixing model, with an isotopic composition being intermediate between the Arabian/Indian end members, and an $\varepsilon Nd(0)$ composition being similar to Arabian values. Thus, the Persian Gulf derived proportions in the lithic fraction of the Arabian Sea sediments during glacial times cannot be distinguished from the Arabian and Indian components (Fig. 64). At this stage, the characterization of provenance based on the isotopic $^{87}Sr/^{86}Sr$ and $\varepsilon Nd(0)$ composition of the clastic fraction reaches its limits, when the mixing involves three major components.

Conclusions

The characterization of provenances for the Arabian Sea clastic sediment fraction reflects various sources and transport pathways of eolian and fluvial particles into this ocean. With respect to the evaluation of the climate related signal in the variability of geochemical properties in sediment core 74KL the following inferences can be drawn:

i) particles deposited in the western Arabian Sea are primarily derived from Arabia during the Holocene

ii) during glacial times, in addition to the prevailing dust discharge from Arabia, large proportions of dust could be derived from sources in Iran, Mesopotamia or the dry Persian Gulf region to be deposited in the northwestern Arabian Sea

ii) contributions from East Africa, being transported directly within southwest monsoon winds, were low during all times, but may contribute minor proportions to sediments in the Gulf of Aden and along the coast of Kenya and Somalia

iv) small dust contributions from an increased northeast monsoon wind intensity during glacial times could have reached the western Arabian Sea

v) riverine contributions from India did not reach the western Arabian Sea during the last 20,000 years at all.

Thus, sediment core 74KL in the western Arabian Sea is most likely to reflect the variability of mass transport in the Arabian dust storms. Variations in the intensity of the northwesterly winds derived from the Persian Gulf region, southwest monsoon and northeast monsoon winds could also be studied at core location 74KL if tracers can be found that can be attributed to each of these transport processes exclusively (see D.2).

C.4. Chemical tracers to monitor the monsoonal climate system in the Arabian Sea

The previous chapters have shown distribution patterns of various trace and major elements (C.1.), their groupings (C.2.), and possible source areas (C.3.). Accordingly, the sedimentation in the western Arabian Sea is largely controlled by dust derived from east Africa, Arabia, the Persian Gulf area and northern India. By simple comparison of the distribution patterns of these elements (Figs. 20-56) with modern surface water properties (Fig. 7), the dispersal of dust over the ocean (Fig. 5) and river suspensions in the ocean (Fig. 6), we observe several similarities between distribution patterns of elements and a potential transport mechanism or source area. In particular:

Southwest monsoon driven upwelling productivity

Regions of intense upwelling are found in the whole western Arabian Sea, with upwelling cells located off Somalia, Oman and over the open ocean along the track of the southwest monsoon jet core, the Findlater Jet (Fig. 7). The upwelling cells in the coastal waters of Oman and Somalia are depicted in none of the distribution patterns of all trace elements studied, because lithic accumulation is too high near the coast and dilutes the flux of biogenic particles significantly (Sirocko, 1991). The open ocean maximum of upwelling intensity is however recorded by biogenic opal content, Zn, Cd, and U content (Figs. 39, 48, 56), which,thus, have a potential to monitor past upwelling strength. U is not very well suited to this task, because U diffuses from the deepwater into the reducing sediments, a process controlled by organic carbon content, thus only indirectly related to surface water properties (Klinkhammer & Palmer, 1991). Cd and Zn, however, parallel nutrient content of ocean water, both globally (Boyle, 1994) and in the Arabian Sea (Saager et al., 1992) (Fig. 7). The bulk Zn content in core 74KL is up to three times as large as in average igneous rocks (Tab. 5, Zn), the bulk Cd content, however, is thirty times higher in core 74KL than in igneous rocks. To approximate the non-lithic Zn proportions we normalized the Zn concentrations to Al. Based on the distribution pattern of Al (Fig. 25), Al is a strictly lithic element in the Arabian Sea sediments (compare Shimmield et al., 1990 a, 1990 b).

Zn/Al (Fig. 67) shows a maximum in the open ocean upwelling region of the western Arabian Sea during the Holocene. The distribution pattern of Zn/Al resembles the distribution pattern of biogenic opal, which was shown to be the sedimentological parameter to correlate best with modern SST variations (Sirocko, 1991). Zn is, however, also highly enriched in core 76128 on the Indian

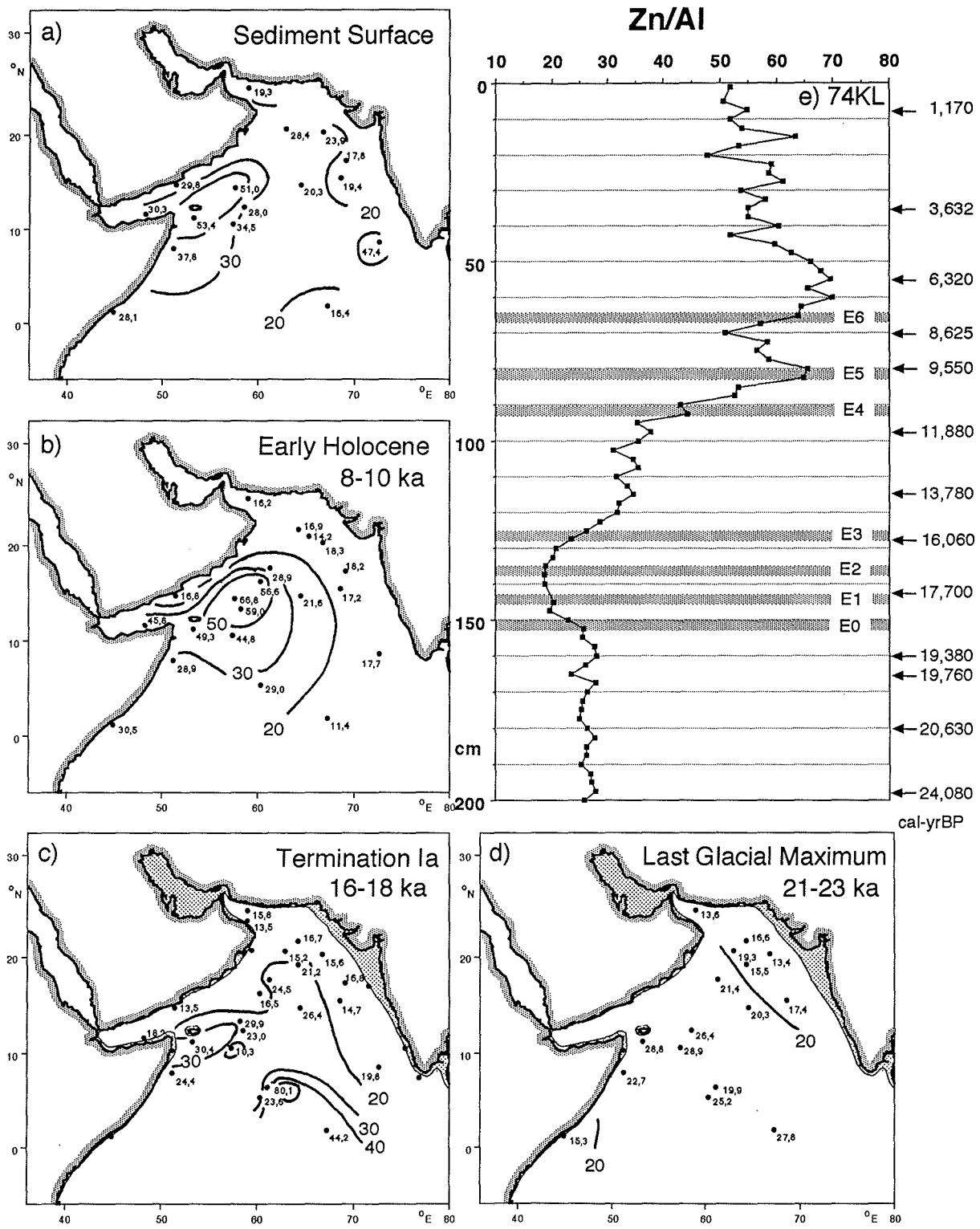

Figure 67. Zn/Al ratio as geochemical tracer of southwest monsoon driven upwelling intensity in the Arabian Sea. (a) at the sediment surface, (b) during the Early Holocene (8000-10,000 cal-yrBP), (c) during Termination Ia (16,000-18,000 cal-yrBP), (d) during the Last Glacial Maximum (21,000-23,000 cal-yrBP), (e) sediment core 74KL; arrows indicate depth of AMS-^{14}C dates, converted to calendar years according to Tab. 1, hatched areas show events as defined in Fig. 12.

continental margin, which cannot be explained by upwelling intensity.

Distribution patterns of Cd content (Fig. 48) and Cd/Al (not shown) reveal maxima on the Carlsberg Ridge, possibly because Cd content is high in the $CaCO_3$ fraction (Boyle, 1992). This $CaCO_3$-bound proportion of Cd limits the application of bulk Cd content as a productivity tracer, even if the biogenic proportion of Cd is higher than for Zn (see above) and Cd is chemically more inert than Zn. A combination of both Cd and Zn contents appears to be the best choice to reconstruct past productivity levels of the surface waters in the western Arabian Sea on a high resolution scale. It would be even better to calculate accumulation rates of biogenic Cd and Zn, but the determination of accumulation rates in core 74KL is only possible on time scales of several thousand years, which is not sufficient to study the history of abrupt climate changes (Tab. 1b).

Other authors (Shimmield et al., 1990 a; Clemens et al., 1991; Emeis, 1993) used the Ba/Al ratio to evaluate changes in the intensity of the southwest monsoon driven ocean upwelling. The areal distribution pattern of Ba (cofb), however, which is identical to the areal distribution pattern of Ba/Al, shows no maximum below the modern upwelling areas, but on the Carlsberg Ridge (not shown). Only accumulation rates of Ba reveal a maximum under the upwelling cells in the western Arabian Sea .The downcore variation of Ba/Al in core 74KL is,however, extremely similar to Zn/Al, thus, Ba/Al can also serve locally as an upwelling indicator, but not when comparing different areas of the Arabian Sea.

The deep-sea record of eolian dust deposition

Contributions from at least four eolian tracks contribute sediments at core location 74KL in the western Arabian Sea (i.e., the southwest monsoon, a southern branch of Arabian northwesterlies, a northern branch of Arabian northwesterlies and the northeast monsoon, Fig. 5). Based on the distribution patterns of various chemical elements in the sediments of the deep Arabian Sea (Fig. 20-56), we can clearly distinguish only 4 elements (Zr, Mg, Al, Rb, Cs) which distribution patterns match the plumes as observed on the satellite pictures.

Zr content (Fig. 68) shows a plume out of east Africa, matching the movement of dust at 850-700 mb level (1-3 km height) as depicted by the southern branch of northwesterlies during the dust outbreak on 26 June 1979 (Fig. 5, Chen, 1986). This southern branch of the northwesterlies merges with the jet core of the southwest monsoon over the ocean. Thus, Zr content still reflects northwesterly winds from Arabia, but incorporates influence from the southwest monsoon. The Zr content should be enriched mostly in the heavy mineral zircon, and only the extremely vigorous southwest monsoon is able to tranport heavy-mineral grains over long distance. Other elements that show maxima

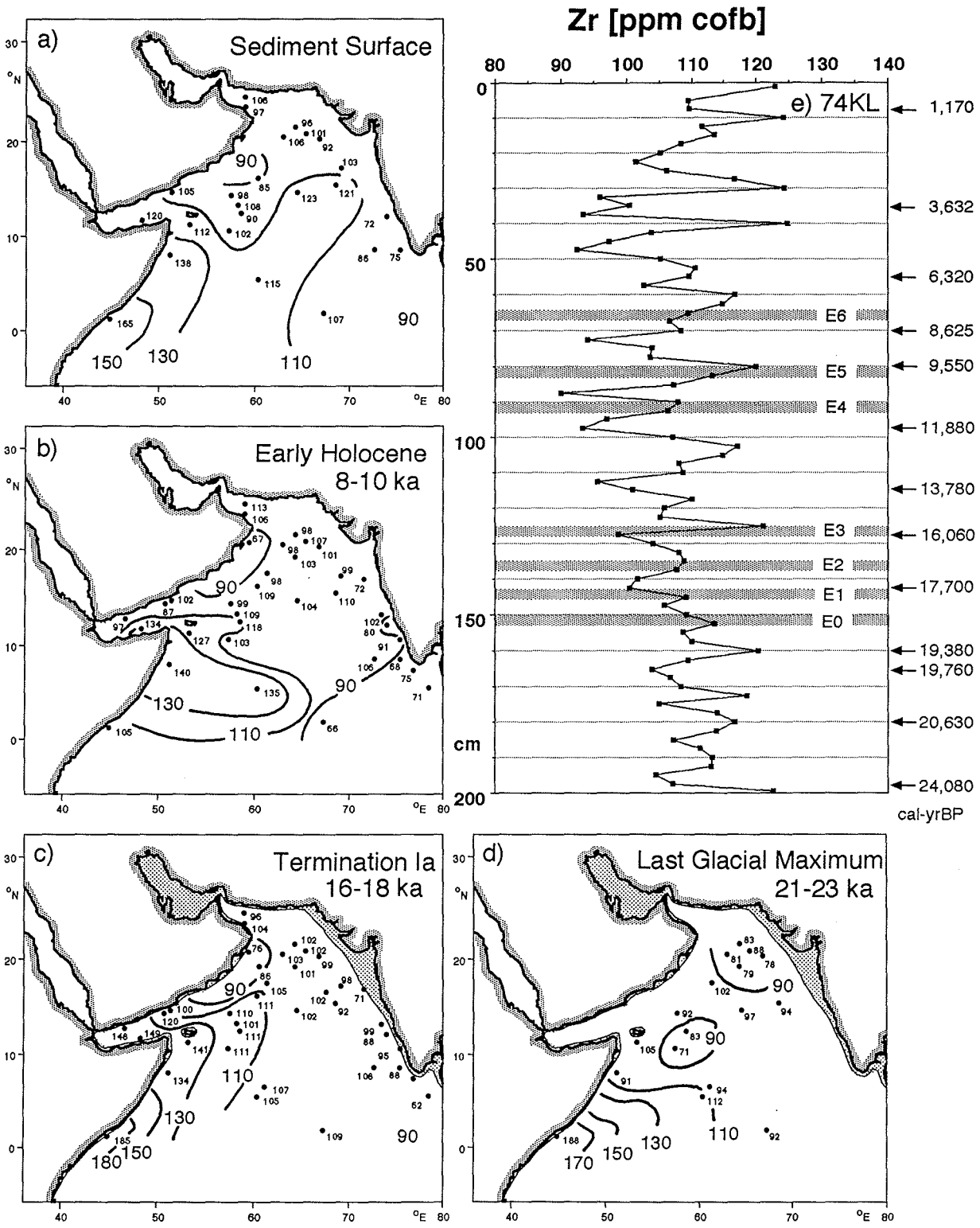

Figure 68. Zr content (ppm cofb) as geochemical tracer of the dust loads transported in the southern branch of Arabian northwesterlies, (a) at the sediment surface, (b) during the Early Holocene (8000-10,000 cal-yrBP), (c) during Termination Ia (16,000-18,000 cal-yrBP), (d) during the Last Glacial Maximum (21,000-23,000 cal-yrBP), (e) sediment core 74KL; arrows indicate depth of AMS-^{14}C dates, converted to calendar years according to Tab. 1, hatched areas show events as defined in Fig. 12.

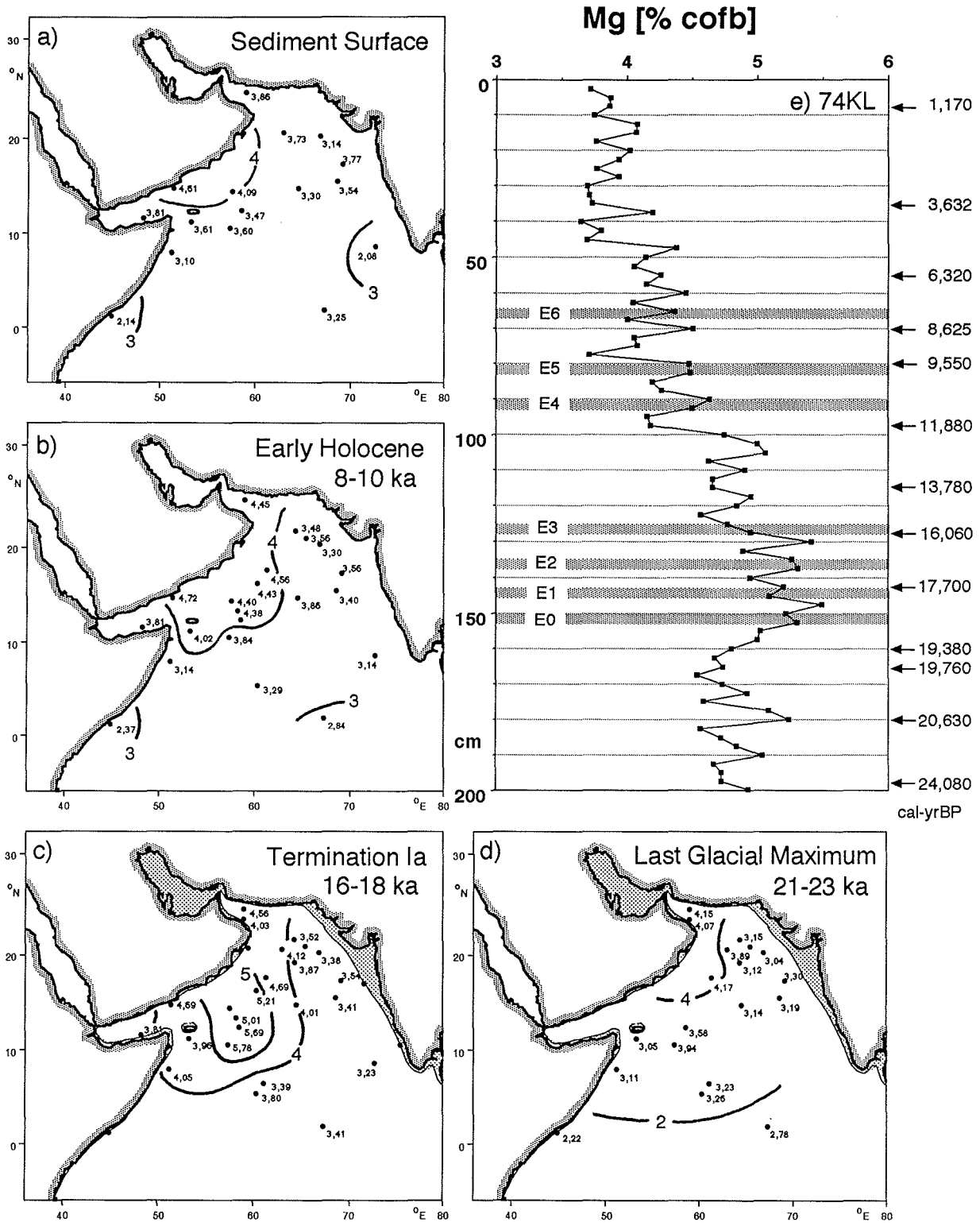

Figure 69. Mg content,(ppm cofb) as geochemical tracer for dust loads transported in the northern branch of Arabian northwesterlies, (a) at the sediment surface, (b) during the Early Holocene (8000-10,000 cal-yrBP), (c) during Termination Ia (16,000-18,000 cal-yrBP), (d) during the Last Glacial Maximum (21,000-23,000 cal-yrBP), (e) sediment core 74KL; arrows indicate depth of AMS-^{14}C dates, converted to calendar years according to Tab. 1, hatched areas show events as defined in Fig. 12.

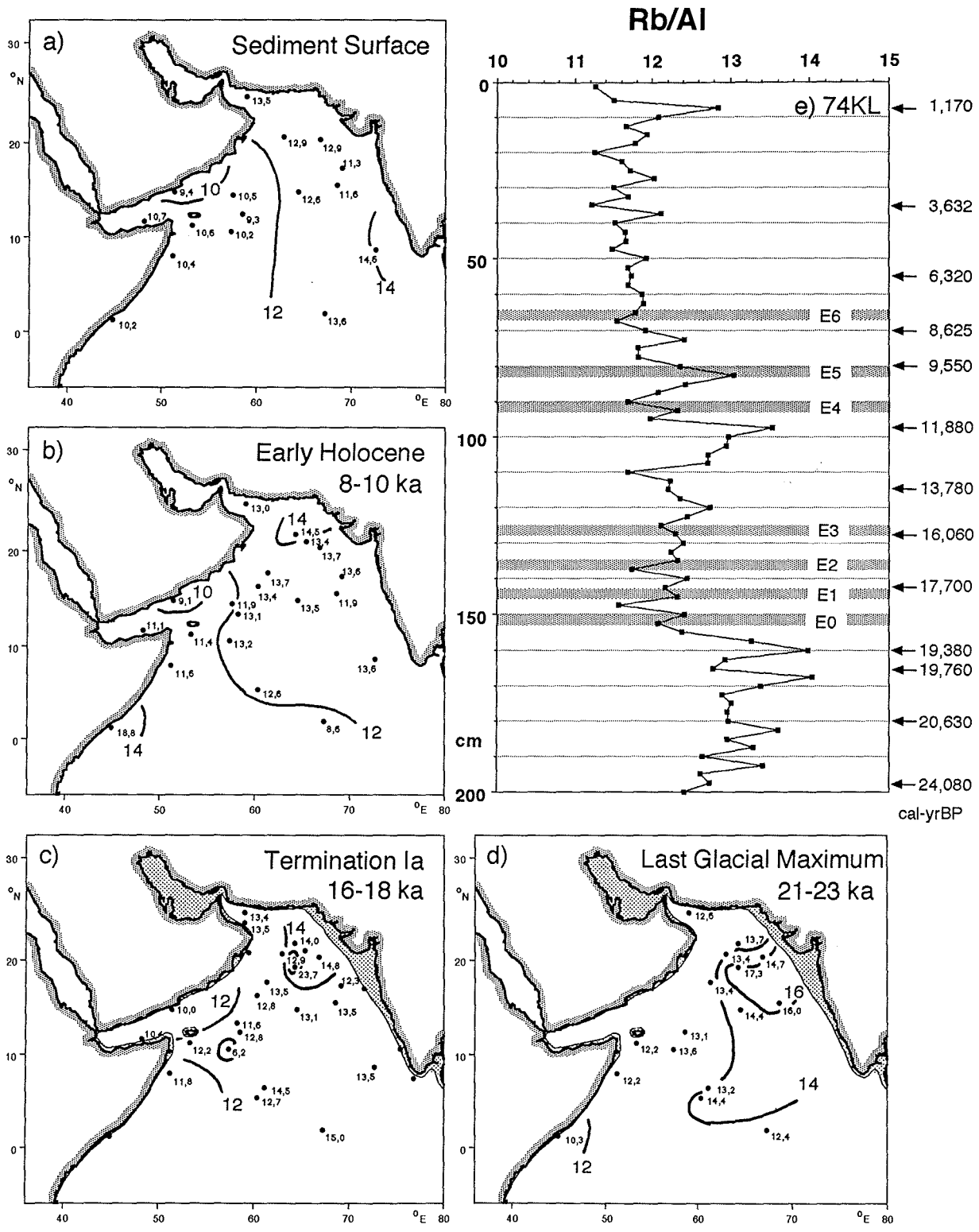

Figure 70. Rb/Al ratio as geochemical tracer of northeast monsoon intensity, (a) at the sediment surface, (b) during the Early Holocene (8000-10,000 cal-yrBP), (c) during Termination Ia (16,000-18,000 cal-yrBP), (d) during the Last Glacial Maximum (21,000-23,000 cal-yrBP), (e) sediment core 74KL; arrows indicate depth of AMS-^{14}C dates, converted to calendar years according to Tab. 2, hatched areas show events as defined in Fig. 12.

near east Africa are Ti and Hf (also frequent in heavy minerals), especially when presented as Ti/Al or Hf/Zr (distribution patterns are not shown, downcore variations in core 74KL are presented in Figs. 32 f, 53 f). The Ti/Al ratio was already used by Shimmield et al. (1990 a) for a reconstruction of the southwest monsoon during the last 350,000 years. The downcore variations of both Ti/Al, and Hf/Zr reveal steep increases during events E4 and E5, which is synchronous with the increases of Zn content, the best tracer of southwest monsoon driven upwelling fertility (see above). Accordingly, the intensification of the southwest monsoon during events E4 and E5 is documented in both the records of dust and upwelling.

The Arabian northwesterlies being the major source of dust in the western Arabian Sea (Fig. 5) are best depicted by the maximum of Mg content off the south Arabian coast (Fig. 69). Mg is both abundant in palygorskite and dolomite, which were shown to be the typical minerals of Arabian derived dust (Sirocko & Lange, 1991; Sirocko & Sarnthein, 1989; Sirocko et al., 1991). Mg/Al ratios are not useful in core 74KL, because both Mg and Al are predominantly contribute by the same transport systems (i.e., the Arabian northwesterlies); accordingly, the Mg/Al is almost constant in 74KL. Minor variations do occur due to the preferential source of Al from the northern branch of the northwesterlies that stem from the Persian Gulf area.

The overwhelming mass of particles in the western Arabian Sea is transported by the northwesterly winds from the Arabian desert and Mesopotamian lowland (Sirocko et al., 1991). Accordingly, dust derived from the northwesterlies must dilute the variations of trace elements being derived from the other, smaller, sources (Fig. 5). To exclude this diluting effect element concentrations were also normalized to Al, which is most abundant in the northern branch of northwesterlies (Fig. 25). Thus, element/Al ratios reflect the variation of the minor transport system relative to the major transport system of the northwesterlies. The disadvantage of the normalisation is, however, that primary variations in the element/Al ratio within the Arabian dust (due to a change of weathering intensity and Al mobilisation in Arabian soils) would be reflected in the ratio. Fortunately, extreme changes in the patterns of soil formation cannot be expected in Arabia during the past 25,000 years, because, despite an early Holocene wet-phase in the area (see chapter D.4.), the Arabian climate stayed between completely arid and semi-arid (Roberts & Wright, 1987).

The distribution pattern of Rb (Fig. 42), in particular after normalisation to Al (Rb/Al, Fig. 70), shows a provenance of Rb in India and Pakistan. The source of Rb could be a suspension of the river Indus or dust plumes that spread during winter and spring in the same area (Fig. 5). The plume of high Rb/Al values was

shifted further to the south during Termination Ia and the LGM. This could imply a southward extent of the northeast monsoon, or a southward dispersal of river suspensions along the continental slope at times of low sealevel. Most probably, the maximum off north India will be a combination of dust and river contributions. At core location 74KL, however, on a ridge in the western Arabian Sea, far away from the Indus and 1000 m above the Indus fan deposits (Fig. 9), the increased glacial Rb content most probably outlines changes in the flux of dust during spring or during the winter northeast monsoon.

The record of river discharge

As indicated above, the Rb/Al ratio in the sediments of the northern Arabian Sea should be affected by changes in the discharge of the river Indus, at core location 74KL, however, Rb is interpreted as reflecting changes in the intensity of dust flux in the northeast monsoon. Unfortunately, the two alternate explanations cannot be tested, because the entrainment area of dust transported in the northeast monsoon lies in the alluvial plains of the Indus (Ackerman & Cox, 1988).

Sc, Ti, As, Sr show maximum values off the rivers Tapti and Narbada (Fig. 31, 32, 41, 43). These elements may well be suited to study the history of river discharge in the eastern Arabian Sea, but their plumes do not reach the western sector of the ocean. Accordingly, the variations of these elements in the sediments of core 74KL must be attributed to changes of the dominating transport system in the western Arbian Sea (i.e., the northwesterlies, or, in case of Ti, the southwest monsoon, see above).

Following the evidence as shown above, we observe empirically that the most appropriate tracers to study the evolution of the monsoonal climate during the past are: Zn/Al - southwest monsoon driven upwelling fertility, Zr content - southern branch of Arabian northwesterlies, Mg content - northern branch of Arabian northwesterlies, Rb/Al - northeast monsoon.

D. Discussion

D.1. Processes affecting the trace element content of deep-sea sediments in the Arabian Sea

Distribution patterns of various elements were presented in chapter C., and those elements that have a potential to be used as tracers of past monsoon intensity were outlined in section C.4. Before we will apply these tracers for a reconstruction of the monsoon intensity, other mechanisms that might affect variations of trace element content in deep-sea sediments are discussed in this chapter. To study the grain-size related processes, the carbonate-and-opal-free silt and clay fraction was measured separately for a few samples of core 74KL. The values for these selected samples are listed in Tab. 13 together with the concentrations of the elements in the bulk fraction. This procedure was done only for the trace elements measured by ICP-MS, but not for the elements measured by ICP and XRF.

Trace element content of the clay fraction

The ratio between trace element contents contained in the clastic <2μm (clay) and the >2μm (silt) fractions shows that Cu, Zn, Ni, Co, Cs, Sc, Mo, Li, Ga, Mn, Pb, Rb, U are enriched in the clay faction, listed in the order of decreasing abundance (Tab. 13 d, Fig. 65 a). Accordingly, these elements should increase in concentration from the last glacial towards the Holocene, because the <2μm grain-size fraction gradually increases from coarse-grained sediments during glacial times to fine-grained sediments during the Holocene (Fig. 19). Indeed, most of the elements listed above show higher values during the Holocene than during the glacial. Only the Rb and Cs contents are lower in the Holocene than in the glacial section. Thus, only Rb and Cs concentrations reflect processes that are independent of grain-size control.

Trace element content of the leachable fraction of the bulk sediment

The average proportion of the leachable fraction in sediment core 74KL (Tab. 13 e, Fig. 65 b) is calculated from the element content in the bulk sediment fraction (cofb) minus the element concentration in the residue fraction after $CaCO_3$ and C_{org} were leached by acetic acid (conc.) and H_2O_2 (Tab. 13 b). Based on this procedure, Mn, Mo and U have a leachable proportion that exceeds 70 % of the bulk element content, whereas Li, Cr, Cu, Zn, Ga, Rb, Zr, Nb, Cs and Hf have leachable proportions of less than 10%.

The process of adsorption (surface complexation) is considered to be the

sediment fraction	core depth [cm]	grain-size < 2um [%]	Li	Sc	Cr	Mn	Co	Ni	Cu	Zn	Ga	Rb	Sr	Y	Zr	Nb	Mo	Cs	Ba	La	Ce	Pr	Nd	Sm	Eu	Gd	Tb	Dy	Ho	Er	Tm	Yb	Lu	Hf	Tl	Pb	U
a) Concentrations of trace elements in the bulk fraction [ppm cofb (carbonate and opal free basis)]																																				
bulk	90		44,8	19,1	145	2100	37,6	241	142	260	15,6	74,1	error	35,6	108	12,0	4,93	5,16	3107	26,0	46,1	6,34	25,9	5,62	1,13	5,70	0,89	5,50	1,172	3,60	0,525	3,39	0,53	2,83	1,09	24,7	14,51
bulk	110		49,2	22,6	156	2240	40,4	239	102	230	15,8	82,2	error	39,9	109	13,1	3,48	5,65	2310	26,4	48,1	6,42	25,9	5,61	1,20	5,84	0,89	5,49	1,161	3,48	0,503	3,37	0,50	2,82	1,32	21,0	16,10
bulk	120		46,8	19,6	158	2230	32,4	218	84	199	14,5	76,6	error	35,6	106	12,6	2,69	5,37	1575	25,0	46,2	6,03	24,2	5,15	1,15	5,28	0,82	4,98	1,049	3,11	0,426	3,02	0,46	2,79	0,95	19,2	10,59
bulk	140		45,6	error	164	1360	33,6	185	65	135	14,9	86,7	error	32,3	102	13,6	2,72	6,02	831	26,1	48,8	6,43	25,2	5,30	1,25	5,83	0,84	4,99	1,045	3,03	0,418	2,82	0,42	2,90	0,86	19,5	8,78
bulk	150		49,9	19,2	172	1310	28,7	200	75	156	14,7	83,5	error	33,3	109	13,2	4,01	5,92	1261	25,8	48,1	6,24	24,9	5,29	1,20	5,37	0,82	4,99	1,036	3,05	0,436	2,92	0,44	2,97	0,93	18,8	11,91
b) Concentrations of trace elements in the clay and silt fraction of the residue after leaching with acidic acid and H2O2 [ppm]																																				
< 2um	90	50,6	47,3	17,3	134	762	32,0	198	187	337	19,1	73,4	70,5	21,2	113	10,8	0,79	6,12	1382	16,9	29,9	3,80	14,1	2,77	0,69	2,73	0,42	2,73	0,576	1,88	0,271	1,94	0,30	2,84	0,53	14,5	2,20
< 2um	110	53,8	52,5	16,9	142	747	34,4	210	149	293	17,7	78,9	58,5	20,4	108	11,1	0,81	6,69	990	17,0	30,7	3,80	14,4	2,83	0,67	2,69	0,41	2,74	0,570	1,83	0,252	1,83	0,29	2,71	0,61	13,0	2,72
< 2um	120	43,0	55,5	18,2	172	339	35,3	225	144	287	18,1	84,8	55,3	19,9	113	12,0	1,12	7,17	808	17,3	31,4	3,88	14,3	2,76	0,66	2,65	0,41	2,66	0,565	1,76	0,265	1,79	0,26	2,91	0,60	12,9	2,50
< 2um	140	36,5	60,6	17,1	172	551	26,1	197	100	211	16,9	94,0	43,7	16,8	106	12,3	0,69	7,71	286	16,3	30,2	3,63	13,2	2,52	0,58	2,43	0,39	2,31	0,496	1,54	0,246	1,61	0,24	2,70	0,59	12,3	2,29
< 2um	150	45,5	60,9	16,7	162	467	23,9	192	116	215	16,7	87,8	51,7	19,7	113	11,5	0,93	7,46	689	18,1	33,4	4,04	15,1	3,00	0,66	2,88	0,44	2,74	0,599	1,83	0,274	1,87	0,28	2,94	0,58	11,8	3,08
> 2um	90	49,4	33,5	10,6	149	412	15,9	103	58	138	13,2	61,9	172,0	22,0	99	12,7	0,48	3,76	2223	19,3	37,5	4,72	18,1	3,81	0,97	3,56	0,52	3,19	0,643	1,91	0,270	1,91	0,28	2,61	0,53	11,5	1,99
> 2um	110	46,2	36,2	10,8	161	420	16,5	111	45	117	13,2	65,3	165,0	22,0	99	13,8	0,45	4,00	1763	19,7	38,4	4,83	18,5	3,85	0,95	3,67	0,53	3,26	0,659	1,92	0,267	1,86	0,26	2,87	0,62	9,6	2,23
> 2um	120	57,0	38,7	11,8	158	448	18,3	117	45	137	13,8	69,6	158,0	22,1	100	14,6	0,61	4,26	1507	20,0	39,2	4,96	19,1	3,86	0,97	3,64	0,55	3,30	0,666	1,96	0,275	1,89	0,27	2,73	0,58	10,1	2,11
> 2um	140	63,5	37,5	10,4	182	449	15,7	113	31	90	12,4	65,7	126,0	19,9	99	14,3	0,63	4,08	535	17,6	34,8	4,39	17,0	3,55	0,89	3,44	0,56	3,13	0,660	1,88	0,315	1,80	0,31	2,85	0,50	8,9	2,15
> 2um	150	54,5	35,0	10,3	170	452	15,4	104	32	95	12,0	62,9	143,0	20,3	102	12,9	0,64	3,83	835	17,6	34,6	4,29	17,0	3,49	0,87	3,37	0,53	3,14	0,624	1,82	0,265	1,75	0,26	2,67	0,46	9,1	2,24
c) Concentrations of trace elements in the residue after leaching with acidic acid and H2O2 [ppm]																																				
bulk	90		40,5	14,0	141	589	24,0	151	123	239	16,2	67,7	120,6	21,6	106	11,7	0,63	4,95	1797	18,1	33,7	4,25	16,1	3,28	0,83	3,14	0,47	2,96	0,609	1,89	0,271	1,93	0,29	2,73	0,53	13,0	2,10
bulk	110		45,0	14,1	151	596	26,1	164	101	212	15,6	72,6	107,7	21,1	104	12,3	0,65	5,45	1347	18,2	34,3	4,28	16,3	3,30	0,80	3,14	0,47	2,98	0,611	1,87	0,259	1,84	0,28	2,78	0,61	11,4	2,49
bulk	120		45,9	14,6	164	401	25,6	163	87	202	15,6	76,1	113,8	21,2	106	13,5	0,83	5,51	1206	18,8	35,8	4,50	17,0	3,39	0,84	3,21	0,49	3,02	0,623	1,87	0,271	1,85	0,27	2,81	0,59	11,3	2,28
bulk	140		45,9	12,8	178	486	19,5	144	56	134	14,0	76,0	96,0	18,8	102	13,6	0,65	5,40	444	17,1	33,1	4,11	15,6	3,17	0,78	3,07	0,50	2,83	0,600	1,76	0,290	1,73	0,29	2,80	0,53	10,1	2,20
bulk	150		46,8	13,2	166	459	19,3	144	70	149	14,1	74,2	101,5	20,0	107	12,3	0,77	5,48	769	17,8	34,1	4,18	16,1	3,27	0,78	3,15	0,48	2,96	0,613	1,82	0,269	1,80	0,27	2,79	0,51	10,3	2,62
d) Ratio between trace element contents contained in the clay and silt fraction																																				
	90		1,4	1,6	0,9	1,8	2,0	1,9	3,2	2,4	1,4	1,2	0,4	1,0	1,1	0,9	1,7	1,6	0,6	0,9	0,8	0,8	0,8	0,7	0,7	0,8	0,8	0,9	0,9	1,0	1,0	1,0	1,1	1,1	1,0	1,3	1,1
	110		1,5	1,6	0,9	1,8	2,1	1,9	3,3	2,5	1,3	1,2	0,4	0,9	1,1	0,8	1,8	1,7	0,6	0,9	0,8	0,8	0,8	0,7	0,7	0,7	0,8	0,8	0,9	1,0	0,9	1,0	1,1	0,9	1,0	1,4	1,2
	120		1,4	1,5	1,1	0,8	1,9	1,9	3,2	2,1	1,3	1,2	0,4	0,9	1,1	0,8	1,8	1,7	0,5	0,9	0,8	0,8	0,7	0,7	0,7	0,7	0,7	0,8	0,8	0,9	1,0	0,9	1,0	1,1	1,0	1,3	1,2
	140		1,6	1,6	0,9	1,2	1,7	1,7	3,2	2,3	1,4	1,4	0,3	0,8	1,1	0,9	1,1	1,9	0,5	0,9	0,9	0,8	0,8	0,7	0,6	0,7	0,7	0,7	0,8	0,8	0,8	0,9	0,8	0,9	1,2	1,4	1,1
	150		1,7	1,6	1,0	1,0	1,6	1,8	3,6	2,3	1,4	1,4	0,4	1,0	1,1	0,9	1,4	1,9	0,8	1,0	1,0	0,9	0,9	0,9	0,8	0,9	0,8	0,9	1,0	1,0	1,0	1,1	1,1	1,1	1,2	1,3	1,4
bulk	Average:		1,5	1,6	1,0	1,3	1,8	1,9	3,3	2,3	1,4	1,3	error	0,9	1,1	0,8	1,6	1,8	0,6	0,9	0,8	0,8	0,8	0,7	0,7	0,8	0,8	0,8	0,9	0,9	0,9	1,0	1,0	1,0	1,1	1,3	1,2
e) Leachable proportion [%] of the bulk element concentration																																				
bulk	90		10	27	2	72	36	37	13	8	-4	9	error	39	2	2	87	4	42	31	27	33	38	42	27	45	47	46	48	47	48	43	46	4	51	47	86
bulk	110		9	38	3	73	35	31	1	8	1	12	error	47	4	6	81	4	42	31	29	33	37	41	33	46	48	46	47	46	49	45	45	1	54	46	85
bulk	120		2	26	-4	82	21	25	-4	-1	-8	1	error	41	0	-7	69	-3	23	25	22	25	30	34	27	39	40	39	41	40	36	39	42	-1	38	41	78
bulk	140		-1		-9	64	42	22	14	0	6	12	error	42	0	1	76	10	47	34	32	36	38	40	38	47	41	43	43	42	31	39	32	4	38	48	75
bulk	150		6	31	3	65	33	28	6	4	4	11	error	40	2	7	81	7	39	31	29	33	35	38	35	41	41	41	41	40	38	38	38	6	44	45	78
bulk	Average:		5	30	-1	71	33	29	6	4	0	9	error	42	2	2	79	5	39	30	28	32	36	39	32	44	43	43	44	43	40	41	40	3	45	45	80

Table 13. Concentrations of trace elements in selected samples of sediment core 74KL. (a) Concentrations in the bulk fraction [ppm cofb (carbonate and opal free basis)], (b) Concentrations in the clay and silt fraction of the residue after leaching with acetic acid and H_2O_2 [ppm], (c) Concentrations in the residue after leaching with acetic acid and H_2O_2 [ppm]. Values are calculated from b) using the grain-size <2 μm values (d) Ratio between trace element contents contained in the clay- and silt fraction, (e) Leachable proportion of the bulk element concentration ((a) minus (c) in percent).

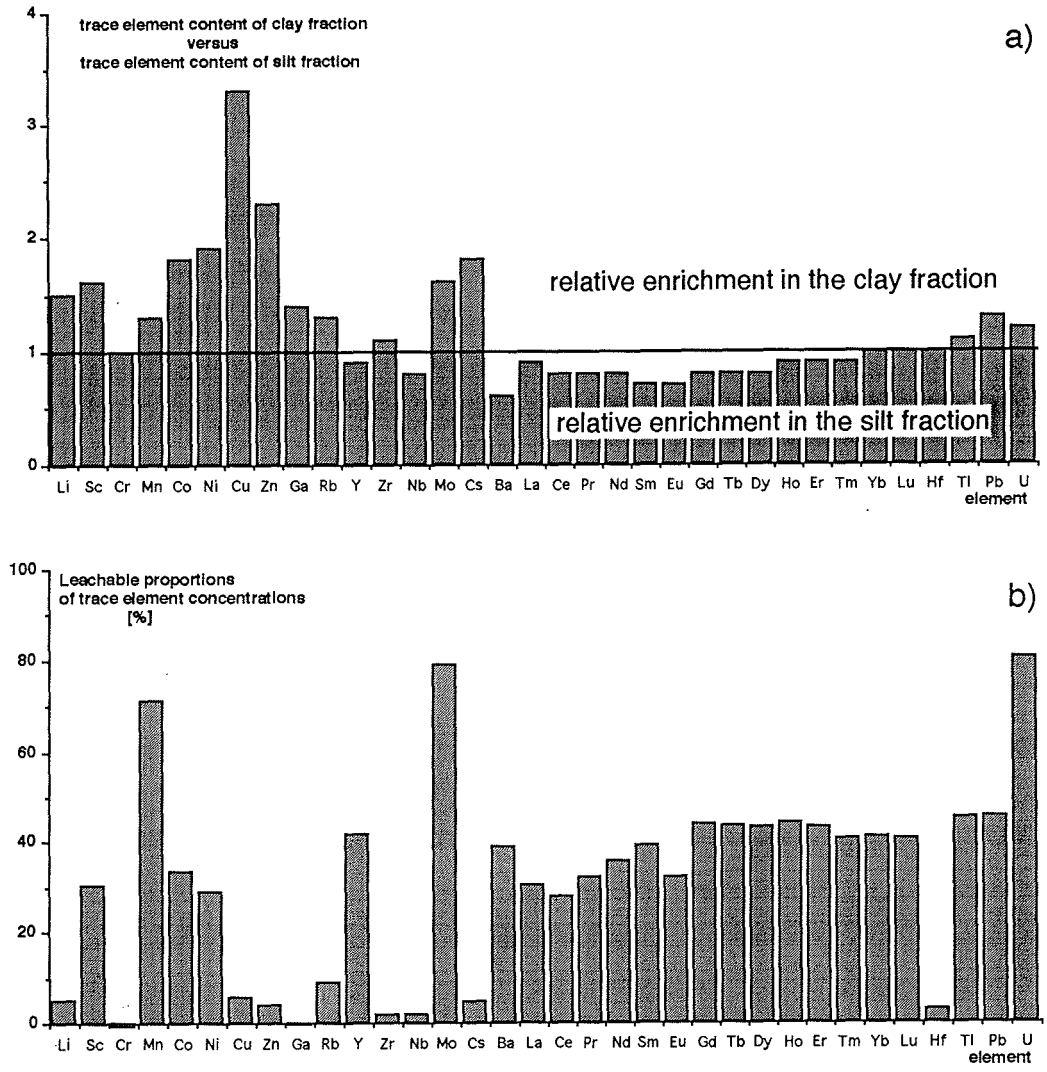

Figure 65. (a) Relative trace element enrichment in the clay and silt fraction, as shown by the ratio between the two fractions [< 2µm/>2µm] (Tab. 13d). (b) Leachable proportion of trace elements [% of element content] .

dominant process in the oceanic scavenging of trace metals (review by (Honeyman et al., 1988)). The specific surface area (m^2/g) of a particle determines the amount of kations that can be adsorbed to it. The largest specific areas are observed for organic matter (800-1000 m^2/g) and smectites (600-800 m^2/g), whereas sand, silt and carbonates reveal values below 1 m^2/g (Scheffer & Schachtschabel, 1992). Organic carbon content is at 6% in modern sediment trap samples in the western Arabian Sea (Nair et al., 1989), 2% in the samples of core 74KL, whereas smectite content can reach 10% of the bulk sample in core 74KL (30% in the clay fraction (Sirocko & Lange, 1991)). Accordingly, both organic

carbon and smectite particles cause a high kation exchange capacity for the sediments in the western Arabian Sea. Zn, and all other elements enriched in nutrient rich waters, must have been transported to the deep ocean by surface complexation. These kations could have been desorbed in the reducing section of the sediments (and being trapped in the small oxigenated surface layer) or are still present in an adsorbed phase. The high content of Zn in the clay fraction (Tab. 13, Fig. 65) suggests the latter explanation. In this case, the weak leachate of acetic acid was not capable in removing strongly adsorbed ions. Accordingly, the variations of Zn in core 74KL still might still reflect the original changes of adsorbed Zn. Hence, Zn could be a reliable tracer of past changes in nutrient content, monitoring the strength of the southwest monsoon.

Trace element content of specific minerals

Quartz, which is the most abundant mineral in the silt fraction of the deep-sea sediments of the Arabian Sea is usually low in trace element content. Other minerals, however, can show extreme enrichment of elements. In particular, three minerals seem to play an important role for the trace element composition of the sediments of the Arabian Sea:

Feldspar, Mica

The areal distribution of Cs and Rb, which were the elements that do not covary with grain-size variations and have a low leachable fraction, show a maximum in the northern Arabian Sea. A similar maximum is observed for K content (Figs. 29, 42, 49), suggesting that Cs and Rb may be frequent in K-rich feldspar. On the other hand, the clay minerals illite or kaolinite are also rich in K. The illite content of the clay fraction has a maximum in the north (Kolla et al., 1981a; Sirocko & Lange, 1991), but feldspar grains (partially altered to chlorite, A. Richter, pers. comm.) are also frequent in the northern Arabian Sea sediments. If the illite bound Cs and Rb proportions were dominating the feldspar-bound proportion, we should find a clear enrichment of Rb and Cs in the clay fraction. According to Fig. 65a, Cs is indeed highly abundant in the clay fraction, but Rb only to a minor degree. Thus, the mineral phase that controls most of the Rb content of Arabian Sea sediments is likely to be feldspar, parts of which are altered to chlorite.

Zircon

Zr, Hf, Ga and the LREE form a group of elements which show a very similar downcore variability in 74KL (Figs. 45, 53, 40, 51). This covariance may be attributed to the common occurrence of these elements in the heavy mineral zircon (Hinton & Upton, 1991), which was observed on smear slides of core 114KK,

which is located in the center of the plume of high Zr content off Somalia. The zircon content is, however, so low that zircons were not apparent in the x-ray diffraction pattern of the silt fraction of Arabian Sea sediments (H. Lange, unpubl. data).

Baryte

Ba is the element most strongly enriched in the silt fraction (Tab. 13, Fig. 65). Thus, the occurrence of Ba is probably linked to silt-sized $BaSO_4$ crystals, which form in biogenic debris while settling through the water column (Bishop et al., 1977). These silt-sized crystals hardly dissolve in the sediments, and are an appropriate tracer to monitor the history of biogenic flux rates (Dymond et al., 1992; Emeis, 1993).

Trace element changes at redox boundaries in the sediments

Besides a synsedimentary enrichment of kations in specific minerals and grain size fractions, a postsedimentary modification of trace element content can occur by diagenetic processes (e.g., Shaw et al., 1990).

The redox boundary near the sediment surface presents a transition zone of decrease in the availability of oxidizing substances to decompose organic compounds (Froelich et al., 1979). Oxygen is still present at the sediment surface, but has been completely consumed for organic carbon remineralisation at the bottom of the bioturbation surface layer (Froelich et al., 1979). The sediment section below this oxic surface layer is reducing, and adsorbed elements, which should be concentrated in the leachable fraction (Fig. 65 b), are mobile in a reducing environment, so that they can diffuse into the surface layer where they can precipitate as oxides and are trapped. Accordingly, deep-sea sediment cores show an enrichment of kations in the uppermost cm below the sediment surface (Shaw et al., 1990). The depth of the oxygenated surface layer varies as a function of C_{org} content, which is the main electron donator for the reduction processes (Finney & Mitchell, 1988).

The C_{org} content of 74KL is 1.3% at the sediment surface (Fig. 21) and indeed only traces of an oxygenated surface layer were observed when the core was recovered, although the surface of the giant box core 74KL was intact on board the ship. Thus, the modern sediments of 74KL were reducing up to the top (Fig. 9).Indeed, none of the various trace elements studied show maximum values in the upper few cm of core 74KL (Figs. 20-56). This might have been different during the past when C_{org} content was lower (Fig. 21). Accordingly, the development of a small oxygenated surface layer could explain the offset between the $\delta^{18}O$ events and nearby changes in trace element content, for example the Ba increase near to

event E4 occurs 2.5 cm below the event (Fig. 50).

Because Zn is one of these elements that could be affected by a diagenetic mobilisation (Shaw et al., 1990), we cannot exclude that the increases of Zn during the abrupt events E3 and E4 are partly due to changes in redox potential at these depths, especially because organic carbon content changes at the same depths. Other processes, however, can provide an alternate explanation for the same observation (see below).

Trace element content of the biogenic fractions

Organic matter can contain primarily the elements Co, Cd, Zn or Ni, but these are not enriched above levels usually found in lithic matter (Collier & Edmond, 1984). The increase in C_{org} content from 30 cm depth to the surface (Fig. 21) is reflected only in the evolution of N, but none of the trace elements. Accordingly, direct contributions from organic tissue have to be regarded as presenting only a minor proportion of the bulk trace element content.

The carbonate fraction contains large proportions of Sr, which is substituting in the crystal lattice for Ca, especially in aragonite. Other elements that have high dissolved ion content in the ocean water (i.e, Zn, Ba, Cd, Cu, REE) are also contained in carbonates, often as organic coatings that are overgrown during calcification (Boyle, 1992).

In 74KL, Ba, Cd, Co, Cu, Mn, Ni, Pb, Y, HREE, Tl, U, Zn reflect the carbonate increase at 127.5-125 cm depth (i.e., during event E3). Distribution patterns of some of these elements (Ba, Cd, REE) also parallel the areal distribution of $CaCO_3$ content, thus showing a general correlation to $CaCO_3$ content. These elements are also high in leachable fraction (Fig. 65b), which corroborates the inference that they are concentrated in the carbonates directly.

In this case, that the carbonate fraction itself contains a significant amount of an element, and the carbonate flux remains constant, but the flux of lithic sediments decreases, the carbonate derived element proportions relatively increase over the lithogenic proportions. When bulk concentration of such an element is expressed on a carbonate-and-opal-free-basis, the reduction in lithogenic flux rates will result in a computed increase in the value of element concentrations (cofb). This process could be partly responsible for the increase of the trace elements being high in the leachable fraction (Fig. 65b) during event E3, because lithic accumulation rates must have decreased near to this event (Tab. 1b).

Biogenic Opal is known to contain significant amounts of Germanium (Mortlock & Froelich, 1989), but to be otherwise barren of trace element content. The development of micro-environments and Ba-sulfate formation, however,

occurs mainly in the organic matter of opaline tests (Bishop et al., 1977). The most pronounced increase in opal occurred between 97.5 and 95.0 cm (Fig. 18) (i.e., very near to the depth where another major transition in the content Mn, Cu, Zn, Cd, Ba, and Pb is observed at 95-92.5 cm), which is 2.5 cm below the major $\delta^{18}O$ event E4. The 2.5 cm offset between the $\delta^{18}O$ event and the respective trace element increase could be caused by the precipitation of trace elements a few cm below the sediment surface at depth of a change in the redox potential of the sediments (see above).

The increase of Ba from the glacial level to the Holocene level could be caused by the increase of opal alone (see calculation on page x), the increase of Zn and other elements at the same depth cannot caused by changes in opal content only, but could be related to the same process that controlled opal content (i.e., the onset of upwelling fertility in the surface water, see below).

The response of trace element content in sediments to changes in deep ocean ventilation

Low oxygen content in the deepwater is often paralleled by sulfide formation, mostly in the form of pyrite (Emeis & Morse, 1993), which can bind large amounts of most other metallic ions (including Zn, one of our potential monsoon tracers) pertinent in the interstitial water of the sediment. Metalliferous coatings can also develop in reducing environments in the inner space of carbonate tests (Boyle, 1992). Accordingly, the history of oxygen content is an important factor for the evaluation of processes affecting trace element content of the Arabian Sea sediments.

Established chemical tracers of anoxic condition in the deepwater are S and Mo (e.g. Seralatan & Hartmann, 1986), elements which reveal highest values between 160-200 cm depth and a sharp transition at 160 cm depth (Figs. 28, 47), compare also factor F7 (Fig. 61). A sluggish ventilation of the Arabian Sea deepwater during glacial times was already observed by Kallel et al. (1988) and Sarkar et al. (1993). The Mo and S records indicate that the end of the bad ventilation occurred abruptly with the end of the Last Glacial Maximum. The low ventilation of the deep Arabian Sea during the LGM is also reflected by negative $\delta^{13}C$ values (-0.7‰) of the benthic foraminifera *Cibicides wuellerstorfi* (Fig. 66).

The section of the LGM in core 74KL (160-200 cm depth) has enriched levels of a large number of kations (i.e., Cr, Mn, Co, Ni, Cu, Zn, Y, Cd, Ba, HREE, Tl, U). Most of these elements, except Mn and Cr, belong to the group of biolimited elements, that are depleted in surface waters but being enriched at depth (Bruland, 1980; German & Elderfield, 1990; Bertram, 1989). Accordingly, it could be assumed that higher productivity during peak glacial times could be responsible for the

enhanced levels of these "nutrient elements". High values of Cr in the same sediment section 160-200 cm (Fig. 33) indicate, however, that this inference could

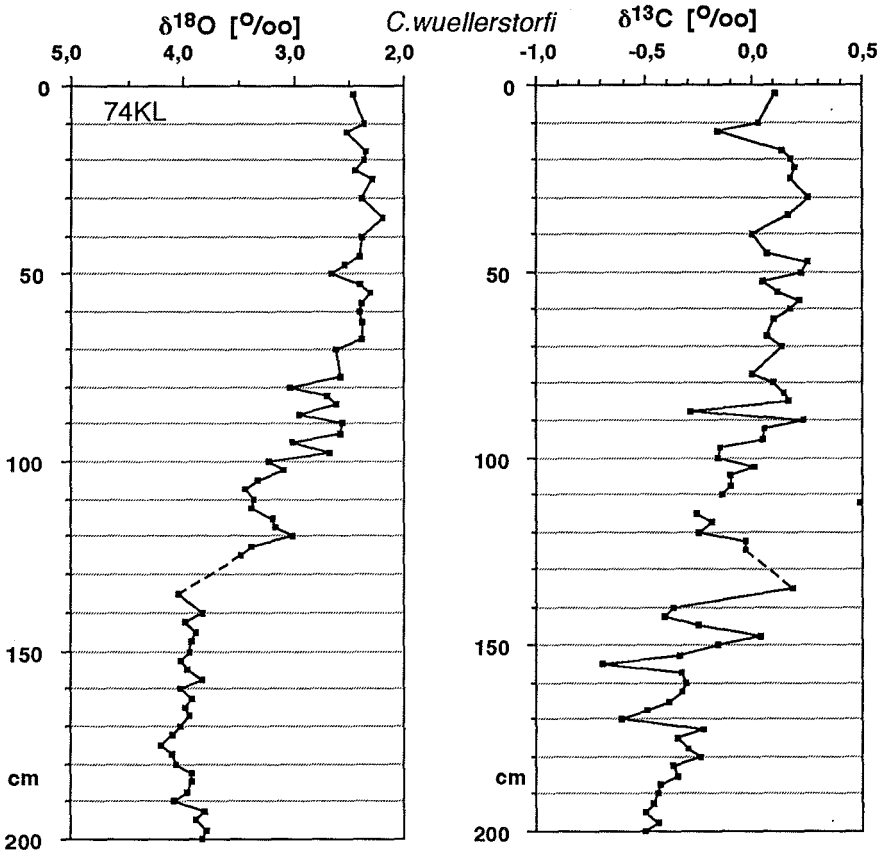

Figure 66. $\delta^{18}O$ and $\delta^{13}C$ of Cibicides wuellerstorfi in sediment core 74KL. Two specimens of 315-400 µm diameter were used for all samples. No specimens were found in the section of the Termination Ia where the line is stippled

be wrong. Cr can be largely enriched in almost anoxic environments; this element is no nutrient element at all, but it can be concentrated in sulfides, which also enrich most other metallic ions being dissolved in the deepwater. Accordingly, an alternate explanation for high trace element content in the sediment section 160-200 cm might be the low ventilation of deepwater during the Last Glacial Maximum. Sediment cores KS8 and 422 in the Gulf of Oman, where glacial $\delta^{13}C$ values reach -0.8 (-1.0 represent conditions of complete anoxia (Shackleton, 1987) show pyrite formation in the LGM section (Appendix 3, 4). Accordingly, low O_2 levels in the deepwater of the Arabian Sea were a widespread phenomenon during the Last Glacial Maximum, with minimum values being found in the very north. We cannot exclude that the high Zn content in the glacial section of core 74KL is partly due to this process.

The response of trace element content in the sediments to changes in the nutrient content of surface waters

Nutrient content of surface water at the location of core 74KL is extremely high during summer (Wyrtki, 1971). The elements Cd and Zn are likely candidates to monitor the history of these nutrients in the water, because the concentrations of their dissolved ions parallel nutrient content on a global scale (Boyle, 1994) and also in the Arabian Sea water (Saager et al., 1992) (Fig. 7). The transfer of these "nutrient elements" to the sediments probably occurs by means of adsorption to large surface areas of clay minerals or organic carbon.

Distribution patterns of Cd and Zn (and U) are the only ones to show maxima in the upwelling areas of the western Arabian Sea (Figs. 39, 48, 56). The downcore profiles of Zn and Cd in core 74KL are in general rather similar, with the exception of a section of low Cd values at 90-95 cm depth (i.e., at a depth level when Zn shows high values). It is striking that spikes of Cd content at 92.5 cm and 82.5-80 cm coincide with $\delta^{18}O$ events E4 and E5 at the same depth (Figs. 12, 48). The other Cd increases at 127.5-125 cm and 70-62.5 cm also coincide with $\delta^{18}O$ events E3 and E6. These spikes are not reflected in the Zn profile, but in the Cd profile only. This discrepancy can be explained by the depth profile of dissolved Cd content in the modern Arabian Sea. Dissolved Cd content and the nutrient PO_4 (Fig. 7) have a nutricline at about 200 m depth (i.e., within the reach of upwelling cells), whereas the nutricline of Zn and H_4SiO_4 is found at about 1000 m depth, well below the depth of modern upwelling cells (Fig. 7). Accordingly, variations of Cd content in the surface water are capable to monitor subtle changes in the intensity of upwelling, whereas Zn content will only reflect major changes in upwelling intensity or intermediate water structure.

D.2. Possible causes of abrupt $\delta^{18}O$ variations in the surface water

The $\delta^{18}O$ record of the surface-dwelling planktonic foraminifera *G.ruber* in core 74KL from the western Arabian Sea is shown in Fig. 12 and is described in detail in chapter B.1. The oxygen isotope composition of core 74KL reveals a succession of abrupt and continuous changes from glacial values near 0‰ to Holocene values averaging -1.75‰ (Fig. 12). Of this range, 1.2‰ can be explained by changes in the global ice volume (Chappell & Shackleton, 1986; Fairbanks, 1989) and 0.55‰ should be of local origin. This local contribution may be reflected particularly in the abrupt events which have a far larger amplitude than the global $\delta^{18}O$ water signal, for example, the 0.5‰ change during event 5 exceeds by 0.35‰ the global increase of 0.15‰ during the synchronous meltwater pulse Ib (Fairbanks, 1989).

To verify that these abrupt changes, which can be observed in core 74KL, are not only confined to the upwelling areas off Arabia we compared them with high resolution records of cores KS8 and 422 from the Gulf of Oman, 900 km further north (Figs. 14, 15). The $\delta^{18}O$ profile of core KS8 shows clearly the $\delta^{18}O$ events 2, 3, 5, moreover, with a larger amplitude than in core 74KL. The variations of $\delta^{18}O$ values in core 422, where the sediment profile is disturbed by a hiatus, have a larger scatter, however, events 5 and 6 are distinct also in core 422 (Fig. 14). Regional variation patterns of the $\delta^{18}O$ amplitude between the last glacial and the Holocene level were first described in the northern Arabian Sea by (Duplessy, 1982). He ascribed the areal changes in the $\delta^{18}O$ amplitude of surface water to changes in surface water salinity. Accordingly, glacial salinity in the surface water of the northern Arabian Sea was higher than today, because the evaporation was assumed to be more intense when precipitation of southwest monsoon rains was low. In addition to evaporation and precipitation, three further mechanisms may be involved as forcing mechanisms of the $\delta^{18}O$ events of abrupt shifts towards lighter $\delta^{18}O$ values:

i) An increased proportion of isotopically light water derived from upwelled intermediate water masses at the water surface. The surface water of the Arabian Sea is up to 0.6‰ heavier in the mixed layer of the uppermost 60 m than the water further below (Fig. 71 b) (Bertram, 1989; Bouvier-Soumagnac & Duplessy, 1985; Ganssen & Kroon, 1991; Zahn & Pedersen, 1991).

ii) A change in the dominant season of test formation of *G.ruber*. Today, *G.ruber* reveals two seasonal maxima of production in the Arabian Sea, one maximum with more positive values occurs during the nutrient-rich summer months, a second one with more negative values is linked to the warm surface waters during winter (Curry et al., 1992).

iii) A marked increase in sea surface temperature (SST). This change, however, appears unlikely, because it would imply warmer SST during the Holocene, just when

upwelling was increased and SST were colder than during the glacial (Prell et al., 1980).

To test which of the three possible mechanisms actually triggered the abrupt $\delta^{18}O$ variations observed in the surface water of the Arabian Sea during the past, we compiled modern $\delta^{18}O$ measurements of seawater from the literature and measured a high resolution profile in the eastern Arabian Sea to better understand the modern control of $\delta^{18}O$ variations in the Arabian Sea (Fig. 71). The $\delta^{18}O$ composition of the surface waters in the southern and northern Indian ocean largely follows the relation described by Craig & Gordon (1965) for the world ocean (Fig. 71. Accordingly, the surface water in the Arabian occupies an intermediate position on a mixing line between water of the southern ocean and the highly saline water of the Persian Gulf and Red Sea. The pronounced local evaporation over the Arabian Sea may contribute to the steep gradient between surface waters and subsurface waters (Fig. 71 b).

Our own water samples from the eastern Arabian Sea were taken during the SO42 cruise at the sediment trap site "EAST" reported by Nair et al. (1989). The $\delta^{18}O$ at EAST reflects the well developed stratification of the surface water during spring before the onset of the southwest monsoon season (Fig. 71 b). Accordingly, $\delta^{18}O$ values reach almost 0.9‰ in the surface water. Below 60 m, the values start to decrease. At 300 m depth they are almost 0.6‰ lighter than at the surface. A similar range of $\delta^{18}O$ variability was reported by Östlund et al. (1987) and Bertram (1989) for the western and equatorial Arabian Sea. The modern salinity in the surface water of the Arabian Sea amounts to near 36.5‰, and near 35.5‰ at 300 m depth (Wyrtki, 1971). Based on the global relation between salinity and $\delta^{18}O$ composition found by Craig & Gordon (1965) (1.75‰ change equals 1.0‰ $\delta^{18}O$ change), the 0.6‰ change between surface water and intermediate water at 300 m depth can be related to salinity only. Accordingly, changes in the stratification of surface water, such as induced by a past intensification of upwelling, can sufficiently affect the $\delta^{18}O$ composition of the surface water and the foraminifera that live in it (*G.ruber* lives in the uppermost 50 m of the ocean, Duplessy & Bé, 1981).

To evaluate whether changes in upwelling intensity have paralleled (and controlled) $\delta^{18}O$ events we compare the *G.ruber* $\delta^{18}O$ profile of core 74KL with the Cd content in the sediment (Figs. 48 and 72), which may serve as tracer of upwelling intensity during the past (chapter D.2.), because the Cd content in ocean water parallels the distribution of PO_4 in the ocean water (Bruland, 1980; Saager et al., 1992) (Fig. 7). The Cd record in core 74KL shows spike-like increases at 177.5, 167.5, 92.5, 80.0, 60.0 and 55.0 cm depth (Figs. 48, 72). The spikes at 177.5, 167.5, 92.5, 80.0 are exactly paralleled by corresponding sharp $\delta^{18}O$ events (Fig. 12), especially during events E4 and E5. The Cd increase at 60.0 cm, after event E6, is not a spike, but the beginning of an extended peak of high Cd content. Accordingly, all abrupt $\delta^{18}O$

decreases in core 74KL (Fig. 12) are paralleled by spikes in Cd content, except for event E3, which lies in the middle of a gradual Cd increase (Fig. 48). Thus, the first upwelling of isotopically light, low-salinity water from intermediate depth at the end of a time of pronounced surface water stratification forms a likely contribution to the abrupt $\delta^{18}O$ events found in the composition of planktonic foraminifera in the Arabian Sea. The other processes listed above (i.e., changes in the seasonality of *G.ruber* growth, water mass characteristics, and the precipitation regime), may modify this primary signal, but will not reach a sufficient order of magnitude.

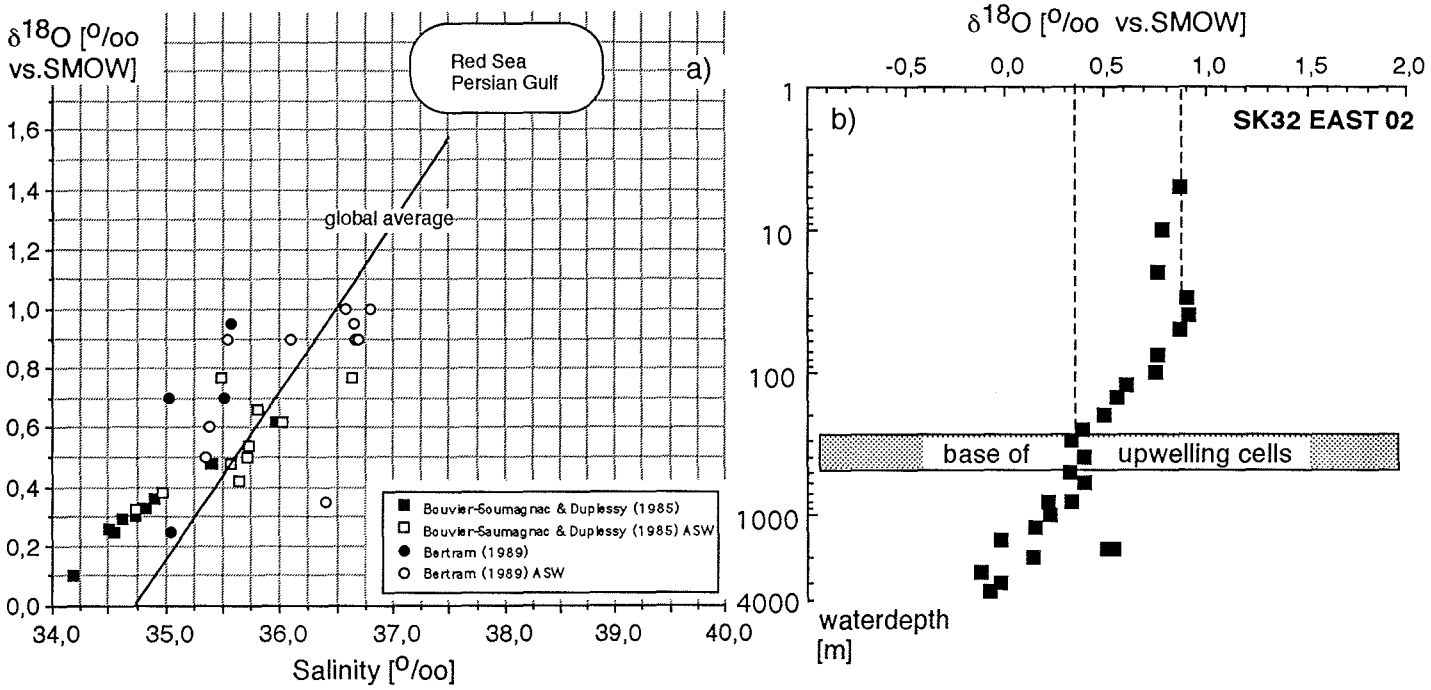

Figure 71. (a) $\delta^{18}O$ [‰ vs. SMOW] of Indian Ocean surface water versus salinity, compiled from Bouvier-Soumagnac & Duplessy (1985) and (Bertram, 1989); as compared to a global regression of Craig & Gordon (1965). The open dots represent data from the Arabian Sea north of the equator (ASW), the filled dots represent data from the southern Indian Ocean (b) $\delta^{18}O$ [‰ vs. SMOW] of water at 7 May 1987 (Erlenkeuser, Ittekkot & Sirocko, unpubl. data). Location of water cast "SK32 EAST 02": 15° 32,00 ´N, 68° 44,81´E (i.e., at sediment trap location EAST (Nair et al., 1989)). The stippled bar indicates source depth of upwelled water originating from about 300 m depth (Prell & Streeter, 1982).

Based on this interpretation, an idealized curve of $\delta^{18}O$ variations in core 74KL can be simulated, if negative $\delta^{18}O$ spikes are applied to all Cd maxima. In summary, the following components may be contained in the $\delta^{18}O$ curve of *G.ruber* in core 74KL (Fig. 72): (a) A global $\delta^{18}O$ decrease of 1.2‰ linked to high-latitude deglaciation (Fairbanks, 1989), (b) spikes of light $\delta^{18}O$ values during initial phases

of upwelling intensification; (c) stepwise changes in oceanic and atmospheric circulation leading to a new equilibrium of precipitation, evaporation and upwelling subsequent to the events. Bioturbating the stacked signal (d) using a convolution technique outlined by Hutson (1980) (M.H. Trauth, unpubl. results) will then result in curve (e), which resembles the genuine record of $\delta^{18}O$ variations in core 74KL fairly closely (f). Only event E3 cannot be reproduced by this procedure. Hence, other processes than the intensification of upwelling must have operated at that time along with the end of global Termination Ia.

The overshot and subsequent relaxation of $\delta^{18}O$ values after events E3, E4, E5 shows that the spike-like decreases of $\delta^{18}O$ values are necessary to produce the observed profile of $\delta^{18}O$ variations in core 7 4KL. The actual duration of these spikes is unknown, but is a crucial test for the validity of our explanation of abrupt $\delta^{18}O$ change in the Arabian Sea. Ultra-high resolution profiles of Cd content and $\delta^{18}O$ variations in cores of 1m/1000yrs sedimentation rate, recovered from the continental margin of Pakistan during cruise "SO90" will serve to determine the rate of change during the $\delta^{18}O$ events on a decadal scale in the near future (F.S. in preparation).

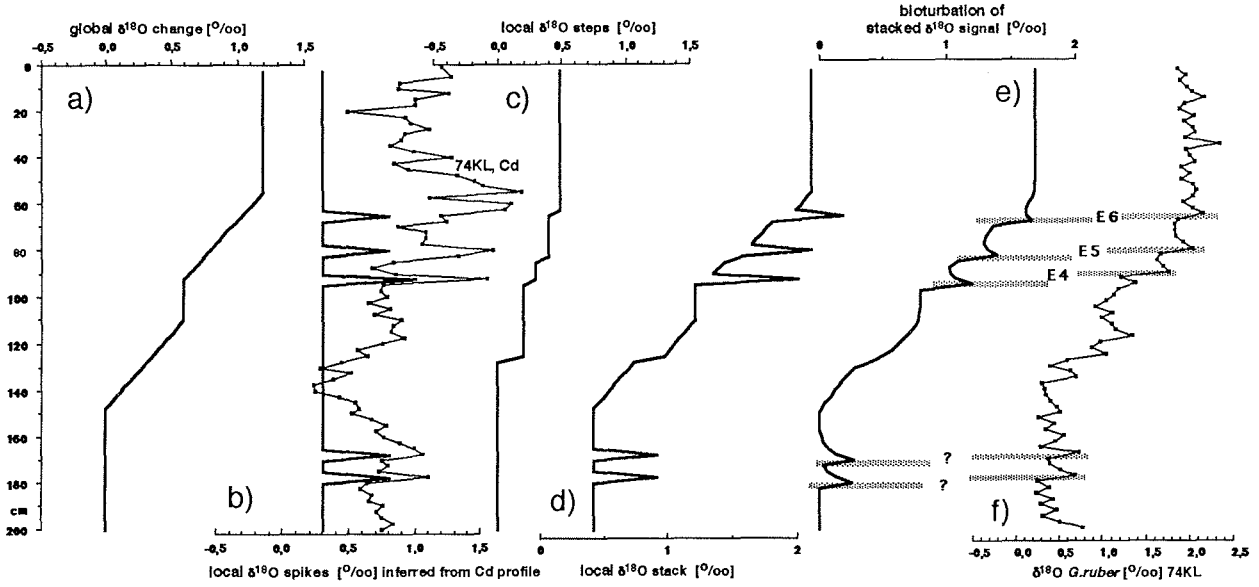

Figure 72 .Components of the $\delta^{18}O$ variability in core 74KL. (a) global decrease of 1.2‰; (b) proposed spikes of light $\delta^{18}O$ values (based on spikes of Cd content in the sediments) during the initial intensification of upwelling; (c) steplike increases to a new equilibrium of evaporation and upwelling; (d) stack of a), b) and c); (e) bioturbation of d) by applying the convolution formula of Hutson (1980) and an impulse response function representing homogenisation of the uppermost 5 cm at the sediment surface; (f) $\delta^{18}O$ variations of G.ruber in core 74KL.

D.3. The evolution of the monsoon climate during the last 25,000 years

The record of core 74KL starts at 20,000 ^{14}C-yrBP (about 24,000 cal-yrBP) subsequent to the Atlantic Heinrich layer H2 near 24,000 cal-yrBP (Bond et al., 1992). Accordingly, the evaluation of the monsoonal climate will start with the Last Glacial Maximum.

The Last Glacial Maximum (LGM): .24,500-18,000 cal-yrBP (21,000 -14,500 ^{14}C-yrBP)

The southwest monsoon and the associated upwelling intensity in the western Arabian Sea (Fig. 67), dust tranport in the northwesterlies (Fig. 68) and the intensity of the northeast monsoon (Fig. 70) remained on an almost constant level during the LGM. The intensity of the northeast monsoon winds was strongest at 19,300-20,000 cal-yrBP (Fig. 70), which is in line with paleoclimatic findings of Fontugne & Duplessy (1986), Sarkar et al. (1990), Van Campo (1986). The intensity of the southwest monsoon, however, was much lower than today, but a little stronger than during Termination Ia (Fig. 67).

The planktonic $\delta^{18}O$ record of core 74KL (Fig. 12) oscillates with amplitudes of up to 0.4‰ during the LGM, amplitudes that exceed the Holocene variability. These $\delta^{18}O$ changes are larger than the analytical error margin and, thus, should reflect a genuine variability in the hydrography of the Arabian Sea, such as changes in evaporation (Duplessy, 1982). Schulz (1994) shows that the faunal planktonic assemblage of the LGM contained large proportions of species (*Neogloboquadrina pachyderma* (sinistral)) probably derived from South Indian Central Waters (SICW). Today this water mass spreads only as far north as the equator and is only rarely encountered in the Arabian Sea (Fig. 7). The occurrence of *N. pachyderma* (sinistral) indicates that the glacial SICW reached as far north as 15°N in the Arabian Sea. The SICW tracer species disappear at 19,000 cal-yrBP when both the southwest and northeast monsoon show a first major change after the LGM (Figs. 67, 70).

The deepwater of the Arabian Sea was poorly ventilated during the LGM, as indicated by low $\delta^{13}C$ values of *C.wuellerstorfi* (-0.5‰) and an enrichment of S, Mo and organic carbon in the glacial section of 74KL (Figs. 61, 66). The deepwater ventilation was further reduced in the Gulf of Oman where S was enriched in the glacial section of core KS8 (Appendix 3), and the $\delta^{13}C$ values of *C.wuellerstorfi* reached almost -1, a value that reflects complete anoxia (Shackleton, 1987; see chapter D.1.).

The onset of Termination Ia (event E0): 18,500 cal-yrBP (15,000 ^{14}C-yrBP)

The definition of event E0, as the other events, is based on an abrupt decrease of $\delta^{18}O$ in core 74KL (Fig. 12). An abrupt change in concentrations of Zn (Fig. 39, 67) and

various other elements precedes the isotopic event by 5 cm, indicating the existance of an oxigenated surface layer of 5 cm thickness during the Termination IA phase when Corg content was low (Fig. 21). The intensity of northwesterlies from Arabia increased at that time (Fig. 69), representing the begin of a deglacial maximum in dust flux to the Arabian Sea during Termination Ia (see below). Accordingly, event E0 should have occurred in the atmospheric circulation of the summer and the winter season, and was probably synchronous with a change in the water mass structure of the Arabian Sea surface waters.

The oxygen content of deep-water in the western Arabian Sea increased rapidly during E0, based on the $\delta^{13}C$ of *C. wuellerstorfi to -0.3‰,* together with a decrease of S and Mo, and the associated factor F4, Figs. 28, 47, 61, 66).

Termination Ia: 18,500-16,000 cal-yrBP (15,000-13,000 ^{14}C-yrBP)

A large number of elements are strongly depleted between 157.5 and 127.5 cm depth (e.g. Ba, Zn, HREE, Figs. 30, 39, 52). Thus, the intensity of the southwest monsoon in the ground level dropped to an outstanding minimum during the Termination Ia, indicating an extremely weak summer circulation over the Arabian Sea (Fig. 67). In contrast Mg content was high during this interval which reflects increased contributions from northwesterly winds from Arabia (Fig. 69). A synchronous minimum of CaCO3 content shows that accumulation rates of clastic sediments also reached a maximum, because the $CaCO_3$ percent value was found to monitor the dilution with lithic mass (C.1. Fig. 17). A maximum of dust discharge from Arabia should reflect most arid conditions on the continent, because modern large-scale dust outbreaks, like the one on 22-26 June 1979 (Fig. 5) occur preferentially during years of extreme drougth in the region (Wolter, 1987).

These hyperarid conditions during Termination Ia have been already mapped by lake level lowstands in Arabia and east Africa, which indicated that 15,000-13,000 ^{14}C-yrBP was the most arid time in the region (McClure, 1976; Roberts & Wright, 1987; Street & Grove, 1979; Street-Perrott et al., 1990). Termination Ia is also characterized by a maximum in the abundance of foraminifera of the tropical factor, lowest SST during summer, and enhanced preservation of planktonic foraminifera (Schulz, 1994). Accordingly, it can be expected that open ocean conditions and almost no upwelling characterized the western Arabian Sea at core location 74KL during the Termination Ia. This climatic extreme occurred during the time of the north Atlantic Heinrich layer H1. This, and other teleconnections between the North Atlantic climate and the monsoon climate are evaluated in chapter D.5.

The events E1 (visible only in the dolomite record) and event E2 (visible only in the $\delta^{18}O$ record) both occurred within Termination Ia.

The end of Termination Ia (event E3): 16,000 cal-yrBP (13,000 ^{14}C cal-yrBP)

Starting at 132 cm, and being accelerated at 127.5 cm Termination Ia found an end during event E3 (Fig. 12) when upwelling fertility increased in the western Arabian Sea (Fig. 67) and also in the Gulf of Oman (see Ba record of KS8, Appendix 3). The dust discharge from Arabia decreased (see Mg content, Fig. 69, and $CaCO_3$ content, Fig. 17), which reflects more humid conditions on that subcontinent. The northeast monsoon, however, remained at the level of the Termination Ia stage and was not affected by event E3. Accordingly, event E3 must have been a summer phenomenon, in contrast to event EO which had affected all seasons.

An increase of amplitude in the variability of most trace elements is found after event E3, see for example Zr, REE, Zn, Cu, probably best documented in the Ga record (Fig. 40). Accordingly, the onset of high frequency, rythmic climate variations during event E3 must be regarded as a signature of variability in the southwest monsoon strength (further discussion in D.6.).

The event E3 is also documented in the $\delta^{18}O$ and carbonate record of sediment core KS8 in the Gulf of Oman (Fig. 14), where pyrite formation (indicating reduced bottom water ventilation), ceased completely during event E3 (Appendix 3). Thus, event E3 is not only pertinent to the wind tracks over the western Arabian Sea, but is documented in the atmospheric circulation, the surface water structure and in the chemistry of the deep ocean.

Bölling, Alleröd Interstadial

Only the carbonate content (being characteristic of the Arabian aridity) shows the full transition from the glacial level towards the Holocene level during event E3. The intensity of the southwest monsoon, northwesterlies, and northeast monsoon, however, remained on a level being intermediate between the Termination Ia and Holocene values (Figs. 67-70).

Younger Dryas: 11,600-12,900 cal-yrBP (9900-11,200 ^{14}C-yrBP)

The duration of the Younger Dryas was best documented in the Greenland ice-cores, which revealed a precise chronology in the annually laminated ice of the GRIP and GISP cores (Alley et al., 1993). Accordingly, the Younger Dryas lasted for 1240 years from 11,640 to 12,900 cal-yrBP (corresponding to depth 95 to 107.5 cm in core 74KL), terminated by an abrupt onset and end that occurred within 25 years or shorter (Alley et al., 1993; Dansgaard et al., 1989).

Since the early days of the Swedish pollen records (review by Björck et al. (1992) increasing evidence was found that the Younger Dryas cold spell was not only restricted to northern Europe and the north Atlantic region (Peteet, 1992), but was

also felt in the climate of the southern hemisphere, the Pacific ocean and on the Asian continent. First evidence by Kudrass et al. (1991) had revealed its existence in the area of the Philippines, where the frequency/magnitude of spring or fall storms was increased during the Younger Dryas, discharging turbidites into the deep Zulu Sea. Further evidence on the existence of the Younger Dryas on land in Africa then came from a sharp drop in lake level and change in faunal assemblage of lake Victoria, indicating lower precipiation in east Africa during the Younger Dryas (Roberts et al., 1993).

In the following, we will explore the 74KL record to understand in more detail which parts of the seasonal monsoon system have reacted during the Younger Dryas. Fig. 73 shows the generalized evolution of the best geochemical tracers that have been defined in chapter D.2. to reconstruct the various parts of the monsoon system during the past. Accordingly, the variability of the summer southwest monsoon showed no response to the Younger Dryas cold spell (Fig. 67). Productivity of surface waters in the western Arabian Sea remained on the level as during the Bölling/Alleröd interstadial and did not change before the Younger Dryas to Preborial transition during event E4. The Younger Dryas is, however, clearly visible in the patterns of dust discharge from the Thar desert in northern India (Rb/Al, Fig. 70). The Younger Dryas cold spell during the northeast monsoon winter season lasted from 13,100 to 11,750 cal-yrBP (108.75 cm to 96.75 cm, i.e., for 1390 years, Fig. 73). The offset of these ages to the respective ages from the Greenland ice-core record (12,900 to 11,640 cal-yrBP) is within the dating precision of the ^{14}C calibration and annual ice layer counting. Most probably, the northeast monsoon followed the climate evolution on the northern hemisphere instantaneously, but leads and lags up to a century cannot be resolved with the dating techniques available at present.

Besides the no-response and full-response modes, two oscillatory modes can be observed in the variability of elements being transported in the Arabian northwesterlies (Fig. 73). A clean sinusoidal mode is pertinent to the dust discharge in the southern branch of the northwesterlies (Zr, Fig. 68). The amplitude of this oscillation starts to increase after event E3 at 127.5 cm depth, and completes a full cycle between 110 cm and 95 cm depth; accordingly, the period of this oscillation is 1450 years (compare D.6. where possible causes of this 1450-year periodicity are discussed). Most elements that are enriched in the mineral zircon and have its source in the southern branch of northwesterlies show this pure sinusoid (e.g. Ga, LREE, Figs. 40, 51).

A modified version of the oscillation mode is visible in the spiked oscillation mode (Fig. 73), which is typical for those lithic elements (Al, Fe, Cr, Li, Figs. 25, 35, 33,

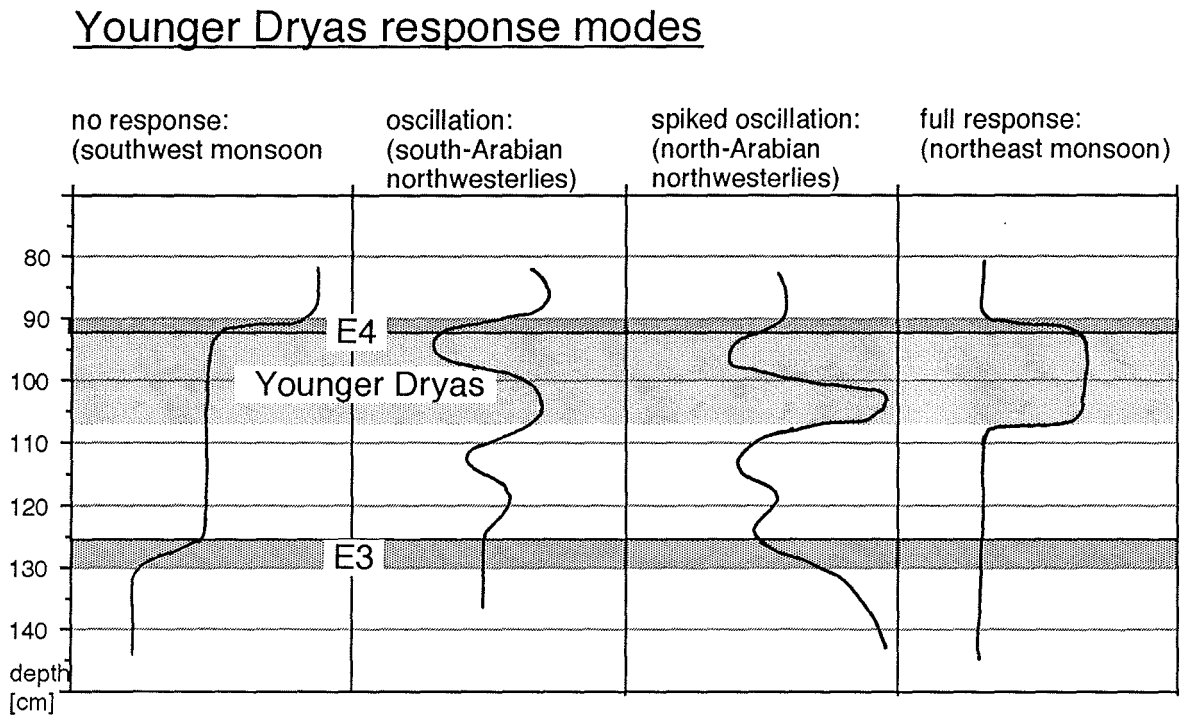

Figure 73 Younger Dryas response modes in sediment core74KL. The profiles are generalized blow-ups of the curves presented in Figs. 67-70.

20), which distribution patterns show a pronounced source area in the north off northern Arabia, Iran, and Pakistan. Profiles of these elements reveal in addition a principle shift from high glacial concentration values to low Holocene values. Superimposed on this trend are the 1450-year oscillation and the Younger Dryas excursion (Fig. 73). Apparently, dust transported in the northern branch of northwesterlies from the Persian Gulf region showed a mixed response, integrating all changes in the Arabian northwesterlies and changes in the northeast monsoon.

In summary, the seasonal parts of the monsoonal climate did not respond coherently to the Younger Dryas cold spell. The southwest monsoon did not respond at all, the northwesterlies continued in the 1450-year oscillation, which reached a minimum during the terminal phase of the Younger Dryas. Thus, it is only the northeast monsoon winter circulation that witnessed a prominent Younger Dryas climate anomaly. Accordingly, only the winter circulation of the seasonal monsoon system appears to be closely tied to the North Atlantic climate.

Younger Dryas to Preborial transition, event E4: 11,600 cal-yrBP (9900 ^{14}C-yrBP)

The intensity of dust transport by northeast monsoon winds declined sharply at the end of the Younger Dryas (Fig. 70). At the same time the largest abrupt change in

the $\delta^{18}O$ of surface waters (Fig. 12) had occurred, paralleled by the strongest geochemical gradient in 74KL, which affects all elements being enriched in ocean water (see D.1). Biogenic opal concentrations (Fig. 18) and *Globigerina bulloides* abundance (Schulz, 1994) also revealed its largest increase during this Younger Dryas to Preborial transition. All these parameters indicate that the largest intensification of the open ocean upwelling conditions at core location 74KL, driven by an increase of southwest monsoon intensity (Fig. 67), occurred during event E4. At this time the southwest monsoon and the northeast monsoon both could have reached a position and strength as being typical for the Holocene level.

The event is also reflected in core KS8, where $\delta^{18}O$ *G. ruber* (Fig. 14), grain size variations, Ba, Cd, (Appendix 3) reveal the major change during the same time interval, showing that event E4 was not a local phenomenon. Instead, the summer and winter climate over the Arabian Sea had changed drastically.

(E5)

$\delta^{18}O$ event E5 occurred during the begin of the Early Holocene interval of maximum northward propagation of the southwest monsoon (see below), and is associated with an increase of the low level southwest monsoon and upwelling fertility in the western Arabian Sea (Fig. 67).

The Early Holocene interval of maximum southwest monsoon intensity, 9900-8600 cal-yrBP, (9200-7850 ^{14}C-yrBP)

An interval of an extreme climatic state could be recorded by the total absence of dolomite dust input from 9900 - 8600 cal-yrBP (85-70cm depth). The distribution pattern of dolomite had been shown to reflect the southeastern extent of spring and summer northwesterly winds from northern Arabia/Oman (Sirocko et al., 1991). In this case, the total absence of dolomite dust over the Arabian Sea during the early Holocene humid interval reveals that southwest monsoon winds had shifted so far north, that the northwesterlies from Oman no longer reached the core position 74KL. A similar pattern is also observed in the Gulf of Oman, where lithogenic carbonate was at a minimum (near 0%, Figs.14, 15) during the same time interval. Thus, it appears that the dolomite-rich northwesterly winds from the Persian Gulf area hardly reached the Arabian Sea at all, but were confined to the Arabian peninsula. An alternate explanation of the same observation could be that vegetation in the Gulf area was widespread during the early Holocene, and that northwesterlies still existed but did non erode any dust from the vegetation covered soils (W.L. Prell, pers. comm.).

Besides dolomite we observe several other elemtents that show extrema at the depth level of the Early Holocene humid phase. Biogenic opal concentrations reveal

a clear maximum, whereas Ni and Co contents show an even more drastic increase (Fig. 36, 37). Both elements can be regarded as having a large biogenically mediated component and the increase of Ni, Co and opal at the same time of the dolomite minimum cannot be interpreted as a simple dilution process, because other elements and $CaCO_3$, which should be a record of lithic dilution, do not react at this depth interval.

Other elements that are affected by this Early Holocene enrichment are Cu, Zn, whereas Ba and Cd are not affected at all. The major feature that Ni and Co have in common, is a frequent occurrence in ultrabasaltic rocks. If this should be the cause for the early Holocene enrichment, we wonder, why Cr, the third element extremely enriched in ultramafic rocks, does not follow the downcore variations of Ni and Co, especially because the distribution patterns of Ni and Cr are quite similar. No obvious answer can be found to this question and we will have to wait for the results of the JGOFS cruises that will provide detailed profiles of concentration of trace elements in the water column and in the pore water (Smith et al., 1991) . At this stage we only observe that all elements that are enriched at 85-70cm depth reveal spatial distribution patterns that show maxima in the outer upwelling regions off the Arabian coast, similar to opal. Accordingly, even if the chemical cause of the Co and Ni enrichment is not fully understood, it appears plausible to interpret the early Holocene maxima of these elements as a record of an extreme stage in the productivity patterns of the Arabian Sea.

The humidity on the continents encompassing the Arabian Sea has been mapped by lake level variations during this time interval (e.g., Gasse et al., 1990; Pachur & Hoelzmann, 1991; Roberts & Wright, 1987; Street & Grove, 1979; Street-Perrott et al., 1990). Accordingly, high lake levels during the early Holocene reached deep into the Sahara, Sudan, Arabia, Pakistan, northern India, and Tibet. This availability of water must not always be regarded as a direct tracer of monsoonal clouds, but once moisture is available on a continent, it migrates by repeated cycles of evaporation and precipitation over large distances. Furthermore, the local climate might responde to various factors controlling the water budget of aquifers. But still, judging from the synchronicity of the onset of strong southwest monsoon winds and heavy rainfall over East Africa at 11,450 cal-yrBP (9900 ^{14}C-yrBP), the moisture seems to be initially derived from monsoonal rains, stemming from the Indian Ocean.

The quasi established interpretation for the increased southwest monsoon strength at this time is a response to the maximum in July solar insolation that occurred in the tropics of the northern hemisphere at about this time (10,000 astronomical years ago at 15^{o}N, 10,400 astronomical years ago at 20^{o}N / 35^{o}N, (Loutre et al., 1992). Following the evidence from numerical model experiments, the

continental Heat Low was strongest during this early Holocene time and the track of the southwest monsoon and its associated pattern of precipitation were expected to have shifted to their northernmost position (Kutzbach & Guetter, 1986; Prell & Kutzbach, 1987).

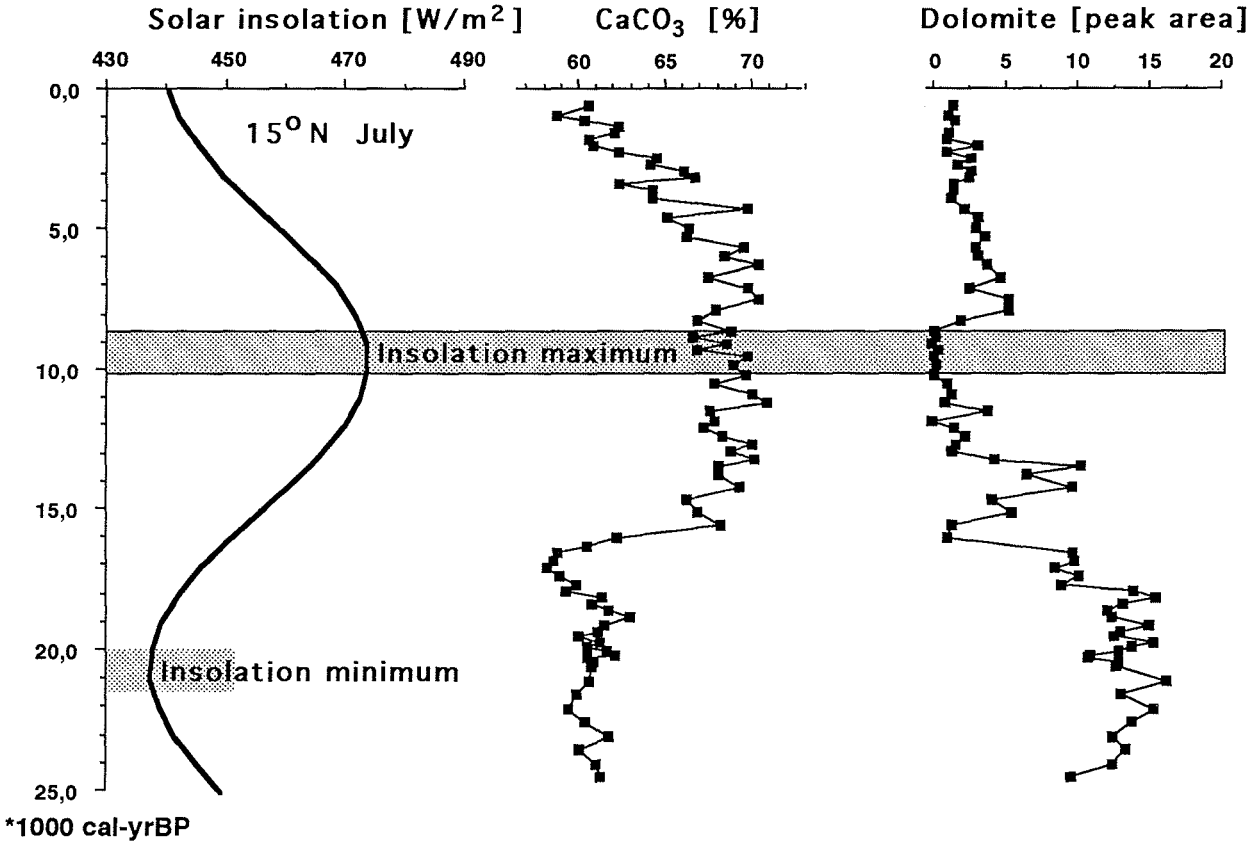

Figure 74. Solar insolation at 15°N, during July, $\delta^{18}O$ Globigerinoides ruber, $CaCO_3$ content and dolomite abundance in sediment core 74KL versus calendar year age.

Fig. 74 shows the July insolation at 15°N and the carbonate and dolomite record of 74KL plotted on a scale of adjusted ages (Tab. 1). The coincidence of the solar insolation maximum with the minimum in dolomite abundance (i.e maximum northward propagation of the southwest monsoon) suggests an immediate reaction of the summer monsoon to the solar insolation strength during the Holocene. The Asian heat low that attracts the southwest monsoon is centered today at 35°N. At this latitude, the insolation maximum had occurred several hundred years earlier (op.cit) and accordingly, a small lag could be possible in the response of southwest monsoon to its solar forcing.

Event E6, and the mid-Holocene interval of high southwest monsoon intensity, (E6) 8050 cal-yrBP (7500 ^{14}C-yrBP)

Following an interval of reduced southwest monsoon strengh between 8600 and 8050 cal-yrBP, a renewed increase in the intensity of the southwest monsoon occurred during event E6, leading to a maximum of southwest monsoon intensity that lasted until 5500 cal-yrBP (Fig. 67). The structure of event E6 and the following interval was similar to event E5 and the subsequent Early Holocene humid interval. However, the southwest monsoon did not migrate so far to the north as it probably had done during the Early Holcene (see above). Accordingly, the mid-Holocene interval of increased upwelling fertility and southwest monsoon strength should have had a smaller effect on the precipiation fields on land, even if the intensity of the southwest monsoon might have been strong over the ocean (maximum values of the Zn/Al record occurred during the mid-Holocene southwest monsoon maximum, Fig. 67). Still, this time interval is characterized by a second period of high lake levels in East Africa (Pachur & Hoelzmann, 1991; Street & Grove, 1979). The age of the interval coincides with the climate optimum at northern latitudes, and thus, the mid-Holocene maximum of southwest monsoon intensity might represent the subtropical equivalent to the Atlanticum of northern Europe.

Finally, the evolution of the southwest monsoon, the northeast monsoon, the northwesterlies, and the deep-water ventilation is summarized in Fig. 75, which presents an overview on the chronology of climate change in the monsoonal circulation as outlined above.

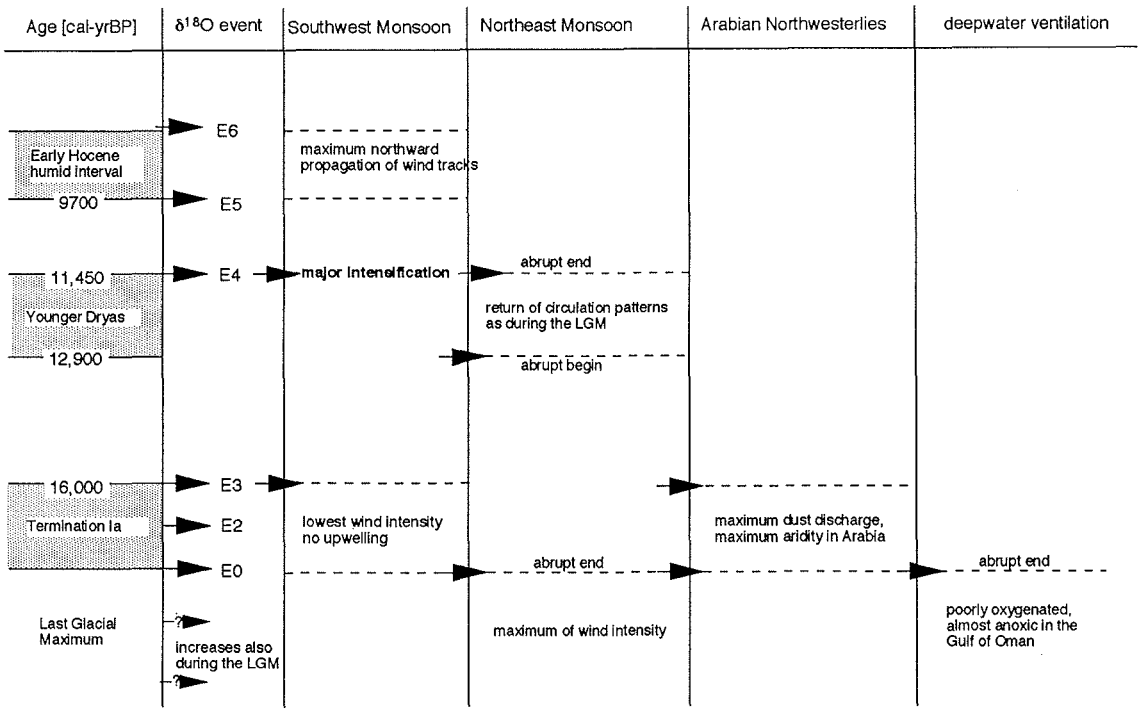

Figure 75. The evolution of the monsoonal climate during the last 25000 years..

D.4. Abrupt changes in monsoonal climate in the context of climatic change on the northern hemisphere

The climate related signals of variations in the geochemical properties of Arabian Sea sediments were evaluated in chapter D.1-D.4. In this chapter the evolution of the monsoonal climate is compared with the history of North Atlantic climate as recorded in the Greenland ice-cores. Large portions of the northern hemisphere are either influenced by Atlantic controlled winds and precipitation (the westwind drift), or by the monsoons (Fig. 1). Thus, one may expect that Europe, north Africa, Asia and the western Pacific have reacted simultanously and coherently, if the Westerlies and the monsoons have changed synchronously during events of abrupt climatic change.

Fig. 76 shows the local Greenland temperature record based on a $\delta^{18}O$ curve of snow (Johnsen et al., 1992)) and the methane content of the ice (Chappellaz et al., 1993). Atmospheric methane [CH_4] concentrations are expected to monitor the global CH_4 concentration, because this gas, which is mostly produced in tropical (i.e., monsoon controlled) wetlands, tundra soils and peat bogs, appears to be well mixed in the atmosphere of both hemispheres within a couple of years. Both the temperature and methane variations in the GRIP record reveal drastic changes at 11,640 cal-yrBP and 14,600 cal-yrBP, which took place within a couple of decades. These findings were exactly duplicated by the ice-core record of the GISP program (Alley et al., 1993; Grootes et al., 1993; Taylor et al., 1993a), hence establishing the abrupt nature of these events, first observed by Dansgaard et al., 1970).

The global methane concentrations show a first increase at 16,600 cal-yrBP, 2000 years prior to the increase in the local Greenland temperature ($\delta^{18}O$) record (Fig. 76). This offset by 2000 years can be in part explained by the depth of pore closure in the ice, which often occurs only at about 70 m depth and hampers the precise correlation of trace gas inclusions in the ice with the ice warve chronology (Oeschger et al., 1985). A time delay of 220-250 years has been observed in the near-surface section of the GISP2 ice-core, however, the time delay can be 2-3 times larger for the glacial section, because glacial snow accumulation rates where 2-3 times lower during the glacial (P. Grootes, pers. comm.). Accordingly, the maximum time shift between the change in atmospheric CH_4 and its record in the ice may amount up to 750 years and hence, the actual atmospheric CH_4 change may have occurred up to 750 years later only about 15,850 cal-yrBP whereas changes in the $\delta^{18}O$ composition of the ice reflect the temperature changes over Greenland instantaneously. This lead of the atmosperic trace gas record has to be considered, when correlating the CH_4 record of the Greenland ice with the evolution of the monsoonal climate as reconstructed from

marine sediment cores.

In Fig. 76 $CaCO_3$ serves as a record of Arabian aridity and Ba as a record of southwest monsoon intensity in the Arabian Sea.

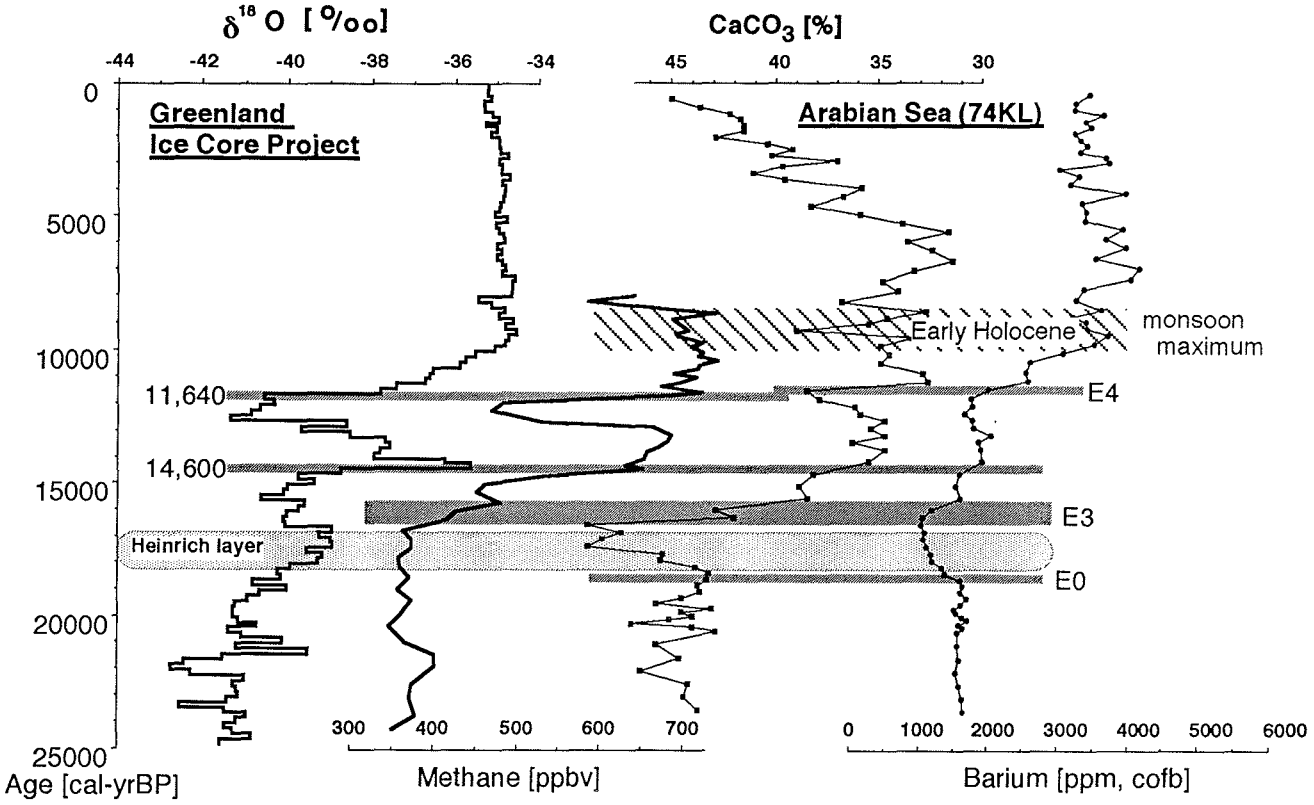

Figure 76. Age correlation between abrupt climatic changes in Greenland (GRIP ice-core) and in the monsoon region. Age (in calendar years) of events in ice-cores and $\delta^{18}O$ data are from Johnsen, et al. (1992), methane concentrations from Chappellaz, et al., (1993). Stippled bars indicate times of abrupt events in monsoonal climate in adjusted calendar years (Fig. 12). Age of Heinrich layer H1 after Bond, et al. (1992) and Maslin (1993). The hatched area represents the early Holocene minimum of dolomite content (Fig. 12).

The beginning of Termination Ia in the monsoonal climate at event E0 near 18,500 cal-yrBP is documented by a slight reduction in the intensity of southwest monsoon driven upwelling productivity (Ba) and a strong decrease of $CaCO_3$ content reflecting the onset of a short phase of maximum aridity in Arabia (Fig. 17). This timespan is paralleled by a slight temperature increase in the Greenland $\delta^{18}O$ record, but not by variations in the CH_4 profile. The subsequent interval of

maximum Arabian aridity (based on a minimum in carbonate content) between 18,000 and 16,500 cal-yrBP is paralleled by an event in the western and central Atlantic where massive iceberg discharge from the decay of the Laurentide ice sheet surged into the north Atlantic producing Heinrich layer 1 (Bond et al., 1992). Maslin (1993) dated the age of the Heinrich layer 1 in five different cores as ranging between 14,800-13,500 ^{14}C-yrBP, corresponding to 18,300 - 17,000 cal-yrBP. Weinelt (1993) and Sarnthein et al. (1994) reported of a further major iceberg surge in the Norwegian Sea originating from the Barents ice shelf and dating to 14,200-13,200 ^{14}C-yrBP, equal to 17,700-16,700 cal-yrBP. This age would put the meltwater event in the Barents Sea to the upper part of the depostition time of the central Atlantic Heinrich layer 1, showing that decay of the Fennoscandian ice sheet occurred at the same time as the decay of the Laurentian ice shield.

Physical links between these events of continental ice sheet decay and maximum aridity in the subtropical climate may be expected. One possible explanation is that the observed synchronicity may result from the weak temperature contrast between a cold mid-latitude and high-latitude North Atlantic during the time of Heinrich layer 1. This would reduce the pressure gradient over the entire Atlantic resulting in a less frequent formation of rain bearing disturbances in the westwind drift, which transported moisture into the Mediterranian, Israel and northern Arabia during the Last Glacial Maximum such as today. Any cessation of these Atlantic-derived cyclones and precipitation during the time of the deposition of the Atlantic Heinrich layer 1, should be reflected on the continents all along the Mediterranian. Accordingly, Syria and Mesopotamia, which receive their modern winter precipitation from the Mediterranian, and central south Arabia that receives summer precipitation from the southwest monsoon were probably not affected from any of these sources during Termination Ia interval when upwelling fertility was lowest in the ocean and aridity on land reached a maximum in the Arabian Sea area (chapter D.4).

The fast increase of carbonate content during event E3 is interpreted as reflecting a reduction of dust flux from Arabia (Fig. 17) and an increase in humidity on the peninsula. This increase started 16,500 cal-yrBP, precisely synchronous with the increase in methane concentrations in the GRIP ice-core record (Fig. 76). Accordingly, the increase in atmospheric methane at 16,500 cal-yrBP could be indeed attributed to a formation of wetlands subsequent to event E3 in the subtropical belt of monsoon-controlled climate (compare Fig. 1).

The local Greenland temperature witnessed its first major rise up to a Holocene level about 2000 years later during a rapid event at 14,600 cal-yrBP (the Bölling) (Fig. 76). This event is more subordinate in the monsoon record at core

74KL, even if the $CaCO_3$ and Ba curves suggest slight further increase of both upwelling fertility in the Arabian Sea and humidity in Arabia.

The intensity of the southwesterly summer monsoon winds as reconstructed from the upwelling history in the Arabian Sea (Zn/Al (Fig. 67) or Ba (Fig. 76)) had its major increase during event E4, at the end of the Younger Dryas (11,640 cal-yrBP), synchronous with a major climatic amelioration in the north Atlantic region and Europe. This age marks the onset of a monsoonal intensity typical of the Holocene (chapter D.4.). It could, however, be that the Arabian Sea event E4 lags the North Atlantic Younger Dryas to Preborial transition by about 150 years, an amount within the error margins of chronology[1] and being based on a 250 year sampling resolution in core 74KL. The highest methane content in the ice-cores is found during the early Holocene (i.e., during the time when dolomite content is lowest in core 74KL, Fig. 12), representing the maximum northward propagation of southwest monsoon wind tracks and precipitation (Sirocko, et al., 1993).

In summary, the almost parallel evolution of the monsoon and the Greenland climate during several events suggest a closely tied physical link between the evolution of North Atlantic oceanography and climate and the monsoons during the last deglacial.

---

[1] An error of +- 150 for the analytical precision of C14 analysis; +- 500 year for the adjustment to calendar years (this error is particularly large in the range of "C14-plateaus" such as found near the end of the Younger Dryas (Bard et al., 1990), (Lotter, 1991), (Becker et al., 1991); several hundred years for the age of surface water (assumed to be 400 years old, Tab. 1), but the age of modern surface waters in the Arabian Sea can reach 800 years in fresh upwelling cells (Uerpmann, 1991). Thus, in theory, the sum of all possible dating errors encountered could add up to as much as 1000 years.

D.5. High-frequency periodicities in the monsoonal climate

Time series analysis on sediment records covering the Quaternary and Tertiary have shown that, on Milankovitch time scales, the monsoon system responds primarily to the precessional cycle of solar radiation (Clemens et al., 1991), a summary of papers in Prell & Niitsuma (1991). There is, however, some discussion on the power of further periodicities, for example the 40,000 year periodicity (Bloemendal & deMenocal, 1989; Prell & van Campo, 1986; Zahn & Pedersen, 1991), moreover on a 100,000 component in the upwelling records from the Oman coast (Anderson & Prell, 1993), being in phase with global ice volume. Accordingly, the Pleistocene variability of monsoons generally follows the strength of solar insolation at low latitudes, in addition it shows some response to a forcing mechanism from the north.

Published time series and spectra on sub-Milancovitch scales from high resolution deep-sea cores in the northern Indian Ocean are rare, such as generally from the whole ocean, and do not cover periods below 2300 years (Pestiaux et al., 1987). Some periodicities reported at 10,200; 4600, 2300 years were explained as combination tones of the orbital precessional and obliquity cycles, thus, representing an internal, but non-linear response of the monsoon system to solar forcing. The time series analyzed in this chapter are the first that reveal periodicities between 2300 years and 900 years in the monsoon region of southern Asia and east Africa.

In previous chapters we have shown that the last glacial to interglacial transition of the $\delta^{18}O$ signal occurred in five distinct steps, with various events being synchronous with events of North Atlantic climate change. When converted into a calendar year time scale we detected a possibly stable time-related pattern in the succession of these events, more precisely, the intervals between events E5-E6, E4-E5, and E1-E3 are constrained to about 1700 years (Sirocko et al., 1993). In search of possible reasons of the 1700 year recurrence period, we now test if the step function of 1700 years is a component of the spectra of periodic variations in core 74KL. Spectral analysis was done using the SPECMAP programs of lagged correlation spectral analysis (Imbrie et al., 1984). To test the statistical stability of the spectra we designed experiments with (i) alternative age models, (ii) spectra on the analytical error of the proxy-data, and (iii) spectra in the depth domain. The average sampling interval of 250-300 years enables us to define periodicities above 900 years, the lowest age of 24,000 cal-yrBP in core 74KL sets the largest periodicity that can be calculated with significance to about 8000 years.

Alternative age models

Adjusted calendar ages can be calculated for ^{14}C-ages from 0 - 10,500 ^{14}C-yrs ago (Becker et al., 1991; Stuiver et al., 1991). For ^{14}C-ages > 10,500 ^{14}C-yrBP there is yet no general agreement on an adjustment, although U/Th dates outline the history of principle changes in the activity of atmospheric ^{14}C (Bard et al., 1990), confirmed by ice warve counts of the Greenland ice-cores (Johnsen et al., 1992). Despite the preliminary nature of any age adjustment model we have to take the risk to convert ^{14}C years into calendar years in order to document time-dependent processes in core 74KL properly. Based on the dates and adjustment scheme as outlined in Tab. 1. we assigned each sample a linearly interpolated age. The first spectra of dolomite content were calculated using both the original ^{14}C stratigraphy and converted calendar-years (Fig. 77). The ^{14}C-time series shows weak periodic variations of dolomite abundance in the silt fraction at 2344, 1415 and 987 years, whereas the calendar-year time series of the same data reveals a clear 1450-year periodicity. The calendar-year adjusted spectrum must be regarded as being more reliable, because the ^{14}C chronology is known to comprise at least two plateaus of constant atmospheric ^{14}C activity at 10,000 ^{14}C-yrBP and 12,700 ^{14}C-yrBP (Lotter, 1991).

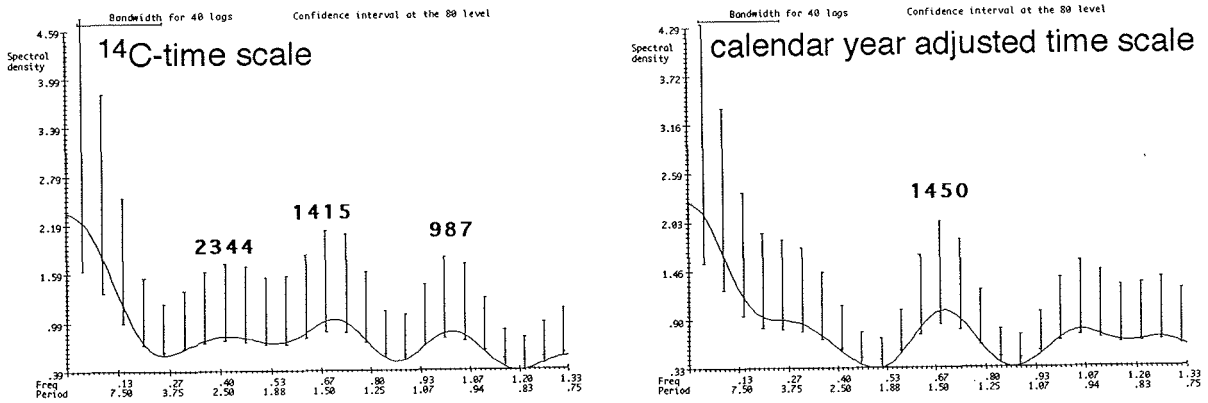

Figure 77. Spectra of dolomite abundance in the silt fraction, core 74KL, prewhitened to a level of 0.8, using different age models (a) original ^{14}C stratigraphy, (b) adjusted ^{14}C ages (Tab. 1).

Pestiaux et al. (1987) also found a 2300-year period in an unadjusted $\delta^{18}O$ record of *G.ruber* in the Arabian Sea. He explained the period as a combination

tone from the major orbital cycles of precession and obliquity. The vaning of the weak 2300 year period in the spectrum on our U/Th-adjusted age model raises the question if any 2300-year period exists at all. On the other hand, weak periodicities near to 2300 years are also observed in the HREE, Hf and Tl records of core 74KL (not shown). If a 2300-year period exists in the monsoonal climate, it may be associated with the waxing and waning of northern ice-sheets such as observed during the Holocene (Denton & Karlén, 1973). The period also appears in the $\delta^{18}O$ record of the Greenland ice-cores over the last glacial and interglacial cycle.

Frequency spectra on the analytical error of the data

The ICP-MS method is a precise analytical technique, showing relative errors between 2% and 7% (Tab. 4). These low errors still introduce noise into the time series. This noise was analyzed by spectral analysis of the relative error values of ICP-MS analysis for several elements. In all cases we could not observe any periodicities at all. Thus, the periodicities in the chemical data ought to reflect the genuine variability of the natural sedimentation regime, even if the amplitude of the periodic variations lies within the relative error of the ICP-MS analytical precision.

A proof for the significance of the major periods is the finding of the same periods in records from different analytical techniques; the 1785-year period is found in the *G.bulloides* abundance (foraminifera counts) and Cd content (AAS); the 1450-year period occurs in the Mg record (ICP), REE (ICP-MS), carbonate and dolomite records.

Frequency spectra in the depth domain

To test a potential influence of diagenetic, depth-dependent processes on the downcore variations of trace elements we ran spectral analysis on several element records versus core depth. Elements that are remobilized by diagenesis, e.g. Mn, do not show any periodic behaviour in the depth domain. Only Cs, an element of lithic origin, similar to Rb, shows a weak periodicity in a 10 cm band. This signal, however, can be explained by the Cs time series itself, which has high power at 950 years, compare Rb (Fig. 78 g). This period translates into a 10 cm depth interval at an average sedimentation rate near 10 cm/1000 yrs, as found in core 74KL (Tab. 1).

Frequency spectra of the seasonal components of the monsoons

Zn/Al, the best geochemical tracer element of surface water productivity does not show any significant periodicity at all (Fig. 78 a), possibly, because the major abrupt changes in the Zn/Al time series are so dominating (Fig. 67) that they

suppress the statistical significance of higher frequencies. In contrast, the Cd content (a tracer of nutrients) and the abundance of *G.bulloides* reveal distinct periodicities at 1785 years and near 1150 years (Fig. 78 b, c), which are attributed to variations in surface water productivity of the western Arabian Sea; *G.bulloides* is regarded as the most reliable upwelling indicator in Arabian Sea sediments (Prell et al., 1980). To our surprise, the 1785-year period is developed also in the variability of winter SST and the variations of the Subpolar and Polar Factor of foraminifera abundance (Schulz, Sirocko & Prell, unpubl. results). The $\delta^{18}O$ record of *G.ruber* exhibits no statistically significant periodicity, because the staircase-like shape of the curve cannot be accounted for by the prewhitening constant of 0.8 that we applied for all records of core 74KL. Nevertheless, the time interval between the abrupt $\delta^{18}O$ events E4-E5 amounts to 1750 years, and the time span between events E5 and E6 to 1650 years (see the 74KL Cd profile for a graphic view of the relations between $\delta^{18}O$ events and Cd spikes). In summary, it turns out that the 1785-year period exerts a dominating control on all records related to the surface water composition at core location 74KL.

The variability of Zr content that represents dust discharge in the southern branch of Arabian northwesterlies shows a broad peak between 1800 and 1300 years, centered near 1550 years (Fig. 78 d). The southern branch of the northwesterlies merges with the jet core of the southwest monsoon over the ocean (Fig. 5, 7); thus the variablity of Zr may incorporate a response signal from both the 1785-year period of the southwest monsoon (see above) and the 1450-year of the northwesterlies (see below). This could explain an average 1550 year period as being found in the spectral variability of Zr.

The variability of Mg content, which reflects the changes in dust discharge by northwesterlies from north Arabia, shows an asymmetric peak near 1470 years (Fig. 78 e). The same, but more pronounced and symmetric periodicity is found at 1450 years in the Factor 2 of the REE data matrix (Fig. 78 f), a factor that can be related to the lithic fraction of the REE, which has most of its variance in the LREE that covary with Zr (Figs. 45, 51). The 1450-year period also occurs in the records of grain-size, dolomite, and $CaCO_3$ content of core 74KL (Figs. 19, 12, 17). Accordingly, the 1450-year period appears to dominate the history of dust discharge from Arabia.

Another pronounced period at 950 years is observed in various records of core 74KL (Fig. 78 d, g). This period is visible in the discharge of dust during summer (Zr), but being strongest in the variability of the winter, northeast monsoon circulation, reconstructed from the record of Rb/Al (Fig. 70).

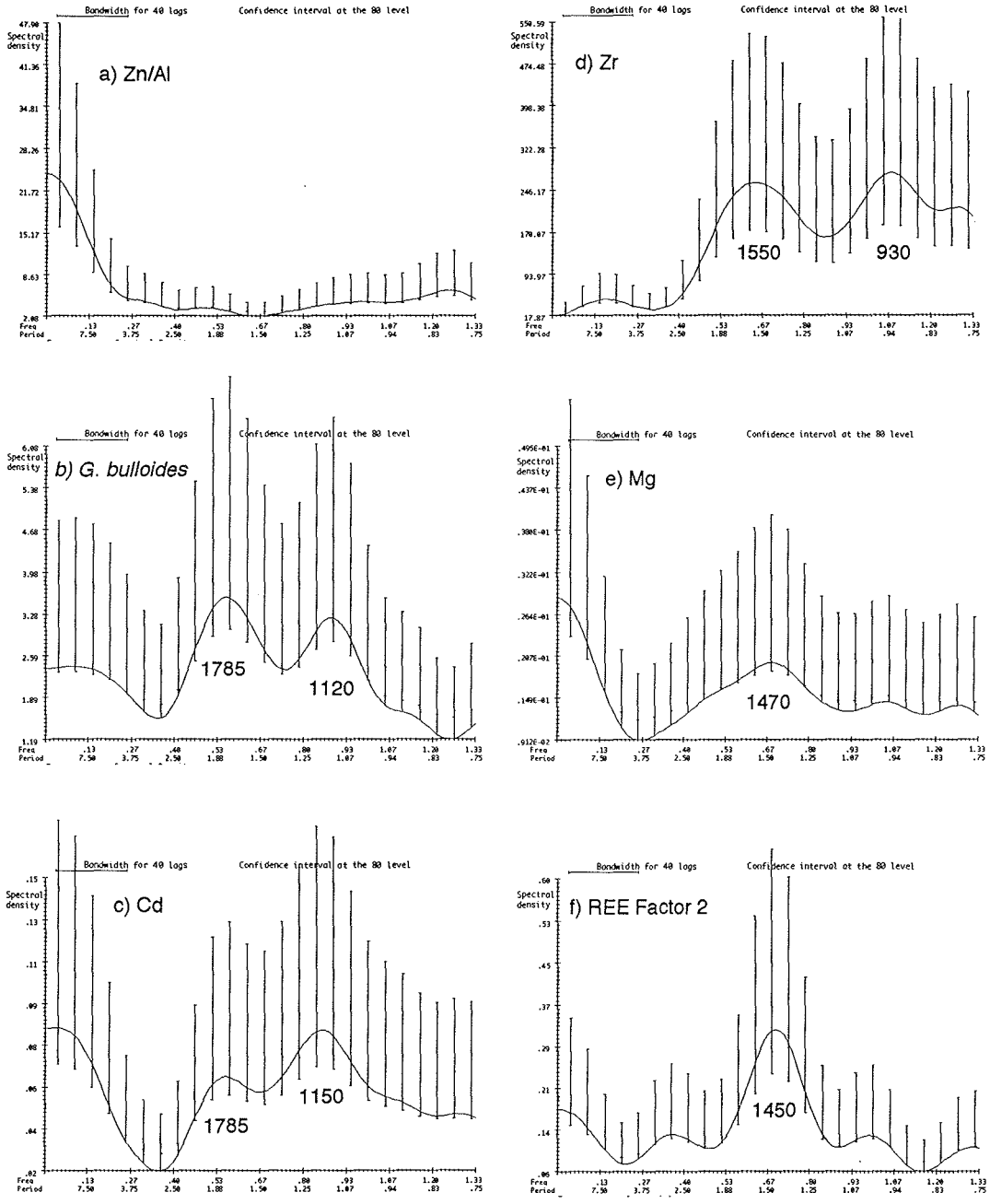

Figure 78. Prewhitened spectra (0.8 level) of geochemical tracers in sediment core 74KL. a) Zn/Al (southwest monsoon driven upwelling), b) Globigerina bulloides (upwelling), (c) Cd content (upwelled nutrients),(d) Zr content (South-Arabian northwesterlies), (e) Mg content (North-Arabian northwesterlies), (f) REE-Factor 2 (Arabian northwesterlies), (g) Rb/Al (northeast monsoon).

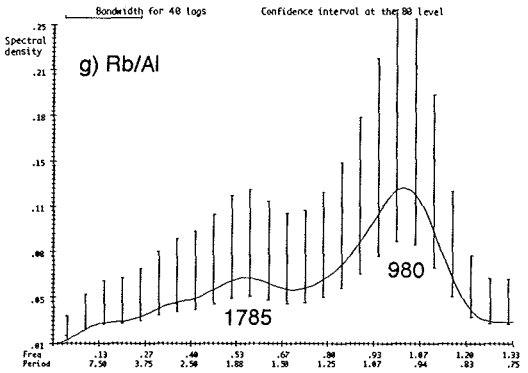

Figure 78. continued

Possible forcing mechanisms of the periodicities at 1785, 1450, 1120, and 950 years

The outlined periodicities have not been observed in geological records of the Indo-Arabian monsoonal climate before. Similar periodicities were, however, found in the U^k_{37} composition of organic matter of deep-sea sediments of the equatorial Atlantic off west Africa where SST variations during Termination II and III reveal periods at 1610-1800 years, 1150-1280 years, and 880-960 years. Accordingly, except for the 1450-year period, the other periodicities of the Asian monsoon climate are also affecting the African monsoonal climate. Thus, the climate variability at these periodicities is not a local process, but reflects climatic variations of the subtropics on a much larger, probably global, scale.

The forcing mechanisms for of all of these periodicites are still unknown. As a first step towards an evaluation of the forcings, we filtered the records at all major periodicities to obtain the variations of their amplitude. The amplitude of the variations in the 1785-year Cd record of surface water nutrients shows that this period became effective after event E4 (Fig. 79 a), that is during the Younger Dryas to Holocene transition. Respective filter series of the *G.bulloides* abundance shows the same pattern. The maximum in variability occurred at 10,000 cal-yrBP during the time of maximum solar insolation at subtropical northern latitudes (Fig. 74). Likewise, the 1150-year period of the Cd record of upwelled nutrients shows a strong increase in amplitude after event E4, and a maximum variability during the early Holocene (Fig. 79 b). Moreover, the filtered time series of the 1150 year period shows the first increase in amplitude after EO, which marks the beginning of the global deglaciation (see D.4).

The record of the Arabian northwesterlies (Mg) shows persistent variability at a 1450-year frequency band (Fig. 79 c). The amplitude was a little lower during glacial times, but increases during the termination to reach a maximum at 10,000 cal-yrBP. The amplitude of the Mg record sligthly decreases during the early Holocene, probably because dolomite, which contributes a large portion of Mg content of the sediment, was almost absent during this interval (Fig. 12). The envelope over the 1450-year amplitude variations reveals a curve near to a 23,000 year oscillation, with its maximum reflecting the July maximum of precession controlled solar insolation in the subtropics (Fig. 74).

The cause of the 1450-year period is not known, but because of the similarity of the envelope to the precession cycle, and because this frequency is a precise harmonic of the Earth´s precessional cycle (1450*16 = 23,200 years), it could be interpreted as an internal response of the precessional cycle. The effect of this cycle on the Quaternary variations in lithic fluxes to the sediments of the Arabian Sea had been demonstrated by Bloemendal & deMenocal (1989) and Clemens et al., (1991) and it does not seem unreasonable that internal responses in the climate system enhance flux rates also at harmonics of the major forcing frequency. In this case, however, the question remains, why this particular band is enhanced in the climate response, whereas the other harmonic tones of precession (i.e., at 2900, 5800, 11600 years) are not visible.

The 950-year period that characterizes the variations in atmospheric circulation is persistent throughout glacial and interglacial times (Fig. 79 d). The amplitude variations show maxima about every 6000 years. The 950-year period in the monsoonal climate might be linked to the gravity field of planets, for example to lunar cylcles, which were claimed to be visible in spectra of modern meteorological data on rainfall intensity in India (Campbell et al., 1983). The 950-year period is near to the largest period that can be calculated from a secular theory of the the long-term planetary motions (Loutre et al., 1992) and was found in the oscillations of ^{14}C activity in the atmosphere and tree rings (Becker et al., 1991; Stuiver et al., 1991). We feel confident that the period existed in the variability of the monsoon summer and winter circulation, because various spectra of faunal, sedimentological, isotope and chemical records in core 74KL reveal some power at frequencies near to 950 years, but any explanation of its forcing mechanism must be regarded as highly speculative at this time.

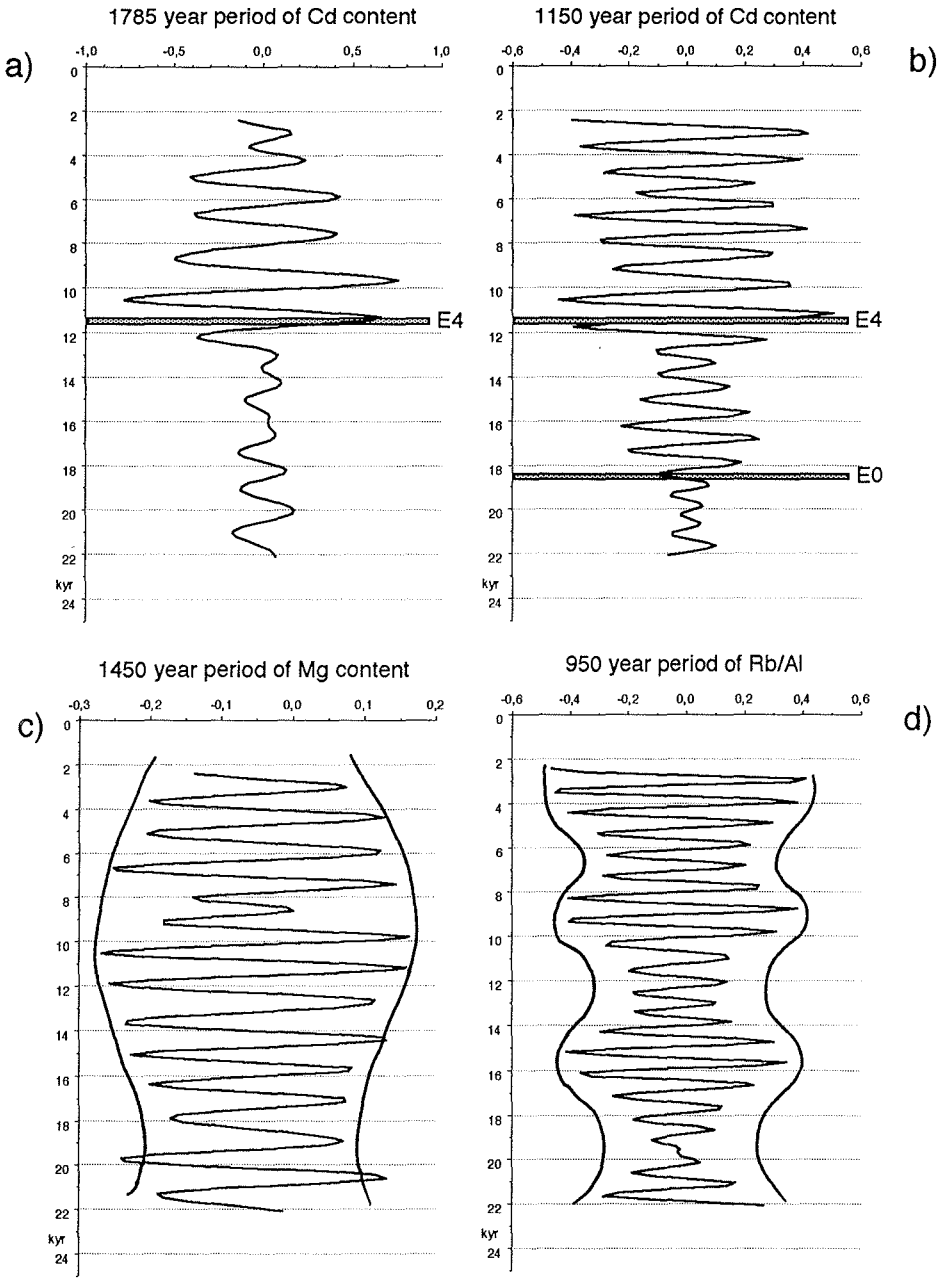

Figure 79. Sinusoids of filtered periods. (a) 1785-year period in the Cd record (surface water nutrient content) (b) 1150-year period in the Cd record, (c) 1450-year period in Mg (dust discharge by Arabian northwesterlies) record, (d) 950-year period in Rb/Al record (dust discharge by the northeast monsoon).

In general, the discussion on the underlying causes and physical forcing mechanisms of periods between 900 and 7000 years remains open. This work is only a first attempt to reconstruct the chronology of atmospheric and oceanographic change in the Indo-Arabian monsoon area on a century-scale; still, the following inferences may be drawn:

The $\delta^{18}O$ events have a 1785-year recurrence period in the Holocene section of core 74KL, starting after event E4 (i.e., after the Younger Dryas to Preborial transition). The same period is found in the abundance of *G.bulloides* and Cd content, which serve as tracers of surface water productivity and nutrients. The 1785-year period is not found prior to event E4. Thus, it represents a mechanism only linked to the southwest monsoon during the Holocene. Abrupt $\delta^{18}O$ variations that also occurred during the glacial and the early deglacial suggest that abrupt $\delta^{18}O$ events can occur independently from the periodic variations of southwest monsoon intensity.

The 1450-year period is dominating the dust discharge from Arabia during glacial and interglacial climatic stages. The amplitude of variability increases slightly during the maximum of the solar insolation intensity at 10,000 cal-yrBP in the subtropics of the northern hemisphere.

Both the 1785-year and the 1450-year period could represent internal harmonics of the Earth´s precessional cycle (1785 years * 13 = 23,205 and 1450 years * 16 = 23,200 years), thus, they could be interpreted as an internal response of the atmospheric circulation to the major precessional forcing period of the monsoons at 23,200 years.

D.6. Experiments with the GISS II Global Circulation Model on links between continental snow cover in Asia, monsoon controlled sedimentation in the Arabian Sea, and North Atlantic climate change

As shown in chapter D.4. the evolution of north Atlantic and monsoonal climates appears to be tied by a number of similarities during the last 25,000 years. For example the last "Heinrich layer 1" (Bond et al., 1992) corresponds to the time of maximum aridity in Arabia, and both the monsoonal and the Atlantic climates witness an extremely fast transition towards the Holocene at the end of the Younger Dryas. A largely synchronous climate evolution of the North Atlantic and the Indian monsoon region leads to the question if there are causal chains, that is about the primary climatic forcing and response systems. We could envision three major mechanisms to explain the synchronicity:

i) an increase in the export of latent and sensible heat by the summer southwest monsoon in combination with an increase of atmospheric moisture content (the most efficient greenhouse gas) heated the northern hemisphere and initialized decay of the continental ice sheets.

ii) the deglaciation of the Fennoscandian ice and surge of the Barents shelf ice (Sarnthein et al., 1992) and/or abrupt decay of the Laurentian ice sheets (Bond et al., 1992; MacAyeal, 1993a; MacAyeal, 1993b) led to large-scale changes in surface air pressure anomalies over the northern hemisphere land and ocean. These anomalies, in turn, correlate with the strength of the subsequent southwest monsoon in Asia (Raman & Maliekal, 1985).

iii) processes external to the North Atlantic and the monsoon area drive the climatic evolution of both regions. For example, "ENSO" events in the Pacific are known to affect climate on a global scale (Cane et al., 1986; Jacobs et al., 1994; Philander et al., 1992)

Which of these scenarios has the highest potential to explain the observed synchronicity can be tested with Numerical Global Circulation Models (GCM). These models are a powerful tool to synthesize climate stages of the past and to explore the sensitivity of the Earth's climate to key parameters of climate forcing (e.g.; Kutzbach & Guetter, 1986; Manabe & Broccoli, 1985; Manabe & Hahn, 1977; Rind, 1987; Joussaume, 1990). The long-term forcing mechanisms of changes in the monsoon system (i.e., solar insolation intensity and mountain uplift) have already been studied extensively (e.g., deMenocal & Rind, 1993; Prell & Kutzbach, 1987; Prell & Kutzbach, 1992; Ruddiman & Kutzbach, 1989); however, these gradual changes cannot explain the short-term variability of the monsoons.

Raymo et al. (1990) already tested the effect of the Arctic sea-ice cover on

short-term climate variability of the northern hemisphere, and found that climatic responses in Asia to changing sea-ice extent are apparent during winter. The response of the southwest monsoon during summer, however, was weak. Accordingly, it remains an open question, how the teleconnections between Atlantic climate and the Indian southwest monsoon might have worked. Changes in the center of the Asian Heat Low itself and their effect on the Atlantic climate have not been tested yet; thus, it is the objective of this chapter.

To simulate a decrease in the intensity of the southwest monsoon, we (David Rind and F.S.) used the GISS II GCM to test scenario i) by exploring the physical relationship between an increase in snow cover in central Asia, which is known to parallel/cause low southwest monsoon intensity (Barnett et al., 1989), and its associated teleconnections to the rest of the world during the Last Glacial Maximum.

The relation between Asian snow cover and the intensity of monsoonal rains was first suggested by Walker (1923), who analyzed the meteorological data of rainfall anomalies in India. The link was recently tested in a numerical model by Barnett et al. (1989), who showed that snow cover in Asia exaggerates a dominating control on the strength and seasonal duration of the Indian monsoon. Thus, snow depth, the extent of snow fields and the seasonal duration between fall and melting of snow are the most likely parameters to explain the interannual variability of the monsoon intensity today (Lautenschlager & Santer, 1991), but possibly also the short-term variations of the past.

The model

The model used in the experiment is the GISS II GCM, as described by Hansen et al., (1983), using a $4^{o}x5^{o}$ grid resolution. The same model was used by Raymo et al., (1990), see above, and by deMenocal & Rind (1993) for a survey of the sensitivity of the Asian and African climate to long term changes in mountain uplift, north Atlantic SST variations, and continental ice sheet extent and elevation. The model has nine atmospheric layers, and is capable of reproducing the major modern atmospheric circulation patterns (Hansen et al., 1983). There are several discrepancies in the modelled and real circulation patterns of the monsoon winter circulation. The pressure gradient between the Asian continent and Indian ocean is about 30% too strong, which results in a slight southward displacement of the northeast monsoon wind trajectories over Pakistan and Iran. In addition, the model produces too much winter precipitation over Asia (4mm/day), and summer southwest monsoon winds do not penetrate sufficiently into the Himlayas. Accordingly, the model output has uncertainties, especially in the region that we are most interested in. As a consequence, we do not discuss the values of our model

calculations, but only present anomaly maps to outline the global patterns of response to large albedo changes on the Asian continent.

Scenario

By contrast to the model as used by deMenocal & Rind (1993), we changed two parameters in our experiment:

i) Following recent evidence the Last Glacial Maximum (LGM) did not occur at 18,000 cal-yrBP, but at 21,500 cal-yrBP (Bard et al., 1990). Hence, the sea surface temperature maps of CLIMAP (1981), which we use as boundary condition, represent the ocean surface at 21,500 calendar yrBP, and the insolation patterns used in the model were taken from that time.

ii) We included a permanent snow field of 1m thickness that covers all grid cells in central Asia where the average altitude exceeds 1000 m in the $4^{o}x5^{o}$ topography input file of the model (Fig. 80).

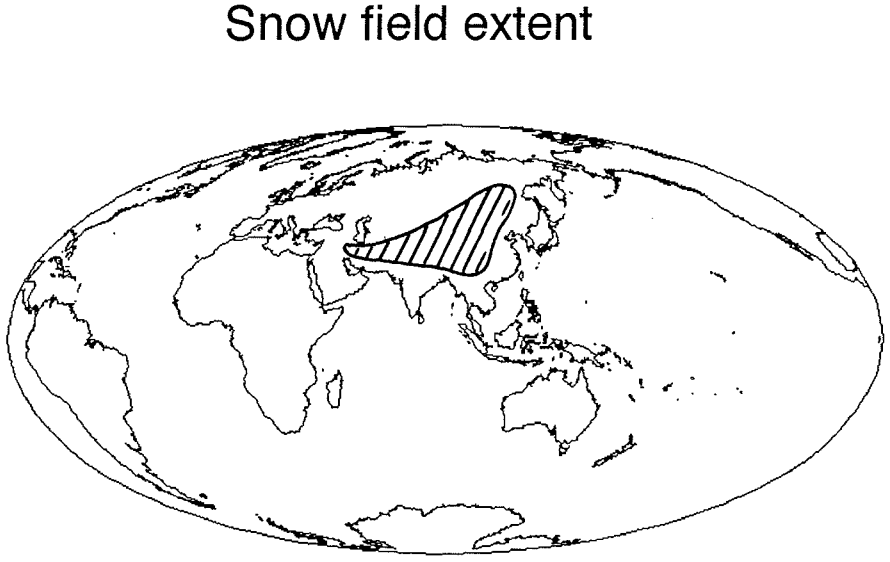

Figure 80. Average elevations in central Asia exceeding1000 m altitude in $4^{o}*5^{o}$ grid boxes. For these grid boxes an artificial one-meter-thick snowfield was prescribed in the boundary conditions of the model.

The extent of a permanent glacial snow field shown in Fig. 80 is certainly unrealistic, even if pollen profiles (Van Zeist & Woldring, 1978) indicate a cold and damp winter and a cold and moist summer in Turkey during the last glacial. A climatic regime similar to the near East can be expected to extend over Iran, north

Pakistan, and the Caspian Sea area all the way to the steppes and loess plateau of central China, compare COHMAP (1993). Field evidence for lowered snowlines by as much as 1200 m was found in Iran (Kuhle, 1974) and around the Tibetan plateau (Kuhle, 1987). This does not imply that we regard the inland ice sheet hypothesis as realistic, but Kuhle´s observation of drastically lowered snowline seems to be valid (F. Lehmkuhl, J. Hövermann, B. Frenzel, G. Kukla, pers.comm.). Our scenario of the permanent snow field will be particularily unrealistic for the summer months, and not comparable to the real world, but still the mechanisms and patterns of the response should allow inferences on those effects that are connected to albedo changes in Asia.

Global climatic effects resulting from increased snow cover in Asia

The effect of an additional snow cover introduced into the boundary conditions is clearly seen in the fields of pressure, temperature and precipitation anomalies all over the world (Figs. 81-83). Responses on land outside of the immediate vicinity of the snow field are weak, except little effects in Europe and in North America, mainly during spring. As a result of the permanent Asian snow field, we observe a pressure-increase over the snow field and its immediate vicinity throughout all months of the year; during winter, this anomaly stretches even into the Arctic. The pressure increase is compensated by a continous lowering of surface air pressure over the west Pacific. The main effect from the increased pressure gradient between Asia and the Pacific is an intensification of cold winds from mainland Asia towards the ocean, cooling the ocean surface water in the western north Pacific dramatically (Fig. 82). The eastern north Pacific, however, receives additional heat during spring and summer, thus increasing also the temperature gradient within this ocean. This result is paralled by severe drought in southern China all year round, because moisture bearing southwest monsoon winds do not reach the continent anymore (Fig. 83). The Atlantic region shows only a little warming during summer as a responses to the Asian snow field. Another teleconnection is observed in the Antarctic where surface air pressure is lowered during winter.

Another effect of the increase in surface air pressure over Asia is a cold anomaly that develops over the northern Indian Ocean during spring and summer, because of a reduction of heat transported by southwest monsoon winds, which are depressed to equatorial latitudes and do not penetrate the Asian continent any more (Fig. 82). As a result the monsoonal winds loose their moisture already over the ocean, leading to a large positive precipitation anomaly in equatorial latitudes of the Indian Ocean during summer.

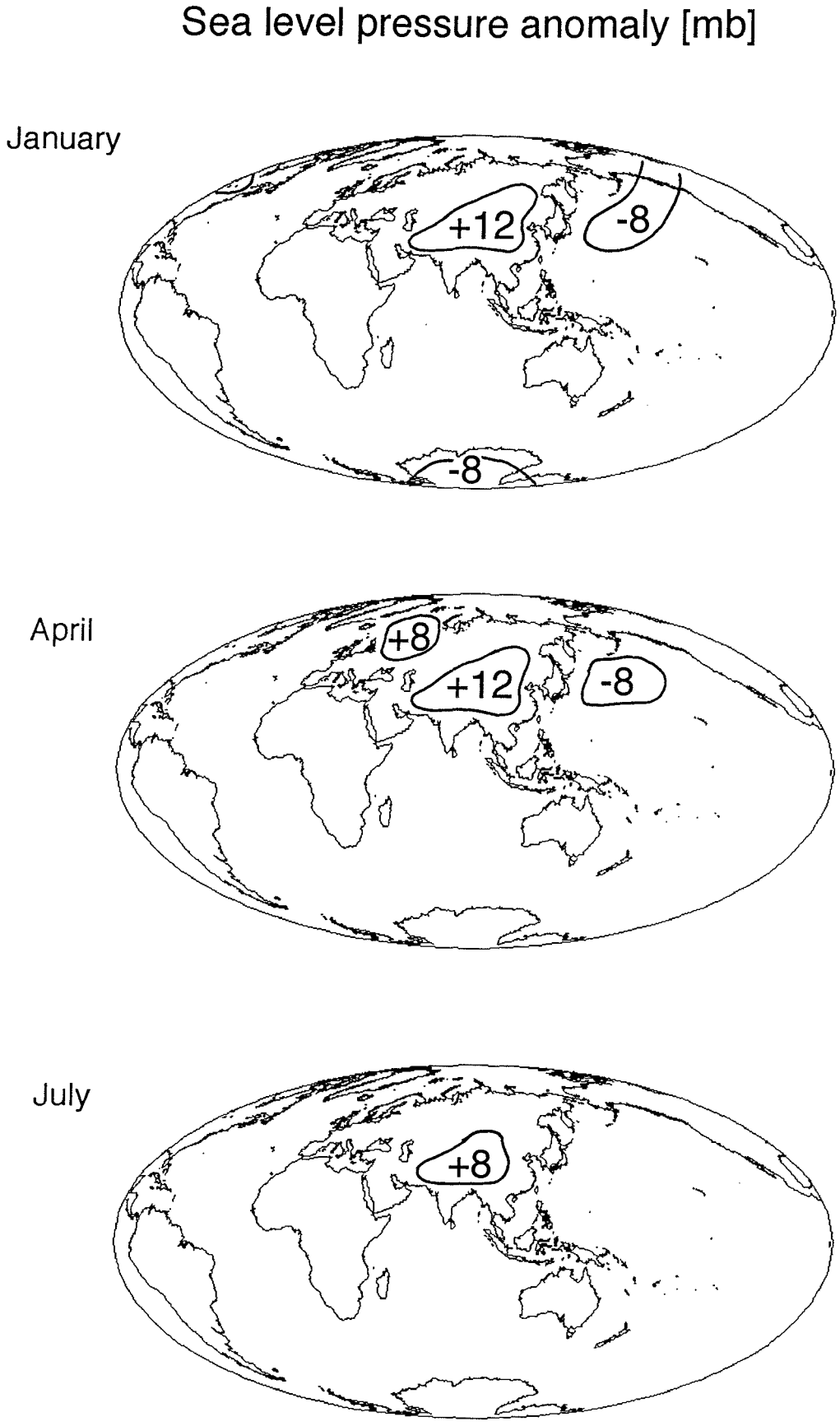

Figure. 81 Sea level pressure [mb] anomaly at 21,500 cal-yrBP (experiment minus control) for January, April and July.

In total, only little effects of the Asian snow field can be found all around the world, except in the Pacific, which is obviously closely coupled to the climatic conditions on land in Asia.

Comparison to the geological record

Some features in the patterns outlined above, agree well with the geological record of Chinese loess and North Pacific deep-sea sediments, indicating that albedo changes in Asia during the last glacial could have been indeed larger than prescribed by the CLIMAP (1981) reconstructions.

The dominating climatic impact of the increased snow cover in Asia will be an intensification and seasonal extent of the winter high pressure cell over Asia. This leads to a low pressure system in the west Pacific, thus, cooling the western part and heating the eastern part of that ocean. It cannot be evaluated if the cooling of the western part of the Pacific would be strong enough to trigger deep water or intermediate water formation, because the GISS II GCM is a strictly atmospheric model, and SST are prescribed by CLIMAP (1981) data. Deep-sea cores from the Pacific had indicated the possibility of glacial deepwater formation in the north Pacific (Dean et al., 1989; Duplessy et al., 1988; Lynch-Stieglitz & Fairbanks, 1994), but these findings are not consistent with the data/interpretation of Keigwin et al. (1992) and Zahn et al. (1991), who showed increased upwelling productivity in the area during that time. Our finding of strong regional contrasts of cooling in the northwestern and heating in the northeastern Pacific may explain this discrepency (Fig. 82).

The increased wind speeds over China and the North Pacific, in combination with the increase in Asian aridity, could also explain the increased glacial loess deposition in China that had occurred mainly during spring (G. Kukla, pers.comm.), which is the season when our model of increased snow cover is most realistic. The glacial long-distance transport of the fine grained fraction of this aerosol dust over the North Pacific should then also occur during spring.

So strong an intensification of winds over the northern Pacific was not shown in other GCM reconstructions of the glacial atmospheric circulation, even if all models that synthesized the climate of the last ice age agree on an intensification of wind strength over mainland China and the northwestern Pacific, already resulting from the changes of boundary conditions as reconstructed by CLIMAP(1981).

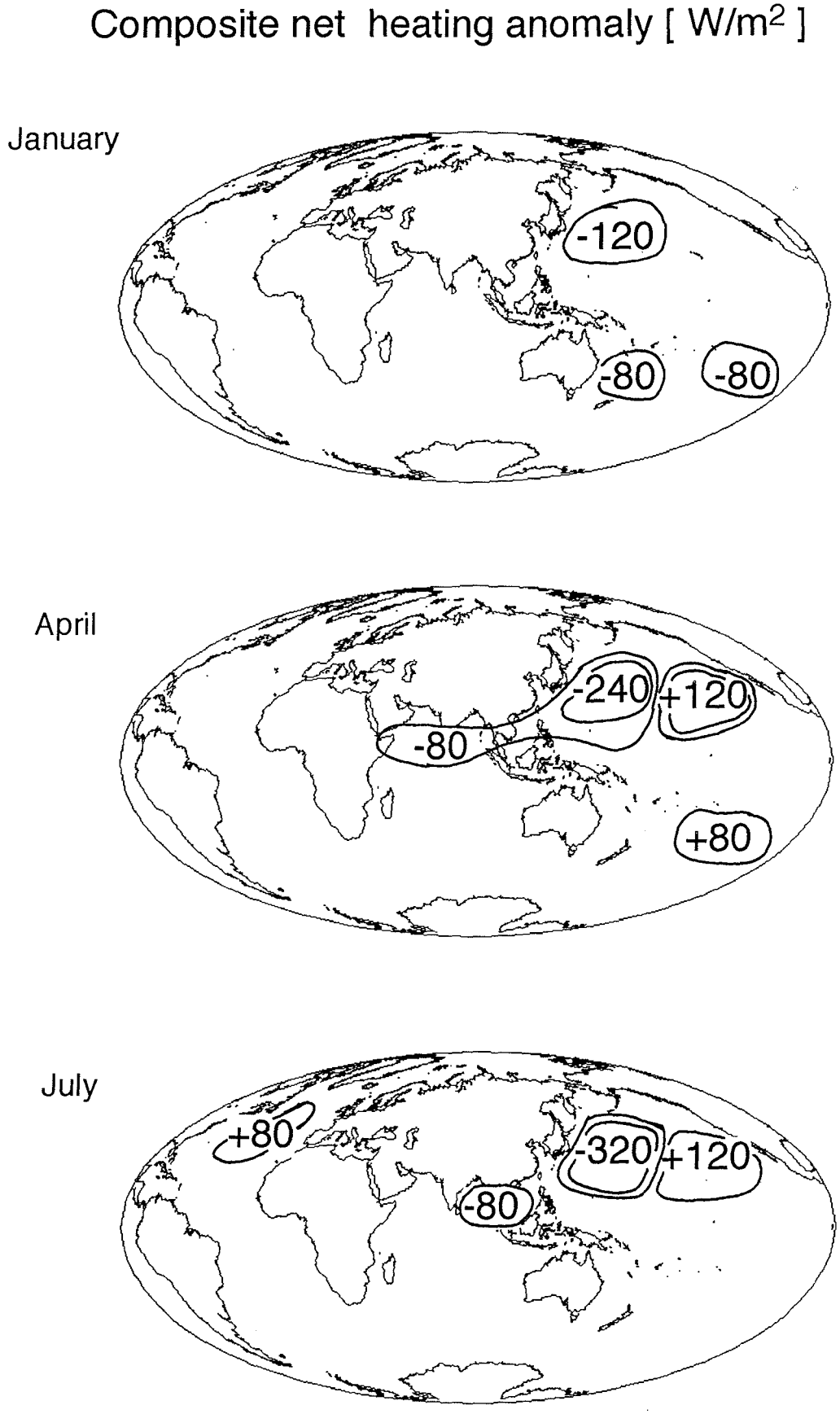

Figure 82. Composite net heating [W/m^2] anomaly at 21,500 cal-yrBP (experiment minus control) for January, April and July.

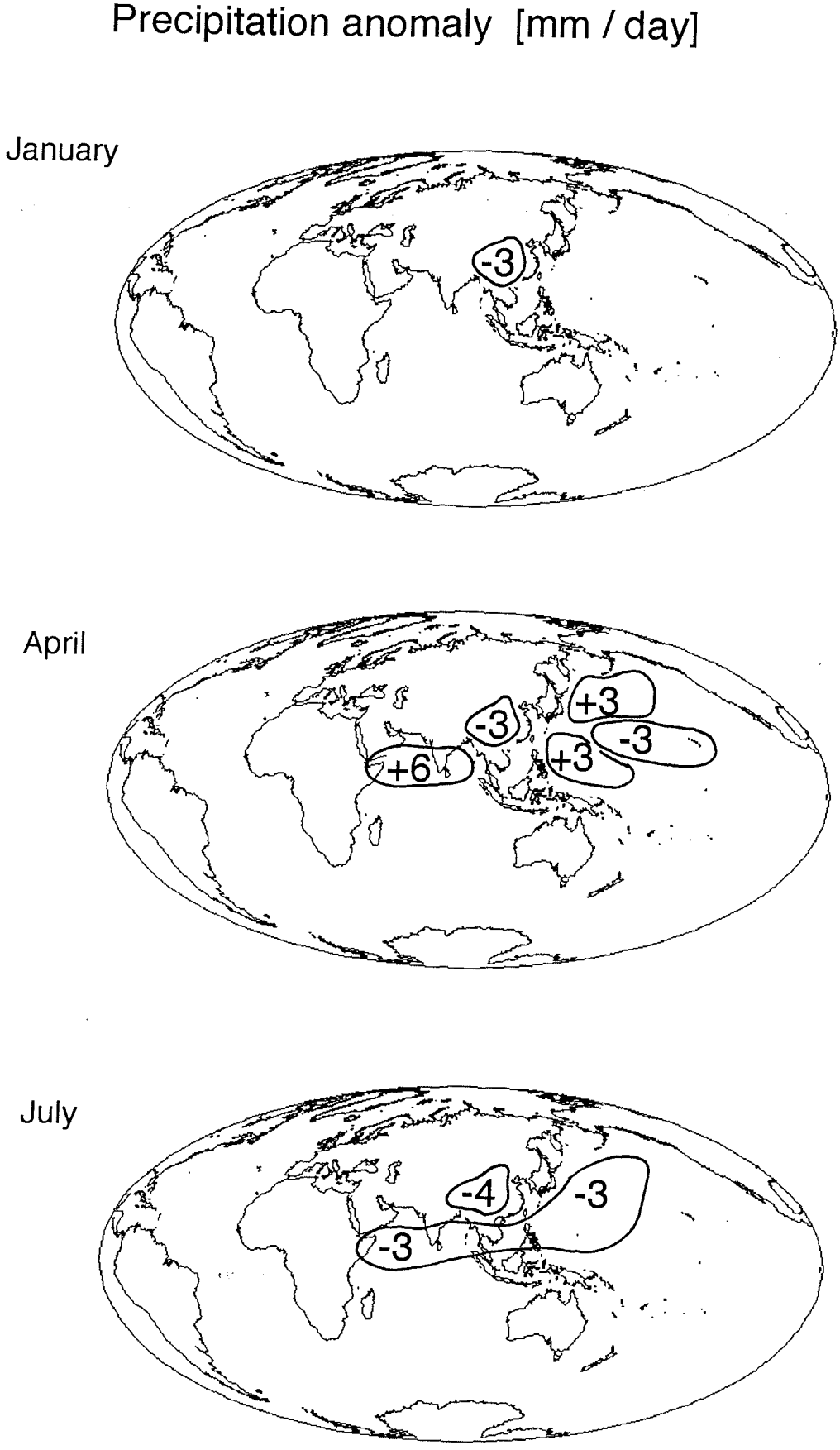

Figure 83. Precipitation [mm/day] anomaly at 21,500 cal-yrBP (experiment minus control) for January, April and July.

Possible forcing mechanisms for synchronous events in the monsoon and the Atlantic climate

The experiment (annual snow cover over all of Asia at elevations > 1000 m) clearly exaggerates the dimension of observed climate change in the region. Still, the results should indicate the direction of response that can be expected from a glacial increase in snow cover over Asia. According to our experiment, a prolonged cold winter season on the Asian continent would produce a slight net warming for the rest of the globe, compensated by a drastic cooling of the northwestern Pacific. The observed coherent abrupt climate change in both the North Atlantic and in the monsoon region at the end of the Younger Dryas is, however, a synchronous warming. Thus, the driving force for a monsoon evolution positively correlated to the Atlantic climate should lie outside the monsoon region, probably in the North Atlantic itself. Which North Atlantic climatic parameter (SST, deepwater formation, sea-ice extent, atmospheric CO_2 variations) could be causing the synchronicity of events cannot be infered from our experiment.

An alternate explanation is provided by a mechanism external to both the Atlantic and the monsoon area, for example in the equatorial Pacific where SST variations control the onset/offset of the ENSO (El Niño, Southern Oscillation). Anomalies in the ENSO intensity are known to be documented in anomalies of the Indian rainfall patterns (Bjerknes, 1969; Walker, 1923), and also in extreme weather conditions over Africa, North America and the central Atlantic (Cane et al., 1986; Philander et al., 1992).

A test for the likelyhood of one or the other explanation may be expected from high resolution reconstructions of past climate changes in the central equatorial Pacific. Unfortunately, such data do not exist at present, because low sedimentation rates limit the time resolution between samples in sediment cores from this key area of tropical climate forcing.

In total, we do not find any evidence in our GCM experiment that an intensification of the southwest monsoon could be forcing the abrupt deglaciation events in the Atlantic. Instead, a warming in the monsoon area would be matched by a cooling in the Atlantic area. Nevertheless, the monsoons could play a role in the spread of abrupt climatic changes in the northern hemisphere by mediating changes from the Atlantic to the Pacific. A warming in the Atlantic region is followed by a warming of Asia during the subsequent winter, a strong summer monsoon, and a warming of the north Pacific, which should have warming effects on the Laurentian ice sheet. In this way, the monsoonal winds in Asia may be an important link that synchronizes warming events on the northern hemisphere.

E. Conclusion

Distribution patterns of $^{143}Nd/^{144}Nd$ and $^{87}Sr/^{86}Sr$ reflect an Arabian provenance of clastic particles in the western Arabian Sea, an Indian provenance in the eastern sector.

Based on their distribution patterns, the following elements appear to be best suited to monitor past monsoon strength in the western Arabian Sea: i) Zr content - dust from east Africa and southern Arabia (transported by northwest winds over the continent, by the mid-tropospheric core layer of the southwest monsoon over the ovean) ii) Mg content-dust from the central Arabian desert and the Persian Gulf region (transported by northwesterly winds), iii) Rb - dust from winter northeast monsoon winds, iv) Zn, Cd - upwelling fertility.

Abrupt decreases in the $\delta^{18}O$ composition of surface water (and planktonic species) can be explained by abrupt increases in upwelling intensity, because upwelling cells feed from a depth where $\delta^{18}O$ values are much lighter than at the surface.

The evolution of the monsoonal climate during the last glacial to interglacial transition showed five distinct intervals, terminated by abrupt beginnings and ends:

The Last Glacial Maximum: -18,000 cal-yrBP (-14,500 ^{14}C-yrBP)
maximum northeast monsoon intensity, low southwest monsoon intensity, sluggish deepwater ventilation

Termination Ia: 18,000-16,000 cal-yrBP (14,500-13,000 ^{14}C-yrBP)
maximum dust flux by northwesterlies from central Arabia (reflecting maximum aridity in Arabia), lowest southwest monsoon intensity, no upwelling activity

Bölling/Alleröd: 16,000-12,900 cal-yrBP (13,000-11,200 ^{14}C-yrBP)
increased humidity in Arabia, intermediate southwest monsoon strength

Younger Dryas: 12,900-11,600 cal-yrBP (11,200-9900 ^{14}C-yrBP)
return of strong northeast monsoon winds, no reaction of southwest monsoon

The Early Holocene 9900-8600 cal-yrBP (9200-7850 ^{14}C-yrBP)
Maximum northward propagation and maximum wind strength of southwest monsoon winds

Abrupt climate change in the monsoon system occurred synchronously with abrupt events in the north Atlantic climate. The major intensification of the southwest monsoon was during the Younger Dryas to Preboreal transition.

Periodic variations in monsoonal climate are found at 1785-, 1450-, 1150- and 950-year periodicities. These periods were already observed in SST variations of the western subtropical Atlantic, suggesting an overall existance of these periods in the climatic variability of the subtropical belt. The 1785-, 1450-, 1150-year periodicities could be explained as harmonic tones of the earth`s precessional cycle.

The cause for abrupt change in monsoonal climate should lie in the Atlantic atmospheric circulation (or external to both the Atlantic and monsoon region), because numerical experiments with changes in the intensity of the monsoons itselft showed no significant effect in temperature fields over the Atlantic region.

Acknowledgments

The study was generously funded over four years by the German Ministery of Research and Technology (grants 07KF0214, 03FO131, "Bundesministerium für Forschung und Technik"). Major parts of the thesis were written at the "Lamont-Doherty Earth Observatory of Columbia University" (New York) where I received a one-year fellowship from the "Max Kade Foundation" (New York) via the "Deutsche Forschungsgemeinschaft" (Bonn). The financial support from these institutions is gratefully acknowledged.

I wish also to express my warm appreciation to a number of individuals, who contributed to this project:

Michael Sarnthein for his scientific guidance;

Dieter Garbe-Schönberg for his close cooperation in running the ICP-MS samples, and his continous effort in improving the accuracy of the data.

Martin Hartmann, Colin Devey, Eckhard Bedbur, Helmut Erlenkeuser (Universität Kiel), Venu Ittekkot (Universität Hamburg), Thomas Wagner (GEOMAR, Kiel), , for providing further analytical capacities;

Thore Meyer, Michael Staubwasser and a large technical staff for running the various analyses;

Jean-Claude Duplessy (CNRS, Gif sur Yvette), Ulrich von Stackelberg (BGR, Hannover), Jean Claude Faugeres (CNRS, Bordeaux), Venu Ittekkot (Universität Hamburg) for sediment samples;

Steven Goldstein (Max-Planck Institut für Chemie, Mainz) for his help in the Nd and Sr isotope analyses;

Wally Broecker for inviting me to Lamont;

Barbara Molfino, Andrew McIntyre and Peter deMenocal for fruitful discussions and providing office and laboratory facilities at Lamont;

David Rind (Goddard Institute for Space Science, NASA, New York) for introducing me to the world of Global Circulation Models;

Albon Man for all the good food and his friendship.

Michael Sarnthein, Rainer Botz, Dieter Garbe-Schönberg, Martin Hartmann, Mark Maslin, Andrew McIntyre, Dan Seidov, and Steven Goldstein improved chapters of this manuscript by a revision of text and data.

G. References

Ackerman, S. A. & Cox, S. K. (1982). The Saudi Arabian heat low: Aerosol distributions and thermodynamic structure. *Journal of Geophysical Research*, **87**(C 11), 8991-9002.

Ackerman, S. A. & Cox, S. K. (1988). Dust outbreaks associated with the southwest monsoon region. *Meteorology and Atmospheric Physics*, **41**(1), 19-34.

Alley, R. B., Meese , D. A., Shuman, C. A., Gow, A. J., Taylor, K. C., Grootes, P. M., White, J. W. C., Ram, M., Waddington, E. D., Mayewski, P. A. & Zielenski, G. A. (1993). Abrupt increase in Greenland snow accumulation at the end of the Younger Dryas event. *Nature*, **362**, 527-529.

Altherr, R., Henjes-Kunst, F. & Baumann, A. (1990). Asthenosphere versus lithosphere as possible sources for basaltic magmas erupted during the formation of the Red Sea; constraints from Sr, Pb and Nd isotopes. *Earth and Planetary Science Letters*, **96**(3-4), 269-286.

Anderson, D. M. & Prell, W. L. (1993). A 300 KYR record of upwelling off Oman during the late Quaternary: Evidence of the Asian southwest monsoon. *Paleoceanography*, **8**(2), 193-208.

Bard, E. & Broecker, W. S. (1992). The last deglaciation: Absolute and Radiocarbon Chronologies. Springer Verlag: Berlin, Heidelberg, New York, London, Paris, Tokyo, Hong Kong, Barcelona, Budapest.

Bard, E., Hamelin, B., Fairbanks, R. G. & Zindler, A. (1990). Calibration of the ^{14}C timescale over the past 30,000 years using mass spectrometric U-Th ages from Barbados corals. *Nature*, **345**, 405-409.

Barnett, T. P., Dümenil, L., Schlese, U., Roeckner, E. & Latif, M. (1989). The effect of Eurasian snow cover on regional and global climate variations. *Journal of the Atmospheric Sciences*, **46**(6), 661-685.

Barrat, J. A., Jahn, B. M., Joron, J. L., Auvray, B. & Hamdi, H. (1990). Mantle heterogeneity in northeastern Africa; evidence from Nd isotopic compositions and hygromagmaphile element geochemistry of basaltic rocks from the Gulf of Tadjoura and southern Red Sea regions. *Earth and Planetary Science Letters*, **101**(2-4), 233-247.

Bauer, S., Hitchcock, G.L. & Olson, B. (1991). Influence of monsoonally-forced Ekman dynamics upon surface layer depth and plankton biomass distribution in the Arabian Sea. *Deep-Sea Research*, **38**(5), 531-553.

Baumann, A., Spies, O. & Lensch, G. (1984). Strontium isotopic composition of post ophiolite Tertiary volcanics between Kashmar, Sabzevar and Quechan/NE Iran. *Neues Jahrbuch für Geologie und Paläontologie, Abhandlungen*, **168**(2-3), 409-416.

Becker, B., Kromer, B. & Trimborn, P. (1991). A stable-isotope tree-ring time-scale of the Late Glacial/Holocene boundary. *Nature*, **353**, 647-648.

Bertram, C. (1989). Nd isotopes and REE distributions in the western basins of the Indian Ocean. Unpubl. PhD thesis, University Cambridge.

Betton, P. J. & Civetta, L. (1984). Strontium and neodymium isotopic evidence for the heterogeneous nature and development of the mantle beneath Afar (Ethiopia). *Earth and Planetary Science Letters*, **71**(1), 59-70.

Biscaye, P. E., Chesselet, R. & Prospero, J. M. (1974). Rb-Sr, $^{87}Sr/^{86}Sr$ isotope system as an index of provenance of continental dusts in the open Atlantic Ocean. *Jour. Recherches Atmospheriques 19744, Numero Special, "Symp. Int'l. sur les Echanges Ocean/Atmosphere de Moitiere a L'Etat Particulaire"*, **8**, 819-829.

Bishop, J. K., Edmond, J. M., Ketten, D. R., Bacon, M. P. & Silker, W. B. (1977). The chemistry, biology, and vertical flux of particulate matter from the upper 400 m of the equatorial Atlantic Ocean. *Deep-Sea Research*, 511-548.

Bjerknes, J. (1969). Atmospheric teleconnections from the equatorial Pacific. *Monthly Weather Review*, **97**(3), 163-172.

Björck, S., Cato, I., Brunnberg, L. & Strömberg, B. (1992). The clay-warve based Swedish time scale and its relation to the Late Weichselian Radiocarbon chronology. In: E. Bard & W. S. Broecker (Eds.), The last deglaciation: Absolute and radiocarbon chronologies NATO ASI series: Springer Verlag, Berlin Heidelberg.

Bloemendal, J. & deMenocal, P. B. (1989). Evidence for a change in the periodicity of tropical climate cycles at 2.4 Myr from whole core magnetic susceptibility measurements. *Nature*, **342**, 897-900.

Bloemendal, J., King, J. W., Hunt, A., Demenocal, P. B. & Hayashida, A. (1993). Origin of the sedimentary magnetic record at Ocean Drilling Program Sites on the Owen Ridge, western Arabian Sea. *Geophysical Research*, **98**(B3), 4199-4219.

Bond, G., Heinrich, H., Huon, S., Broecker, W. S., Labeyrie, L., Andrews, J., McManus, J., Clasen, S., Tedesco, K., Jantschik, R. & Simet, C. (1992). Evidence for massive discharges of icebergs into the glacial Northern Atlantic. *Nature*, **360**, 245-249.

Bouvier-Soumagnac, Y. & Duplessy, J.-C. (1985). Carbon and oxygen isotopic composition of planktonic foraminifera from laboratory culture, plankton tows and recent sediment: implications for the reconstruction of paleoclimatic conditions and of the global carbon cycle. *Journal of Foraminiferal Research*, **15**(4), 302-320.

Boyle, E. A. (1992). Cadmium and $\partial^{13}C$ Paleochemical ocean distributions during the stage 2 glacial maximum. *Annu. Rev. Earth Planet. Sci.*, **20**, 245-287.

Boyle, E. A. (1994). A comparision of carbon isotopes and cadmium in the modern adn glacial maximum ocean: can we account for the discrepancies? In: R. Zahn, T. F. Pedersen, M. A. Kaminski, L. Labeyrie (Eds.), Carbon cycling in the glacial ocean: constraints on the ocean´s role in global change. NATO ASI Series I, Vol. 17. (pp. 167-194). Springer Verlag: Berlin, Heidelberg, New York, London, Paris, Tokyo, Hong Kong, Barcelona, Budapest.

Brock, J. C., McClain, C. R., Anderson, D. M., Prell, W. L. & Hay, W. W. (1992). Southwest monsoon circulation and environments of recent planktonic foraminifera in the northwestern Arabian Sea. *Paleoceanography*, 7(6), 799-813.

Broecker, W. S. (1992). Defining the boundaries of the late -glacial isotope episodes. *Quaternary Research*, **38**, 135-138.

Broecker, W. S., Andree, M., Wolfli, W., Oeschger, H., Bonani, G., Kennett, J. & Peteet, D. (1988). The chronology of the last deglaciation: implications to the cause of the Younger Dryas event. *Paleoceanography*, **31**(1), 1-19.

Broecker, W. S. & Peng, T.-H. (1982). Tracers in the Sea. Eldigio Press: New York.

Bruland, K. W. (1980). Oceanographic distributions of cadmium, zinc, nickel and copper in the North Pacific. *Earth and Planetary Science Letters*, **47**, 176-198.

Campbell, W. H., Blechmann, J. B. & Bryson, R. A. (1983). Long-period tidal forcing of Indian monsoon rainfall: an hypothesis. *Journal of Climate and Applied Meteorology*, 22(2), 287-296.

Cane, M. A., Zebiak, S. E. & Dolan, S. C. (1986). Experimental forcast of El Nino. *Nature*, **321**, 827-832.

Chapman, R. W. (1978). Geology. In: S. S. Al Sayari & J. G. Zoetl (Eds.), Quaternary period in Arabia Springer-Verlag: Wien, New York.

Chappell, J. & Shackleton, N. J. (1986). Oxygen isotopes and sea level. *Nature*, **324**, 137-140.

Chappellaz, J., Blunier, T., Raynaud, D., Barnola, J. M., Schwander, J. & Stauffer, B. (1993). Synchrounous changes in atmospheric CH4 and Greenland climate between 40 and 8kyr BP. *Nature*, **366**, 443-445.

Chen, F. H. (1986). Analyses of a major dust outbreak over the Arabian Sea during monex. Unpubl. Thesis, University of Wisconsin, Madison.

Clemens, S., Prell, W., Muray, D., Shimmield, G. & Weedon, G. (1991). Forcing mechanism of the Indian Ocean monsoon. *Nature*, **353**, 720-725.

Clemens, S. C. & Prell, W. L. (1990). Late pleistocene variability of Arabian Sea summer monsoon winds and continental aridity: eolian record from the lithogenic components of deep sea sediments. *Paleoceanography*, 5(2), 109-145.

CLIMAP (1981). Seasonal reconstructions of the Earth's surface at the last glacial maximum. *The Geological Society of America, Map and Chart Series*, MC-36.

Collier, R. & Edmond, J. (1984). The trace element geochemistry of marine biogenic particulate matter. *Progress in Oceanography*, **13**, 113-199.

Craig, H. & Gordon, L. I. (1965). Isotopic oceanography: Deuterium and oxygen-18 variation in the ocean and marine atmosphere. In: D. R. Schink & J. T. Corless (Eds.), Proc. Symp. Marine Geochemistry, University of Rhode Island, Oct. 29&30, 1964. Graduate School of Oceanography, University of Rhode Island.:

Currie, R. I., Fisher, A. E. & Hargreaves, P. M. (1973). Arabian Sea Upwelling. In: B. Zeitschel & S. A. Gerlach (Eds.), The biology of the Indian Ocean (pp. 37-52). Springer-Verlag: Berlin, Heidelberg, New York.

Curry, W. B., Ostermann, D. R., Guptha, M. V. S. & Ittekkot, V. (1992). Foraminiferal production and monsoonal upwelling in the Arabian Sea: evidence from sediment traps. In: E. Summerhayes, W. L. Prell, K. C. Emeis (Eds.), Upwelling systems: Evolution since the Early Miocene (pp. 93-106). The Geological Society: London.

Dansgaard, W., Johnsen, S. J., Clausen, H. B. & Langway Jr., C. C. (1970). Climatic record revealed by the Camp Century ice core. In: K. Turekian (Ed.), Late Cenozoic ice ages (pp. 37-56). Yale University Press:

Dansgaard, W., White, J. W. C. & Johnsen, S. J. (1989). The abrupt termination of the Younger Dryas climate event. *Nature*, **339**, 532-533.

Dean, W. E., Gardner, J. V. & Hemphill-Haley, E. (1989). Changes in redox conditions in deep-sea sediments of the subarctic north Pacific ocean: possible evidence for the presence of North Pacific deep water. *Paleoceanography*, **4**(6), 639-653.

deMenocal, P. B. & Rind, D. (1993). Sensetivity of Asian and African climate to variations in seasonal insolation, glacial ice cover, sea surface temperature, and Asian Orography. *Journal of Geophysical Research*, **98**(D4), 7265-7287.

Denton, G. H. & Karlén, W. (1973). Holocene climatic variations - Their pattern and possible cause. *Quaternary Research*, **3**, 155-205.

Devey, C., Garbe-Schönberg, D., Stoffers, P., Chauvel, C. & Mertz, D. F. (1994). Geochemical effects of dynamic melting beneath ridges: reconciling major and trace element variations in Kolbensey (and global) mid ocean ridge basalts. *Journal of Geophysical Research*, **99**, 9077-9095.

Duplessy, J. C. (1982). Glacial to interglacial contrasts in the northern Indian Ocean. *Nature*, **295**, 494-498.

Duplessy, J. C. & Bé, A. W. H. (1981). Oxygen and carbon isotopic composition and biogeographic distribution of planktonic foraminifera in the Indian Ocean.

Paleogeography, Paleoclimatology, Paleoecology, **33**, 9-46.

Duplessy, J. C., Shackleton, N. J., Fairbanks, R. G., Labeyrie, L., Oppo, D. & Kallel, N. (1988). Deepwater source variations during the last climatic cycle and their impact on the global deepwater circulation. *Paleoceanography*, 3(3), 343-360.

Duyverman, H. J., Harris, N. B. W. & Hawkesworth, C. J. (1982). Crustal accretion in the Pan African; Nd and Sr isotope evidence from the Arabian Shield. *Earth and Planetary Science Letters*, **59**(2), 315-326.

Dymond, J., Suess, E. & Lyle, M. (1992). Barium in deep-sea sediment: a geochemical proxy for palaeoproductivity. *Palaeoceanography*, 7(2), 163-181.

Elderfield, H. (1990). Tracers of ocean palaeoproductivity and palaeochemistry: an introduction. *Palaeoceanography*, 5(5), 711-717.

Emeis, K.-C. (1993). Geochemische Auftriebsindikatoren in Sedimenten des Nordwestlichen Arabischen Meeres. unpubl. Habilitation thesis, University of Kiel.

Emeis, K. C. & Morse, J. W. (1993). Zur Systematik der Kohlenstoff-Schwefel-Eisen Verhältnisse in Auftriebssedimenten. *Geologische Rundschau*, **82**, 604-618.

Fairbanks, R. G. (1989). A 17,000-year glacio-eustatic sea level record: influence of glacial melting rates on the Younger Dryas event and deep-ocean circulation. *Nature*, **342**, 637-642.

Faugères, J. C. & Gonthier, E. (1981). Les argiles des sédiments marins du Quaternaire récent dans le Golf d' Aden et la Mer d'Oman. *Oceanologica Acta*, 4(4), 395-399.

Findlater, J. (1969). A major low level air current near the Indian Ocean during the northern summer. *Qart. J. R. Met. Soc.*, **95**, 362-380.

Findlater, J. (1974). An extreme wind speed in the low-level jet-stream system of the western Indian Ocean. *Meteorological Magazine*, **103**, 201-205.

Finney, B. P. & Mitchell, W. L. (1988). Sedimentation at Manop Site H (eastern equatorial Pacific) over the past 400,000 years: climatically induced redox variations and their effects on transitions metal cycling. *Palaeoceanography*, 3(2), 169-189.

Fontugne, M. R. & Duplessy, J. C. (1986). Variations of the monsoon regime during the upper quaternary: evidence from carbon isotopic record of organic matter in north Indian Ocean sediment cores. *Palaeogeography, Palaeoclimatology, Palaeoecology*, **56**, 69-88.

Froelich, P. N., Blanc, V., Mortlock, R. A., Chillrud, S. N., Dunstan, W., Udomkit, A. & Peng, T.-H. (1992). River fluxes of dissolved silica to the ocean were higher during glacials: Ge/Si in diatoms, rivers, and oceans. *Paleooceanography*, 7(6), 739-767.

Froelich, P. N., Klinkhammer, G. P., Bender, M. L., Luedtke, N. A., Heath, G. R., Cullen, D., Dauphin, P., Hammond, D. & Hartman, B. (1979). Early oxydation of organic matter in pelagic sediments of the eastern equatorial Atlantic: suboxic diagenesis. *Geochimica et Cosmochimica Acta*, **43**, 1075-1090.

Ganssen, G. & Kroon, D. (1991). Evidence for Red Sea surface circulation from oxygen isotopes of modern surface waters and planktonic foraminiferal tests. *Paleoceanography*, **6**(1), 73-82.

Garbe-Schönberg, C.-D. (1993). Simultanous determination of thirty seven trace elements in twenty-eigth international rock standards by ICP-MS. *Geostandard Newsletters*, **17**(1), 81-97.

Gasse, F., Téhet, R., Durand, A., Gilbert, E. & Fontes, J.-C. (1990). The arid-humid transition in the Sahara and the Sahel during the last deglaciation. *Nature*, **346**, 141-146.

GEBCO (1975). General Bathymetric Chart of the oceans No. 5.05). Canadian Hydrographic Service, Ottawa.

German, C. R. & Elderfield, H. (1990). Rare earth elements in the NW Indian Ocean. *Geochimica et Cosmochimica Acta*, **54**, 1929-1940.

Goldstein, S. J. & Jacobsen, S. B. (1987). The Nd and Sr isotopic sytematics of river-water dissolved material: implications for the sources and Nd and Sr in seawater. *Chemical Geology (Isotope Geoscience section)*, **66**(245-272).

Goldstein, S. L., O'Nions, R. K. & Hamilton, P. J. (1984). A Sm-Nd isotopic study of atmospheric dusts and particulates from major river systems. *Earth and Planetary Science Letters*, **70**, 221-236.

Govindaruju, K. (1989). Compilation of working values and sample description for 272 geostandards. *Geostandard Newsletters*, **13**(1-113).

Grootes, P. M., Stuiver, M., White, J. W. C., Johnsen, S. & Jouzel, J. (1993). Comparison of oxygen isotope records from the GISP2 and GRIP Greenland ice cores. *Nature*, **366**, 552-554.

Grousset, F. E. & Biscaye, P. E. (1989). Nd and Sr isotopes as tracers of wind transport in Atlantic aerosols and surface sediments. In: M. Leinen & M. Sarnthein (Eds.), Paleoclimatology and Paleometeorology: Modern and Past Patterns of Glacial Atmospheric Transport. - NATO ASI Series, C, Math. and Phys. Sciences (pp. 385-400). Kluwer Academic Publishers: Dordrecht, Boston, London.

Grousset, F. E., Biscaye, P. E., Zindler, A., Chester, R. & Prospero, J. (1988). Neodymium isotopes as tracers of marine sediments and aerosols: north Atlantic. *Earth and Planetary Science Letters*, **87**, 367-378.

Grousset, F. E. & Chesselet, R. (1986). The Holocene sedimentary regime in the northern Mid-Atlantic Ridge region. *Earth and Planetary Science Letters*,

78, 271-287.

Guptha, M. V. S. & Hashimi, N. H. (1985). Fluctuation in glacial and interglacial sediment discharge of the river Indus as seen in a core from the Arabian Sea. *Ind. Journal of Marine Sciences*, **14**, 66-70.

Haake, B., Ittekkot, V., Ramaswamy, V., Nair, R. R. & Honjo, S. (1992). Fluxes of amino acids and hexosamines to the deep Arabian Sea. *Marine Chemistry*, **40**, 291-314.

Haake, B., Ittekot, V., Rixen, T., Ramaswamy, V., Nair, R. R. & Curry, W. B. (1993). Seasonality and interannual variability of particle fluxes to the deep Arabian Sea. *Deep-Sea Research*, **40**, 1323-1344.

Hansen, J., Russel, G., Rind, D., Stone, P., Lacis, A., Lebedeff, S., Ruedy, R. & Travis, L. (1983). Efficient three dimensional global models for climate studies: Models I and II. *Monthly Weather Review*, **111**, 609-662.

Harris, N. B. W., Hawkesworth, C. J. & Ries, A. C. (1984). The crustal evolution in North-east and East Africa from model Nd ages. *Nature*, **309**, 773-776.

Harris, N. B. W. & Marzouki, F. M. H. (1986). The Jabel Said complex, Arabian shield: geochemical constraints on the origin of peralkaline and releated granites. *Journal of Geological Society*, **143**, 287-295.

Hashimi, N. H., Scholten, J. & Sirocko, F. (1984). Sediment Cores. In: Sedimentation Processes in the Arabian Sea, Cruise Report "Sonne 42" pp. 62-69). Hamburg: University of Hamburg, Institute of Biogeochemisty marine Chemistry.

Hastenrath, S. & Lamb, P. J. (1979). Climatic Atlas of the Indian Ocean. University of Wisconsin Press: Madison, Wisconsin.

Hastenrath, S. & Lamb, P. J. (1980). On the heat budget of hydrosphere and atmosphere in the Indian Ocean. *Physical Oceanography*, **10**(5), 649-708.

Hermelin, J. O. R. & Shimmield, G. B. (1990). The importance of the oxygen minimum zone and sediment geochemistry in the distribution of recent benthic Foraminifera in the northwest Indian Ocean. *Marine Geology*, **91**, 1-29.

Hinton, R. W. & Upton, B. G. J. (1991). The chemistry of zircon: Variations within and between large crystals from syenite and alkali basalt xenoliths. *Geochimica et Cosmochimica Acta*, **55**, 3287-3302.

Honeyman, B. D., Balistrieri, L. S. & Murray, J. W. (1988). Oceanic trace metal scavenging: the importance of particle concentration. *Deep-Sea Research*, **35**(2), 227-246.

Hutson, W. H. (1980). Bioturbation of deep-sea sediments: oxygen isotopes and stratigraphic uncertainty. *Geology*, **8**(127-130).

Imbrie, J., Hays, J. D., Martinson, D. G., McIntire, A., Mix, A. C., Morley, J. J., Pisias, N. G., Prell, W. L. & Shackleton, N. J. (1984). The orbital theory of pleistocene

climate: support from a revised chronology of the marine $\partial^{18}O$ record. In: A. L. Berger et al. (Ed.), Milankovitch and Climate, Part 1 (pp. 269-305).

Ittekkot, V., Haake, B., Bartsch, M., Nair, R. R. & Ramaswamy, V. (1992). Organic carbon removal in the sea: the continental connection. In: C. P. Summerhays, W. L. Prell, K. C. Emeis (Eds.), Upwelling systems: Evolution since the Early Miocene (pp. 167-176). Geological Society Special Publication: Blackwell, London.

Ittekot, V. & Zhang, S. (1989). Patterns of particulate nitrogen transport in world rivers. *American Geophysical Union*, **3**(4), 383-391.

Jacobs, G. A., Hurlburt, H. E., Kindle, J. C., Metzger, E. J., Mitchell, J. L., Teague, W. J. & Wallcraft, A. J. (1994). Decadal-scale trans-Pacific propagation and warming effects of an El Nino anomaly. *Nature*, **370**, 360-363.

Jacobsen, S. B. & Wasserburg, G. J. (1980). Sm-Nd isotopic evolution of chondrites. *Earth and Planetary Science Letters*, **50**, 139.

Johnsen, S. J., Clausen, H. B., Dansgaard, W., Fuhrer, K., Gundestrup, N., Hammer, C. U., Iversen, P., Jouzel, J., Staufer, B. & Steffensen, J. P. (1992). Irregular glacial interstadials recorded in a new Greenland ice core. *Nature*, **359**, 311-313.

Joussaume, S. (1990). Three-dimensional simulations of the atmospheric cycle of desert dust particles using a general circulation model. *Journal of Geophysical Research*, **95**(2), 1909-1941.

Jung, G., Keller, J., Khorasani, R., Marcks, C., Baumann, A. & Horn, P. (1984). Petrology of the Tertiary magmatic activity in the northern Lut area, East Iran. *Neues Jahrbuch für Geologie und Paläontologie, Abhandlungen*, **168**(2-3), 417-467.

Kallel, N., Labeyrie, L. D., Juillet-Leclerc, A. & Duplessy, J.-C. (1988). A deep hydrological front between intermediate and deep-water masses in the glacial Indian Ocean. *Nature*, **333**, 651-655.

Katyal, J. C. & Sharma, B. D. (1991). DTPA-extractable and total Zn, Cu, Mn, and Fe in Indian soils and their association with some soil properties. *Geoderma*, **49**, 165-179.

Keeling, C. D., Moss, B. J. & Whorf, T. P. (1987). Measurements of the concentrations of atmospheric CO2 at Mauna Loa Observatory, Hawaii, 1958-1986. Final report for the Carbon dioxide Information Center, Oak Ridge, USA.

Keigwin, L. D., Jones, G. A. & Froelich, P. N. (1992). A 15,000 year paleoenvironmental record from Meiji seamount, far northwest Pacific. *Earth and Planetary Science Letters*, **111**, 425-440.

Klinkhammer, G. P. & Palmer, M. R. (1991). Uranium in the oceans: Where it goes and why. *Geochimica et Cosmochimica Acta*, **55**, 1799-1806.

Kolla, V., Bê, A. W. H. & Biscaye, P. E. (1976a). Calcium carbonate distribution in the surface sediments of the Indian Ocean. *Journal of Geophysical Research*, **81**(15), 2605-2616.

Kolla, V. & Biscaye, P. E. (1973). Clay mineralogy and sedimentation in the eastern Indian Ocean. *Deep-Sea Research*, **20**, 727-738.

Kolla, V. & Biscaye, P. E. (1977). Distribution and origin of quartz in the sediments of the Indian Ocean. *Journal of Sedimentary Petrologists*, **47**(2), 642-649.

Kolla, V., Henderson, L. & Biscaye, P. (1976b). Clay mineralogy and sedimentation in the western Indian Ocean. *Deep-Sea Research*, **23**, 949-961.

Kolla, V., Kostecki, J. A., Robinson, F., Biscaye, P. E. & Ray, P. K. (1981a). Distribution and origin of clay minerals and quartz in surface sediments of the Arabian Sea. *Journal of Sedimentary Petrologists*, **51**(2), 563-569.

Kolla, V., Ray, P. K. & Kostecki, J. A. (1981b). Surficial sediments of the Arabian Sea. *Marine Geology*, **41**, 183-204.

Kröner, A., Pallister, J. S. & Fleck, R. J. (1992). Age of initial oceanic magmatism in the Late Proterozoic Arabian Shield. *Geology*, **20**, 803-806.

Kudrass, H. R., Erlenkeuser, H., Vollbrecht, R. & Weiss, W. (1991). Global nature of the Younger Dryas cooling event inferred from oxygen isotope data from Sulu Sea cores. *Nature*, **349**, 406-408.

Kuhle, M. (1974). Vorläufige Ausführung morphologischer Feldarbeitsergebnisse aus dem S/E-Iranischen Hochgebirge am Beispiel des Kuh-I-Jupar. *Zeitschrift für Geomorphologie N.F.*, **18**(4), 472-483.

Kuhle, M. (1987). Subtropical mountain- and highland-glaciation as ice age triggers and the waning of the glacial periods in the Pleistocene. *GeoJournal*, **14**(4), 393-421.

Kukal, Z. & Saadallah, A. (1973). Aeolian admixtures in the sediments of the Northern Persian Gulf. In: B. H. Purser (Ed.), The Persian Gulf (pp. 115-123). Springer Verlag: Berlin, Heidelberg, New York.

Kutzbach, J. E. & Guetter, P. J. (1986). The influence of changing orbital parameters and surface boundary conditions on climate simulations for the past 18,000 years. *Journal of the Atmospheric Science*, **43**(16), 1726-1759.

Labeyrie, L. D., Duplessy, J. C. & Blanc, P. L. (1987). Variations in mode of formation and temperature of oceanic deep waters over the past 125,000 years. *Nature*, **327**, 477-482.

Lautenschlager, M. & Santer, B. D. (1991). Atmospheric response to a hypothetical Tibetan ice sheet. *Journal of Climate*, **4**(4), 386-394.

Lehman, S. J. & Keigwin, L. D. (1992). Sudden changes in North Atlantic circulation during the last deglaciation. *Nature*, **356**, 757-762.

Lightfoot, P. C., Hawkesworth, C. J., Devey, C. W., Rogers, N. W. & Van Calsteren, P.

W. C. (1990). Source and differentiation of Deccan trap lavas: Implications of geochemical and mineral chemical variations. *Journal of Petrology*, **31**(5), 1165-1200.

Lotter, A. F. (1991). Absolute dating of the late-glacial period in Switzerland using annually laminated sediments. *Quaternary Research*, **35**, 321-330.

Loutre, M. F., Berger, A., Bretagnon, P. & Blanc, P.-L. (1992). Astronomical frequencies for climate research at the decadal to century time scale. *Climate Dynamics*, 7, 181-194.

Luther, M. E. & O´Brien, J. J. (1990). Variability in upwelling fields in the northwestern Indian Ocean 1. model experiments for the past 18,000 years. *Paleoceanography*, 5(3), 433-445.

Lynch-Stieglitz, J. & Fairbanks, R. G. (1994). A conservative tracer for glacial ocean circulation from carbon isotope and paleonutrient measurements in benthic foraminifera. *Nature*, **369**, 308-310.

Lynch-Stieglitz, J., Fairbanks, R. G. & Christopher, D. C. (subm.). Glacial-interglacial history of Antarctic intermediate water: Relative strengths of Antarctic vs. Indian Ocean sources. *Paleoceanography*.

MacAyeal, D. R. (1993a). Binge/purge oscillations of the Laurentide ice sheet as a cause of the north Atlantic Heinrich events. *Paleoceanography*, **8**(6), 775-784.

MacAyeal, D. R. (1993b). A low order model of the Heinrich event cycle. *Paleoceanography*, **8**(6), 767-773.

Manabe, S. & Broccoli, A. J. (1985). The influence of continental ice sheets on the climate of an ice age. *Journal of Geophysical Research*, **90**, 2167.

Manabe, S. & Hahn, D. G. (1977). Simulation of the tropical climate of an ice age. *Journal of Geophysical Research*, **82**(27), 3889-3911.

Marchig, V. (1972). Zur Geochemie rezenter Sedimente des Indischen Ozeans. *"Meteor" Forschungs-Ergebnisse, C*, **11**, 1-104.

Marchig, V. (1974). Zur Geochemie rezenter Sedimente des Indischen Ozeans II, Arabisches Meer, afrikanischer Kontinentalrand und Vergleich mit dem indisch-pakistanischen Kontinentalrand. *"Meteor" Forschungs-Ergebnisse, C*, **18**, 1-34.

Martin, J.-M. & Meybeck, M. (1979). Elemental mass balance of material carried by major world rivers. *Marine Chemistry*, 7, 173-206.

Martin, J. H. & Knauer, G. A. (1973). The elemental composition of plankton. *Geochimica et Cosmochimica Acta*, **37**, 1639-1653.

Maslin, M. (1993). A study of the palaeoceanography of the NE Atlantic in the late Pleistocene. unpubl. PhD thesis, University of Cambridge.

McClure, H. A. (1976). Radiocarbon chronology of late Quaternary lakes in the

Arabian Desert. *Nature*, **263**, 755-756.

McDonald, W. F. (1938). Atlas of Climatic Charts of the Oceans no.1, charts 59-62. U.S. Deptartment of Agriculture, Weather Bureau: Washington D.C.

Middleton, N. J. (1986). A geography of dust storms in South-west Asia. *Journal of Climatology*, **6**, 183-196.

Milliman, J. D. & Meade, R. H. (1983). World-wide delivery of river sediments to the oceans. *Journal of Geology*, **91**, 1-21.

Millisenda, C. C., Liew, T. C., Hofmann, A. W. & Köhler, H. (1994). Nd isotopic mapping of the Sri Lanka basement: update and additional constraints from Sr isotopes. *Precambrian Research*, **66**, 95-110.

Millisenda, C. C., Liew, T. C., Hofmann, A. W. & Kröner, A. (1988). Isotopic mapping of age provinces in Precambrian high-grade terrains: Sri Lanka. *Journal of Geology*, **96**, 608-615.

Mortlock, R. A. & Froelich, P. N. (1989). A simple method for the rapid determination of biogenic opal in pelagic marine sediments. *Deep-Sea Research*, **36**(9), 1415-1426.

Mosley, F. & Abbots, I. L. (1979). The ophiolite melange of Masirah, Oman. *J. Geol. Soc. London*, **136**, 713-724.

Moyes, J., Duprat, J., Faugeres, J.-C., Gonthier, E. & Pujol, C. (1978). Etudes stratigraphique et sedimentologique. In: O. 4 (Ed.), Golf d`Aden, Mer d`Oman (pp. 189-263).

Müller, G. (1967). The HCl-souble iron, manganese, and copper contents of recent Indian Ocean sediments off the eastern coast of Somalia. *Mineralium Deposita*, **2**, 54-61.

Murray, D. W. & Prell, W. L. (1991). Pliocene to pleistocene variations in calcium carbonate, organic carbon, and opal on the Owen Ridge, northern Arabian Sea. *Proceedings of the Ocean Drilling Program, Scientific Results*, **117**, 343-363.

Nair, R. R., Ittekkot, V., Manganini, S. J., Ramaswamy, V., Haake, B., Degens, E. T., Desai, B. N. & Honjo, S. (1989). Increased particle flux to the deep ocean related to monsoons. *Nature*, **338**, 749-751.

Oeschger, H., Stauffer, B., Finkel, R. & Langway Jr., C. C. (1985). Variations of the CO2 concentration of occluded air and of anions and dust in polar ice cores. In: E. T. Sundquist & W. S. Broecker (Eds.), The carbon cycle and athmosperic CO2: Natural variations archean to present (pp. 133-142). American Geophysical Union: Washington, D.C.

Olausson, E. & Olsson, I. U. (1968). Varve stratigraphy in a core from the Gulf of Aden. *Palaeogeography, Palaeoclimatology, Palaeoecology*, **6**, 87-103.

Östlund, H. G., Craig, H., Broecker, W. S. & Spencer, D. (1987). GEOSECS - Atlantic,

Pacific, and Indian Ocean expeditions. National Science Foundation: Washington D.C.

Pachur, H.-J. & Hoelzmann, P. (1991). Paleoclimatic implications of late Quaternary Lacustrine Sediments in Western Nubia, Sudan. *Quaternary Research*, **36**, 257-276.

Paropkari, A. L. (1990). Geochemistry of sediments from the Mangalore-Cochin shelf and upper slope off southwest India: geological and environmental factors controlling dispersal of elements. *Chemical Geology*, **81**, 99-119.

Paropkari, A. L., Prakash Babu, C. & Mascarenhas, A. (1992). A critical evaluation of depositional parameters controlling the variability of organic carbon in the Arabian Sea sediments. *Marine Geology*, **107**, 213-226.

Pearson, G. W., Pilcher, J.R., Baillie, M.G.L., Corbett, D.M. & Qua, B. (1986). High precision 14C measurement of Irish oaks to show the natural C14 variations from AD 1840-5210 BC. *Radiocarbon*, **28**(2B), 911-934.

Pedersen, T., Shimmield, G. B. & Price, N. B. (1992). Lack of enhanced preservation of organic matter in sediments under the oxygen minimum on the Oman margin. *Geochimica Cosmochimica Acta*, **56**, 545-551.

Pestiaux, P., Duplessy, J. C. & Berger, A. (1987). Paleoclimatic variability at frequencies ranging fom 10^{-4} cycles per year to 10^{-3} cycle per year - Evidence for nonlinear behaviour of the climate system. In: M. Rampino, et al, (Eds.), Climate History. van Norstrand.

Peteet, D. M. (1992). The palynological expression of the Younger Dryas event - Europe versus Eastern North America. In: E. Bard & W. S. Broecker (Eds.), The last deglaciation: absolute and radiocarbon chronologies. (pp. 327-344). Springer Verlag: Berlin, Heidelberg, New York, London, Paris, Tokyo, Hong Kong, Barcelona, Budapest.

Peterson, L. C. & Prell, W. L. (1985). Carbonate preservation and rates of climatic change: An 800 kyr record from the Indian Ocean. In: E. T. Sundquist & W. S. Broecker (Eds.), The carbon cycle and atmospheric CO_2: Natural variation archean to present. Geophysical Monograph, 32. (pp. 251-269).

Philander, S. G. H., Pacanowski, R. C., Lau, N.-C. & Nath, M. J. (1992). Simulation of ENSO with a global atmospheric GCM coupled to a high resolution, tropical Pacific Ocean GCM. *Journal of Climate*, **5**, 308-328.

Prell, W. L. (1984). Variation of moonsoonal upwelling: a response to changing solar radiation. In: "Climate Processes and Climate Sensitivity", Geophysical Monograpg 29, Maurice Ewing Vol. 5. American Geophysical Union.

Prell, W. L., Hutson, W. H., Williams, D. F., Bé, A. W., Geitzrenauer, K. & Molfino, B.

(1980). Surface circulation of the Indian Ocean during the last glacial maximum, approximately 18,000 yr B.P. *Quaternary Research*, **14**, 309-336.

Prell, W. L. & Kutzbach, J. E. (1987). Monsoon variability over the past 150,000 years. *Journal of Geophysical Research*, **92**(D7), 8411-8425.

Prell, W. L. & Kutzbach, J. E. (1992). Sensetivity of the Indian monsoon to changes in orbital parameters, glacial and tectonic boundary conditions and atmospheric CO2 concentration. .

Prell, W. L. & Niitsuma, N. (1991). Proceedings of the Ocean Drilling Program, part B: scientific results, Leg 117.

Prell, W. L. & Streeter, H. F. (1982). Temporal and spatial patterns of monsoonal upwelling along Arabia: a modern analogue for the interpretation of quaternary SST anomalies. *Journal of Marine Research*, **40**(1), 143-155.

Prell, W. L. & van Campo, E. (1986). Coherent response of Arabian Sea upwelling and pollen transport to late Quaternary monsoonal winds. *Nature*, **323**, 526-528.

Pye, K. (1987). Aeolian dust and dust deposits. Academic Press: University of Cambridge.

Ramage, C. S. & Raman, C. V. R. (1972). Meteorological atlas of the international Indian Ocean expedition. Upper Air. U.S. National Science Foundation and India Meteorological Department.:

Raman, C. R. V. & Maliekal, J. A. (1985). A "northern oscillation" relating northern hemispheric pressure anomalies and the Indian summer monsoon? *Nature*, **314**, 430-432.

Raymo, M. E., Rind, D. & Ruddiman, W. F. (1990). Climatic effects of reduced arctic sea ice limits in the GISS II general circulation model. *Paleoceanography*, **5**(3), 367-382.

Raymo, M. E. & Ruddiman, W. F. (1992). Tectonic forcing of late Cenozoic climate. *Nature*, **359**, 117-122.

Raynaud, D., Chapellaz, J., Barnola, J. M., Korotkevich, Y. S. & Lorius, C. (1988). Climatic and CH_4 cycle implications of glacial-interglacial CH_4 change in the Vostok ice core. *Nature*, **333**, 655-657.

Reemtsma, T. & Ittekkot, V. (1992). Determination of factors controlling the fatty acid composition of settling particles in the water column by principal-component analysis and their quantitative assessment by multiple regression. *Org. Geochem.*, **18**(1), 121-129.

Reischmann, T. (submitted). Isotope mapping of the Arabian-Nubian Shield: Implications for late Proterozoic crustal growth. *Geology*.

Rind, D. (1987). Components of the Ice Age circulation. *Journal of Geophysical Research*, **92**(D4), 4241-4281.

Roberts, N., Taieb, M., Barker, P., Damnati, B., Icole, M. & Williamson, D. (1993). Timing of the Younger Dryas event in East Africa from lake level changes. *Nature*, **366**, 146-148.

Roberts, N. & Wright, H. E. (1987). Vegetational, lake-level and climatic history of the near east and southwest Asia. In: J. E. Kutzbach, P. Street F.A., W. F. Ruddiman, T. WEbb III, W. F. Wright Jr (Eds.), Global climates for 9000 and 6000 years ago - COHMAP (Cooperative Holocene Mapping Project)

Ruddiman, W. F. & Kutzbach, J. E. (1989). Forcing of late Cenozoic northern hemisphere climate by plateau uplift in southern Asia and the American West. *Journal of Geophysical Research*, **94**, 18,409-18,427.

Saager, P. M., DeBaar, H. J. W. & Howland, R. J. (1992). Cd, Zn, Ni and Cu in the Indian Ocean. *Deep-Sea Research*, **39**, 9-35.

Sarkar, A., Ramesh, R., Bhattacharya, S. K. & Rajagopalan, G. (1990). Oxygen isotopes evidence for a stronger winter monsoon current during the last glaciation. *Nature*, **343**, 549-551.

Sarnthein, M. (1972). Sediments and history of the postglacial transgression in the Persian Gulf and northwest Gulf of Oman. *Marine Geology*, **12**, 245-266.

Sarnthein, M., Jansen, E., Arnold, M., Duplessy, J. C., Erlenkeuser, H., Flatoy, A., Veum, T., Vogelsang, E. & Weinelt, M. (1992). $d^{18}O$ time-slice reconstruction of meltwater anomalies at Termination I in the North Atlantic between 50 and 80°N. In: E. Bard & W. S. Broecker (Eds.), The Last Deglaciation: Absolute and Radiocarbon Chronologies. (pp. 183-200). Springer Verlag: Berlin, Heidelberg, New York, London, Paris, Tokyo, Hong Kong, Barcelona, Budapest.

Sarnthein, M., Winn, K., Duplessy, J. C. & Fontugne, M. R. (1988). Global variations of surface ocean productivity in low and mid latitudes: influence on CO2 reservoirs of the deep ocean and atmosphere during the last 21,000 years. *Paleoceanography*, **3**(3), 361-399.

Sarnthein, M., Winn, K., Jung, S. J. A., Duplessy, J.-C., Labeyrie, L., Erlenkeuser, H. & Ganssen, G. (1994). Changes in east Atlantic deepwater circulation over the last 30,000 years: Eight time slice reconstrunctions. *Paleoceanography*, **9**(2), 209-267.

Scheffer, F. & Schachtschabel, P. (1992). Lehrbuch der Bodenkunde. Ferdinand Enke Verlag: Stuttgart.

Scholten, J. C. (1987). Ein Beitrag zur Geochemie und Sedimentationsgeschichte am Carlsberg- und Mittel-Indischen Rücken. unpubl. PHD-Thesis, Ruprecht-Karls-University Heidelberg.

Schott, F. & Fieux, M. (1985). The Somali current in autumn 1984, before the onset of the north-east monsoon. *Nature*, **315**, 50-52.

Seralatan, P. & Hartmann, M. (1986). Molybdenum and vanadium in sediment cores from the NW-African continental margin and their relations to climatic and environmental conditions. *"Meteor" Forschungs Ergebnisse*, C(40), 1-17.

Shackleton, N. J. (1987). The carbon isotope record of the Cenocoic: history of organic burial and of oxygen in the ocean and atmosphere. In: J. Brooks & A. J. Fleet (Eds.), Marine Petroleum Source Rocks (pp. 423-434). Geological Society Special Publication:

Shankar, R., Subbarao, K. V. & Kolla, V. (1987). Geochemistry of surface sediments from the Arabian Sea. *Marine Geology*, **76**, 253-279.

Shaw, T. J., Gieskes, J. M. & Jahnke, R. A. (1990). Early diagenesis in differing depositional environments: The response of transition metals in pore water. *Geochimica et Cosmochimica Acta*, **54**, 1233-1246.

Shimmield, G. B., Mowbray, S. R. & Weedon, G. P. (1990a). A 350ka history of the Indian southwest monsoon-evidence from deep-sea cores, northwest Arabian Sea. *Transactions of the Royal Society of Edinburgh: Earth Sciences*, **81**, 289-299.

Shimmield, G. B., Price, N. B. & Pedersen, T. F. (1990b). The influence of hydrography, bathymetry and productivity on sediment type and composition of the Oman Margin and in the northwest Arabian Sea. In: A. H. F. Robertson, M. P. Searle, A. C. Ries (Eds.), The geology and tectonics of the Oman region. (pp. 759-769). Geological Society Special Publication:

Sirocko, F. (1989). Zur Akkumulation von Staubsedimenten im nördlichen Indischen Ozean: Anzeiger der Klimageschichte Arabiens und Indiens. *Berichte-Reports, Geol.-Paläont. Inst. Univ. Kiel*, **27**, 114.

Sirocko, F. (1991). Deep-Sea sediments of the Arabian Sea: a paleoclimatic record of the Southwest Asian summer monsoon. *Geologische Rundschau*, **80**(3), 557-566.

Sirocko, F. & Ittekkot, V. (1992). Organic carbon accumulation rates in the Holocene and Glacial Arabian Sea: Implications for the global CO2 budget. *Climate Dynamics*, **7**, 167-172.

Sirocko, F. & Lange, H. (1991). Clay mineral accumulation rates in the Arabian Sea during the Late Quaternary. *Marine Geology*, **97**, 105-119.

Sirocko, F. & Sarnthein, M. (1989). Wind-borne deposits in the Northwestern Indian Ocean: record of Holocene sediments versus modern satellite data. In: M. Leinen & M. Sarnthein (Eds.), Paleoclimatology and Paleometeorology: Modern and Past Patterns of Glacial Atmospheric Transport. - NATO ASI Series, C, Math. and Phys. Sciences (pp. 401-433). Kluwer Academic Publishers: Dordrecht, Boston, London.

Sirocko, F., Sarnthein, M., Erlenkeuser, H., Lange, H., Arnold, M. & Duplessy, J. C.

(1993). Century-scale events in monsoonal climate over the past 24,000 years. *Nature*, **364**, 322-324.

Sirocko, F., Sarnthein, M., Lange, H. & Erlenkeuser, H. (1991). The atmospheric summer circulation and coastal upwelling in the Arabian Sea during the Holocene and the last glaciation. *Quaternary Research*, **36**, 72-93.

Slater, R. D. & Kroopnick, P. (1984). Controls on dissolved oxygene distribution and organic carbon deposition in the Arabian Sea. In: B. U. Haq & J. D. Milliman (Eds.), Marine geology and oceanography of Arabian Sea and coastal Pakistan (pp. 305-313). Van Nostrand Reinhold Company: New York.

Smith, S. L., Banse, K., Cochran, J. K., Codispoti, L. A., Ducklow, H. W., Luther, M. E., Olson, D. B., Petersen, W. T., Prell, W. L., Surgi, N., Swallow, J. C. & Wishner, K. (1991). U.S. JGOFS: Arabian Sea Process Study, Planning report No. 13). Woods Hole Oceanographic Institution.

Stewart, R. A., Pilkley, O. H. & Nelson, B. W. (1965). Sediments of the northern Arabian Sea. *Marine Geology*, **3**, 411-427.

Street, F. A. & Grove, A. T. (1979). Global maps of lake-level fluctations since 30,000 yr B.P. *Quaternary Research*, **12**, 83-118.

Street-Perrott, F. A., Mitchell, J. F. B., Marchand, D. S. & Brunner, J. S. (1990). Milankovitch and albedo forcing of the tropical monsoons: a comparison of geological evidence and numerical simulations for 9000 yr.B.P. *Transactions of the Royal Society of Edinburgh: Earth Science*, **81**, 407-427.

Stuiver, M., Branziunas, T. F., Becker, B. & Kromer, B. (1991). Climatic, Solar, Oceanic and Geomagnetic Influences on Late-Glacial and Holocene Athmospheric $^{14}C/^{12}C$ Change. *Quaternary Research*, **35**, 1-24.

Taylor, K. C., Hammer, C. U., Alley, R. B., Clausen, H. B., Dahl-Jensen, D., Gow, A. J., Gundestrop, N. S., Kipfstuhl, J., Moore, J. C. & Waddlington, E. D. (1993a). Electrical conductivity measurements from the GISP2 and GRIP Greenland ice cores. *Nature*, **366**, 549-552.

Taylor, K. C., Lamorey, G. W., Doyle, G. A., Alley, R. B., Grootes, P. M., Mayewski, P. A., White, J. W. C. & Barlow, L. K. (1993b). The flickering switch of late Pleistocene climate change. *Nature*, **361**, 432-436.

Topping, G. (1969). Concentrations of Mn, Co, Fe, and Zn in the northern Indian Ocean. *Journal of Marine Resarch*, **27**, 318-326.

Turekian, K. K. & Wedepohl, K. H. (1961). Distribution of the elements in some major units of the earth´s crust. *Geological Society of America Bulletin*, **72**, 175-192.

Uerpmann, H. P. (1991). Radiocarbon dating of shell middens in the Sultanate of Oman. *Pact*, **4**(5), 335-347.

Van Campo, E. (1986). Monsoon fluctuations in two 20,000-Yr B.P. oxygene-

isotope/pollen records off Southwest India. *Quaternary Research*, **26**, 376-388.

Van Zeist, W. & Woldring, H. (1978). A postglacial pollen diagram from lake Van in east Anatolia. *Review of Palaeobotany and Palynology*, **26**, 249-276.

Von Stackelberg, U. (1972). Faziesverteilung in Sedimenten des indisch-pakistanischen Kontinentalrandes. *"Meteor" Forschungs-Ergebnisse,C*, **9**, 1-73.

Walker, G. T. (1923). Correlations in seasonal variations of Weather VIII: a preliminary study of world weather. *Memoirs of Indian Meteorological Department*, **24**(4), 75-131.

Weinelt, M. (1993). Veränderungen der Oberflächenzirkulation im Europäischen Nordmeer während der letzten 60.000 Jahre - Hinweise aus stabilen Isotopen. *Berichte aus dem Sonderforschungsbereich 313*, **41**, 1-106.

Weinelt, M. S., Sarnthein, M., Vogelsang, E. & Erlenkeuser, H. (1991). Early decay of Barents shelf ice sheet - spread of stable isotope signals across the eastern Norwegian Sea. *Norsk Geologisk Tidskrift*, **71**, 137-140.

Winn, K., Sarnthein, M. & Erlenkeuser, H. (1991). d18O Stratigraphy and Chronology of Kiel Sediment Cores from the East Atlantic. *Berichte-Reports Geol. Paleont. Inst. Univ. Kiel*, **45**, 1-99.

Wolter, K. (1987). Modes of surface circulation and climate over the tropical Atlantik, Eastern Pacific, and Indian Oceans. Unpubl. PHD-Thesis, University of Madison-Wisconsin.

Wyrtki, K. (1971). Oceanographic Atlas of the International Indian Ocean Expedition. National Science Foundation: Washington.

Zahn, R. & Pedersen, T. F. (1991). Late pleistocene evolution of surface and mid-depth hydrography at the oman margin: planktonic and benthic isotopes records at site 724. In: L. Prell & N. Niitsuma (Eds.), Proceedings of the Ocean Drilling Program, part B: scientific results, Leg 117 (pp. 291-308).

Zahn, R., Pedersen, T. F., Bornhold, B. D. & Mix, A. C. (1991). Water mass conversion in the glacial subarctic Pacific (54N, 148W): physical constraints and the benthic-planktonic stable isotope record. *Paleoceanography*, **6**(5), 543-560.

Zobel, B. (1973). Biostratigraphische Untersuchungen an Sedimenten des indisch-pakistanischen Kontinentalrandes. *"Meteor" Forschungs-Ergebnisse, C*, **12**, 9-73.

Appendix

The entire data file is available upon request from the German "Past Global Changes" (PAGES-) marine data repository SEDAN (grobe@awi-bremerhaven.de).

Appendix 1) Time-slice samples

Table 1) Chemical composition at the sediment surface. Concentration values in the bulk fraktion (% or ppm), concentration values expressed on a carbonate and opal free basis (% or ppm, cofb)

Table 2) Chemical composition at the depth level of the early Holocene (8000-10,000 cal-yrBP). Concentration values in the bulk fraktion (% or ppm), concentration values expressed on a carbonate and opal free basis (% or ppm, cofb)

Table 3) Chemical composition at the depth level of the Termination Ia (16,000-18,000 cal-yrBP). Concentration values in the bulk fraktion (% or ppm), concentration values expressed on a carbonate and opal free basis (% or ppm, cofb)

Table 4) Chemical composition at the depth level of the Last Glacial Maximum (21,000-23,000 cal-yrBP). Concentration values in the bulk fraktion (% or ppm), concentration values expressed on a carbonate free basis (% or ppm, cfb)

Appendix 2) Sediment core 74KL

Table 1) Sedimentology, isotope and mineral composition
Table 2) Geochemical concentration values in the bulk fraktion (% or ppm), concentration values expressed on a carbonate and opal free basis (% or ppm, cofb)

Appendix 3) Sediment core KS8

Table 1) Sedimentology, isotope and mineral composition
Table 2) Geochemical concentration values in the bulk fraktion (% or ppm), concentration values expressed on a carbonate free basis (% or ppm, cfb)

Appendix 4) Sediment core 422

Table 1) Sedimentology, isotope and mineral composition

Appendix 5) Sediment core 36KL

Table 1) Geochemical concentration values in the bulk fraktion (% or ppm), concentration values expressed on a carbonate free basis (% or ppm, cfb)

Appendix 6) Sediment cores 243 and 280

Table 1) Isotope composition

core	depth	w.depth	CaCO3	Opal	Biogenic	< 2 µm	area	Corg	N	S	SiO2	TiO2	Al2O3	Fe2O3	MnO	MgO	CaO	P2O5	Si	Ti	Al	Fe	Mn	Mg	Ca, bulk	Ca, mar.	Ca, lith.	P	Li	Na	K	Sc
	cm	m	%	%	%	%	m2	%	%	%	wt%	wt%	wt%	wt%	wt%	wt%	wt%	wt%	wt%	%	%	%	%	%	%	%	%	%	%	ppm	%	%	ppm
15KL	0-5	3920	64,6	1,9	66,5	59,2	19,8	0,83	0,07	0,101	16,2	0,26	4,22	2,18	0,229	1,83	41,4	0,222	7,6	0,154	2,23	1,52	0,177	1,10	29,6	25,9	3,7	0,048	15,9	1,33	1,48	5,66
26KL	0-5	3776	54,0	2,4	56,4	64,4	26,1	0,58	0,08	0,040	24,0	0,43	6,69	3,57	0,129	2,56	34,0	0,205	11,2	0,256	3,54	2,50	0,100	1,55	24,3	21,6	2,7	0,045	15,9	1,66	1,86	7,68
36KL	0-5	2055	72,1	1,2	73,3	46,4	13,2	0,41	0,05	0,087	14,3	0,25	3,84	2,10	0,042	1,67	47,7	0,149	6,7	0,149	2,03	1,47	0,032	1,01	34,1	28,9	5,3	0,033	20,4	1,38	0,78	9,81
51KL	0-5	2644	45,5	1,6	47,1	49,6	20,4	0,64	0,10	0,092																18,2			22,7	1,83	1,58	14,20
57KL	0-5	3422	33,2	2,4	35,6	54,8	23,9	1,29	0,16	0,136	35,2	0,47	8,79	4,36	0,496	3,98	20,8	0,247	16,5	0,282	4,65	3,05	0,384	2,40	14,9	13,3	1,6	0,054	25,0	2,20	1,83	12,30
64KL		3281																														
70KL	0-10	3810	67,7			56,0		1,21	0,12	0,141																27,1						
71KL	0-20	4029	47,8	4,6	52,4			2,28	0,20	0,505																19,1			18,1	1,98	1,16	10,60
74KL	9-15	3212	59,0	7	66,0	50,0	23,0	1,51	0,18	0,211	21,0	0,21	3,45	1,86	0,095	2,31	37,8	0,170	9,8	0,128	1,83	1,30	0,073	1,39	27,0	23,6	3,4	0,037	13,6	2,06	0,73	8,86
79KL	0-2	4351	41,2	7,4	48,6	63,4		1,60	0,18	0,276																16,5			13,6	3,22	1,17	15,40
82KL	0-2	4416	45,1	5,1	50,2	62,0		1,29	0,11	0,252	26,4	0,32	5,20	2,85	0,900	2,87	29,2	0,211	12,3	0,192	2,75	1,99	0,697	1,73	20,9	18,1	2,8	0,046	6,8	2,42	1,47	6,12
87KL	0-5	3773	74,5	4,3	78,8	60,8	19,5	0,42	0,06	0,208	11,8	0,14	2,27	1,26	0,385	1,26	47,3	0,142	5,5	0,081	1,20	0,88	0,298	0,76	33,8	29,8	4,0	0,031	15,9	2,10	0,50	8,39
5KL		3335																														
11KL	0-5	3859	77,2	3,3	80,5	75,2		0,44	0,05	0,178																30,9			15,9	1,59	0,46	3,13
18KL	0-10	3035	85,5	2,2	87,7	74,6	11,5	0,31	0,05	0,176	4,9	0,06	1,16	0,78	0,044	0,66	55,8	0,081	2,3	0,038	0,62	0,54	0,034	0,40	39,9	34,2	5,6	0,018	15,9	1,52	0,26	2,07
105KK	3-7	3535	65,7	7	72,7	63,5		1,46	0,12	0,145	17,6	0,19	2,89	1,57	0,046	1,63	41,5	0,148	8,2	0,113	1,53	1,10	0,036	0,99	29,7	26,3	3,4	0,032	6,8	1,90	1,12	4,52
114KK	3-8	3843	67,6	5,8	73,4	68,8	24,2	0,77	0,12	0,151	16,5	0,22	3,24	1,71	0,098	1,37	42,0	0,193	7,7	0,132	1,72	1,20	0,076	0,83	30,0	27,1	2,9	0,042	11,3	1,63		4,92
143KK	12-19	1522	48,5	2	50,5	58,5	25,4	1,56	0,17	0,148	26,6	0,62	7,32	3,80	0,036	1,76	30,5	0,168	12,5	0,370	3,87	2,66	0,028	1,06	21,8	19,4	2,4	0,037	6,8	1,73	1,66	7,78
182SK	4-8	2234	62,1	2,7	64,8	73,2		0,67	0,10	0,181	12,8	0,20	3,69	1,84	0,091	1,22	27,5	0,158	6,0	0,119	1,95	1,29	0,070	0,73	19,6	24,9	-5,2	0,034	20,4	1,69	1,16	5,88
223SK	8-15	2686	46,0	1,1	47,1	52,4	32,6	0,67	0,08	0,118	29,0	0,47	7,75	4,12	0,096	2,75	28,1	0,209	13,5	0,280	4,10	2,88	0,075	1,66	20,1	18,4	1,7	0,046	20,4	1,66	2,06	8,72
232SK	5-10	3098	37,3	1,4	38,7	52,4	23,8	0,96	0,11	0,139																14,9			27,2	1,82	1,78	9,25
76123	5,5	2631	40,0			76,1																				16,0						
76125	6,5	1878	37,0	0,5	37,5	80,4																				14,8			40,9	2,74	2,19	9,10
76127	4,5	1610	26,1	0,5	26,6	83,6																				10,5			36,4	2,24	2,40	9,60
76128	6,5	1712	26,0			71,0																				10,4						
76132		1430																														
76135	4,5	1895	44,0			49,2																				17,6						
76136	5,5	1649	42,0			48,4																				16,8						
77191	21,5	1254				84,4																										
77194	11,5	1222				79,6																										
77200	4,5	2910	58,0			50,8																				23,2						
77202	8	2427	52,0			40,4																				20,8						
77203	0-20	2442	35,0			49,0																				14,0						
422	0-10	2732	12,4	2,5	14,9	61,0	15,7	2,05	0,26	0,180	45,0	0,62	12,83	6,24	0,084	5,44	7,7	0,238	21,0	0,373	6,79	4,36	0,065	3,28	5,5	5,0	0,6	0,052	43,2	2,11	2,87	14,20
KS8	2-4	2900	11,2	2,7	13,9	54,8		1,62	0,20	0,135																4,5			38,6	1,95	3,41	20,20
243	0-3	1041	55,5	0,2	55,7			2,58	0,24	0,192	22,7	0,30	4,28	1,70	0,027	3,38	34,4	0,181	10,6	0,178	2,26	1,19	0,021	2,04	24,6	22,2	2,4	0,040	11,3	1,64	0,91	10,50
280	0-3	2106	36,0	3,6	39,6		25,7	1,95	0,22	0,188	30,4	0,54	7,79	4,74	0,243	3,82	24,0	0,215	14,2	0,322	4,12	3,32	0,188	2,30	17,1	14,4	2,7	0,047	18,1	2,34	1,61	12,50

Appendix 1, Table 1) Chemical composition at the sediment surface. Concentration values in the bulk fraktion (% or ppm), concentration values expressed on a carbonate and opal free basis (% or ppm, cofb)

	87	85	84	86	675	676	677	700	81	679	680	681	83	682	1	82	684	685	686	687	688	689	650	651	652	653	654	655	656	691	654	655
core	Cr	Co	Ni	Cu	Zn	Ga	As	Rb	Sr	Y	Zr	Nb	Mo	Cd	Cs	Ba	La	Ce	Pr	Nd	Sm	Eu	Gd	Tb	Dy	Ho	Er	Tm	Yb	Lu	Hf	Tl
	ppm	ppm	ppm	ppm	ppm	ppm	ppm	ppm	ppm	ppm	ppm	ppm	ppm	ppm	ppm	ppm	ppm	ppm	ppm	ppm	ppm	ppm	ppm	ppm	ppm	ppm	ppm	ppm	ppm	ppm	ppm	ppm
15KL	44,6	18,96	106,2	63,0	45,4	5,87	6,47	28,2	1155	19,1	41,1	5,12	3,04	0,292	2,10	732	11,60	17,9	2,74	10,68	2,20	0,544	2,30	0,340	2,18	0,482	1,420	0,220	1,420	0,220	1,04	0,24
26KL	67,2	18,64	83,4	75,4	68,8	8,35	7,78	41,2	955	19,2	52,6	6,92	2,38	0,264	2,98	682	14,50	24,4	3,34	12,68	2,68	0,637	2,80	0,400	2,48	0,518	1,520	0,220	1,500	0,220	1,34	0,24
36KL	41,2	8,93	36,1	28,6	36,2	4,57	3,04	23,0	980	11,9	27,5	3,60	0,45	0,207	1,72	294	8,46	13,6	1,87	7,26	1,53	0,367	1,58	0,260	1,48	0,331	0,980	0,140	0,920	0,140	0,73	0,12
51KL	83,4	20,70	95,2	53,0	74,3	9,23	5,20	54,1	746	16,8	53,6	7,18	1,19	0,213	4,08	603	14,90	26,7	3,36	12,60	2,64	0,606	2,59	0,400	2,31	0,507	1,510	0,200	1,420	0,220	1,48	0,32
57KL	105,0	35,50	151,0	83,0	132,0	10,60	5,74	60,1	618	21,4	68,4	15,90	2,64	0,340	4,27	904	17,20	31,7	4,00	14,40	3,03	0,705	2,98	0,430	2,67	0,575	1,770	0,250	1,760	0,250	2,43	0,53
64KL																																
70KL																																
71KL	103,0	14,40	108,0	40,4	56,2	6,26	4,80	29,7	862	12,3	40,6	4,96	2,75	0,884	2,02	438	9,74	17,9	2,26	8,78	1,92	0,452	1,88	0,300	1,74	0,359	1,080	0,150	0,980	0,160	1,03	0,26
74KL	41,8	11,80	84,2	51,5	93,1	5,25	2,28	19,1	977	13,1	33,2	4,20	1,08	0,689	1,37	1256	8,82	14,7	1,99	7,87	1,75	0,443	1,75	0,290	1,67	0,374	1,130	0,170	1,110	0,180	0,91	0,39
79KL	63,0	26,10	155,0	104,0	152,0	8,56	2,95	30,5	773	20,6	55,7	5,89	2,68	0,168	2,11	1604	14,80	26,0	3,49	13,50	3,02	0,745	3,13	0,510	2,94	0,625	1,830	0,270	1,820	0,290	1,36	0,25
82KL	46,4	26,80	109,2	79,2	77,0	6,70	5,48	25,6	694	19,4	44,6	5,78	5,28	0,316	1,76	922	12,82	21,6	3,12	11,90	2,74	0,657	2,80	0,400	2,48	0,506	1,520	0,220	1,420	0,220	1,10	0,18
87KL	32,8	11,10	84,0	51,7	41,5	3,43	1,76	12,3	1246	13,2	21,7	2,77	2,15	0,171	0,81	881	8,50	11,1	1,90	7,62	1,72	0,427	1,74	0,280	1,71	0,372	1,130	0,160	1,010	0,160	0,49	0,13
5KL																																
11KL	18,2	7,68	33,8	54,6	26,1	3,17	2,62	14,5	1185	16,4	22,4	7,60	1,05	0,207	1,02	853	9,89	12,9	2,26	8,79	2,01	0,483	2,02	0,320	1,97	0,422	1,190	0,170	1,160	0,170	0,86	0,27
18KL	11,1	6,12	19,6	37,7	10,1	1,95	1,47	8,4	1208	14,7	13,2	3,57	0,69	0,199	0,64	914	7,74	8,7	1,71	7,20	1,64	0,425	1,79	0,270	1,62	0,374	1,050	0,160	0,970	0,160	0,47	0,14
105KK	33,4	6,68	41,0	39,6	81,6	4,52	1,53	16,3	1158	14,8	30,6	3,60	0,66	0,312	0,94	762	9,46	13,4	2,12	8,20	1,76	0,406	1,82	0,250	1,68	0,336	1,020	0,120	1,020	0,120		
114KK	25,4	9,48	33,6	50,0	64,8	4,94	2,18	17,8	1141	15,8	36,6	4,78	0,78	0,199	0,92	774	11,34	16,6	2,66	10,20	2,08	0,501	2,18	0,300	1,94	0,391	1,200	0,140	1,120	0,140	0,78	
143KK	48,4	9,24	34,6	29,4	108,8	9,04	1,84	39,6	1091	16,9	81,8	14,20	0,78	0,329	1,68	362	17,60	33,6	4,12	15,58	3,18	0,730	2,90	0,440	2,44	0,514	1,460	0,200	1,320	0,200	2,00	0,26
182SK	44,6	13,32	50,6	39,2	92,4	5,68	3,46	28,4	1022	15,6	30,2	3,80	0,80	0,243	1,86	1052	11,80	19,8	2,56	10,26	2,04	0,522	2,08	0,300	1,84	0,391	1,160	0,140	1,100	0,140	0,64	
223SK	68,0	16,58	69,0	45,2	98,2	8,78	7,62	53,0	796	17,3	48,6	6,66	0,32	0,176	3,76	448	15,30	28,0	3,60	12,58	2,92	0,594	2,74	0,380	2,32	0,460	1,400	0,180	1,320	0,180	1,12	
232SK	85,5	20,30	100,0	64,2	86,3	10,20	3,43	59,8	659	18,0	58,7	9,91	0,73	0,461	4,80	686	16,80	30,2	3,85	14,90	3,04	0,637	2,81	0,420	2,49	0,529	1,540	0,230	1,570	0,230	1,74	0,47
76123																																
76125	73,6	14,80	74,5	49,8	227,0	10,10	2,77	47,1	716	18,4	46,6	6,75	0,67	0,880	2,86	1097	16,90	31,0	3,82	14,70	2,71	0,642	2,67	0,410	2,52	0,483	1,470	0,200	1,410	0,200	1,29	0,36
76127	113,0	23,70	101,0	60,8	11481,0	10,80	9,15	54,4	508	15,3	52,8	7,58	26,60	1,300	3,74	692	15,20	29,6	3,62	13,20	2,48	0,582	2,41	0,370	2,18	0,441	1,300	0,170	1,280	0,180	1,46	0,39
76128																																
76132																																
76135																																
76136																																
77191																																
77194																																
77200																																
77202																																
77203																																
422	157,0	25,80	163,0	51,5	131,0	14,70	3,99	92,0	251	17,6	90,4	11,60	0,61	0,300	7,26	451	20,30	40,0	4,63	17,60	3,62	0,836	3,41	0,520	3,2	0,664	1,980	0,290	1,960	0,290	2,54	0,50
KS8	162,0	23,80	161,0	53,2	100,0	15,80	3,62	104,0	200	18,8	83,5	10,20	1,08	0,361	8,53	417	24,40	48,5	5,50	20,40	3,98	0,869	3,62	0,550	3,17	0,656	1,990	0,280	1,950	0,300	2,48	0,66
243	92,2	6,92	51,5	23,9	67,5	9,67	2,29	21,2	680	11,4	46,3	4,57	0,79	0,397	1,12	178	8,83	15,8	2,09	8,22	1,72	0,411	1,75	0,280	1,57	0,349	0,980	0,140	0,970	0,140	1,19	0,15
280	75,0	12,60	115,0	51,0	125,0	5,00	4,09	43,9	669	19,5	72,4	10,30	1,90	0,300	2,66	1119	17,20	33,0	3,93	14,90	3,13	0,752	3,02	0,480	2,76	0,578	1,710	0,240	1,580	0,250	1,79	0,42

Appendix 1, Table 1) continued (sediment surface samples)

core	Pb	U	Corg	N	S	Si opal cor	Ti	Al	Fe	Mn	Mg	Ca, lith.	P	Li	Na	K	Sc	Cr	Co	Ni	Cu	Zn	Ga	As	Pb	Sr/Ca	Y	Zr	Nb	Mo	Cd	Cs
	ppm	ppm	% cofb	% cofb	% cofb	% cofb	% cofb	% cofb	% cofb	% cofb	% cofb	% cofb	% cofb	ppm cofb	% cofb	% cofb	ppm cofb	ppm cofb	ppm cofb	ppm cofb	ppm cofb	ppm cofb	ppm cofb	ppm cofb	ppm cofb	ppm cofb		ppm cofb	ppm cofb	ppm cofb	ppm cofb	ppm cofb	ppm cofb
15KL	6,92	0,72	2,48	0,21	0,30	19,9	0,459	6,66	4,54	0,529	3,30	11,1	0,144	47,3	3,96	4,42	16,9	133	56,6	317	188	136	17,5	19,3	84,2	44,7	57,0	123	15,3	9,07	0,87	6,27
26KL	8,54	0,98	1,33	0,18	0,09	23,2	0,588	8,12	5,73	0,229	3,54	6,2	0,102	36,4	3,81	4,26	17,6	154	42,8	191	173	158	19,2	17,8	94,5	44,2	44,0	121	15,9	5,46	0,61	6,83
36KL	5,62	0,67	1,54	0,19	0,33	23,0	0,556	7,62	5,51	0,121	3,77	19,7	0,122	76,5	5,17	2,92	36,7	154	33,4	135	107	136	17,1	11,4	86,1	33,9	44,6	103	13,5	1,69	0,78	6,44
51KL	12,20	1,41	1,21	0,19	0,17									42,9	3,45	2,99	26,8	158	39,1	180	100	140	17,4	9,8	102,3	40,9	31,8	101	13,6	2,25	0,40	7,71
57KL	15,30	1,83	2,00	0,25	0,21	23,8	0,437	7,22	4,73	0,597	3,73	2,4	0,084	38,8	3,42	2,84	19,1	163	55,1	234	129	205	16,5	8,9	93,3	46,5	33,2	106	24,7	4,10	0,53	6,63
64KL																																
70KL																																
71KL	6,34	4,45	4,79	0,42	1,06									38,1	4,15	2,45	22,3	216	30,3	227	85	118	13,2	10,1	62,4	45,0	25,8	85	10,4	5,78	1,86	4,24
74KL	6,88	4,90	4,44	0,53	0,62	19,2	0,377	5,37	3,83	0,215	4,09	10,1	0,109	39,9	6,06	2,15	26,1	123	34,7	248	151	274	15,4	6,7	56,2	41,4	38,5	98	12,4	3,18	2,03	4,03
79KL	12,20	1,17	3,11	0,35	0,54									26,4	6,26	2,27	30,0	123	50,8	302	202	296	16,7	5,7	59,3	46,9	40,1	108	11,5	5,21	0,33	4,11
82KL	8,36	0,78	2,59	0,22	0,51	20,0	0,386	5,53	4,00	1,399	3,47	5,7	0,092	13,6	4,85	2,96	12,3	93	53,8	219	159	155	13,5	11,0	51,4	38,4	39,0	90	11,6	10,60	0,63	3,53
87KL	4,41	0,51	1,98	0,28	0,98	16,5	0,383	5,67	4,15	1,407	3,60	18,7	0,146	74,8	9,90	2,38	39,6	155	52,4	396	244	196	16,2	8,3	58,0	41,8	62,3	102	13,1	10,14	0,81	3,82
5KL																																
11KL	5,98	0,41	2,26	0,26	0,91									81,3	8,15	2,35	16,1	93	39,4	173	280	134	16,3	13,4	74,4	38,3	84,1	115	39,0	5,38	1,06	5,23
18KL	3,22	0,30	2,52	0,41	1,43	10,3	0,311	5,00	4,41	0,276	3,25	45,9	0,144	128,9	12,34	2,11	16,8	90	49,8	159	307	82	15,9	12,0	68,1	35,3	119,5	107	29,0	5,61	1,62	5,20
105KK	4,56	2,30	5,35	0,44	0,53	18,1	0,414	5,60	4,03	0,130	3,61	12,4	0,119	24,7	6,95	4,09	16,6	122	24,5	150	145	299	16,6	5,6	59,6	44,0	54,2	112	13,2	2,42	1,14	3,44
114KK	12,94	1,20	2,89	0,45	0,57	18,7	0,495	6,45	4,50	0,286	3,10	11,1	0,159	42,5	6,14		18,5	95	35,6	126	188	244	18,6	8,2	66,9	42,2	59,4	138	18,0	2,93	0,75	3,46
143KK	7,58	2,16	3,15	0,34	0,30	23,3	0,747	7,82	5,37	0,056	2,14	4,8	0,074	13,6	3,49	3,36	15,7	98	18,7	70	59	220	18,3	3,7	80,0	56,2	34,1	165	28,7	1,58	0,66	3,39
182SK	7,30	0,66	1,90	0,28	0,51	13,4	0,337	5,54	3,67	0,199	2,08	-14,8	0,098	58,0	4,81	3,30	16,7	127	37,8	144	111	263	16,1	9,8	80,7	41,1	44,3	86	10,8	2,27	0,69	5,28
223SK	10,20	1,38	1,27	0,15	0,22	24,6	0,529	7,76	5,45	0,141	3,14	3,2	0,086	38,6	3,13	3,90	16,5	129	31,3	130	85	186	16,6	14,4	100,2	43,2	32,7	92	12,6	0,60	0,33	7,11
232SK	13,80	2,27	1,57	0,18	0,23									44,4	2,97	2,90	15,1	139	33,1	163	105	141	16,6	5,6	97,6	44,1	29,4	96	16,2	1,19	0,75	7,83
76123																																
76125	11,10	6,22												65,4	4,38	3,51	14,6	118	23,7	119	80	363	16,2	4,4	75,4	48,3	29,4	75	10,8	1,07	1,41	4,58
76127	100,00	9,62												49,5	3,05	3,27	13,1	154	32,3	138	83	15642	14,7	12,5	74,1	48,6	20,8	72	10,3	36,24	1,77	5,10
76128																																
76132																																
76135																																
76136																																
77191																																
77194																																
77200																																
77202																																
77203																																
422	18,10	3,16	2,41	0,31	0,21	23,4	0,439	7,98	5,13	0,076	3,86	0,7	0,061	50,7	2,48	3,37	16,7	184	30,3	192	61	154	17,3	4,7	108,1	50,6	20,7	106	13,6	0,72	0,35	8,53
KS8	17,30	3,06	1,88	0,23	0,16									44,9	2,27	3,96	23,5	188	27,6	187	62	116	18,4	4,2	120,8	44,6	21,8	97	11,8	1,25	0,42	9,91
243	3,79	2,47	5,82	0,54	0,43	23,8	0,401	5,11	2,68	0,047	4,61	5,3	0,089	25,5	3,71	2,06	23,7	208	15,6	116	54	152	21,8	5,2	47,9	30,6	25,7	105	10,3	1,78	0,90	2,53
280	9,92	2,15	3,23	0,36	0,31	20,7	0,534	6,82	5,49	0,311	3,81	4,5	0,078	30,0	3,87	2,67	20,7	124	20,9	190	84	207	8,3	6,8	72,7	46,4	32,3	120	17,1	3,15	0,50	4,40

Appendix 1, Table 1) continued (sediment surface samples)

core	Ba	La	Ce	Pr	Nd	Sm	Eu	Gd	Tb	Dy	Ho	Er	Tm	Yb	Lu	Hf	Tl	Pb	U
	ppm cofb	ppm cofb	ppm cofb	ppm cofb	ppm cofb	ppm cofb	ppm cofb	ppm cofb	ppm cofb	ppm cofb	ppm cofb	ppm cofb	ppm cofb	ppm cofb	ppm cofb	ppm cofb	ppm cofb	ppm cofb	ppm cofb
15KL	2185	34,6	53,6	8,18	31,9	6,57	1,62	6,87	1,015	6,51	1,44	4,24	0,657	4,24	0,657	3,10	0,716	20,7	2,15
26KL	1564	33,3	56,0	7,66	29,1	6,15	1,46	6,42	0,917	5,69	1,19	3,49	0,505	3,44	0,505	3,07	0,550	19,6	2,25
36KL	1101	31,7	50,9	7,00	27,2	5,73	1,37	5,92	0,974	5,54	1,24	3,67	0,524	3,45	0,524	2,73	0,449	21,0	2,51
51KL	1140	28,2	50,5	6,35	23,8	4,99	1,15	4,90	0,756	4,37	0,96	2,85	0,378	2,68	0,416	2,80	0,605	23,1	2,67
57KL	1404	26,7	49,2	6,21	22,4	4,70	1,09	4,63	0,668	4,15	0,89	2,75	0,388	2,73	0,388	3,77	0,823	23,8	2,84
64KL																			
70KL																			
71KL	920	20,5	37,6	4,75	18,4	4,03	0,95	3,95	0,630	3,66	0,75	2,27	0,315	2,06	0,336	2,16	0,546	13,3	9,35
74KL	3694	25,9	43,2	5,85	23,1	5,15	1,30	5,15	0,853	4,91	1,10	3,32	0,500	3,26	0,529	2,68	1,147	20,2	14,41
79KL	3121	28,8	50,6	6,79	26,3	5,88	1,45	6,09	0,992	5,72	1,22	3,56	0,525	3,54	0,564	2,65	0,486	23,7	2,28
82KL	1851	25,7	43,4	6,27	23,9	5,50	1,32	5,62	0,803	4,98	1,02	3,05	0,442	2,85	0,442	2,21	0,361	16,8	1,57
87KL	4156	40,1	52,4	8,96	35,9	8,11	2,01	8,21	1,321	8,07	1,75	5,33	0,755	4,76	0,755	2,31	0,613	20,8	2,41
5KL																			
11KL	4374	50,7	66,2	11,59	45,1	10,31	2,48	10,36	1,641	10,10	2,16	6,10	0,872	5,95	0,872	4,41	1,385	30,7	2,10
18KL	7431	62,9	70,9	13,90	58,5	13,33	3,46	14,55	2,195	13,17	3,04	8,54	1,301	7,89	1,301	3,82	1,138	26,2	2,44
105KK	2791	34,7	49,1	7,77	30,0	6,45	1,49	6,67	0,916	6,15	1,23	3,74	0,440	3,74	0,440			16,7	8,42
114KK	2910	42,6	62,3	10,00	38,3	7,82	1,88	8,20	1,128	7,29	1,47	4,51	0,526	4,21	0,526	2,93		48,6	4,51
143KK	731	35,6	67,9	8,32	31,5	6,42	1,47	5,86	0,889	4,93	1,04	2,95	0,404	2,67	0,404	4,04	0,525	15,3	4,36
182SK	2989	33,5	56,1	7,27	29,1	5,80	1,48	5,91	0,852	5,23	1,11	3,30	0,398	3,13	0,398	1,82		20,7	1,88
223SK	847	28,9	52,9	6,81	23,8	5,52	1,12	5,18	0,718	4,39	0,87	2,65	0,340	2,50	0,340	2,12		19,3	2,61
232SK	1119	27,4	49,3	6,28	24,3	4,96	1,04	4,58	0,685	4,06	0,86	2,51	0,375	2,56	0,375	2,84	0,767	22,5	3,70
76123																			
76125	1755	27,0	49,6	6,11	23,5	4,34	1,03	4,27	0,656	4,03	0,77	2,35	0,320	2,26	0,320	2,06	0,576	17,8	9,95
76127	943	20,7	40,3	4,93	18,0	3,38	0,79	3,28	0,504	2,97	0,60	1,77	0,232	1,74	0,245	1,99	0,531	136,2	13,11
76128																			
76132																			
76135																			
76136																			
77191																			
77194																			
77200																			
77202																			
77203																			
422	530	23,9	47,0	5,44	20,7	4,25	0,98	4,01	0,611	3,76	0,78	2,33	0,341	2,30	0,341	2,98	0,588	21,3	3,71
KS8	484	28,3	56,3	6,39	23,7	4,62	1,01	4,20	0,639	3,68	0,76	2,31	0,325	2,26	0,348	2,88	0,767	20,1	3,55
243	402	19,9	35,7	4,72	18,6	3,88	0,93	3,95	0,632	3,54	0,79	2,21	0,316	2,19	0,316	2,69	0,339	8,6	5,58
280	1853	28,5	54,6	6,51	24,7	5,18	1,25	5,00	0,795	4,57	0,96	2,83	0,397	2,62	0,414	2,96	0,695	16,4	3,56

Appendix 1, Table 1) continued (sediment surface samples)

core	depth	w.depth	CaCO3	Opal	Biogenic	< 2 µm	area	Corg	N	S	SiO2	TiO2	Al2O3	Fe2O3	MnO	MgO	CaO	P2O5	Si	Ti	Al	Fe	Mn	Mg	Ca, bulk	Ca, mar.	Ca, lith.	P	Li	Na	K	Sc
	cm	m	%	%	%	%	m2	%	%	%	wt%	wt%	wt%	wt%	wt%	wt%	wt%	wt%	%	%	%	%	%	%	%	%	%	%	ppm	%	%	ppm
15KL	16-20	3920	69,1	1,1	70,2	54,6	15,7	0,48	0,06	0,113	15,3	0,24	4,11	2,11	0,055	1,91	43,7	0,151	7,1	0,146	2,17	1,48	0,042	1,15	31,2	27,7	3,6	0,033	22,7	1,47	0,82	6,70
26KL	15-19	3776	59,9	2,2	62,1	64,0	29,6	0,55	0,06	0,135	19,8	0,47	5,71	3,61	0,105	2,13	36,6	0,168	9,2	0,281	3,02	2,53	0,081	1,29	26,1	24,0	2,2	0,037	34,1	1,68	0,96	9,86
36KL	8-12	2055	62,4	1,1	63,5	51,5	17,0	0,38	0,04	0,103	19,2	0,33	5,16	2,72	0,055	2,16	37,8	0,181	9,0	0,198	2,73	1,90	0,043	1,30	27,0	25,0	2,0	0,040	25,0	1,37	1,00	7,28
51KL	28-32	2644	54,4	1,0	55,4	51,0	16,0	0,53	0,06	0,139	24,7	0,36	6,49	3,26	0,058	2,63	33,9	0,180	11,6	0,215	3,43	2,28	0,045	1,59	24,2	21,8	2,4	0,039	22,7	1,72	1,35	6,89
57KL	28-32	3422	50,0	1,2	51,2	52,4	18,7	0,59	0,08	0,105																20,0			25,0	1,61	1,43	8,43
64KL	8-12	3281	58,8	1,4	60,2	52,0	17,0	0,66	0,07	0,122																23,5			22,7	1,63	1,06	7,31
70KL	18-22	3810	61,2	1,4	62,6	51,6	18,4	0,67	0,06	0,112	20,0	0,28	4,83	2,35	0,090	2,83	37,5	0,183	9,3	0,171	2,56	1,64	0,070	1,70	26,8	24,5	2,3	0,040	25,0	1,58	1,10	5,76
71KL	38-40	4029	67,8	3,0	70,8	55,6	18,3	0,65	0,05	0,114	16,5	0,20	3,44	1,77	0,119	2,15	41,8	0,170	7,7	0,120	1,82	1,24	0,092	1,29	29,9	27,1	2,7	0,037	20,4	1,54	0,81	5,07
74KL	62-66	3212	66,8	5,7	72,5	61,0	17,8	1,16	0,12	0,208	16,2	0,15	2,63	1,46	0,098	2,01	41,7	0,155	7,6	0,092	1,39	1,02	0,076	1,21	29,8	26,7	3,1	0,034	18,1	1,93	0,91	3,79
79KL	38-42	4351	66,5	4,0	70,5	59,0	19,9	0,88	0,08	0,134	16,3	0,18	3,20	1,77	0,185	2,14	42,0	0,154	7,6	0,111	1,69	1,24	0,143	1,29	30,0	26,6	3,4	0,034	20,4	1,65	0,77	4,80
82KL	8-10	4416	54,3	7,1	61,4	63,0	36,3	1,07	0,11	0,167																21,7			20,4	1,91	0,95	6,75
87KL	58-62	3773	75,5	5,0	80,5	66,8	16,7	0,59	0,06	0,141	12,0	0,12	1,98	1,22	0,057	1,24	46,6	0,146	5,6	0,072	1,05	0,85	0,044	0,75	33,3	30,2	3,1	0,032	18,1	1,56	0,48	3,00
5KL		3335																														
11KL	11-14	3859	79,7	2,8	82,5	71,0	17,0	0,19	0,05	0,121	9,4	0,14	2,42	1,46	0,126	0,95	48,8	0,142	4,4	0,086	1,28	1,02	0,097	0,58	34,9	31,9	2,9	0,031	20,4	1,24	0,47	4,51
18KL	17-21	3035	83,2	2,5	85,7	73,0	9,1	0,36	0,01	0,157	5,9	0,08	1,42	0,91	0,055	0,67	52,6	0,146	2,8	0,046	0,75	0,64	0,043	0,41	37,6	33,3	4,3	0,032	15,9	1,22	0,31	1,77
105KK	57-62	3535	72,2	7,7	79,9	74,0	16,2	0,82	0,09	0,181	14,6	0,15	2,10	1,12	0,026	1,34	45,6	0,158	6,8	0,089	1,11	0,78	0,020	0,81	32,6	28,9	3,7	0,035	13,6	1,81	0,48	3,40
114KK	44-48	3843	70,8	5,2	76,0	74,8	21,2	0,86	0,07	0,133	14,0	0,21	2,79	1,48	0,026	1,25	44,1	0,134	6,5	0,125	1,48	1,04	0,020	0,75	31,5	28,3	3,1	0,029	20,4	1,52	0,60	4,04
143KK	156-162	1522	41,4	2,1	43,5	63,6	43,2	1,21	0,10	0,252	29,3	0,85	8,54	4,90	0,044	2,22	24,5	0,193	13,7	0,510	4,52	3,43	0,034	1,34	17,5	16,6	0,9	0,042	27,2	1,78	1,57	16,02
182SK	27-32	2234	44,9	1,4	46,3	73,0	25,9	0,83	0,07	0,137	27,4	0,48	8,45	4,38	0,051	2,79	28,1	0,177	12,8	0,286	4,47	3,06	0,040	1,68	20,1	18,0	2,1	0,039	40,9	1,86	1,71	9,66
223SK	19-14	2686	53,2	2,4	55,6	51,0	12,7	0,53	0,06	0,109	24,3	0,39	6,41	3,36	0,064	2,43	31,7	0,214	11,4	0,234	3,39	2,35	0,049	1,46	22,7	21,3	1,4	0,047	27,2	1,76	1,34	8,84
232SK	22-27	3098	46,6	1,5	48,1	48,5	16,1	0,54	0,06	0,107	30,0	0,41	8,06	3,71	0,075	3,00	27,9	0,233	14,0	0,246	4,27	2,60	0,058	1,81	20,0	18,7	1,3	0,051	29,5	1,63	1,70	8,68
76123	18,5	2631	45,0	0,5	45,5	82,3																				18,0			34,1	2,10	1,96	7,94
76125	50,5	1878	41,0	0,5	41,5	80,0																				16,4			34,1	2,00	1,96	13,40
76127	18	1610	23,9	0,5	24,4	78,0																				9,6			29,5	3,42	2,53	18,70
76128	77	1712	23,2	0,2	23,4	81,2																				9,3			59,1	2,23	2,70	24,40
76132	18,5	1430	63,0	0,2	63,2	70,5																				25,2			36,4	2,15	0,69	5,34
76135	108,5	1895	55,0	0,4	55,4	70,7																				22,0			11,3	1,71	1,44	5,01
76136	38,5	1649	37,0	0,4	37,4	28,0																				14,8			15,9	1,80	1,53	7,34
77191	401,5	1254	55,5	0,5	56,0	86,0																				22,2			29,5	1,84	1,66	6,81
77194	149	1222	11,8	0,5	12,3	84,4																				4,7			79,6	2,69	2,79	17,30
77200	18,5	2910				51,3																										
77202	53,5	2427	57,0			50,8																				22,8						
77203	75	2442	36,5	2,6	39,1	58,7																				14,6			18,1	1,86	1,35	6,41
422	126-130	2732	25,2	2,7	27,9	60,9	20,1	0,56	0,12	0,235	41,0	0,58	12,02	5,78	0,091	5,32	13,3	0,250	19,1	0,345	6,36	4,04	0,071	3,21	9,5	10,1	-0,6	0,055	47,7	1,87	2,79	11,50
KS8	105-112	2900	23,3	1,3	24,6	55,0		0,99	0,99	0,229																9,3			36,4	1,99	2,55	10,90
243	60	1041	54,1	1,6	55,7		9,0	2,31	0,18	0,240	24,1	0,32	4,41	1,78	0,028	3,47	35,2	0,147	11,3	0,191	2,33	1,24	0,022	2,09	25,2	21,7	3,5	0,032	11,3	1,42	0,90	12,40
280	60	2106	60,1	2,4	62,5		17,8	1,18	0,11	0,194	18,5	0,32	4,62	2,81	0,171	2,52	38,8	0,178	8,7	0,189	2,44	1,97	0,133	1,52	27,7	24,1	3,6	0,039	18,1	1,76	0,98	7,70

Appendix 1, Table 2) Chemical composition at the depth level of the early Holocene (8000-10,000 cal-yrBP). Concentration values in the bulk fraktion (% or ppm), concentration values expressed on a carbonate and opal free basis (% or ppm, cofb)

core	Cr	Co	Ni	Cu	Zn	Ga	As	Rb	Sr	Y	Zr	Nb	Mo	Cd	Cs	Ba	La	Ce	Pr	Nd	Sm	Eu	Gd	Tb	Dy	Ho	Er	Tm	Yb	Lu	Hf	Tl
	ppm	ppm	ppm	ppm	ppm	ppm	ppm	ppm	ppm	ppm	ppm	ppm	ppm	ppm	ppm	ppm	ppm	ppm	ppm	ppm	ppm	ppm	ppm	ppm	ppm	ppm	ppm	ppm	ppm	ppm	ppm	ppm
15KL	49,3	9,83	50,7	48,5	46,9	6,35	4,40	29,3	1195	13,3	31,1	5,40	0,58	0,165	1,88	502	9,38	16,2	2,11	8,65	1,77	0,419	1,70	0,268	1,63	0,355	1,050	0,163	1,040	0,157	0,86	0,12
26KL	64,1	14,20	47,8	57,3	52,0	8,56	2,24	36,1	4040	11,7	41,6	5,66	0,68	0,113	2,24	263	10,40	19,0	2,42	9,93	2,03	0,514	2,05	0,304	1,77	0,365	1,010	0,147	0,969	0,141	1,18	0,18
36KL	55,0	13,50	47,3	27,7	49,7	7,71	4,32	37,0	1124	13,1	36,0	5,74	0,51	0,221	2,47	260	11,50	20,4	2,72	10,40	2,07	0,475	1,97	0,299	1,81	0,375	1,100	0,160	1,040	0,156	0,94	0,16
51KL	62,4	14,90	64,6	40,5	48,8	7,61	2,69	46,0	828	15,7	47,6	8,15	0,46	0,446	3,57	572	12,30	22,0	2,77	10,50	2,22	0,500	2,18	0,317	1,94	0,420	1,240	0,181	1,230	0,182	1,35	0,27
57KL	86,2	15,20	101,0	60,0	85,4	9,71	2,55	52,3	802	14,3	47,7	7,12	0,42	0,414	3,81	693	13,60	25,6	3,13	11,80	2,40	0,534	2,24	0,342	2,03	0,446	1,320	0,196	1,310	0,204	1,41	0,40
64KL	65,5	14,90	60,3	52,3	58,1	7,77	4,42	40,3	1020	15,5	40,8	6,10	0,53	0,153	2,91	639	12,90	21,7	2,83	11,50	2,35	0,550	2,28	0,348	2,13	0,446	1,350	0,198	1,390	0,215	1,16	0,17
70KL	62,0	10,20	90,6	46,0	74,0	6,53	1,83	35,0	1013	11,8	36,7	5,30	0,30	0,564	2,53	394	10,20	19,3	2,32	9,50	1,85	0,437	1,82	0,281	1,64	0,344	1,010	0,150	1,020	0,156	1,06	0,40
71KL	46,4	14,80	141,0	62,3	103,0	5,74	3,37	24,3	1202	12,9	31,8	4,03	1,15	0,919	1,71	700	8,96	15,5	2,03	8,05	1,69	0,420	1,76	0,271	1,73	0,360	1,070	0,160	1,120	0,173	0,83	0,58
74KL	34,1	10,50	82,4	48,1	93,1	4,68	2,59	16,6	1186	11,8	27,3	3,04	1,49	0,745	1,14	1151	7,42	12,2	1,65	6,91	1,41	0,375	1,52	0,231	1,47	0,316	0,953	0,136	0,987	0,151	0,67	0,40
79KL	39,1	15,20	117,0	69,2	99,8	6,14	2,69	22,2	1240	13,1	32,3	3,91	0,71	0,684	1,64	799	8,61	15,1	1,99	8,02	1,78	0,426	1,78	0,271	1,71	0,367	1,080	0,155	1,080	0,170	0,74	0,59
82KL	47,7	17,20	118,4	104,0	105,0	7,93	2,53	30,0	1004	19,5	45,4	6,63	0,52	0,769	2,05	987	14,20	23,4	3,39	13,60	2,83	0,690	2,96	0,450	2,74	0,575	1,670	0,237	1,610	0,243	1,22	0,49
87KL	21,0	6,96	51,9	50,1	46,9	3,73	1,84	13,8	1292	10,8	20,0	2,92	0,55	0,619	0,92	690	6,77	10,5	1,55	6,57	1,34	0,345	1,46	0,221	1,38	0,291	0,859	0,127	0,847	0,128	0,51	0,25
5KL																																
11KL	23,0	7,47	37,1	60,4	37,2	4,13	1,99	16,2	1338	15,9	23,6	4,13	0,80	0,234	0,94	800	9,82	13,7	2,24	9,00	1,89	0,476	2,01	0,309	1,88	0,414	1,230	0,171	1,170	0,178	0,61	0,08
18KL	8,4	6,27	14,1	34,0	8,6	1,49	1,50	6,5	1229	13,8	9,5	3,49	0,36	0,276	0,45	881	7,58	7,1	1,63	6,72	1,48	0,386	1,65	0,248	1,5	0,328	0,952	0,134	0,913	0,130	0,35	0,06
105KK	20,9	4,45	29,8	35,9	54,7	4,23	0,99	12,7	1279	10,3	25,6	3,94	0,40	0,479	0,74	567	7,21	10,3	1,56	6,44	1,31	0,331	1,41	0,211	1,32	0,284	0,822	0,114	0,794	0,121	0,63	0,09
114KK	21,6	5,47	32,4	44,8	42,6	5,05	1,24	17,1	1155	11,0	33,5	5,80	0,44	0,465	0,93	581	8,57	13,7	2,01	7,98	1,64	0,381	1,64	0,248	1,53	0,315	0,900	0,131	0,864	0,132	0,87	0,14
143KK	98,8	20,40	72,0	48,6	138,0	21,70	3,54	85,0	1462	10,4	59,4	9,18	1,46	0,386	3,84	598	38,80	78,4	9,70	36,90	7,32	1,730	6,46	0,978	5,6	1,080	3,080	0,451	2,960	0,432	1,54	0,36
182SK	78,5	12,20	75,2	43,1	79,1	11,60	4,09	60,9	858	17,7	56,7	10,40	0,64	0,358	4,27	679	17,20	30,9	3,86	14,70	3,00	0,686	2,88	0,426	2,53	0,526	1,520	0,220	1,480	0,222	1,82	0,31
223SK	64,8	12,20	58,8	50,1	62,0	8,15	2,36	46,5	868	13,7	44,9	9,01	1,14	0,486	3,53	455	13,10	24,3	3,21	13,10	2,45	0,616	2,73	0,430	2,54	0,513	1,430	0,219	1,270	0,237	1,74	0,24
232SK	77,5	14,00	79,6	47,5	72,1	9,96	2,72	62,0	757	15,4	50,8	11,10	0,57	0,473	4,83	652	16,00	31,1	3,87	14,30	3,19	0,714	2,86	0,426	2,64	0,508	1,410	0,238	1,390	0,212	1,95	0,40
76123	60,6	9,87	59,1	39,7	245,0	9,87	3,80	42,5	712	11,3	38,9	7,36	1,02	*	2,23	830	15,90	32,3	3,76	14,40	2,64	0,617	2,44	0,353	2,01	0,387	1,150	0,151	1,110	0,156	1,09	0,48
76125	81,1	23,00	79,4	80,3	115,0	12,50	4,04	49,0	716	17,6	40,0	6,89	2,71	0,749	3,24	1072	17,40	31,4	3,80	14,80	4,04	1,000	3,48	0,589	3,05	0,657	1,860	0,324	2,180	0,308	1,84	0,68
76127	119,0	34,60	98,5	105,0	2452,0	15,40	4,47	68,9	528	16,0	60,7	9,62	6,52	1,170	5,33	701	16,90	33,2	4,07	14,30	5,11	1,250	4,46	0,708	3,61	0,743	2,100	0,405	2,400	0,414	2,74	0,88
76128	147,0	38,30	104,0	124,0	178,0	19,10	4,94	85,7	554	18,5	77,8	11,70	6,29	0,543	6,33	598	19,40	37,1	4,60	17,70	6,56	1,600	5,23	0,824	3,92	0,880	2,540	0,514	3,070	0,507	3,07	0,95
76132	36,4	6,20	20,8	19,2	30,4	4,54	5,46	19,0	5237	5,6	26,4	4,36	0,54	0,070	1,20	53	5,66	11,8	1,50	6,08	1,36	0,341	1,22	0,196	1,17	0,226	0,678	0,088	0,555	0,081	0,78	0,08
76135	58,1	6,58	58,7	30,9	61,4	5,09	3,63	21,9	865	11,1	38,9	5,72	1,05	0,830	1,36	871	9,06	16,2	2,15	8,38	1,81	0,455	1,82	0,271	1,74	0,358	1,080	0,141	1,060	0,149	0,85	0,22
76136	69,8	9,20	48,5	22,9	64,8	8,78	2,83	42,8	659	12,7	60,6	10,80	1,83	0,322	2,03	300	14,70	30,6	3,66	14,40	2,93	0,697	2,72	0,421	2,41	0,484	1,370	0,203	1,300	0,184	1,74	0,25
77191	61,6	10,50	60,2	32,1	348,0	7,84	4,45	37,4	1069	12,8	33,0	5,31	10,30	0,964	1,61	346	16,70	30,1	3,69	13,40	2,32	0,477	2,18	0,301	1,81	0,348	1,010	0,133	0,898	0,131	0,82	0,28
77194	137,0	24,70	86,5	44,2	147,0	17,10	9,94	86,8	306	18,1	79,5	11,80	1,97	0,639	5,88	386	22,50	46,0	5,27	20,00	3,75	0,849	3,44	0,513	3,08	0,576	1,660	0,229	1,600	0,220	2,28	0,44
77200																																
77202																																
77203	101,0	10,40	89,1	31,5	66,9	7,09	5,29	35,1	611	9,6	40,6	6,01	2,95	0,709	2,56	558	10,60	20,9	2,50	9,81	1,94	0,474	1,82	0,273	1,67	0,344	1,020	0,148	1,050	0,151	1,14	0,20
422	133,0	19,80	145,0	40,2	103,0	13,30	4,36	83,0	429	19,7	81,5	10,20	1,07	0,416	6,80	440	17,80	37,4	4,24	16,10	2,98	0,711	2,73	0,416	2,46	0,507	1,480	0,220	1,510	0,227	2,31	0,47
KS8	131,0	17,00	138,0	34,1	89,3	13,00	4,02	79,1	516	18,7	79,7	10,90	0,68	0,393	6,32	358	17,00	35,3	4,12	15,30	2,99	0,682	2,64	0,405	2,38	0,480	1,400	0,211	1,400	0,211	2,08	0,43
243	99,8	7,51	53,1	23,6	39,2	5,13	4,55	21,3	727	11,0	45,3	4,86	0,87	0,657	1,08	201	8,76	15,8	2,09	8,07	1,73	0,435	1,71	0,274	1,61	0,320	0,945	0,135	0,962	0,144	1,22	0,22
280	48,6	10,70	101,0	49,7	112,0	20,00	2,54	27,1	1109	15,6	50,2	6,19	0,76	0,104	1,78	1309	11,20	20,5	2,49	9,51	2,02	0,511	2,02	0,318	1,97	0,410	1,300	0,171	1,220	0,190	1,18	0,55

Appendix 1, Table 2) continued (Early Holocene samples)

core	Pb	U	Corg	N	S	Si opal cor	Ti	Al	Fe	Mn	Mg	Ca, lith.	P	Li	Na	K	Sc	Cr	Co	Ni	Cu	Zn	Ga	As	Rb	Sr/Ca	Y	Zr	Nb	Mo	Cd	Cs
	ppm	ppm	% cofb	% cofb	% cofb	% cofb	% cofb	% cofb	% cofb	% cofb	% cofb	% cofb	% cofb	ppm cofb	% cofb	% cofb	ppm cofb	ppm cofb	ppm cofb	ppm cofb	ppm cofb	ppm cofb	ppm cofb	ppm cofb	ppm cofb	ppm cofb		ppm cofb	ppm cofb	ppm cofb	ppm cofb	ppm cofb	ppm cofb
15KL	5,83	0,66	1,61	0,20	0,38	22,2	0,489	7,29	4,95	0,142	3,86	12,0	0,111	76,1	4,95	2,76	22,5	165	33,0	170	163	157	21,3	14,8	98,3	43,2	44,6	104	18,1	1,95	0,55	6,31
26KL	6,63	2,51	1,45	0,16	0,35	21,7	0,741	7,98	6,67	0,215	3,40	5,7	0,097	89,9	4,43	2,54	26,0	169	37,5	126	151	137	22,6	5,9	95,3	168,4	30,9	110	14,9	1,79	0,30	5,91
36KL	7,34	0,97	1,04	0,11	0,28	23,2	0,542	7,48	5,21	0,117	3,56	5,5	0,108	68,4	3,74	2,73	19,9	151	37,0	130	76	136	21,1	11,8	101,4	45,0	35,9	99	15,7	1,40	0,61	6,77
51KL	8,52	2,15	1,19	0,13	0,31	24,9	0,482	7,70	5,11	0,101	3,56	5,4	0,088	50,9	3,86	3,03	15,4	140	33,4	145	91	109	17,1	6,0	103,1	38,0	35,2	107	18,3	1,03	1,00	8,00
57KL	10,30	3,20	1,21	0,16	0,22									51,2	3,29	2,93	17,3	177	31,1	207	123	175	19,9	5,2	107,2	40,1	29,3	98	14,6	0,86	0,85	7,81
64KL	9,48	0,87	1,66	0,18	0,31									57,0	4,09	2,66	18,4	165	37,4	152	131	146	19,5	11,1	101,3	43,3	38,9	103	15,3	1,33	0,38	7,31
70KL	7,23	3,93	1,79	0,16	0,30	23,2	0,456	6,84	4,39	0,186	4,56	6,1	0,107	66,8	4,22	2,94	15,4	166	27,3	242	123	198	17,5	4,9	93,6	41,3	31,6	98	14,2	0,80	1,51	6,76
71KL	6,74	5,53	2,23	0,17	0,39	21,6	0,409	6,23	4,24	0,316	4,43	9,4	0,127	69,9	5,26	2,76	17,4	159	50,7	483	213	353	19,7	11,5	83,2	44,3	44,2	109	13,8	3,94	3,15	5,86
74KL	5,93	4,26	4,22	0,44	0,75	17,8	0,333	5,07	3,70	0,277	4,40	11,2	0,123	65,9	7,01	3,31	13,8	124	38,2	300	175	339	17,0	9,4	60,4	44,3	42,9	99	11,1	5,42	2,71	4,15
79KL	7,13	4,59	2,98	0,27	0,45	19,5	0,375	5,74	4,20	0,486	4,38	11,4	0,114	69,2	5,61	2,60	16,3	133	51,5	397	235	338	20,8	9,1	75,3	46,6	44,4	109	13,3	2,41	2,32	5,56
82KL	8,62	4,11	2,77	0,28	0,43									52,9	4,94	2,45	17,5	124	44,6	307	269	272	20,5	6,6	77,7	46,2	50,5	118	17,2	1,35	1,99	5,31
87KL	3,67	3,00	3,03	0,31	0,72	16,8	0,368	5,37	4,38	0,227	3,84	15,8	0,164	93,0	8,01	2,48	15,4	108	35,7	266	257	241	19,1	9,4	70,8	42,7	55,4	103	15,0	2,82	3,17	4,72
5KL																																
11KL	4,91	0,41	1,09	0,29	0,69	17,5	0,490	7,33	5,85	0,556	3,29	16,8	0,177	116,6	7,11	2,67	25,8	131	42,7	212	345	213	23,6	11,4	92,6	41,9	90,9	135	23,6	4,57	1,34	5,37
18KL	3,18	0,24	2,52	0,07	1,10	11,2	0,324	5,27	4,47	0,299	2,84	30,1	0,223	110,9	8,56	2,18	12,4	59	43,8	99	238	60	10,4	10,5	45,5	36,9	96,5	66	24,4	2,52	1,93	3,15
105KK	3,51	2,91	4,08	0,45	0,90	16,0	0,442	5,53	3,90	0,099	4,02	18,4	0,172	67,6	9,01	2,37	16,9	104	22,1	148	179	272	21,0	4,9	63,2	44,2	51,2	127	19,6	1,99	2,38	3,68
114KK	3,55	3,16	3,58	0,29	0,55	17,1	0,519	6,15	4,32	0,083	3,14	13,1	0,122	85,1	6,33	2,49	16,8	90	22,8	135	187	178	21,0	5,2	71,3	40,7	45,8	140	24,2	1,83	1,94	3,88
143KK	16,00	6,05	2,14	0,18	0,45	22,5	0,904	8,00	6,07	0,061	2,37	1,6	0,075	48,2	3,15	2,78	28,4	175	36,1	127	86	244	38,4	6,3	150,4	88,2	18,4	105	16,2	2,58	0,68	6,80
182SK	10,27	2,83	1,55	0,13	0,25	22,6	0,532	8,33	5,70	0,074	3,14	3,9	0,072	76,2	3,46	3,19	18,0	146	22,7	140	80	147	21,6	7,6	113,4	47,7	33,0	106	19,4	1,19	0,67	7,95
223SK	8,89	1,81	1,19	0,14	0,24	23,1	0,526	7,64	5,30	0,111	3,30	3,1	0,105	61,4	3,97	3,02	19,9	146	27,5	132	113	140	18,4	5,3	104,7	40,7	30,9	101	20,3	2,57	1,09	7,95
232SK	12,60	2,66	1,04	0,12	0,21	25,7	0,474	8,22	5,00	0,112	3,48	2,5	0,098	56,9	3,13	3,28	16,7	149	27,0	153	92	139	19,2	5,2	119,5	40,6	29,7	98	21,4	1,10	0,91	9,31
76123	13,20	4,95												62,5	3,85	3,59	14,6	111	18,1	108	73	450	18,1	7,0	78,0	39,5	20,7	71	13,5	1,87		4,09
76125	10,90	3,93												58,2	3,41	3,35	22,9	139	39,3	136	137	197	21,4	6,9	83,8	43,6	30,1	68	11,8	4,63	1,28	5,54
76127	32,10	4,22												39,0	4,53	3,34	24,7	157	45,8	130	139	3243	20,4	5,9	91,1	55,2	21,2	80	12,7	8,62	1,55	7,05
76128	13,40	5,37												77,2	2,91	3,52	31,9	192	50,0	136	162	232	24,9	6,4	111,9	59,6	24,2	102	15,3	8,21	0,71	8,26
76132	4,46	3,60												98,8	5,83	1,86	14,5	99	16,8	57	52	83	12,3	14,8	51,6	207,6	15,2	72	11,8	1,47	0,19	3,26
76135	5,11	5,56												25,3	3,84	3,23	11,2	130	14,8	132	69	138	11,4	8,1	49,1	39,3	24,9	87	12,8	2,35	1,86	3,05
76136	8,30	3,22												25,3	2,87	2,45	11,7	112	14,7	77	37	104	14,0	4,5	68,4	44,5	20,3	97	17,3	2,92	0,51	3,24
77191	13,50	5,98												67,1	4,19	3,77	15,5	140	23,9	137	73	791	17,8	10,1	85,0	48,1	29,1	75	12,1	23,41	2,19	3,66
77194	13,30	6,89												90,8	3,06	3,18	19,7	156	28,2	99	50	168	19,5	11,3	99,0	64,8	20,6	91	13,5	2,25	0,73	6,70
77200																																
77202																																
77203	7,41	5,69												29,8	3,05	2,22	10,5	166	17,1	146	52	110	11,6	8,7	57,6	41,8	15,8	67	9,9	4,84	1,16	4,20
422	14,40	3,46	0,78	0,17	0,33	24,8	0,479	8,83	5,61	0,098	4,45	-0,8	0,076	66,2	2,60	3,86	16,0	184	27,5	201	56	143	18,4	6,0	115,1	42,5	27,3	113	14,1	1,48	0,58	9,43
KS8	11,83	3,33	1,31	1,31	0,30									48,2	2,64	3,38	14,5	174	22,5	183	45	118	17,2	5,3	104,9	55,3	24,8	106	14,5	0,90	0,52	8,38
243	3,69	5,82	5,21	0,41	0,54	23,8	0,431	5,26	2,81	0,049	4,72	7,9	0,073	25,5	3,21	2,03	28,0	225	17,0	120	53	88	11,6	10,3	48,1	33,6	24,8	102	11,0	1,96	1,48	2,44
280	7,71	4,14	3,15	0,29	0,52	20,1	0,505	6,52	5,25	0,354	4,05	9,7	0,104	48,4	4,70	2,61	20,5	130	28,5	269	133	299	53,3	6,8	72,3	46,1	41,6	134	16,5	2,03	0,28	4,75

Appendix 1, Table 2) continued (Early Holocene samples)

core	Ba	La	Ce	Pr	Nd	Sm	Eu	Gd	Tb	Dy	Ho	Er	Tm	Yb	Lu	Hf	Tl	Pb	U
	ppm	cofbppm	cofbppm	cofbppm	cofbppm	cofbppm	cofbppm	cofbppm	cofbppm	cofbppm	cofbppm	cofbppm	cofbppm	cofbppm	cofbppm	cofbppm	cofbppm	cofbppm	cofb
15KL	1685	31,5	54,4	7,08	29,0	5,94	1,41	5,70	0,899	5,47	1,19	3,52	0,547	3,49	0,527	2,89	0,403	19,6	2,21
26KL	694	27,4	50,1	6,39	26,2	5,36	1,36	5,41	0,802	4,67	0,96	2,66	0,388	2,56	0,372	3,11	0,475	17,5	6,62
36KL	712	31,5	55,9	7,45	28,5	5,67	1,30	5,40	0,819	4,96	1,03	3,01	0,438	2,85	0,427	2,58	0,438	20,1	2,66
51KL	1283	27,6	49,3	6,21	23,5	4,98	1,12	4,89	0,711	4,35	0,94	2,78	0,406	2,76	0,408	3,03	0,605	19,1	4,82
57KL	1420	27,9	52,5	6,41	24,2	4,92	1,09	4,59	0,701	4,16	0,91	2,70	0,402	2,68	0,418	2,89	0,820	21,1	6,56
64KL	1606	32,4	54,5	7,11	28,9	5,90	1,38	5,73	0,874	5,35	1,12	3,39	0,497	3,49	0,540	2,91	0,427	23,8	2,19
70KL	1053	27,3	51,6	6,20	25,4	4,95	1,17	4,87	0,751	4,39	0,92	2,70	0,401	2,73	0,417	2,83	1,070	19,3	10,51
71KL	2397	30,7	53,1	6,95	27,6	5,79	1,44	6,03	0,928	5,92	1,23	3,66	0,548	3,84	0,592	2,84	1,986	23,1	18,94
74KL	4185	27,0	44,4	6,00	25,1	5,13	1,36	5,53	0,840	5,35	1,15	3,47	0,495	3,59	0,549	2,44	1,455	21,6	15,49
79KL	2708	29,2	51,2	6,75	27,2	6,03	1,44	6,03	0,919	5,80	1,24	3,66	0,525	3,66	0,576	2,51	2,000	24,2	15,56
82KL	2557	36,8	60,6	8,78	35,2	7,33	1,79	7,67	1,166	7,10	1,49	4,33	0,614	4,17	0,630	3,16	1,269	22,3	10,65
87KL	3538	34,7	53,8	7,95	33,7	6,87	1,77	7,49	1,133	7,08	1,49	4,41	0,651	4,34	0,656	2,62	1,282	18,8	15,38
5KL																			
11KL	4571	56,1	78,3	12,80	51,4	10,80	2,72	11,49	1,766	10,74	2,37	7,03	0,977	6,69	1,017	3,49	0,457	28,1	2,34
18KL	6161	53,0	49,7	11,40	47,0	10,35	2,70	11,54	1,734	10,49	2,29	6,66	0,937	6,38	0,909	2,45	0,420	22,2	1,68
105KK	2821	35,9	51,2	7,76	32,0	6,52	1,65	7,01	1,050	6,57	1,41	4,09	0,567	3,95	0,602	3,13	0,448	17,5	14,48
114KK	2421	35,7	57,1	8,38	33,3	6,83	1,59	6,83	1,033	6,38	1,31	3,75	0,546	3,60	0,550	3,63	0,583	14,8	13,17
143KK	1058	68,7	138,8	17,17	65,3	12,96	3,06	11,43	1,731	9,91	1,91	5,45	0,798	5,24	0,765	2,73	0,637	28,3	10,71
182SK	1264	32,0	57,5	7,19	27,4	5,59	1,28	5,36	0,793	4,71	0,98	2,83	0,410	2,76	0,413	3,39	0,577	19,1	5,27
223SK	1025	29,5	54,7	7,23	29,5	5,52	1,39	6,15	0,968	5,72	1,16	3,22	0,493	2,86	0,534	3,92	0,541	20,0	4,08
232SK	1256	30,8	59,9	7,46	27,6	6,15	1,38	5,51	0,821	5,09	0,98	2,72	0,459	2,68	0,408	3,76	0,771	24,3	5,13
76123	1523	29,2	59,3	6,90	26,4	4,84	1,13	4,48	0,648	3,69	0,71	2,11	0,277	2,04	0,286	2,00	0,881	24,2	9,08
76125	1832	29,7	53,7	6,50	25,3	6,91	1,71	5,95	1,007	5,21	1,12	3,18	0,554	3,73	0,526	3,15	1,162	18,6	6,72
76127	927	22,4	43,9	5,38	18,9	6,76	1,65	5,90	0,937	4,78	0,98	2,78	0,536	3,17	0,548	3,62	1,164	42,5	5,58
76128	781	25,3	48,4	6,01	23,1	8,56	2,09	6,83	1,076	5,12	1,15	3,32	0,671	4,01	0,662	4,01	1,240	17,5	7,01
76132	144	15,4	32,1	4,08	16,5	3,70	0,93	3,32	0,533	3,18	0,61	1,84	0,239	1,51	0,220	2,12	0,217	12,1	9,78
76135	1953	20,3	36,3	4,82	18,8	4,06	1,02	4,08	0,608	3,90	0,80	2,42	0,316	2,38	0,334	1,91	0,493	11,5	12,47
76136	479	23,5	48,9	5,85	23,0	4,68	1,11	4,35	0,673	3,85	0,77	2,19	0,324	2,08	0,294	2,78	0,399	13,3	5,14
77191	786	38,0	68,4	8,39	30,5	5,27	1,08	4,95	0,684	4,11	0,79	2,30	0,302	2,04	0,298	1,86	0,636	30,7	13,59
77194	440	25,7	52,5	6,01	22,8	4,28	0,97	3,92	0,585	3,51	0,66	1,89	0,261	1,82	0,251	2,60	0,502	15,2	7,86
77200																			
77202																			
77203	916	17,4	34,3	4,11	16,1	3,19	0,78	2,99	0,448	2,74	0,56	1,67	0,243	1,72	0,248	1,87	0,328	12,2	9,34
422	610	24,7	51,9	5,88	22,3	4,13	0,99	3,79	0,577	3,41	0,70	2,05	0,305	2,09	0,315	3,20	0,652	20,0	4,80
KS8	475	22,5	46,8	5,46	20,3	3,97	0,90	3,50	0,537	3,16	0,64	1,86	0,280	1,86	0,280	2,76	0,570	15,7	4,42
243	454	19,8	35,7	4,72	18,2	3,91	0,98	3,86	0,619	3,63	0,72	2,13	0,305	2,17	0,325	2,75	0,497	8,3	13,14
280	3491	29,9	54,7	6,64	25,4	5,39	1,36	5,39	0,848	5,25	1,09	3,47	0,456	3,25	0,507	3,15	1,467	20,6	11,04

Appendix 1, Table 2) continued (Early Holocene samples)

core	depth	w.depth	CaCO3	Opal	Biogenic	< 2 µm	area	Corg	N	S	SiO2	TiO2	Al2O3	Fe2O3	MnO	MgO	CaO	P2O5	Si	Ti	Al	Fe	Mn	Mg	Ca, bulk	Ca, mar.	Ca, lith.	P	Li	Na	K	Sc
	cm	m	%	%	%	%	m2	%	%	%	wt%	wt%	wt%	wt%	wt%	wt%	wt%	wt%	%	%	%	%	%	%	%	%	%	%	ppm	%	%	ppm
15KL	35-39	3920	51,4	1,8	53,2	55,0	17,9	0,44	0,04	0,103	26,2	0,37	6,30	4,70	0,051	3,11	31,0	0,183	12,2	0,221	3,34	3,28	0,039	1,88	22,2	20,6	1,6	0,040	18,1	1,35	2,04	6,53
26KL	78-82	3776	48,4	1,1	49,5	48,4	16,7	0,75	0,09	0,187	28,5	0,49	7,81	3,69	0,067	2,85	28,9	0,222	13,3	0,296	4,13	2,58	0,052	1,72	20,7	19,4	1,3	0,048	34,1	1,56	1,57	8,49
36KL	26-30	2055	56,2	1,4	57,6	50,0	19,7	0,62	0,06	0,113	23,4	0,38	5,98	3,11	0,035	2,49	35,4	0,170	11,0	0,230	3,16	2,18	0,027	1,50	25,3	22,5	2,8	0,037	20,4	1,44	1,22	6,21
51KL	78-82	2644	35,8	1,4	37,2	41,0	21,7	0,67	0,06	0,088																14,3			27,2	1,68	1,96	9,12
57KL	78-82	3422	36,1	1,8	37,9	44,5	22,5	0,75	0,07	0,114	36,0	0,47	8,50	3,88	0,085	4,24	21,7	0,207	16,8	0,282	4,50	2,71	0,066	2,56	15,5	14,5	1,1	0,045	27,2	1,69	1,86	8,38
64KL	58-62	3281	35,7	1,2	36,9	54,0	24,4	0,71	0,05	0,102	28,1	0,40	6,66	3,23	0,109	4,05	34,8	0,205	13,1	0,239	3,52	2,26	0,085	2,44	24,9	14,3	10,6	0,045	34,1	1,59	2,17	9,73
70KL	58-62	3810	52,9	1,6	54,5	46,0	18,8	0,84	0,07	0,122	24,1	0,35	5,62	3,01	0,072	3,54	34,6	0,163	11,3	0,208	2,98	2,11	0,056	2,14	24,7	21,2	3,5	0,036	22,7	1,42	1,36	6,54
71KL	70-74	4029	48,0	1,4	49,4	52,5	26,2	0,55	0,05	0,124	28,5	0,41	6,93	3,35	0,081	4,37	28,2	0,202	13,3	0,248	3,67	2,34	0,062	2,64	20,2	19,2	0,9	0,044	27,2	1,56	1,59	7,62
74KL	138-142	3212	56,2	1,8	58,0	47,0	23,1	0,51	0,07	0,196																22,5			20,4	1,68	1,29	6,02
79KL	79-83	4351	52,6	1,0	53,6	51,6	23,1	1,23	0,10	0,167	23,6	0,33	5,51	2,76	0,161	3,86	32,8	0,120	11,0	0,201	2,92	1,93	0,125	2,33	23,4	21,1	2,4	0,026	22,7	1,56	1,33	5,91
82KL	58-62	4416	54,2	2,4	56,6	54,0	27,8	0,77	0,04	0,116	23,7	0,33	5,36	2,75	0,085	4,10	34,1	0,207	11,1	0,200	2,84	1,93	0,066	2,47	24,4	21,7	2,7	0,045	22,7	1,58	1,46	6,23
87KL	94-98	3773	65,3	2,4	67,7	59,0	22,7	0,51	0,05	0,140																			22,7	1,32	0,94	4,68
5KL	30-33	3335	77,6	2,0	79,6	62,0	15,8	0,35	0,07	0,122	9,9	0,15	2,59	1,46	0,057	1,15	48,3	0,154	4,6	0,091	1,37	1,02	0,044	0,69	34,5	31,1	3,5	0,034	9,0	0,87	0,97	5,16
11KL	41-44	3859	64,2	3,5	67,7	43,0	26,3	0,34	0,04	0,166	17,9	0,27	4,67	2,62	0,592	2,03	41,4	0,160	8,4	0,160	2,47	1,83	0,459	1,23	29,6	25,7	3,9	0,035	20,4	1,75	1,02	7,51
18KL	33-37	3035	83,8	2,4	86,2	73,0	10,6	0,14	0,04	0,138	7,0	0,09	1,62	1,04	0,043	0,78	50,8	0,132	3,3	0,057	0,86	0,73	0,033	0,47	36,3	33,6	2,7	0,029	9,0	1,02	0,92	5,05
105KK	111-119	3535	68,6	3,0	71,6	70,8	23,2	0,74	0,07	0,203	16,6	0,23	3,36	1,71	0,040	1,86	41,7	0,190	7,8	0,139	1,78	1,20	0,031	1,12	29,8	27,5	2,4	0,042	25,0	1,16	0,85	4,50
114KK	104-108	3843	74,8	3,3	78,1	68,0	18,8	0,47	0,08	0,145	12,7	0,17	2,67	1,30	0,039	1,47	45,6	0,143	5,9	0,104	1,41	0,91	0,030	0,89	32,6	29,9	2,6	0,031	18,1	1,33	0,65	3,29
143KK	215-220	1522	63,5	1,3	64,8	63,0	19,4	0,75	0,08	0,182																25,4			20,4	1,32	0,96	4,35
182SK	38-44	2234	40,0	2,0	42,0	69,0	36,2	0,91	0,10	0,145	30,1	0,49	8,78	4,84	0,052	3,11	24,3	0,189	14,1	0,292	4,65	3,39	0,040	1,87	17,3	16,0	1,3	0,041	36,4	1,83	1,82	12,70
223SK	67-72	2686	37,5	1,5	39,0	39,0	18,6	0,71	0,06	0,111	35,7	0,50	8,95	4,24	0,062	3,42	23,4	0,192	16,7	0,298	4,74	2,97	0,048	2,06	16,7	15,0	1,7	0,042	29,5	1,40	1,82	11,80
232SK	77-82	3098	35,4	1,7	37,1	40,0	16,6	0,89	0,09	0,119	38,7	0,51	9,08	4,14	0,079	3,67	22,2	0,197	18,1	0,303	4,81	2,89	0,061	2,21	15,8	14,2	1,7	0,043	27,2	1,62	1,91	12,00
76123	58,5	2631	57,0	0,0	57,0	75,6																				22,8			11,3	1,32	1,35	5,03
76125	88,5	1878	42,0	0,0	42,0	76,4																				16,8			36,4	1,72	2,20	8,57
76127	37,5	1610	18,2	0,0	18,2	74,0																				7,3			52,3	2,28	2,77	13,90
76128	188,5	1712	23,0	0,0	23,0	73,7																				9,2			45,5	2,04	2,59	14,90
76132	189,5	1430	68,5	0,0	68,5	70,0																				27,4			22,7	1,78	1,14	4,80
76135	207,5	1895	52,0	1,0	53,0	48,6																				20,8			11,3	1,24	1,72	6,13
76136	76,5	1649	35,0	0,6	35,6	17,5																				14,0			6,8	1,47	2,16	8,79
77191	659,5	1254	76,0			73,3																				30,4						
77194	315,5	1222	14,0	0,0	14,0	78,3																				5,6			81,9	1,80	2,47	16,20
77200	45	2910	46,0	0,0	46,0	50,6																				18,4			18,1	1,41	2,07	8,47
77202	133,5	2427	43,0	0,9	43,9	44,5																				17,2			11,3	1,22	1,98	7,26
77203	225	2442	39,5	0,0	39,5	37,2																				15,8			6,8	1,27	1,90	6,83
422	156-160	2732	28,1	1,1	29,2	42,0	23,3	1,53	0,12	0,451	38,2	0,52	9,40	4,48	0,079	5,35	17,7	0,175	17,9	0,314	4,98	3,14	0,061	3,22	12,7	11,3	1,4	0,038	34,1	1,56	1,98	13,70
KS8	235-347	2900	29,7	1,4	31,1	45,2		0,80	0,07	0,189	39,9	0,52	9,51	4,26	0,080	4,61	18,5	0,193	18,6	0,311	5,03	2,98	0,062	2,78	13,2	11,9	1,3	0,042	29,5	1,56	1,99	13,20
243	170	1041	50,7	0,0	50,7		15,7	1,80	0,12	0,310	25,6	0,35	4,97	2,09	0,035	3,83	31,5	0,133	12,0	0,210	2,63	1,46	0,027	2,31	22,5	20,3	2,2	0,029	13,6	1,35	0,97	13,30
280	120	2106	56,2	2,2	58,4		20,3	0,49	0,05	0,160	22,2	0,42	5,67	3,11	0,148	3,15	34,6	0,162	10,4	0,253	3,00	2,17	0,115	1,90	24,8	22,5	2,2	0,035	18,1	1,60	1,12	9,11

Appendix 1, Table 3) Chemical composition at the depth level of the Termination Ia (16,000-18,000 cal-yrBP). Concentration values in the bulk fraktion (% or ppm), concentration values expressed on a carbonate-and-opal-free-basis (% or ppm, cofb)

core	Cr	Co	Ni	Cu	Zn	Ga	As	Rb	Sr	Y	Zr	Nb	Mo	Cd	Cs	Ba	La	Ce	Pr	Nd	Sm	Eu	Gd	Tb	Dy	Ho	Er	Tm	Yb	Lu	Hf	Tl
	ppm	ppm	ppm	ppm	ppm	ppm	ppm	ppm	ppm	ppm	ppm	ppm	ppm	ppm	ppm	ppm	ppm	ppm	ppm	ppm	ppm	ppm	ppm	ppm	ppm	ppm	ppm	ppm	ppm	ppm	ppm	ppm	ppm
15KL	69,9	10,80	80,0	39,6	88,2	7,48	8,02	43,6	819	14,2	47,7	5,96	1,06	0,236	3,08	447	12,60	23,3	2,95	10,90	2,34	0,546	2,34	0,350	2,18	0,450	1,320	0,200	1,280	0,190	1,28	0,27
26KL	65,9	11,50	52,2	30,4	60,8	9,17	4,05	55,9	2427	11,9	46,3	7,95	0,56	0,742	3,90	228	13,40	25,6	3,10	11,90	2,48	0,561	2,38	0,350	2,11	0,428	1,200	0,170	1,110	0,160	1,28	0,45
36KL	58,4	10,10	47,6	24,4	53,3	6,43	2,06	39,0	821	12,1	41,6	6,22	0,24	0,148	2,78	312	11,00	19,7	2,52	9,86	2,10	0,472	2,01	0,310	1,88	0,395	1,170	0,160	1,090	0,160	1,12	0,21
51KL	88,0	15,00	68,9	28,3	69,0	10,00	3,08	66,3	549	14,5	63,8	9,23	0,34	0,287	4,75	332	16,20	31,8	3,75	14,60	3,07	0,646	2,85	0,430	2,58	0,510	1,490	0,210	1,450	0,210	1,88	0,38
57KL	104,0	16,50	88,7	33,0	68,4	9,36	3,29	58,1	515	13,9	64,2	8,89	0,50	0,314	4,17	325	15,70	31,1	3,62	13,80	2,93	0,628	2,75	0,410	2,48	0,499	1,460	0,210	1,400	0,210	1,83	0,54
64KL	89,3	17,70	72,3	35,9	74,7	11,70	4,17	83,5	533	15,3	63,6	10,30	0,40	0,247	6,15	373	17,60	34,9	4,11	16,00	3,24	0,687	3,00	0,450	2,71	0,549	1,580	0,230	1,530	0,230	1,70	0,46
70KL	86,9	15,30	96,2	35,5	72,8	6,64	3,15	40,3	771	12,1	48,0	6,46	0,58	0,687	2,89	405	11,10	21,0	2,55	9,99	2,19	0,506	2,16	0,320	1,99	0,405	1,200	0,180	1,150	0,180	1,27	0,52
71KL	96,2	15,10	86,5	32,9	60,6	7,71	2,72	47,1	661	12,9	56,0	7,60	0,52	0,307	3,42	264	12,40	24,1	2,90	11,40	2,44	0,558	2,40	0,360	2,24	0,447	1,300	0,190	1,260	0,190	1,54	0,38
74KL	79,5	12,40	67,8	26,6	58,7	5,87	2,89	33,5	800	11,3	46,1	6,10	1,31	0,288	2,28	305	9,90	18,5	2,33	9,08	1,99	0,473	2,00	0,310	1,88	0,386	1,120	0,160	1,070	0,150	1,21	0,28
79KL	72,5	12,00	103,0	40,9	87,1	6,19	3,18	33,8	832	12,8	46,8	6,53	1,13	0,829	2,53	461	10,90	20,8	2,53	9,82	2,21	0,521	2,21	0,340	2,1	0,430	1,270	0,180	1,190	0,180	1,25	0,66
82KL	68,7	9,39	77,7	38,7	65,1	6,52	1,72	36,3	863	12,9	48,2	6,66	0,59	0,406	2,70	282	11,30	20,7	2,72	10,40	2,31	0,529	2,26	0,340	2,13	0,436	1,260	0,180	1,220	0,180	1,29	0,35
87KL	47,7	6,45	52,2	31,8	47,2	5,02	1,70	28,3	1048	11,6	36,0	5,13	0,40	0,283	2,12	330	9,31	15,7	2,09	8,31	1,81	0,412	1,81	0,280	1,72	0,351	1,020	0,150	1,000	0,140	0,90	0,26
5KL	25,2	11,60	34,8	45,4	110,0	3,62	2,55	19,9	1198	11,8	21,8	2,57	1,24	0,349	1,38	660	8,04	12,7	2,15	6,55	2,13	0,420	1,55	0,280	1,61	0,376	1,040	0,150	1,100	0,180	0,51	0,24
11KL	44,7	24,60	82,3	72,5	58,3	5,92	3,89	31,4	1014	16,1	33,9	8,18	3,27	0,205	2,66	717	12,30	18,4	2,99	11,40	3,21	0,872	3,17	0,480	2,73	0,593	1,760	0,300	1,720	0,290	1,21	0,35
18KL	18,0	12,60	25,8	32,6	37,9	2,42	1,58	12,9	1147	14,6	15,0	2,03	1,67	0,303	0,93	788	9,23	9,9	2,11	7,50	2,07	0,537	2,23	0,340	1,92	0,418	1,240	0,140	1,200	0,170	0,59	0,10
105KK	37,7	7,22	46,0	36,6	54,1	4,80	2,21	21,6	1167	13,3	40,1	6,15	1,13	0,105	1,42	463	10,50	14,9	2,36	9,28	1,98	0,467	2,09	0,310	1,96	0,405	1,170	0,160	1,090	0,170	1,03	0,26
114KK	25,5	5,07	32,7	24,9	34,4	3,49	0,96	16,6	1196	10,8	29,4	4,90	0,59	0,499	1,12	486	8,37	12,1	1,85	7,42	1,57	0,374	1,65	0,240	1,56	0,323	0,930	0,130	0,880	0,130	0,72	0,14
143KK	31,7	5,61	23,0	15,8	38,1	5,46	1,56	26,9	1362	10,8	65,2	11,20	0,43	0,257	1,16	176	11,80	21,0	2,73	10,00	2,07	0,480	1,99	0,300	1,81	0,354	1,040	0,140	0,940	0,140	1,65	0,13
182SK	88,1	14,30	84,4	67,0	92,0	11,30	2,61	62,8	729	19,1	62,5	10,60	1,93	0,863	4,67	707	17,60	30,9	4,00	14,80	3,71	0,917	3,37	0,540	3,08	0,678	1,880	0,300	1,960	0,320	2,09	0,47
223SK	88,1	15,10	66,0	58,3	74,0	11,90	3,21	70,0	666	17,2	60,2	9,95	1,98	0,287	5,41	363	17,40	31,1	3,86	15,20	4,11	0,865	3,46	0,530	2,82	0,586	1,790	0,300	1,730	0,300	1,83	0,57
232SK	95,7	18,60	80,4	57,3	80,1	11,10	4,10	67,3	562	16,6	63,9	9,51	2,12	0,494	5,06	401	17,00	31,2	4,01	15,10	3,71	0,862	3,54	0,530	2,91	0,601	1,860	0,310	1,930	0,310	2,12	0,57
76123	25,6	10,50	41,2	26,5	84,2	5,30	2,54	29,0	812	11,7	26,8	3,44	0,60	0,831	1,62	659	10,70	19,0	2,51	9,43	1,70	0,379	1,73	0,260	1,55	0,303	0,850	0,110	0,830	0,110	0,66	0,20
76125	68,8	14,40	63,2	35,1	92,2	9,87	2,79	53,7	883	16,8	51,0	7,39	0,42	0,785	3,64	410	16,90	29,8	3,73	14,20	2,58	0,540	2,52	0,370	2,3	0,448	1,320	0,180	1,240	0,170	1,34	0,30
76127	124,0	16,60	87,6	48,3	1545,0	14,60	8,13	78,8	460	17,3	71,9	12,40	5,37	0,879	5,69	440	18,20	36,1	4,35	16,60	3,36	0,750	3,05	0,470	2,8	0,546	1,580	0,230	1,560	0,230	2,16	0,40
76128	119,0	17,30	74,8	50,5	104,0	14,00	10,78	71,4	863	17,7	76,0	10,30	4,55	0,414	4,90	259	16,40	31,4	3,99	15,80	3,28	0,752	3,16	0,500	2,92	0,575	1,640	0,230	1,530	0,220	2,28	0,32
76132	32,9	6,37	19,6	18,9	42,0	3,75	6,20	17,4	6053	5,5	22,5	2,71	1,35	0,009	1,14	45,4	4,84	9,8	1,23	4,66	1,12	0,258	1,24	0,170	0,97	0,181	0,530	0,070	0,460	0,070	0,59	0,10
76135	66,1	8,12	54,4	21,9	54,7	6,14	2,65	29,4	882	13,9	56,3	7,97	1,00	0,629	2,01	171	11,60	21,6	2,77	11,40	2,30	0,487	2,25	0,350	2,06	0,410	1,160	0,160	1,090	0,150	1,68	0,16
76136	102,0	11,30	57,3	24,7	92,9	10,10	2,59	46,3	677	19,5	95,4	15,70	1,50	0,396	2,40	224	19,40	39,1	4,78	17,40	3,72	0,756	3,37	0,530	3,02	0,606	1,730	0,240	1,580	0,240	2,53	0,26
77191																																
77194	158,0	18,60	81,6	35,8	138,0	18,40	11,44	81,3	407	16,7	81,9	13,60	1,89	0,622	5,43	242	24,50	50,3	5,59	20,00	4,01	0,868	3,37	0,500	2,78	0,560	1,630	0,230	1,480	0,210	2,25	0,37
77200	76,5	23,20	85,0	38,5	140,0	9,11	7,33	41,4	771	16,8	54,9	8,26	1,54	0,196	3,69	325	15,10	29,6	3,70	13,20	2,73	0,588	2,68	0,390	2,33	0,485	1,410	0,200	1,300	0,200	1,35	0,24
77202	106,0	12,50	72,8	22,4	94,7	7,16	3,17	42,0	665	12,9	48,0	6,82	1,01	0,387	2,80	282	11,50	23,4	2,91	10,70	2,23	0,489	2,19	0,320	1,92	0,383	1,130	0,160	1,000	0,150	1,15	0,23
77203	145,0	13,60	85,9	21,1	91,3	7,01	4,75	37,0	657	12,1	46,1	6,66	1,40	0,426	2,38	240	11,70	23,4	2,79	10,50	2,19	0,491	2,03	0,310	1,78	0,361	1,060	0,140	0,970	0,150	1,20	0,21
422	147,0	22,90	108,0	56,2	78,8	12,30	6,36	66,7	426	16,1	67,8	9,51	3,33	0,313	5,04	205	15,30	29,7	3,66	14,90	3,81	1,000	3,50	0,500	3,18	0,641	1,830	0,340	1,840	0,330	2,36	0,60
KS8	139,0	20,30	96,7	52,5	68,1	11,70	4,84	67,9	520	15,9	71,8	9,70	2,52	0,221	5,04	215	17,20	32,9	4,04	14,50	4,10	1,000	3,80	0,570	3,17	0,617	1,870	0,330	2,000	0,320	2,36	0,83
243	94,4	9,12	58,2	22,5	35,5	6,86	4,38	26,3	706	12,0	49,2	5,59	1,63	0,520	1,46	134	9,91	18,3	2,39	9,33	2,07	0,486	2,00	0,310	1,82	0,368	1,060	0,150	1,030	0,150	1,22	0,24
280	63,5	10,00	62,5	28,7	54,7	8,72	2,01	31,3	961	14,8	62,0	8,53	0,57	0,362	1,94	189	12,10	24,0	2,89	11,20	2,39	0,536	2,31	0,360	2,09	0,430	1,220	0,170	1,150	0,170	1,55	0,29

Appendix 1, Table 3) continued (Termination Ia samples)

core	Pb	U	Corg	N	S	Si opal cor	Ti	Al	Fe	Mn	Mg	Ca, lith.	P	Li	Na	K	Sc	Cr	Co	Ni	Cu	Zn	Ga	As	Pb	Sr/Ca	Y	Zr	Nb	Mo	Cd	Os
	ppm	ppm	% cofb	% cofb	% cofb	% cofb	% cofb	% cofb	% cofb	% cofb	% cofb	% cofb	% cofb	ppm cofb	% cofb	% cofb	ppm cofb	ppm cofb	ppm cofb	ppm cofb	ppm cofb	ppm cofb	ppm cofb	ppm cofb	ppm cofb	ppm cofb		ppm cofb	ppm cofb	ppm cofb	ppm cofb	ppm cofb	ppm cofb
15KL	8,44	1,12	0,94	0,09	0,22	24,3	0,471	7,13	7,02	0,084	4,01	3,4	0,085	38,8	2,88	4,37	14,0	149	23,1	171	85	188	16,0	17,1	93,2	39,8	30,3	102	12,7	2,26	0,50	6,58
26KL	8,40	3,65	1,49	0,18	0,37	25,4	0,585	8,18	5,11	0,102	3,41	2,6	0,096	67,5	3,08	3,10	16,8	130	22,8	103	60	120	18,2	8,0	110,7	125,2	23,6	92	15,7	1,11	1,47	7,72
36KL	6,89	1,06	1,46	0,14	0,27	24,3	0,542	7,46	5,14	0,065	3,54	6,5	0,087	48,1	3,40	2,89	14,6	138	23,8	112	58	126	15,2	4,9	92,0	36,5	28,5	98	14,7	0,57	0,35	6,56
51KL	11,67	3,08	1,07	0,10	0,14									43,4	2,68	3,11	14,5	140	23,9	110	45	110	15,9	4,9	105,6	38,3	23,1	102	14,7	0,54	0,46	7,56
57KL	10,80	3,01	1,21	0,11	0,18	25,7	0,455	7,25	4,37	0,106	4,12	1,7	0,073	43,9	2,71	3,00	13,5	167	26,6	143	53	110	15,1	5,3	93,6	35,6	22,4	103	14,3	0,81	0,51	6,71
64KL	14,10	3,97	1,13	0,08	0,16	19,9	0,379	5,58	3,58	0,134	3,87	16,8	0,071	54,0	2,52	3,44	15,4	142	28,1	115	57	118	18,5	6,6	132,3	37,3	24,2	101	16,3	0,63	0,39	9,75
70KL	7,72	4,11	1,85	0,15	0,27	23,1	0,456	6,54	4,63	0,122	4,69	7,7	0,078	49,9	3,12	3,00	14,4	191	33,6	211	78	160	14,6	6,9	88,6	36,4	26,6	105	14,2	1,27	1,51	6,35
71KL	8,66	2,87	1,09	0,10	0,25	25,0	0,491	7,25	4,62	0,123	5,21	1,9	0,087	53,8	3,09	3,14	15,1	190	29,8	171	65	120	15,2	5,4	93,1	34,4	25,5	111	15,0	1,03	0,61	6,76
74KL	6,60	3,01	1,21	0,17	0,47									48,6	4,00	3,06	14,3	189	29,5	161	63	140	14,0	6,9	79,8	35,6	26,9	110	14,5	3,12	0,69	5,43
79KL	8,22	4,31	2,65	0,22	0,36	22,8	0,432	6,29	4,16	0,269	5,01	5,1	0,057	48,9	3,37	2,87	12,7	156	25,9	222	88	188	13,3	6,9	72,8	39,5	27,6	101	14,1	2,44	1,79	5,45
82KL	7,06	2,74	1,77	0,09	0,27	22,9	0,460	6,53	4,44	0,152	5,69	6,2	0,104	52,3	3,64	3,37	14,4	158	21,6	179	89	150	15,0	4,0	83,6	39,8	29,7	111	15,3	1,36	0,94	6,22
87KL	5,27	2,09	1,58	0,15	0,43									70,2	4,09	2,92	14,5	148	20,0	162	98	146	15,5	5,3	87,6	40,1	35,9	111	15,9	1,24	0,88	6,56
5KL	5,49	0,49	1,72	0,34	0,60	18,1	0,447	6,73	5,00	0,217	3,39	17,1	0,165	44,3	4,25	4,76	25,3	124	56,9	171	223	539	17,7	12,5	97,5	38,6	57,8	107	12,6	6,08	1,71	6,76
11KL	6,80	0,93	1,05	0,12	0,51	20,9	0,495	7,66	5,67	1,420	3,80	12,1	0,108	63,2	5,41	3,16	23,3	138	76,2	255	224	180	18,3	12,0	97,2	39,4	49,8	105	25,3	10,12	0,63	8,24
18KL	3,69	0,32	1,01	0,29	1,00	15,5	0,411	6,21	5,26	0,241	3,41	19,7	0,209	65,4	7,42	6,68	36,6	130	91,3	187	236	275	17,5	11,4	93,5	34,2	105,8	109	14,7	12,10	2,20	6,74
105KK	3,46	5,49	2,61	0,25	0,71	22,4	0,488	6,26	4,22	0,108	3,96	8,3	0,146	87,9	4,08	2,98	15,8	133	25,4	162	129	190	16,9	7,8	76,1	42,5	46,8	141	21,7	3,98	0,37	5,00
114KK	3,18	3,26	2,15	0,37	0,66	20,0	0,475	6,45	4,16	0,137	4,05	11,9	0,143	82,8	6,09	2,95	15,0	116	23,2	149	114	157	15,9	4,4	75,8	39,9	49,3	134	22,4	2,69	2,28	5,11
143KK	4,49	3,93	2,13	0,23	0,52									58,0	3,74	2,73	12,4	90	15,9	65	45	108	15,5	4,4	76,4	53,6	30,7	185	31,8	1,22	0,73	3,30
182SK	10,60	3,90	1,57	0,17	0,25	22,7	0,504	8,01	5,84	0,069	3,23	2,3	0,071	62,7	3,16	3,13	21,9	152	24,7	146	116	159	19,5	4,5	108,3	45,5	32,9	108	18,3	3,33	1,49	8,05
223SK	11,90	2,72	1,16	0,10	0,18	26,2	0,488	7,77	4,86	0,079	3,38	2,8	0,069	48,4	2,30	2,98	19,3	144	24,8	108	96	121	19,5	5,3	114,8	44,4	28,2	99	16,3	3,25	0,47	8,87
232SK	12,90	3,18	1,41	0,14	0,19	27,5	0,482	7,64	4,60	0,098	3,52	2,6	0,068	43,3	2,57	3,04	19,1	152	29,6	128	91	127	17,6	6,5	107,0	39,6	26,4	102	15,1	3,37	0,79	8,04
76123	6,63	5,07												26,3	3,08	3,14	11,7	60	24,4	96	62	196	12,3	5,9	67,4	35,6	27,2	62	8,0	1,40	1,93	3,77
76125	18,40	4,88												62,7	2,96	3,80	14,8	119	24,8	109	61	159	17,0	4,8	92,6	52,5	29,0	88	12,7	0,72	1,35	6,28
76127	30,40	5,42												63,9	2,79	3,39	17,0	152	20,3	107	59	1889	17,8	9,9	96,3	63,1	21,1	88	15,2	6,56	1,07	6,96
76128	10,80	5,05												59,0	2,64	3,37	19,4	155	22,5	97	66	135	18,2	14,0	92,7	93,7	23,0	99	13,4	5,91	0,54	6,36
76132	11,90	3,51												72,0	5,65	3,61	15,2	104	20,2	62	60	133	11,9	19,7	55,2	220,7	17,4	71	8,6	4,29	0,03	3,62
76135	5,63	4,20												24,1	2,63	3,67	13,0	141	17,3	116	47	116	13,1	5,6	62,6	42,4	29,6	120	17,0	2,13	1,34	4,28
76136	7,83	2,87												10,5	2,28	3,35	13,6	158	17,5	89	38	144	15,7	4,0	71,9	48,3	30,3	148	24,4	2,33	0,61	3,73
77191																																
77194	16,20	5,03												95,2	2,10	2,87	18,8	184	21,6	95	42	160	21,4	13,3	94,5	72,6	19,4	95	15,8	2,20	0,72	6,31
77200	10,50	1,14												33,6	2,61	3,83	15,7	142	43,0	157	71	259	16,9	13,6	76,7	41,9	31,1	102	15,3	2,85	0,36	6,83
77202	8,12	3,43												20,2	2,17	3,54	12,9	189	22,3	130	40	169	12,8	5,7	74,9	38,6	23,0	86	12,2	1,80	0,69	4,99
77203	6,76	3,24												11,2	2,10	3,14	11,3	240	22,5	142	35	151	11,6	7,9	61,2	41,5	20,0	76	11,0	2,31	0,70	3,93
422	10,20	3,14	2,16	0,17	0,64	24,5	0,444	7,03	4,43	0,087	4,56	2,0	0,054	48,1	2,20	2,80	19,4	208	32,3	153	79	111	17,4	9,0	94,2	37,9	22,7	96	13,4	4,70	0,44	7,12
KS8	13,80	2,64	1,16	0,10	0,27	26,1	0,452	7,30	4,33	0,090	4,03	1,9	0,061	42,8	2,27	2,89	19,2	202	29,5	140	76	99	17,0	7,0	98,5	43,7	23,1	104	14,1	3,66	0,32	7,31
243	4,42	4,89	3,65	0,24	0,63	24,3	0,425	5,34	2,97	0,056	4,69	4,5	0,059	27,5	2,74	1,98	27,0	191	18,5	118	46	72	13,9	8,9	53,3	34,8	24,3	100	11,3	3,31	1,05	2,96
280	6,26	3,01	1,18	0,12	0,38	22,4	0,607	7,21	5,22	0,276	4,57	5,4	0,085	43,6	3,84	2,70	21,9	153	24,0	150	69	131	21,0	4,8	75,2	42,7	35,6	149	20,5	1,37	0,87	4,66

Appendix 1, Table 3) continued (Termination Ia samples)

core	Ba	La	Ce	Pr	Nd	Sm	Eu	Gd	Tb	Dy	Ho	Er	Tm	Yb	Lu	Hf	Tl	Pb	U
	ppm cofb	ppm cofb	ppm cofb	ppm cofb	ppm cofb	ppm cofb	ppm cofb	ppm cofb	ppm cofb	ppm cofb	ppm cofb	ppm cofb	ppm cofb	ppm cofb	ppm cofb	ppm cofb	ppm cofb	ppm cofb	ppm cofb
15KL	955	26,9	49,8	6,30	23,3	5,00	1,17	5,00	0,748	4,66	0,96	2,82	0,427	2,74	0,406	2,74	0,577	18,0	2,39
26KL	451	26,5	50,7	6,14	23,6	4,91	1,11	4,71	0,693	4,18	0,85	2,38	0,337	2,20	0,317	2,53	0,891	16,6	7,23
36KL	736	25,9	46,5	5,94	23,3	4,95	1,11	4,74	0,731	4,43	0,93	2,76	0,377	2,57	0,377	2,64	0,495	16,3	2,50
51KL	529	25,8	50,6	5,97	23,2	4,89	1,03	4,54	0,685	4,11	0,81	2,37	0,334	2,31	0,334	2,99	0,605	18,6	4,90
57KL	523	25,3	50,1	5,83	22,2	4,72	1,01	4,43	0,660	3,99	0,80	2,35	0,338	2,25	0,338	2,95	0,870	17,4	4,85
64KL	591	27,9	55,3	6,51	25,4	5,13	1,09	4,75	0,713	4,29	0,87	2,50	0,365	2,42	0,365	2,69	0,729	22,3	6,29
70KL	890	24,4	46,2	5,60	22,0	4,81	1,11	4,75	0,703	4,37	0,89	2,64	0,396	2,53	0,396	2,79	1,143	17,0	9,03
71KL	522	24,5	47,6	5,73	22,5	4,82	1,10	4,74	0,711	4,43	0,88	2,57	0,375	2,49	0,375	3,04	0,751	17,1	5,67
74KL	726	23,6	44,0	5,55	21,6	4,74	1,13	4,76	0,738	4,48	0,92	2,67	0,381	2,55	0,357	2,88	0,667	15,7	7,17
79KL	994	23,5	44,8	5,45	21,2	4,76	1,12	4,76	0,733	4,53	0,93	2,74	0,388	2,56	0,388	2,69	1,422	17,7	9,29
82KL	650	26,0	47,7	6,27	24,0	5,32	1,22	5,21	0,783	4,91	1,00	2,90	0,415	2,81	0,415	2,97	0,806	16,3	6,31
87KL	1022	28,8	48,6	6,47	25,7	5,60	1,28	5,60	0,867	5,33	1,09	3,16	0,464	3,10	0,433	2,79	0,805	16,3	6,47
5KL	3235	39,4	62,3	10,54	32,1	10,44	2,06	7,60	1,373	7,89	1,84	5,10	0,735	5,39	0,882	2,50	1,176	26,9	2,40
11KL	2220	38,1	57,0	9,26	35,3	9,94	2,70	9,81	1,486	8,45	1,84	5,45	0,929	5,33	0,898	3,75	1,084	21,1	2,88
18KL	5710	66,9	71,4	15,29	54,3	15,00	3,89	16,16	2,464	13,91	3,03	8,99	1,014	8,70	1,232	4,28	0,725	26,7	2,32
105KK	1630	37,0	52,5	8,31	32,7	6,97	1,64	7,36	1,092	6,90	1,43	4,12	0,563	3,84	0,599	3,63	0,915	12,2	19,33
114KK	2219	38,2	55,3	8,45	33,9	7,17	1,71	7,53	1,096	7,12	1,47	4,25	0,594	4,02	0,594	3,29	0,639	14,5	14,89
143KK	500	33,5	59,7	7,76	28,4	5,88	1,36	5,65	0,852	5,14	1,01	2,95	0,398	2,67	0,398	4,69	0,369	12,8	11,16
182SK	1219	30,3	53,3	6,90	25,5	6,40	1,58	5,81	0,931	5,31	1,17	3,24	0,517	3,38	0,552	3,60	0,810	18,3	6,72
223SK	595	28,5	51,0	6,33	24,9	6,74	1,42	5,67	0,869	4,62	0,96	2,93	0,492	2,84	0,492	3,00	0,934	19,5	4,46
232SK	638	27,0	49,6	6,38	24,0	5,90	1,37	5,63	0,843	4,63	0,96	2,96	0,493	3,07	0,493	3,37	0,906	20,5	5,06
76123	1533	24,9	44,2	5,84	21,9	3,95	0,88	4,02	0,605	3,60	0,70	1,98	0,256	1,93	0,256	1,53	0,465	15,4	11,79
76125	707	29,1	51,4	6,43	24,5	4,45	0,93	4,34	0,638	3,97	0,77	2,28	0,310	2,14	0,293	2,31	0,517	31,7	8,41
76127	538	22,2	44,1	5,32	20,3	4,11	0,92	3,73	0,575	3,42	0,67	1,93	0,281	1,91	0,281	2,64	0,489	37,2	6,63
76128	336	21,3	40,8	5,18	20,5	4,26	0,98	4,10	0,649	3,79	0,75	2,13	0,299	1,99	0,286	2,96	0,416	14,0	6,56
76132	144	15,4	31,1	3,90	14,8	3,56	0,82	3,94	0,540	3,08	0,57	1,68	0,222	1,46	0,222	1,87	0,317	37,8	11,14
76135	364	24,7	46,0	5,89	24,3	4,89	1,04	4,79	0,745	4,38	0,87	2,47	0,340	2,32	0,319	3,57	0,340	12,0	8,94
76136	348	30,1	60,7	7,42	27,0	5,78	1,17	5,23	0,823	4,69	0,94	2,69	0,373	2,45	0,373	3,93	0,404	12,2	4,46
77191																			
77194	281	28,5	58,5	6,50	23,3	4,66	1,01	3,92	0,581	3,23	0,65	1,90	0,267	1,72	0,244	2,62	0,430	18,8	5,85
77200	602	28,0	54,8	6,85	24,4	5,06	1,09	4,96	0,722	4,31	0,90	2,61	0,370	2,41	0,370	2,50	0,444	19,4	2,11
77202	503	20,5	41,7	5,19	19,1	3,98	0,87	3,90	0,570	3,42	0,68	2,01	0,285	1,78	0,267	2,05	0,410	14,5	6,11
77203	397	19,3	38,7	4,61	17,4	3,62	0,81	3,36	0,512	2,94	0,60	1,75	0,231	1,60	0,248	1,98	0,347	11,2	5,36
422	290	21,6	41,9	5,17	21,0	5,38	1,41	4,94	0,706	4,49	0,91	2,58	0,480	2,60	0,466	3,33	0,847	14,4	4,44
KS8	312	25,0	47,8	5,86	21,0	5,95	1,45	5,52	0,827	4,60	0,90	2,71	0,479	2,90	0,464	3,43	1,205	20,0	3,83
243	272	20,1	37,1	4,85	18,9	4,20	0,99	4,06	0,629	3,69	0,75	2,15	0,304	2,09	0,304	2,47	0,487	9,0	9,92
280	454	29,1	57,7	6,95	26,9	5,75	1,29	5,55	0,865	5,02	1,03	2,93	0,409	2,76	0,409	3,73	0,697	15,0	7,24

Appendix 1, Table 3) continued (Termination Ia samples)

core	depth	w.depth	CaCO3	Opal	Biogenic	< 2 µm	area	Corg	N	S	SiO2	TiO2	Al2O3	Fe2O3	MnO	MgO	CaO	P2O5	Si	Ti	Al	Fe	Mn	Mg	Ca, bulk	Ca, mar.	Ca, lith.	P	Li	Na	K	Sc
	cm	m	%	%	%	%	m2	%	%	%	wt%	wt%	wt%	wt%	wt%	wt%	wt%	wt%	%	%	%	%	%	%	%	%	%	%	ppm	%	%	ppm
15KL	50-54	3920	47,4	0,9	47,4			0,29	0,06	0,110	24,0	0,38	6,29	2,98	0,042	2,74	27,2	0,166	11,2	0,226	3,33	2,08	0,032	1,65	19,4	19,0	0,4	0,036				7,04
26KL	103-107	3776	35,5	1,6	35,5			0,73	0,07	0,194	32,7	0,51	8,96	4,28	0,067	3,41	21,0	0,199	15,3	0,307	4,74	2,99	0,052	2,06	15,0	14,2	0,8	0,043				10,10
36KL	43-47	2055	55,3	1,3	55,3			0,67	0,06	0,127	24,0	0,40	6,09	3,13	0,036	2,45	34,4	0,192	11,2	0,237	3,22	2,19	0,028	1,48	24,6	22,1	2,4	0,042				
51KL	130-134	2644	35,7	1,5	35,7			0,71	0,06	0,221																14,3						9,17
57KL	118-122	3422	36,7	1,6	36,7			1,47	0,13	0,297	34,5	0,46	8,14	3,91	0,117	4,08	24,0	0,201	16,1	0,276	4,31	2,73	0,091	2,46	17,1	14,7	2,5	0,044				8,66
64KL	96-100	3281	34,6	1,0	34,6			0,71	0,06	0,119	33,9	0,50	9,66	4,36	0,076	3,38	21,2	0,225	15,8	0,301	5,11	3,05	0,059	2,04	15,1	13,9	1,3	0,049				10,30
70KL	82-86	3810	44,1	1,9	44,1			1,80	0,09	0,149	29,4	0,42	6,99	3,38	0,111	3,87	27,2	0,197	13,8	0,253	3,70	2,37	0,086	2,33	19,5	17,6	1,8	0,043				8,05
71KL		4029																														
74KL	200-204	3212	55,2	1,9	55,2			1,23	0,08	0,333																22,1						5,63
79KL		4351								0,189																						
82KL	100-105	4416	51,5	2,9	51,5			0,38	0,07		20,9	0,29	4,83	2,50	0,070	2,87	30,7	0,143	9,8	0,172	2,56	1,75	0,055	1,73	22,0	20,6	1,3	0,031				6,22
87KL	118-122	3773	71,3	2,3	71,3			0,54	0,09	0,122	13,4	0,18	3,03	1,66	0,058	1,88	42,0	0,155	6,3	0,109	1,60	1,16	0,045	1,13	30,1	28,5	1,5	0,034				4,44
5KL	48-52	3335	68,0	1,6	68,0			0,42	0,04	0,117	14,8	0,24	3,98	2,16	0,112	1,72	41,5	0,145	6,9	0,142	2,11	1,51	0,087	1,03	29,7	27,2	2,5	0,032				5,08
11KL	65-69	3859	61,6	2,0	61,6			0,40	0,04	0,146	18,4	0,27	4,74	3,05	0,060	2,07	36,7	0,205	8,6	0,162	2,51	2,14	0,046	1,25	26,2	24,7	1,5	0,045				5,39
18KL	43-47	3035	82,1	2,4	82,1			0,14	0,04	0,136	7,8	0,11	1,85	1,20	0,037	0,82	50,0	0,143	3,6	0,065	0,98	0,84	0,029	0,50	35,7	32,9	2,8	0,031				2,70
105KK	138-143	3535	66,9	*1	66,9			0,67	0,07	0,232	17,6	0,22	3,24	1,64	0,033	1,68	40,1	0,185	8,2	0,132	1,72	1,14	0,026	1,01	28,6	26,8	1,8	0,040				5,31
114KK	137-141	3843	72,4	*1	72,4			0,72	0,08	0,157	12,6	0,17	2,52	1,34	0,025	1,43	43,0	0,148	5,9	0,101	1,33	0,94	0,019	0,86	30,7	29,0	1,7	0,032				3,98
143KK	253-258	1522	61,4	1,3	61,4			1,34	0,11	0,324	19,6	0,39	4,69	2,24	0,020	1,42	37,3	0,182	9,1	0,234	2,48	1,56	0,016	0,86	26,7	24,6	2,1	0,040				4,38
182SK		2234																														
223SK	98-103	2686	39,1	*1	39,1			0,76	0,08	0,141	36,0	0,49	8,95	3,96	0,070	3,07	24,4	0,253	16,8	0,293	4,74	2,77	0,054	1,85	17,4	15,7	1,8	0,055				8,94
232SK	110-115	3098	34,2	1,4	34,2			1,29	0,07	0,258	36,3	0,48	8,67	4,06	0,101	3,44	22,4	0,208	16,9	0,285	4,59	2,84	0,079	2,07	16,0	13,7	2,3	0,045				8,62
76123	78,50	2631	60,0	*1	60,0																					24,0						
76125	132,50	1878	42,0	*1	42,0																					16,8						
76127	57,50	1610	21,3	*1	21,3																					8,5						
76128	255,00	1712	16,7	*1	16,7																					6,7						
76132		1430																														
76135	247,50	1895	48,4	*1	48,4																					19,4						
76136	134,50	1649	19,0	*1	19,0																					7,6						
77191		1254																														
77194	389,00	1222	12,3	*1	12,3																					4,9						
77200	69,50	2910	50,0	*1	50,0																					20,0						
77202	198,00	2427	45,4	*1	45,4																					18,2						
77203	368,50	2442	39,0	*1	39,0																					15,6						
422	184-188	2732	25,0	1,2	26,2			1,55	0,11	0,565	39,4	0,53	9,47	4,54	0,072	5,07	17,5	0,302	18,4	0,318	5,01	3,18	0,056	3,06	12,5	10,0	2,5	0,066				10,70
KS8	285-292	2900	31,2	*1	31,2			1,27	0,08	0,346	40,0	0,52	9,50	4,39	0,073	4,64	17,1	0,223	18,7	0,312	5,03	3,07	0,056	2,80	12,2	12,5	-0,3	0,049				
243		1041																														
280		2106																														

*1: biogenic opal not determined, thus, element concentrations are expressed only on the carbonate-free-basis (cfb)

Appendix 1, Table 4) Chemical composition at the depth level of the Last Glacial Maximum (21,000-23,000 cal-yrBP). Concentration values in the bulk fraktion (% or ppm), concentration values expressed on a carbonate-free-basis (% or ppm, cfb)

core	Cr	Co	Ni	Cu	Zn	Ga	As	Rb	Sr	Y	Zr	Nb	Mo	Cd	Cs	Ba	La	Ce	Pr	Nd	Sm	Eu	Gd	Tb	Dy	Ho	Er	Tm	Yb	Lu	Hf	Tl
	ppm	ppm	ppm	ppm	ppm	ppm	ppm	ppm	ppm	ppm	ppm	ppm	ppm	ppm	ppm	ppm	ppm	ppm	ppm	ppm	ppm	ppm	ppm	ppm	ppm	ppm	ppm	ppm	ppm	ppm	ppm	ppm
15KL	67,5	9,34	70,0	37,8	67,7	7,84		47,9	765	16,9	51,3	6,24	0,22		3,45	394	13,30	24,8	3,13	12,60	2,58	0,553	2,48	0,377	2,42	0,489	1,490	0,212	1,430	0,214	1,41	0,31
26KL	89,4	13,10	81,0	41,8	82,5	11,60		76,1	630	18,2	60,6	8,60	0,39		5,19	512	16,20	30,9	3,81	15,10	3,02	0,625	2,82	0,438	2,69	0,536	1,620	0,238	1,540	0,228	1,59	0,39
36KL																																
51KL	86,0	13,40	67,0	27,4	65,1	10,20		69,6	577	16,3	56,7	8,31	0,49		4,80	325	16,30	32,3	3,89	15,20	3,14	0,651	2,82	0,460	2,58	0,528	1,530	0,239	1,430	0,232	1,67	0,41
57KL	94,4	17,00	103,0	35,6	83,0	9,04		57,6	580	15,0	51,2	7,15	1,43		4,01	355	14,20	28,0	3,40	13,20	2,73	0,573	2,49	0,388	2,34	0,465	1,400	0,208	1,350	0,212	1,45	0,65
64KL	90,6	18,40	79,1	38,6	79,5	11,90		88,4	583	16,9	51,9	9,06	0,35		6,06	360	17,40	34,6	4,11	15,90	3,15	0,637	2,87	0,446	2,64	0,528	1,550	0,223	1,470	0,219	1,40	0,49
70KL	102,0	14,80	113,0	38,6	79,1	8,15		49,6	686	17,1	56,8	6,79	0,60		3,46	376	13,70	26,1	3,25	13,00	2,69	0,592	2,68	0,403	2,43	0,513	1,530	0,216	1,450	0,217	1,55	0,48
71KL																																
74KL	80,4	10,00	72,0	28,4	58,0	5,73		32,1	893	13,9	41,4	5,31	2,57		2,22	412	10,00	18,0	2,38	9,46	2,01	0,394	1,98	0,293	1,88	0,373	1,130	0,160	1,110	0,159	1,09	0,31
79KL																																
82KL	61,8	10,50	83,6	32,4	67,5	5,94		33,6	839	15,5	40,4	4,96	0,82		2,42	320	11,70	20,1	2,80	11,30	2,32	0,511	2,32	0,358	2,21	0,443	1,310	0,183	1,240	0,177	0,97	0,38
87KL	35,2	7,97	59,5	24,8	46,3	3,79		21,8	1143	11,3	20,5	3,44	0,91		1,60	505	8,71	13,3	2,03	8,35	1,69	0,368	1,77	0,262	1,63	0,352	1,020	0,145	0,909	0,139	0,53	0,33
5KL	37,4	19,10	46,6	28,2	41,9	4,66		27,9	1084	16,6	30,1	4,38	0,50		2,07	584	11,50	17,2	2,67	10,50	2,16	0,442	2,22	0,360	2,11	0,456	1,350	0,202	1,240	0,204	0,89	0,17
11KL	43,1	8,04	59,9	45,9	63,2	5,99		36,2	1020	19,0	42,9	5,01	0,20		2,52	683	13,30	19,8	3,15	12,90	2,67	0,558	2,70	0,425	2,13	0,548	1,620	0,227	1,480	0,221	1,11	0,27
18KL	16,7	5,47	19,3	28,1	27,3	2,42		12,2	1100	17,0	16,4	2,16	0,27		0,85	786	9,72	10,3	2,27	9,63	2,08	0,428	2,23	0,346	2,19	0,460	1,340	0,186	1,200	0,182	0,48	0,09
105KK	34,1	6,09	41,6	33,7	49,4	4,65		20,9	1121	15,3	34,7	5,28	1,18		1,35	604	11,10	16,3	2,56	10,40	2,15	0,443	2,22	0,329	2,07	0,433	1,270	0,182	1,170	0,170	0,89	0,22
114KK	25,8	4,15	30,9	24,8	30,3	3,11		16,3	1228	11,9	25,2	3,85	0,48		1,09	365	8,43	12,1	1,99	7,94	1,62	0,345	1,69	0,255	1,58	0,323	0,984	0,139	0,894	0,129	0,71	0,14
143KK	30,0	5,06	24,0	15,6	37,9	5,43		25,6	1183	12,3	72,7	12,20	0,72		1,05	279	12,60	22,6	2,91	11,30	2,19	0,480	1,96	0,301	1,82	0,369	1,110	0,156	1,090	0,152	1,85	0,14
182SK																																
223SK	77,9	13,60	62,8	27,5	63,5	9,89		69,5	746	16,4	47,7	8,87	0,56		4,95	320	16,80	32,6	3,96	15,20	3,08	0,635	2,78	0,435	2,55	0,531	1,440	0,214	1,380	0,226	1,47	0,43
232SK	88,1	20,20	93,3	32,6	76,1	9,72		63,0	574	16,0	54,4	8,73	1,48		4,75	343	16,10	31,6	3,86	14,50	3,12	0,673	2,80	0,468	2,5	0,562	1,520	0,280	1,470	0,269	1,52	0,57
76123																																
76125																																
76127																																
76128																																
76132																																
76135																																
76136																																
77191																																
77194																																
77200																																
77202																																
77203																																
422	139,0	14,50	107,0	27,8	68,2	10,30		63,3	357	16,2	62,0	8,44	1,83		4,72	222	15,50	30,8	3,75	14,20	2,98	0,697	2,74	0,448	2,5	0,542	1,500	0,242	1,520	0,237	1,69	0,36
KS8																																
243																																
280																																

Appendix 1, Table 4) continued (Last Glacial Maximum samples)

core	Pb	U	Corg	N	S	Si opal co	Ti	Al	Fe	Mn	Mg	Ca, lith.	P	Li(Flame)	Na	K	Sc	Cr	Co	Ni	Cu	Zn	Ga	As	Pb	Sr/Ca	Y	Zr	Nb	Mo	Cd	Cs
	ppm	ppm	% cofb	% cofb	% cofb	% cofb	% cofb	% cofb	% cofb	% cofb	% cofb	% cofb	% cofb	ppm cofb	% cofb	% cofb	ppm cofb	ppm cofb	ppm cofb	ppm cofb	ppm cofb	ppm cofb	ppm cofb	ppm cofb	ppm cofb		ppm cofb	ppm cofb	ppm cofb	ppm cofb	ppm cofb	ppm cofb
15KL	8,63	4,75	0,55	0,11	0,21	20,5	0,429	6,33	3,96	0,062	3,14	0,8	0,069				13,4	128	17,7	133	72	129	14,9		91,0	40,3	32,1	97	11,9	0,41		6,55
26KL	12,00	2,30	1,13	0,11	0,30	22,5	0,476	7,36	4,64	0,081	3,19	1,3	0,067				15,7	139	20,3	126	65	128	18,0		118,0	44,3	28,2	94	13,3	0,61		8,05
36KL			1,50	0,13	0,28	23,7	0,531	7,21	4,90	0,062	3,30	5,4	0,093																			
51KL	12,70	2,86	1,10	0,09	0,34												14,3	134	20,8	104	43	101	15,9		108,2	40,4	25,3	88	12,9	0,77		7,46
57KL	11,30	4,11	2,32	0,21	0,47	24,3	0,437	6,80	4,32	0,143	3,89	3,9	0,069				13,7	149	26,9	163	56	131	14,3		91,0	39,5	23,7	81	11,3	2,26		6,33
64KL	15,20	2,35	1,09	0,09	0,18	23,5	0,461	7,82	4,67	0,090	3,12	1,9	0,075				15,8	139	28,1	121	59	122	18,2		135,2	42,1	25,9	79	13,9	0,54		9,27
70KL	9,53	2,89	3,22	0,16	0,27	23,0	0,452	6,61	4,23	0,154	4,17	3,3	0,077				14,4	182	26,5	202	69	141	14,6		88,7	38,9	30,6	102	12,1	1,07		6,19
71KL																																
74KL	6,90	3,39	2,74	0,18	0,74												12,6	179	22,3	161	63	129	12,8		71,6	40,4	31,0	92	11,8	5,73		4,95
79KL																																
82KL	6,81	3,03	0,78	0,14		17,4	0,355	5,28	3,60	0,112	3,58	2,8	0,065				12,8	128	21,7	172	67	139	12,3		69,3	40,7	32,0	83	10,2	1,69		4,99
87KL	4,60	4,09	1,88	0,31	0,42	18,1	0,381	5,58	4,03	0,157	3,94	5,3	0,117				15,4	122	27,7	207	86	161	13,2		75,9	40,1	39,3	71	12,0	3,15		5,57
5KL	6,16	0,69	1,31	0,12	0,37	19,3	0,445	6,58	4,71	0,271	3,23	7,7	0,099				15,9	117	59,6	146	88	131	14,6		87,1	39,8	51,8	94	13,7	1,57		6,46
11KL	6,42	2,77	1,04	0,10	0,38	20,0	0,422	6,54	5,56	0,121	3,26	4,0	0,117				14,0	112	20,9	156	120	165	15,6		94,3	41,3	49,5	112	13,1	0,51		6,57
18KL	6,49	0,36	0,78	0,22	0,76	14,1	0,364	5,49	4,69	0,161	2,78	15,9	0,175				15,1	94	30,6	108	157	153	13,5		68,3	33,4	95,2	92	12,1	1,52		4,74
105KK	3,78	5,51	2,02	0,21	0,70		0,398	5,18	3,46	0,077	3,05	5,6	0,122				16,0	103	18,4	126	102	149	14,0		63,1	41,9	46,2	105	15,9	3,56		4,08
114KK	3,46	3,54	2,61	0,29	0,57		0,365	4,82	3,39	0,070	3,11	6,3	0,117				14,4	93	15,0	112	90	110	11,3		59,0	42,4	43,1	91	13,9	1,74		3,95
143KK	4,71	3,97	3,47	0,28	0,84	22,1	0,605	6,43	4,05	0,041	2,22	5,4	0,103				11,3	78	13,1	62	40	98	14,1		66,3	48,1	31,8	188	31,6	1,87		2,72
182SK																																
223SK	12,00	3,15	1,25	0,13	0,23		0,482	7,78	4,55	0,089	3,04	2,9	0,091				14,7	128	22,3	103	45	104	16,2		114,1	47,6	26,9	78	14,6	0,92		8,13
232SK	13,00	3,44	1,96	0,11	0,39	24,8	0,434	6,98	4,32	0,119	3,15	3,6	0,069				13,1	134	30,7	142	50	116	14,8		95,8	41,9	24,3	83	13,3	2,25		7,22
76123																																
76125																																
76127																																
76128																																
76132																																
76135																																
76136																																
77191																																
77194																																
77200																																
77202																																
77203																																
422	10,50	3,01	2,10	0,15	0,77	24,2	0,430	6,79	4,30	0,076	4,15	3,4	0,089				14,5	188	19,6	145	38	92	14,0		85,8	35,7	22,0	84	11,4	2,48		6,40
KS8			1,85	0,12	0,50		0,453	7,31	4,46	0,082	4,07	-0,4	0,071																			
243																																
280																																

Appendix 1, Table 4) continued (Last Glacial Maximum samples)

core	Ba	La	Ce	Pr	Nd	Sm	Eu	Gd	Tb	Dy	Ho	Er	Tm	Yb	Lu	Hf	Tl	Pb	U
	ppm cofb	ppm cofb	ppm cofb	ppm cofb	ppm cofb	ppm cofb	ppm cofb	ppm cofb	ppm cofb	ppm cofb	ppm cofb	ppm cofb	ppm cofb	ppm cofb	ppm cofb	ppm cofb	ppm cofb	ppm cofb	ppm cofb
15KL	749	25,3	47,1	5,95	23,9	4,90	1,05	4,71	0,716	4,60	0,93	2,83	0,403	2,72	0,407	2,68	0,579	16,4	9,02
26KL	794	25,1	47,9	5,91	23,4	4,68	0,97	4,37	0,679	4,17	0,83	2,51	0,369	2,39	0,354	2,47	0,602	18,6	3,57
36KL																			
51KL	505	25,3	50,2	6,05	23,6	4,88	1,01	4,38	0,715	4,01	0,82	2,38	0,372	2,22	0,361	2,60	0,637	19,7	4,45
57KL	561	22,4	44,2	5,37	20,9	4,31	0,91	3,93	0,613	3,70	0,73	2,21	0,329	2,13	0,335	2,29	1,019	17,9	6,49
64KL	551	26,6	52,9	6,29	24,3	4,82	0,97	4,39	0,682	4,04	0,81	2,37	0,341	2,25	0,335	2,14	0,756	23,3	3,59
70KL	672	24,5	46,7	5,81	23,2	4,81	1,06	4,79	0,720	4,34	0,92	2,74	0,386	2,59	0,388	2,77	0,862	17,0	5,17
71KL																			
74KL	919	22,3	40,1	5,31	21,1	4,48	0,88	4,42	0,653	4,19	0,83	2,52	0,357	2,48	0,355	2,43	0,682	15,4	7,56
79KL																			
82KL	660	24,1	41,5	5,78	23,3	4,79	1,05	4,79	0,739	4,56	0,91	2,70	0,378	2,56	0,365	2,01	0,774	14,0	6,25
87KL	1757	30,3	46,3	7,06	29,1	5,88	1,28	6,16	0,912	5,67	1,22	3,55	0,505	3,16	0,484	1,83	1,159	16,0	14,23
5KL	1824	35,9	53,7	8,34	32,8	6,75	1,38	6,93	1,124	6,59	1,42	4,22	0,631	3,87	0,637	2,76	0,515	19,2	2,17
11KL	1780	34,7	51,6	8,21	33,6	6,96	1,45	7,03	1,107	5,55	1,43	4,22	0,591	3,86	0,576	2,89	0,701	16,7	7,22
18KL	4401	54,4	57,7	12,71	53,9	11,65	2,40	12,49	1,937	12,26	2,58	7,50	1,041	6,72	1,019	2,68	0,510	36,3	2,01
105KK	1824	33,5	49,2	7,73	31,4	6,49	1,34	6,70	0,994	6,25	1,31	3,84	0,550	3,53	0,513	2,67	0,658	11,4	16,64
114KK	1322	30,5	43,8	7,21	28,8	5,87	1,25	6,12	0,923	5,72	1,17	3,56	0,503	3,24	0,467	2,57	0,500	12,5	12,82
143KK	722	32,6	58,5	7,53	29,3	5,67	1,24	5,07	0,779	4,71	0,96	2,87	0,404	2,82	0,393	4,79	0,365	12,2	10,28
182SK																			
223SK	526	27,6	53,5	6,50	25,0	5,06	1,04	4,57	0,714	4,19	0,87	2,37	0,351	2,27	0,371	2,41	0,698	19,7	5,17
232SK	522	24,5	48,0	5,87	22,0	4,74	1,02	4,26	0,712	3,80	0,85	2,31	0,426	2,24	0,409	2,31	0,859	19,8	5,23
76123																			
76125																			
76127																			
76128																			
76132																			
76135																			
76136																			
77191																			
77194																			
77200																			
77202																			
77203																			
422	301	21,0	41,7	5,08	19,2	4,04	0,94	3,71	0,607	3,39	0,73	2,03	0,328	2,06	0,321	2,29	0,493	14,2	4,08
KS8																			
243																			
280																			

Appendix 1, Table 4) continued (Last Glacial Maximum samples)

sample	Age	Dry Dens	Water content	>63 um	G.ruber	G.ruber 18 O	G.ruber 13 C	CaCO3 18 O	CaCO3 13 C	CaCO3	CaCO3 lith.	CaCO3 marine	C.wuell. 18 O	C.wuell. 13 C	specific area	<2 um new	N	C org	C/N	Palyg.	Quarz 1.run	Dolomit 1.run	Quarz 2.run	Dolomit 2.run	Quarz mean	Dolomit mean
cm	cal.yrBP	g/ccm	%	%	#/g	‰ PDB	‰ PDB	‰ PDB	‰ PDB	%	%	%	‰ PDB	‰ PDB	m2/g	%	%	%		%	impulse	impulse	impulse	impulse	impulse	impulse
2,50	0,61	0,47	64,2	4,63	8,33	-1,62	1,32	-1,83	-0,55	60,63	2,91	57,72	2,47	0,11			0,16	1,26	7,90	24,00	16,80	1,22	16,80	1,20	16,80	1,21
5,00	0,95	0,52	61,2	4,29	10,00	-1,73	1,43	-1,80	-0,52	58,79	0,96	57,83					0,18	1,26	6,97	31,00	18,10	0,30	16,00	1,70	17,05	1,00
7,50	1,17			4,12	2,06	-1,66	1,49	-1,83	-0,54	60,37	2,36	58,01					0,18	1,28	7,09	26,00	17,80	0,70	15,90	2,00	16,85	1,35
10,00	1,39	0,54	60,5	3,60	5,41	-1,74	1,56	-1,78	-0,46	62,28	0,58	61,70	2,37	0,03			0,19	1,21	6,35							
12,50	1,62			3,96	4,95	-1,79	1,09	-1,76	-0,53	62,11	-0,44	62,55	2,53	-0,16			0,18	1,16	6,43	21,00	18,20	0,80	15,60	1,10	16,90	0,95
15,00	1,84	0,54	60,3	4,17	5,21	-1,94	1,06	-1,84	-0,47	60,67	-1,49	62,16					0,18	1,26	7,00	30,00	20,00	0,70	14,80	1,00	17,40	0,85
17,50	2,07			3,96	5,94	-1,71	1,29	-1,85	-0,52	60,80	1,98	58,82	2,36	0,13			0,17	1,17	6,91	31,00	18,90	3,70	18,20	2,20	18,55	2,95
20,00	2,29	0,57	59,1	4,90	11,76	-1,65	1,13	-1,75	-0,52	62,31	1,43	60,88	2,37	0,17			0,16	1,11	6,96		17,20	1,00	16,70	0,60	16,95	0,80
22,50	2,51			3,31	6,61	-1,82	1,34	-1,70	-0,46	64,52	-1,85	66,37	2,44	0,19			0,13	0,95	7,29	27,00	22,20	4,00	18,80	1,00	20,50	2,50
25,00	2,74	0,63	55,8	3,96	9,90	-1,70	1,34	-1,87	-0,50	64,14	2,54	61,60	2,29	0,17			0,13	0,96	7,41	26,00	20,50	1,80	17,30	1,40	18,90	1,60
27,50	2,96			4,17	15,00	-1,79	1,48	-1,77	-0,51	66,15	-0,31	66,46					0,12	0,83	6,93	27,00	18,80	4,00	19,30	1,00	19,05	2,50
30,00	3,18	0,68	53,4	4,26	14,36	-1,82	1,51	-1,74	-0,55	66,75	-1,28	68,03	2,39	0,25			0,12	0,81	6,75	22,00	19,00	2,60	19,90	1,90	19,45	2,25
32,50	3,41			4,46	26,11	-1,71	1,42	-1,83	-0,49	62,29	1,74	60,55					0,13	0,88	6,73	18,00	16,10	1,10	13,60	1,30	14,85	1,20
35,00	3,63	0,68	53,1	4,72	35,43	-2,11	1,33	-1,79	-0,50	64,21	-5,28	69,49	2,20	0,16			0,15	0,92	6,17	33,00	14,50	1,70	15,00	0,70	14,75	1,20
37,50	3,97			6,04	21,43	-1,72	1,41	-1,72	-0,47	64,28	1,00	64,28					0,12	0,81	6,72	25,00	19,80	1,30	19,10	0,90	19,45	1,10
40,00	4,30	0,69	53,1	5,82	24,34	-1,77	1,36	-1,67	-0,54	69,81	-1,65	71,46	2,38	0,00			0,10	0,56	5,63	30,00	19,30	1,70	16,90	2,20	18,10	1,95
42,50	4,64			5,29	20,63	-1,82	1,49	-1,76	-0,55	65,12	-0,93	66,05					0,11	0,64	5,78	25,00	18,20	2,70	17,50	3,20	17,85	2,95
45,00	4,98	0,53	61,2	7,07	28,26	-1,67	1,32	-1,68	-0,47	66,30	0,15	66,15	2,40	0,07			0,10	0,64	6,44	18,00	21,50	3,20	18,80	2,40	20,15	2,80
47,50	5,31			6,21	31,06	-1,77	1,39	-1,72	-0,51	66,20	-0,78	66,98	2,54	0,25			0,10	0,66	6,56	25,00	20,00	4,00	18,90	2,70	19,45	3,35
50,00	5,65	0,68	53,0	6,19	24,74	-1,67	1,36	-1,70	-0,56	69,56	0,48	69,08	2,66	0,22	18,76		0,10	0,78	7,83	29,00	20,90	2,60	17,10	3,00	19,00	2,80
52,50	5,98			7,10	30,97	-1,80	1,41	-1,66	-0,52	68,36	-2,28	70,64	2,41	0,05			0,12	0,84	6,97	19,00	17,90	2,80	17,20	3,10	17,55	2,95
55,00	6,32	0,67	53,3	8,51	42,55	-1,84	1,31	-1,64	-0,59	70,39	-3,38	73,77	2,32	0,12	19,10		0,09	0,72	8,04	26,00	21,20	3,20	16,80	3,90	19,00	3,55
57,50	6,71			7,32	31,71	-1,80	1,19	-1,67	-0,60	67,48	-2,09	69,57	2,38	0,21			0,10	1,13	11,32	13,00	19,70	4,60	15,90	4,30	17,80	4,45
60,00	7,09	0,69	52,3	8,57	40,00	-1,69	1,29	-1,64	-0,68	69,76	-0,81	70,57	2,41	0,17	18,50		0,10	0,70	6,99	27,00	18,70	1,50	16,70	3,00	17,70	2,25
62,50	7,48			8,26	41,32	-1,79	1,35	-1,68	-0,66	70,40	-1,84	72,24	2,38	0,10			0,10	0,64	6,42	7,00	19,50	6,00	14,40	4,00	16,95	5,00
65,00	7,86	0,66	54,0	8,33	25,00	-1,91	1,32	-1,79	-0,76	67,93	-1,99	69,92			20,60		0,10	0,80	7,98	11,00	18,30	5,30	16,70	4,90	17,50	5,10
67,50	8,25			7,09	29,79	-1,62	1,14	-1,67	-0,78	66,81	0,76	66,05	2,39	0,07		55,89	0,11	0,83	7,57	12,00	25,00	-0,50	19,30	3,90	22,15	1,70
70,00	8,63	0,65	54,4	8,59	33,13	-1,58	0,99	-1,71	-0,90	68,72	2,02	66,70	2,63	0,13	20,37	51,87	0,11	0,81	7,40	8,00	22,60	-0,50	22,20	0,20	22,40	-0,15
72,50	8,86			7,98	28,19			-1,52	-0,73	66,53						54,88	0,11	0,91	8,24	13,00	22,60	0,02	19,40	0,00	21,00	0,01
75,00	9,09	0,68	53,4	8,98	24,55	-1,60	1,19	-1,58	-0,77	68,50	-0,31	68,81			18,60	54,04	0,12	0,86	7,17	19,00	19,10	-0,40	18,40	0,00	18,75	-0,20
77,50	9,32			8,21	26,15	-1,69	1,18	-1,46	-0,72	66,78	-3,56	70,34	2,58	0,00		53,58	0,12	0,93	7,72	14,00	20,50	-0,40	17,90	0,70	19,20	0,15
80,00	9,55	0,70	52,0	7,31	31,96	-1,79	1,09	-1,32	-0,76	69,80	-7,79	77,59	3,04	0,10	23,80	53,28	0,11	0,75	6,85	9,00	23,20	-0,20	20,30	0,00	21,75	-0,10
82,50	9,88			8,33	26,92	-1,41	1,10	-1,47	-0,80	68,93	0,90	68,03	2,70	0,14		53,28	0,12	0,83	6,90	11,00	22,20	-0,06	19,80	0,10	21,00	0,02
85,00	10,22	0,71	51,0	9,27	15,89	-1,38	1,05	-1,29	-0,62	69,64	-1,36	71,00	2,63	0,16	18,70	54,95	0,09	0,67	7,48	13,00	26,70	-0,10	19,90	0,00	23,30	-0,05
87,50	10,55			11,11	24,56	-1,45	1,01	-1,27	-0,76	67,84	-2,68	70,52	2,95	-0,29		52,18	0,09	0,99	10,99	11,00	25,80	0,80	23,60	0,90	24,70	0,85
90,00	10,88	0,78	49,0	11,84	26,32	-1,51	1,16	-1,37	-0,88	70,02	-2,18	72,20	2,56	0,23	18,90	50,06	0,09	0,69	7,64	8,00	28,80	0,90	22,10	1,40	25,45	1,15
92,50	11,21			12,50	31,73	-0,97	0,87	-1,18	-0,77	70,89	2,96	67,93	2,59	0,06		49,98	0,10	0,51	5,13		24,50	0,30	23,40	1,10	23,95	0,70
95,00	11,55	0,79	48,1	12,50	48,00	-1,14	0,86	-1,09	-0,73	67,55	-0,69	68,24	3,02	0,05	18,40	47,86	0,07	0,81	11,63	8,00	24,60	3,30	23,80	3,70	24,20	3,50
97,50	11,88			14,49	58,94	-0,94	0,94	-1,02	-0,77	67,76	1,07	66,69	2,69	-0,15		49,76	0,07	0,46	6,55	6,00	31,50	-0,40	30,50	0,00	31,00	-0,20
100,00	12,15	0,85	46,1	12,43	55,37	-0,88	1,03	-0,84	-0,68	67,19	-0,52	67,71	3,23	-0,16	19,50	46,66	0,06	0,32	5,29	7,00	28,30	0,90	30,90	1,50	29,60	1,20
102,50	12,42			9,24	35,87	-0,79	0,85	-0,90	-0,64	68,30	1,44	66,86	3,10	0,01		43,33	0,07	0,37	5,34	7,00	31,10	1,40	27,90	2,50	29,50	1,95
105,00	12,69			8,70	43,48	-0,67	0,89	-1,01	-0,69	69,94	4,46	65,48	3,32	-0,10	18,30	43,65	0,06	0,42	6,95	7,00	33,50	1,30	26,10	1,50	29,80	1,40
107,50	12,97			10,19	27,18	-0,87	0,84	-0,74	-0,57	68,80	-1,74	70,54	3,45	-0,10		45,12	0,09	0,60	6,71	7,00	32,00	1,60	24,20	0,60	28,10	1,10
110,00	13,24	0,85	45,3	7,89	35,53	-0,74	0,65	-0,88	-0,79	70,07	1,86	68,21	3,37	-0,14	17,90	46,21	0,08	0,56	7,02	10,00	30,20	3,90	26,90	4,20	28,55	4,05
112,50	13,51			8,91	30,69	-0,85	0,94	-0,96	-0,68	68,00	1,45	66,55	3,39	0,49		41,89	0,10	0,68	6,80	1,00	25,40	9,50	21,10	10,60	23,25	10,05
115,00	13,78			9,25	42,77	-0,89	1,06	-1,01	-0,80	68,10	1,60	66,50	3,18	-0,26	14,10	43,72	0,07	0,69	9,83	8,00	28,10	5,30	27,40	7,30	27,75	6,30
117,50	14,24			8,88	35,51	-1,09	0,69	-0,95	-0,79	69,26	-1,97	71,23	3,17	-0,19		41,95	0,12	0,64	5,32	8,00	26,70	9,40	26,30	9,60	26,50	9,50
120,00	14,69	0,79	48,6	8,82	29,41	-0,73	0,83	-0,77	-0,68	66,18	0,50	65,68	3,02	-0,25	18,40	43,02	0,09	0,57	6,32	9,00	30,10	4,20	26,50	3,60	28,30	3,90
122,50	15,15			10,00	41,05	-0,62	0,70	-0,73	-0,65	66,81	1,37	65,44	3,39	-0,03		41,37	0,08	0,38	4,79	7,00	31,50	4,90	25,60	5,40	28,55	5,15
125,00	15,60			10,20	41,84	-0,79	0,54	-0,91	-0,71	68,15	1,57	66,58	3,49	-0,03	17,80	45,18	0,08	0,50	6,27	6,00	34,80	1,10	33,20	1,00	34,00	1,05
127,50	16,06			9,22	76,70	-0,34	0,70	-0,61	-0,57	62,17	2,97	59,20				40,80	0,06	0,34	5,66	8,00	34,10	0,60	32,70	1,00	33,40	0,80
130,00	16,33	0,88	44,8	8,63	44,67	-0,15	0,67	-0,64	-0,81	60,43	5,06	55,37					0,05	0,27	5,37						#DIV/0!	#DIV/0!
132,50	16,61			5,42	29,17	-0,39	0,56	-0,77	-0,63	58,76	3,98	54,78				37,67	0,07	0,23	3,27	7,00	31,80	9,50	29,20	9,50	30,50	9,50
135,00	16,88			8,22	41,10	-0,45	0,66	-0,71	-0,62	58,57	2,74	55,83	4,05	0,18	22,75	36,14	0,06	0,24	4,03	6,00	29,50	10,70	25,30	8,70	27,40	9,70
137,50	17,15			5,46	30,03	-0,05	0,59	-0,71	-0,61	58,13	6,45	51,68				38,16	0,06	0,28	4,74	5,00	30,10	9,00	25,70	7,40	27,90	8,20
140,00	17,43	0,91	43,2	5,91	33,76	-0,08	0,65	-0,68	-0,54	58,89	5,97	52,92	3,83	-0,37	23,40	36,55	0,06	0,35	5,89	6,00	27,90	9,30	27,90	10,70	27,90	10,00
142,50	17,70			6,25	42,97	-0,09	0,74	-0,72	-0,53	59,85	6,38	53,47	3,99	-0,41		37,39	0,08	0,40	4,98	6,00	28,90	8,40	32,20	9,00	30,55	8,70
145,00	17,94			6,64	35,68	-0,15	0,76	-0,58	-0,57	59,22	4,35	54,87	3,88	-0,25	21,10	37,48	0,08	0,50	6,30	8,00	31,50	14,90	27,70	12,50	29,60	13,70
147,50	18,18			6,15	26,23	-0,22	0,53	-0,58	-0,45	61,33	3,82	57,51	3,92	0,04		35,59	0,08	0,53	6,63	8,00	26,90	14,80	23,00	15,60	24,95	15,20
150,00	18,42	0,87	44,7	5,83	29,17	-0,26	0,31	-0,55	-0,52	60,69	3,07	57,62	3,95	-0,16	18,80	45,47	0,08	0,60	7,47	8,00	26,70	12,70	29,50	13,30	28,10	13,00

Appendix 2, Table 1) Sediment core 74KL, sedimentology, isotope and mineral composition

sample	Age	Dry Dens	Water content	>63 um	G.ruber	G.ruber 18 O	G.ruber 13 C	CaCO3 18 O	CaCO3 13 C	CaCO3	CaCO3 lith.	CaCO3 marine	C.wuell. 18 O	C.wuell. 13 C	specific area	<2 um new	N	C org	C/N	Palyg.	Quarz 1.run	Dolomit 1.run	Quarz 2.run	Dolomit 2.run	Quarz mean	Dolomit mean
cm	cal.yrBP	g/ccm	%	%	#/g	‰ PDB	‰ PDB	‰ PDB	‰ PDB	%	%	%	‰ PDB	‰ PDB	m2/g	%	%	%		%	impulse	impulse	impulse	impulse	impulse	impulse
152,50	18,66			5,51	18,90	-0,01	0,66	-0,63	-0,53	61,69	6,39	55,30	4,02	-0,34		41,90	0,10	0,74	7,37	7,00	33,80	15,40	24,40	8,50	29,10	11,95
155,00	18,90			4,65	23,26	-0,19	0,75	-0,49	-0,51	62,90	3,25	59,65	3,96	-0,69		37,39	0,10	0,74	7,42	8,00	26,10	13,90	23,30	10,40	24,70	12,15
157,50	19,14			4,75	22,78	-0,09	0,69	-0,61	-0,46	61,48	5,41	56,07	3,83	-0,33		37,39	0,13	0,87	6,71	6,00	27,40	14,30	21,90	15,20	24,65	14,75
160,00	19,38	0,83	46,7	5,26	25,56	-0,30	0,69	-0,57	-0,48	61,12	2,90	58,22	4,02	-0,31		38,35	0,12	0,87	7,21	5,00	32,20	16,10	21,70	9,70	26,95	12,90
162,50	19,57			3,88	12,62	-0,20	0,52	-0,60	-0,50	60,02	4,14	55,88	3,93	-0,30		35,88	0,12	0,86	7,15	7,00	30,80	15,20	25,50	9,50	28,15	12,35
165,00	19,76			4,86	25,91	-0,04	0,81	-0,53	-0,39	61,27	5,04	56,23	3,98	-0,39		35,23	0,11	0,81	7,34	10,00	29,70	16,70	30,10	13,40	29,90	15,05
167,50	19,91			5,00	18,18	-0,47	0,81	-0,63	-0,44	60,53	1,75	58,78	3,95	-0,49		38,08	0,12	0,92	7,64	5,00	30,00	14,60	25,10	12,50	27,55	13,55
170,00	20,05	0,80	44,5	4,98	20,90	-0,12	0,66	-0,53	-0,54	61,56	4,29	57,27	4,02	-0,61		39,12	0,12	0,93	7,77	6,00	35,60	14,90	23,20	10,60	29,40	12,75
172,50	20,19			4,12	10,82	-0,13	0,61	-0,56	-0,45	62,05	4,55	57,50	4,10	-0,23		39,69	0,12	0,74	6,20	8,00	30,40	12,90	26,40	8,50	28,40	10,70
175,00	20,34			4,12	16,48	-0,26	0,64	-0,64	-0,48	60,49	4,00	56,49	4,20	-0,35		39,76	0,12	0,90	7,51	6,00	30,80	11,20	27,50	9,80	29,15	10,50
177,50	20,48			3,91	11,07	-0,43	0,58	-0,62	-0,42	60,83	2,07	58,76	4,11	-0,30		39,09	0,11	0,85	7,73	7,00	27,70	13,80	24,10	11,60	25,90	12,70
180,00	20,63	0,84	46,1	3,69	17,51	0,01	0,95	-0,48	-0,30	60,70	4,95	55,75	4,06	-0,24		38,33	0,11	0,87	7,87	4,00	30,60	14,60	25,70	10,40	28,15	12,50
182,50	21,12			3,99	11,23	-0,13	0,87	-0,56	-0,34	60,64	4,44	56,20	3,93	-0,37		37,97	0,12	0,87	7,28	7,00	31,30	17,80	23,80	14,40	27,55	16,10
185,00	21,62			4,11	11,64	0,02	0,74	-0,65	-0,41	59,85	6,66	53,19	3,92	-0,35		36,62	0,11	0,78	7,07	7,00	28,60	12,60	24,70	13,10	26,65	12,85
187,50	22,11			4,05	8,11	-0,17	0,47	-0,68	-0,49	59,40	5,20	54,20	3,96	-0,43		36,61	0,12	0,80	6,68	7,00	34,60	16,70	29,80	13,60	32,20	15,15
190,00	22,60	0,82	46,8	4,17	17,26	-0,03	0,86	-0,71	-0,57	60,32	6,87	53,45	4,09	-0,44		36,36	0,12	0,83	6,93	7,00	33,00	15,00	26,00	12,30	29,50	13,65
192,50	23,09			3,77	7,53	-0,22	0,71	-0,78	-0,55	61,66	5,97	55,69	3,82	-0,46		37,98	0,12	0,74	6,17	5,00	33,40	8,60	29,30	15,80	31,35	12,20
195,00	23,59			4,18	13,69	-0,05	0,86	-0,82	-0,62	59,95	7,76	52,19	3,88	-0,50		37,77	0,12	0,80	6,63	6,00	31,00	15,20	24,10	11,00	27,55	13,10
197,50	24,08			5,38	23,08	-0,24	0,64	-0,96	-0,73	60,94	7,62	53,32	3,79	-0,44		36,66	0,13	0,88	6,75	6,00	28,70	15,10	31,60	9,50	30,15	12,30
200,00	24,57	0,83	46,1	3,57	6,12	-0,51	0,64	-0,90	-0,70	61,19	4,35	56,84	3,84	-0,50		38,98	0,12	0,78	6,48	7,00	34,00	8,70	28,30	10,10	31,15	9,40

Appendix 2, Table 1) continued (core 74KL)

depth	Dry Dens	CaCO3 HH	CaCO3 K1	CaCO3 K2	Opal	Biogenic	< 2 µm	area	Corg	N	S	SiO2	TiO2	Al2O3	Fe2O3	MnO	MgO	CaO	P2O5	Si	Ti	Al	Fe	Mn	Mg	Ca, bulk	Ca, mar.	Ca, lith.	P	Al	Fe	Mg	Na	K	Li
	g/ccm	%	%	%	%	%	%	m2	%	%	%	wt%	wt%	wt%	wt%	wt%	wt%	wt%	wt%	%	%	%	%	%	%	%	%	%	%	%	%	%	%	%	ppm
1,25	0,47	60,6	55,00	55,50	8,6	69,2			1,26	0,16	0,223															24,3			1,78	1,21	1,35	2,10	0,67	12,01
5	0,52	58,8	56,40	55,40	8,2	67,0			1,26	0,16	0,23	21,5	0,23	3,66	2,02	0,068	2,36	36,7	0,132	10,0	0,136	1,94	1,41	0,052	1,43	26,2	23,5	2,7	0,029	1,81	1,22	1,37	1,73	0,69	11,89
7,5		60,4	57,80	58,00	8,0	68,4			1,26	0,16	0,225																24,2			1,67	1,16	1,32	1,89	0,69	10,29
10	0,54	62,3	58,30	58,00	7,7	70,0			1,21	0,19	0,206	21,0	0,22	3,62	1,94	0,074	2,36	38,3	0,125	9,8	0,134	1,91	1,35	0,058	1,42	27,3	24,9	2,4	0,027	1,79	1,21	1,28	1,27	0,68	12,31
12,5		62,1	58,50	58,60	7,4	69,5			1,16	0,16	0,243																24,9			1,73	1,18	1,39	1,79	0,68	10,28
15	0,54	60,7	58,50	58,60	7,6	68,3			1,26	0,18	0,251	20,4	0,21	3,43	1,88	0,067			0,121	9,5	0,126	1,82	1,31	0,052			24,3		0,026	1,75	1,19	1,38	1,83	0,67	10,63
17,5		60,8	57,10	58,40	7,5	68,3			1,17	0,17	0,232																24,3			1,64	1,12	1,34	2,07	0,70	10,06
20	0,57	62,3	59,60	61,20	7,5	69,8			1,11	0,16	0,229	20,4	0,21	3,37	1,85	0,080	2,27	38,5	0,155	9,5	0,123	1,79	1,29	0,062	1,37	27,5	24,9	2,6	0,034	1,64	1,09	1,33	1,87	0,66	10,95
22,5		64,5	60,80	61,00	6,6	71,1			0,95	0,13	0,224																25,8			1,56	1,06	1,29	1,90	0,67	9,66
25	0,63	64,1	59,80	62,10	7,4	71,5			0,96	0,13	0,246	18,8	0,19	3,18	1,71	0,074	2,11	40,8	0,143	8,8	0,117	1,68	1,19	0,057	1,27	29,1	25,7	3,5	0,031	1,49	1,03	1,24	1,71	0,63	9,04
27,5		66,2	63,00	62,50	7,0	73,2			0,83	0,12	0,231																26,5			1,46	0,98	1,18	1,69	0,63	9,95
30	0,68	66,8	60,30	64,00	7,8	74,6			0,81	0,12	0,193	18,1	0,18	2,98	1,63	0,086	1,99	40,5	0,184	8,5	0,108	1,58	1,14	0,066	1,20	29,0	26,7	2,2	0,040	1,50	0,99	1,18	1,54	0,63	10,02
32,5		62,3	58,90	58,60	9,4	71,7			0,88	0,13	0,244																24,9			1,34	0,84	1,17	2,65	0,63	8,42
35	0,68	64,2	60,40	59,70	9,1	73,3			0,92	0,15	0,225	21,0	0,16	2,65	1,44	0,094	1,88	39,2	0,246	9,8	0,096	1,40	1,00	0,073	1,14	28,0	25,7	2,3	0,054	1,35	0,90	1,14	1,91	0,59	8,69
37,5		64,3	64,20	61,30	7,2	71,5			0,81	0,12	0,253																25,7			1,38	0,91	1,20	2,26	0,65	10,24
40	0,69	69,8	63,30	62,70	7,4	77,2			0,56	0,10	0,195	18,0	0,17	2,83	1,56	0,099	1,90	40,9	0,144	8,4	0,101	1,50	1,09	0,077	1,14	29,2	28,0	1,3	0,031	1,38	0,91	1,07	1,58	0,61	9,50
42,5		65,1	61,70	62,30	7,0	72,1			0,64	0,11	0,239																26,1			1,37	0,94	1,19	2,38	0,66	9,77
45	0,53	66,3	64,10	64,30	6,6	72,9			0,64	0,10	0,234	16,5	0,16	2,74	1,53	0,079	1,90	42,1	0,144	7,7	0,098	1,45	1,07	0,061	1,15	30,1	26,5	3,5	0,031	1,29	0,91	1,08	1,80	0,58	9,39
47,5		66,2	66,10	66,10	6,9	73,1			0,66	0,10	0,266																26,5			1,25	0,83	1,18	2,65	0,60	9,78
50	0,68	69,6	66,40	66,30	6,4	76,0		18,76	0,78	0,10	0,187	15,4	0,15	2,59	1,42	0,078	1,78	43,3	0,138	7,2	0,092	1,37	1,00	0,060	1,07	31,0	27,9	3,1	0,030	1,22	0,87	1,04	1,47	0,58	9,47
52,5		68,4	66,40	65,60	6,2	74,6			0,84	0,12	0,209																27,4			1,25	0,85	1,11	1,77	0,61	9,49
55	0,67	70,4	67,60	67,60	6,2	76,6		19,1	0,72	0,09	0,174	15,7	0,16	2,59	1,42	0,084	1,83	43,6	0,360	7,3	0,094	1,37	1,00	0,065	1,10	31,1	28,2	2,9	0,079	1,21	0,89	1,12	1,55	0,59	10,22
57,5		67,5	68,60	68,40	6,5	74,0				0,10	0,195																27,0			1,28	0,86	1,03	1,25	0,56	9,73
60	0,69	69,8	66,70	66,30	7,7	77,5		18,5	0,70	0,10	0,221	15,8	0,16	2,56	1,47	0,091	1,89	43,6	0,227	7,4	0,093	1,35	1,02	0,071	1,14	31,2	28,0	3,2	0,049	1,23	0,90	1,14	1,50	0,57	11,15
62,5		70,4	65,20	66,50	6,7	77,1			0,64	0,10	0,209																28,2			1,30	0,85	1,14	1,50	0,59	9,52
65	0,66	67,9	65,90	65,80	7,2	75,1		20,6	0,80	0,10	0,184	16,4	0,16	2,63	1,52	0,092	1,98	43,2	0,130	7,7	0,095	1,39	1,07	0,071	1,19	30,9	27,2	3,7	0,028	1,29	0,93	1,18	1,54	0,59	8,96
67,5		66,8	63,20	64,40	6,7	73,5	55,9		0,83	0,11	0,256																26,7			1,33	0,94	1,21	2,10	0,63	9,88
70	0,65	68,7	67,30	66,20	7,1	75,8	51,9	20,37	0,81	0,11	0,32	16,1	0,16	2,56	1,43	0,091	1,93	42,5	0,123	7,5	0,095	1,35	1,00	0,070	1,16	30,4	27,5	2,9	0,027	1,27	0,90	1,16	1,37	0,59	10,48
72,5		66,5	65,40	64,10	7,0	73,5	54,9		0,91	0,11	0,171																25,6			1,23	0,81	1,12	2,02	0,61	9,89
75	0,68	68,5	64,50	64,90	8,3	75,8	54,0	18,6	0,86	0,12	0,251	17,8	0,15	2,50	1,38	0,092	1,92	40,7	0,139	8,3	0,091	1,32	0,97	0,071	1,16	29,1	27,4	1,7	0,030	1,28	0,83	1,11	1,52	0,57	9,35
77,5		66,8	61,00	59,90	8,0	74,8	53,6		0,93	0,12	0,201																26,7			1,32	0,84	1,15	1,81	0,62	9,98
80	0,70	69,8	66,70	66,10	8,2	78,0	53,3	23,8	0,75	0,11	0,222	16,7	0,16	2,56	1,41	0,079	1,95	42,0	0,127	7,8	0,096	1,35	0,98	0,061	1,18	30,0	28,0	2,1	0,028	1,27	0,85	1,13	1,35	0,59	10,15
82,5		68,9	65,10	65,60	7,6	76,5	53,3		0,83	0,12	0,222																27,6			1,20	0,84	1,23	1,56	0,61	10,32
85	0,71	69,6	65,50	64,70	6,4	76,0	55,0	18,7	0,67	0,09	0,259	17,2	0,17	2,89	1,66	0,086	2,16	41,3	0,126	8,0	0,105	1,53	1,16	0,066	1,30	29,5	27,9	1,6	0,027	1,35	0,93	1,18	1,44	0,63	10,55
87,5		67,8	65,10	66,10	5,6	73,4	52,2			0,09	0,165																27,2			1,34	0,95	1,25	1,35	0,64	10,66
90	0,78	70,0	67,10	66,50	5,3	75,3	50,1	18,9	0,69	0,09	0,211	15,4	0,18	2,83	1,61	0,079	2,21	43,1	0,146	7,2	0,106	1,50	1,13	0,061	1,33	30,8	28,0	2,8	0,032	1,46	0,98	1,28	1,45	0,64	11,08
92,5		70,9	67,40	67,60	4,7	75,6	50,0		0,51	0,10	0,195																28,4			1,48	0,94	1,26	1,44	0,69	11,42
95	0,79	67,6	61,50	60,70	5,1	72,7	47,9	18,4		0,07	0,207	15,5	0,18	2,90	1,68	0,072	2,26	42,8	0,114	7,2	0,106	1,54	1,18	0,056	1,37	30,6	27,1	3,5	0,025	1,55	1,03	1,39	1,46	0,68	11,91
97,5		67,8	62,10	65,90	3,8	71,6	49,8		0,46	0,07	0,227																27,2			1,46	0,98	1,43	2,11	0,77	12,14
100	0,85	67,2	63,80	64,60	3,9	71,1	46,7	19,5	0,32	0,06	0,187	17,0	0,22	3,49	1,83	0,080	2,62	41,1	0,128	8,0	0,129	1,85	1,28	0,062	1,58	29,4	26,9	2,5	0,028	1,75	1,11	1,53	1,42	0,79	12,59
102,5		68,3	64,10	62,60	3,4	71,7	43,3		0,37	0,07	0,217																27,4			1,69	1,17	1,63	1,23	0,73	13,27
105		69,9	65,30	64,50	3,6	73,5	43,7	18,3	0,42	0,06	0,226	16,6	0,22	3,54	1,74	0,074	2,61	40,6	0,146	7,8	0,130	1,87	1,22	0,057	1,57	29,0	28,0	1,1	0,032	1,79	1,09	1,57	1,26	0,68	14,20
107,5		68,8	64,60	64,20	3,8	72,6	45,1		0,60	0,09	0,231																27,6			1,63	1,01	1,46	1,36	0,66	12,56
110	0,85	70,1	65,30	65,20	4,1	74,2	46,2	17,9	0,56	0,08	0,221	15,9	0,21	3,24	1,72	0,086	2,52	41,3	0,117	7,4	0,124	1,71	1,20	0,067	1,52	29,5	28,1	1,4	0,026	1,64	1,10	1,50	1,31	0,66	12,71
112,5		68,0	63,70	64,00	3,6	71,6	41,9		0,68	0,10	0,289																27,2			1,55	1,01	1,53	1,90	0,68	12,39
115		68,1	65,30	65,00	3,6	71,7	43,7	14,1	0,69	0,07	0,208	15,5	0,20	3,14	1,70	0,086	2,48	41,1	0,221	7,3	0,120	1,66	1,19	0,067	1,49	29,4	27,3	2,1	0,048	1,56	1,05	1,45	1,54	0,67	12,49
117,5		69,3	64,50	64,90	3,4	72,7	42,0		0,64	0,12	0,281																27,8			1,67	1,22	1,59	1,23	0,71	13,98
120	0,79	66,2	61,80	62,70	3,3	69,5	43,0	18,4	0,57	0,09	0,239	16,6	0,23	3,58	1,94	0,094	2,77	39,9	0,125	7,8	0,140	1,90	1,35	0,073	1,67	28,5	26,5	2,0	0,027	1,77	1,20	1,69	1,34	0,76	14,29
122,5		66,8	61,10	61,00	3,0	69,8	41,4		0,38	0,08	0,328																26,7			1,86	1,20	1,64	1,67	0,82	15,56
125		66,2	61,50	60,80	3,2	71,4	45,2	17,8	0,50	0,08	0,231	18,7	0,26	4,11	2,18	0,081	3,13	38,2	0,143	8,7	0,154	2,17	1,52	0,063	1,88	27,3	27,3	0,0	0,031	1,92	1,34	1,68	1,26	0,84	14,47
127,5		62,2	57,10	56,70	3,1	65,3	40,8		0,34	0,06	0,185																24,9			2,22	1,65	1,97	1,54	0,97	17,03
130	0,88	60,4	58,00	58,40	3,2	63,6			0,27	0,05	0,181	21,9	0,30	4,85	2,51	0,084	3,64	35,7	0,177	10,2	0,182	2,57	1,76	0,065	2,20	25,5	24,2	1,3	0,039	2,42	1,58	2,10	1,30	1,03	20,12
132,5		58,8	51,00	51,90	3,2	62,0	37,7		0,23	0,07	0,27																23,5			2,62	1,70	2,24	1,49	1,12	20,05
135		58,6	52,60	51,20	3,0	61,6	36,1	22,75	0,24	0,06	0,227	23,1	0,32	5,25	2,63	0,078	3,86	33,5	0,232	10,8	0,193	2,78	1,84	0,060	2,33	23,9	23,5	0,5	0,051	2,86	1,67	2,34	1,30	1,11	18,39
137,5		58,1	51,70	51,50	3,1	61,2	38,2		0,28	0,06	0,229																23,3			2,82	1,78	2,40	1,31	1,14	18,11
140	0,91	58,9	51,00	52,50	2,8	61,7	36,6	23,4	0,35	0,06	0,192	23,3	0,32	5,22	2,83	0,078	3,96	33,6	0,140	10,9	0,194	2,76	1,98	0,060	2,39	24,0	23,6	0,4	0,030	2,56	1,82	2,28	1,26	1,12	17,44
142,5		59,9	54,60	54,60	2,7	62,6	37,4		0,40	0,08	0,217																24,0			2,58	1,82	2,22	0,92	0,82	19,15
145		59,2	54,50	54,50	2,6	61,8	37,5	21,1	0,50	0,08	0,225	22,1	0,31	4,99	2,61	0,070	3,80	35,5	0,155	10,3	0,188	2,64	1,83	0,054	2,29	25,3	23,7	1,6	0,034	2,40	1,63	2,18	1,43	1,05	16,05
147,5		61,3	56,20	55,80	2,6	63,9	35,6		0,53	0,08	0,235																24,5			2,54	1,60	2,26	1,12	1,02	17,80
150	0,87	60,7	56,80	55,80	2,6	63,3	45,5	18,8	0,60	0,08	0,195	20,7	0,29	4,69	2,29	0,069	3,53	36,3	0,151	9,7	0,174	2,48	1,60	0,054	2,13	25,9	24,3	1,6	0,033	2,36	1,49	2,12	1,14	1,00	18,31
152,5		61,7	56,70	55,50	2,9	64,6	41,9		0,74	0,10	0,225																24,7			2,32	1,45	2,14	1,65	1,02	17,69
155		62,9	56,30	56,50	3,0	65,9	37,4		0,74	0,10	0,281	21,0	0,30	4,71	2,52	0,086	3,60	38,3	0,142	9,8	0,178	2,49	1,76	0,066	2,17	27,4	25,2	2,2	0,031	2,26	1,57	2,04	1,38	1,22	15,01
157,5		61,5	56,40	56,00	2,8	64,3	37,4		0,87	0,13	0,253																24,6			2,18	1,56	2,04	1,59	1,48	15,56
160	0,83	61,1	55,50	56,00	3,0	64,1	38,4		0,87	0,12	0,234	21,0	0,30	4,71	2,47	0,098	3,51	36,6	0,143	9,8	0,178	2,49	1,73	0,076	2,12	26,1	24,5	1,7	0,031	2,16	1,51	1,99	1,33	0,93	19,75
162,5		60,0	54,30	54,20	2,5	62,5	35,9		0,86	0,12	0,362																24,0			2,28	1,56	2,02	1,88	0,96	18,88
165		61,3	56,90	55,60	2,7	64,0	35,2		0,81	0,11	0,391	20,6	0,29	4,64	2,48	0,084	3,47	36,9	0,135	9,6	0,173	2,46	1,73	0,065	2,09	26,4	24,5	1,8	0,030	2,16	1,61	1,91			16,21
167,5		60,5	55,50	55,70	2,7	63,2	38,1		0,92	0,12	0,361																24,2			2,06	1,39	1,90	1,77	0,93	18,51
170	0,80	61,6	58,00	55,40	2,4	64,0	39,1		0,93	0,12	0,293	20,8	0,30	4,61	2,50	0,091	3,46	36,9	0,140	9,7	0,178	2,44	1,75	0,070	2,08	26,4	24,7	1,7	0,031	2,22	1,48	1,97	1,33	0,92	19,44
172,5		62,1	54,90	54,50	2,8	64,9	39,7		0,74	0,12	0,323																24,9			2,38	1,60	2,08	1,09	0,91	17,47
175		60,5	53,10	55,40	2,5	63,0	39,8		0,90	0,12	0,379	21,4	0,30	4,81	2,70	0,085	3,56	37,1	0,137	10,0	0,182	2,54	1,89	0,066	2,15	26,5	24,2	2,3	0,030	2,36	1,65	2,04	1,37	0,97	19,24
177,5		60,8	56,00	54,80	2,6	63,4	39,1		0,85	0,11	0,291																24,3			2,40	1,77	2,10	1,20	0,97	18,90
180	0,84	60,7	57,10	57,90	2,8	63,5	38,3		0,87	0,11	0,317	23,0	0,33	5,14	2,76	0,099	3,75	39,7	0,161	10,7	0,195	2,72	1,93	0,077	2,26	28,3	24,3	4,0	0,035	2,36	1,67	2,10	1,21	0,97	18,30
182,5		60,6	54,30	54,90	2,6	63,2	38,0		0,87	0,12	0,364																24,3			2,28	1,55	1,97	1,34	0,97	17,70
185		59,9	55,40	54,40	2,7	62,6	36,6		0,78	0,11	0,455	22,3	0,32	5,02	2,67	0,102	3,67	37,6	0,344	10,4	0,193	2,66	1,87	0,079	2,21	26,9	24,0	2,9	0,075	2,40	1,61	1,97	1,51	0,99	18,76
187,5		59,4	53,50	53,00	2,7	62,1	36,6		0,80	0,12	0,4																23,8			2,34	1,69	2,12	1,82	1,01	19,63
190	0,82	60,3	55,80	54,60	2,5	62,8	36,4		0,83	0,12	0,351	21,5	0,31	4,83	2,66	0,087	3,51	37,9	0,155	10,1	0,185	2,56	1,86	0,067	2,12	27,1	24,1	3,0	0,034	2,34	1,65	2,10	1,44	0,98	15,74
192,5		61,7	55,60	54,90	2,5	64,2	38,0		0,74	0,12	0,291																24,7			2,14	1,56	1,96	1,78	0,96	16,63
195		60,0	56,30	56,00	2,7	62,7	37,8		0,80	0,12	0,348	21,2	0,31	4,76	2,55	0,094	3,46	38,7	0,144	9,9	0,183	2,52	1,79	0,073	2,08	27,7	24,0	3,6	0,031	2,32	1,60	1,94	1,41	0,95	18,99
197,5		60,9	55,80	55,30	2,2	63,1	36,7		0,88	0,13	0,364																24,4			2,30	1,54	1,98	1,68	0,95	18,15
200	0,83	61,2	55,10	55,40	2,7	63,9	39,0		0,78	0,12	0,383	22,2	0,32	5,00	2,62	0,096	3,55	38,3	0,117	10,4	0,191	2,65	1,83	0,074	2,14	27,4	24,5	2,9	0,026	2,44	1,67	2,08	1,46	0,97	16,22

Appendix 2, Table 2) Sediment core 74KL, chemical concentration values in the bulk fraktion (% or ppm), concentration values expressed on a carbonate and opal free basis (% or ppm, cofb)

depth	Sc	Cr	Mn	Co	Ni	Cu	Zn	Ga	Pb	Sr	Y	Zr	Nb	Mo	Cd	Cs	Ba	La	Ce	Pr	Nd	Sm	Eu	Gd	Tb	Dy	Ho	Er	Tm	Yb	Lu	Hf	Ta	Tl	Pb
	ppm	ppm	%	ppm	ppm	ppm	ppm	ppm	ppm	ppm	ppm	ppm	ppm	ppm	ppm	ppm	ppm	ppm	ppm	ppm	ppm	ppm	ppm	ppm	ppm	ppm	ppm	ppm	ppm	ppm	ppm	ppm	ppm	ppm
1,25	8,64	39,8	0,061	12,1	79,7	46,0	104,1	5,43	22,3	967	14,2	37,9	4,02	0,83	0,97	1,55	1389	9,21	15,7	2,19	8,83	1,91	0,38	2,02	0,31	1,95	0,42	1,25	0,180	1,24	0,200	0,94	0,270	0,320	7,83
5	7,72	39,5	0,058	11,0	78,1	46,7	104,2	5,45	21,7	960	14,4	36,1	3,96	0,63	1,10	1,50	1391	9,34	15,9	2,22	8,99	1,93	0,39	2,05	0,32	1,99	0,43	1,30	0,190	1,28	0,200	0,93	0,270	0,320	8,06
7,5	8,23	39,3	0,043	14,1	78,3	48,0	99,1	5,44	21,0	931	14,0	34,7	3,81	0,68	0,74	1,45	1321	9,15	15,3	2,20	8,77	1,91	0,40	2,18	0,32	1,93	0,42	1,26	0,180	1,25	0,200	0,83	0,250	0,310	7,90
10	7,65	38,3	0,038	9,6	73,3	48,0	100,9	5,59	21,8	989	14,8	37,3	3,97	0,47	0,70	1,57	1450	9,68	16,3	2,28	9,13	1,93	0,39	2,05	0,32	2,04	0,43	1,30	0,190	1,29	0,200	0,89	0,260	0,280	7,94
12,5	7,06	36,9	0,041	12,4	77,9	48,1	101,2	5,20	20,0	915	13,7	34,0	3,56	0,62	1,00	1,41	1350	9,10	15,2	2,17	8,75	1,86	0,40	2,17	0,31	1,94	0,42	1,26	0,180	1,27	0,200	0,81	0,240	0,300	7,52
15	8,16	40,7	0,047	16,5	87,6	52,9	122,3	5,50	22,1	1011	14,8	36,0	3,84	0,91	0,84	1,57	1451	9,29	15,3	2,17	8,55	1,91	0,39	2,11	0,32	1,93	0,43	1,27	0,190	1,28	0,200	0,87	0,240	0,390	7,60
17,5	6,74	36,8	0,060	14,0	87,0	41,6	96,5	4,98	19,5	913	13,4	34,4	3,50	1,21	0,84	1,36	1330	8,75	14,5	2,10	8,41	1,84	0,38	2,07	0,31	1,87	0,41	1,22	0,180	1,24	0,200	0,88	0,240	0,490	7,80
20	6,23	31,8	0,048	9,3	66,3	36,0	77,8	4,69	17,8	920	12,6	31,8	3,21	0,86	0,41	1,32	1300	8,39	13,8	1,98	7,93	1,71	0,39	1,85	0,28	1,76	0,38	1,16	0,170	1,14	0,170	0,75	0,220	0,290	6,38
22,5	8,9	34,1	0,057	13,5	82,4	44,6	99,5	4,61	18,5	1004	12,7	29,3	3,15	1,24	0,71	1,31	1288	8,41	14,0	2,03	8,25	1,78	0,37	2,02	0,29	1,77	0,38	1,16	0,170	1,15	0,180	0,75	0,220	0,480	7,31
25	7,11	35,0	0,046	13,8	80,3	43,0	95,6	4,58	18,5	1001	12,5	30,3	3,19	1,08	0,73	1,25	1230	8,02	13,2	1,93	7,73	1,69	0,35	1,92	0,28	1,72	0,37	1,12	0,160	1,12	0,180	0,77	0,210	0,370	6,95
27,5	5,96	35,7	0,046	12,9	75,6	43,7	100,0	4,68	19,5	1088	13,0	31,2	3,23	0,99	0,76	1,33	1310	8,16	13,2	1,90	7,52	1,61	0,33	1,82	0,27	1,69	0,37	1,11	0,160	1,11	0,180	0,75	0,210	0,370	6,37
30	5,95	36,0	0,053	15,4	81,8	44,5	89,9	4,67	19,5	1100	13,2	31,6	3,32	1,24	0,62	1,36	1262	8,16	13,5	1,92	7,44	1,64	0,34	1,92	0,27	1,69	0,37	1,12	0,170	1,12	0,180	0,77	0,210	0,430	6,58
32,5	6,45	30,5	0,056	16,7	97,8	38,0	82,8	3,99	15,8	939	11,0	27,1	2,68	1,75	0,67	1,10	1083	7,00	11,5	1,69	6,86	1,47	0,32	1,67	0,24	1,52	0,33	0,98	0,140	1,00	0,160	0,69	0,190	0,470	6,15
35	7,35	28,7	0,053	17,7	87,7	41,1	84,8	4,11	17,4	1050	11,8	26,8	2,87	1,19	0,58	1,22	1143	7,31	12,0	1,72	6,70	1,50	0,32	1,71	0,25	1,51	0,33	0,98	0,150	1,00	0,160	0,63	0,180	0,410	5,81
37,5	9,46	36,5	0,057	11,0	87,2	38,8	84,8	4,32	17,9	1036	11,4	25,6	2,94	1,59	0,74	1,24	1165	7,30	12,2	1,74	7,10	1,53	0,29	1,81	0,25	1,56	0,34	1,01	0,150	1,01	0,160	0,67	0,200	0,460	6,37
40	5,37	31,7	0,055	11,3	83,4	41,0	92,7	4,17	17,0	1067	11,5	28,5	2,89	1,25	0,76	1,21	1216	7,21	11,9	1,71	6,91	1,49	0,29	1,63	0,25	1,54	0,33	1,03	0,150	1,03	0,160	0,72	0,190	0,420	6,08
42,5	7,03	31,4	0,049	9,2	71,0	40,7	80,5	4,20	17,5	1045	11,6	29,0	2,92	1,52	0,62	1,22	1214	7,22	12,0	1,72	6,92	1,49	0,29	1,63	0,25	1,57	0,34	1,05	0,150	1,04	0,160	0,73	0,190	0,430	6,04
45	5,96	29,7	0,042	9,6	67,4	40,3	85,7	4,02	16,3	1028	11,0	26,4	2,72	1,10	0,68	1,14	1201	6,76	11,0	1,58	6,49	1,40	0,27	1,49	0,23	1,44	0,31	0,97	0,140	0,98	0,150	0,65	0,180	0,340	5,40
47,5	7,59	25,6	0,048	7,6	62,9	41,9	84,5	3,77	15,3	1022	10,5	24,9	2,48	1,69	0,93	1,11	1186	6,60	10,8	1,56	6,24	1,34	0,26	1,46	0,23	1,43	0,31	0,94	0,130	0,93	0,140	0,57	0,170	0,480	5,10
50	5,73	28,0	0,046	8,7	67,1	43,4	89,7	3,99	16,1	1146	10,3	25,3	2,64	1,04	0,91	1,14	1265	6,67	11,0	1,57	6,43	1,39	0,27	1,48	0,23	1,45	0,31	0,96	0,140	0,95	0,150	0,62	0,170	0,390	5,95
52,5	4,70	30,3	0,052	9,0	64,4	42,3	94,6	4,10	17,0	1111	11,7	28,1	2,77	1,19	1,00	1,14	1239	6,96	11,5	1,63	6,37	1,39	0,28	1,55	0,23	1,47	0,32	0,99	0,150	0,99	0,150	0,65	0,180	0,430	6,03
55	4,73	29,3	0,049	9,3	64,6	41,1	91,4	3,92	15,4	1130	8,9	25,6	2,56	1,01	1,10	1,13	1247	6,65	11,0	1,57	6,37	1,35	0,26	1,46	0,23	1,44	0,31	0,95	0,140	0,92	0,150	0,64	0,180	0,380	6,62
57,5	4,90	31,4	0,058	13,0	78,7	45,8	96,0	4,13	16,6	1110	10,3	26,7	2,69	1,06	0,76	1,16	1213	6,69	10,9	1,54	6,07	1,35	0,27	1,56	0,22	1,40	0,31	0,95	0,140	0,92	0,150	0,62	0,180	0,390	5,91
60	5,83	29,6	0,060	12,7	82,0	45,6	94,3	3,98	15,4	1112	10,9	26,2	2,57	1,55	1,01	1,15	1264	6,86	11,5	1,64	6,59	1,40	0,28	1,54	0,24	1,53	0,33	1,01	0,140	1,01	0,160	0,67	0,170	0,530	6,65
62,5	6,57	30,5	0,066	15,1	90,3	47,5	95,2	4,18	16,8	1129	9,7	26,3	2,73	1,28	1,00	1,17	1243	6,91	11,5	1,65	6,63	1,46	0,30	1,71	0,24	1,51	0,33	0,99	0,140	0,98	0,150	0,67	0,190	0,450	6,76
65	4,99	32,7	0,056	14,9	82,1	46,3	93,0	4,06	16,1	1033	11,1	27,3	2,66	1,37	0,78	1,08	1094	6,46	11,0	1,58	6,39	1,39	0,29	1,60	0,23	1,48	0,32	0,97	0,140	0,97	0,150	0,67	0,180	0,450	6,32
67,5	5,84	32,8	0,069	11,6	81,5	43,1	81,1	3,94	15,6	1009	10,6	28,3	2,60	1,78	0,86	1,14	1115	6,79	11,4	1,62	6,55	1,40	0,30	1,64	0,24	1,49	0,32	1,01	0,150	1,00	0,160	0,71	0,190	0,540	6,46
70	4,88	32,6	0,059	10,7	67,8	42,2	70,2	4,05	16,0	1101	9,5	26,3	2,68	1,37	0,56	1,17	1158	6,51	11,4	1,58	6,33	1,40	0,26	1,45	0,22	1,41	0,31	0,94	0,140	0,90	0,150	0,66	0,180	0,390	6,21
72,5	6,67	30,5	0,057	9,5	68,6	42,7	74,7	3,90	15,8	1034	10,3	25,0	2,61	1,84	0,75	1,12	1098	6,31	11,1	1,51	6,04	1,33	0,25	1,37	0,21	1,38	0,30	0,93	0,130	0,91	0,140	0,60	0,170	0,480	6,42
75	3,91	25,1	0,057	11,0	73,5	37,0	69,1	3,67	14,1	951	9,6	24,1	2,47	1,62	0,66	1,07	1028	6,16	10,6	1,44	5,86	1,28	0,31	1,40	0,21	1,31	0,29	0,89	0,120	0,88	0,130	0,53	0,160	0,470	5,94
77,5	5,41	33,2	0,058	15,4	94,4	45,2	79,3	3,96	16,1	1089	10,2	26,2	2,63	1,77	0,70	1,15	1125	6,61	11,6	1,60	6,58	1,45	0,27	1,47	0,22	1,41	0,31	0,96	0,140	0,95	0,150	0,67	0,170	0,470	6,80
80	4,82	33,8	0,056	12,2	78,5	43,4	85,8	3,94	16,1	1098	9,6	26,5	2,70	1,57	0,91	1,18	1082	6,56	11,5	1,57	6,29	1,37	0,27	1,40	0,22	1,40	0,30	0,92	0,130	0,89	0,140	0,65	0,180	0,420	6,68
82,5	5,02	32,8	0,060	15,3	92,2	43,3	82,7	3,97	16,5	1118	9,8	26,6	2,75	1,81	0,81	1,20	1087	6,58	11,6	1,59	6,39	1,40	0,27	1,45	0,22	1,41	0,31	0,94	0,140	0,90	0,140	0,70	0,180	0,430	6,48
85	6,01	31,4	0,055	9,4	62,6	37,1	73,3	3,95	17,0	1028	10,1	25,7	2,84	1,42	0,53	1,23	939	6,63	11,6	1,60	6,42	1,42	0,28	1,45	0,22	1,41	0,30	0,90	0,130	0,89	0,140	0,67	0,190	0,350	6,16
87,5	4,87	31,1	0,063	10,6	67,0	37,9	73,4	3,81	16,7	1085	8,5	23,9	2,71	1,54	0,48	1,20	853	6,29	11,2	1,55	6,17	1,37	0,27	1,35	0,21	1,31	0,28	0,85	0,120	0,80	0,130	0,64	0,180	0,290	6,70
90	4,74	35,8	0,052	9,3	59,6	35,1	64,3	3,86	18,3	1101	8,8	26,7	2,96	1,22	0,56	1,28	769	6,44	11,4	1,57	6,42	1,39	0,28	1,41	0,22	1,36	0,29	0,89	0,130	0,84	0,130	0,70	0,200	0,270	6,10
92,5	5,03	37,9	0,054	9,0	60,2	35,9	67,0	3,98	18,5	1071	7,2	26,0	2,95	1,21	0,98	1,32	770	6,40	11,4	1,55	6,23	1,31	0,26	1,36	0,20	1,26	0,27	0,82	0,120	0,76	0,120	0,67	0,200	0,320	6,34
95	4,98	37,2	0,048	9,8	60,1	30,9	56,2	3,87	19,1	1066	7,4	28,5	3,04	0,99	0,55	1,37	618	6,32	11,4	1,54	6,21	1,30	0,28	1,35	0,21	1,27	0,27	0,80	0,110	0,75	0,120	0,68	0,200	0,350	5,63
97,5	6,17	36,8	0,049	9,1	59,5	31,2	55,9	3,96	19,6	1032	9,6	26,5	3,07	1,32	0,56	1,40	529	6,63	12,0	1,61	6,43	1,35	0,30	1,43	0,22	1,34	0,28	0,84	0,120	0,82	0,120	0,70	0,210	0,310	5,57
100	5,91	44,3	0,053	12,8	66,0	32,1	64,7	4,59	24,0	1008	10,9	30,9	3,73	1,24	0,60	1,62	543	7,41	13,5	1,79	6,88	1,49	0,33	1,66	0,24	1,45	0,31	0,90	0,130	0,89	0,140	0,84	0,240	0,320	5,64
102,5	5,79	49,3	0,050	13,5	67,9	31,3	61,6	4,74	26,1	1032	10,9	33,1	3,99	0,92	0,49	1,75	486	7,59	14,0	1,83	7,14	1,56	0,36	1,72	0,25	1,52	0,32	0,96	0,140	0,91	0,140	0,87	0,250	0,350	5,77
105	5,66	44,8	0,052	9,5	61,2	28,8	62,2	4,44	23,0	1046	9,2	30,5	3,62	1,02	0,57	1,67	500	7,28	13,5	1,77	7,10	1,51	0,33	1,52	0,24	1,47	0,31	0,91	0,130	0,85	0,130	0,84	0,240	0,350	5,89
107,5	5,41	50,2	0,043	9,7	59,6	28,5	61,1	4,20	21,9	1045	10,0	29,7	3,49	0,84	0,51	1,52	523	6,89	12,7	1,69	6,82	1,49	0,32	1,50	0,23	1,43	0,30	0,89	0,130	0,86	0,130	0,83	0,230	0,300	5,41
110	5,85	40,3	0,058	10,4	61,8	28,2	59,4	4,08	21,3	1094	10,3	28,1	3,39	0,90	0,61	1,46	597	6,82	12,4	1,66	6,69	1,45	0,31	1,51	0,23	1,42	0,30	0,90	0,130	0,87	0,130	0,73	0,230	0,340	5,44
112,5	6,51	38,7	0,060	10,6	65,9	28,5	60,8	3,90	20,4	1072	10,2	27,2	3,25	1,22	0,63	1,39	577	6,59	12,1	1,59	6,52	1,40	0,30	1,49	0,22	1,39	0,30	0,88	0,130	0,85	0,130	0,71	0,220	0,370	5,53
115	6,55	41,3	0,061	10,6	58,4	27,0	62,4	4,00	21,5	1050	10,2	28,6	3,39	1,00	0,61	1,41	594	6,90	12,4	1,65	6,49	1,41	0,31	1,52	0,22	1,38	0,30	0,89	0,130	0,85	0,130	0,75	0,230	0,360	5,42
117,5	5,47	41,9	0,064	12,1	65,6	28,1	58,6	4,16	21,6	1048	10,7	30,0	3,59	1,06	0,66	1,55	577	7,27	13,3	1,75	7,02	1,50	0,33	1,55	0,25	1,51	0,32	0,94	0,130	0,90	0,140	0,80	0,240	0,460	5,85
120	5,98	48,1	0,068	9,9	66,5	25,5	60,6	4,43	23,4	973	10,9	32,3	3,84	0,82	0,61	1,64	481	7,63	14,1	1,84	7,39	1,57	0,35	1,61	0,25	1,52	0,32	0,95	0,130	0,92	0,140	0,85	0,260	0,290	5,87
122,5	7,36	46,0	0,060	10,9	61,9	25,2	55,5	4,49	24,1	964	10,9	31,7	3,93	1,02	0,48	1,70	452	7,86	14,6	1,92	7,59	1,64	0,38	1,66	0,26	1,61	0,33	0,99	0,140	0,95	0,140	0,89	0,270	0,340	6,25
125	6,31	52,7	0,055	13,2	63,5	27,5	58,9	4,76	28,2	1002	11,6	34,7	4,42	0,91	0,49	1,83	460	8,13	14,9	1,96	7,53	1,67	0,37	1,80	0,26	1,59	0,33	0,98	0,140	0,92	0,140	0,93	0,280	0,350	5,99
127,5	6,79	56,8	0,049	10,7	63,9	24,3	57,9	5,05	29,1	839	11,2	34,3	4,60	0,90	0,42	2,01	333	8,41	16,0	2,10	8,36	1,79	0,40	1,78	0,27	1,66	0,35	1,03	0,150	0,96	0,140	0,94	0,310	0,300	6,31
130	7,32	61,5	0,051	11,5	68,0	24,0	52,7	5,43	31,3	778	11,7	37,9	4,97	0,72	0,30	2,22	279	9,28	17,7	2,29	9,02	1,92	0,44	1,90	0,29	1,80	0,37	1,08	0,150	1,02	0,150	1,09	0,340	0,270	6,32
132,5	8,11	65,9	0,048	11,0	69,6	27,1	58,7	5,82	34,2	755	12,3	41,1	5,53	0,90	0,54	2,37	271	9,75	18,8	2,40	9,64	2,05	0,47	2,07	0,31	1,89	0,38	1,15	0,160	1,07	0,160	1,18	0,380	0,320	7,10
135	7,85	63,8	0,053	12,8	73,9	26,4	53,1	5,81	33,6	714	12,5	41,8	5,47	0,89	0,42	2,37	305	10,19	19,3	2,54	10,67	2,09	0,49	2,29	0,33	1,98	0,40	1,16	0,170	1,11	0,170	1,17	0,390	0,340	7,40
137,5	20,3	66,1	0,049	14,5	76,6	26,7	57,1	6,00	34,9	725	12,8	41,9	5,54	1,07	0,27	2,36	297	10,18	19,2	2,57	10,00	2,16	0,50	2,30	0,33	1,98	0,41	1,19	0,170	1,14	0,170	1,17	0,390	0,320	7,76
140	11,9	62,8	0,052	12,9	70,7	25,0	51,6	5,70	33,2	722	12,4	38,9	5,22	1,04	0,28	2,30	318	9,99	18,7	2,46	9,66	2,03	0,48	2,23	0,32	1,91	0,40	1,16	0,160	1,08	0,160	1,11	0,360	0,330	7,46
142,5	18,9	63,5	0,048	11,1	65,4	49,2	86,50	5,71	33,1	797	12,5	37,6	5,19	1,07	0,44	2,28	353	9,39	17,9	2,36	9,52	2,09	0,46	2,04	0,31	1,89	0,38	1,12	0,160	1,07	0,160	1,09	0,370	0,320	6,67
145	7,40	68,6	0,045	12,7	68,9	27,6	52,6	5,44	32,0	780	12,8	41,7	5,03	1,24	0,57	2,18	367	9,73	18,2	2,42	9,55	2,04	0,47	2,17	0,32	1,90	0,40	1,17	0,160	1,11	0,160	1,18	0,350	0,340	7,33
147,5	7,83	59,2	0,047	9,8	64,8	26,6	54,1	5,56	32,6	855	12,8	38,2	5,07	1,19	0,56	2,26	429	9,54	18,0	2,37	9,49	2,01	0,45	2,02	0,30	1,87	0,39	1,14	0,160	1,08	0,160	1,04	0,340	0,320	6,84
150	7,04	63,0	0,048	10,5	73,3	27,4	57,2	5,38	30,6	864	12,2	40,1	4,85	1,47	0,52	2,17	463	9,47	17,6	2,29	9,13	1,94	0,44	1,97	0,30	1,83	0,38	1,12	0,160	1,07	0,160	1,09	0,330	0,340	6,89
152,5	7,80	61,7	0,059	11,0	79,7	29,3	65,9	5,37	31,1	926	13,2	40,2	4,91	1,97	0,63	2,19	574	10,03	18,8	2,46	9,73	2,08	0,45	2,05	0,32	1,98	0,41	1,23	0,180	1,15	0,180	1,13	0,330	0,340	7,46
155	7,22	57,9	0,055	16,8	98,4	30,4	61,9	5,17	29,1	873	13,0	37,0	4,64	2,07	0,70	2,01	565	9,49	17,3	2,33	9,26	2,04	0,45	2,19	0,31	1,91	0,40	1,18	0,170	1,16	0,170	1,04	0,320	0,590	7,33
157,5	6,35	60,9	0,063	14,5	86,7	30,2	61,8	5,08	27,5	822	13,3	39,4	4,51	2,18	0,67	1,92	576	9,54	17,4	2,33	9,21	1,98	0,45	2,17	0,32	1,87	0,39	1,17	0,170	1,13	0,170	1,06	0,320	0,460	7,28
160	6,23	69,2	0,066	12,7	84,3	28,3	64,0	5,39	29,7	875	12,3	43,1	4,97	2,28	0,72	2,08	618	9,58	17,8	2,33	9,22	1,97	0,43	1,99	0,31	1,89	0,40	1,17	0,170	1,13	0,170	1,15	0,330	0,460	7,12
162,5	6,75	72,0	0,057	11,4	78,3	29,8	63,3	5,22	29,9	882	13,0	41,0	4,72	2,69	0,87	2,10	607	9,59	18,0	2,35	9,21	1,98	0,43	1,96	0,30	1,91	0,40	1,19	0,170	1,12	0,170	1,14	0,320	0,460	7,17
165	5,28	60,21	0,055	10,8	76,8	27,9	55,2	4,96	28,59	849	12,66	37,4	4,58	2,32	0,94	1,962	530	8,94	16,33	2,16	8,67	1,86	0,41	1,89	0,29	1,8	0,38	1,13	0,16	1,08	0,16	1,01	0,310	0,600	6,54
167,5	6,16	64,1	0,055	13,8	84,3	28,0	59,6	5,05	28,0	833	12,6	39,3	4,46	3,16	1,01	1,98	554	8,99	16,6	2,17	8,58	1,88	0,41	1,89	0,30	1,85	0,39	1,14	0,160	1,08	0,170	1,06	0,310	0,720	6,32
170	7,05	62,4	0,062	12,7	82,9	28,0	61,5	5,26	29,3	892	13,3	39,0	4,58	2,39	0,71	2,07	587	9,61	17,6	2,31	9,22	1,96	0,44	2,03	0,31	1,93	0,41	1,21	0,170	1,13	0,170	1,10	0,310	0,400	7,00
172,5	6,83	71,7	0,062	16,2	82,2	29,9	68,0	5,55	32,6	882	13,7	41,6	5,07	2,03	0,73	2,18	617	9,76	17,6	2,32	9,21	1,97	0,45	2,17	0,31	1,91	0,41	1,21	0,180	1,16	0,180	1,09	0,320	0,420	7,47
175	6,58	70,1	0,058	13,5	83,0	30,3	63,6	5,37	30,3	876	12,2	38,9	4,70	2,73	0,71	2,06	575	9,43	17,3	2,29	9,22	1,97	0,44	2,06	0,32	1,94	0,41	1,21	0,170	1,14	0,170	1,07	0,320	0,530	6,98
177,5	6,37	76,7	0,057	12,9	79,1	30,1	64,5	5,50	31,3	886	12,2	41,7	4,94	2,45	1,05	2,20	608	9,69	17,9	2,39	9,59	2,05	0,44	2,10	0,32	1,99	0,42	1,23	0,180	1,19	0,180	1,16	0,340	0,630	7,30
180	6,48	75,3	0,063	16,5	95,0	32,2	67,1	5,62	32,9	921	13,9	42,6	5,00	3,31	0,62	2,18	562	9,94	18,1	2,39	9,39	2,00	0,45	2,13	0,32	1,94	0,41	1,20	0,180	1,15	0,170	1,05	0,320	0,430	6,93
182,5	7,68	68,3	0,061	14,7	87,0	30,6	67,6	5,66	33,1	885	14,2	41,9	5,03	2,92	0,58	2,17	568	9,97	18,1	2,38	9,33	2,05	0,45	2,13	0,32	1,93	0,41	1,20	0,180	1,15	0,180	1,11	0,320	0,410	6,97
185	7,46	66,2

depth	U	Corg	N	S	Si opal cor	Ti	Al	Fe	Mn	Mg	Ca, lith.	P	Al	Fe	Mg	Na	K	Li	Sc	Cr	Mn	Co	Ni	Cu	Zn	Ga	Pb	Sr/Ca	Y	Zr	Nb	Mo	Cd	Cs	Ba
	ppm	% corb	% corb	% corb	% corb	% corb	% corb	% corb	% corb	% corb	% corb	% corb	% corb	% corb	% corb	% corb	% corb	ppm corb	ppm corb	ppm corb	ppm corb	ppm corb	ppm corb	ppm corb	ppm corb	ppm corb	ppm corb	ppm corb		ppm corb	ppm corb	ppm corb	ppm corb	ppm corb	ppm corb	ppm corb
1,25	3,56	4,09	0,52	0,72									5,795	3,924	4,398	6,83	2,16	39,01	28,1	129	0,198	39,4	259	150	338	17,6	72,4	39,9	46,1	123,0	13,1	2,70	3,15	5,04	4513
5	3,24	3,82	0,55	0,70	18,8	0,412	5,87	4,26	0,159	4,32	8,2	0,088	5,480	3,692	4,159	5,26	2,09	36,04	23,4	120	0,176	33,2	237	142	316	16,5	65,8	40,8	43,6	109,5	12,0	1,91	3,33	4,53	4218
7,5	5,12	4,05	0,57	0,71									5,267	3,737	4,186	5,96	2,18	32,53	26,0	124	0,136	44,5	248	152	313	17,2	66,5	38,5	44,2	109,6	12,0	2,15	2,34	4,58	4178
10	4,52	4,03	0,63	0,69	20,8	0,445	6,37	4,51	0,192	4,73	8,0	0,091	5,951	4,014	4,254	4,23	2,26	40,96	25,4	127	0,126	31,9	244	160	336	18,5	72,4	39,6	49,1	124,1	13,2	1,56	2,33	5,21	4827
12,5	4,98	3,81	0,59	0,80									5,882	3,884	4,560	5,87	2,24	33,72	23,2	121	0,134	40,7	256	158	332	17,1	65,7	36,8	45,0	111,6	11,7	2,03	3,28	4,62	4427
15	5,72	3,97	0,57	0,79	18,9	0,397	5,72	4,15	0,164			0,083	5,524	3,739	4,357	5,77	2,12	33,52	25,7	128	0,148	52,1	276	167	386	17,3	69,6	41,6	46,6	113,5	12,1	2,87	2,85	4,94	4574
17,5	5,55	3,69	0,54	0,73									5,168	3,517	4,210	6,53	2,19	31,70	21,2	116	0,189	44,1	274	131	304	15,7	61,5	37,5	42,1	108,4	11,0	3,81	2,65	4,29	4192
20	4,32	3,68	0,53	0,76	20,0	0,407	5,91	4,29	0,206	4,53	8,6	0,112	5,417	3,623	4,391	6,20	2,19	36,26	20,6	105	0,159	30,7	220	119	258	15,5	58,9	36,9	41,7	105,3	10,6	2,85	1,36	4,37	4305
22,5	5,56	3,29	0,45	0,78									5,398	3,661	4,450	6,57	2,33	33,41	30,8	118	0,197	46,6	285	154	344	16,0	64,2	38,9	43,9	101,5	10,9	4,29	2,46	4,52	4458
25	6,89	3,37	0,46	0,86	18,8	0,410	5,90	4,19	0,200	4,46	12,1	0,110	5,241	3,606	4,343	5,98	2,21	31,71	24,9	123	0,161	48,4	282	151	335	16,1	64,9	39,0	43,7	106,2	11,2	3,72	2,56	4,38	4315
27,5	5,34	3,10	0,45	0,86									5,439	3,669	4,416	6,31	2,36	37,15	22,2	133	0,172	48,2	282	163	374	17,5	72,7	41,1	48,4	116,6	12,1	3,70	2,91	4,98	4895
30	5,52	3,19	0,47	0,76	19,0	0,425	6,20	4,49	0,262	4,73	8,7	0,158	5,890	3,906	4,646	6,07	2,49	39,43	23,4	142	0,209	60,5	322	175	354	18,4	76,8	41,1	51,9	124,4	13,1	4,88	2,44	5,37	4968
32,5	5,53	3,11	0,46	0,86									4,726	2,986	4,153	9,38	2,24	29,79	22,8	108	0,198	59,0	346	135	293	14,1	55,7	37,7	38,8	96,0	9,5	6,19	2,37	3,90	3832
35	4,88	3,45	0,56	0,84	20,9	0,358	5,25	3,76	0,272	4,26	8,6	0,201	5,041	3,386	4,277	7,14	2,20	32,53	27,5	107	0,199	66,4	329	154	318	15,4	65,1	40,8	44,2	100,5	10,7	4,46	2,17	4,57	4281
37,5	4,16	2,84	0,42	0,89									4,839	3,203	4,214	7,94	2,27	35,96	33,2	128	0,200	38,7	306	136	298	15,2	62,7	40,2	40,0	93,4	10,3	5,58	2,60	4,37	4090
40	4,76	2,46	0,44	0,86	21,8	0,443	6,57	4,79	0,337	5,02	5,5	0,138	6,061	4,000	4,693	6,95	2,68	41,67	23,5	139	0,241	49,4	366	180	406	18,3	74,6	38,2	50,3	124,8	12,7	5,48	3,33	5,31	5332
42,5	4,11	2,29	0,38	0,86									4,893	3,367	4,277	8,54	2,36	35,00	25,2	112	0,176	33,1	254	146	288	15,0	62,8	40,1	41,4	103,8	10,5	5,44	2,22	4,38	4349
45	4,29	2,36	0,37	0,86	17,0	0,362	5,34	3,94	0,227	4,23	13,0	0,116	4,741	3,348	3,996	6,62	2,15	34,60	22,0	109	0,155	35,2	248	148	316	14,8	60,0	38,7	40,5	97,4	10,0	4,06	2,51	4,20	4427
47,5	4,49	2,45	0,37	1,06									4,664	3,094	4,396	9,86	2,22	36,37	28,2	95	0,179	28,4	234	156	314	14,0	57,1	38,6	39,1	92,6	9,2	6,29	3,46	4,13	4411
50	5,01	3,24	0,42	0,78	17,7	0,382	5,69	4,14	0,251	4,47	12,8	0,125	5,058	3,611	4,343	8,13	2,40	39,37	23,8	117	0,191	36,0	279	180	373	16,6	66,8	41,1	42,9	105,3	11,0	4,33	3,79	4,73	5261
52,5	4,62	3,31	0,47	0,82									4,920	3,353	4,377	6,98	2,40	37,35	18,5	119	0,205	35,6	253	166	373	16,1	66,9	40,5	46,1	110,5	10,9	4,68	3,94	4,50	4877
55	5,26	3,08	0,38	0,74	18,9	0,403	5,85	4,26	0,280	4,71	12,6	0,336	5,183	3,815	4,772	6,62	2,52	43,68	20,2	125	0,210	39,6	276	176	391	16,7	65,9	40,1	38,1	109,6	10,9	4,32	4,70	4,83	5334
57,5	4,92		0,38	0,75									4,908	3,301	3,978	4,82	2,15	37,43	18,8	121	0,223	49,8	303	176	369	15,9	63,8	41,1	39,5	102,7	10,3	4,08	2,92	4,45	4666
60	4,77	3,11	0,44	0,98	16,8	0,415	6,02	4,55	0,314	5,08	14,3	0,220	5,467	3,982	5,076	6,67	2,54	49,56	25,9	131	0,267	56,5	364	203	419	17,7	68,6	39,8	48,3	116,6	11,4	6,89	4,49	5,09	5617
62,5	5,16	2,79	0,44	0,91									5,658	3,711	4,969	6,57	2,56	41,54	28,7	133	0,288	66,1	394	207	416	18,3	73,2	40,1	42,2	114,7	11,9	5,59	4,37	5,10	5425
65	4,84	3,21	0,40	0,74	17,3	0,382	5,58	4,27	0,264	4,79	14,7	0,114	5,171	3,736	4,722	6,19	2,36	35,89	20,0	131	0,224	59,8	329	186	373	16,3	64,5	38,0	44,3	109,5	10,7	5,49	3,13	4,32	4386
67,5	5,13	3,13	0,42	0,97									5,033	3,532	4,550	7,94	2,39	37,26	22,0	124	0,260	43,8	307	183	306	14,9	59,0	37,7	39,9	106,6	9,8	6,72	3,24	4,29	4205
70	4,78	3,34	0,45	1,32	17,5	0,394	5,59	4,12	0,291	4,80	11,9	0,111	5,230	3,704	4,768	5,65	2,44	43,21	20,1	135	0,243	43,9	280	174	289	16,7	66,1	40,0	39,1	108,4	11,1	5,65	2,31	4,81	4778
72,5	4,22	3,43	0,41	0,84									4,646	3,070	4,224	7,60	2,29	37,30	25,1	115	0,215	35,9	259	161	282	14,7	59,4	38,8	38,8	94,1	9,8	6,94	2,83	4,22	4141
75	4,18	3,71	0,52	1,08	19,0	0,394	5,71	4,17	0,308	5,01	7,1	0,131	5,515	3,591	4,782	6,58	2,48	40,33	16,9	108	0,246	47,5	317	159	298	15,8	60,8	34,7	41,5	104,0	10,7	5,99	2,85	4,62	4436
77,5	4,67	3,69	0,48	0,80									5,231	3,313	4,566	7,17	2,46	39,53	21,4	132	0,230	61,0	374	179	314	15,7	63,8	40,7	40,5	103,7	10,4	7,01	2,77	4,55	4457
80	5,23	3,40	0,50	1,01	18,0	0,434	6,14	4,46	0,276	5,33	9,3	0,126	5,762	3,848	5,109	6,13	2,68	46,05	21,8	153	0,254	55,1	356	197	389	17,9	73,0	39,3	43,5	120,0	12,3	7,12	4,13	5,35	4910
82,5	4,44	3,53	0,51	0,94									5,086	3,581	5,213	6,64	2,61	43,86	21,3	139	0,255	65,0	392	184	352	16,9	70,0	40,5	41,7	113,2	11,7	7,70	3,44	5,09	4621
85	4,82	2,79	0,38	1,08	21,0	0,436	6,37	4,85	0,276	5,42	6,8	0,114	5,635	3,860	4,918	5,99	2,62	43,97	25,0	131	0,229	39,0	261	154	306	16,4	70,8	36,9	42,2	107,2	11,8	5,92	2,21	5,11	3914
87,5	3,56		0,34	0,70									5,053	3,577	4,699	5,08	2,41	40,12	18,3	117	0,237	40,0	252	143	276	14,3	62,7	40,0	31,9	90,1	10,2	5,80	1,81	4,51	3210
90	3,59	2,79	0,36	0,85	19,1	0,429	6,05	4,56	0,246	5,39	11,3	0,128	5,884	3,952	5,169	5,84	2,59	44,76	19,1	145	0,210	37,6	241	142	260	15,6	74,1	39,3	35,6	107,9	12,0	4,93	2,26	5,16	3107
92,5	4,22	2,09	0,41	0,80									6,038	3,837	5,148	5,87	2,62	46,72	20,6	155	0,221	36,7	246	147	274	16,3	75,5	37,7	29,4	106,3	12,1	4,95	4,01	5,39	3148
95	4,36		0,26	0,76	17,7	0,388	5,64	4,32	0,206	5,01	12,6	0,091	5,870	3,793	5,091	5,34	2,50	43,68	18,3	137	0,176	35,9	220	113	206	14,2	69,9	39,4	27,1	97,1	11,2	3,63	2,02	5,01	2268
97,5	3,89	1,62	0,25	0,80									5,121	3,454	5,023	7,42	2,69	42,70	21,7	129	0,172	32,1	209	110	197	13,9	69,1	38,0	33,7	93,3	10,8	4,64	1,97	4,92	1862
100	3,77	1,11	0,21	0,65	21,2	0,447	6,40	4,43	0,215	5,48	8,6	0,097	6,058	3,856	5,310	4,92	2,74	43,56	20,5	153	0,183	44,4	228	111	224	15,9	83,1	37,5	37,8	107,1	12,9	4,29	2,08	5,60	1879
102,5	3,89	1,31	0,25	0,77									6,687	4,150	5,747	4,34	2,58	46,90	20,4	174	0,177	47,6	240	111	218	16,7	92,4	37,7	38,5	117,1	14,1	3,25	1,73	6,19	1718
105	4,19	1,58	0,23	0,85	23,0	0,491	7,06	4,58	0,215	5,93	4,0	0,120	6,764	4,109	5,934	4,77	2,58	53,54	21,3	169	0,198	35,6	231	109	235	16,7	86,7	37,4	34,8	114,8	13,6	3,85	2,15	6,31	1884
107,5	4,40	2,19	0,33	0,84									5,938	3,671	5,337	4,97	2,41	45,77	19,7	183	0,157	35,4	217	104	223	15,3	79,8	37,9	36,5	108,1	12,7	3,06	1,86	5,54	1905
110	4,16	2,17	0,31	0,86	21,5	0,479	6,64	4,65	0,258	5,88	5,6	0,099	6,354	4,237	5,812	5,05	2,55	49,18	22,6	156	0,224	40,4	239	102	230	15,8	82,2	39,0	39,9	108,6	13,1	3,48	2,36	5,65	2310
112,5	4,17	2,39	0,35	1,02									5,434	3,540	5,361	6,66	2,38	43,54	22,9	136	0,211	37,4	232	93	214	13,7	71,8	39,4	36,0	95,6	11,4	4,29	2,21	4,88	2027
115	3,64	2,43	0,25	0,73	19,8	0,423	5,87	4,19	0,235	5,27	7,5	0,170	5,496	3,715	5,126	5,44	2,38	44,06	23,1	146	0,215	37,5	206	95	220	14,1	75,8	38,5	36,1	101,0	12,0	3,53	2,15	4,96	2094
117,5	3,93	2,34	0,44	1,03									6,103	4,474	5,821	4,49	2,61	51,18	20,0	153	0,234	44,4	240	103	215	15,2	79,1	37,8	39,0	110,0	13,1	3,88	2,42	5,67	2113
120	3,23	1,87	0,29	0,78	20,4	0,458	6,22	4,44	0,238	5,48	6,6	0,090	5,788	3,933	5,532	4,39	2,48	46,82	19,6	158	0,223	32,4	218	84	199	14,5	76,6	36,7	35,6	105,9	12,6	2,69	2,00	5,37	1575
122,5	3,57	1,26	0,27	1,09									6,182	3,967	5,439	5,55	2,72	51,61	24,4	152	0,199	36,2	205	83	184	14,9	80,0	36,0	36,2	105,2	13,0	3,38	1,53	5,65	1500
125	3,15	1,75	0,28	0,81	25,3	0,539	7,60	5,32	0,220	6,59	-0,1	0,109	6,725	4,698	5,886	4,41	2,94	50,56	22,1	184	0,192	46,0	222	96	206	16,6	98,7	36,7	40,5	121,1	15,5	3,18	1,71	6,39	1610
127,5	3,05	0,98	0,17	0,53									6,397	4,766	5,665	4,43	2,79	49,07	19,6	164	0,141	30,9	184	70	167	14,5	83,9	33,7	32,2	98,8	13,3	2,59	1,21	5,79	959
130	3,04	0,74	0,14	0,50	24,0	0,499	7,05	4,82	0,179	6,03	3,6	0,106	6,643	4,326	5,764	3,56	2,82	55,21	20,1	169	0,140	31,6	187	66	145	14,9	85,9	32,2	32,2	104,1	13,6	1,98	0,82	6,10	765
132,5	3,35	0,61	0,18	0,71									6,893	4,462	5,893	3,93	2,96	52,75	21,3	173	0,126	29,0	183	71	154	15,3	90,0	32,1	32,3	108,1	14,5	2,37	1,42	6,24	712
135	3,65	0,62	0,16	0,59	24,5	0,503	7,23	4,78	0,157	6,06	1,2	0,132	6,918	4,344	6,086	3,38	2,88	47,83	20,4	166	0,138	33,2	192	69	138	15,1	87,4	30,4	32,6	108,8	14,2	2,31	1,09	6,17	793
137,5	3,41	0,72	0,15	0,59									7,263	4,584	6,181	3,37	2,95	46,64	52,2	170	0,126	37,4	197	69	147	15,5	89,9	31,1	33,0	107,8	14,3	2,76	0,70	6,08	765
140	3,36	0,91	0,16	0,50	25,0	0,507	7,21	5,17	0,157	6,24	1,2	0,080	6,690	4,751	5,958	3,29	2,92	45,57	31,0	164	0,136	33,6	185	65	135	14,9	86,7	30,6	32,3	101,7	13,6	2,72	0,73	6,02	831
142,5	3,21	1,07	0,21	0,58									6,896	4,865	5,934	2,45	2,19	51,17	50,5	170	0,128	29,6	175	131	231	15,2	86,6	33,2	33,3	100,6	13,9	2,86	1,18	6,09	944
145	4,14	1,31	0,21	0,59	23,9	0,492	6,92	4,78	0,142	6,00	4,3	0,089	6,289	4,282	5,713	3,75	2,74	42,05	19,4	180	0,118	33,3	180	72	138	14,2	83,9	32,9	33,5	109,2	13,2	3,25	1,49	5,72	963
147,5	3,93	1,47	0,22	0,65									7,039	4,423	6,263	3,11	2,82	49,32	21,7	164	0,130	27,3	180	74	150	15,4	90,4	34,8	35,3	105,9	14,1	3,30	1,55	6,26	1190
150	4,37	1,84	0,22	0,53	23,1	0,475	6,77	4,37	0,146	5,80	4,4	0,090	6,433	4,051	5,779	3,11	2,73	49,90	19,2	172	0,131	28,7	200	75	156	14,7	83,5	35,5	33,3	109,3	13,2	4,01	1,42	5,92	1261
152,5	4,11	2,09	0,28	0,64									6,559	4,088	6,050	4,65	2,89	50,00	22,1	174	0,167	31,2	225	83	186	15,2	87,9	37,6	37,2	113,6	13,9	5,57	1,78	6,19	1622
155	6,08	2,17	0,29	0,83	24,7	0,521	7,33	5,17	0,195	6,37	6,4	0,091	6,637	4,616	5,991	4,05	3,57	44,06	21,2	170	0,162	49,5	289	89	182	15,2	85,5	34,6	38,1	108,7	13,6	6,08	2,06	5,89	1660
157,5	5,01	2,43	0,36	0,71									6,100	4,354	5,708	4,44	4,13	43,52	17,8	170	0,176	40,5	242	84	173	14,2	77,0	33,4	37,3	110,1	12,6	6,10	1,87	5,37	1611
160	4,29	2,43	0,33	0,65	23,4	0,498	6,96	4,82	0,212	5,90	4,6	0,087	6,025	4,223	5,551	3,72	2,59	55,09	17,4	193	0,184	35,4	235	79	178	15,0	82,8	35,8	34,3	120,3	13,9	6,36	2,01	5,81	1725
162,5	4,32	2,30	0,32	0,97									6,087	4,170	5,393	5,02	2,56	50,41	18,0	192	0,152	30,4	209	80	169	13,9	79,9	36,7	34,7	109,4	12,6	7,18	2,32	5,61	1620
165	4,99	2,25	0,31	1,09	23,2	0,480	6,82	4,81	0,180	5,81	5,1	0,082	6,002	4,468	5,318			45,04	14,7	167	0,153	30,0	213	77	153	13,8	79,4	34,6	35,2	103,9	12,7	6,45	2,61	5,45	1472
167,5	6,69	2,50	0,33	0,98									5,596	3,781	5,161	4,81	2,52	50,27	16,7	174	0,149	37,8	229	76	162	13,7	75,9	34,4	34,3	106,8	12,1	8,58	2,74	5,37	1504
170	4,18	2,59	0,33	0,81	23,8	0,496	6,79	4,86	0,195	5,80	4,7	0,085	6,171	4,114	5,470	3,71	2,56	54,02	19,6	173	0,172	35,3	230	78	171	14,6	81,4	36,2	36,8	108,4	12,7	6,64	1,97	5,76	1631
172,5	3,63	2,11	0,34	0,92									6,778	4,551	5,923	3,11	2,60	49,75	19,4	204	0,177	46,1	234	85	194	15,8	92,9	35,5	39,0	118,5	14,4	5,78	2,08	6,22	1756
175	4,84	2,43	0,32	1,02	23,9	0,493	6,87	5,10	0,178	5,80	6,2	0,081	6,378	4,464	5,513	3,71	2,62	51,98	17,8	190	0,157	36,4	224	82	172	14,5	81,9	36,2	32,9	105,1	12,7	7,38	1,92	5,57	1553
177,5	5,33	2,32	0,30	0,80									6,565	4,830	5,744	3,29	2,66	51,70	17,4	210	0,156	35,3	216	82	176	15,0	85,5	36,4	33,3	114,0	13,5	6,70	2,87	6,01	1663
180	4,04	2,39	0,30	0,87	25,8	0,536	7,46	5,30	0,211	6,20	11,1	0,096	6,471	4,568	5,758	3,33	2,65	50,17	17,8	206	0,173	45,2	260	88	184	15,4	90,2	37,9	38,2	116,7	13,7	9,08	1,70	5,99	1540
182,5	3,87	2,37	0,33	0,99									6,198	4,214	5,350	3,64	2,84	48,12	20,9	186	0,166	39,9	236	83	184	15,4	89,9	36,5	38,5	113,8	13,7	7,94	1,58	5,91	1545
185	4,04	2,09	0,29	1,22	24,5	0,515	7,11	5,00	0,212	5,93	7,7	0,201	6,423	4,309	5,283	4,04	2,65	50,20	20,0	177	0,182	37,5	224	79	180	15,0	83,8	36,9	37,4	107,2	13,4	9,39	1,79	5,87	1554
187,5	5,41	2,11	0,32	1,06									6,176	4,461	5,595	4,79	2,67	51,80	16,8	194	0,150	34,5	212	75	165	14,1	79,6	36,1	36,5	111,3	12,2	9,00	1,74	5,67	1486
190	4,86	2,23	0,32	0,94	23,9	0,499	6,89	5,00	0,182	5,70	8,0	0,091	6,296	4,430	5,652	3,88	2,63	42,35	16,9	208	0,159	41,0	232	79	168	14,4	80,6	36,0	36,6	113,2	12,6	7,24	1,99	5,42	1550
192,5	3,83	2,07	0,33	0,81									5,973	4,365	5,459	4,96	2,67	46,42	19,5	197	0,167	39,1	220	82	174	15,0	86,9	37,4	38,4	113,1	13,0	9,82	1,87	5,87	1629
195	4,80	2,14	0,32	0,93	23,2	0,490	6,75	4,78	0,195	5,58	9,8	0,084	6,214	4,296	5,191	3,78	2,54	50,86	19,5	163	0,158	36,3	299	77	173	14,0	79,4	39,5	37,2	104,6	12,5	7,93	1,98	5,87	1657
197,5	4,45	2,38	0,35	0,99									6,230	4,172	5,374	4,55	2,58	49,17	17,3	180	0,157	35,5	234	80	183	14,6	83,5	39,3	32,0	107,1	13,1	8,94	2,19	5,83	1596
200	4,94	2,16	0,33	1,06	25,3	0,528	7,33	5,07	0,205	5,94	8,0	0,071	6,757	4,636	5,760	4,04	2,69	44,90	17,4	212	0,163	45,2	252	82	188	15,2	86,3	38,1	38,2	122,6	13,8	8,31	1,97	6,09	1540

Appendix 2, Table 2) continued (geochemistry of core 74KL)

depth	La	Ce	Pr	Nd	Sm	Eu	Gd	Tb	Dy	Ho	Er	Tm	Yb	Lu	Hf	Ta	Tl	Pb	U
	ppm	ppm	ppm	ppm	ppm	ppm	ppm	ppm	ppm	ppm	ppm	ppm	ppm	ppm	ppm	ppm	ppm	ppm	ppm
1,25	29,9	50,9	7,11	28,7	6,20	1,23	6,56	1,007	6,33	1,36	4,06	0,585	4,03	0,650	3,05	0,88	1,04	25,4	11,6
5	28,3	48,2	6,73	27,2	5,85	1,18	6,21	0,970	6,03	1,30	3,94	0,576	3,88	0,606	2,82	0,82	0,97	24,4	9,8
7,5	28,9	48,4	6,95	27,7	6,04	1,26	6,89	1,012	6,10	1,33	3,98	0,589	3,95	0,632	2,62	0,79	0,98	25,0	16,2
10	32,2	54,3	7,59	30,4	6,42	1,30	6,82	1,065	6,79	1,43	4,33	0,632	4,29	0,666	2,96	0,87	0,93	26,4	15,0
12,5	29,9	49,9	7,12	28,7	6,10	1,31	7,12	1,017	6,36	1,38	4,13	0,590	4,17	0,656	2,66	0,79	0,98	24,7	16,3
15	29,3	48,2	6,84	27,0	6,02	1,23	6,65	1,009	6,09	1,36	4,00	0,599	4,04	0,631	2,74	0,76	1,23	24,0	18,0
17,5	27,6	45,8	6,62	26,5	5,80	1,20	6,52	0,977	5,89	1,29	3,84	0,567	3,91	0,630	2,77	0,76	1,54	24,6	17,5
20	27,8	45,7	6,56	26,3	5,66	1,29	6,13	0,927	5,83	1,26	3,84	0,563	3,77	0,563	2,48	0,73	0,96	21,1	14,3
22,5	29,1	48,4	7,02	28,5	6,18	1,28	6,99	1,003	6,12	1,31	4,01	0,588	3,98	0,623	2,60	0,76	1,66	25,3	19,2
25	28,1	46,3	6,77	27,1	5,93	1,23	6,73	0,982	6,03	1,30	3,93	0,561	3,93	0,631	2,70	0,74	1,30	24,4	24,2
27,5	30,5	49,5	7,10	28,1	6,01	1,23	6,80	1,009	6,31	1,38	4,15	0,598	4,15	0,672	2,80	0,78	1,38	23,8	19,9
30	32,1	53,0	7,56	29,3	6,46	1,34	7,56	1,063	6,65	1,46	4,41	0,669	4,41	0,709	3,03	0,83	1,69	25,9	21,7
32,5	24,8	40,8	5,98	24,3	5,20	1,13	5,91	0,849	5,38	1,17	3,47	0,495	3,54	0,566	2,44	0,67	1,66	21,8	19,6
35	27,4	44,8	6,44	25,1	5,62	1,20	6,40	0,936	5,66	1,24	3,67	0,562	3,75	0,599	2,36	0,67	1,54	21,8	18,2
37,5	25,6	42,9	6,11	24,9	5,37	1,02	5,65	0,878	5,48	1,19	3,55	0,527	3,55	0,562	2,35	0,70	1,62	22,4	14,6
40	31,6	52,3	7,50	30,3	6,54	1,27	7,15	1,096	6,75	1,45	4,52	0,658	4,52	0,702	3,16	0,83	1,84	26,7	20,9
42,5	25,9	42,8	6,16	24,8	5,34	1,04	5,84	0,896	5,62	1,22	3,76	0,537	3,73	0,573	2,61	0,68	1,54	21,6	14,7
45	24,9	40,6	5,83	23,9	5,16	1,00	5,49	0,848	5,31	1,14	3,58	0,516	3,61	0,553	2,40	0,66	1,25	19,9	15,8
47,5	24,5	40,3	5,80	23,2	4,98	0,97	5,43	0,855	5,32	1,15	3,50	0,483	3,46	0,521	2,12	0,63	1,79	22,7	16,7
50	27,7	45,7	6,53	26,7	5,78	1,12	6,16	0,957	6,03	1,29	3,99	0,582	3,95	0,624	2,58	0,71	1,62	24,8	20,8
52,5	27,4	45,4	6,42	25,1	5,47	1,10	6,10	0,905	5,79	1,26	3,90	0,590	3,90	0,590	2,56	0,71	1,69	23,7	18,2
55	28,4	47,1	6,71	27,2	5,77	1,11	6,24	0,984	6,16	1,33	4,06	0,599	3,93	0,641	2,74	0,77	1,63	28,3	22,5
57,5	25,7	42,0	5,92	23,3	5,19	1,04	6,00	0,846	5,39	1,19	3,65	0,539	3,54	0,577	2,38	0,69	1,50	22,7	18,9
60	30,5	51,3	7,29	29,3	6,22	1,24	6,84	1,067	6,80	1,47	4,49	0,622	4,49	0,711	2,98	0,76	2,36	29,6	21,2
62,5	30,2	50,3	7,20	28,9	6,37	1,31	7,47	1,048	6,59	1,44	4,32	0,611	4,26	0,655	2,93	0,83	1,96	29,5	22,5
65	25,9	44,1	6,33	25,6	5,57	1,16	6,41	0,922	5,93	1,28	3,89	0,561	3,89	0,601	2,69	0,72	1,80	25,3	19,4
67,5	25,6	42,8	6,11	24,7	5,28	1,13	6,19	0,906	5,62	1,21	3,81	0,566	3,77	0,604	2,68	0,72	2,04	24,4	19,4
70	26,9	47,0	6,52	26,1	5,77	1,07	5,98	0,907	5,82	1,28	3,88	0,577	3,71	0,619	2,72	0,74	1,61	25,6	19,7
72,5	23,8	41,7	5,69	22,8	5,02	0,94	5,17	0,792	5,20	1,13	3,51	0,490	3,43	0,526	2,26	0,64	1,81	24,2	15,9
75	26,6	45,7	6,21	25,3	5,52	1,34	6,04	0,906	5,65	1,25	3,84	0,518	3,80	0,561	2,29	0,69	2,03	25,6	18,0
77,5	26,2	45,6	6,34	26,1	5,75	1,07	5,83	0,872	5,59	1,23	3,80	0,555	3,77	0,594	2,66	0,67	1,86	26,9	18,5
80	29,8	52,0	7,12	28,5	6,22	1,23	6,35	0,998	6,35	1,36	4,17	0,590	4,04	0,635	2,95	0,82	1,91	30,3	23,7
82,5	28,0	49,2	6,76	27,2	5,95	1,15	6,17	0,936	6,00	1,32	4,00	0,595	3,83	0,595	2,98	0,77	1,83	27,6	18,9
85	27,6	48,4	6,67	26,8	5,92	1,17	6,04	0,917	5,88	1,25	3,75	0,542	3,71	0,584	2,79	0,79	1,46	25,7	20,1
87,5	23,7	42,2	5,84	23,2	5,16	1,02	5,08	0,791	4,93	1,05	3,20	0,452	3,01	0,489	2,41	0,68	1,09	25,2	13,4
90	26,0	46,1	6,34	25,9	5,62	1,13	5,70	0,889	5,50	1,17	3,60	0,525	3,39	0,525	2,83	0,81	1,09	24,7	14,5
92,5	26,2	46,7	6,34	25,5	5,36	1,06	5,56	0,818	5,15	1,10	3,35	0,491	3,11	0,491	2,74	0,82	1,31	25,9	17,3
95	23,2	41,6	5,65	22,8	4,77	1,03	4,95	0,770	4,66	0,99	2,93	0,403	2,75	0,440	2,49	0,73	1,28	20,6	16,0
97,5	23,9	42,1	5,66	22,6	4,75	1,06	5,03	0,774	4,71	0,98	2,95	0,422	2,88	0,422	2,46	0,74	1,09	19,6	13,7
100	25,7	46,6	6,20	23,8	5,16	1,14	5,75	0,831	5,02	1,07	3,12	0,450	3,08	0,485	2,91	0,83	1,11	19,5	13,1
102,5	26,8	49,4	6,47	25,2	5,51	1,27	6,08	0,884	5,37	1,13	3,39	0,495	3,22	0,495	3,08	0,88	1,24	20,4	13,7
105	27,4	51,0	6,67	26,8	5,69	1,24	5,73	0,905	5,54	1,17	3,43	0,490	3,20	0,490	3,17	0,90	1,32	22,2	15,8
107,5	25,1	46,4	6,16	24,9	5,43	1,17	5,47	0,838	5,21	1,09	3,24	0,474	3,14	0,474	3,03	0,84	1,09	19,7	16,0
110	26,4	48,1	6,42	25,9	5,61	1,20	5,84	0,890	5,49	1,16	3,48	0,503	3,37	0,503	2,82	0,89	1,32	21,0	16,1
112,5	23,2	42,4	5,59	22,9	4,92	1,05	5,24	0,773	4,89	1,05	3,09	0,457	2,99	0,457	2,50	0,77	1,30	19,4	14,7
115	24,3	43,9	5,82	22,9	4,97	1,09	5,36	0,776	4,87	1,06	3,14	0,459	3,00	0,459	2,65	0,81	1,27	19,1	12,8
117,5	26,6	48,5	6,41	25,7	5,49	1,21	5,67	0,915	5,53	1,17	3,44	0,476	3,29	0,513	2,93	0,88	1,68	21,4	14,4
120	25,0	46,2	6,03	24,2	5,15	1,15	5,28	0,819	4,98	1,05	3,11	0,426	3,02	0,459	2,79	0,85	0,95	19,2	10,6
122,5	26,1	48,3	6,37	25,2	5,44	1,26	5,51	0,862	5,34	1,09	3,28	0,464	3,15	0,464	2,95	0,90	1,13	20,7	11,8
125	28,4	52,0	6,85	26,3	5,84	1,29	6,29	0,909	5,56	1,15	3,43	0,489	3,22	0,489	3,25	0,98	1,22	20,9	11,0
127,5	24,2	46,1	6,05	24,1	5,16	1,15	5,13	0,778	4,78	1,01	2,97	0,432	2,77	0,403	2,71	0,89	0,86	18,2	8,8
130	25,5	48,7	6,29	24,8	5,27	1,21	5,22	0,796	4,94	1,02	2,96	0,412	2,80	0,412	2,99	0,93	0,74	17,3	8,3
132,5	25,7	49,4	6,31	25,4	5,39	1,24	5,45	0,816	4,97	1,00	3,03	0,421	2,82	0,421	3,10	1,00	0,84	18,7	8,8
135	26,5	50,2	6,61	27,8	5,44	1,27	5,96	0,858	5,10	1,04	3,07	0,442	2,89	0,442	3,04	1,01	0,88	19,2	9,5
137,5	26,2	49,6	6,62	25,8	5,56	1,29	5,92	0,850	5,10	1,06	3,06	0,438	2,94	0,438	3,01	1,00	0,82	20,0	8,8
140	26,1	48,8	6,43	25,2	5,30	1,25	5,83	0,836	4,99	1,05	3,03	0,418	2,82	0,418	2,90	0,94	0,86	19,5	8,8
142,5	25,1	47,7	6,31	25,4	5,59	1,23	5,45	0,829	5,05	1,02	2,99	0,428	2,86	0,428	2,91	0,99	0,86	17,8	8,6
145	25,5	47,6	6,34	25,0	5,35	1,23	5,69	0,839	4,98	1,05	3,07	0,419	2,91	0,419	3,09	0,92	0,89	19,2	10,8
147,5	26,4	49,7	6,57	26,3	5,57	1,25	5,60	0,831	5,18	1,08	3,16	0,443	2,99	0,443	2,88	0,94	0,89	19,0	10,9
150	25,8	48,1	6,24	24,9	5,29	1,20	5,37	0,818	4,99	1,04	3,05	0,436	2,92	0,436	2,97	0,90	0,93	18,8	11,9
152,5	28,4	53,3	6,95	27,5	5,88	1,27	5,80	0,905	5,54	1,16	3,48	0,509	3,25	0,509	3,19	0,93	0,96	21,1	11,6
155	27,9	50,7	6,84	27,2	5,99	1,32	6,43	0,910	5,61	1,17	3,47	0,499	3,41	0,499	3,05	0,94	1,73	21,5	17,9
157,5	26,7	48,7	6,52	25,8	5,54	1,26	6,07	0,895	5,23	1,09	3,27	0,476	3,16	0,476	2,97	0,90	1,29	20,4	14,0
160	26,7	49,6	6,50	25,7	5,49	1,20	5,55	0,865	5,27	1,12	3,26	0,474	3,15	0,474	3,21	0,92	1,28	19,9	12,0
162,5	25,6	48,0	6,27	24,6	5,29	1,15	5,23	0,801	5,10	1,07	3,18	0,454	2,99	0,454	3,04	0,85	1,23	19,1	11,5
165	24,8	45,4	6,00	24,1	5,17	1,14	5,25	0,806	5,00	1,06	3,14	0,445	3,00	0,445	2,81	0,86	1,67	18,2	13,9
167,5	24,4	45,0	5,89	23,3	5,11	1,11	5,13	0,815	5,03	1,06	3,10	0,435	2,93	0,462	2,88	0,84	1,96	17,2	18,2
170	26,7	49,0	6,42	25,6	5,45	1,22	5,64	0,862	5,36	1,14	3,36	0,473	3,14	0,473	3,06	0,86	1,11	19,5	11,6
172,5	27,8	50,2	6,61	26,2	5,61	1,28	6,18	0,883	5,44	1,17	3,45	0,513	3,30	0,513	3,10	0,91	1,20	21,3	10,3
175	25,5	46,8	6,19	24,9	5,32	1,19	5,57	0,865	5,24	1,11	3,27	0,459	3,08	0,459	2,89	0,86	1,43	18,9	13,1
177,5	26,5	49,0	6,54	26,2	5,61	1,20	5,74	0,875	5,44	1,15	3,36	0,492	3,25	0,492	3,17	0,93	1,72	20,0	14,6
180	27,3	49,7	6,55	25,7	5,48	1,23	5,84	0,877	5,32	1,12	3,29	0,494	3,15	0,466	2,88	0,88	1,18	19,0	11,1
182,5	27,1	49,2	6,47	25,4	5,57	1,22	5,79	0,870	5,25	1,11	3,26	0,489	3,13	0,489	3,02	0,87	1,11	18,9	10,5
185	26,9	48,8	6,50	26,2	5,62	1,23	5,75	0,910	5,43	1,15	3,43	0,482	3,24	0,482	2,97	0,94	1,31	19,9	10,8
187,5	25,7	47,6	6,26	24,7	5,23	1,21	5,44	0,845	5,23	1,11	3,25	0,475	3,11	0,475	3,09	0,84	1,45	18,9	14,3
190	26,0	47,1	6,41	25,5	5,46	1,24	6,06	0,888	5,41	1,13	3,42	0,484	3,28	0,511	3,15	0,86	1,21	19,9	13,1
192,5	26,5	47,8	6,39	25,1	5,44	1,23	5,75	0,865	5,39	1,14	3,38	0,502	3,29	0,502	3,13	0,87	1,03	18,9	10,7
195	26,4	47,9	6,35	25,6	5,52	1,23	5,60	0,857	5,38	1,15	3,40	0,482	3,27	0,509	2,79	0,88	1,45	19,6	12,9
197,5	26,1	47,4	6,31	25,2	5,31	1,19	5,42	0,840	5,15	1,08	3,25	0,461	3,06	0,461	2,87	0,89	1,30	19,3	12,1
200	28,5	51,2	6,95	27,7	5,95	1,33	6,62	0,942	5,79	1,25	3,66	0,526	3,49	0,526	3,35	0,97	1,22	21,4	13,7

Appendix 2, Table 2) continued (geochemistry of core 74KL)

sample	Lithology depth of	CaCO3	CaCO3 lith.	CaCO3 marine	CaCO3 d18 O	CaCO3 d13 C	G.ruber d18 O	G.ruber d13 C	C.wuell. d18 O	C.wuell. d13 C	<2 um	>6 um	>20 um	N	C org	pyrite 1 traces	pyrite #	>63um	pyrite	occurrence gypsum	S
cm	silt layer	%	%	%	%oPDB	%oPDB	%oPDB	%oPDB	%oPDB	%oPDB	%	%	%	%	%	2 abundant	#	g	#/g	pieces	%
3,00		13,08	5,42	7,66	-3,58	-1,55	-1,87	1,04			54,00	22,00	4,00	0,17	1,03	0,00				0,00	0,167
10,00																0,00				0,00	
21,00		13,57			-3,34	-1,50			2,79	-0,05	61,00	19,00	5,00	0,21	1,55	0,00				0,00	0,143
25,00											57,00	21,00	9,00			0,00				0,00	
31,00		16,90	1,72	15,18	-2,12	-0,66	-1,68	1,11			58,00	20,00	7,00	0,18	1,20	0,00				0,00	0,219
36,00		16,14	3,07	13,07	-2,68	-1,17	-1,90	1,07	2,65	0,06	58,00	20,00	6,00	0,16	1,01	0,00				0,00	
41,00		16,50	6,40	10,10	-3,33	-1,26	-1,64	1,03	2,53	-0,02	60,00	18,00	6,00	0,18	1,16	0,00				0,00	0,187
46,00		17,14	4,49	12,65	-2,73	-0,95	-1,57	0,92			62,00	16,00	4,00	0,15	0,92	0,00				0,00	
50,00					-3,05	-1,19					60,00	17,00	5,00			0,00				0,00	0,167
56,00		20,55	3,96	16,59	-2,56	-0,96	-1,74	1,12			63,00	16,00	5,00	0,15	1,12	0,00				0,00	
61,00		23,61	2,74	20,87	-2,42	-0,58	-1,95	1,19	2,42	-0,06	61,00	18,00	6,00	0,14	0,94	0,00				0,00	0,217
66,00		23,51	3,65	19,86	-2,63	-0,91	-2,01	0,90	2,48	0,00	60,00	19,00	6,00	0,14	0,91	0,00				0,00	
71,00		24,39	3,46	20,93	-2,61	-1,19	-2,05	0,72	2,41	0,00	62,00	17,00	4,00	0,15	1,40	1,00				0,00	0,201
75,00											54,00	24,00	10,00			0,00				0,00	
81,00		26,04	8,55	17,49	-2,89	-1,04	-1,37	1,00			55,00	25,00	12,00	0,10	0,63	0,00				0,00	0,180
86,00		21,16	3,59	17,57	-2,48	-0,88	-1,76	0,84	2,80	0,06	66,00	14,00	4,00	0,11	0,66	0,00				0,00	
91,00		22,57	2,84	19,73	-2,52	-0,80	-2,02	0,85	2,62	0,01	63,00	15,00	5,00	0,12	0,77	0,00				0,00	0,204
96,00		23,97	1,95	22,02	-2,16	-0,66	-1,82	0,80	2,50	-0,04	64,00	15,00	4,00	0,11	0,77	0,00				0,00	
99,00											62,00	15,00	5,00			0,00				0,00	0,193
106,00		23,03	0,65	22,38	-2,21	-0,59	-2,10	0,76			65,00	14,00	4,00	0,12	0,74	0,00				0,00	
111,00		25,53	4,15	21,38	-2,50	-0,78	-1,82	0,62	2,67	0,07	57,00	21,00	6,00	0,09	0,54	0,00				0,00	0,199
116,00	118	36,44	-2,42	38,86	-1,67	0,53	-1,94	0,61			55,00	27,00	9,00			0,00				0,00	
120,00											49,00	29,00	8,00			0,00				0,00	0,135
126,00		31,20	3,94	27,26	-2,33	-0,68	-1,80	0,91	2,89	0,03	58,00	24,00	10,00	0,07	0,42	0,00				0,00	
131,00		22,88	1,38	21,50	-2,58	-1,10	-2,36	0,84	2,98	0,08	59,00	20,00	6,00	0,09	0,42	0,00				0,00	0,141
136,00		25,45	4,98	20,47	-2,38	-1,22	-1,50	0,92			60,00	20,00	7,00	0,08	0,35	0,00				0,00	
140,00									2,52	-0,15	57,00	20,00	7,00			0,00	0,00	0,60	0,00	0,00	0,142
146,00		30,38	6,50	23,88	-1,96	-0,87	-0,86	0,77	2,97	-0,01	47,00	25,00	9,00	0,07	0,45	0,00	0,00	1,00	0,00	0,00	
151,00		29,37	9,14	20,23	-2,06	-0,57	-0,28	0,87	2,56	-0,14	51,00	32,00	14,00	0,07	0,47	0,00	2,00	1,50	1,33	0,00	0,143
156,00		28,10	8,23	19,87	-2,14	-0,75	-0,54	0,95	2,96	0,05	51,00	32,00	16,00	0,07	0,39	0,00	0,00	1,00	0,00	0,00	
160,00									3,01	-0,13	52,00	29,00	14,00			0,00	0,00	0,70	0,00	0,00	0,165
166,00	165	30,04	5,09	24,95	-1,78	-0,66	-0,92	1,05			53,00	30,00	14,00			1,00	2,00	2,10	0,95	0,00	
171,00		30,28	7,77	22,51	-1,80	-0,63	-0,35	0,78	3,21	-0,28	58,00	24,00	8,00	0,09	0,63	0,00	0,00	1,10	0,00	0,00	0,200
176,00		32,21	6,18	26,03	-1,70	-0,63	-0,68	0,54	3,18	-0,28	59,00	24,00	9,00	0,09	0,56	0,00	0,00	1,70	0,00	0,00	
180,00									3,21	-0,32	58,00	22,00	8,00			0,00	0,00	1,00	0,00	0,00	0,273
186,00		31,08	6,28	24,80	-1,97	-1,12	-0,95	0,81	3,25	-0,28	57,00	25,00	11,00	0,08	0,48	1,00	0,00	1,20	0,00	0,00	
191,00		31,69	9,16	22,53	-2,09	-0,83	-0,50	0,59	3,39	-0,26	55,00	28,00	13,00	0,09	0,55	0,00	0,00	1,60	0,00	0,00	
196,00		30,71	7,71	23,00	-2,06	-0,96	-0,74	0,26	3,45	-0,37	59,00	24,00	8,00	0,09	0,49	1,00	0,00	1,10	0,00	0,00	
198,00									3,13	-0,39	51,00	27,00	10,00			0,00	0,00	1,00	0,00	0,00	0,196
206,00		34,14	15,85	18,29	-2,71	-0,91	0,14	0,68	3,46	-0,22	43,00	43,00	21,00	0,05	0,23	0,00	0,00	0,80	0,00	0,00	
211,00		32,50	15,48	17,02	-2,78	-1,08	0,15	-0,01			47,00	37,00	15,00	0,06	0,21	1,00	1,00	0,80	1,25	0,00	0,153
216,00		34,43	13,23	21,20	-2,30	-0,89	0,01	-0,25	3,62	-0,13	43,00	46,00	26,00	0,06	0,37	1,00	1,00	0,70	1,43	0,00	
222,00											44,00	39,00	17,00				3,00	0,40	7,50	0,00	0,178
226,00		33,10	13,41	19,69	-2,52	-0,93	-0,15	0,53	3,40	-0,23	42,00	44,00	24,00	0,06	0,41	2,00	5,00	0,70	7,14	0,00	
231,00		34,59	18,55	16,04	-2,99	-1,11	0,49	0,48	3,67	-0,24	48,00	39,00	18,00	0,05	0,36	1,00	2,00	0,60	3,33	0,00	0,214
236,00		33,78	17,31	16,47	-2,83	-1,15	0,50	0,57	3,67	-0,19	43,00	42,00	21,00	0,05	0,24	1,00	0,00	0,50	0,00	0,00	
240,00							0,47	0,41			45,00	37,00	17,00				13,00	0,50	26,00	0,00	0,136
246,00		33,47			-2,35	-0,87			3,72	-0,32	50,00	35,00	16,00	0,06	0,24	1,00	2,00	0,40	5,00	0,00	
251,00		35,59	13,02	22,57	-2,08	-0,59	0,18	0,74	3,69	-0,24	52,50	29,00	8,00	0,06	0,40	1,00	3,00	0,30	10,00	0,00	0,208
256,00		34,59	16,69	17,90	-2,76	-0,92	0,26	0,55	3,33	-0,25	45,00	42,00	21,00	0,06	0,35	2,00	13,00	0,30	43,33	0,00	
260,00									3,62	-0,20	40,00	45,00	23,00				4,00	0,30	13,33		0,134
266,00		33,47	15,17	18,30	-2,44	-0,96	0,51	0,52	3,98	-0,21	51,50	33,50	10,50	0,06	0,24	1,00	4,00	0,40	10,00	0,00	
271,00		31,91	17,03	14,88	-2,94	-1,00	0,56	0,80	4,06	-0,55	47,00	40,00	20,00	0,06	0,35	2,00	16,00	0,50	32,00	0,00	0,221
276,00		31,70	16,07	15,63	-2,86	-1,08	0,37	0,74	4,21	-0,34	47,00	39,00	17,00	0,06	0,40	1,00	1,00	0,40	2,50	0,00	
280,00									4,12	-0,62	44,00	41,00	20,00				2,00	0,50	4,00		0,184
286,00		31,23	17,17	14,06	-3,07	-0,98	0,51	0,93	4,29	-0,56	53,00	34,00	13,00	0,09	0,60	1,00	8,00	0,30	26,67	0,00	
291,00	290	30,41	15,54	14,87	-2,86	-1,05	0,42	0,97	4,16	-0,61	47,00	38,00	17,00			2,00	13,00	0,60	21,67	0,00	0,311
296,00		32,19	16,20	15,99	-2,98	-1,22	0,08	0,82	4,04	-0,49	50,00	38,00	18,00	0,10	0,69	2,00	26,00	0,70	37,14	0,00	
299,00											43,00	41,00	21,00			2,00	10,00	0,30	33,33	0,00	0,398
301,00		30,26	13,00	17,26	-2,51	-0,94	0,12	0,52	4,12	-0,51	47,00	39,00	16,00	0,11	1,44	2,00	11,00	0,50	22,00	0,00	
306,00		30,14	15,09	15,05	-2,93	-1,23	0,15	0,49	4,34	-0,53	51,00	35,00	14,00	0,10	0,96	2,00	6,00	0,50	12,00	0,00	
311,00		30,04	14,64	15,40	-2,73	-0,98	0,38	0,57	4,31	-0,46	52,00	35,00	14,00	0,12	1,00	2,00	11,00	0,60	18,33	0,00	0,648
316,00		32,85	18,22	14,63	-3,14	-1,35	0,42	0,44			45,00	38,00	15,00	0,11	1,03	1,00	3,00	0,50	6,00	1,00	
321,00		31,35	15,23	16,12	-2,75	-1,22	0,32	0,52	4,25	-0,60	44,00	43,00	19,00	0,13	1,14	1,00	2,00	0,70	2,86	0,00	0,784
326,00		30,65	17,33	13,32	-3,24	-1,06	0,35	0,36	3,87	-0,59	44,00	40,00	17,00	0,11	1,07	2,00				0,00	

Appendix 3, Table 1) Sediment core KS8, sedimentology, isotope and mineral composition

sample	Lithology	CaCO3	CaCO3	CaCO3	CaCO3	CaCO3	G.ruber	G.ruber	C.wuell.	C.wuell.				N	C org	pyrite				occurrence	S
	depth of		lith.	marine	d18 O	d13 C	d18 O	d13 C	d18 O	d13 C	<2 um	>6 um	>20 um			1 traces	pyrite #	>63um	pyrite	gypsum	
cm	silt layer	%	%	%	%oPDB	%oPDB	%oPDB	%oPDB	%oPDB	%oPDB	%	%	%	%	%	2 abundant	#	g	#/g	pieces	%
331,00		30,25	15,24	15,01	-2,79	-1,01	0,47	0,35	4,19	-0,56	46,00	38,00	17,00	0,13	1,15	0,00	0,00	0,70	0,00	0,00	0,611
336,00	335	33,56	11,25	22,31	-2,27	-0,95	-0,39	0,62	4,11	-0,60	51,00	34,00	13,00			2,00	4,00	0,70	5,71	0,00	
341,00	341	37,34	16,76	20,58	-2,61	-0,84	0,15	0,64	4,21	-0,67	44,00	41,00	17,00	0,11	0,44	2,00	50,00	1,40	35,71	1,00	0,543
346,00	346	31,06	14,18	16,88	-2,75	-1,09	-0,02	1,05	3,55	-0,40	49,00	38,00	17,00	0,12	1,12	2,00	43,00	0,80	53,75	1,00	
350,00	350				-2,47	-1,01					43,00	41,00	20,00				29,00	1,00	29,00		
356,00	356	31,25	15,12	16,13	-2,80	-1,55	0,20	0,87	4,24	-0,76	44,00	40,00	18,00	0,11	1,34	2,00	19,00	0,70	27,14	1,00	0,478
361,00	depths	32,23	15,76	16,47	-2,78	-1,03	0,30	0,31	3,93	-0,47	50,00	36,00	15,00	0,12	1,10	2,00	10,00	0,90	11,11	1,00	0,742
366,00	of coral	32,02	17,73	14,29	-3,13	-1,12	0,43	0,41	4,15	-0,57	45,00	43,00	19,00	0,12	1,00	1,00	6,00	0,60	10,00	1,00	
371,00	occurence	26,26	13,17	13,09	-2,95	-1,18	0,12	0,16	4,18	-0,77	50,00	33,00	12,00	0,11	0,84	1,00	5,00	0,60	8,33	1,00	0,685
376,00		30,43			-2,95	-1,10			4,02	-0,79	45,00	41,00	18,00	0,13	1,07	0,00	1,00	0,30	3,33	1,00	
380,00											42,00	41,00	20,00				17,00	0,50	34,00		0,582
386,00		30,26	13,38	16,88	-2,63	-1,03	0,04	0,90	4,23	-0,65	47,00	40,00	16,00	0,11	1,03	2,00	9,00	0,70	12,86	1,00	
391,00		27,76	14,54	13,22	-3,11	-1,23	0,07	0,49	3,92	-0,87	44,00	41,00	18,00	0,11	0,93	2,00	41,00	0,50	82,00	1,00	0,448
396,00		27,47	15,29	12,18	-3,25	-1,56	0,20	0,59	3,91	-0,63	48,00	37,00	13,00	0,11	0,73	2,00	13,00	0,50	26,00	1,00	
401,00		29,94	12,66	17,28	-2,67	-1,49	-0,23	0,35	4,25	-0,68	44,00	44,00	22,00	0,14	1,54						0,487
406,00		23,70			-3,63	-1,64					53,00	34,00	12,00	0,17	1,40						
411,00		26,88			-2,91	-1,21					50,00	37,00	14,00	0,17	1,88						
416,00		24,98			-3,59	-1,51					48,00	36,00	13,00	0,17	1,56						
421,00		26,56			-3,47	-1,33					50,00	36,00	13,00	0,18	1,71						
426,00	426	34,13			-2,84	-1,16					46,00	39,00	17,00	0,11	0,99						
431,00		29,73			-3,21	-1,11					49,00	37,00	13,00	0,07	0,46						
436,00		30,10			-3,53	-1,32					52,00	32,00	11,00	0,07	0,46						
441,00		28,89			-3,66	-1,33					45,00	40,00	17,00	0,09	0,48						
446,00	445	26,48			-3,13	-1,12					51,00	36,00	16,00	0,12	0,90						
451,00		26,03			-3,79	-1,32					42,00	41,00	16,00	0,11	0,73						
456,00		26,41			-3,47	-1,08					38,00	48,00	21,00	0,10	0,79						
461,00		26,73			-3,58	-1,32					49,00	36,00	12,00	0,09	0,65						
466,00		27,36	12,62	14,74	-2,81	-1,00	-0,08	0,80	3,90	-0,50	46,00	38,00	17,00	0,13	1,09						
471,00		23,76			-3,52	-1,44			4,06	-0,36	45,00	38,00	16,00	0,13	0,96						
476,00		25,93			-2,95	-1,21					46,00	39,00	17,00	0,09	0,65						
481,00		25,67	14,98	10,69	-3,46	-1,20	0,10	0,96			45,00	42,00	20,00	0,12	0,87						
486,00		25,20	12,80	12,40	-3,23	-1,60	-0,37	0,80	3,68	-0,60	46,00	38,00	19,00	0,11	0,80						
491,00		22,23	12,57	9,66	-3,67	-1,54	-0,64	0,80	3,90	-0,44	47,00	37,00	15,00	0,09	0,74						
496,00		26,31	14,13	12,18	-3,37	-1,29	-0,32	0,59			45,00	40,00	19,00	0,10	0,68						
501,00		24,12	15,33	8,79	-3,85	-1,56	-0,10	0,83	4,00	-0,49	51,00	33,00	14,00	0,14	1,16						
504,00		23,47	15,30	8,17	-3,89	-1,78	0,06	0,64			50,00	34,00	15,00	0,13	1,22						
506,00		27,57	14,37	13,20	-3,30	-1,36	-0,36	0,69	3,76	-0,41	49,00	34,00	15,00	0,12	0,91						
511,00		27,59	13,55	14,04	-3,19	-1,36	-0,48	0,73	3,71	-0,34	48,00	37,00	17,00	0,09	0,60						
516,00		23,05	6,05	17,00	-1,90	-1,29	-0,44	0,87	3,50	-0,22	50,00	33,00	12,00	0,10	0,70						
521,00		26,72	10,44	16,28	-2,49	-1,01	-0,24	0,51			53,00	31,00	11,00	0,11	0,80						
526,00	525	29,83	6,80	23,03	-2,07	-0,86	-0,91	0,85			48,00	36,00	15,00	0,14	1,32						
531,00		21,48	10,98	10,50	-3,19	-1,85	-0,25	0,73			48,00	35,00	13,00	0,15	1,25						
536,00		26,83	11,25	15,58	-2,80	-1,32	-0,49	0,60	3,59	-0,46	50,00	35,00	17,00	0,13	1,00						
541,00		26,88	15,64	11,24	-3,35	-1,47	0,34	0,64	3,40	-0,31	50,00	36,00	16,00	0,08	0,63						
546,00		28,14	15,45	12,69	-3,20	-1,50	0,21	0,68	3,22	-0,43	47,00	38,00	18,00	0,07	0,40						
551,00		29,00			-2,91	-1,37			3,64	-0,29	47,00	38,00	17,00	0,08	0,52						
556,00		26,03			-3,06	-1,35			3,60	-0,42	52,00	34,00	15,00	0,10	0,64						
561,00		24,86			-3,10	-1,39			3,51	-0,49	48,00	36,00	15,00	0,12	0,85						
566,00		23,94			-3,20	-1,43			3,78	-0,52	53,00	31,00	12,00	0,12	0,94						
571,00	572	16,29			-4,04	-1,93			3,89	-0,59	45,00	36,00	11,00	0,16	1,39						
576,00		23,55			-3,21	-1,59			3,95	-0,53	51,00	33,00	13,00	0,10	0,74						
581,00		29,35			-3,38	-1,46					41,00	44,00	23,00	0,07	0,48						
586,00		24,48			-3,21	-1,24			3,59	-0,41	41,00	47,00	23,00	0,05	0,40						
591,00		28,94			-2,77	-1,17			3,50	-0,62	44,00	42,00	17,00	0,06	0,39						
596,00		30,18			-2,20	-1,00			3,78	-0,59	45,00	41,00	19,00	0,08	0,58						
601,00		27,67			-2,05	-0,94					48,00	37,00	13,00	0,07	0,48						
604,00		27,30			-2,09	-1,12					49,00	35,00	14,00	0,08	0,67						

Appendix 3, Table 1) continued (core KS8)

depth	CaCO3	Li	Sc	Cr	Mn	Co	Ni	Cu	Zn	Ga	Rb	Sr	Y	Zr	Nb	Mo	Cs	Ba	La	Ce	Pr	Nd	Sm	Eu	Gd	Tb	Dy	Ho
cm	%	ppm	ppm	ppm	ppm	ppm	ppm	ppm	ppm	ppm	ppm	ppm	ppm	ppm	ppm	ppm	ppm	ppm	ppm	ppm	ppm	ppm	ppm	ppm	ppm	ppm	ppm	ppm
61	23,6	41,3	11,4	159	1245	32,9	173	50,8	115,0	12,7	91,0	386	18,8	80,0	8,98	0,73	6,96	496	20,0	38,8	4,43	16,7	3,34	0,67	3,02	0,46	2,89	0,59
70	24,4	41,3	11,3	158	1278	31,6	174	53,4	139,0	12,6	88,4	396	18,6	80,0	8,67	1,12	6,74	513	19,2	38,3	4,40	16,6	3,27	0,67	3,08	0,45	2,83	0,58
80	26,1	40,7	10,4	147	722	22,2	133	41,8	94,2	12,0	84,6	424	18,0	76,4	8,61	0,46	6,36	381	18,3	36,6	4,23	16,0	3,21	0,66	2,89	0,46	2,72	0,54
91	22,6	46,4	11,3	144	673	24,2	144	51,1	107,0	13,4	93,4	371	18,5	77,3	9,06	0,64	7,10	549	20,7	41,1	4,62	17,6	3,53	0,71	3,11	0,46	2,82	0,60
99	22,8	45,3	11,2	145	625	23,7	143	45,9	98,5	12,7	89,8	372	18,0	76,5	8,39	0,46	6,76	505	19,5	38,6	4,38	16,1	3,29	0,68	2,89	0,44	2,77	0,56
110	25,5	45,8	11,3	147	615	22,4	132	39,3	90,8	12,4	86,8	457	17,3	79,1	8,07	0,33	6,43	410	18,0	35,8	4,06	15,3	3,05	0,63	2,69	0,43	2,66	0,54
120	21,2	46,0	11,7	159	872	24,9	142	39,9	93,7	13,4	94,8	351	19,4	84,6	9,09	0,30	7,20	427	21,2	42,2	4,77	17,9	3,67	0,73	3,20	0,49	3,06	0,62
131	22,9	48,1	11,4	145	765	22,3	125	38,0	88,6	13,6	96,4	356	19,0	83,2	9,38	0,48	7,24	376	21,3	42,9	4,84	18,0	3,66	0,77	3,24	0,51	3,01	0,64
140	24,8	51,4	13,0	150	690	22,8	126	37,9	92,0	14,4	102,0	446	19,9	85,3	9,70	0,45	7,64	379	22,4	44,9	5,06	18,8	3,88	0,79	3,27	0,52	3,16	0,65
148	30,4	41,1	10,4	126	693	17,9	102	33,9	77,2	11,4	77,5	526	16,3	72,1	8,00	0,39	5,76	274	17,3	34,3	3,98	14,8	3,09	0,68	2,72	0,44	2,57	0,54
156	28,1	41,8	10,5	128	548	16,1	101	32,3	77,4	11,3	79,5	470	17,2	75,7	8,32	0,30	5,97	270	17,6	35,2	4,07	15,6	3,23	0,68	2,82	0,43	2,69	0,55
160	26,5	42,5	10,6	131	541	16,8	102	31,7	77,4	11,1	79,0	498	17,3	75,8	8,25	0,31	5,89	270	17,3	34,8	4,02	15,3	2,99	0,66	2,83	0,44	2,65	0,54
171	30,3	42,5	9,9	120	586	18,2	101	32,2	73,3	10,8	76,3	575	16,5	70,5	7,99	0,41	5,77	290	16,7	33,7	3,93	14,5	3,02	0,66	2,65	0,43	2,59	0,52
180	30,9	41,8	10,6	128	530	18,6	112	30,5	69,2	10,9	76,6	582	16,3	67,9	7,83	0,53	5,69	288	16,8	33,8	3,90	14,9	3,10	0,62	2,67	0,41	2,55	0,52
190	31,7	40,1	9,5	123	622	17,8	105	30,9	74,5	10,5	74,2	453	16,8	67,2	7,74	0,51	5,56	281	16,6	33,0	3,90	14,6	2,99	0,61	2,65	0,41	2,53	0,51
198	29,7	40,8	9,6	138	564	16,5	109	28,9	70,6	10,5	73,8	454	16,8	72,7	7,88	0,43	5,58	219	16,6	33,0	3,92	15,0	3,00	0,65	2,73	0,42	2,64	0,52
210	32,5	36,3	8,8	129	570	14,8	89	26,1	62,3	9,5	64,6	441	16,1	68,7	7,52	0,37	4,67	212	15,5	30,9	3,71	14,2	2,89	0,63	2,57	0,41	2,50	0,50
222	33,1	35,6	8,8	123	508	14,8	92	27,3	61,3	9,1	61,3	510	15,9	65,7	7,69	0,35	4,48	208	14,7	29,2	3,51	13,4	2,91	0,63	2,58	0,39	2,41	0,48
231	34,6	36,0	9,3	114	594	15,1	88	23,6	63,2	9,4	62,6	461	16,2	62,9	7,70	0,43	4,52	199	15,1	30,0	3,60	14,0	2,86	0,62	2,62	0,38	2,49	0,50
240	30,4	35,4	11,1	131	535	15,5	97	30,8	70,4	11,4	77,2	482	17,5	70,8	9,35	0,64	5,68	204	17,6	34,8	4,06	15,7	3,06	0,67	2,83	0,45	2,72	0,54
250	35,6	33,0	10,8	141	603	14,9	94	28,9	65,1	10,3	67,5	538	17,0	68,9	8,71	0,75	4,77	203	15,2	30,0	3,58	13,8	2,90	0,63	2,74	0,42	2,54	0,52
260	32,1	32,9	10,5	142	537	13,6	88	28,8	66,6	10,1	66,9	424	16,8	68,8	8,64	0,72	4,72	215	15,6	30,8	3,68	14,2	2,96	0,65	2,80	0,42	2,53	0,53

Appendix 3, Table 2) Sediment core KS8, chemical concentration values in the bulk fraktion (% or ppm), concentration values expressed on a carbonate free basis (% or ppm, cfb)

depth cm	Er ppm	Tm ppm	Yb ppm	Lu ppm	Hf ppm	Ta ppm	Tl ppm	Pb ppm	U ppm	Li ppm cofb	Sc ppm cofb	Cr ppm cofb	Mn ppm cofb	Co ppm cofb	Ni ppm cofb	Cu ppm cofb	Zn ppm cofb	Ga ppm cofb	Rb ppm cofb	Sr/Ca	Y ppm cofb	Zr ppm cofb	Nb ppm cofb	Mo ppm cofb	Cs ppm cofb	Ba ppm cofb	La ppm cofb	Ce ppm cofb
61	1,76	0,26	1,69	0,26	2,12	1,13	0,59	24,2	3,85	54,06	14,9	208	1630	43,1	226	66,5	151	16,6	119	40,8	24,6	105	11,8	0,95	9,11	649	26,2	50,8
70	1,78	0,25	1,66	0,25	2,00	1,08	0,55	17,8	3,98	54,63	14,9	209	1690	41,8	230	70,6	184	16,7	117	40,5	24,6	106	11,5	1,48	8,92	679	25,4	50,7
80	1,68	0,24	1,62	0,23	2,06	1,07	0,43	14,3	3,43	55,07	14,1	199	977	30,0	180	56,6	127	16,2	114	40,6	24,4	103	11,7	0,63	8,61	516	24,8	49,5
91	1,77	0,28	1,74	0,26	2,17	1,15	0,50	17,5	3,61	59,95	14,6	186	870	31,3	186	66,0	138	17,3	121	41,0	23,9	100	11,7	0,83	9,17	709	26,7	53,1
99	1,75	0,25	1,73	0,26	2,15	1,05	0,48	16,0	3,51	58,68	14,5	188	810	30,7	185	59,5	128	16,5	116	40,7	23,3	99	10,9	0,59	8,76	654	25,3	50,0
110	1,65	0,23	1,72	0,24	2,18	0,99	0,44	13,2	3,56	61,48	15,2	197	826	30,1	177	52,8	122	16,6	117	44,8	23,2	106	10,8	0,44	8,63	550	24,2	48,1
120	1,87	0,26	1,88	0,26	2,39	1,11	0,42	16,0	3,04	58,38	14,8	202	1107	31,6	180	50,6	119	17,0	120	41,4	24,6	107	11,5	0,38	9,14	542	26,9	53,6
131	1,85	0,30	1,91	0,29	2,43	1,14	0,52	20,3	2,58	62,39	14,8	188	992	28,9	162	49,3	115	17,6	125	38,8	24,6	108	12,2	0,63	9,39	488	27,6	55,6
140	1,93	0,29	1,96	0,29	2,58	1,17	0,50	16,0	3,13	68,35	17,3	199	918	30,3	168	50,4	122	19,1	136	44,9	26,5	113	12,9	0,60	10,16	504	29,8	59,7
148	1,60	0,25	1,57	0,25	2,06	0,97	0,37	14,0	5,61	59,05	14,9	181	996	25,7	147	48,7	111	16,4	111	43,2	23,4	104	11,5	0,56	8,28	394	24,9	49,3
156	1,65	0,24	1,66	0,25	2,19	0,99	0,36	13,7	2,87	58,14	14,6	178	762	22,4	140	44,9	108	15,7	111	41,8	23,9	105	11,6	0,42	8,30	376	24,5	49,0
160	1,66	0,24	1,59	0,23	2,13	0,98	0,33	12,4	2,95	57,82	14,4	178	736	22,9	139	43,1	105	15,1	107	46,9	23,5	103	11,2	0,42	8,01	367	23,5	47,3
171	1,54	0,23	1,53	0,24	1,96	1,00	0,40	12,2	3,05	60,98	14,2	172	841	26,1	145	46,2	105	15,5	109	47,4	23,7	101	11,5	0,59	8,28	416	24,0	48,4
180	1,55	0,22	1,49	0,22	2,00	0,98	0,39	12,2	3,29	60,49	15,3	185	767	26,9	162	44,1	100	15,8	111	47,0	23,6	98	11,3	0,76	8,23	417	24,3	48,9
190	1,54	0,22	1,49	0,22	1,93	0,95	0,36	12,7	3,42	58,71	13,8	180	911	26,1	154	45,2	109	15,4	109	35,7	24,6	98	11,3	0,74	8,14	411	24,3	48,3
198	1,61	0,23	1,55	0,23	2,00	0,98	0,33	12,5	3,1	58,04	13,7	196	802	23,5	155	41,1	100	14,9	105	38,2	23,9	103	11,2	0,61	7,94	312	23,6	46,9
210	1,58	0,22	1,50	0,20	2,13	0,93	0,27	14,4	2,65	53,78	13,1	191	844	21,9	132	38,7	92	14,1	96	33,9	23,9	102	11,1	0,55	6,92	314	23,0	45,8
222	1,49	0,19	1,42	0,20	1,94	0,90	0,27	10,5	2,87	53,21	13,1	184	759	22,1	137	40,8	92	13,7	92	38,5	23,8	98	11,5	0,52	6,70	311	22,0	43,6
231	1,48	0,21	1,37	0,19	1,82	0,93	0,28	19,2	2,85	55,05	14,2	174	908	23,1	134	36,1	97	14,3	96	33,3	24,8	96	11,8	0,66	6,91	304	23,1	45,9
240	1,53	0,24	1,50	0,23	2,04	0,75	0,39	12,1	2,66	50,86	15,9	188	769	22,3	139	44,3	101	16,4	111	39,6	25,1	102	13,4	0,93	8,16	293	25,3	50,0
250	1,54	0,22	1,43	0,22	1,72	0,68	0,34	11,1	2,57	51,23	16,8	219	936	23,1	146	44,9	101	16,0	105	37,8	26,4	107	13,5	1,17	7,41	315	23,6	46,6
260	1,55	0,23	1,49	0,22	1,91	0,69	0,32	11,3	2,36	48,45	15,5	209	791	20,0	130	42,4	98	14,9	99	33,0	24,7	101	12,7	1,06	6,95	317	23,0	45,4

Appendix 3, Table 2) continued (geochemistry of core KS8)

depth	Pr	Nd	Sm	Eu	Gd	Tb	Dy	Ho	Er	Tm	Yb	Lu	Hf	Ta	Tl	Pb	U
cm	ppm cofb	ppm cofb	ppm cofb	ppm cofb	ppm cofb	ppm cofb	ppm cofb	ppm cofb	ppm cofb	ppm cofb	ppm cofb	ppm cofb	ppm cofb	ppm cofb	ppm cofb	ppm cofb	ppm cofb
61	5,80	21,9	4,37	0,87	3,95	0,60	3,78	0,77	2,30	0,340	2,21	0,34	2,77	1,48	0,768	31,7	5,04
70	5,82	22,0	4,33	0,88	4,07	0,59	3,74	0,76	2,35	0,336	2,20	0,33	2,65	1,43	0,733	23,5	5,26
80	5,72	21,7	4,34	0,90	3,91	0,62	3,68	0,73	2,27	0,322	2,19	0,31	2,79	1,45	0,585	19,4	4,64
91	5,97	22,7	4,56	0,91	4,02	0,60	3,64	0,77	2,29	0,359	2,25	0,34	2,80	1,49	0,643	22,6	4,66
99	5,67	20,9	4,26	0,88	3,74	0,57	3,59	0,73	2,27	0,326	2,24	0,34	2,78	1,36	0,624	20,7	4,55
110	5,45	20,5	4,09	0,85	3,61	0,57	3,57	0,72	2,21	0,307	2,31	0,32	2,93	1,33	0,595	17,7	4,78
120	6,05	22,7	4,66	0,92	4,06	0,62	3,88	0,78	2,37	0,324	2,39	0,33	3,03	1,41	0,536	20,3	3,86
131	6,28	23,3	4,75	0,99	4,20	0,66	3,90	0,82	2,40	0,389	2,48	0,38	3,15	1,48	0,676	26,3	3,35
140	6,73	25,0	5,16	1,04	4,35	0,69	4,20	0,87	2,57	0,387	2,61	0,39	3,43	1,56	0,668	21,3	4,16
148	5,72	21,3	4,44	0,97	3,91	0,63	3,69	0,77	2,30	0,358	2,26	0,36	2,96	1,40	0,532	20,1	5,61
156	5,66	21,7	4,49	0,95	3,92	0,60	3,74	0,77	2,29	0,328	2,31	0,35	3,05	1,37	0,494	19,1	3,99
160	5,47	20,8	4,07	0,90	3,85	0,60	3,61	0,73	2,26	0,322	2,16	0,31	2,90	1,33	0,449	16,9	4,01
171	5,64	20,8	4,33	0,94	3,80	0,61	3,72	0,75	2,21	0,333	2,20	0,34	2,81	1,43	0,571	17,5	4,38
180	5,64	21,6	4,49	0,90	3,86	0,59	3,69	0,75	2,24	0,318	2,16	0,32	2,89	1,42	0,559	17,7	4,76
190	5,71	21,4	4,38	0,89	3,88	0,61	3,70	0,75	2,25	0,324	2,18	0,32	2,83	1,39	0,523	18,6	5,01
198	5,58	21,3	4,27	0,92	3,88	0,59	3,76	0,75	2,29	0,323	2,20	0,32	2,84	1,39	0,471	17,8	4,41
210	5,50	21,0	4,28	0,93	3,81	0,61	3,70	0,75	2,34	0,330	2,22	0,30	3,16	1,37	0,404	21,3	3,93
222	5,25	20,0	4,35	0,94	3,86	0,59	3,60	0,72	2,23	0,287	2,12	0,30	2,90	1,34	0,398	15,7	4,29
231	5,50	21,4	4,37	0,95	4,01	0,59	3,81	0,76	2,26	0,320	2,09	0,29	2,78	1,42	0,425	29,4	4,36
240	5,83	22,6	4,40	0,96	4,07	0,64	3,91	0,78	2,20	0,342	2,16	0,33	2,93	1,08	0,565	17,4	3,82
250	5,56	21,4	4,50	0,98	4,25	0,65	3,94	0,81	2,39	0,334	2,22	0,34	2,67	1,05	0,526	17,2	3,99
260	5,42	20,9	4,36	0,96	4,12	0,62	3,73	0,77	2,28	0,333	2,19	0,32	2,81	1,02	0,470	16,6	3,48

Appendix 3, Table 2) continued (geochemistry of core KS8)

depth	dry density	>63um	CaCO3	CaCO3 d18 O	CaCO3 d13 C	CaCO3 lith.	CaCO3 marine	G.ruber d18 O	G.ruber d13 C	C.wuell. d18 O	C.wuell. d13 C	grain size in lithic fraction <2 um	>6 um	>20 um	N	C org	pyrite	pyrite
cm	g/ccm	%	%	%oPDB	%oPDB	%	%	%oPDB	%oPDB	%oPDB	%oPDB	%	%	%	%	%	#	#/g
2,50	0,79	0,92	11,60	-3,38	-1,27	4,22	7,38	-1,88	1,20			57,70	14,10	12,60	0,29	1,88	0,00	0,00
6,00	0,82	0,31	12,20	-3,12	-1,27										0,32	2,00	0,00	0,00
8,00	0,83	1,21	12,10	-3,22	-1,22	3,41	8,69	-2,13	0,99			57,50	16,00	5,50	0,32	1,94	0,00	0,00
10,00	0,85	0,59	13,00	-3,15	-0,70	3,96	9,04	-1,90	0,99			61,20	13,00	3,50	0,29	1,85	0,00	0,00
12,00	0,82	0,61	12,60	-3,05	-1,35							66,30	13,10	5,60	0,35	1,99	0,00	0,00
14,00	0,84	2,67	10,60	-3,20	-1,15	3,47	7,13	-1,84	1,02	2,08	-0,13	57,00	16,00	5,50	0,28	1,86	0,00	0,00
16,00	0,81	0,62	12,50	-3,01	-1,21	2,26	10,24	-2,35	0,95	2,79	0,15	57,00	16,00	5,50	0,30	1,96	0,00	0,00
18,00	0,82	0,91	12,40	-3,34	-1,02	4,30	8,10	-1,93	1,17	2,59	0,00	57,50	16,50	6,50	0,30	1,88	0,00	0,00
20,00	0,82	0,61	11,30	-3,01	-1,13	3,29	8,01	-1,78	1,12	2,06	-0,37	60,60	15,00	5,20	0,29	1,82	0,00	0,00
22,00	0,80	0,63	13,40	-2,69	-1,03	2,91	10,49	-1,77	1,14	2,79	0,23	60,00	12,50	3,20	0,29	1,78	0,00	0,00
24,00	0,83	0,90	12,40	-2,99	-1,28							63,30	13,90	4,40	0,27	1,85	0,00	0,00
26,00	0,85	2,65	13,30	-2,77	-1,13					2,79	0,02	59,00	12,00	3,00	0,23	1,73	0,00	0,00
28,00	0,85	1,18	13,00	-2,80	-0,95	2,88	10,12	-1,89	1,06	2,67	0,17	64,00	12,00	1,70	0,25	1,62	0,00	0,00
30,00	0,86	1,46	14,20	-2,78	-0,95	2,04	12,16	-2,24	1,12	2,55	0,15	62,10	13,80	3,80	0,24	1,59	0,00	0,00
32,00	0,87	1,43	13,50	-2,84	-0,86					2,69	-0,05	52,00	17,20	5,20	0,20	1,16	0,00	0,00
34,00	0,86	1,74	14,00	-2,75	-1,00	2,09	11,91	-2,18	0,87	2,63	0,31	65,60	12,20	4,40	0,18	1,28	0,00	0,00
36,00	0,84	0,59	13,70	-3,44	-0,76	5,12	8,58	-1,91	1,29	2,57	0,17	58,50	13,50	5,00	0,18	1,40	0,00	0,00
38,00	0,82	0,91	15,00	-2,87	-0,99	3,63	11,37	-1,87	1,13	2,53	-0,01	54,90	17,20	5,00	0,20	1,18	0,00	0,00
40,00	0,85	1,47	15,00	-2,67	-0,85	1,50	13,50	-2,30	1,14	2,52	-0,08	59,00	12,90	5,20	0,17	1,22	0,00	0,00
42,00	0,89	2,25	15,90	-2,50	-0,71	2,13	13,77	-1,96	0,81	2,28	-0,02	66,50	12,60	4,50	0,24	1,19	0,00	0,00
44,00	0,86	1,45	18,30	-2,62	-0,73	3,03	15,27	-1,95	0,86	2,27	0,13	52,20	16,10	5,60	0,24	1,15	0,00	0,00
46,00	0,86	2,31	20,50	-2,47	-0,57	1,99	18,51	-2,09	1,12	2,52	0,23				0,21	1,20	0,00	0,00
48,00	0,83	1,20	17,90	-2,54	-0,69	2,57	15,33	-1,96	0,48	2,54	0,24	61,00	14,70	5,70	0,22	1,14	0,00	0,00
50,00	0,83	0,91	17,00	-2,79	-0,81	2,25	14,75	-2,30	1,23	2,39	-0,01	69,40	11,20	4,00	0,18	1,18	0,00	0,00
52,00	0,87	1,72	21,10	-2,45	-0,56	1,69	19,41	-2,14	0,72	2,46	-0,02	62,50	14,40	6,00	0,24	1,29	0,00	0,00
54,00	0,87	1,15	28,90	-2,21	-0,49	1,38	27,52	-2,02	1,07	2,57	0,00				0,18	1,16	0,00	0,00
56,00	0,82	1,79	21,60	-2,24	-0,40	0,34	21,26	-2,18	0,83	2,63	0,18				0,19	1,13	0,00	0,00
58,00	0,86	2,31	19,70	-2,55	-0,59	1,38	18,32	-2,29	1,25	2,44	0,20	55,20	15,00	5,00	0,20	1,26	2,00	0,50
60,00	0,89	1,64	21,30	-2,78	-0,57	3,67	17,63	-2,11	1,19	2,38	0,10				0,17	1,14	0,00	0,00
62,00	0,94	1,60	31,50	-2,16	-0,25	0,48	31,02	-2,10	1,06	2,50	0,04	61,10	17,70	6,80	0,18	1,53	0,00	0,00
64,00	0,95	1,05	23,70	-3,06	-0,68	5,74	17,96	-2,12	1,17	2,39	0,08	53,00	20,40	7,60	0,13	1,27	0,00	0,00
66,00	0,83	2,10	24,50	-2,58	-0,53	1,54	22,96	-2,35	1,02	2,51	0,04	59,00	14,50	5,50	0,16	1,31	0,00	0,00
68,00	1,11	6,08	28,80	-2,71	-0,74	4,50	24,30	-2,10	0,86	2,17	0,02	59,50	24,50	16,50	0,21	1,14	0,00	0,00
70,00	0,87	1,13	16,60	-2,84	-0,88							67,50	11,00	1,70	0,16	1,05	0,00	0,00
72,00	0,86	0,87	17,20	-2,64	-0,68	1,19	16,01	-2,39	1,31			66,30	13,70	4,20	0,17	1,22	0,00	0,00
74,00	0,88	1,14	18,90	-2,61	-0,75	1,99	16,91	-2,21	1,17	2,46	0,00	60,00	13,20	3,00	0,22	1,26	0,00	0,00
76,00	0,84	2,07	18,60	-2,60	-0,68	3,32	15,28	-1,86	1,22	2,38	-0,05				0,21	1,19	0,00	0,00
78,00	0,88	1,42	19,90	-2,56	-0,60							63,00	11,60	3,20	0,19	1,16	0,00	0,00
80,00	0,88	1,42	19,70	-2,52	-0,58	2,98	16,72	-1,90	0,69	2,43	0,05	64,20	12,40	3,70	0,17	1,07	0,00	0,00
82,00	0,87	0,86	20,80	-2,83	-0,62	3,54	17,26	-2,18	0,92	2,51	0,19	62,80	12,40	3,90	0,17	1,18	1,00	0,25
84,00	0,84	1,45	22,40	-2,49	0,10	3,18	19,22	-1,91	1,19			56,50	15,80	4,50	0,19	1,27	1,00	0,24
86,00	0,89	1,12	25,40	-1,88	0,13	-0,63	26,03	-1,98	0,96	2,57	0,10	60,90	13,60	4,00	0,18	1,55	0,00	0,00
88,00	0,87	1,41	24,00	-2,00	-0,25	0,64	23,36	-1,89	1,01	2,25	0,01	56,90	16,00	5,00	0,18	1,29	0,00	0,00
90,00	0,98	2,73	28,20	-2,07	-0,14	-1,75	29,95	-2,30	0,73	2,46	0,00	60,00	18,00	5,00	0,15	1,44	0,00	0,00
92,00	0,87	1,40	18,90	-2,45	-0,63	0,21	18,69	-2,41	0,99	2,06	0,09	62,00	16,80	7,00	0,18	1,15	0,00	0,00
94,00	0,86	1,46	19,50	-2,42	-0,58	1,13	18,37	-2,20	0,70	1,88	-0,13	68,80	11,20	4,00	0,20	1,02	0,00	0,00
96,00	0,86	1,70	19,90	-2,29	-0,56	1,63	18,27	-1,96	0,82	2,36	0,03	58,00	16,00	7,00	0,19	1,06	0,00	0,00
98,00	0,90	1,11	19,70	-2,32	-0,42	1,25	18,45	-2,07	1,00	2,43	0,10				0,24	1,04	0,00	0,00
100,00	0,90	1,11	20,30	-2,45	-0,52					2,46	0,21	65,00	12,00	3,00	0,18	1,06	0,00	0,00
102,00	0,91	1,93	21,30	-2,19	-0,42	0,65	20,65	-2,07	1,00	2,21	-0,02	62,00	13,80	4,20	0,19	1,12	0,00	0,00
104,00	0,92	1,36	22,50	-2,06	-0,49	-0,65	23,15	-2,17	0,96			61,90	15,50	5,70	0,19	1,04	0,00	0,00
106,00	0,90	1,39	21,00	-2,50	-0,15	2,20	18,80	-2,09	0,91	2,52	0,10	70,00	10,60	3,70	0,20	1,03	0,00	0,00
108,00	0,90	2,16	21,20					-1,94	0,75	2,69	0,12	67,70	11,00	4,00	0,19	1,11	0,00	0,00
110,00	0,88	1,14	21,10	-2,15	-0,50	0,74	20,36	-2,01	1,04	2,26	-0,07	65,30	12,90	4,70	0,19	1,05	0,00	0,00
112,00	0,90	1,36	23,20	-2,01	-0,15	-2,58	25,78	-2,41	0,76	2,59	0,28	61,50	11,80	4,00	0,15	1,04	0,00	0,00
114,00	0,89	1,37	22,00	-2,15	-0,39	1,79	20,21	-1,81	1,23	1,94	-0,28	62,00	11,60	3,20	0,17	0,94	0,00	0,00
116,00	0,88	1,39	21,00	-2,21	-0,44	-1,23	22,23	-2,42	0,95	2,69	0,14	58,30	14,80	1,80	0,13	0,96	0,00	0,00
118,00	0,87	1,40	19,50	-2,53	-0,61	1,60	17,90	-2,22	0,91	2,32	0,04	68,00	10,00	1,50	0,17	1,10	0,00	0,00
120,00	0,86	2,55	20,70	-2,11	-0,50	-0,72	21,42	-2,24	0,90	1,85	-0,28	64,80	11,50	3,50	0,13	0,89	0,00	0,00
122,00	0,87	1,68	21,30					-2,13	1,25	2,67	-0,05	67,20	9,80	2,50	0,13	0,86	0,00	0,00
124,00	0,89	1,92	21,20	-2,22	-0,46	0,22	20,98	-2,18	0,96	2,58	0,14	69,40	10,40	4,00	0,10	0,81	0,00	0,00
126,00	0,90	1,94	21,20	-2,30	-0,53	0,06	21,14	-2,29	0,69	2,88	-0,25	61,80	11,50	3,80	0,11	0,80	0,00	0,00
128,00	0,92	1,90	21,70	-2,19	-0,54	3,12	18,58	-1,55	0,93	2,62	-0,03	61,70	13,80	4,30	0,12	0,77	0,00	0,00
130,00	0,94	1,87	22,10	-2,19	-0,48	2,19	19,91	-1,77	0,77	2,58	0,08	60,50	11,20	3,00	0,12	0,79	0,00	0,00
132,00	0,95	1,89	21,30	-2,14	-0,47	2,13	19,17	-1,71	1,07	2,46	0,03	60,40	11,90	4,50	0,04	0,83	0,00	0,00

Appendix 4, Table 1) Sediment core 422, sedimentology, isotope and mineral composition

depth	dry density	>63um	CaCO3	CaCO3 d18 O	CaCO3 d13 C	CaCO3 lith.	CaCO3 marine	G.ruber d18 O	G.ruber d13 C	C.wuell. d18 O	C.wuell. d13 C	grain size in lithic fraction <2 um	>6 um	>20 um	N	C org	pyrite	pyrite
cm	g/ccm	%	%	%oPDB	%oPDB	%	%	%oPDB	%oPDB	%oPDB	%oPDB	%	%	%	%	%	#	#/g
134,00	0,96	2,09	23,30	-2,46	-0,49	2,73	20,57	-1,99	0,65	2,73	0,20	65,60	11,00	1,00	0,12	0,91	0,00	0,00
136,00	0,98	3,30	22,80	-1,95	-0,46	-0,06	22,86	-1,96	0,78	2,70	0,04	65,20	12,00	4,80	0,10	0,78	0,00	0,00
138,00	1,01	2,73	20,60	-3,48	-0,79	8,86	11,74	-1,58	0,91	2,62	0,06				0,10	0,73	0,00	0,00
140,00	0,98	4,09	24,50	-2,41	-0,81	4,42	20,08	-1,62	0,89	2,68	0,00	65,00	13,50	5,00	0,08	0,70	0,00	0,00
142,00	0,99	3,96	23,10	-1,94	-0,47	0,56	22,54	-1,84	1,03	2,90	0,17	68,00	12,50	4,00	0,09	0,70	0,00	0,00
144,00	0,96	3,07	26,90	-1,83	-0,26					2,65	0,08	67,40	13,70	2,60	0,10	1,09	0,00	0,00
146,00	1,02	1,22	28,60	-1,60	0,01	1,06	27,54	-1,43	0,86	1,98	-0,18	60,40	16,70	5,20	0,07	0,97	0,00	0,00
148,00	1,20	8,33	33,40	-2,35	-0,58	9,31	24,09	-0,94	1,03	2,27	0,15	64,00	28,50	16,00	0,06	1,60	3,00	0,75
149,00	1,26	7,69	28,60	-2,92	-1,33					3,37	-0,33	51,50	32,60	15,40	0,07	1,43	0,00	0,00
151,00	1,20	1,88	28,90	-2,87	-1,32	10,92	17,98	-0,97	0,87			48,50	37,50	16,00	0,15	1,70	5,00	1,25
152,00	1,21	3,54	26,10	-2,78	-0,91	10,59	15,51	-0,58	0,75	2,96	-0,42	52,50	29,80	12,50	0,15	1,22	2,00	0,57
154,00	1,17	3,09	29,40	-2,93	-1,28	14,48	14,92	0,05	0,43	3,48	-0,18	47,50	37,50	18,50	0,12	1,88	4,00	0,85
156,00	1,11	1,31	27,40	-3,33	-1,25	15,71	11,69	0,26	0,43	3,88	-0,58	67,50	26,50	9,00	0,14	1,84	7,00	1,46
158,00	1,11	1,87	27,70	-3,09	-1,25	14,33	13,37	0,03	0,79			54,60	30,00	12,50	0,13	1,91	6,00	1,25
160,00	1,14	2,10	27,90	-3,22	-1,29							50,20	31,50	10,50	0,16	1,98	0,00	0,00
162,00	1,16	2,94	26,40	-3,26	-1,42	13,99	12,41	-0,17	0,90			41,00	41,50	21,00	0,11	1,64	0,00	0,00
164,00	1,16	2,52	28,20	-3,14	-1,35	13,85	14,35	-0,38	0,46	3,80	-0,62	49,00	34,50	15,50	0,13	1,72	0,00	0,00
166,00	1,16	1,89	26,30	-3,31	-1,45							52,70	31,30	16,00	0,13	1,35	0,00	0,00
168,00	1,17	2,34	26,20	-3,35	-1,29					4,08	-0,53	36,50	44,50	20,20	0,11	1,44	5,00	1,25
170,00	1,20	2,08	26,30					-0,62	0,79			44,00	41,50	21,00	0,25	1,67	1,00	0,25
172,00	1,16	1,94	26,50	-3,13	-1,32	12,97	13,53	-0,38	0,84			46,30	35,20	17,00	0,13	1,23	2,00	0,50
174,00	1,17	2,71	26,80	-3,74	-1,68					4,14	-0,51	44,70	35,00	13,20	0,13	1,51	2,00	0,49
176,00	1,20	1,67	26,90	-3,65	-1,64	16,62	10,28	0,15	0,60	4,05	-0,54	52,80	29,70	11,00	0,17	1,36	1,00	0,25
178,00	1,14	2,15	26,90	-3,10	-1,40	14,67	12,23	0,38	0,42			51,40	29,70	9,90	0,12	1,91	4,00	0,98
180,00	1,14	1,93	26,50	-3,09	-1,36	14,14	12,36	0,24	0,39	3,85	-0,38	47,00	37,50	18,20	0,17	1,75	0,00	0,00
182,00	1,13	2,80	26,30	-2,99	-1,37	13,39	12,91	0,13	0,80			53,10	31,10	13,90	0,17	1,36	0,00	0,00
184,00	1,15	2,33	26,60	-2,95	-1,25					3,97	-0,76				0,13	1,90	0,00	0,00
186,00	1,17	2,71	25,70	-3,01	-1,36	12,15	13,55	-0,33	0,71	3,92	-0,58	30,00	34,50	16,50	0,13	1,78	5,00	1,22
188,00	1,20	2,30	26,80	-3,03	-1,27	12,59	14,21	-0,40	0,95	3,95	-0,40	53,00	32,20	15,50	0,13	1,84	2,00	0,50
190,00	1,19	2,31	27,20	-3,11	-1,33					3,87	-0,39	53,40	33,00	16,50	0,08	1,15	1,00	0,25
192,00	1,17	2,56	24,30	-3,01	-1,34					3,85	-0,24				0,08	1,20	2,00	0,50
194,00	1,21	2,89	28,20	-3,32	-1,41	15,24	12,96	-0,17	0,85			46,60	39,00	18,50	0,04	1,38	4,00	1,00
196,00	1,20	2,29	27,00	-3,06	-1,36	12,95	14,05	-0,35	0,81						0,04	1,16	4,00	1,00
198,00	1,22	2,45	28,30	-3,09	-1,39					3,81	-0,44	51,60	34,20	15,80	0,06	1,08	9,00	2,25
200,00	1,21	2,21	28,10	-3,63	-1,69					3,86	-0,55	56,70	32,20	16,10	0,10	0,84	1,00	0,24
202,00	1,29	3,02	29,30	-2,95	-1,23							46,00	39,50	19,20	0,07	1,13	1,00	0,24
204,00	1,30	3,26	29,90	-2,90	-1,36					4,00	-0,64	45,00	41,00	18,00	0,05	1,19	0,00	0,00
206,00	1,33	3,11	30,00	-3,03	-1,35					3,86	-0,31	43,50	41,80	21,00	0,04	1,41	0,00	0,00
208,00	1,32	2,65	31,30	-3,02	-1,47					3,78	-0,32	45,50	39,50	20,00	0,09	1,23	0,00	0,00
210,00	1,35	5,18	29,30	-3,03	-1,36	14,03	15,27	-0,30	0,73	3,59	-0,54	45,30	35,30	17,10	0,09	1,29	99,00	25,00
212,00	1,36	2,95	28,70	-3,19	-1,25					3,84	-0,69	43,50	40,50	21,00	0,02	1,26	42,00	10,50
214,00	1,32	2,46	27,90	-3,26	-1,49	15,80	12,10	0,32	0,86	3,93	-0,31	45,00	38,50	19,50	0,09	0,81	28,00	7,00
216,00	1,36	1,80	28,40	-3,09	-1,21					3,74	-0,39				0,03	0,98	7,00	1,71
218,00	1,30	2,11	28,30	-3,43	-1,23										0,03	0,83	20,00	5,00
220,00	1,35	2,23	29,10	-3,35	-1,26					3,90	-0,25	52,80	33,00	14,00	0,08	1,31	29,00	7,25
222,00	1,36	2,39	28,40	-3,22	-1,22					3,77	-0,39				0,02	1,23	45,00	11,25
224,00	1,35	2,78	28,40	-3,14	-1,25	15,17	13,23	0,14	0,29			46,50	37,50	17,50	0,02	0,79	26,00	6,50
226,00	1,36	2,39	28,40	-3,67	-1,22	16,95	11,45	-0,22	0,42	3,50	-0,48	50,50	35,00	16,00	0,03	0,69	63,00	15,75
228,00	1,37	2,00	28,20	-3,65	-1,23					3,04	-0,76	48,00	36,50	17,20	0,05	1,09	41,00	10,25
230,00	1,38	2,30	28,20	-3,27	-1,12					3,92	-0,34				0,15	1,35	85,00	20,73
232,00	1,40	2,67	28,10	-3,07	-1,21					3,18	-0,82	53,80	32,00	14,00	0,08	1,06	82,00	20,50
234,00	1,38	2,17	28,20	-3,07	-1,28					3,85	-0,46	59,50	29,00	13,00	0,06	1,33	71,00	17,75

Appendix 4, Table 1) continued (core 422)

depth cm	G.ruber d18O	CaCO3 %	Li ppm	Sc ppm	Cr ppm	Mn ppm	Co ppm	Ni ppm	Cu ppm	Zn ppm	Ga ppm	Pb ppm	Sr ppm	Y ppm	Zr ppm	Nb ppm	Mo ppm	Cs ppm	Ba ppm	La ppm	Ce ppm	Pr ppm	Nd ppm	Sm ppm	Eu ppm	Gd ppm	Tb ppm	Dy ppm
1,0	-2,0	72,4	10,3	4,4	33,3	349	8,5	32,4	23,4	34,3	3,73	20,7	857	9,7	18,9	3,60	0,44	1,46	271	7,4	11,8	1,70	6,7	1,43	0,34	1,51	0,22	1,44
2,0		72,4	11,0	5,2	34,5	384	10,3	33,8	22,6	33,7	3,76	20,8	912	12,7	26,7	3,70	0,49	1,53	295	7,9	12,1	1,78	7,2	1,47	0,37	1,60	0,26	1,65
3,0		72,4	11,6	13,3	35,9	314	9,5	31,7	23,3	34,6	4,28	21,2	910	12,1	27,0	4,45	1,38	1,56	303	8,3	12,8	1,89	7,4	1,73	0,46	1,68	0,31	1,64
4,0		71,8	11,3	17,0	34,4	282	8,8	33,7	23,1	31,3	4,24	19,9	896	11,7	26,4	4,13	1,27	1,65	278	7,9	12,4	1,84	7,6	1,93	0,49	1,80	0,33	1,63
5,0	-1,5	72,9	11,4	16,3	32,3	218	6,8	33,1	23,7	32,4	4,14	19,2	880	11,4	24,9	4,05	1,21	1,61	271	7,4	12,0	1,69	6,7	1,80	0,39	1,77	0,30	1,64
6,0		72,7	11,6	20,9	33,3	224	7,2	32,9	22,5	31,0	4,28	19,1	872	11,4	24,7	4,04	1,42	1,56	281	7,5	12,0	1,80	6,9	1,64	0,45	1,85	0,32	1,60
7,0		74,4	10,9	3,1	35,6	217	6,7	31,8	24,3	36,3	3,83	20,7	969	12,1	26,9	3,86	0,39	1,53	284	7,6	11,7	1,67	6,8	1,39	0,35	1,52	0,24	1,53
8,0		70,6	12,7	4,0	38,6	267	8,5	35,2	25,4	39,3	4,36	23,4	993	12,0	29,4	4,05	0,35	1,69	277	8,1	12,9	1,81	7,2	1,48	0,37	1,55	0,25	1,51
9,0		69,2	14,1	4,7	40,6	334	9,9	38,8	26,3	43,8	4,84	26,2	1006	12,7	31,8	4,38	0,43	1,91	312	10,4	14,3	1,97	7,8	1,66	0,39	1,68	0,27	1,64
10,0	-1,9	70,8	12,8	4,5	36,0	329	9,3	35,9	24,4	39,6	4,34	23,3	1011	11,8	27,8	3,89	0,31	1,71	249	8,2	13,2	1,88	7,2	1,53	0,35	1,56	0,24	1,48
11,0		70,0	13,2	4,3	37,5	361	10,4	38,9	25,1	41,5	4,55	24,3	988	12,3	32,4	4,48	0,50	1,86	262	9,1	14,6	2,00	7,8	1,64	0,42	1,71	0,29	1,69
12,0		71,3	12,3	3,8	36,8	325	9,5	35,0	25,0	36,8	4,27	22,7	940	12,4	29,6	4,03	0,35	1,72	273	8,4	13,3	1,90	7,5	1,59	0,37	1,55	0,27	1,60
13,0		65,9	15,1	4,9	44,0	341	9,6	41,7	26,5	45,6	5,28	28,8	951	12,8	34,5	4,75	0,34	2,19	256	9,6	16,2	2,19	8,6	1,85	0,42	1,87	0,29	1,76
14,0		53,8	21,3	6,7	59,2	540	15,7	55,4	31,4	55,0	7,45	42,3	965	14,6	46,4	6,66	0,58	3,11	251	12,3	22,4	2,82	10,9	2,27	0,54	2,26	0,35	2,14
15,0		52,0	22,5	7,4	60,1	449	13,2	54,0	30,0	56,9	7,61	44,6	973	15,3	46,0	7,33	0,79	3,32	263	12,9	23,3	2,99	11,6	2,48	0,60	2,42	0,39	2,20
16,0		53,4	22,1	7,3	58,0	335	9,6	51,8	27,3	55,6	7,38	43,0	944	14,3	43,6	6,80	0,58	3,21	271	12,3	22,3	2,86	11,2	2,32	0,55	2,26	0,37	2,08
17,0	-0,3	54,8	20,9	6,9	57,7	312	9,0	48,0	26,9	50,6	7,05	41,6	905	14,1	42,9	6,42	0,48	3,11	269	11,8	21,3	2,72	10,5	2,13	0,53	2,08	0,35	1,96
18,0		55,7	20,7	6,7	56,3	317	9,8	50,1	24,2	49,8	6,84	40,6	901	14,3	41,2	6,28	0,46	3,00	282	11,8	21,0	2,71	10,5	2,20	0,54	2,13	0,34	1,94
19,0		53,4	21,5	6,5	58,1	298	9,3	48,9	25,5	49,4	7,15	42,7	874	14,3	42,5	6,42	0,43	3,21	284	12,0	21,5	2,77	10,7	2,20	0,49	2,22	0,35	2,00
20,0	-0,5	54,4	23,5	8,0	57,9	232	8,6	49,0	26,6	50,8	6,79	41,9	789	14,7	43,2	6,48	0,47	3,14	301	12,3	21,9	2,78	10,9	2,34	0,52	2,22	0,37	2,05
21,0		54,1	22,3	8,2	53,3	274	8,6	42,9	21,3	48,4	6,97	40,3	830	14,0	39,3	6,03	0,53	2,92	298	11,4	20,4	2,65	10,5	2,26	0,53	2,13	0,35	1,98

Appendix 5, Table 1) Sediment core 36KL, chemical concentration values in the bulk fraktion (% or ppm), concentration values expressed on a carbonate free basis (% or ppm, cfb)

depth cm	Ho ppm	Er ppm	Tm ppm	Yb ppm	Lu ppm	Hf ppm	Ta ppm	Tl ppm	Pb ppm	Bi ppm	Th ppm	U ppm	Li ppm cofb	Sc ppm cofb	Cr ppm cofb	Mn ppm cofb	Co ppm cofb	Ni ppm cofb	Cu ppm cofb	Zn ppm cofb	Ga ppm cofb	Rb ppm cofb	Sr/Ca	Y ppm cofb	Zr ppm cofb	Nb ppm cofb	Mo ppm cofb	Cs ppm cofb
1,0	0,31	0,88	0,13	0,84	0,14	0,54	0,35	0,14	5,76	0,14	1,36	0,60	37,3	15,8	121	1264	30,6	117	84,8	124	13,5	75,0	29,6	35,1	68,5	13,0	1,61	5,29
2,0	0,35	1,02	0,15	1,04	0,16	0,96	0,37	0,12	5,42	0,14	1,97	0,65	39,9	19,0	125	1391	37,3	122	81,9	122	13,6	75,4	31,5	46,0	96,7	13,4	1,76	5,54
3,0	0,42	1,07	0,22	1,05	0,21	0,89	0,58	0,25	5,58	0,55	1,93	0,68	42,0	48,2	130	1138	34,2	115	84,4	125	15,5	76,8	31,4	43,8	97,8	16,1	5,00	5,65
4,0	0,42	1,11	0,21	1,25	0,22	1,02	0,50	0,25	5,36	0,54	1,92	0,66	40,1	60,3	122	1000	31,1	120	81,9	111	15,0	70,6	31,2	41,5	93,6	14,6	4,50	5,85
5,0	0,37	1,03	0,17	1,08	0,20	0,73	0,43	0,27	5,02	0,47	1,81	0,61	42,1	60,1	119	804	25,0	122	87,5	120	15,3	70,8	30,1	42,1	91,9	14,9	4,46	5,94
6,0	0,37	1,10	0,22	1,14	0,26	1,06	0,48	0,24	5,39	0,51	1,85	0,67	42,5	76,6	122	821	26,3	121	82,4	114	15,7	70,0	30,0	41,8	90,5	14,8	5,20	5,71
7,0	0,33	0,97	0,14	0,94	0,14	0,62	0,49	0,12	5,14	0,19	1,76	0,57	42,6	12,2	139	848	26,3	124	94,9	142	15,0	80,9	32,5	47,3	105,1	15,1	1,52	5,98
8,0	0,33	0,98	0,14	0,95	0,14	0,75	0,50	0,12	5,69	0,17	1,90	0,64	43,2	13,7	131	908	28,9	120	86,4	134	14,8	79,6	35,1	40,8	100,0	13,8	1,18	5,75
9,0	0,35	1,00	0,15	0,96	0,15	0,81	0,52	0,14	6,24	0,15	2,06	0,73	45,8	15,4	132	1084	32,2	126	85,4	142	15,7	85,1	36,3	41,2	103,2	14,2	1,39	6,20
10,0	0,32	0,95	0,14	0,89	0,14	0,73	0,45	0,13	5,80	0,11	1,94	0,68	43,8	15,3	123	1127	31,8	123	83,6	136	14,9	79,8	35,7	40,4	95,2	13,3	1,05	5,86
11,0	0,37	1,03	0,17	1,01	0,17	0,79	0,51	0,15	6,20	0,21	2,11	0,72	44,0	14,5	125	1203	34,7	130	83,7	138	15,2	81,0	35,3	41,0	108,0	14,9	1,67	6,20
12,0	0,36	1,05	0,15	1,00	0,16	0,74	0,46	0,13	5,73	0,19	2,00	0,67	42,9	13,1	128	1132	33,1	122	87,1	128	14,9	79,1	32,9	43,2	103,1	14,0	1,22	5,99
13,0	0,37	1,10	0,16	1,04	0,16	0,94	0,52	0,17	6,54	0,17	2,45	0,83	44,3	14,4	129	1000	28,1	122	77,7	134	15,5	84,5	36,0	37,5	101,2	13,9	1,01	6,42
14,0	0,46	1,25	0,18	1,20	0,19	1,25	0,70	0,22	8,97	0,17	2,95	1,19	46,1	14,6	128	1169	34,0	120	68,0	119	16,1	91,6	44,8	31,6	100,4	14,4	1,25	6,73
15,0	0,47	1,27	0,21	1,25	0,21	1,30	0,76	0,30	9,05	0,40	3,57	1,28	46,9	15,4	125	935	27,5	113	62,5	119	15,9	92,9	46,7	31,9	95,8	15,3	1,64	6,92
16,0	0,44	1,24	0,20	1,17	0,19	1,03	0,72	0,25	8,45	0,28	2,59	1,18	47,4	15,7	124	719	20,6	111	58,6	119	15,8	92,3	44,2	30,7	93,6	14,6	1,25	6,89
17,0	0,43	1,20	0,18	1,11	0,18	1,16	0,68	0,25	8,46	0,22	2,67	1,14	46,2	15,3	128	690	20,0	106	59,5	112	15,6	92,0	41,2	31,2	94,9	14,2	1,06	6,88
18,0	0,43	1,20	0,18	1,12	0,18	1,16	0,66	0,21	8,42	0,17	2,64	1,08	46,7	15,2	127	716	22,0	113	54,6	112	15,4	91,6	40,4	32,3	93,0	14,2	1,04	6,77
19,0	0,42	1,21	0,18	1,13	0,18	1,19	0,68	0,21	8,68	0,16	2,58	1,11	46,1	14,0	125	639	20,0	105	54,7	106	15,3	91,6	40,9	30,7	91,2	13,8	0,91	6,89
20,0	0,43	1,25	0,19	1,14	0,19	1,03	0,70	0,24	8,20	0,25	3,48	2,71	51,5	17,6	127	509	18,9	107	58,3	111	14,9	91,9	36,2	32,2	94,7	14,2	1,03	6,89
21,0	0,42	1,19	0,18	1,14	0,18	1,22	0,67	0,22	8,43	0,21	2,28	1,05	48,6	17,8	116	597	18,6	93	46,4	105	15,2	87,8	38,3	30,5	85,6	13,1	1,15	6,36

Appendix 5, Table 1) continued (geochemistry of core 36KL)

depth	Ba	La	Ce	Pr	Nd	Sm	Eu	Gd	Tb	Dy	Ho	Er	Tm	Yb	Lu	Hf	Ta	Tl	Pb	U
cm	ppm cofb	ppm cofb	ppm cofb	ppm cofb	ppm cofb	ppm cofb	ppm cofb	ppm cofb	ppm cofb	ppm cofb	ppm cofb	ppm cofb	ppm cofb	ppm cofb	ppm cofb	ppm cofb	ppm cofb	ppm cofb	ppm cofb	ppm cofb
1,0	982	26,7	42,8	6,16	24,2	5,18	1,24	5,47	0,81	5,22	1,11	3,17	0,46	3,04	0,51	1,95	1,27	0,50	20,9	2,19
2,0	1069	28,6	43,8	6,45	26,1	5,33	1,36	5,80	0,94	5,98	1,25	3,70	0,54	3,77	0,57	3,49	1,35	0,43	19,6	2,36
3,0	1098	30,0	46,4	6,85	26,9	6,27	1,66	6,09	1,12	5,94	1,54	3,88	0,81	3,80	0,77	3,21	2,11	0,91	20,2	2,46
4,0	986	28,0	44,0	6,52	27,0	6,84	1,75	6,38	1,17	5,78	1,49	3,94	0,73	4,43	0,77	3,62	1,78	0,90	19,0	2,35
5,0	1000	27,5	44,3	6,24	24,8	6,64	1,43	6,53	1,10	6,05	1,38	3,80	0,64	3,99	0,74	2,68	1,60	0,99	18,5	2,26
6,0	1029	27,6	44,0	6,59	25,4	6,01	1,64	6,78	1,16	5,86	1,36	4,03	0,79	4,18	0,95	3,88	1,77	0,89	19,7	2,46
7,0	1109	29,6	45,7	6,52	26,5	5,43	1,37	5,94	0,92	5,98	1,27	3,79	0,55	3,68	0,55	2,42	1,91	0,48	20,1	2,21
8,0	942	27,4	43,9	6,16	24,4	5,03	1,24	5,27	0,84	5,14	1,12	3,33	0,49	3,24	0,46	2,55	1,71	0,41	19,4	2,17
9,0	1013	33,8	46,4	6,40	25,4	5,39	1,27	5,45	0,86	5,32	1,14	3,25	0,49	3,11	0,47	2,64	1,68	0,45	20,3	2,38
10,0	853	28,0	45,2	6,44	24,7	5,24	1,19	5,34	0,82	5,07	1,08	3,25	0,48	3,06	0,49	2,50	1,52	0,43	19,9	2,31
11,0	873	30,3	48,7	6,67	25,9	5,47	1,41	5,70	0,98	5,63	1,24	3,43	0,55	3,37	0,56	2,62	1,69	0,51	20,7	2,40
12,0	951	29,3	46,3	6,62	26,0	5,54	1,27	5,40	0,94	5,57	1,25	3,66	0,53	3,48	0,57	2,57	1,61	0,45	20,0	2,32
13,0	751	28,2	47,5	6,42	25,3	5,43	1,24	5,48	0,84	5,16	1,07	3,23	0,48	3,05	0,47	2,76	1,51	0,49	19,2	2,44
14,0	543	26,6	48,5	6,10	23,6	4,91	1,16	4,89	0,75	4,63	0,99	2,71	0,40	2,60	0,40	2,71	1,50	0,47	19,4	2,58
15,0	548	26,9	48,5	6,23	24,2	5,17	1,25	5,04	0,82	4,58	0,98	2,65	0,44	2,60	0,44	2,71	1,59	0,61	18,9	2,67
16,0	582	26,4	47,9	6,14	24,0	4,98	1,17	4,85	0,79	4,46	0,94	2,66	0,43	2,51	0,40	2,21	1,54	0,53	18,1	2,53
17,0	595	26,1	47,1	6,02	23,2	4,71	1,16	4,60	0,78	4,34	0,96	2,65	0,40	2,46	0,39	2,57	1,51	0,56	18,7	2,52
18,0	637	26,6	47,4	6,12	23,7	4,97	1,22	4,81	0,77	4,38	0,96	2,71	0,40	2,53	0,40	2,62	1,49	0,47	19,0	2,44
19,0	609	25,8	46,1	5,94	23,0	4,72	1,06	4,76	0,74	4,29	0,91	2,60	0,38	2,42	0,38	2,55	1,46	0,46	18,6	2,38
20,0	660	27,0	48,0	6,10	23,9	5,13	1,14	4,87	0,82	4,50	0,94	2,74	0,41	2,50	0,42	2,26	1,54	0,52	18,0	5,94
21,0	649	24,8	44,4	5,77	22,9	4,92	1,16	4,64	0,77	4,31	0,92	2,59	0,40	2,48	0,39	2,66	1,46	0,47	18,4	2,29

Appendix 5, Table 1) continued (geochemistry of core 36KL)